

# ***The status of graphite development for gas cooled reactors***

*Proceedings of a Specialists Meeting  
held in Tokai-mura, Japan, 9–12 September 1991*



INTERNATIONAL ATOMIC ENERGY AGENCY

IAEA

**THE STATUS OF GRAPHITE DEVELOPMENT FOR GAS COOLED REACTORS**  
**IAEA, VIENNA, 1993**  
**IAEA-TECDOC-690**  
**ISSN 1011-4289**

Printed by the IAEA in Austria  
February 1993

## FOREWORD

The Specialists Meeting on the Status of Graphite Development for Gas Cooled Reactors was held at the Japan Atomic Energy Research Institute (JAERI), Tokai-mura, Japan, from 9 to 12 September 1991. The meeting was convened by the International Atomic Energy Agency on the recommendation of the International Working Group on Gas Cooled Reactors. It was attended by 61 participants from France, Germany, Japan, the United Kingdom, the United States of America and the former Union of Soviet Socialist Republics. The meeting was chaired by Dr. S. Saito of JAERI, and covered the following:

- Overview of National Programmes
- Design Criteria, Fracture Mechanisms and Component Tests
- Materials Development and Properties
- Non-destructive Examinations, Inspections and Surveillance.

The participants presented 33 papers on behalf of their countries. Each presentation was followed by an open discussion in the general area covered by the paper.

During the meeting, JAERI provided tours of the Helium Engineering Demonstration Loop (HENDEL) and the Naka Fusion Research Establishment, and a visit was made to the HTTR construction site at the Oarai Research Establishment to view the progress of construction.

At the end of the meeting an open discussion was held regarding the direction for future international collaboration.

## *EDITORIAL NOTE*

*In preparing this material for the press, staff of the International Atomic Energy Agency have mounted and paginated the original manuscripts as submitted by the authors and given some attention to the presentation.*

*The views expressed in the papers, the statements made and the general style adopted are the responsibility of the named authors. The views do not necessarily reflect those of the governments of the Member States or organizations under whose auspices the manuscripts were produced.*

*The use in this book of particular designations of countries or territories does not imply any judgement by the publisher, the IAEA, as to the legal status of such countries or territories, of their authorities and institutions or of the delimitation of their boundaries.*

*The mention of specific companies or of their products or brand names does not imply any endorsement or recommendation on the part of the IAEA.*

*Authors are themselves responsible for obtaining the necessary permission to reproduce copyright material from other sources.*

*This text was compiled before the recent changes in the former Union of Soviet Socialist Republics.*



## CONTENTS

SUMMARY OF THE SPECIALISTS MEETING .....	7
SUMMARY OF NATIONAL PROGRAMMES (Session I) .....	29
<b>DESIGN CRITERIA, FRACTURE MECHANISMS AND COMPONENT TESTS — Part A</b> (Session II)	
A microstructurally based fracture model for nuclear graphite .....	49
<i>T.D. Burchell</i>	
Burst tests to measure the tangential strength of CFC tubes .....	59
<i>M. Roedig, W. Baur, B. Woschek</i>	
Spatial variability in the tensile strength of an extruded nuclear-grade graphite .....	64
<i>J.P. Strizak</i>	
Evaluations of the fracture mechanical properties of fuel compacts for the HTTR, with emphasis on thermal shock resistances and neutron irradiation effects .....	70
<i>S. Sato, A. Kurumada, K. Kawamata, N. Suzuki, M. Kaneko, K. Fukuda</i>	
A method for assessing the effects of graphite property variability on core structural integrity criteria .....	78
<i>R.C.B. Judge</i>	
<b>DESIGN CRITERIA, FRACTURE MECHANISMS AND COMPONENT TESTS —</b> <b>Part B (Session II)</b>	
Bending fatigue behavior of nuclear-grade graphite under impact loading .....	87
<i>M. Futakawa, K. Kikuchi, Y. Muto, H. Shibata</i>	
Component test of the core support post of the HTTR .....	95
<i>M. Ishihara, T. Iyoku, N. Takikawa, S. Shiozawa, K. Jinza, N. Tsuji, T. Miki</i>	
Assessment of the load capacity of the dowel and socket system in the HTTR hexagonal block .....	105
<i>N. Takikawa, M. Ishihara, T. Iyoku, S. Shiozawa, M. Tokumitsu, S. Koe, M. Uno</i>	
The vibrational characteristics of the keyed graphite components in the HTTR .....	113
<i>M. Futakawa, H. Shirai, T. Iyoku, S. Shiozawa, S. Takada</i>	
<b>MATERIALS DEVELOPMENT AND PROPERTIES — Part A (Session III)</b>	
Fabrication of HTGR core components by the method of volume gas-phase impregnation of porous media with pyrocarbon — Main characteristics of the materials and products .....	123
<i>V.F. Zelenskij, V.A. Gurin, Yu.F. Konotop, Yu.A. Deryuga, V.V. Kolosenko</i>	
Development of graphite for fuel element sleeves in advanced gas cooled reactors .....	134
<i>D.P. Burridge, J.E. Naylor</i>	
Mechanical properties and thermal shock resistances of recently developed high performance graphites .....	140
<i>S. Sato, K. Kawamata, A. Kurumada, A. Chiba</i>	
<b>MATERIALS DEVELOPMENT AND PROPERTIES — Part B (Session III)</b>	
Behavior of gas desorption and gas permeability of carbon materials .....	149
<i>M. Okada, T. Sogabe</i>	
Relation between gasification rates and gas desorption behavior with metallic impurities of carbon and graphite materials for the HTTR .....	159
<i>S. Nomura, H. Imai, K. Fujii, M. Shindo</i>	
Corrosion behavior of sintered pellet of graphite and boron carbide in helium containing water vapor .....	169
<i>K. Fujii, S. Nomura, H. Imai, M. Shindo</i>	

Effect of atmosphere on the bend strength of nuclear graphite .....	177
<i>T. Maruyama</i>	
Corrosion tests of matrix graphites .....	183
<i>A.I. Vavilin, E.T. Kulikov, S.I. Mozzherin, A.S. Chernikov</i>	

### **MATERIALS DEVELOPMENT AND PROPERTIES — Part C (Session III)**

Engineering thermomechanics of nuclear graphites under neutron irradiation, oxidation and transient heatup: A review .....	195
<i>T. Arai</i>	
A review of irradiation creep in reactor graphite .....	200
<i>B.T. Kelly</i>	
Specific behavior of reflector and matrix graphite under high temperature irradiation .....	205
<i>P.A. Platonov, V.I. Karpukhin, Ya.I. Shtrombakh, V.M. Alekseev, O.K. Chugunov, B.A. Gurovich, E.I. Trofimchuk</i>	
Irradiation behavior of boronated graphite for the HTTR .....	210
<i>H. Matsuo, F. Kobayashi, K. Sawa</i>	
Capsule design, fabrication and irradiation for tensile creep test on HTGR graphites at 1200°C in the JMTR .....	219
<i>T. Saito, T. Kikuchi, T. Arai, H. Ugachi</i>	
Strength analysis code for graphite structural components in uranium-graphite nuclear reactors .....	225
<i>B.S. Rodchenkov, P.A. Platonov, V.N. Manevskij, B.A. Kashirin, O.K. Chugunov</i>	

### **MATERIALS DEVELOPMENT AND PROPERTIES — Part D (Session III)**

The effect of volume on the tensile strength of several nuclear-grade graphites .....	233
<i>J.P. Strizak</i>	
The effects of specimen geometry and size on the fracture toughness of nuclear graphites .....	241
<i>G.R. Romanoski, T.D. Burchell</i>	
Cumulative fatigue damage on HTGR graphite .....	248
<i>S. Ishiyama, M. Eto</i>	
Fracture behavior of nuclear graphites under compressive impact loading .....	256
<i>H. Ugachi, M. Ishihara, S. Ishiyama, M. Eto</i>	

### **NON-DESTRUCTIVE EXAMINATIONS, INSPECTIONS AND SURVEILLANCE — Part A (Session IV)**

Radiolytic corrosion of graphite surveillance and lessons drawn from the operation of the Bugey-1 reactor .....	265
<i>A. Petit, C. Phalippou, M. Brié</i>	
Graphite surveillance in N reactor .....	273
<i>E.M. Woodruff</i>	
Non-destructive testing and acceptance test for HTTR graphite components .....	281
<i>N. Takikawa, T. Iyoku, S. Shiozawa, N. Ooka, M. Kambe, A. Ide</i>	

### **NON-DESTRUCTIVE EXAMINATIONS, INSPECTIONS AND SURVEILLANCE — Part B (Session IV)**

Non-destructive test of HTGR graphite components .....	291
<i>M. Ishihara, T. Ishii, S. Ishiyama, M. Eto</i>	
The correlation of hardness with Young's modulus and strengths of nuclear carbon materials .....	299
<i>T. Oku, S. Ohta, M. Eto</i>	
Quantitative analysis of trace amounts of impurities contaminating pure graphite with ICP-MS and metal atomizer FLAAS .....	304
<i>T. Miyatani, H. Suzuki, O. Yoshimoto</i>	
List of Participants .....	309

## SUMMARY OF THE SPECIALISTS MEETING

At the invitation of the Government of Japan, the International Atomic Energy Agency convened a Specialists Meeting on the Status of Graphite Development for Gas Cooled Reactors in Tokai-mura, Japan, from 9 to 12 September 1991. The meeting was hosted by the Japan Atomic Energy Research Institute (JAERI) at the Tokai Research Establishment. The meeting was held within the framework of the International Working Group on Gas Cooled Reactors (IWGGCR) which had recommended at its last meeting that the IAEA convene this Graphite Specialists Meeting.

Dr. S. Saito, Deputy Director, Department of HTTR Project of JAERI, was chairman of the meeting.

Opening remarks were provided by Dr. N. Shikazono, Deputy Director General, Tokai Research Establishment, JAERI. Dr. Shikazono welcomed the many distinguished experts gathering for the meeting. He noted that the last Graphite Meeting held five years ago had also been hosted by JAERI at Tokai. Since then there has been continuous progress in many aspects of HTGR technologies, but there has been also a worldwide change of social attitude toward nuclear energy. Fortunately, JAERI was able to obtain the approval and the budget for the HTTR programme from the Japanese Government in 1990. JAERI started the construction of the reactor in March 1991. Dr. Shikazono expressed sincere appreciation for the strong support of the international HTGR community for the HTTR programme.

The purpose of the meeting was to provide an international forum for a comprehensive review and discussion of the status of graphite development for gas cooled reactors. The meeting was divided into the following sessions:

- Session I: The status and future plans for the graphite development for gas cooled reactors - Overview.
- Session II: Design criteria, fracture mechanisms and components tests.
- Session III: Materials development and properties.
- Session IV: Non-destructive examinations, inspections and surveillance.
- Session V: Summarizing discussion.

Tours of the Helium Engineering Demonstration Loop (HENDEL), and the Naka Fusion Research Establishment were conducted and a visit was made to the HTTR construction site at the Oarai Research Establishment to view the progress of construction.

The meeting was attended by 17 foreign participants representing France (2), Germany (1), the USSR (6), the UK (4), USA (3) and the IAEA (1).

These proceedings contain all 33 papers which were presented at the meeting as well as summaries of the sessions (Sessions II-IV are presented in this Summary, while Session I is summarized separately).

The status of the HTGR programme in Japan was presented. Efforts are now focused on construction of the HTTR which is scheduled for start-up in 1996. Various R&D activities have been conducted to support its licensing. Regarding graphite, the isotropic fine-grained graphite IG-110 has been developed and characterized for the HTTR core and core support structures. JAERI has completed testing of these structures to demonstrate their structural integrity. This includes full scale testing of the fracture strength of core support posts, the dowel and socket system of the core graphite blocks, and the keyed graphite components of the core bottom

structure under seismic event conditions. The effects of oxidation on the fracture strength was included in these tests. Also, evaluations of fracture mechanical properties of graphites for HTTR fuel compacts have been determined. Acceptance tests for the HTTR graphite components were described.

Methods to determine the extremely low impurity level of nuclear graphite have been developed by JAERI in collaboration with a manufacturer and were reported.

For the HTTR, boronated graphite is a candidate material for control rods, burnable poison, reserve shutdown material and neutron shielding. Boronated graphite has been irradiated up to a fast neutron fluence of  $2 \times 10^{21}$  neutrons/cm<sup>2</sup> at HTTR operating temperatures in the JMTR and results of the irradiation behaviour were presented.

Finally, development of high performance graphites was described. Some of these graphites are in use as rocket nozzles and as armor tiles of the first wall of fusion machines, and may have possible future application in HTGR core components.

In the USSR, HTGR activities have focused on design and development of the 200 MW(th) modular type VGM reactor and on the 1060 MW(th) integrated design, the VG-400 system. The very high strength GR-1 graphite has been developed especially for HTGRs. Design activities for the graphite reflector of the VGM reactor to achieve acceptable thermal stresses were described. The behaviour of reflector graphite and fuel element matrix graphite properties for neutron fluences up to  $2.5 \times 10^{22}$  neutrons/cm<sup>2</sup> were presented. Also, results of investigation of matrix graphite corrosion in helium containing water vapour were reported.

In the USA, the programme to characterize graphite properties and graphite behaviour under reactor conditions was outlined. Areas of continuing concern include irradiation creep, the effect of oxidation on graphite properties and development of fracture criteria. Results of a joint ORNL/JAERI effort to determine the fracture toughness of various nuclear graphites were reported and included investigation of the effect of the test specimen geometry and size on fracture toughness. Development of a model for predicting the fracture probability as a function of stress based on inputs related to the graphite microstructure and specimen size was described and compared with experimental data.

In the UK, about 15% of the total electricity is generated by graphite moderated, carbon dioxide cooled reactors of the Magnox and AGR type. No new gas cooled reactors are foreseen in the UK for the foreseeable future. Graphite research has been greatly decreased as a result of recent changes in the structure and of the electricity supply industry and in the UK's nuclear power research establishment. As a result, the only new data will come from operating reactors, and the emphasis is on maximizing the life of the reactors' graphite moderator.

Related to assuring long lifetime of the AGRs, a programme has been under way for several years to develop improved graphite for the fuel element sleeve which is the prime structural member of the AGR fuel element. This programme has progressed to the current stage in which pilot loadings of the new graphite sleeves are currently under irradiation in AGR reactors, and the programme was reported in detail.

Also, in regard to determination of core lifetime, development of a probabilistic method for assessing the effects of graphite property variability on core structural integrity was reported. The aim is to account for inherent redundancies in the core structure that would allow a small number of cracked graphite bricks to exist without compromising safety, and thereby ultimately modify the current policy that none of the bricks should fail. Work is currently under way, applying the proposed methodology to an AGR core.

In Germany, while the industry has greatly reduced their efforts to commercialize the HTR, the KFA Forschungszentrum Juelich is proceeding with HTR research on a lower level in connection with some industry development work geared towards a modular HTR of Siemens design. International co-operative efforts in graphite development are being continued. In particular, the US/FRG co-operation under the umbrella agreement and the KFA/JAERI agreement may be mentioned. Irradiation creep, high fast neutron fluence impact on graphitic material and its behaviour at accident conditions (air/water ingress) are the main topics.

In France, of the original eight Magnox type gas cooled reactors only the St. Laurent A2 and the Bugey-1 reactors are still in operation, and they are scheduled for shutdown in 1992 and 1994 respectively. There is a major graphite oxidation problem in the Bugey reactor which results from radiolytic activation of the carbon dioxide coolant causing oxidation of the graphite, a phenomena termed radiolytic oxidation. Continued operation of this reactor depends on results of careful monitoring of the variation in physical properties of the core graphite. Currently the mean weight loss of the most corroded area of the core is around 30%. Careful analysis has shown that no severe degradation of the mechanical properties of the graphite occurs at these oxidation levels. The experience gained from operation of this reactor was presented in detail.

In summary, graphite technology has progressed by means of long term development programmes financed by individual countries for their particular use, and each country's graphite behaves differently and depends on the source of the coke the manufacturing process. However, there are some clear trends common to most GCR graphites on the basis of which design criteria, component integrities, in-service inspection, etc. can be discussed internationally.

In comparison with the previous Specialists Meeting on Graphite also held at Tokai-mura, Japan, in 1986 the present meeting dealt more with the advanced materials, the experience of reactor operation including surveillance and advanced design concepts. Also, considerable graphite development activities which were conducted to prepare for licensing and construction of the HTTR were reported.

During the summarizing discussion the specialists recommended graphite technology development activities which they felt would be especially fruitful areas for future international co-operation. The delegation from the Soviet Union suggested that a programme be stated to establish international structural design criteria specifying limiting stresses for graphite components for nuclear reactors and suggested that this might begin with a round-robin strength calculation for a selected component, and comparison of failure criteria. Review and comparison of fracture criteria and design criteria for core life (design allowable stress levels) and methods of selecting allowable stress levels used in different countries was also recommended by other participants. Such activities could be carried out through a series of workshops.

TABLE I. AREAS OF INTEREST FOR FUTURE INTERNATIONAL COLLABORATION

	Japan	USA	UK	Germany	France	USSR
Material properties /irradiation	X	X	X	X		X
Radiolytic oxidation			X		X	
Irradiation creep	X	X	X	X		X
Structural criteria	X	X	X		X	X
In-reactor NDE and ISI	X		X			
Corrosion due to air and water ingress	X	X	X	X		X

Other areas in which several participants expressed interest regarding international collaboration were:

- a review of irradiation creep data and establishment of a suitable model for predicting creep,
- effects of oxidation on physical properties.

Table I lists those topics which were suggested for future international collaboration and notes those countries which expressed an interest in collaboration on these topics.

It was noted that only a few results of the effects on graphite due to air or water ingress were presented, but that this is of considerable international interest from the safety viewpoint.

The participants were generally of the opinion that Graphite Specialists Meetings should be held at least every five years, and preferably every three to four years. Finally, it was the consensus that future meetings should focus on more specialized topics within the field of graphite development for GCRs.

## Session II (Part A)

### DESIGN CRITERIA, FRACTURE MECHANISMS AND COMPONENT TESTS

Chairmen: M. Brié, S. Sato

Dr. T.D. Burchell of ORNL (USA) presented a paper entitled "A microstructurally based fracture model for nuclear graphite". He reports the physical basis of, and assumptions behind, a fracture model for nuclear graphites. Microstructurally related inputs, such as filler particle size, filler particle fracture toughness ( $K_{IC}$ ), density, pore size distribution, number of pores and specimen geometry (size and volume) were utilized in the model. The model was applied to two graphites, Great Lakes Carbon Corporation grade H-451 and Toyo Tanso grade IG-110. For each graphite, the predicted tensile failure probabilities were compared with experimental data generated using ASTM standard C-749 tensile test specimens. The predicted failure probabilities were in close agreement with the experimental data, particularly in the case of the H-451. The model was also shown to qualitatively predict the influence on the failure probabilities of changes in filler particle size, density, pore size, pore size distribution, number of pores and specimen geometry (stressed volume). The good performance was attributed to the sound physical basis of the model, which recognizes the dominant role of porosity in controlling crack initiation and propagation during graphite fracture.

Dr. M. Roedig, Research Center Juelich (Germany), presented a paper entitled "Burst tests to measure the tangential strength of CFC tubes". The aim of this paper was to measure the tangential strength in burst test of carbon fiber reinforced composites and to compare the results with those of less sophisticated experiments, such as split-disk-test (ASTM standard D2290.69). For different reasons such as mountability, edge effects which influence the stress distribution, no pure tensile stresses can be assumed in the split disk test. The internal pressure tests were performed with tube segments made of CFC (carbon fiber reinforced composites). A finite element study was performed in order to estimate the influence of the reinforcements. For a given geometry, the split disk test underestimated the tangential strength at least by a factor of two.

Mr. J.P. Strizak of ORNL (USA) presented a paper entitled "Spatial variability in the tensile strength of an extruded nuclear-grade graphite". He presented the results of a study on spatial variations in the strength of nuclear-grade H-451 graphite. The tensile properties of H-451 were examined extensively in the past in order to characterize the variability of strength within billets, between billets, and between lots. However, the variability within a billet was, for the most part, studied only casually. The problem appeared to be the strong influence of a limited sampling plan in describing the mean strength and the variability. Therefore, an extensive, statistically sound sampling plan was devised to fully characterize the spatial variability within a single billet. Test specimens were machined to conform to ASTM C749-87, "Standard Test Method for Tensile Stress-Strain of Carbon and Graphite". Test results were obtained for four specimen sizes having gage diameters of 6.35, 9.53, 15.88, and 25.40 mm with respective gage-section volumes of 1407, 3163, 12,577, and 51,483 mm<sup>3</sup>. A new fracture model developed by Dr. Burchell was applied to the data with encouraging results. This probabilistic failure criteria combine a microstructural basis with a fracture-mechanics approach to failure.

Prof. S. Sato of Ibaraki University (Japan) presented a paper entitled "Evaluations of the fracture mechanical properties of fuel compacts for

HTTR, with emphasis on thermal shock resistances and neutron irradiation effects". He reported on the fuel compact models using SiC kernel coated particles instead of UO<sub>2</sub>-kernel coated particles as the nuclear fuel for High Temperature Engineering Test Reactor (HTTR). The specimen preparations were made under the same conditions as the real fuel compact. The mechanical and fracture mechanics properties were studied at room temperature. The thermal shock resistance and fracture toughness for thermal stresses in the fuel compact were emphasizingly determined by means of Joule heating at a central area of the disk specimens. Then these model specimens were neutron irradiated in the Japan Material Testing Reactor (JMTR) up to  $1.7 \times 10^{21}$  n/cm<sup>2</sup> (E>29fJ) at 900°C ± 50°C and the effects on a series of fracture mechanical properties were also evaluated in comparison with the cases of graphite IG-110 as the core materials in the HTTR.

Dr. R.C.B. Judge of AEA Reactor Services (UK) presented a paper entitled "A method for assessing the effects of graphite property variability on core structural integrity criteria". He reported on the Reserve Strength Factor (RSF) as the factor of safety used in assessments of advanced gas cooled reactor core integrity. Values of RSF currently used are based on engineering judgement. These values were related to variability due to inhomogeneity of graphite, systematic error in the calculation route and uncertainties in property measurement. A probabilistic approach, bringing the safety assessment of the graphite core into line with other reactor components, was described in this paper. A probability distribution for the RSF may be obtained by repeatedly following the full calculation route. In each iteration, appropriate values for the key parameters were obtained using the Latin Hypercube sampling technique. The number of key parameters were kept to a minimum by first using sensitivity calculations to eliminate the less important ones.

Material properties were reported from tests on small specimens. The variability in these properties is, intuitively, expected to be greater than that found in the brick (on which the RSF calculations are based). In the case of the non-destructive properties these size effects were treated by applying the central limit theorem. Core brick strength was obtained from a series of on-going experiments. The statistical distribution of brick strength was assumed to follow a Weibull function fitted to small specimen data.

This proposed methodology is currently being applied to an advanced gas cooled reactor core.



## Session II (Part B)

### DESIGN CRITERIA, FRACTURE MECHANISMS AND COMPONENT TESTS

Chairmen: T.D. Burchell, S. Shiozawa

In session II-B, a total of 4 papers were presented concerning the structural integrity of graphite core and core support components during seismic events. These activities were performed in support of the JAERI High Temperature Engineering Test Reactor (HTTR) which is currently under construction in Japan.

The first paper, presented by Dr. M. Futakawa, was entitled "Bending fatigue behavior of HTGR graphite under impact loading". Impact strength and impact fatigue behaviour of graphite material were examined using a pendulum-type impact bending machine. The observed impact behaviour was explained by a beam model taking into account the contact behaviour described by the Hertzian theory. The impact strength of graphite was lower in comparison with nonimpact fatigue strength. During discussion of this paper the mechanism responsible for the observed strength differences was questioned. A full explanation of this phenomena is not currently available, but Dr. Futakawa reported that further work is planned to resolve this matter.

The remaining papers were concerned with full scale testing of HTTR core and core support graphite components.

Mr. M. Ishihara presented a paper entitled "Component test of core support post of HTTR". The core support post is an important component from a reactor safety point of view, since its failure may result in the direct degradation of the core. Full-scale model and half-scale model component tests were carried out to confirm the structural integrity of the core support post during a seismic event. Moreover, the effect of oxidation on the fracture strength was examined to simulate possible air ingress accidents, such as primary circuit rupture. The test results have shown the complete validity of the design, i.e., the fracture strength is at least five times larger than the design stress during a seismic event, even after the most severe air ingress accident. A question was asked on the degree of the oxidation. It was confirmed that pre-test oxidation was done in a manner to ensure that the profile across the core support post was at least the same as, or more severe than that estimated by analysis. It is hoped that an analytical approach to explain the test results can be developed in the near future.

The third presentation, made by Mr. M. Uno, was entitled "Assessment of dowel and socket system load capacity in HTTR hexagonal graphite block". The dimensional alignment of the HTTR core graphite blocks is preserved during a seismic event by dowel pins at the top of each block and mating sockets at the bottom of each block. Full-scale shear strength tests were conducted to verify design allowable loads for the dowel and socket system. A simple model was successfully employed to predict the fracture strength of the dowel and socket system using uniaxial fracture strength.

Finally, Mr. H. Shirai gave a presentation entitled "The vibrational characteristics of the keyed graphite component in the HTTR". The seismic response of a keyed graphite component generally exhibited non-linear collision behaviour, and was too complicated to be understood from a calculational analysis alone. First, a basic vibrational test was performed to develop an analytical code suitable for predicting the

nonlinear vibrational behaviour of the structure. A non-linear stiffness model was incorporated in the analytical code. This method was verified by 1/5-scale and 1/3-scale experimental prototypes of the HTTR core bottom structure.

Valuable data can be obtained from large scale seismic tests. The Japanese, living in a country prone to earthquakes, have done excellent work in the field of seismic analysis. It is hoped that data obtained here will be widely utilized for verifying other seismic analytical codes developed in other countries.

In summary, JAERI has been successful in conducting extensive efforts to demonstrate the structural integrity of core and core support graphite components of the HTTR. At the same time, much data on the fracture strengths of the components, which cannot be obtained by laboratory tests using small-sized specimens, has been accumulated. It is hoped that efforts will continue to develop analytical models to explain component test results from the fundamental mechanical properties of graphite.

### Session III (Part A)

#### MATERIALS DEVELOPMENT AND PROPERTIES

Chairmen: B.T. Kelly, T. Arai

Three papers were presented in this session:

- (1) "Fabrication of HTGR core components by the method of volume gas-phase impregnation of porous media with pyrocarbon: main characteristics of the materials and products" by V.F. Zelensky et al.
- (2) "Development of graphite for fuel element sleeves in advanced gas-cooled reactors" by D.P. Burridge and J. Naylor.
- (3) "Mechanical properties and thermal shock resistances of recently developed high performance graphites" by S. Sato et al.

The first paper developed the fabrication of a range of materials using the technology of carbon deposition from gas at about 1000°C to form solid bonding granular material including graphite, fuel particles for the HTGR and boron carbide neutron absorbing particles. This technology has found extensive application in the space industry but it now was believed to be ready for application to HTGR core components. The properties of the graphite based materials (GSP) were shown to be superior to industrial graphites and comparable to carbon-carbon composites.

The behaviour under irradiation testing of fuel core materials (GPP) and spherical fuel and absorbing elements prepared in this way was found to be highly satisfactory ( $R/B - 10^{-6}$  for the former and small dimensional changes for the latter). However, while the data was regarded as promising for the use of such materials it was not regarded as being sufficient for supporting their use.

A comparison of the costs of fabrication by these and more conventional methods would have been interesting.

The second paper concerned the development of a new graphite for the fuel sleeves of the United Kingdom's advanced gas cooled reactors using a new coke. The reactor system is mature and the properties required for such a graphite are well known. The paper describes the required conditions and properties. The results of laboratory examination and initial production followed by adequate irradiation data to permit a pilot loading of five fuel stringers (40 elements) in an advanced gas cooled reactor which will be examined after burnups of 9-24 GWd/t. The third paper examined the properties of high performance graphites developed by Japanese manufacturers in the 14 years since the graphite IG-110 was selected as the core material for the HTTR. A wide range of properties were determined in the unirradiated state and demonstrated to be comparable to, or better than the IG-110 properties. However only the latter is supported by substantial data on the effects of irradiation and a very considerable amount of work would be required to qualify one or more of these alternative materials.

An underlying theme of these papers was the major effort required to demonstrate the suitability of one graphite for reactor use.

### Session III (Part B)

#### MATERIALS DEVELOPMENT AND PROPERTIES

Chairmen: O. Chugunov, T. Maruyama

The papers presented in this session dealt with the two main problems of HTGR: (1) the influence of helium coolant containing water vapour on the physical-mechanical properties of graphite, and (2) the influence of graphite burn-off on the cleanliness of helium coolant and radiolytic corrosion.

As for the first problem, the reports deal with the influence of helium coolant parameters (water vapour concentration, temperature and pressure) on the mechanical properties of matrix and block graphite and integrity of construction of reactor and the influence of different metallic impurities including boron. The second problem was considered from the point of view of gas desorption and gas permeability of carbon materials.

The first paper, presented by Dr. Okada, showed the results of measurements of gas desorption and permeability of carbon materials. Gas species released from isotropic graphite, carbon/carbon composites and B<sub>4</sub>C-graphite materials were analyzed using the Thermal Desorption Spectrometer. It was shown that purification and pre-baking treatment of graphite materials reduced the amount of gas desorption, and that addition of boron by 1% suppressed the desorption of CO and CO<sub>2</sub>. In regard to gas permeation property, impregnation of glass and resin to the graphite material as well as PyC coating are effective in reducing gas permeability.

In the second paper, presented by Dr. Nomura, the relation between gasification rates and gas desorption behaviour with metallic impurities of carbon and graphite materials was presented. The gasification rates by water and CO were strongly dependent upon the kinds of metallic impurities and their concentration. It was pointed out that the addition of small amounts of Si are effective in reducing the desorption of gases from graphite materials.

The third paper, reported by Dr. Fujii, dealt with the problem of integrity of the sintered pellet and control rod system of the HTTR reactor because of the oxidation of B<sub>4</sub>C in helium containing water vapour at up to 1000°C. It is shown that the oxidation by water of the sintered pellet does not simply increase with temperature caused by formation of B<sub>2</sub>O<sub>3</sub>. The addition of boron decreased the oxidation rate of graphite by H<sub>2</sub>O. For the sintered pellet containing 30% boron which is the same specification as one in the reserved shutdown system of the HTTR the mutual adhesion yielded when above 2% of boron contained in the sintered pellet was oxidized and temperature exceeded the melting point of produced B<sub>2</sub>O<sub>3</sub> of 577°C even temporarily. The sintered pellets for the reserved shutdown system are stored in the hopper at 400°C and the environment in the hopper is the primary coolant which is helium containing 0.2 ppm water vapour, so that the mutual adhesion does not occur. The environmental effect on mechanical properties of graphite was reported by Dr. Maruyama. The effect of test environment on bend strength and fracture toughness of fine-grained isotropic graphites was very large. The bend strength increased if it was measured in vacuum or in dry helium. In the measurement of high temperature strength, it was shown that a substantial portion of the increase in strength at high temperature might originate from the removal of gases from the materials. Fracture toughness also increased if it was measured in vacuum. From these experimental results, it was shown

that when we evaluate mechanical properties of graphite materials, the effect of test environments should be taken into consideration.

The last paper is about the influence of corrosion on two kinds of matrix graphites: molded graphite based on calcinated coke and graphite based on uncalcinated coke in the temperature range 400-1200°C and at the water vapour concentration in helium of 0.01-1 vol%.

The authors concluded that in the tested temperature range the corrosion has a volumetric character. The corrosion resistance of matrix graphite based on calcinated coke is higher than that for the graphite based on uncalcinated coke. For the first type of material corrosion has an anisotropic character and is higher in the direction parallel to the axis of spherical fuel element molding.

With increase of metallic impurities, particularly iron, in the graphite the corrosion rate of the material increases. The corrosion rate of the irradiated matrix graphite based on calcinated coke is less than the unirradiated ones by a factor of 2.

To sum up, we consider the results of the work reported in this session to be very interesting and useful for HTGR reactor operation. There were no discussion in the session because of shortage of time, but the reports were received with great interest.

### Session III (Part C)

#### MATERIALS DEVELOPMENT AND PROPERTIES

Chairmen: B.T. Kelly, H. Matsuo

Six papers were presented in this session:

- (1) "Engineering thermomechanics of nuclear graphites under neutron irradiation, oxidation and transient heatup - A review" by T. Arai
- (2) "Review of irradiation creep in reactor graphite" by B.T. Kelly
- (3) "The specific behavior of the reflector and matrix graphite under high temperature irradiation" by P.A. Platonov et al.
- (4) "Irradiation behavior of boronated graphite for HTTR" by M. Matsuo et al.
- (5) "Capsule design, fabrication and irradiation for transient creep test on HTGR graphites at 1200°C in JMTR" by T. Saito et al.
- (6) "Main statements of strength analysis code for graphite structural components in uranium graphite nuclear reactors" by B. Rodchenkov et al.

The first paper described the current state of understanding of graphite irradiation behaviour, particularly with respect to non-isothermal behaviour. The paper provides many references to available work, excluding creep, and discusses the Graphite Damage Model (GDM) which uses numerical fitting of a limited set of processes to interpolate and extrapolate behaviour. The paper emphasizes the very wide range of data necessary on a single graphite, with sufficient understanding to extrapolate and interpolate.

The second paper described the UK database on irradiation creep in graphite and pointed out that the simple visco-elastic laws obtained were deceptively simple. The changes in thermal expansion with creep strain, both parallel and perpendicular to the stress, and the large changes in Young's Modulus to structural changes meant that the model must be corrected and recent data indicated that current methods may be incorrect. It was concluded that stress calculations in components are less reliable the larger the creep strains involved.

The third paper described the changes in properties and dimensions of a variety of graphites developed in the USSR for the UG-400 and VGM reactors. An increase in thermal expansion is observed at high doses, following the decrease often observed is a new phenomenon in graphite of this type which is not understood.

The next paper described the behaviour of boronated graphite made from  $B_4C$  granules and a graphite matrix used for neutron absorbing elements. The data presented showed satisfactory behaviour but the discussion emphasized the difficulty in obtaining appropriate data on such materials because the boron carbide responds to thermal neutrons and swells due to the  $B^{10}(n, \alpha) Li^7$  reaction with the recoil particles damaging the local graphite matrix, while the graphite responds to fast neutrons. The relative effects of these two processes in the real reactor situation was not clear.

The detailed design of a capsule (now being irradiated) to measure tensile irradiation creep at 1200°C was described. The current performance appeared very satisfactory.

Finally the paper from the USSR presented the conditions to which graphite is subjected and the criteria used to calculate stresses and

strains in the material are given. The limiting states permitted are described including:

- (a) Critical fluence above which the properties deteriorate
- (b) Failure due to stress
- (c) Excessive creep strains ( $>0.02$ )
- (d) Excessive cracking.

However, the creep model was not described in detail, nor the justification for use of the various limiting parameters. The background to the choices would be of great interest.

The session gave the impression that all participants are able to generate good data in isothermal irradiations with, for graphite, good agreement in observed behaviour and use of identical dose scales. There are, as highlighted by the first two papers, considerable differences in possible methods of applying results, particularly to non-isothermal conditions (normal for operating reactors) and also to the application of creep multi-axial high creep strain situations ( $>0.5\%$ ). Increased collaboration and information exchange in these areas is highly desirable.

### Session III (Part D)

#### MATERIALS DEVELOPMENT AND PROPERTIES

Chairmen: M. Roedig, K. Kikuchi

In the first two papers, the influence of specimen geometry and sampling on strength and fracture toughness was discussed. In the other two papers, the influence of loading conditions was investigated.

Firstly Dr. Strizak of ORNL presented a paper entitled "The effect of volume on the tensile strength of several nuclear-grade graphites". The influence of stress volume on the tensile strength of two graphites, H-451 and IG-110, was discussed. Before, the variability of tensile strength within a billet was investigated only casually. The problem was the influence of a limited sampling plan in describing the mean strength and the variability. Therefore, an extensive sampling plan was devised to characterize the spatial variability within a single billet. The effect of stress volume was re-examined by comparing the strengths of four (H451) and three (IG-110) specimen sizes.

The tensile strength of both graphites increased with specimen size, which was contrary to the predictions of the popular Weibull model. But it has been found before, that stress decreases rapidly as the specimen size approaches the grain size of the graphite. A modified Weibull model introduced by Ho takes the grain size effect into consideration but does not consider the spatial variations noted particularly in H-451. The experimental data show that the grain size effect is overestimated by this model. The new fracture model by Dr. Burchell, presented at this conference, incorporates microstructural elements, specimen size, and fracture toughness. An initial evaluation of this model using the experimental data shows promise for the description of the volume effect.

Secondly Dr. Burchell of ORNL presented a paper entitled "The effects of specimen geometry and size on the fracture toughness of nuclear graphite". Various fracture toughness measuring techniques have been applied to graphite IG-110. Test geometries were compact tension (CT), disc compact tension (DCT), short rod (SR), chevron notch short rod (CNSR), cylindrical bend specimen (BS), and centrally slotted disk (CSD). With specimens which allow slow crack propagation (CNSR, CT) higher fracture toughness values are measured than in specimens which show a rapid crack growth (CSD). This was attributed to a specimen size effect.

Therefore a further investigation has been performed to study the influence of the specimen size. This has been done for three graphites (H-451, S-2020 and IG-110) on CNSR specimens. Three specimen diameters have been used (12.7, 19, and 25.4 mm). Fracture toughness increased with increasing specimen size. This was explained by increasing R-curve behaviour during crack extension. The latter may be attributed to nonlinear fracture process, including microcracking residual strain in the crack wake region and grain bridging between crack flank surfaces.

Thirdly Dr. Ishiyama of JAERI presented a paper entitled "Cumulative Fatigue Damage on HTGR Graphite". Two-step fatigue tests were performed to investigate a cumulative damage of fine-grained isotropic graphite IG-110.

Peak load was changed from high level to low (HL mode) and from low level to high (LH mode) during a life of specimen. Then fatigue life was found to be shorter than expected for HL mode and longer for LH mode. It was found that Miner's rule couldn't describe lives of HL and LH modes



because the maximum stress had a strong influence to the next load step mode. This was explained as being due to the different size of the process zone ahead of the cracks at high and low stress levels.

New empirical equations were proposed to express cumulative fatigue damage for these two-step tests.

Finally M. Ugachi presented a paper entitled "Fracture behavior of nuclear graphite under compressive impact loading". Compressive load tests were carried out at various strain rates from  $10^{-4}$  to  $10^2$  (1/s) for two kinds of nuclear grade graphites, IG-11 and PGX. MTS machine of model 5041 was used for impact test of high strain rate.

Two types of cylindrical specimens, 12.5 mm in diameter with 25 mm length and 25 mm in diameter with 50 mm length, were employed in this experiment.

Compressive fracture strength, strain at fracture, specimen volume and Poisson's ratio were shown as a function of strain rate. Compressive strength increased slightly up to strain rate of  $10^2$  (1/s) and then decreased drastically. Poisson's ratio increased with strain rate and compressive stress, and reached 1/3 at strain rate over  $10^2$  (1/s), which is the theoretical value of elastic behaviour.

## Session IV (Part A)

### NON-DESTRUCTIVE EXAMINATIONS, INSPECTIONS AND SURVEILLANCE

Chairmen: D.P. Burridge, A. Ide

The three papers presented in this session covered three different areas of non-destructive examination, inspection and surveillance. The Japanese paper described non-destructive testing and acceptance testing of HTTR components, the French paper described surveillance of an operating reactor core to support its continued operation, whilst the US paper described surveillance of a closed reactor from which useful information arising from 24 years of operation could be obtained.

The French paper provides an outline of the Bugey-1 reactor which is graphite moderated and cooled with carbon dioxide. The unirradiated properties of the graphite are included in the paper. The core bricks are affected by dimensional change and radiolytic oxidation. To minimise radiolytic oxidation, methane is added to the coolant but this can give problems of deposition on the clad. To monitor weight loss arising from radiolytic oxidation, samples are taken from the highest power channels and their density determined. The most affected samples are subjected to compressive strength measurements and additional samples are taken parallel to the channel wall. The mean radial weight loss in the most affected areas is 30% with maximum values of 35%. The compressive strength values have been plotted as a function of weight loss.

The mechanical behaviour of the core is predicted by the INCA code which uses weight loss data determined by the USURE code. The agreement between calculated and experimental results is generally good although some tuning of parameters is necessary. There is now confidence that the reactor can operate until its planned closure in 1994. However, further sampling is planned to monitor core behaviour.

The paper by Mr. Woodruff represented a unique opportunity to provide data from a reactor that had operated for over 24 years. The graphite in the fuelled region had experienced the full cycle of transverse contraction, turnaround and growth. The graphite used was anisotropic and therefore not representative of modern nuclear graphites. As a consequence the radiation induced changes were greater than modern graphites. The paper describes the core, irradiation experiments to predict dimensional change and inspection techniques. Inspection techniques included the use of calipers, a theodolite, transducers, bore scopes and CCTV cameras. A large amount of data is presented in the paper covering block measurement, stack profiles, layer displacement and stack motion. The paper concludes that future cores should be designed to allow access for surveillance equipment and that irradiation testing to full reactor life exposure should be conducted on graphites before use in a reactor core.

The paper by JAERI and Fuji Electric provided an outline specification for acceptance testing of the PGX and IG-110 graphites that are to be used in the HTTR reactor. This included mechanical testing, chemical analysis, ultrasonic testing and eddy current testing. Graphite shows a wide scatter in the strength data and therefore three different strength classes have been identified for each grade. Each strength class will be used for an application appropriate to the design stresses of the component.

All three papers proved interesting. Although the French and the US paper dealt with grades of graphite that would not be used for future nuclear applications, important lessons could be derived. The French had

identified a method of ensuring the core would remain operational until the planned closure of the reactor. Mr. Woodruff recommended that future cores should be constructed of material that had been irradiated to full reactor life exposure and the access for surveillance equipment should be a design feature for graphite cores. In contrast, the Japanese dealt with the specification for modern nuclear grade graphites. It was interesting to note the tests applied and the specified limits. The inclusion of non-destructive testing information was particularly useful.

## Session IV (Part B)

### NON-DESTRUCTIVE EXAMINATIONS, INSPECTIONS AND SURVEILLANCE

Chairmen: E.M. Woodruff, S. Ishiyama

Mr. Ishii, Japan Atomic Energy Research Institute, presented a paper entitled "Non-destructive test of HTGR graphite components". The main purpose of this paper was to show the optimized regulation and applicability of C-scan imaging eddy-current technique to detect a defect and the surface of IG-110 and PGX graphite plates. The recommended liftoff (The distance between eddy-current probe and surface of graphite plate) of within 0.1mm to 0.3mm and a scanning speed of from 20 mm/s to 30 mm/s to measure the diameter of a hole drilled in the surface of graphite plates, and the minimum and maximum measurable hole diameters and depths are also reported.

The eddy-current technique is expected to be very useful for the acceptance test of HTGR graphite components and more detailed information of penny shaped defect will be required by this technique.

Dr. Oku, Ibaraki University (Japan), presented a paper entitled "The correlation of hardness with Young's modulus and strength of nuclear carbon materials". The main aim of the paper is to obtain the correlation of Vickers hardness to Young's modulus, bending strength and compressive strength. A good correlation and applicability of microhardness test techniques to evaluate the strength of graphite materials is demonstrated.

The microhardness test technique has the advantage of evaluating the mechanical properties of graphite materials using very small specimens.

The last paper is entitled "Quantitative analysis of trace amounts of impurities contaminating in the pure graphite with ICP-MS and metal atomizer FLAAS".

The development of modern analytic capabilities for the analysis of impurities in graphite is most appropriate at this time. The work presented here demonstrates improved detection limits and the applicability of the methods for high purity nuclear graphite. Repeatability of results for this and less pure graphite still need to be demonstrated.

The US ASTM Subcommittee on Nuclear Graphite, C5.05, is currently reviewing the Standard Method for Chemical Analysis of Graphite (ASTM C560-88). An obvious deficiency requiring revision is the use of outdated analytic procedures. The work reported here is a good step in that direction.

The next step should be an effort to determine if the methods are suitable for use at other laboratories including manufacturers or their service contract labs. The question is "Can other labs obtain comparable results?" Round robin analyses have been used in the past for this purpose but it was 30 years ago for nuclear graphite.

The next stage would be to reach consensus among potential users. The methods are both reliable and economically feasible if they were to be used for quality control during production or incorporated in purchase specifications.

Interaction with the current ASTM activity would be mutually beneficial. It is being co-ordinated by the ORNL representatives on the committee (Dr. Burchell et al.)

Some consideration should also be given to the application of the results of chemical analysis in calculations of neutron absorption cross-section. The availability of test reactors for that purpose has diminished if not disappeared in most countries and chemical method of determination is the only alternative.



# SUMMARY OF NATIONAL PROGRAMMES

(Session I)





## 1. INTRODUCTION

Graphite research and development activities in Japan, Russia, Germany, the USA, France and the United Kingdom have led to improved understanding of graphite behaviour in gas-cooled reactors since the IAEA Specialists Meeting on Graphite Component Structural Design which was held in Tokai, Japan in 1986. The following reports the status of graphite research and development programmes in these countries in the context of their national gas-cooled reactor programmes.

## 2. STATUS OF THE HTGR PROGRAMME IN JAPAN (S. Saito, Japan Atomic Energy Research Institute)

The HTGR development programme has a long history in Japan. The JAERI started the HTGR development programme in 1969 so as mainly to construct an experimental reactor for direct heat application, along with the Japanese industries. The energy situation, however, has changed remarkably in Japan during the last 20 years. Then, in 1987, the construction of the High Temperature Engineering Test Reactor (HTTR) was decided instead of an experimental HTGR. The HTTR aims at establishing and upgrading the technology basis necessary for an HTGR, serving at the same time as a potential tool for new and innovative basic researches. The budget for the construction of the HTTR was finally approved by the Government in 1989 and the JAERI submitted immediately the safety analysis report of the HTTR to the Government. After about a two year safety review by the Government, the installation permit was issued in November 1990, and the construction was started in March 1991 at the Oarai Research Establishment. The excavation of ground has been already completed. The manufacturing of the containment vessel is being proceeded in the factories, and other reactor equipments are being designed for fabrication at the industrial side. It will take about five years for the completion of the HTTR facility and the first criticality will be attained in FY 1996.

The JAERI has carried out various kinds of research and development for the HTTR licensing and construction. Several new materials and equipments have been developed together with specific considerations in the design of the HTTR in order to realize the reactor outlet coolant temperature of 950°C. As for graphite, the isotropic fine-grained IG-110 with very high strength and corrosion resistance was developed to be used in the core and important parts of the core support structures in the HTTR.

Although the definite programme of the second HTGR following the HTTR is not established in Japan, several studies by the Japan Atomic Industrial Forum and Research Association on HTGR plants have been made for introduction of HTGRs for nuclear heat application and electricity generation for the future programme of energy supply.

### 2.1. Outline of the HTTR design

The HTTR consists of a reactor pressure vessel, a primary cooling loop with an intermediate helium-helium heat exchanger (IHX) and a pressurized water cooler (PWC) in parallel, an auxiliary cooling system, reactor vessel cooling system and related components. The reactor pressure vessel (RPV) is 13.2 m high and 5.5 m in inner diameter, and contains a prismatic

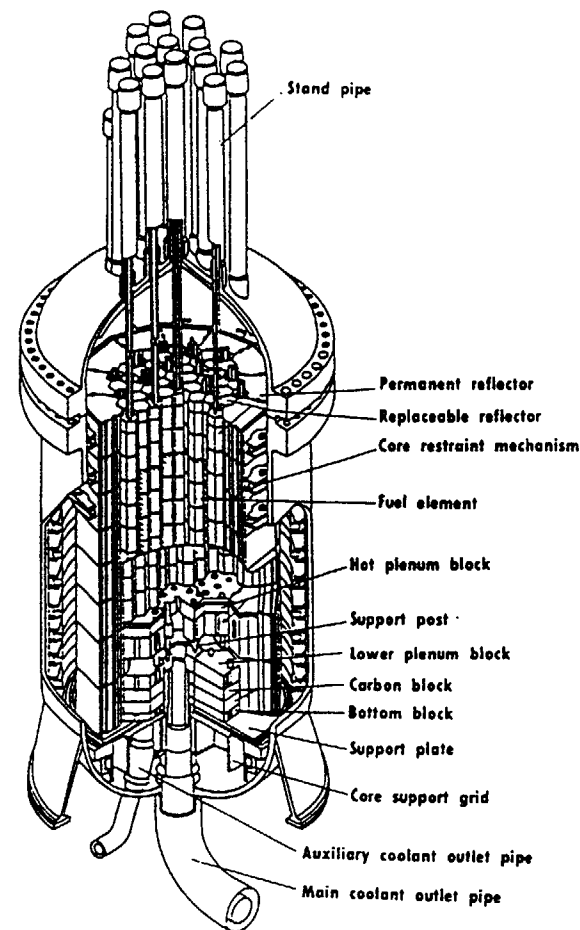


FIG. 2.1. Bird's eye view of reactor vessel and core.

30 MW(th) core and reactor internal structures as shown in Fig. 2.1. The reactor outlet coolant temperature is 850°C at the rated operation and 950°C at the high temperature test operation. Major specifications of the HTTR are listed in Table 2.1.



Reactivity control is provided by control rods, which are individually supported by drive mechanisms contained in the stand-pipes connected to the hemispherical top head of the RPV and inserted into the fuel region and replaceable reflector region. The reactor shutdown from a high temperature condition is made by the insertion of 9 pairs of control rods in the reflector region at first, and then 7 pairs of control rods in the fuel region are inserted in the condition of core temperature lower than 900°C. Back-up shutdown capability is provided by insertion of boron carbide/graphite pellets into separate holes in the control rod guide blocks.

#### Fuel

A fuel block which holds fuel rods in it is a pin-in-block type hexagonal block of 58 cm in height, 36 cm across flats as shown in Fig. 2.3. The fuel consists of coated particles of low enriched uranium oxide whose average uranium enrichment is 6% and the kernel diameter is 600  $\mu\text{m}$ . The particles are bonded together with graphite powder in fuel compacts, which are contained in a graphite sleeve to form a fuel rod. The fuel rods are contained within vertical holes with 4.1 cm in diameter of the graphite blocks. Helium gas flows downward through the gap between the vertical hole and a fuel rod to remove the heat produced by fission and gamma heating.

#### Reactor cooling systems

The reactor cooling systems are composed of a primary cooling system (PCS), an auxiliary cooling system (ACS) and two vessel cooling systems (VCSs) as shown in Fig. 2.4.

The cooling circuit of the PCS is separated into two lines outside the RPV. The heated helium gas is cooled by a 10 MW He-He IHX in one line or cooled directly by a 20 MW PWC in the other line. The demonstration plant for application of nuclear heat as process heat will be connected with the outlet of the secondary side of the IHX in future.

In order to maintain the integrity of the reactor cooling system against the severe high pressure and high temperature condition, various considerations are taken in the design. A co-axial double piping system as shown in Fig. 2.5 is adopted in the primary circuit. Cold gas of about 400°C flows the annular space between the inner and outer pipes toward reactor inlet, while hot gas from the reactor flows inside the inner pipe. Temperature of the inner pipe is almost the same as that of the outer pipe because the inside of the inner pipe is thermally insulated by Kaowool and lined with Hastelloy-XR, which is a specifically developed heat resisting super alloy with high corrosion resistivity at high temperature. The pressure boundary is formed by the outer pipe, thus the inner pipe is designed only to withstand the pressure difference between the inside and the outside of the inner pipe.

The IHX is a vertical helical coil counter-flow type heat exchanger as shown in Fig. 2.6. Primary coolant flows on the shell side with secondary coolant flowing on the tube side. Then, heat transfer tubes in the IHX form the primary coolant pressure boundary under the high temperature condition.

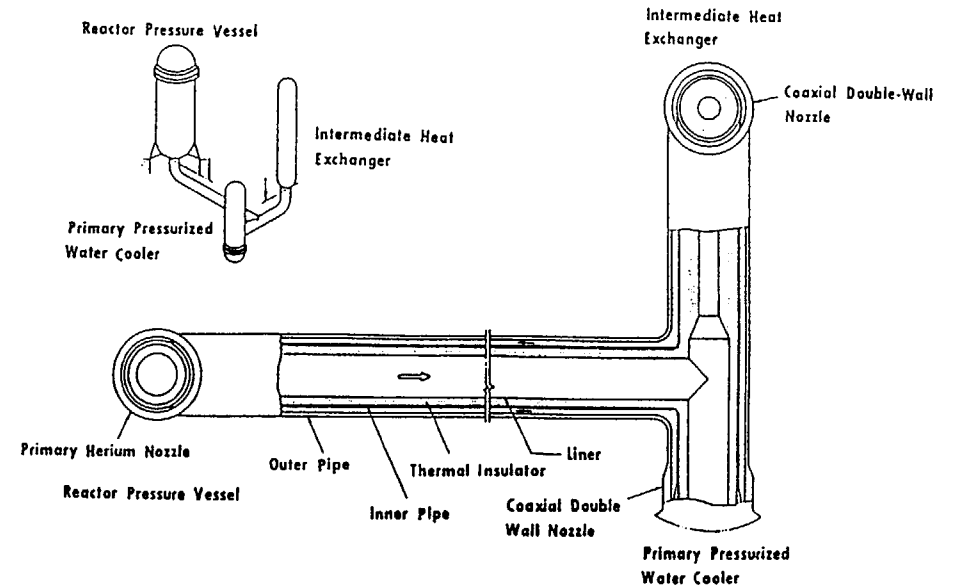


FIG. 2.5. Coaxial double piping.

In order to maintain the integrity of the tubes, mechanical loading on the tubes is reduced by minimizing pressure difference to only 0.1 MPa in a normal operation. In addition, Hastelloy-XR is used at high temperature structures such as heat transfer tubes, tube sheets, tube support structures, a centre pipe and a liner.

The ACS is operated when there is a trouble in the PCS but flow path in the primary cooling circuit is still kept. Two sets of VCSs are operated during normal operation in order to cool biological shield around the RPV and serve to cool the RPV and the core in the accident like pipe break of the PCS in which the flow path in the primary cooling circuit is not kept.

#### Irradiation capability

Many possible irradiation regions are reserved in the HTTR to be served as an irradiation test reactor in order to promote innovative high temperature basic researches as well as to irradiate fuels and materials for HTGR as illustrated in Fig. 2.7.

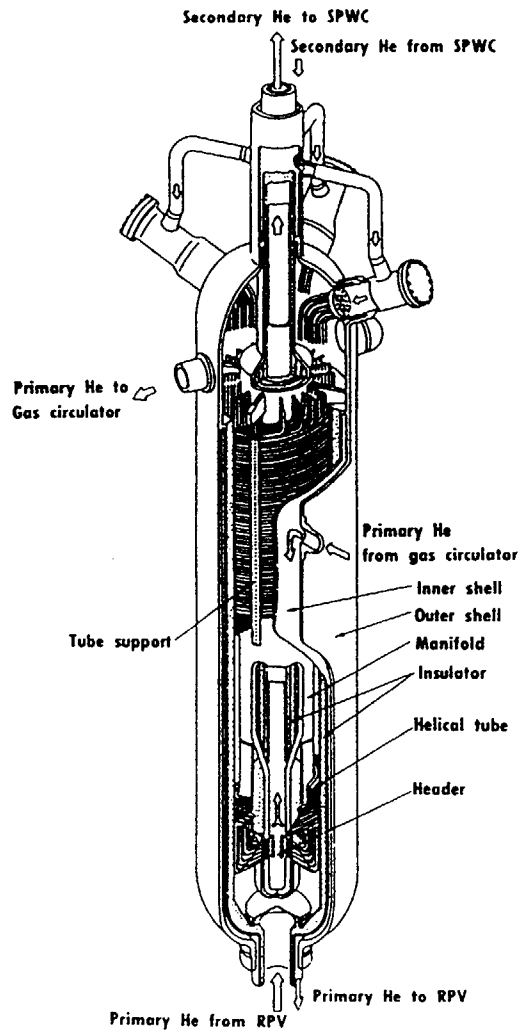


FIG. 2.6. Intermediate heat exchanger (10 MW).

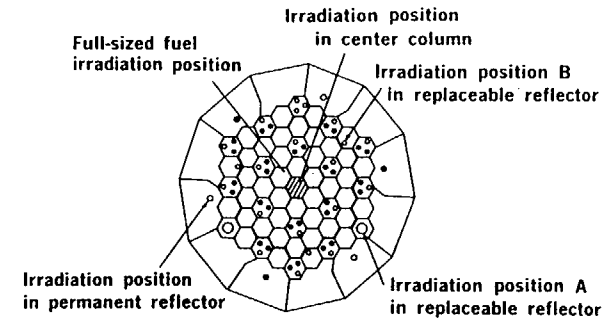


FIG. 2.7. Sample irradiation positions in core and reflector.

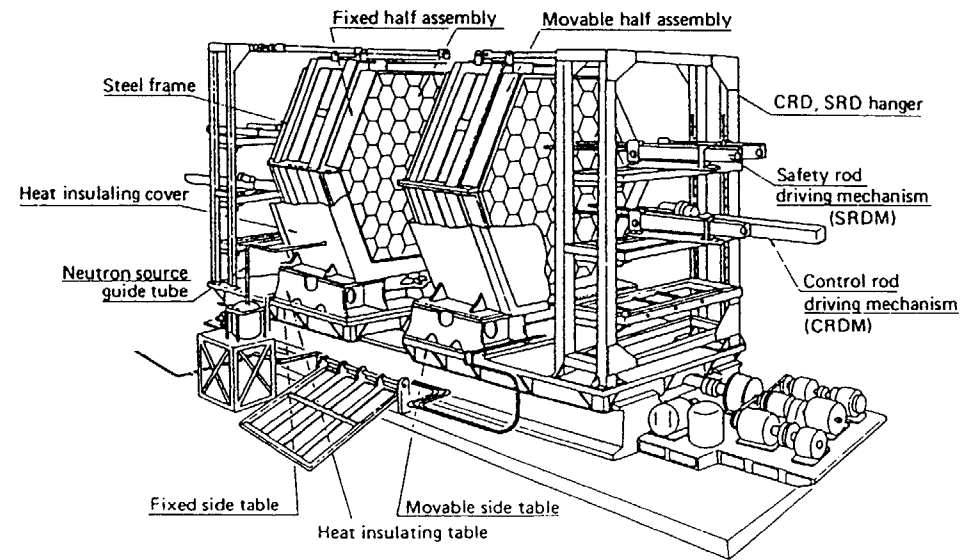


FIG. 2.8. Schematic view of the VHTRC.

## 2.2. Major research and development for the HTTR

### Core neutronics

In order to verify the adequacy of computer codes related to the core neutronics design of the HTTR, various experiments have been conducted using a critical assembly, the VHTRC (Very High Temperature Reactor Critical Assembly). A schematic view of the VHTRC is shown in Fig. 2.8. The major items investigated are (a) critical mass, (b) temperature coefficient of reactivity, (c) neutron flux distribution and (d) reactivity worth of the HTTR control rod and burnable poison rod.

As an example, a comparison of the effective multiplication factor obtained by the calculation and experiments is shown in Fig. 2.9. The calculated results are in very good agreement with the experimental ones.

### Thermohydraulics

The HENDEL (Helium Engineering Demonstration Loop) was constructed to perform large scale demonstration tests of high temperature components for HTGRs in March 1982. The HENDEL consists of Mother (M), Adapter (A) and Test (T) sections. The Mother and Adapter (M+A) sections circulate helium gas at a flow rate of 4 kg/s, a pressure of 4 MPa and temperature of 1000°C at maximum. The M+A sections have been operated for more than 14 000 hours since 1982. The test section is made up of the Fuel Stack Test Section and the In-core Structure Test Section. Many valuable data such as leakage flow, pressure drop, temperature distribution have been obtained from the HENDEL and other small scale experimental facilities.

A comparison of fuel temperature distributions obtained by the calculation and experiment in the HENDEL is shown in Fig. 2.10. The calculated results are in good agreement with the experimental results.

### Fuel

Performance of the HTTR design reference fuel under normal reactor conditions has been tested in the Oarai Gas Loop No.1 (OGL-1) at the JMTR and the capsule irradiation experiments. Fractional release (R/B) of fission products ( $^{88}\text{Kr}$ ) from the fuel element remained in the order of  $10^{-6}$  during the irradiation, showing good performance.

Concerning the fission product release at the elevated temperature up to 2400°C, the out-of-pile isothermal heating and transient heatup tests on the irradiated coated particles have been carried out and revealed that the integrity of the fuel was maintained up to 1900°C.

### Materials

- (1) Graphite and carbon

The JAERI together with a private company developed a new description isotropic fine-grained graphite, IG-110, which has very high strength and corrosion resistance. These properties are shown in Fig. 2.11 compared with other conventional graphites. Figure 2.11 also shows that IG-110 has rather small dimensional change induced by neutron irradiation, which is quite desirable to the reactor design.

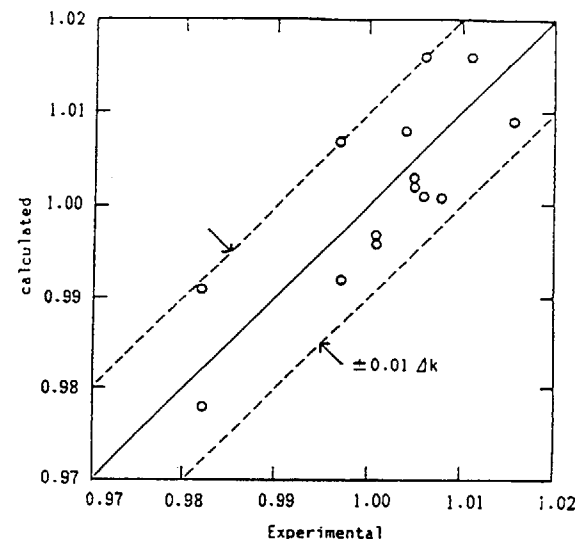


FIG. 2.9. Experimental and calculated effective multiplication factors.

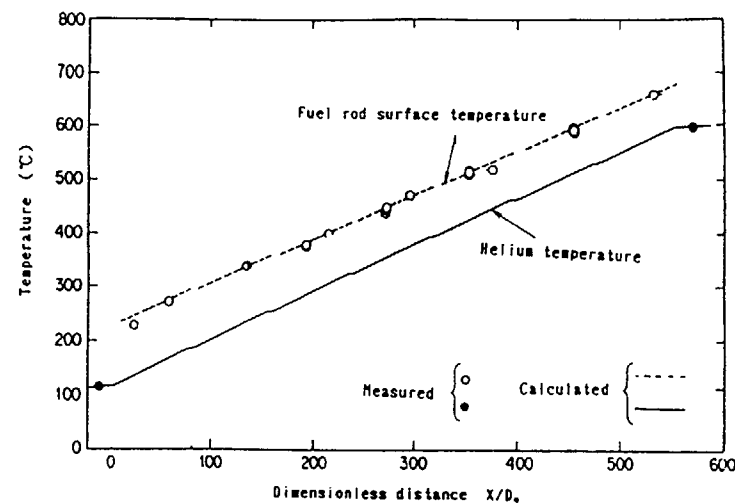


FIG. 2.10. Experimental and calculated fuel temperature.

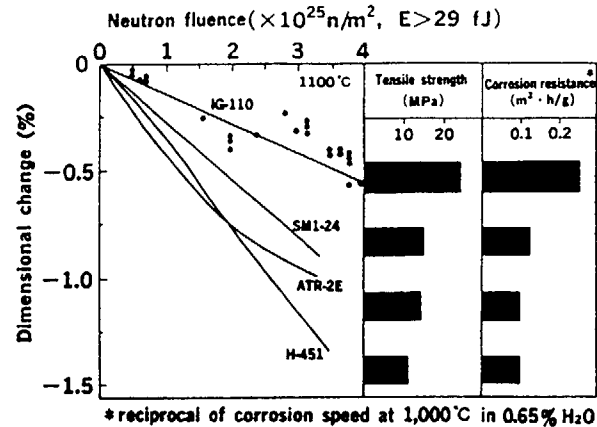


FIG. 2.11. Dimensional change by irradiation, tensile strength and corrosion resistance of various graphites.

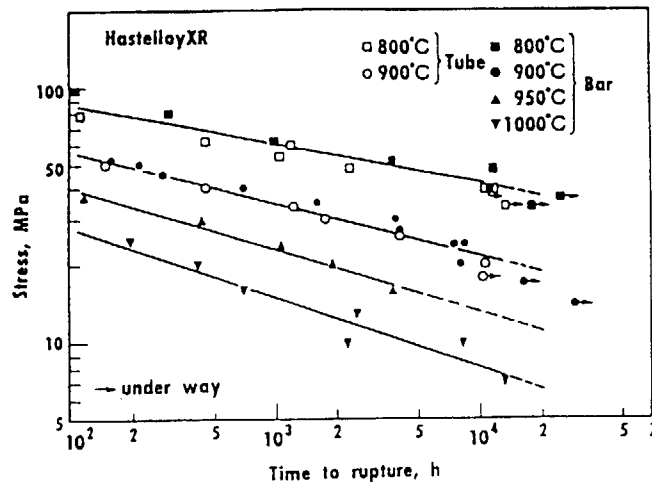


FIG. 2.12. Long term creep rupture data for Hastelloy XR in JAERI type helium gas.

The JAERI has accumulated the data required for the design of the HTTR, such as corrosion, thermal conductivity, tensile and compression strength, impact strength, high temperature Young's modulus, fracture mechanics properties, low cycle fatigue life, irradiation creep properties and so on, for IG-110, PGX and ASR-ORB which will be used in the HTTR.

The JAERI has also developed the graphite component design criteria and inspection criteria for the HTTR, and these criteria are authorized by the Government.

## (2) Metals

The tests for creep, fatigue, fracture toughness, corrosion and other critical items have been made for the accumulation of design data of Hastelloy-XR, which is a modified version of Hastelloy-X and is used for the IHX. Creep-rupture tests under helium environment simulating HTTR condition have been performed for 3x10<sup>4</sup> hours as shown in Fig. 2.12.

In the HTTR, 2 1/4Cr-1Mo steel is used for the pressure boundary components (pressure vessel, pipes, etc.). The data similar to those required for Hastelloy-XR have been accumulated also for 2 1/4Cr-1Mo steel.

## High temperature nuclear heat application

### (1) Hydrogen production by the IS process

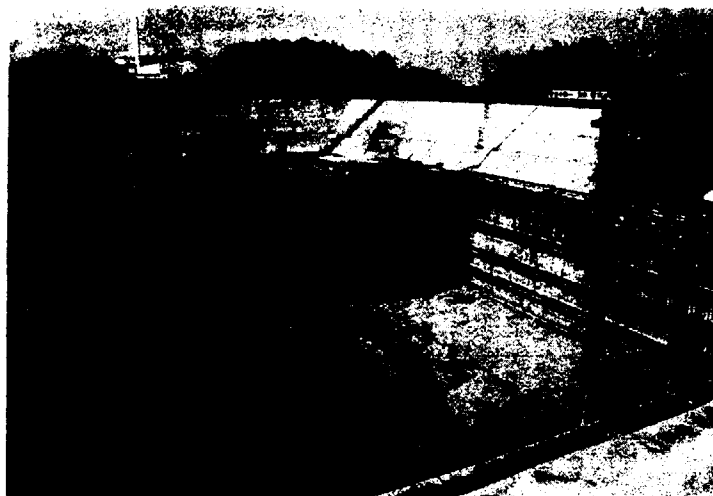
For utilization of high temperature heat from the HTGRs, the thermochemical hydrogen production process, i.e. the Iodine-Sulfur (IS) process, has been studied in the JAERI. The IS process produces hydrogen by water splitting with the combination of 3 reactions, that is, Bunsen reaction, decomposition of hydrogen iodide and decomposition of sulfuric acid. A hydrogen production rate of 1 litre/cycle was confirmed in a laboratory-scale test and a bench-scale apparatus has been installed for demonstration of continuous process and is under test operation.

### (2) Hydrogen production by high temperature electrolysis of steam

Hydrogen production by high temperature electrolysis of steam is also one of a candidate of nuclear heat application. A fundamental study on material selection of solid electrolytes and ceramics electrodes for application to electrolysis of steam has been carried out by measuring electrical conductivity and phase stability in the JAERI.

Concurrent with the above JAERI's activities, various vendor sponsored studies have been carried out.

In July 1990 a working group within the Japan Atomic Industrial Forum was organized to evaluate possible contribution of heat application of HTGR to the global environmental problem and to find out the way to promote it. Typical candidates for HTGR heat application have been evaluated and their system arrangements are proposed. The candidates are cogeneration, methanol production from fossil fuels and methanol or steel production by hydrogen by means of high temperature steam electrolysis. The study working group will complete the report in fall 1991.



**Photo 1. Excavation of ground.**



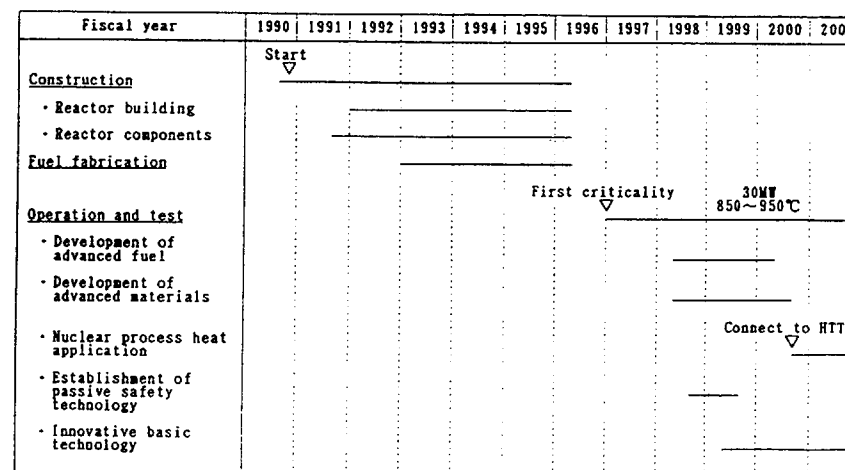
**Photo 2. Examination of supporting foundation.**

The Research Association on HTGR Plant was formed in April, 1985 to investigate more immediate potential of HTGRs for electrical power generation in Japan. The association surveyed several types of HTGR power plants and assessed the applicability of modular HTGR under siting conditions typical of Japan.

### 2.3. Construction of HTTR

In accordance with the Government's decision of financial support for the construction of the HTTR in January 1989, the JAERI submitted the safety analysis report of the HTTR to the Government for the safety review in February 1989. After about two years' safety review by the Science and Technology Agency (STA) at the first step and the Nuclear Safety Commission (NSC) at the second step, the installation permit was issued in November 1990 by the Government. The construction of the HTTR facility including the reactor building and reactor components was initiated on the site in the Oarai Research Establishment, JAERI, in March 1991. The excavation of ground and the examination of supporting foundation by the Government have been already completed as shown in Photos 1 and 2. The construction of concrete base-matt will be initiated in the late fall this year. The manufacturing of containment vessel is being proceeded in the factories, and it will be transported to Oarai site in the middle of 1992. Other reactor equipments are being designed for fabrication at the industrial side.

It will take about six years for the completion of the HTTR facility and the first criticality will be attained in FY 1996 as shown in Fig. 2.13.



**FIG. 2.13. Schedule of construction and operation.**

The JAERI plans, as illustrated in Fig. 2.13, to make material and fuel irradiation tests and safety demonstration tests after attaining the rated power and coolant temperature. Furthermore, a heat utilization system is planned to be connected to the HTTR and demonstrated at the early stage, which will be first challenge in the world.

#### 2.4. International Co-operation

In order to promote HTGR research and development most efficiently, the JAERI has proceeded with international co-operation with the research organizations mainly in the Federal Republic of Germany, the United States of America, the United Kingdom and the People's Republic of China. The co-operation is basically based on the agreements between the governments as shown in Fig. 2.14.

Since 1979, the collaboration with the Juelich Research Center (KFA) has been carried out in the area of fuel, graphite, metals, instrumentation, components and safety. In 1988, the KFA-JAERI agreement was revised to include joint projects. Joint experiments at the AVR reactor for testing the high temperature fission chambers and measuring the neutron flux in the steam generator were carried out successfully. Since May 1988, JAERI has participated in the safety-related experiments of the AVR investigation programme such as LOCA simulation tests.

The JAERI also made an agreement with the US Department of Energy to promote the programme for HTGRs in the fields of fission chamber, fuel performance, graphite, metal and design. Recently, the JAERI also initiated the information exchange on gas cooled reactors with the Soviet Union as well as with the United Kingdom.

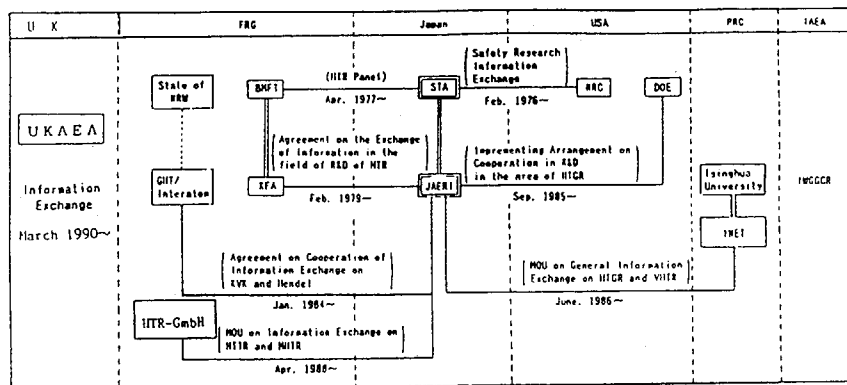


FIG. 2.14. Scheme of international co-operation.

#### 3. STATUS OF ACTIVITIES IN THE SOVIET UNION INVESTIGATING GRAPHITE BEHAVIOUR IN VGM MODULAR REACTOR CONDITIONS AND THE PROBLEMS OF ITS OPERABILITY (I.S. Mosevitskij, V.S. Popov, I.E. Golubev, I.V. Kurchatov Institute of Atomic Energy, Moscow)

A modular reactor VGM is a reactor with graphite fuel spheres and graphite reflector. A reactor design description with main characteristics is given in [1]. Providing the reflector operability is one of the main tasks to be solved in designing this and any other HTGR reactors. This problem arises because a reflector operates under high temperatures and considerable fast neutron fluence acquired during reactor life. The task of a designer is to develop a design which would not require reflector replacement or repair. Such a reactor may require new graphite materials. The paper reviews the results of studies concerning some of these problems as applied to a VGM graphite reflector.

##### 3.1. Reflector design and features of graphite operation

Upper and lower axial and radial reflectors are assembled of different-configuration graphite blocks. A radial reflector incorporates internal and external blocks, the radial dimension being 200 and 700 mm and the height 250 mm each (Fig. 3.1). The internal blocks have 60 X 260 mm channels for absorbing ball system (ABS). The channels can be filled with small balls absorbing neutrons. The thickness of wall between the ABS-channel and the internal reflector surface is 60 mm. The external graphite blocks have 140 mm diam. channels to accommodate control rods (24 pos) and to pass "cold" helium from the bottom to the top of the reactor, to the core inlet (72 pos). The lower reflector consists of the blocks with 20 mm diam. channels for hot helium.

The radial and lower axial reflector graphite blocks operate under high loadings. Fig. 3.2 shows for the helium temperature 950°C and 750°C the height distribution of the internal reflector temperature and of fast neutron fluence ( $E > 0.1$  MeV) for a 40 years service time.

The lower reflector is at the temperature near the helium temperature. It is positioned in the region of a low fluence.

The temperature fields and thermal stresses in the graphite blocks depend on the reflector cooling conditions. In normal operation the cooling depends on the positions of the cold gas channels, channels with control rods ABS-channels and on the heat exchange with gas in these channels. These factors may vary to some extent and be optimized in reactor designing, therefore it would be reasonable to investigate the effect of these factors. For example it is feasible to vary the gas flowrate through channels housing control rods and through ABS ones, thus affecting heat removal from a reflector at the places of their positioning.

When estimating the lifetime of the reflector, the effects of corrosion should be taken into account. Chemically active oxidizing components in the coolant cannot be completely removed. To preserve an oxide film coating the primary metallic components (in the first place, on the helium-helium heat exchanger tubes), it is necessary to follow certain requirements imposed on the oxidation potential and partial impurity



FIG. 3.1. Shape and size of reflector blocks.

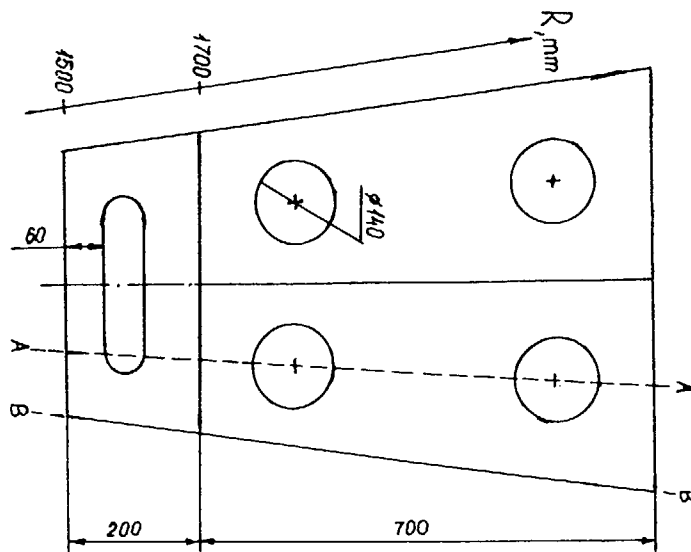
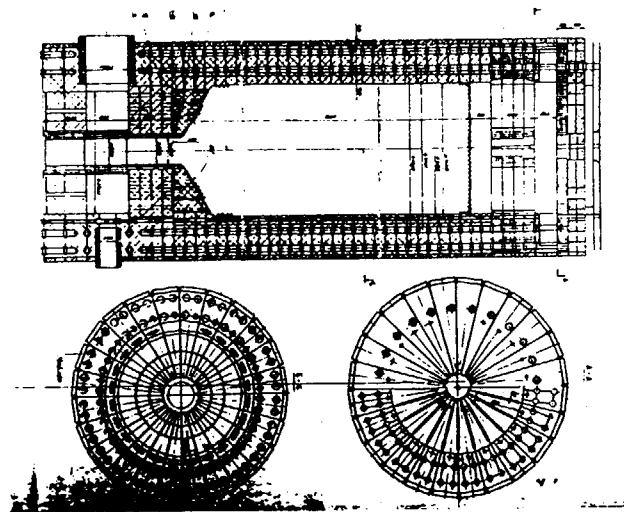


FIG. 3.2. Height distribution of radial reflector internal surface temperature and fast neutron fluence. Z is the distance from the pebble bed upper level.

pressures in the coolant. The upper limit for the oxidizing component pressure should be defined by the admissible corrosion levels in the fuel and the reflector.

### 3.2. Radiation stability of reflector graphite

It is known that graphite operational reliability under irradiation depends on the temperature at which irradiation occurs. To take into account this effect in reactor design, a critical fluence criterion was introduced in [2]. It permits the operability of the graphite irradiated without mechanical loads at a specified temperature to be estimated. This criterion is the fast neutron fluence at which starts a quick swelling of the graphite and degradation of its properties because of structural changes. The critical fluence,  $F_{cr}$ , decreases with increasing temperature: the  $F_{cr}(T)$  function characterizes the graphite radiation stability, permits different graphites to be compared and their operability under design conditions to be estimated. Fig. 3.3 shows these functions obtained for two graphites, including a pilot-scale GR-1 graphite developed in the USSR especially for HTGR reactors. This is a material manufactured on the base of non-calcinated coke. It exhibits a higher radiation stability than the conventional graphites. The comparison of operation conditions of VGM radial reflector graphite with the  $F_{cr}(T)$ -function (Fig. 3.3) shows that conventional graphite does not provide the required lifetime at  $T_{he}=950^\circ\text{C}$ , while GR-1 graphite is shown to be applicable for fabrication of the VGM reflectors. The range over which a GR-1 critical fluence margin for a radial reflector is minimal corresponds to a temperature range of 600 to  $900^\circ\text{C}$  and to a zone located at the depth of  $Z=3.5\text{--}8\text{m}$  from the upper level of pebble-bed. As for the lower reflector, it will have a higher critical fluence margin than the radial reflector.

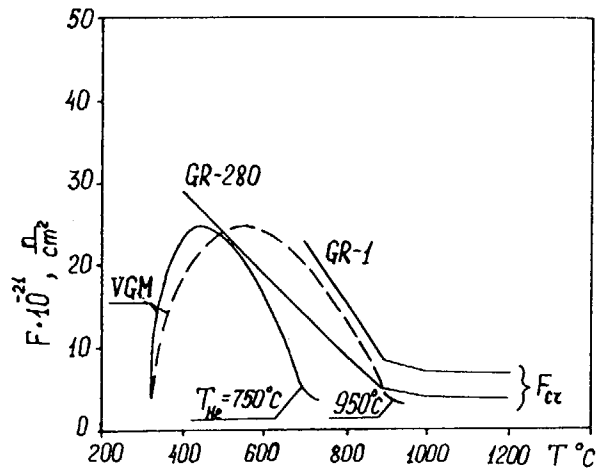


FIG. 3.3. Dependence of critical fluence  $F_{cr}$  on irradiation temperature and operating conditions of VGM radial reflector.

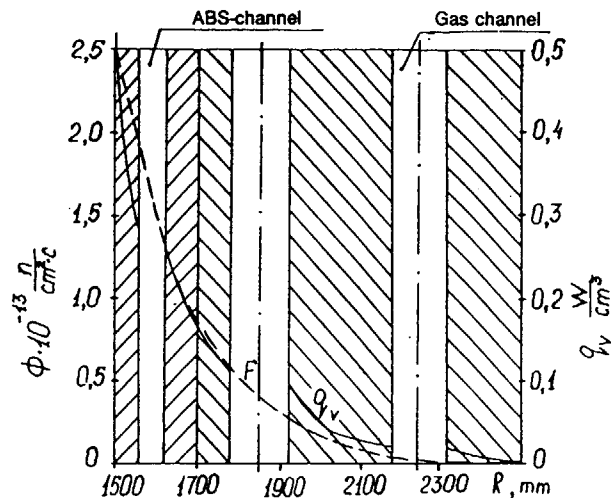


FIG. 3.4. Distribution of power density and fast neutron fluence over reflector (at the A-ray).

### 3.3. Temperature fields and thermal stresses

The temperature fields were calculated in the 2-D X-Y geometry taking into account real geometric shapes and sizes of the graphite blocks and the channels in them. The conditions of heat exchange with the core were given by the heat transfer coefficient  $\alpha_c = 2000 \text{ W/m}^2\text{K}$  and the gas temperature,  $T_c$ , in the core. The heat exchange in the channels was given by the heat-transfer coefficient  $\alpha_{ch} = 500 \text{ W/m}^2\text{K}$  (basic version), and a temperature of this gas,  $T_g$ . There was practically no heat removal on the external reflector side. The calculations were performed for various reflector height cross-sections. The distributions of power density and fast neutron fluence were taken from reactor physics calculations (Fig. 3.4).

Since the graphite heat conductivity depends strongly on temperature  $T$  and fast neutron fluence  $F$  the dependences  $\lambda(T, F)$  obtained for laboratory GR-1 samples were used. At the same time, in order to get conservative estimates, the calculations were carried out using  $\lambda = 20 \text{ W/mK}$  and taking into account the fact that F-effect is the stronger, the higher is for non-irradiated graphite.

Analysis of thermal stresses in the internal block was performed according to a specially developed code. The method of analysis is developed for a 3-D geometry taking into account the development of anisotropic radiation-induced changes and fast neutron-induced graphite radiation creep. When developing the algorithm 3-D 8-node oblique finite elements were used. The calculation region was selected taking into account symmetry conditions and was divided into three layers in height and 81 finite elements in each layer. So that an internal block got divided into 7-10 elements along the radius and 9-10 elements along the width. External load was neglected.

Estimation of the operability under thermal stress was performed according to a criterion of a "maximal tensile stress". Admissible value of this stress was assumed to be 15 MPa, i.e. it was assumed that upon achieving this value some finite element should develop cracks.

Fig. 3.5 shows temperature distributions along the radii passing through the cooling channel centres and along the lateral graphite block surfaces (rays A and B in Fig. 3.1) for two cross-sections at different heights ( $Z=2.5 \text{ m}$  and  $Z=4 \text{ m}$ ). It was assumed here that there is no heat removal from ABS-channel,  $T_g = 300^\circ\text{C}$ ,  $\lambda = 20 \text{ W/mK}$ . It is seen that the external reflector blocks are at a relatively low temperature, mainly depending on the heat exchange conditions in the channels. The internal block temperature was mainly defined by heat transfer from the core and varied considerably along the height and the radius.

In order to estimate the effect of heat removal conditions, calculations were performed for a cross-section at height  $Z = 2.5 \text{ m}$  ( $T_c = 550^\circ\text{C}$ ) with a maximal fast neutron flux at varying of heat transfer coefficient in cooling channels ( $\alpha_{ch} = 25\text{--}1000 \text{ W/m}^2\text{K}$ ) and also with a simultaneous heat removal from ABS-channel ( $\alpha_{ABS} = 200 \text{ W/m}^2\text{K}$ ,  $T_g = 500^\circ\text{C}$  and  $300^\circ\text{C}$ ). The reduction in convective heat exchange in cooling channels turned to reduce the temperature non-uniformity in the internal graphite blocks while application of cooling to ABS-channels increases it

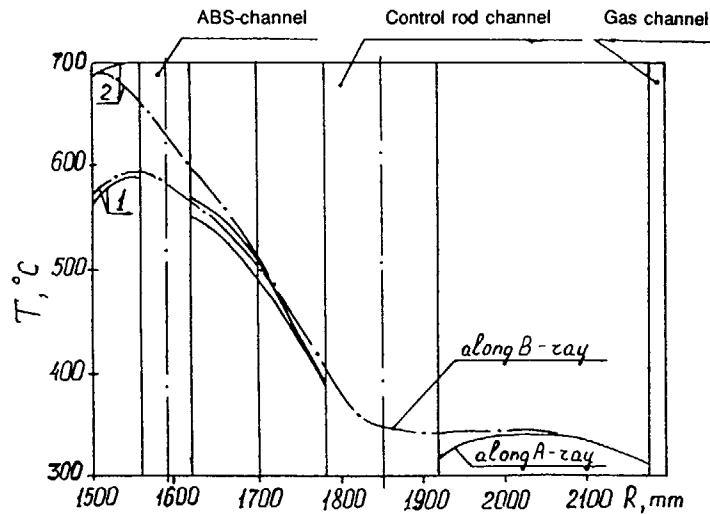


FIG. 3.5. Temperature distribution in a reflector. 1:  $Z = 2.5$  m; 2:  $Z = 4.0$  m.

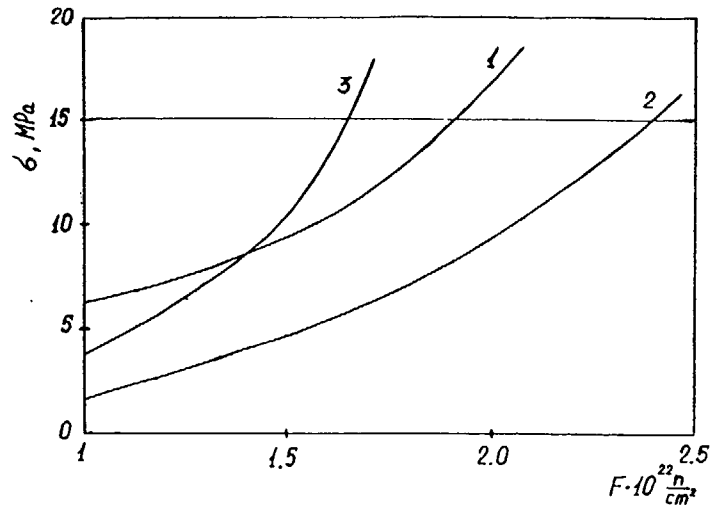


FIG. 3.6. Dependence of maximal tensile stress in the internal block on neutron fluence ( $E > 0.1$  MeV):

1.  $\alpha_{ch} = 500$  W/m<sup>2</sup>K,  $\alpha_{ABS} = 0$
2.  $\alpha_{ch} = 300$  W/m<sup>2</sup>K,  $\alpha_{ABS} = 0$
3.  $\alpha_{ch} = 300$  W/m<sup>2</sup>K,  $\alpha_{ABS} = 200$  W/m<sup>2</sup>K.

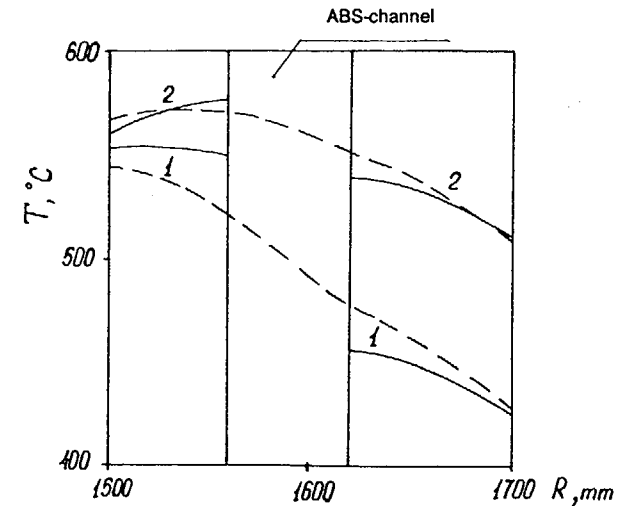


FIG. 3.7. Temperature distribution in the internal block: 1.  $\lambda = \lambda(T)$  at  $F = 0$ ; 2.  $\lambda = \lambda(T, F)$  at  $F = 2.5 \cdot 10^{22}$  n/cm<sup>2</sup>.

sharply despite some decrease in a maximal temperature value. The highest thermal load was on the area between the ABS-channel and the lateral block surface. Fig. 3.6 for  $Z = 2.5$  m shows variation of the maximum stress in the function of fast neutron fluence for various variants of heat exchange in the conservative approximation ( $\lambda = 20$  W/mK). It should be pointed out that for all variants the maximum stress developed in the same finite element. It is evident that in the above variants a required fluence of  $2.5 \times 10^{22}$  n/cm<sup>2</sup> is not achieved. A reduction in the heat removal decreases essentially the thermal stresses and increases the lifetime before cracks start to form, thus bringing the lifetime to the required level. To assess the degree of conservatism the calculations were performed for initial (before irradiation) dependence  $\lambda(T)$  and for  $\lambda(T, F)$  at a maximum fluence  $F = 2.5 \times 10^{22}$  n/cm<sup>2</sup> (Fig. 3.7). The  $\lambda$ -values for these variants for the internal graphite block lied within the range 61 to 68 W/mK and 39 to 38 W/mK, respectively. It is seen that with  $\lambda$  decreasing due to irradiation the temperature difference across the block reduces from 139° to 71°C. However, in the further  $\lambda$  reduction to 20 W/mK the temperature difference again begins to rise. Comparison of maximal thermal stress and the time of achieving the limiting values for versions with  $\lambda = 20$  W/mK and  $\lambda = 39$ -38 W/mK shows that the difference is but slight.

On the basis of the calculations performed, preliminary recommendations can be given: to reduce convective heat exchange in channels located closer to the core, and to introduce no cooling gas into

ABS-channels. It should be noted that it is necessary to perform calculations of some cross-sections in height with  $Z > 2.5$  m in which thermal stresses may be higher despite decrease in the fluency. Calculations of the  $Z = 4.0$  m cross-sections showed that a zone of stresses exceeding specified value includes a greater number of finite elements than that in a  $Z = 2.5$  m cross-section. This zone is at the same place (between the ABS-channel and the lateral block side).

### 3.4 Corrosion effect on the reflector

The oxidizing components will act most strongly on the thin-walled parts of the blocks which are at the highest temperatures, such as the inner wall of the ABS-channel (60 mm in thickness) and the passages (10 mm in thickness) between the channels to remove hot gas in the bottom reflector. The ABS-channel wall will be subject not only to radiation and corrosion but also to friction and wear due to the fuel element and absorbing ball movement. Corrosion can cause more intensive wear. No data on this effect are available; therefore we assume that the graphite layer be worn out in which corrosion-induced reduction in the density is more than 20%, which corresponds to more than 60% loss in strength of this layer.

In this case it is assumed that in the beginning the surface corrosion reaches 20%, then wear begins and the front of 20% corrosion moves deep into the wall. The value of this corrosion wear and relative reduction in the average graphite density along the direction into the bulk of the wall ( $\Delta\gamma/\gamma$ ) are assumed to be a characteristic of corrosion effect.

Corrosion calculations were performed in terms of the wear corrosion model of a flat graphite wall [3] taking into account the profile of corrosion in graphite depth is determined by a corrosion rate constant  $K_p$ , and local water pressure  $P_{H2O}$ :

$$\frac{1}{\gamma} \frac{d\gamma}{dq} = -K_p \cdot P_{H2O}; \quad K_p = K_0 \cdot \exp\left(-\frac{E}{RT}\right)$$

The adopted values  $K_0 = 26.8$  (bar.s)<sup>-1</sup> and  $E = 137000$  J/mole were obtained for one of reactor-grade graphites and did not allow for radiation effect. For a graphite temperature of 750°C and 950°C the characteristic corrosion depth at which corrosion rate is changed by a factor of  $e$  were 7 mm and 1.9 mm respectively.

The corrosion effects on the above parts of the reflector and the fuel elements were compared taking into account the 40 year service life of the reflector and the time of fuel element passage through the core. At the accepted values of the permissible degree of corrosion for these parts the values of water pressure permissible for them are comparable. However the corrosion of the passages in the bottom reflector turned out to be decisive. For this reason the thickness of the passages must be increased. After 40 years of operation under conditions with a helium temperature of 950°C the relative wear of the ABS-channel wall will be 0.3 mm/ $\mu$  bar  $H_2O$ , the relative reduction in the average density of graphite in this wall being 0.3%/ $\mu$  bar, while for the 10 mm thick passage the latter value will be 1.7%/ $\mu$  bar. In the case of the operation with a helium temperature of 750°C, these values will be 0.07%/ $\mu$  bar and

0.46%/ $\mu$  bar, respectively. These data should be taken into consideration in choosing the permissible partial pressure of water in the coolant.

The effect of radiation induced qualitative change in the graphite corrosion characteristics found recently by F.F. Zherdev and his colleagues at the I.V. Kurchatov Institute of Atomic Energy seems to be of interest and importance [4]. They investigate the interaction of graphites with water vapour in helium and showed that during reactor irradiation the corrosion rate after a small drop started to rise. This effect being stronger at lower temperatures. For B-15-grade graphite irradiated at the temperature of 500 to 700°C up to a fluence of  $1.3 \times 10^{22}$  n/cm<sup>2</sup> ( $E > 0.18$  MeV) the corrosion rate at 950°C increased almost thrice and at 750°C it increased by a factor of 400. The authors explain this phenomenon as radiation induced damage of inter-crystallite borders and growth of crystallite surface of high reactivity (perpendicular to basic planes). This effect in GR-1 graphite has not been analysed in detail. However, it has been found that in irradiated and non-irradiated samples the 1/T dependence of the reaction rate constant is not exponential but is of the S-shape character with a maximum at 900°C. It seems to be associated with specific features of GR-1 graphite structure. The influence of these factors on the reflector operability requires additional analysis.

GR-1 graphite developed for HTGR reactors meets the requirements of radiation stability for VGM reflector conditions. To improve its stability against thermal stress the further efforts are required on optimizing the design and coolant conditions of the reflector. It is also necessary to continue the analysis of GR-1 real corrosion characteristics and of corrosion effects on the reflector.

### 4. STATUS OF HTR DEVELOPMENT IN GERMANY (M. Roedig, Forschungszentrum, Juelich)

The HTR development in Germany is based on spherical fuel elements. The first experimental facility, the small prototype AVR reactor, became operational in the late sixties ( $W_{th} = 46$  MW,  $W_{el} = 15$  MW). After more than 21 years of successful operation it was shut down at the end of 1988, having produced about 1.7 TW of electricity. Based on the favourable operational experience, the THTR 300 was designed and constructed by the companies ABB and HRB. It had a power rating of 750 MW(th) providing about 300 MW(e) output. Electricity production began in 1985, and after extensive commissioning trials, the plant was handed over to the utility in 1987. Mid-1989 it was shut down, more or less for political reasons. At the present time two HTR concepts are being followed up:

- The HTR module, a small reactor (approx. 200 MW(th) with a steel pressure vessel for process heat or electricity generation, designed by the Siemens/KWU group.
- The HTR 500, a medium sized reactor (approx. 550 MW(e) with a prestressed concrete vessel for electricity generation, designed by ABB Company.

Some technical data for both reactor types are given in Table 4.1. As no project is in sight, the work for the HTR 500 has been drastically reduced. The erection of two HTR module plants in the former German

TABLE 4.1. TECHNICAL DATA FOR GERMAN HTR MODULE AND HTR 500 REACTORS

HTR 500
ELECTRIC POWER GENERATION (1390 MW(th), 550 MW(e))
PEBBLE BED CORE 7 m $\phi$ , 5.4 m IN HEIGHT
<sup>235</sup> U ENRICHMENT 9%
HELIUM INLET TEMPERATURE 260°C, OUTLET TEMPERATURE 700°C
HTR MODULE
ELECTRIC POWER (200 MW(th)) OR PROCESS HEAT (170 MW(th)) GENERATION
PEBBLE BED CORE 3 m $\phi$ , 9.4 m IN HEIGHT
<sup>235</sup> U ENRICHMENT 8 %
HELIUM INLET TEMPERATURE 250°C, OUTLET TEMPERATURE 700°C
TWO INDEPENDENT SHUT DOWN SYSTEMS IN THE REFLECTOR REGION (NO ABSORBER RODS IN THE PEBBLE BED)
LIMITATION OF MAX. FUEL TEMPERATURE IN CASE OF ACCIDENTS TO 1600°C (IN NORMAL OPERATION TO 850°C)

Democratic Republic has been under discussion. The status of the German HTR situation can be summarized as follows:

- great progress was made in technical areas,
- the German industrial effort faltered,
- the programme of the Research Center Juelich (KFA) has been funded in 1991/92 after some reductions for the 5 new German States,
- international co-operation exists with the USSR, Japan, the USA and China.

Present development goals for the HTR are given in Table 4.2.

A survey on the history of the German graphite development programme for HTR is given in Table 4.3. The present research activities are listed in Table 4.4, the programme structure is given in Table 4.5.

TABLE 4.2. DEVELOPMENT GOALS FOR THE HTA PROJECT

A. <u>Demonstration of HTR specific safety features</u>
<ul style="list-style-type: none"> <li>- Improved analysis methods</li> <li>- Validation of codes and data bases</li> <li>- Reduction of uncertainties</li> </ul>
Thermohydraulic analyses of HTR plant in normal operation and in accidents
Large scale component testing under transient conditions
Source term analysis and dose rate determination in hypothetical accidents
Improved methods for safety and risk analyses
Core heatup simulation test with irradiated fuel elements
Post-irradiation examination of AVR and THTR - documentation of operational experience
B. <u>Demonstration of safe disposal of HTR fuel</u>
Dry storage in transport casks for 40 years
Direct terminal storage without reprocessing in deep salt mines
C. <u>Materials development programme</u>
Irradiation testing of high quality TRISO fuel elements
Investigation in the effects of massive water and air ingress; feasibility studies of corrosion resistant fuel and graphite
Demonstration of graphite behaviour based on new raw materials; development of irradiation induced creep model
Process technology and demonstration programme for metals and ceramics in high temperature applications

TABLE 4.3. HISTORY OF THE GERMAN GRAPHITE DEVELOPMENT PROGRAMME

---

1960:	Reactor grade graphite must be highly purified
1973:	Studies on behaviour under fast neutrons reactor graphite should be isotropic optimization of coke base: petrol - pitch - soot - fluid - Gilsonite (THTR)
1973:	Reactor graphite should be produced from national resources coal tar pitch isotropy postulate led to - introduction of special pitch coke - development of the secondary coke technique - optimization of the pressing method: extrusion isostatic pressing densification by vibration
1977:	Irradiation testing in HFIR and HFR geared to THTR follow-up designs: HTGR 1160 HHT NPW HTR 500 MODULAR HTR  In parallel: optimization of production with respect to strength and homogeneity

---

TABLE 4.4. RESEARCH ACTIVITIES FOR GRAPHITE IN GERMANY

- 
- |     |   |
|-----|---|
| (1) | IRRADIATION DATA FOR DIFFERENT GRAPHITES<br>NEUTRON FLUENCE UP TO $4 \times 10^{22}/\text{cm}^2$ (EDN) AT TEMPERATURES 300-1100°C   |
| (2) | INFLUENCE OF PRODUCTION LOT OF A GRAPHITE TYPE<br>INFLUENCE OF INHOMOGENEITIES INFLUENCE OF A NEW COKE BASE   |
| (3) | MEASUREMENT OF DESIGN DATA:<br>INFLUENCE OF FAST NEUTRONS ON<br>- DIMENSIONAL CHANGES<br>- DENSITY<br>- YOUNG'S MODULUS<br>- THERMAL CONDUCTIVITY<br>- COEFFICIENT OF THERMAL EXPANSION |
| (4) | CREEP EXPERIMENTS<br>DIMENSIONAL CHANGES OF SPECIMENS AS A FUNCTION OF NEUTRON FLUENCE UNDER EXTERNAL LOADS (TENSION, COMPRESSION) FOR DIFFERENT TEMPERATURES                           |
| (5) | POST-IRRADIATION EXAMINATIONS OF AVR REFLECTOR  |
-

TABLE 4.5. DEVELOPMENT AND TESTING OF HTGR REACTOR GRAPHITE

Programme Structure		
Application	Side / Bottom / Top Reflector Fuel Element Matrix	
Irradiation Testing of Pilot-/Production Scale Material		
* Material Comparison		(HFIR)
Joint Experimental Programme		
* Basic Property Test Programme		(HFR)
Change of dimension, density, Young's Modulus, thermal conductivity, CTE (300-900°C)		
KFA Experimental Programme		
* Creep Test Programme		
KFA experimental programme		(HFR)
tensile load, isothermal		
Joint experimental programme		
tensile load, isothermal		(HFR)
temperature change		
load change		(HFIR/HFR)

#### 5. GRAPHITE DEVELOPMENT FOR GAS COOLED REACTORS IN THE USA (Timothy D. Burchell, Oak Ridge National Lab., Oak Ridge, USA)

The research on graphite is sponsored by the Division of MHTGRs, Office of Advanced Reactor Programs, US Department of Energy, under contract with Martin Marietta Energy Systems, Inc.

Modular High Temperature Gas Cooled Reactor (MHTGR) graphite activities in the USA currently include the following research and development tasks: coke examination; effects of irradiation; variability of physical properties (mechanical, thermal-physical, and fracture); fatigue behaviour, oxidation behaviour; NDE techniques; structural design criteria; and carbon-carbon composite control rod clad materials. These tasks support nuclear grade graphite manufacturing technology including nondestructive examination of billets and components. Moreover, data shall be furnished to support design and licensing of the graphite components for the MHTGR.

The coke examination subtask involves examination of the structure and properties of selected isotropic cokes and the graphites manufactured from them. Correlations will be established between coke properties and graphite irradiation performance. It is anticipated that this work will guide the selection of cokes for future production of nuclear grade graphites in the USA.

Graphite is an inherently variable material. Consequently, activities are in hand to characterize the variations of mechanical, thermal-physical, and fracture properties, both within and between billets of graphite. Moreover, the fatigue behaviour of candidate graphites is being elucidated. These activities are summarized below.

Graphite Physical Property Data to be Acquired by the US MHTGR Program:

- Thermal conductivity
- Coefficient of thermal expansion
- Strengths
  - Tensile
  - Flexural
  - Compressive
- Strain to failure
- Elastic constants
- Fracture toughness,  $K_{Ic}$
- Strain energy release rate,  $G_{Ic}$
- Constant life fatigue diagrams
- Fatigue strength
- Minor law verification.

Graphite oxidation behaviour must be quantified for design and life prediction purposes. Required data include air and steam oxidation kinetics and oscillation-depth profiles. The effect of oxidative weight loss on the physical properties must additionally be determined.

The Oak Ridge National Laboratory (ORNL) is working to provide experimental data on the multiaxial stress analysis and structural design criteria. Moreover, this work will be utilized in the preparation of the subsection of the ASME boiler and pressure vessel code for HTGR graphite core support structures. Efforts are also being directed toward developing non-destructive examination techniques for graphite core components. These include Eddy-current methods for detecting surface breaking flaws in the core support posts and fuel-element, fuel-coolant channel webs, and ultrasonic techniques for billet screening prior to component machining.

Carbon-carbon composite materials are being evaluated for application as a high-temperature control rod clad material. A carbon-carbon composite element has been designed and will be tested to demonstrate the feasibility of the product form. A full database for the selected carbon-carbon composite material will be acquired for component design purposes. Data are required for the mechanical, thermal-physical, and fracture properties. Moreover, the effects of neutron damage and oxidation on properties will be determined.

Irradiation experiments are being conducted to increase the current database on the effect of neutron damage on graphite properties. Increased

effort is being directed toward conducting graphite irradiation creep experiments.

Several research and development areas continue to give cause for concern to the US MHTGR graphite programme. These are: (i) repeatability of graphite material, i.e., assuring continued graphite availability and materials properties when sources of feedstock materials have to be changed; (ii) developing a graphite failure criteria which may be applied for design purposes; (iii) quantifying the effects of oxidation on graphite physical properties; and (iv) expanding the current database on irradiation induced creep of graphites. These areas of concern are currently being addressed through the US MHTGR graphite technology development programme at ORNL.

#### 6. THE CURRENT SITUATION REGARDING NUCLEAR POWER AND GRAPHITE RESEARCH IN THE UNITED KINGDOM (J. Wilson, AEA Technology, Harwell Laboratory, United Kingdom)

The United Kingdom generates about 15% of its electricity supply from nuclear power, all, except a small proportion, from carbon dioxide cooled graphite moderated reactors of two types:

(a) The so-called Magnox reactors - a series of evolving reactor designs based on the original "Calder Hall" design, using natural uranium clad with Magnox alloy in a moderator using needle coke graphites.

(b) The advanced gas cooled reactors (AGRs), based on the original Windscale AGR design using enriched uranium oxide fuel clad in stainless steel in a moderator using isotropic graphite based on gilsonite coke. A total of seven AGR twin reactor stations have been completed and are operating, the last two stations Heysham II and Torness as recently as 1988.

It is not expected that any further graphite moderated reactors will be built. Currently only one nuclear power station is under construction, a pressurised water reactor at Sizewell on the same site as a Magnox twin reactor station. Planning permission exists to build a second PWR at Hinkley Point, but the United Kingdom Government intends to review the future of nuclear power in 1994.

The further development of nuclear power in the United Kingdom must be seen against great changes in the structure of the electricity generating industry in the United Kingdom. A few years ago generation was provided by a small number of publicly (eg Government) owned Generating Boards, two of which operated nuclear power stations, the Central Electricity Generating Board (CEGB) and the South of Scotland Electricity Board (SSEB). The United Kingdom Government, following its philosophy of putting previously state-owned industries into private hands decided to break the existing Boards into smaller units and sell them. It proved impossible to persuade the market to purchase nuclear stations and these were eventually separated from the others and two state-owned nuclear companies formed - Nuclear Electric and Scottish Nuclear with a requirement to produce power as cheaply as possible which has led to a very substantial reduction in R/D on the two main reactor types.

At the same time the Government owned United Kingdom Atomic Energy Authority which had previously carried out most of the research for nuclear power in the United Kingdom (fission and fusion) (CEGB had also a significant research arm) was required to become a contract research organization (AE Technology) and, as a result, was split into 10 separate businesses. It proved impossible to continue to operate the two Material Testing Reactors DIDO and PLUTO and the graphite irradiation experiments were terminated. At the same time, the government funding for fast reactors and fusion was sharply reduced with both national programmes seen to terminate in the mid 1990s. AEAT's graphite research now concentrates on the analysis of graphite core behaviour in the gas-cooled Reactor Assessment Department of the Safety and Performance Division at Risley. Limited work is carried out under contract to NE/SN on core brick failure modelling, but the materials teams have been distributed.

Nuclear power, in part due to the United Kingdom's financial structures, is currently seen to be expensive, as well as not popular with the general public. The building of new power stations depends upon the Government review in 1994 and is likely to concern only the possibility of further PWR's (fast reactors are not seen as viable for 30-40 years and fusion further still in the future). Two of our three political parties (Labour Party and Social Democrats) are committed to not building further nuclear power stations.

The consequences for graphite research are:

- (1) No new data will be generated except for the special monitoring samples removed from each reactor.
- (2) A strong emphasis is placed on the expected life of the reactor moderators and what it is determined by. Possibilities are:
  - (a) Excessive weight loss due to radiolytic oxidation;
  - (b) Numbers of cracked core bricks;
  - (c) Bore distortion.

The designed life is 25 full power years corresponding to  $1.5 \times 10^{22}$  n.cm<sup>-2</sup> (EDN),  $55 \times 10^3$  wh.g<sup>-1</sup> energy deposition.

A considerable effort is being devoted to these aspects. Recent experimental studies have shown that our calculational methods are quite good up to  $1 \times 10^{22}$  n.cm<sup>-2</sup> (EDN) but that for higher doses the interaction which occurs between radiation damage and radiolytic oxidation is significant and difficult to model introducing considerable increases in uncertainty.

#### 7. GRAPHITE RESEARCH IN FRANCE (M. Brié, Commissariat à l'Energie Atomique, Paris, France)

The studies jointly defined by CEA and EDF to meet safety authorities requirements are maintained for the surveillance of both gas cooled reactors, SAINT LAURENT A2 and BUGEY 1, still in operation. The six other gas cooled reactors are shut down.

With regard, more particularly, to the BUGEY 1 reactor, the aim of these studies is to forecast as a function of time the mechanical behaviour



of the most corroded areas of the moderator. These studies are based, on the one hand, on the examinations and measures of the evolution of graphite physical characteristics of the most sensitive areas; on the other hand, the behaviour of these parts, by means of both calculation codes : "USURE" code is a calculation of radiolytic corrosion rate as a function of lifetime of the reactor and "INCA" code is a thermomechanical calculation allowing to forecast the mechanical behaviour of graphite block as a function of time.

The shutdown of these reactors is scheduled for June 1992 for SAINT LAURENT A2 and April 1994 for BUGEY 1.

The consequence of this decision is the stop of the manufacture activity of BUGEY 1 fuel element take into account of present stock; as well as the control activity of these fuel elements in great part managed by the CEA.

In the field of thermonuclear fusion reactor and in the framework of the "Next European Torus" programme, it must be pointed out that irradiation tests were carried out in PETTEN and PHENIX reactors in order to determine the variation of thermal and mechanical properties of some graphite. The aim of these studies is to select these materials for the components of the first limiters and divertors of TOKAMAK reactors.

Since 1979, there has been no development and research programme at the CEA in the field of high temperature reactor. However, the CEA is still interested in the MHTGR and makes its own assessment of concepts developed abroad, such as the MHTGR.

It must be pointed out that France participates in the study carried out by Martin Marietta Energy Systems (ORNL, USA) on the migration of fission products. The tests for this study are conducted in the COMEDIE loop in operation in the SILOE reactor at Grenoble.

#### REFERENCES

- [1] Ponomares-Stepnoy, N.N., et. al., Development prospects of high temperature gas-cooled reactors and the role in nuclear power, 11th International Conference on HTGRs, June 19-20, 1989.
- [2] Platonov, P.A., Shtrombakh, Ya.I., Karpukhin, V.I., Alekseev, V.M., Guovich, B.A., Chugnov, O.K. Influence of radiation on HTGR graphite properties. Report to the Soviet-German seminar. "HTGR fuel element and graphite", Moscow, 1990.
- [3] Mosevitskij, I.S., Djakov, A.V., Problems of investigation of HTGR fuel elements under loss-of-pressure accident conditions. IAEA Specialists Meeting on Behaviour of Gas-Cooled Reactor Fuel under Accident Conditions, 5-8 November, 1990, Oak Ridge, USA.
- [4] Zherdev, F.F., Komissarov, I.E., Kuzmichev, V.A., Gurovich, B.A., Effect of neutron radiation on kinetics of reactor graphite corrosion. Report to the Soviet-German seminar "HTGR fuel element and graphite", Juelich, 1991.

#### DISCUSSION

##### Questions or Comments on Japanese Programme

Name: Dr. T. Burchell

What process heat utilization system do you envisage for the HTTR?

Answer:

Although the hydrogen productions by water splitting with thermechemical method and also by high-temperature electrolysis of steam have been studied for long time in the JAERI, we have not succeeded in developing large scaled system enough to be connected to the HTTR. Then, probably we will select a steam reformer to produce hydrogen and methanol as the first system for the HTTR.

##### Questions or Comments on Russian Programme

Name: T. Oku

Could you give some more information on GR-1, GR-280 and B-15 graphites?

Answer:

The first paper of session III-A (Manufacture of HTGR Core Components by Methods of Volume-Gas Phase Impregnation of Porous Media with Pyrocarbon) will give the answer.

##### Questions or Comments on US Programme

Name: S. Shiozawa

How idea or plan for in-service NDT of core support structures such as core support posts?

Answer:

A two level NDE system is envisaged:

- (i) visual inspection using video camaras
- (ii) Eddy current based, non-contacting, NDE system remotely operated. These two systems will allow for TST. In addition the core support posts are designed to be removable. Thus, core support posts could, if required, be removed via the refueling machine.

##### Questions or Comments on US Programme

Name: S. Saito

Are you considering to use different graphites for civilian MHTGR from those for NPR?

Answer:

The civilian MHTGR and NPR MHTGR are expected to use the same grades of nuclear graphites.

Questions or Comments on US Programme

Name: J. Wilson

Could Dr. Burchell explain why the control rod temperatures are as high as 1600°C.

Answer:

Dr. Burchell replied that these temperatures were reached under fault conditions where cooling of the core was by radial conduction.

Questions or Comments on US Programme

Name: M. Brié

In which experimental reactor are carried out your tests under irradiation?

Answer:

The following materials test reactors will be utilized:

High Flux Isotope Reactor (HFIR) at ORNL, USA.

Bulk Shielding Reactor (BSR) at ORNL, USA.

University of Buffalo MRT, New York State USA.

Ford Nuclear Reactor, University of Michigan, USA.

Collaborative Experiments are being performed at JAERI using JMTR and with the KFA using HFR at Petten.

**DESIGN CRITERIA, FRACTURE MECHANISMS  
AND COMPONENT TESTS**

**Part A**

**(Session II)**

**Chairmen**

**M. BRIÉ**

France

**S. SATO**

Japan



# A MICROSTRUCTURALLY BASED FRACTURE MODEL FOR NUCLEAR GRAPHITE\*

T.D. BURCHELL

Oak Ridge National Laboratory,  
Oak Ridge, Tennessee,  
United States of America

## Abstract

This paper reports the physical basis of, and assumptions behind, a fracture model for nuclear graphites. Microstructurally related inputs, such as filler particle size, filler particle fracture toughness ( $K_{IC}$ ), density, pore size distribution, number of pores and specimen geometry (size and volume), are utilized in the model. The model has been applied to two graphites, Great Lakes Carbon Corporation grade H-451 and Toyo Tanso grade IG-110. For each graphite, the predicted tensile failure probabilities are compared with experimental data generated using ASTM Standard C-749 tensile test specimens. The predicted failure probabilities are in close agreement with the experimental data, particularly in the case of the H-451. The model is also shown to qualitatively predict the influence on the failure probabilities of changes in filler particle size, density, pore size, pore size distribution, number of pores and specimen geometry (stressed volume). The good performance is attributed to the sound physical basis of the model, which recognizes the dominant role of porosity in controlling crack initiation and propagation during graphite fracture.

## 1.0 INTRODUCTION

Gas-cooled reactors such as the U.S. designed Modular High-Temperature Gas-Cooled Reactor (MHTGR), and the Japanese High Temperature Test Reactor (HTTR), use near-isotropic or isotropic grade graphites as the nuclear moderator and for the major core structural components. During operation the reactor core graphite is subject to complex stresses, such as thermal stresses and stresses caused by neutron-damage induced dimensional changes. Moreover, seismic and static forces act on the graphite core components. These stresses acting singularly or in combination should not be sufficient to cause failure of the graphite core components. Consequently accurate predictions of core brick stresses are of key importance. However, if safety margins are to be demonstrated, a credible and acceptable failure criteria for graphite must be available, against which the probability of failure can be accurately predicted.

---

\* Research sponsored by the Division of MHTGRs, Office of Advanced Reactor Programs, US Department of Energy, under contract DE-AC05-84OR21400 with Martin Marietta Energy Systems, Inc.

In their review of fracture in graphite, Tucker, Rose and Burchell<sup>1</sup> assessed the performance of several failure theories when applied to graphite. These theories included the Weibull theory, the Rose-Tucker model, Fracture Mechanics, Critical Strain Energy, Critical Stress and Critical Strain Theories. While no single criteria could satisfactorily account for all the situations they examined, their review showed that a combination of the fracture mechanics and a microstructurally based fracture criteria might offer the most versatile approach to modelling fracture in graphite.

This paper gives a full account of a model which combines a fracture mechanics failure criteria and a microstructurally based description of graphite failure. The physical basis and assumptions behind the model are reported and the necessary microstructural inputs for the model are discussed. The model predictions are compared with experimental tensile strength data for two nuclear grade graphites. The performance of the model in predicting the influence of changes in microstructural features on the failure probability is discussed.

## 2.0 THE MECHANISM OF FRACTURE IN GRAPHITE

A microstructural study of fracture in graphite<sup>2</sup> has revealed the manner in which certain microstructural features influence the process of crack initiation and propagation in nuclear graphites; the principal observations are summarized below.

### 2.1 POROSITY

Two important roles of porosity in the fracture process have been identified. Firstly, the interaction between the applied stress field and the pores will cause localized stress intensification, promoting crack initiation from favorably oriented pores at low applied stresses. Secondly, propagating cracks can be drawn toward pores in their vicinity, presumably under the influence of the stress field around the pore. In some instances such pore/crack encounters serve to accelerate crack growth; however, occasionally a crack will be arrested by a pore, and does not break free until higher applied stresses are attained. Pores of many shapes and sizes are observed in the microstructure of a graphite. The larger, more slit-shaped pores being more damaging to the graphite.

## 2.2 THE BINDER PHASE

Two arbitrarily defined types of microstructure can be identified in the binder phase: (i) domains, which are regions of common basal plane alignment extending over linear dimensions greater than  $100\mu\text{m}$ , and (ii) mosaics, which are regions of small randomly-oriented pseudo-crystallites with linear dimensions of common basal plane orientation of less than about  $10\mu\text{m}$ . Cleavage of domains can occur at stresses well below the fracture stress, and such regions can act as sites for crack initiation, particularly when in the vicinity of pores. Fracture of mosaic regions is usually only observed at stresses close to the fracture stress. At lower stresses, propagating cracks which encounter such regions are arrested or deflected.

## 2.3 FILLER PARTICLES

Coke filler particles with good basal plane alignment are highly susceptible to microcracking along basal planes at low stresses. This cleavage is facilitated by the needle-like cracks which lie parallel to the basal planes, and are formed by anisotropic contraction of the filler-coke particles during the calcination process. Frequently, when a crack propagating through the binder phase encounters a well aligned filler particle, it takes advantage of the easy cleavage path and propagates through the particle. However, the reverse process, i.e., propagation of a crack initiated in the filler particle into the binder phase, was much less commonly observed.

## 2.4 FRACTURE MECHANISM

Based on the forgoing discussion of graphite fracture processes, it is evident that the microstructure plays a dominant role in controlling the fracture behavior of the material. Therefore, any new fracture model should attempt to capture the essence of the microstructural processes influencing fracture. Particularly, a fracture model should embody the following: (i) the distribution of pore sizes; (ii) the initiation of cracks from stress raising pores, and (iii) the propagation of cracks to a critical length prior to catastrophic failure of the graphite (i.e., subcritical growth). The fracture model<sup>3</sup> presented here recognizes these aspect of graphite fracture, and applies a fracture mechanics criteria to describe steps (ii) and (iii) above.

## 3.0 THE FRACTURE MODEL

### 3.1 MODELLING THE GRAPHITE MICROSTRUCTURE

The microstructure of graphite is considered to be comprised of an array of cubic particles, each particle being equal to the mean filler particle size ( $a$ ). Each of these particles is assumed to contain a plane of weakness oriented at some angle  $\theta$  to the applied stress (Fig. 1). Moreover, pores are randomly scattered about the microstructure, their size (cross-section) being log-normally distributed.

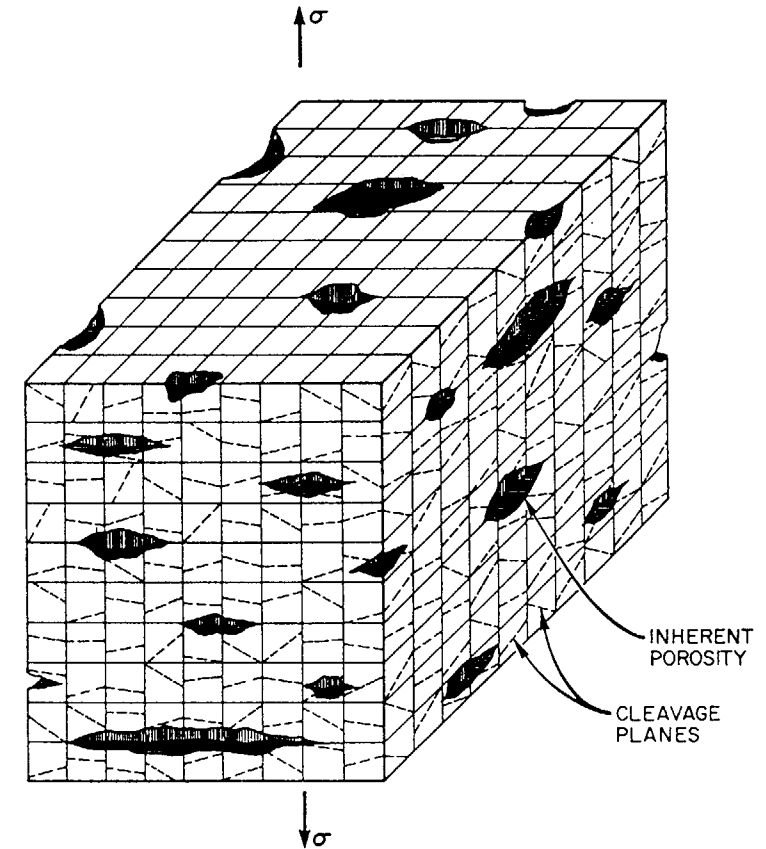


Figure 1. Graphite Microstructure as Conceived in the Fracture Model

Such pores have a stress intensification factor ( $K_i$ ) associated with them, which is quantifiable in terms of the applied stress and the pore half length  $c$  according to the principles of linear elastic fracture mechanics (LEFM). Cracks are considered to initiate from these pores, and propagate by fracturing along the planes of weakness in the cubic particles of the graphite.

A fracture mechanics criteria is developed to determine if fracture will occur on such planes in the vicinity of pores. A critical stress intensity factor ( $K_{Ic}$ ) is ascribed to the particles, and when this is exceeded by the stress intensity factor ( $K_I$ ) on the plane of weakness ( $K_I$  is a function of  $K_i$  and  $\theta$ ) the particle is deemed to have failed. The initiating pore will then have grown from its original length  $c$  to  $c+a$ , where  $a$  is the particle size. In three dimensions the probability  $P(n)$  that the crack will traverse all  $n$  of the particles in the row ahead of it is  $P(n)=P(i)^n$ . The probability  $P(f)$  that the defect  $c$  will grow to length  $c+ia$ , fracturing  $i$  rows of particles may then be determined. Failure of the graphite is deemed to occur when the stress intensity factor ( $K_i$ ) associated with the propagating defect,  $c+ia$ , exceeds a critical value which is related to the particle  $K_{Ic}$ . Moreover, there is a finite probability that the initiating defect (pore) exists, which is calculable from the pore size distribution. These two probabilities may be combined to determine the failure probability. The total failure probability that an inherent defect will initiate a crack which propagates to cause fracture, which is a function of the number of pores in the specimen and their size distribution, may then be defined for any applied stress.

### 3.2 A FRACTURE CRITERION FOR PARTICLES IN THE GRAPHITE MICROSTRUCTURE

The stress  $\sigma'_{yy}$  perpendicular to a plane  $x'$  at angle  $\theta$  to the  $x$ -axis at a point distance  $r$  from a crack tip (Fig. 2) may be written as:

$$\sigma'_{yy} = \frac{K_i}{\sqrt{(2\pi r)}} \cos^3\left(\frac{\theta}{2}\right) \quad (1)$$

where  $K_i$  is the stress intensity factor of the crack length  $2c$  under applies stress  $\sigma$ . The stress  $\sigma'_{yy}$  may also be defined in terms of the stress intensity factor  $K_I$  of the plane  $x'$  at angle  $\theta$  from  $x$ :

$$\sigma'_{yy} = \frac{K_I}{\sqrt{(2\pi r)}} \quad (2)$$

where

$$K_I = K_i \cos^3\left(\frac{\theta}{2}\right) \quad (3)$$

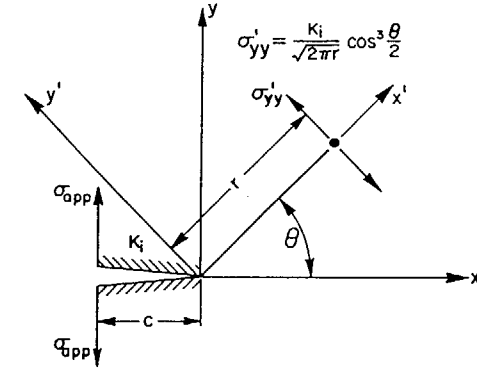


Figure 2. The Stress  $\sigma'_{yy}$  acting on a point distance  $r$  along a plane  $x'$  rotated through angle  $\theta$  from the plane  $x$ .

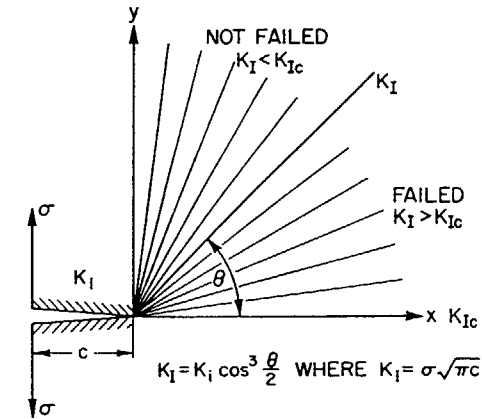


Figure 3. Schematic illustration of the failure criterion.

At the moment of particle failure

$$K_I = K_{Ic} \cos^3 \left( \frac{\theta}{2} \right) = K_{Ic} \quad (4)$$

where  $K_{Ic}$  is the critical stress intensity factor associated with fracture of the graphite particles. A criterion for the fracture of the particles may thus be defined. When  $K_I$  of a plane at angle  $\theta$  (which is a function of the  $K_I$  associated with the defect length  $c$ ) exceeds  $K_{Ic}$  then all of the planes at angle less than  $\theta$  may be assumed to have failed (Fig. 3). From equation (4), at fracture,

$$\left( \frac{K_{Ic}}{K_I} \right) = \cos^3 \left( \frac{\theta}{2} \right) \quad (5)$$

thus,

$$\theta = 2 \cos^{-1} \left( \frac{K_{Ic}}{K_I} \right)^{1/3} \quad (6)$$

For crack in tension,  $K_I$  is defined as

$$K_I = \sigma_{app} \sqrt{\pi c} \quad (7)$$

substituting equation (7) in equation (6) we get

$$\theta = 2 \cos^{-1} \left[ \frac{K_{Ic}}{\sigma_{app} \sqrt{\pi c}} \right]^{1/3} \quad (8)$$

From equation (8) above we see that  $\theta$  is a function of the applied stress,  $\sigma_{app}$ , and the crack half length  $c$ . Figure 4 shows a crack of half length  $c$  under applied stress  $\sigma$ . The crack front abuts a row of  $n$  particles, where  $n=b/a$ , and  $b$  is the breadth of the specimen. For a given  $\sigma$  and  $c$  the angle  $\theta$  below which a particle may be assumed to have failed is given by equation (8). For simplicity the orientation of these planes about the  $z$  axis is considered to be uniform. Therefore, the fraction of the particle that is potentially fractured is given by  $2\theta/180^\circ$  or  $2\theta/\pi$ . This is also the probability,  $P_i$ , that the particle has failed. Thus we may write:

$$P_i = \frac{2\theta}{\pi} \quad (9)$$

Substituting for  $\theta$  from equation (6):

$$P_i = \frac{4}{\pi} \cos^{-1} \left( \frac{K_{Ic}}{K_I} \right)^{1/3} \quad (10)$$

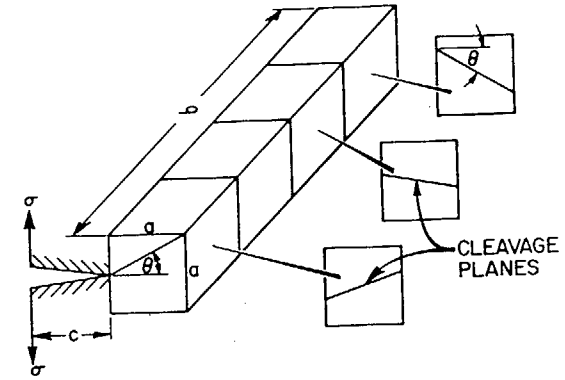


Figure 4. A row of graphite particles ahead of a crack length  $c$  and breadth  $b$ .

The limits of probability of particle failure may now be defined:

$$(a) \quad P_i = 0$$

i.e., the particle cannot fail, this occurs when  $K_I \leq K_{Ic}$ .

$$(b) \quad P_i = 1$$

i.e., particle cleavage is certain to occur. This happens when:

$$P_i = 1 = \frac{4}{\pi} \cos^{-1} \left( \frac{K_{Ic}}{K_I} \right)^{1/3} \quad (11)$$

that is when

$$\left( \frac{K_{Ic}}{K_I} \right)^{1/3} = \cos \left( \frac{\pi}{4} \right) = \frac{1}{\sqrt{2}} \quad (12)$$

or

$$\left( \frac{K_{Ic}}{K_I} \right) = \left( \frac{1}{\sqrt{2}} \right)^3 = \frac{1}{2\sqrt{2}} \quad (13)$$

Hence, when  $K_I \geq 2\sqrt{2}K_{Ic}$  a particle ahead of the crack front is certain to fracture.



$$(c) \quad 0 \leq P_i \leq 1$$

This corresponds to the condition  $K_{Ic} \leq K_i \leq 2\sqrt{2}K_{Ic}$  when the probability of a particle failing in the row ahead of the crack front is given by equation (10).

### 3.3 DEFINING THE PROBABILITY THAT FAILURE WILL OCCUR FROM A PORE OF HALF LENGTH $c$

Equation (9) gives the probability that one particle has fractured. However there are  $n=b/a$  particles in the entire row, therefore:

$$P(n) = (P_i)^n = \left( \frac{2\theta}{\pi} \right)^{b/a} \quad (14)$$

now substituting for  $\theta$  from equation (8)

$$P(n) = \left[ \frac{4}{\pi} \cos^{-1} \left( \frac{K_{Ic}}{\sigma_{app} \sqrt{\pi c}} \right)^{1/3} \right]^{b/a} \quad (15)$$

This is the probability that the initial pore of length  $c$  will grow from length  $c$  to length  $c+a$ , where  $a$  is the particle size, by fracturing all  $n$  particles. Similarly, the probability that the crack will grow from length  $c+a$  to length  $c+2a$  is:

$$P(n) = \left[ \frac{4}{\pi} \cos^{-1} \left( \frac{K_{Ic}}{\sigma \sqrt{\pi (c+a)}} \right)^{1/3} \right]^{b/a} \quad (16)$$

Because the crack must extend from  $c$  to  $c+a$  before it can extend from  $c+a$  to  $c+2a$ , the probability that the crack will grow from  $c$  to  $c+2a$  is given by the product of equations (15) and (16). Thus, the probability that the crack will grow from  $c$  to  $c+ia$ , fracturing  $i$  rows of particles can be written as:

$$P(n) = \prod_{i=0}^i \left[ \frac{4}{\pi} \cos^{-1} \left( \frac{K_{Ic}}{\sigma \sqrt{\pi (c+ia)}} \right)^{1/3} \right]^{b/a} \quad (17)$$

taking logarithms

$$\ln P_f = \frac{b}{a} \sum_{i=0}^i \ln \left[ \frac{4}{\pi} \cos^{-1} \left( \frac{K_{Ic}}{\sigma \sqrt{\pi (c+ia)}} \right)^{1/3} \right] \quad (18)$$

which may be approximated to

$$\ln P_f = \frac{b}{a} \int_0^i \ln \left[ \frac{4}{\pi} \cos^{-1} \left( \frac{K_{Ic}}{\sigma \sqrt{\pi (c+ia)}} \right)^{1/3} \right] di \quad (19)$$

This is the probability that failure will occur due to the propagation of one tip of the initial defect  $c$  under stress  $\sigma$ , where  $K_{Ic}$  is the critical stress intensity factor of the filler particle and  $a$  is the filler particle size.

### 3.4 DEFINING THE TOTAL PROBABILITY OF FAILURE FOR THE GRAPHITE SPECIMEN

The graphite microstructure is assumed to contain a log-normal distribution of pores. In these circumstances, for a specific defect, the probability that its length falls between  $c$  and  $c+dc$  is  $f(c)dc$ , with  $f(c)$  defined as:

$$f(c) = \text{Constant} \times \exp \left[ -\frac{1}{2} \left( \frac{\ln 2c - \ln S_0}{\ln S_d} \right)^2 \right] \quad (20)$$

Where  $S_0$  is the mean pore size and  $S_d$  is a constant reflecting the spread of the distribution. The probability that one tip of a single defect will cause failure under applied stress  $\sigma$  may now be defined from equations (19) and (20) as:

$$\int_0^\infty f(c) \cdot P_f(\sigma, c) dc \quad (21)$$

However there are  $NV$  such defects in the specimen, where  $N$  is the number of pores per unit volume and  $V$  is the specimen volume. Each has a survival probability of one minus its failure probability, i.e.,

$$P_s = 1 - \int_0^\infty f(c) \cdot P_f(\sigma, c) dc \quad (22)$$

The total survival probability of the volume  $V$  under stress  $\sigma$ , containing  $2NV$  crack tips, is thus  $(P_s)^{2NV}$ , and the total probability of failure of the specimen or stressed volume may be written as:

$$P_{tot} = 1 - (P_s)^{2NV} = 1 - \left[ 1 - \int_0^\infty f(c) \cdot P_f(\sigma, c) dc \right]^{2NV} \quad (23)$$

#### 4.0 FRACTURE MODEL PERFORMANCE

##### 4.1 INPUT PARAMETERS

The following input parameters are required to code the model:

Particle Critical Stress Intensity Factor,  $K_{Ic}$  ( $\text{MN}\cdot\text{m}^{-3/2}$ )  
 Mean Filler Particle Size,  $a$  (m)  
 Mean Pore Size (log-normal distribution),  $S_o$  (m)  
 Standard Deviation (log-normal distribution),  $S_d$   
 Density,  $p$  ( $\text{g}/\text{cm}^3$ )  
 Number of Pores per Unit Volume,  $N$  ( $\text{m}^{-3}$ )  
 Stressed Volume,  $V$  ( $\text{m}^3$ )  
 Specimen Breadth,  $b$  (m).

The values used for the two graphites modelled in this work are given in Table 1.

Details of the mean filler particle and pore sizes have been obtained for IG-110 from various sources.<sup>4,5</sup> For H-451, the data are experimental measurements. The particle  $K_{Ic}$  is taken as one tenth of the graphites bulk  $K_{Ic}$  as reported by Romanoski and Burchell.<sup>6</sup> The ratio  $K_{Ic}$  (bulk) to  $K_{Ic}$  (particle) was arbitrarily chosen as 10. However, particle fracture will occur along the weak planes between the crystallographic  $a$  planes. Consequently, a reduced  $K_{Ic}$  would be anticipated for such a fracture process. Moreover,  $K_{Ic}$  has been shown to reduce with volume<sup>6</sup> and the particle volume much less than that of the fracture mechanics specimens that would typically be used to determine bulk  $K_{Ic}$ . The stressed volume is taken to be the volume of graphite within the gauge length of the tensile specimens modelled (ASTM C749, type 113).<sup>7</sup> Further details of the specimen geometry are given by Strizak.<sup>8</sup>

The specimen breadth is taken as the dimensions of a square with the same cross-sectional area as the cylindrical ASTM tensile specimens. The number of pores per unit volume ( $N$ ) is calculated as follows:

$$N = \frac{4F}{S_o^2 \pi} \quad (24)$$

where

$$F = \frac{2.26 - p}{2.26} \quad (25)$$

and where  $p$  is the graphite bulk density and  $2.26 \text{ g}/\text{cm}^3$  is the theoretical crystal density. There are

Table 1. Model Input Parameters for Grade H-451 and IG-110 Graphites

Model Input Parameters	Grade H-451	Grade IG-110
Particle $K_{Ic}$ ( $\text{MN}\cdot\text{m}^{-3/2}$ )	0.135	0.098
Mean Part. Size, $a$ (mm)	0.50	0.020
Density, $p$ ( $\text{g}/\text{cm}^3$ )	1.79	1.75
Mean Pore Size, $S_o$ ( $\mu\text{m}$ )	4.1	3.6
Standard Dev., $S_d$	1.75	1.66
No. Pores per $\text{m}^3$ , $N$ ( $\text{m}^{-3}$ )	$1.58 \times 10^{10}$	$2.19 \times 10^{10}$
Specimen Volume, $V$ ( $\text{m}^3$ )	$3.17 \times 10^{-6}$	$3.17 \times 10^{-6}$
Specimen Breadth, $b$ (mm)	8.44	8.44

certain assumptions inherent in this approach to calculating  $N$ . Firstly, it is assumed that all pores are spherical and of the same size (given by the mean of the pore-size distribution). Secondly, it is assumed that the fractional pore area (as observed from a metallographic section) equals the bulk pore volume as calculated above. These stereographic assumptions may be valid for an ideal system containing randomly distributed spherical pores of identical size, but unfortunately graphite is far from ideal in this respect.

##### 4.2 COMPARISONS OF MODEL PREDICTIONS AND EXPERIMENTAL DATA

Experimental strength data were taken for two nuclear graphites, Great Lakes Carbon Corporation grade H-451 and Toyo Tanso Company grade IG-110, using ASTM C749 type 113 tensile specimens. For each material the model was coded with the input parameters shown in Table 1. The predicted failure probabilities are compared with the experimental data in Figs. 5 and 6. In the case of H-451 (Fig. 5) the prediction of the failure probability distribution is excellent. The very close agreement of the predicted and experimental mean (50% failure probability) tensile strength of the graphite is particularly encouraging. Moreover, the shape of the distribution is correctly predicted for this graphite grade. However, the agreement between experimental data and model prediction is less good in the case of IG-110 graphite (Fig. 6). This is perhaps evidence that the failure mechanism assumed in the model is less applicable to fine grained graphites such as IG-110. Indeed, it has been shown that fine-grained graphites exhibit much less sub-critical cracking, or process-zone activity

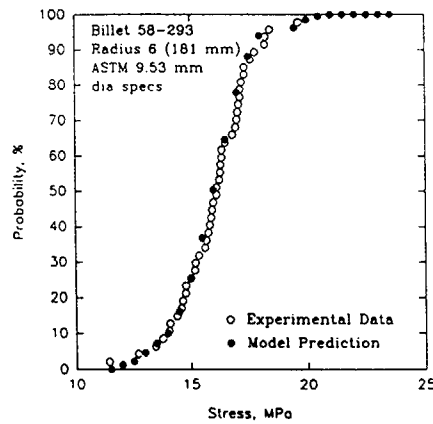


Figure 5. Comparison of predicted and experimental failure probabilities for grade H-451 graphite.

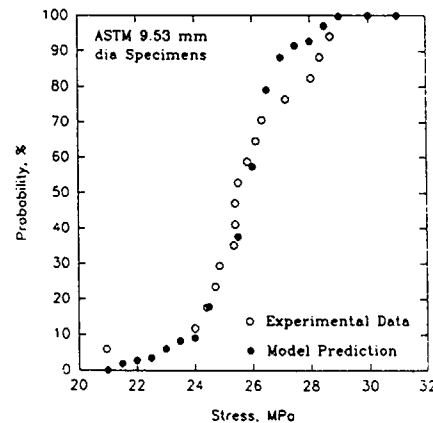


Figure 6. Comparison of predicted and experimental failure probabilities for grade IG-110 graphite.

during fracture than do coarser-grained graphites.<sup>2</sup> Quantitatively, this is shown by the lower bulk  $K_{Ic}$  of IG-110 compared with that of H-451.<sup>6</sup> Despite the poorer performance in the latter case, the model does display considerable versatility in being able to predict the behavior of two graphites with significantly different microstructures.

#### 4.3 THE INFLUENCE OF INPUT PARAMETER VARIATION ON MODEL PERFORMANCE

To assess the physical soundness of the fracture model a series of cases were run using the H-451 ASTM type 113 as the base case. In each set of model cases, one of the input parameters was systematically varied, while the other parameters were held constant. The model inputs can be categorized into three general groups: (i) particle related ( $K_{Ic}$  and  $a$ ), (ii) porosity related input parameters ( $p$ ,  $S_o$ ,  $S_d$  and  $N$ ), and (iii) specimen geometry related parameters ( $V$  and  $b$ ). The model response to variations of input parameters in each of these categories is discussed below.

##### 4.3.1 Particle Related Inputs

Figure 7 shows the influence of particle  $K_{Ic}$  on the predicted failure probabilities for H-451. In this figure, as in all of the figures in section 4.3, the center distribution is the prediction shown in Fig. 5. The model is clearly very sensitive to variations in the particle  $K_{Ic}$ , small changes in  $K_{Ic}$  causing large changes in the predicted mean strength. The model predicts increased strength with increasing  $K_{Ic}$ . This is not generally the case with graphites, the stronger graphites usually exhibit lower toughness. However, here we are not adjusting other parameters such as pore size and distribution, and filler particle size, which would change markedly from coarse to fine grained graphites. The effect of one of these input parameters, mean filler particle size, is shown in Fig. 8. The model is less sensitive to changes in particle size than in  $K_{Ic}$ . Moreover, the prediction of a lower strength for coarser particle size graphites is qualitatively correct. This result reinforces the view that the basis of the model is physically sound.

##### 4.3.2 Porosity Related Inputs

The influence of density on the predicted failure distributions is shown in Fig. 9. Three densities are considered, ranging from 1.65 to 1.95 g/cm<sup>3</sup>. The dependence of density is weak, but is qualitatively correct, i.e., lower strengths are predicted for lower density graphites. Again, one must consider that in reality lower density grade graphites would vary significantly in the number, mean size, and shape

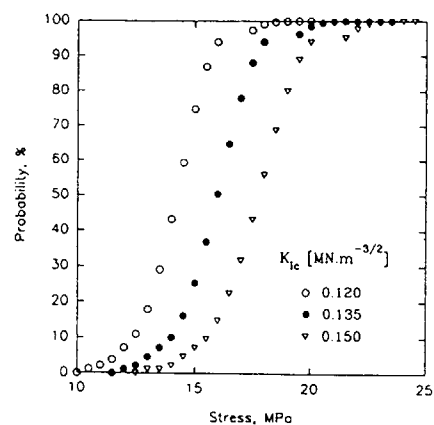


Figure 7. The influence of particle  $K_{Ic}$  on the predicted failure probability.

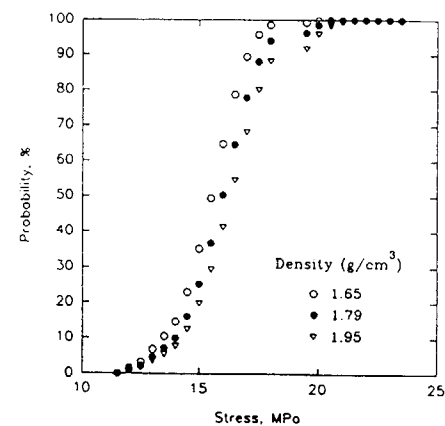


Figure 9. The influence of density on the predicted failure probability.

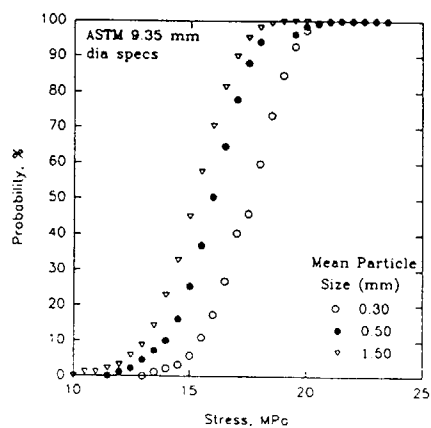


Figure 8. The influence of mean particle size (a) on the predicted failure probability.

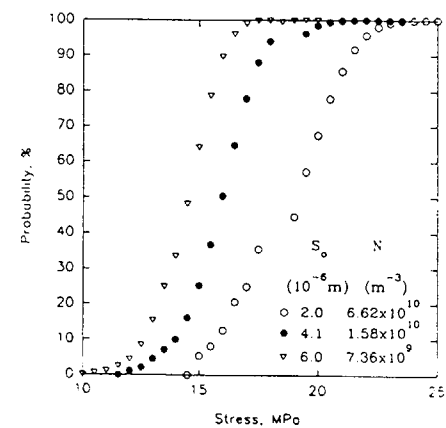


Figure 10. The influence of mean pore size ( $S_0$ ) and number ( $N$ ) on the predicted failure probability.

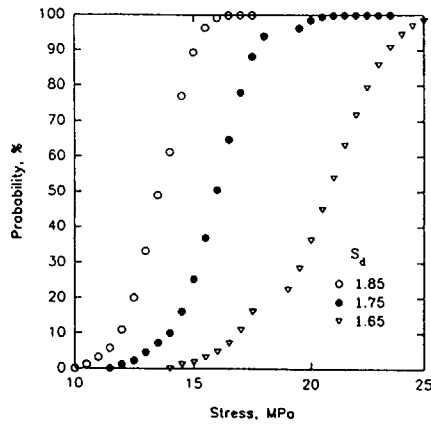


Figure 11. The influence of pore size distribution width ( $S_d$ ) on the predicted failure probability.

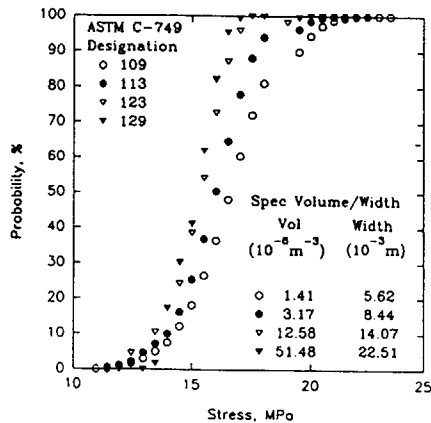


Figure 12. The influence of specimen size ( $V$  and  $b$ ) on the predicted failure probability.

of their pores. In the model, density is linked to the number of pores ( $N$ ) as described previously. The influence of  $N$  on the predicted failure distributions is shown in Fig. 10. Here changes in the number of pores have been achieved by taking three different mean pore sizes, 2.0, 4.1, and 6.0  $\mu\text{m}$ . The corresponding values of  $N$  are then  $6.62 \times 10^{10}$ ,  $1.58 \times 10^{10}$ , and  $7.36 \times 10^9$ . The number and mean size of the pores have a significant effect on the predicted failure probabilities, which is not surprising, when one considers the importance of porosity in the initiation and propagation of cracks during graphite fracture. Again, the model is qualitatively correct, predicting lower strengths for graphites with larger and more numerous pores. The last input parameter in this category is the standard deviation of the log-normal pore size distribution ( $S_d$ ). A large value of  $S_d$  is indicative of a wide pore size distribution, such as might be observed in a coarse-grained graphite. The influence of  $S_d$  on the predicted failure probabilities is shown in Fig. 11. The model is extremely sensitive to small changes in this input parameter. Reducing  $S_d$  from 1.75 to 1.65 causes an increase in the predicted mean strength from 16 MPa to approximately 21 MPa. Again, the model is qualitatively correct. The large effect of  $S_d$  variations is reasonable given the prominent role of porosity in graphite fracture processes. The good performance of the model in accounting for changes in input parameters in this category can be attributed to the sound physical basis of the fracture model.

#### 4.3.3 Specimen Geometry Related Inputs

Variations of specimen geometry were modeled by inputting the stressed volumes and appropriate equivalent beam breadths for the four recommended ASTM C749 tensile test specimens. The value of  $V$  and  $b$  are shown in Fig. 12 along with the models predicted failure probabilities. The model predicts an increasing strength with decreasing specimen volume, which is in agreement with other failure theories such as the Weibull model. The model is more sensitive to increases of stress volume at small initial volumes than it is for increases at larger volumes. This is apparent from a comparison of the predictions from specimen types 109 and 113, and of types 123 and 129. The effect of stress volume on the strength of H-451 and IG-110 is discussed in detail elsewhere.<sup>8</sup>

#### 5.0 CONCLUSIONS

A fracture model has been developed and applied to predict tensile strength distributions for two nuclear grade graphites. The models performance was assessed by comparison of prediction with experimental data, and was found to be remarkably good, particularly for the medium-grained H-451 graphite. Moreover, the model demonstrated a high degree of versatility in predicting the failure

probability distribution for the fine-grained grade IG-110 graphite. The effects of varying the microstructural inputs to the model were investigated. The model behavior is quantitatively correct with respect to changes in filler particle size, density, pore size and shape, the number of pores and the specimen geometry (stressed volume). The impressive performance is attributed the sound physical basis of the fracture model, which recognizes the dominant role of porosity in the graphite fracture process.

#### REFERENCES

1. M. O. Tucker, A. P. G. Rose and T. D. Burchell. "The Fracture of Polygranular Graphite," *Carbon*, Vol. 24. No. 5, pp. 581-602, 1986.
2. T. D. Burchell, M. O. Tucker and B. McEnaney. "Qualitative and Quantitative Studies of Fracture in Nuclear Graphites," in *Proc. Materials for Nuclear Reactor Core Application*, BNES, London, 1987.
3. T. D. Burchell. "Studies of Fracture in Nuclear Graphite," Ph.D. Thesis, University of Bath, UK, 1986.
4. Manufactures Product Literature, Toyo Tanso Graphite Company Ltd.
5. S. Sato, K. Kawamata, A. Kurumada, H. Ugachi and H. Awaji. "Degradation of Thermal Shock Resistance and the Fracture Toughness of Reactor Graphite Subjected to Neutron Irradiation," in *Proc. IAEA Specialist's Meeting on Graphite Component Structural Design, JAERI Tokai, Japan, Sept. 8-11, 1986*, p.144, 1987.
6. G. R. Romanoski and T. D. Burchell. "Specimen Size Effects on Fracture Toughness of Nuclear Graphites," in *Proc. IAEA Specialist's Meeting on The Present Status of Graphite Development for Gas-Cooled Reactors, JAERI Tokai, Japan, Sept 9-12, 1991*.
7. ASTM Standard C749-87, "Standard Test Method for Tensile Stress-Strain of Carbon and Graphite," *Annual Book of ASTM Standards*, Vol. 1501, 1990.
8. J. P. Strizak. "The Effect of Volume on the Tensile Strength of Several Nuclear Grade Graphites," in *Proc. IAEA Specialist's Meeting on The Present Status of Graphite Development for Gas-Cooled Reactors, JAERI Tokai, Japan, Sept 9-12, 1991*.

#### DISCUSSION

##### Questions or Comments

Name: I.S. Mosevitskii

Can you use your model for matrix graphite?

If not, change must be made?

##### Answer:

The fracture model has been developed for conventional nuclear grade graphite. However it should be applicable to any graphite with suitable variation to the input parameters. I am not fully familiar with the details of your matrix graphite but I am confident that it could be modeled using a microstructural fracture approach. Perhaps such a model would assume the fuel particles to be particles of zero strength (or large pores?). If the fuel particles are modeled pores they would contribute significantly to the fracture process.

##### Questions or Comments

Name: Chugunov

What is the difference between  $K_{IC}$  for the bulk of the graphites and the  $K_{IC}$  for a single crystallite?

##### Answer:

Particle  $K_{IC}$  is assumed to be associated with particle cleavage along crystallographic basal planes. Therefore it will be significantly less than  $K_{IC}$  value measured by LEFM tests on a bulk graphite, which measures more model tortuous - crack path fractures. In the model we arbitrarily set ( $K_{IC}$ ) particle =  $1/10(K_{IC})$  bulk i.e. one order of magnitude less than bulk  $K_{IC}$ .

## BURST TESTS TO MEASURE THE TANGENTIAL STRENGTH OF CFC TUBES

M. ROEDIG\*, W. BAUR\*\*, B. WOSCHEK\*

\*Institut für Reaktorwerkstoffe,  
Forschungszentrum Jülich GmbH,  
Jülich

\*\*Sigri GmbH\*

Germany

### Abstract

*Carbon fiber reinforced composites (CFC) are considered as graphite/metal substitute material for certain structural components in modern HTR design. Internal pressure tests have been performed with tube segments made of CFC. The aim of the investigations was to value the failure of components under hoop stress and to compare the results to those obtained in relatively simple tests as split disk tests. The internal pressure was generated by gas and water.*

*The main problem in the experiments was to prevent leakage at the end of the tubes without applying uncontrolled bending moments. Design methods supported by finite element calculations, helped to reduce these bending moments which could not avoided totally however. Therefore the results of the burst tests must be considered as conservative. But compared to the split disk tests, the failure stress is twice as high as for the latter. Therefore it can be assumed, that for the given geometry, the split disk tests underestimate the tangential strength at least by a factor of two.*

### 1. Aim

Carbon fiber reinforced composites (CFC) are considered as graphite/metal substitute material for certain structural components in modern HTR design. In a cooperation of the Institute for Reactor Materials and Sigri GmbH, internal pressure tests have been performed with tube segments made of CFC.

The aim of the experiments was to measure the tangential strength in burst tests and to compare the results with those of less sophisticated experiments, as split-disk-tests (ASTM Standard D2290-69).

The split disk test is usually used for semi-empiric comparison of ring shaped testing specimens. The grips for these tests are two half-cylinders with an outer diameter corresponding to the inner diameter of the ring specimen to be tested (cp. Fig. 1). During the experiment the specimen is loaded by these half-cylinders. For the evaluation, a pure tangential tensile stress is assumed in both halves of the ring-specimen. Therefore the ultimate tangential tensile stress (UTS) is:

$$UTS = F / (2 \cdot t \cdot l)$$

F: force

t: wall thickness

l: width of the ring

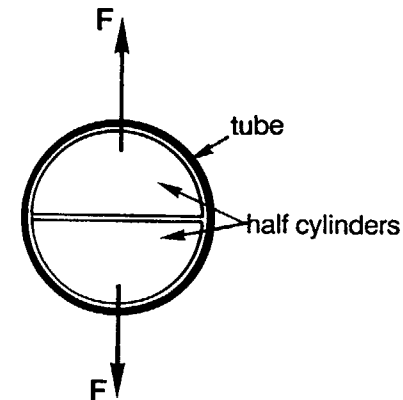


Fig. 1: Split disk test

\* Now FFT GmbH, Mengen, Germany.

In reality however the stress stage is more complicated and for the following reasons no pure tensile stresses can be assumed:

- For reasons of mountability the outer diameter of the grips has to be smaller than the inner diameter of the ring specimen to be tested.
- No ideal contact between grips and ring specimens is given due to surface roughness effects.
- The stress distribution is influenced by edge effects.

So the aim of the burst tests was to compare the results with those of the relatively simple split disk test and get an information on the grade of conservativity of the latter.

## 2. Tested Material and Specimens

The CFC material to be tested was CC 2001 G made by SIGRI. The technical data are given in Fig. 2.

The inner tube wall is a roving tissue of 0.2 mm thickness. Above this tissue are windings of carbon fibers under an angle of  $\pm 15^\circ$  to the tangential direction. The outer wall consists of a layer of matrix material without reinforcement of fibers. This means, that the effect of reinforcement is given only in directions near to the tangential direction.

Material data:

Material:	Sigri CC 2001 G
final temperature treatment:	2000°C
density:	1.3 - 1.5 g/cm <sup>3</sup>
bending strength (tang.):	280 - 350 MPa
tensile strength (tang.):	380 - 470 MPa
dyn. Young's modulus:	110 - 130 GPa

Tube dimensions:

outer diameter:	331 mm
wall thickness:	3 - 4.5 mm
length:	150 mm, 700 mm

Fig. 2: Technical data of CFC material CC2001G

The number of specimens tested are:

- 10 tube segments of 700 mm width (pressurized by water),
- 12 tube segments of 150 mm width (pressurized by gas),
- 15 split disk specimens of 6.3 mm width.

## 3. Burst Tests with gas as a pressurizing medium

It was intended to perform the experiments in such a way that by the sealing system no axial stresses were applied. In this case a uniaxial stress state would be achieved in the tube wall. The idea was to use a materials testing machine in closed loop operation so that only the sealing force was achieved. This concept of sealing is shown in Fig. 3.

The internal pressure was produced from a helium bottle (cp. Fig. 4). The needle valve behind the pressure reducer was used to shelter the pressure reducer from shocks during the failure of the tube. A filler body was brought into the tube specimen to reduce the released potential energy during failure. Four pairs of extensometers were mounted on the inside and on the outside of the tube in order to measure the change of the internal and the external diameter.

The failure stress of nine short tubes (length = 150 mm) is given in Fig. 9 (marked "2"). The mean values were:

mean failure stress: 249 MPa

standard deviation: 41 MPa

95%-confidence range for the mean value: 218...445 MPa

All specimens failed near to the edges of the tube.

The reason was, that the applied sealing force exceeded the failure stress of the tube in axial direction. To get the information about axial strength of the tube, pure compression tests were performed (cp. Fig. 5). It can be seen that from a stress of approximately 12 MPa irreversible deformations take place. So it must be assumed that near the edges a complex state of stresses occurs, and so the maximum hoop stress calculated from the burst pressure underestimates the tangential strength of the tube material.



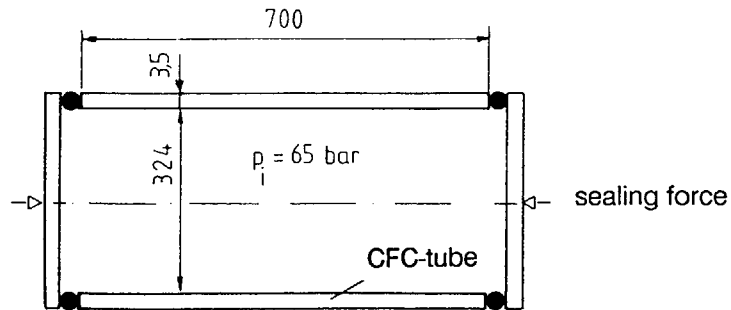


Fig. 3: Sealing by O-rings

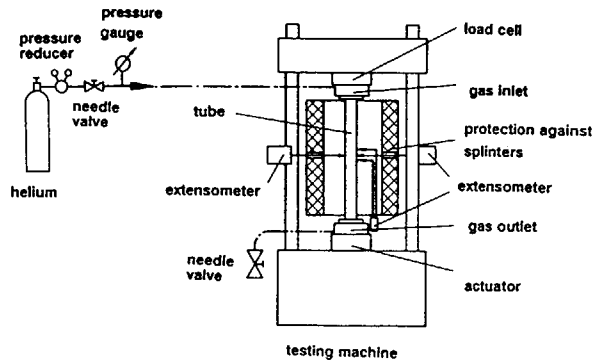


Fig. 4: Gas pressuring system

#### 4. Burst Tests with water as a pressurizing medium

Due to the experimental problems described in chapter 3, another testing technique was developed. Lip sealings were used to avoid damage of the tube while applying the sealing forces (cp. Fig. 6). Now it was no longer necessary to perform the experiments in a testing machine and water could be used as a pressurizing medium.

In the first two tests it was found that the tubes were destroyed near the edges as well. The results for these two tubes are shown in Fig. 9 they are marked by "3a".

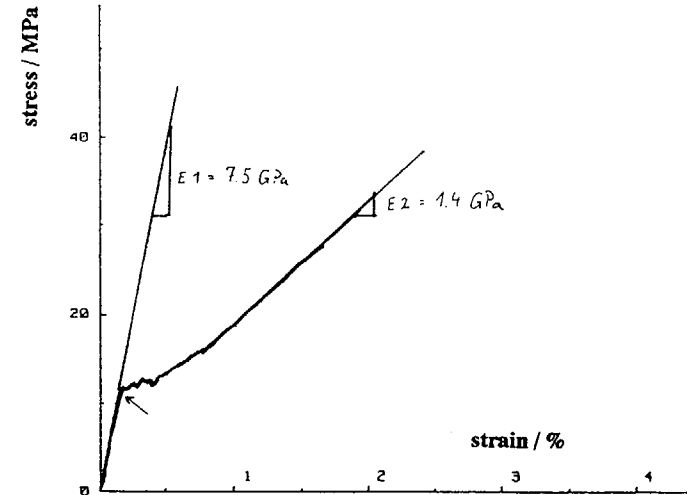


Fig. 5: Stress strain diagram for a tube under axial compression

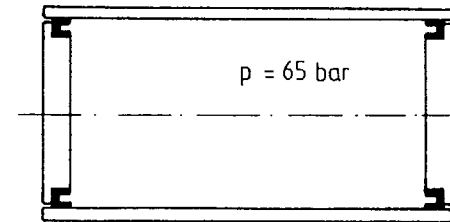
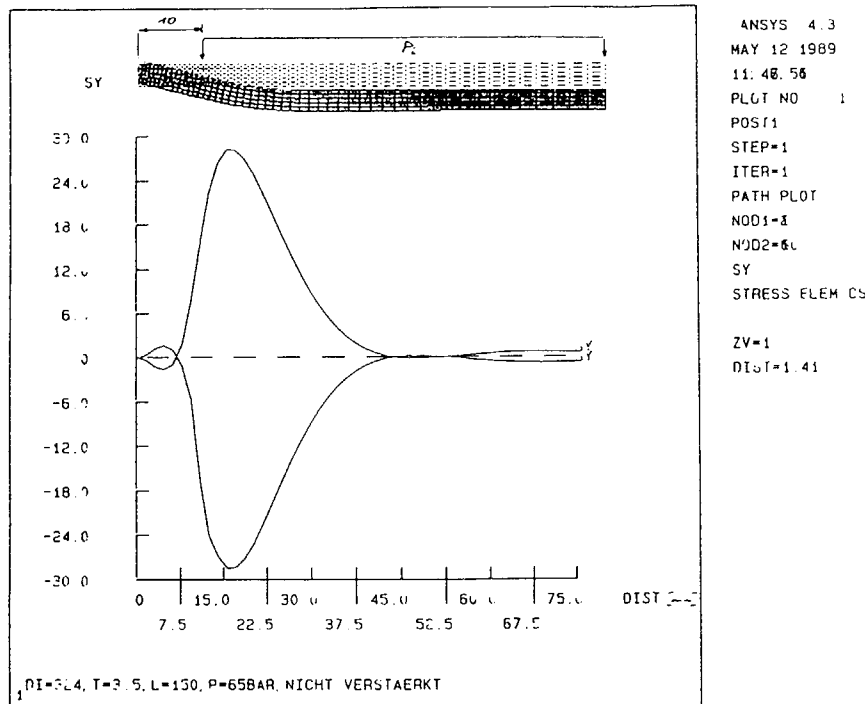


Fig. 6: Lip sealing concept

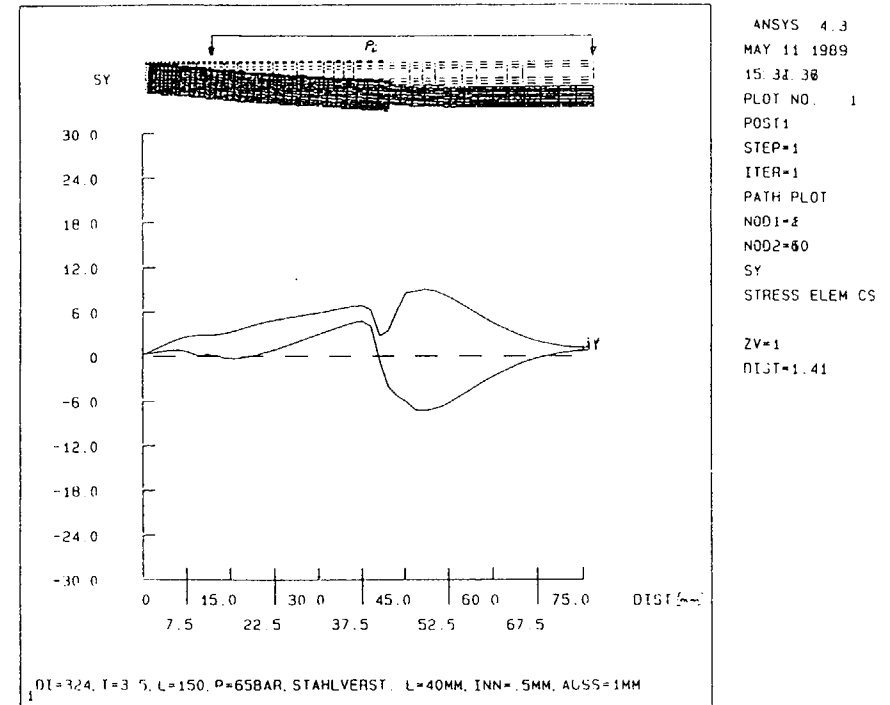
In order to understand these phenomenon, an analysis of the deformations and stress distributions was performed with the finite element code ANSYS. In Fig. 7 the distribution of axial stresses in the tube wall is shown. An internal pressure of 65 bars was assumed which is the approximate mean burst pressure. About 16 mm from the tube edge, a maximum of the bending stress of 28 MPa is found. This is compared to the results of the simple axial compression test (cp. Fig. 5).



outer diameter: 324 mm, wall thickness: 3.5 mm, length: 150 mm  
no reinforcement sheets

**Fig. 7:** Axial stress in the inner and outer tube wall (without reinforcements)

The reason for the high axial stresses now is the large difference in axial and tangential stiffness of the tube. The small part of the edges of the tube, which is not pressure loaded remains on its position while the pressure loaded part gets a radial deformation (cp. top of Fig. 7). The result is a high curvature in axial direction near the edges which leads to the bending stresses. To avoid the curvature, it was necessary to reinforce the tubes by metal sheets in the region near the sealings.

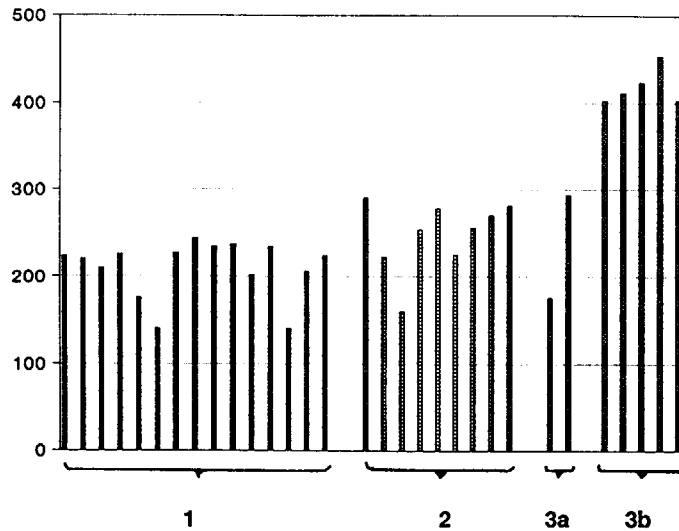


outer diameter: 324 mm, wall thickness: 3.5 mm, length: 150 mm  
inner reinforcement: steel 0.5 mm thick, 40 mm long  
outer reinforcement: steel 1 mm thick, 40 mm long

**Fig. 8:** Axial stress in the inner and outer tube wall (with reinforcements)

A finite element study has been performed in order to estimate the influence of the reinforcements. Calculations were made for several widths of the reinforcement zone, for reinforcements on the inner and/or the outer tube wall, and for reinforcement materials of different stiffness. Fig. 8 gives the final configuration of the reinforcements (inside: 40 mm long, 0.5 mm thick, outside: 40 mm long, 1 mm thick, sheet material: steel). The finite element calculation shows, that the axial stresses are drastically reduced by the reinforcement.

ultimate hoop stress [MPa]



1: split disk tests

2: burst tests (series 1):  
tube length: 150 mm  
pressure medium: gas

3: burst tests (series 2)  
tube length: 700 mm  
pressure medium: water  
a) without reinforcements  
b) with reinforcements

Fig. 9: Experimental results for all specimens

In burst test with tubes reinforced by steel sheets a much higher failure stress is found (cp. Fig. 9 - results are marked "3b"). Mean values were:

mean failure stress: 419 MPa  
standard deviation: 21 MPa  
95 % confidence range for the mean value: 393...445 MPa

## 5. Result of Split Disk Tests and Discussion

Nine split disk tests have been performed. The results are given in Fig. 9 (marked by "1"). Mean values are:

mean failure stress: 210 MPa  
standard deviation: 33 MPa  
95 % confidence level for the mean value: 192...228 MPa.

The failure strength of the tubes pressurized by gas (249 MPa) lies approximately 20 % higher than the split disk test. This difference however is not significant according to the 95 % confidence limit. For the tubes reinforced by steel sheets, significantly higher failure stresses are found. The final stresses are nearly as double as high as for the tubes without reinforcement. This confirms the result of the finite element calculation on the influence of reinforcements. But it must be mentioned, that by the reinforcement bending moments can be reduced but can not be totally avoided. Therefore it must be mentioned, that the failure stresses found in these experiments are still below the true tangential strength and hence conservative. Therefore it can be assumed, that for the given geometry, the split disk test underestimated the tangential strength at least by a factor of two.

## DISCUSSION

Questions or Comments

Name: R. Judge

1 Did you use strain gauges on the specimens?

No - But extensometers were used to measure the change in diameter.

2 Did you consider loading by rubber membrane?

We considered rubber membrane loading, but we did not use it because we were afraid of edge effects.

## SPATIAL VARIABILITY IN THE TENSILE STRENGTH OF AN EXTRUDED NUCLEAR-GRADE GRAPHITE\*

J.P. STRIZAK

Oak Ridge National Laboratory,  
Oak Ridge, Tennessee,  
United States of America

### Abstract

This report will present the results of a study on spatial variations in the strength of nuclear-grade H-451 graphite. The tensile properties of H-451 were examined extensively in the past in order to characterize the variability of strength within billets, between billets, and between lots. But the variability within a billet was, for the most part, studied only casually. The problem appeared to be the strong influence of a limited sampling plan in describing the mean strength and the variability. Therefore, an extensive, statistically sound sampling plan has been devised to fully characterize the spatial variability within a single billet.

Test specimens were machined to conform to ASTM C749-87, "Standard Test Method for Tensile Stress-Strain of Carbon and Graphite." Test results have been obtained for four specimen sizes having gage diameters of 6.35, 9.53, 15.88, and 25.40 mm with respective gage-section volumes of 1407, 3163, 12,577, and 51,482 mm<sup>3</sup>.

A new fracture model developed by Burchell was applied to the data with encouraging results. This probabilistic failure criteria combines a microstructural basis with a fracture-mechanics approach to failure.

### 1. INTRODUCTION

Grade H-451 near-isotropic graphite is the reference graphite for High-Temperature Gas-Cooled Reactor (HTGR) applications in the U.S. The variability and statistical distribution of the graphite strength (tensile, compressive, fatigue, flexure, and fracture toughness) must be considered in the design of critical HTGR core components. A fracture model based on the governing role of flaws in the microstructure of the brittle graphite material, and relating the probability of failure to the volume of material under stress would be a useful engineering design tool. The model could be combined with finite-element stress analysis to show compliance with reliability requirements for critical HTGR structural components.

\* Research sponsored by the Division of MHTGRs, Office of Advanced Reactor Programs, US Department of Energy, under contract DE-AC05-84OR21400 with Martin Marietta Energy Systems, Inc.

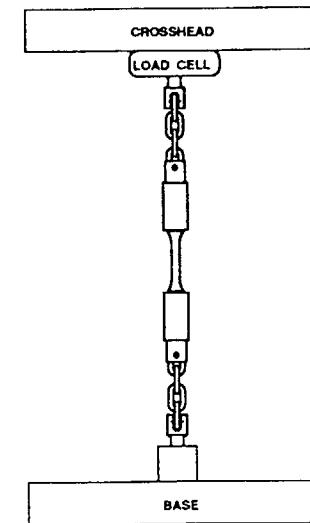


Fig. 1. Schematic diagram of tensile testing load train.

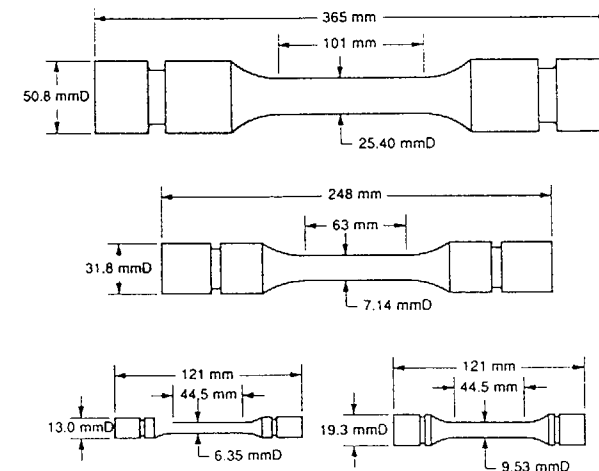


Fig. 2. Tensile specimen sizes.

Work is currently underway to validate the existing data base on H-451 graphite for more demanding HTGR applications, and to improve the statistical distributions used in probabilistic analysis. New data on the variability of tensile strength within an H-451 graphite billet is presented herein.

## 2. EXPERIMENTAL PROCEDURE

Tensile tests at room temperature were conducted according to the ASTM C749-87 [1] method for tensile testing of graphite. Tests were performed on a microprocessor based Instron electro-mechanical test system equipped with specimen grips incorporating chain links which serve to minimize parasitic stresses. Figure 1 shows a schematic drawing of the test system and the specimen gripping arrangement. All tests regardless of specimen size were conducted at a constant extension rate (cross-head speed) of  $8.5 \times 10^{-3}$  mm/s. Only the fracture strength of each specimen was recorded; no strain measurements were taken in this study on the dependence of tensile strength on location within the material.

Four specimen sizes having gage diameters of 6.35, 9.53, 15.88, and 25.40 mm were machined such that the specimens were axially aligned with the longitudinal axis of the graphite billet (log). Schematic drawings of the test specimens are shown in Fig. 2, and gage section volumes are listed in Table 1.

Table 1. Tensile specimen stress volumes

Gage diameter (mm)	Gage length (mm)	Stress volume (mm <sup>3</sup> )
6.35	44.44	1,407
9.53	44.44	3,163
15.88	63.50	12,577
25.40	101.60	51,482

## 3. MATERIAL: GRADE H-451 GRAPHITE

Grade H-451, manufactured by Great Lakes Carbon Corporation, is a near-isotropic, petroleum-coke based, medium-grained graphite that has been heat treated to 2,650°C and gas purified. The graphite is extruded into billets measuring 432-mm diameter by 813-mm long. An entire

billet was consumed for tensile testing to determine the effects of 1) specimen size on strength, and 2) spatial variability of strength throughout the billet. The former is the topic of another presentation by the author at this IAEA Specialist's Meeting [2].

Prior to specimen fabrication, the billet of H-451 was cut into slabs. The various specimen sizes were machined from the slabs as indicated in Fig. 3. Two specimen sizes, i.e., 6.35 and 9.53-mm gage diameters, were machined from all six (6) locations along the length of the billet. At two locations along the billet length, i.e., positions 2 and 5 in Fig. 3, all four specimen sizes were available

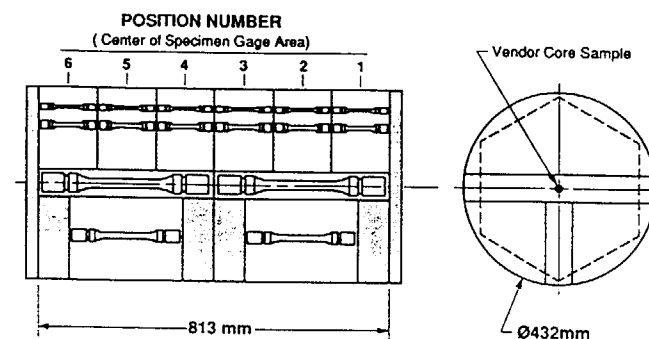


Fig. 3. H-451 graphite billet slabbing plan.

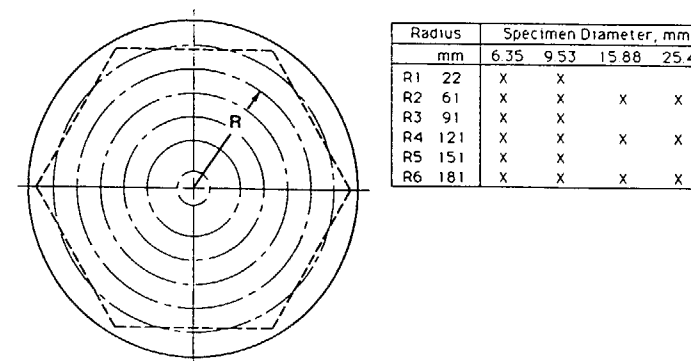


Fig. 4. Radial locations for tensile specimens in H-451 billet.

through the cross-section of the billet. Additionally, at each position along the billet length, the specimens were located at six specific radial positions through the cross-section of the billet, as shown in Fig. 4. All four specimens were obtained at the radii designated as R2, R4, and R6, while only the 6.35 and 9.53-mm gage diameter specimens were obtainable at radii R1, R3, and R6. The specimen yield from the billet included 160 of the 6.35-mm diameter specimens, 158 of the 9.53-mm diameter specimens, 20 of the 15.88-mm diameter specimens and 18 of the 25.40-mm diameter specimens. A total of 356 tensile tests were conducted.

#### 4. RESULTS

Analysis of the large body of data for grade H-451 graphite obtained in this study has just begun. Observations presented herein focus on test results for the 9.53-mm diameter specimens taken at all 6 locations along the billet length and all 6 radial locations through the cross-section of the billet (see Figs. 3 and 4), thus characterizing the entire billet.

In Figs. 5 through 10, the measured tensile strengths for the 9.35 mm diameter specimens at the various radial locations through the billet cross-section are plotted for each of the six locations along the billet length. Using a different approach, the same strength data are plotted in Figs. 11 through 15 as a function of position along the billet length for each radial location through the billet cross-section. The first set of figures (Fig. 5 through 10) serves to highlight variations in strength from the outer edge of the billet in toward the central axis of the billet. The second set of figures (Figs. 11 through 15) promotes observations on the variation in strength from one end of the billet to the other.

#### 5. DISCUSSION

The various data sets plotted in Figs. 5 through 11 are summarized in Fig. 16. The mean tensile strengths for the various locations along the length of the billet are plotted as a function of the radial distance out from the center of the billet as shown in Fig. 16. In general, the H-451 graphite becomes progressively weaker in moving from the outer surface of the billet towards the central axis of the billet, i.e., traversing from R6 to R1. However, there is one exception; the strength changes very little near the end of the billet (position 6) opposite the end where the vendor core sample was removed and tested to determine the overall billet strength classification. In fact, there appears to be an indication that material from the central portion of the billet cross-section may be slightly stronger compared with the outer edge at this end of the billet.

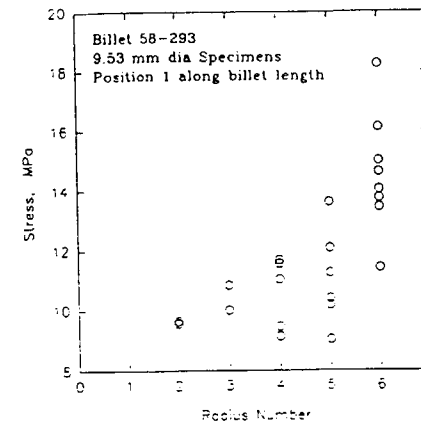


Fig. 5. Tensile strength vs. radius number at position 1.

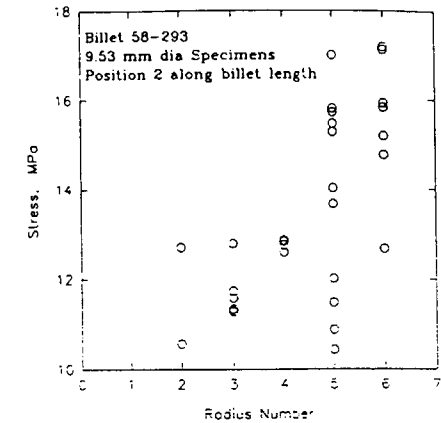


Fig. 6. Tensile strength vs. radius number at position 2.

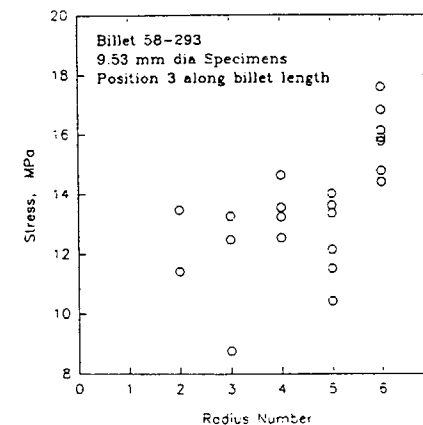


Fig. 7. Tensile strength vs. radius number at position 3.

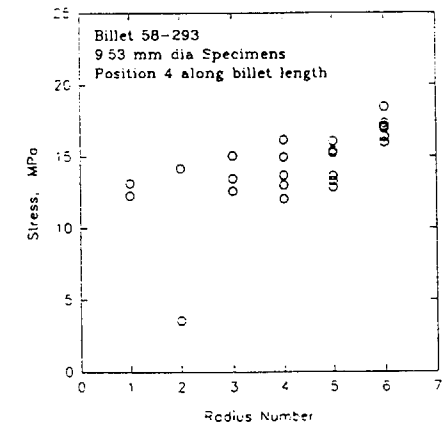


Fig. 8. Tensile strength vs. radius number at position 4.

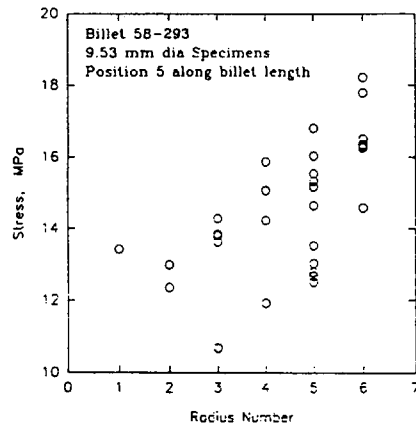


Fig. 9. Tensile strength vs radius number at position 5.

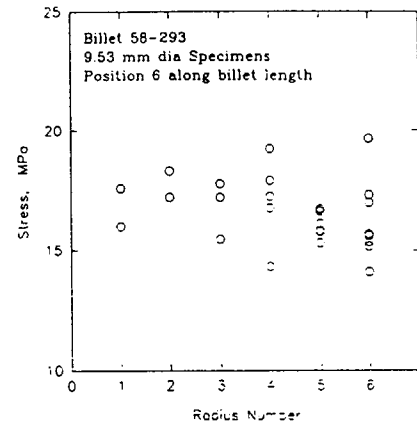


Fig. 10. Tensile strength vs radius number at position 6.

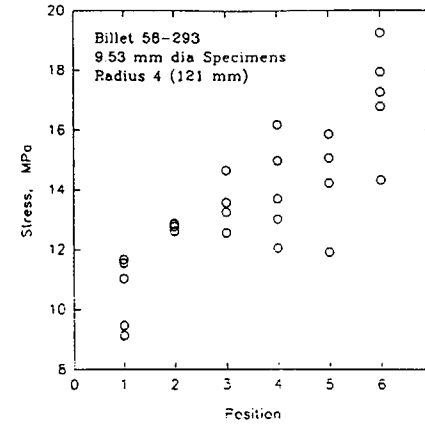


Fig. 13. Tensile strength vs position at radius 4.

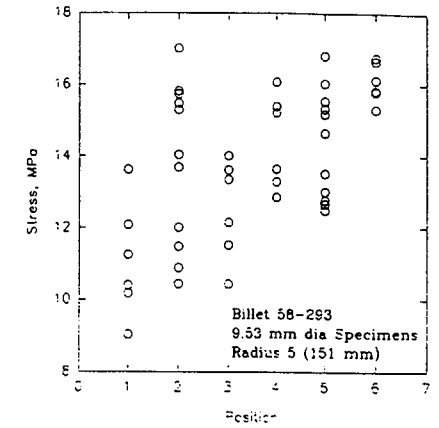


Fig. 14. Tensile strength vs position at radius 5.

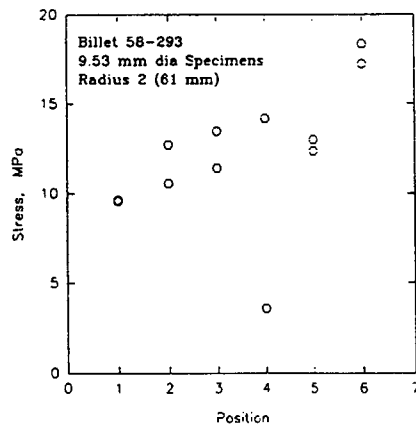


Fig. 11. Tensile strength vs position at radius 2.

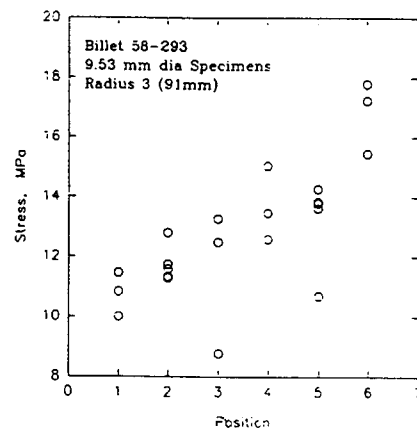


Fig. 12. Tensile strength vs position at radius 3.

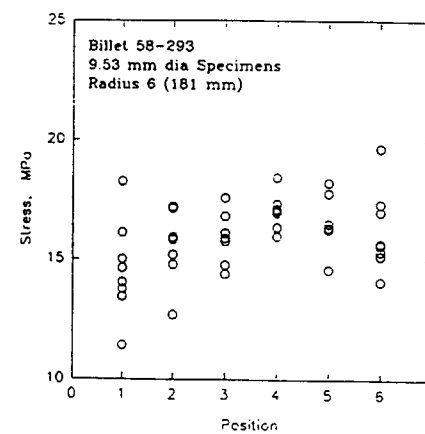


Fig. 15. Tensile strength vs position at radius 6.

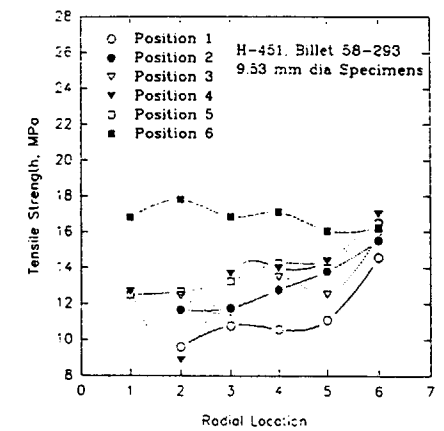


Fig. 16. Radial variations in tensile strength.

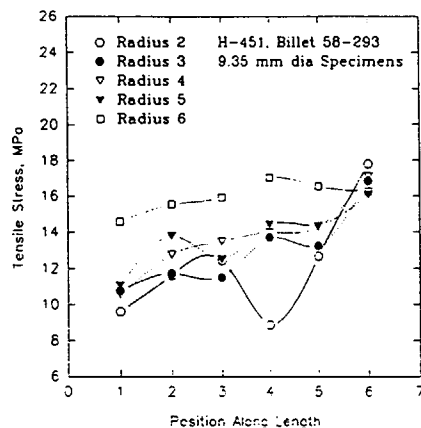


Fig. 17. Spatial variations in tensile strength along billet length.

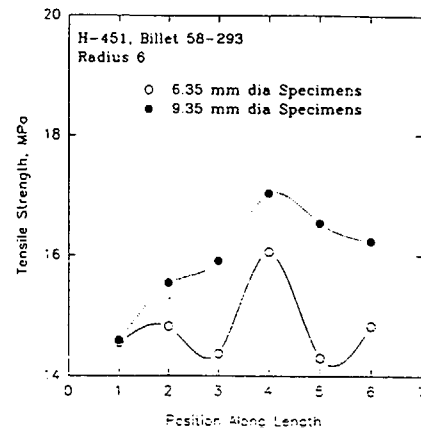


Fig. 18. Specimen volume effect on spatial variation.

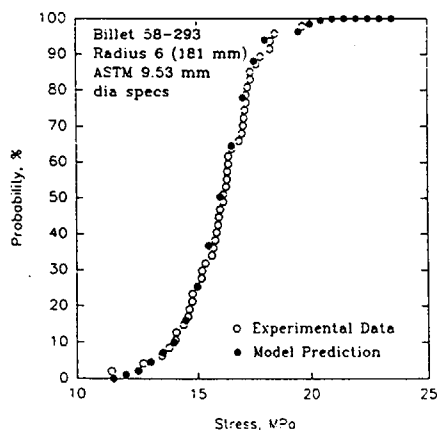


Fig. 19. Fracture model predictions at radius 6 near edge of billet.

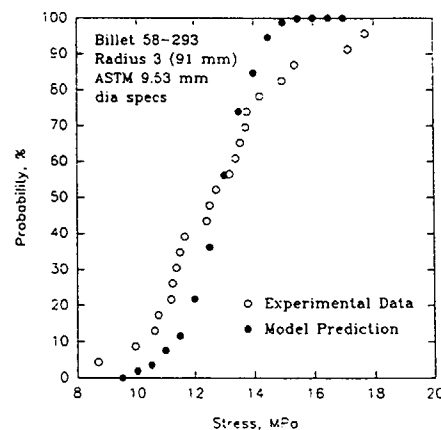


Fig. 20. Fracture model predictions at radius 3 near center of billet.

Fig. 16 also suggests that there are variations in strength from one end of the billet to the other. This is best illustrated in Fig. 17. In general, H-451 graphite becomes progressively stronger in moving from the core sample end of the billet on to the opposite end. This trend holds true for material from the central portion of the material, i.e., radial locations R1 through R5. However, near the outer edge of the material (radial location R6) the trend appears to be reversed.

As pointed out by Price [3], strength variations are common in extruded graphite such as H-451 and result from the alignment of coke particles during extrusion, distribution of impregnant carbon following the impregnant process, and the following heat treatment of the billets. Work is currently underway to relate the expected microstructural variations to the systematic strength variations (edge to center, and also along the billet length) observed in the H-451 billet tested during this study. Characterization of the strength variations in H-451 graphite must also consider the effect of specimen size on strength.

This point is illustrated in Fig. 18 where the mean strength for 9.35 and 6.35-mm diameter specimens taken from material near the outer edge of the billet cross-section (radial location R6) are plotted as a function of position along the length of the billet. At one end of the billet the strength of the two specimen sizes are essentially the same. However, the strengths diverge at the other end of the billet with the 6.35-mm specimens being weaker. The effect of specimen size on the strength of H-451 is discussed in another report presented by the author at this IAEA meeting [2].

As mentioned in the introduction to this report, a fracture model based on the governing role of flaws in the microstructure of graphite and relating the probability of failure to the volume of the material would be a useful engineering design tool. A potential model introduced by Burchell [4.5] has been applied to the experimental data obtained in this study on the spatial variations in the strength of H-451 graphite. The model utilizes microstructurally related parameters including filler particle size, filler particle fracture toughness, density, pore size distribution and number of pores, as well as specimen geometry parameters such as, size (dimensions) and volume. The physical basis of the model is discussed by Burchell [6] at this IAEA meeting.

Figure 19 demonstrates good agreement between the model predictions for the strength of 9.35-mm diameter specimens taken near the outer edge of the billet cross-section (radial position R6). Similarly, reasonable agreement is observed in Fig. 20 for material nearer the central axis of the billet (radial location R3) when appropriate (estimated) changes were made to the various microstructural parameters of the model based on the measured density of the tested specimens, and the effect of specimen size on the fracture toughness of H-451 reported by Romanoski [7].



## 6. CONCLUSIONS

The tensile strength of grade H-451 nuclear graphite exhibits a dependence on location within the billet. Generally, the strength near the edge of the billet was stronger than at the central area of the billet. Further, the strength was found to progressively increase from one end of the billet to the other. Characterization of the spatial variations in strength, however, must also consider the observed stress volume (specimen size) effect. A new fracture model incorporating microstructural elements, as well as the fracture toughness of the material, showed good agreement with the limited experimental data on H-451 analyzed to date, and shows promise for characterizing the interaction of volume effects and microstructural variations through the bulk of the material.

## REFERENCES

1. ASTM Standard C749-87, "Standard Test Method for Tensile Stress-Strain of Carbon and Graphite," Annual Book of ASTM Standards, Vol. 15.01, 1990.
2. J. P. Strizak "The Effect of Volume on the Tensile Strength of Several Nuclear-Grade Graphites," Proceedings IAEA Specialist's Meeting on the Present Status of Graphite Development for Gas-Cooled Reactors, September 9-12, 1991, Japan Atomic Energy Research Institute, Tokai-mura, Ibaraki-Ken, Japan.
3. R. J. Price, "Statistical Study of the Strength of Near Isotropic Graphite," GA-A13955, General Atomic Company, San Diego, California, U.S.A., May 1976.
4. T. D. Burchell, "Studies of Fracture in Nuclear Graphite", Ph.D. Thesis, University of Bath, United Kingdom, 1986.
- 6. T. D. Burchell and M. D. Tucker, "A New Fracture Criterion for Graphites," Proceedings, XVII<sup>th</sup> Biennial Conference on Carbon, July 19-24, 1987, pp. 486-487, Worchester Polytechnic Institute, Worchester, Massachusetts.
7. T. D. Burchell, "A Microstructurally Based Fracture Model for Nuclear Graphites," Proceedings IAEA Specialist's Meeting on the Present Status of Graphite Development for Gas-Cooled Reactors, September 9-12, 1991, Japan Atomic Energy Research Institute, Tokai-mura, Ibaraki-Ken, Japan.
8. G. R. Romanoski and T. D. Burchell, "Specimen Size Effect on Fracture Toughness of Nuclear Graphites," Proceedings Twentieth Biennial Conference on Carbon, University of California, Santa Barbara, California, U.S.A., June 23-28, 1991, pp. 584-585.

## DISCUSSION

### Questions or Comments

Name: T. Arai

I would like to know which type of theoretical statistical distribution fits to the measured tensile strength, at respective location or total, and/or the predicted tensile strength.

### Answer:

Paper on volume effects gives figures showing that test results for the 4 specimen sizes follow a "normal" distribution; these results are for specimens of the outer edge of the billet (R6). Data for R4 (not given in the report) also follow a normal distribution. There is some indications of departure from a normal distribution at low stresses. It has suggested that this may be due to desperate flaws. Review of previous dates on H-451 indicated that the strength data was equally well described by normal and Weibull distributions.

### Questions or Comments

Name: K. Kikuchi

I understood new model to explain tensile strength of H451. Could new model apply for stress-gradient field using the same microstructural parameters with tensile field?

### Answer:

I believe the model could be applied to a stress gradient field provided that the microstructural variations can be described by an empirical relationship. Our continuing work will attempt to map the variations in microstructural parameters in the H-451 billet.

# EVALUATIONS OF THE FRACTURE MECHANICAL PROPERTIES OF FUEL COMPACTS FOR THE HTTR, WITH EMPHASIS ON THERMAL SHOCK RESISTANCES AND NEUTRON IRRADIATION EFFECTS

S. SATO, A. KURUMADA, K. KAWAMATA

Faculty of Engineering,  
Ibaraki University,  
Hitachi-shi, Ibaraki-ken

N. SUZUKI, M. KANEKO

Tokai Works,  
Nuclear Fuel Industries, Ltd,  
Tokai

K. FUKUDA

Tokai Research Establishment,  
Japan Atomic Energy Research Institute,  
Tokai-mura, Naka-gun, Ibaraki-ken

Japan

## Abstract

The High Temperature Engineering Testing Reactor (HTTR), currently under development by Japan Atomic Energy Research Institute (JAERI), uses fuel rods, which contain so called "fuel compact" of pellets and a form of fuel made by sintering coated  $UO_2$  fuel kernel dispersed in natural graphite matrix in graphite sleeves. The spherical  $UO_2$  fuel kernel in the fuel compact is covered with several layers of carbon and SiC. The primary objective of this study was to investigate the mechanical, fracture mechanics properties and the thermal shock resistances of the fuel compact. Disk or rod-shaped fuel compact specimens were prepared by using SiC-kernel coated particles instead of  $UO_2$  particles, and by following otherwise the same manufacturing process as that for the real fuel compact. A series of experimental studies were then carried out by using these model specimens. These model specimens were further neutron irradiated in JMTR for fluences up to  $1.7 \times 10^{21}$  n/cm<sup>2</sup> (E<29fJ) at high temperature (900°C ( $\pm 50^\circ$ C)) to study the effects of neutron irradiation on the fracture mechanical properties. In this study, all the fractures were found to occur in the matrix or at the interfaces of kernel particles. No fracture of the SiC-kernel coated particles themselves was found.

## 1. Introduction

High Temperature Engineering Testing Reactor (HTTR), currently under development by Japan Atomic Energy Research Institute (JAERI), uses fuel rods, which contain so called "fuel compact" of ten-odd pellets and a form of fuel made by sintering coated  $UO_2$  fuel kernel dispersed in natural graphite matrix in graphite sleeves. The spherical  $UO_2$  fuel kernel in the fuel compact is covered with several layers of carbon and SiC by CVD. The SiC and high density carbon layers form a strong barrier to confine radioactive substances produced by nuclear fission. The matrix graphite functions as a secondary barrier having high thermal resistance and conductivity. Steady efforts have been made for many years to study the fuel compact, for example, by irradiation tests using the material testing reactor (JMTR)<sup>(1)</sup>. Studies on the fracture mechanical properties of the compact itself, however, are relatively scarce.

The primary objective of this study was to investigate the mechanical, fracture mechanics properties and the thermal shock resistances of the fuel compact. Disk or rod-shaped fuel compact specimens were prepared by using SiC-kernel coated particles instead of  $UO_2$  particles, and by following otherwise the same manufacturing process as that for the real fuel compact. A series of experimental study was then carried out by using these model specimens. These model specimens were further neutron irradiated in JMTR for fluences up to  $1.7 \times 10^{21}$  n/cm<sup>2</sup> (E<29fJ) at high temperature (900°C ( $\pm 50^\circ$ C)) to study the effects of neutron irradiation on the fracture mechanical properties. In this study, all the fractures were found to occur in the matrix or at the interfaces of kernel particles. No fracture of the SiC-kernel coated particles themselves was found. This study, in effect, is equivalent to a macroscopic evaluation of the performances of fuel compact matrix and its kernel interfaces. The data obtained in this study were compared with those for graphite IG-110<sup>(2)</sup>, the core material of HTTR.

## 2. Preparation of Fuel Compact Model

### 2.1 Fuel compact model

Figure 1 shows the process diagram for preparing the specimen of the fuel compact model. To simulate the real fuel compact, SiC-kernels coated particles were used in lieu of  $UO_2$ -kernel particles. The SiC-kernel are particles obtained by sintering the granulated mixture of SiC powder, binder, and solvent. The SiC kernels were coated successively with a layer of high density pyrolytic carbon, SiC, and another layer of high density pyrolytic carbon to shape them into coated particles similar to the real fuel particles. The coated particles were about 900  $\mu$ m in diameter and 2.1g/cm<sup>3</sup> in density. Subsequent process of preparation is essentially identical to that for the real fuel compact containing  $UO_2$ -kernel<sup>(3)</sup>. Photo. 1 shows typical cross sections of the fuel compact model. SiC-kernels have somewhat larger diameters than those of  $UO_2$  kernels. Except for not having a buffer layer, the coated layers of SiC and pyrolytic carbons are quite similar in appearance to the real coated layers. The matrix of graphite is also quite similar to the real fuel compact<sup>(4)</sup>.

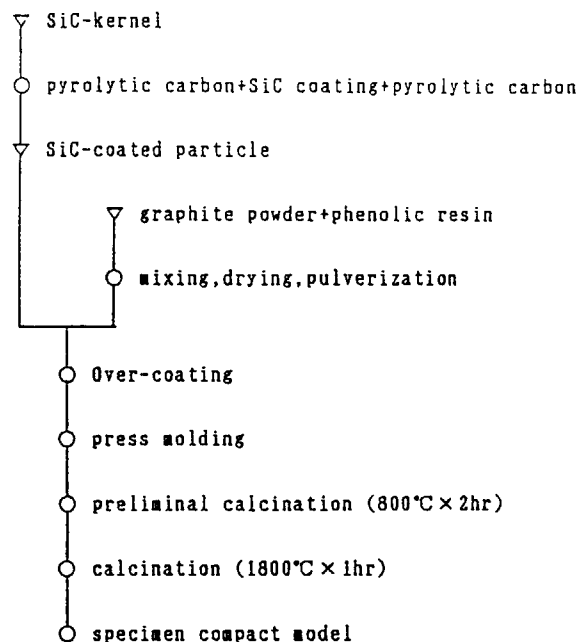


FIG. 1. Manufacturing process of the specimen of the fuel compact model.

The volumetric packing fraction of the coated particles and the matrix density were adjusted to match the respective values of 30% and 1.70 g/cm<sup>3</sup> for the HTTR fuel. The coated particles were further coated with fine graphite powder made of 64 % natural graphite powder (Kropfmühl Co., Germany), 16 % artificial graphite powder (Ringsdorf Co., Germany) and 20% phenol resin, while wetting their surfaces with a solvent. The coated particles were measured and hot-press molded using metal dies to obtain the required diameter and height. The molded bodies were then calcined in 800 °C nitrogen atmosphere for 2 hours to carbonize phenol resin. Thereafter, they were sintered in 1800 °C vacuum for 1 hour and used directly as specimens without machining. As shown in photographs 2 and 3 to be discussed later, a slight swelling of the specimen surfaces was found in the portion of coated particles. The same phenomenon has been observed for the real fuel compact. It is believed to be caused by the difference in shrinkages relative to the matrix during the sintering processes. Table 1 shows the measured results of the dimension, matrix density and volumetric packing fraction of SiC-kernel coated particles of the prepared specimens.

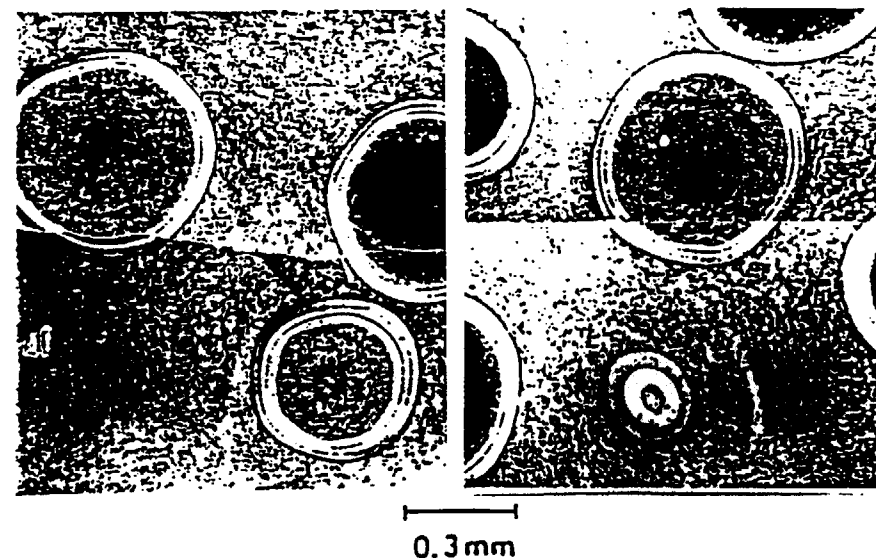


Photo 1. Microscopic structure of the fuel compact model.

TABLE 1. SPECIMEN CHARACTERISTICS (MEAN VALUE)

specimen	size (mm)	density of matrix (g/cm <sup>3</sup> )	volume fraction of SiC-kernel coated particle (%)
(I)	φ 20.09 × 2.05	1.87	30.2
(II)	φ 20.03 × 4.94	1.73	29.1
(III)	φ 8.00 × 80.13	1.70	28.8
(IV)	φ 8.01 × 14.90	1.88	28.5

## 2.2 Fuel compact matrix

To study the physical properties of fuel matrix, specimens which do not contain fuel particles were also prepared. They were prepared by undergoing the same heat treatments as the mold disk (φ30×3mm), using material having the same composition as that described in the previous section. The apparent density of the matrix material was 1.71g/cm<sup>3</sup>.

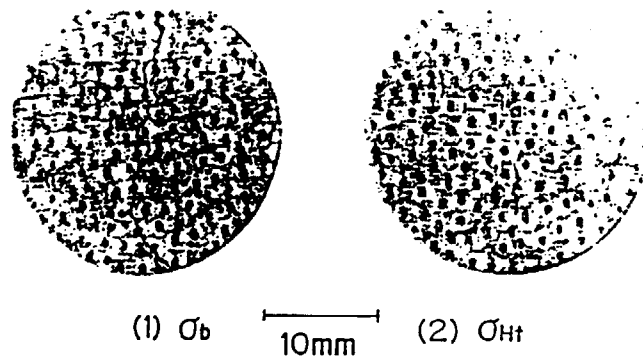


Photo 2. Typical fractures in the diametral compression (left) and bending tests (right) of the fuel compact disk specimens.

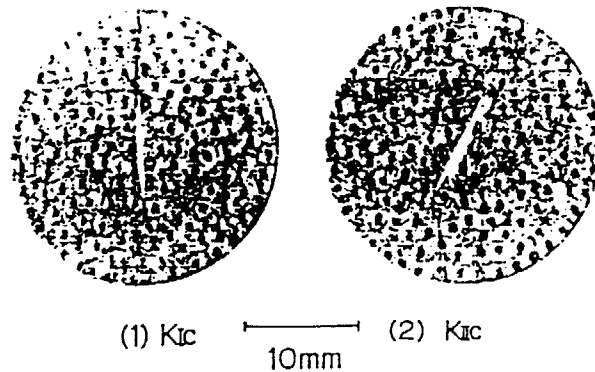


Photo 3. Typical fractures in mode I (left) and mode II (right) fracture toughness tests of the fuel compact disk specimens.

### 3. Experimental Methods

By using specimens having the shapes and dimensions as shown in Table 1 as the fuel compact model, a series of mechanical and fracture mechanics tests as well as thermal shock tests were carried out. That is to say, ① bending strength  $\sigma_b$  test by a ball indenter<sup>(6)</sup>, ② diametral compression strength  $\sigma_{Ht}$  by circular anvils<sup>(6)</sup>, ③ mode I and II fracture toughness  $K_{Ic}$ ,  $K_{IIc}$  tests<sup>(7,8)</sup>, ④ thermal shock resistance  $\Delta$  ( $=\sigma_t k/E\alpha$ ,  $\sigma_t$  is tensile strength,  $k$  is thermal conductivity,  $E$  is Young's modulus and  $\alpha$  is thermal expansivity) test<sup>(10)</sup> and ⑤ thermal shock fracture toughness  $\nabla$  ( $=K_{Ic}k/E\alpha$ ,  $K_{Ic}$  is mode I fracture toughness value) test<sup>(11)</sup>, and thermal diffusivity  $\chi$  test<sup>(16)</sup> were carried out. The details are shown in each reference. Fig.2 shows the essentials of the experimental methods using disk type specimens.

#### 3.1 Neutron irradiation

Table 2 shows the irradiation conditions of fuel compact model specimens in JMTR. Those for the case of graphite IG-110<sup>(2)</sup>, a core material in HTTR, are also shown. As both of these conditions are similar and close to the actual situation in HTTR, a comparison of irradiation effects can be made between the two.

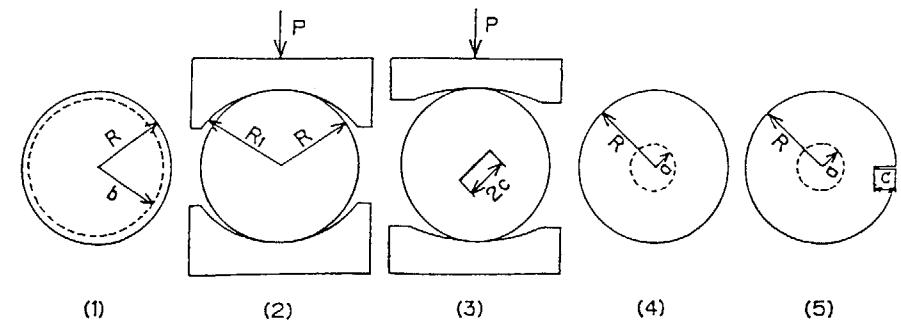


FIG. 2. Measuring methods for disk specimens.

TABLE 2. NEUTRON IRRADIATION CONDITIONS IN THE JMTR

specimen	Capsule number	Neutron flux ( $n/cm^2s$ , $E>29fJ$ )	Temperature ( $^{\circ}C$ )	Neutron fluence ( $n/cm^2$ , $E>29fJ$ )
Fuel compact	87H-33u	$3.28 \times 10^{14}$	900 (850~950)	$1.7 \times 10^{21}$
graphite IG-110	80H-31u	$1.10 \times 10^{14}$	925 (850~1000)	$(1.1-1.5) \times 10^{21}$

TABLE 3. MEAN VALUES OF EXPERIMENTAL RESULTS OF THE FUEL COMPACT MODEL BEFORE AND AFTER NEUTRON IRRADIATIONS AND THEIR COMPARISONS WITH GRAPHITE IG-110

Material	TP	Fuel compact model		graphite IG-110	
Irradiation	N	before	after	before	after
Bulk density	4	1.82	1.84	1.75	1.75
$\gamma$ (g/cm <sup>3</sup> )			(1.01)		(1.00)
Dimensional change	4	-	-	-	-
(%)			(-0.58)		(-0.04)
Young's modulus	4	8.89	9.97	7.80	11.8
E (GPa)			(1.45)		(1.51)
Compressive strength	4	25.7	35.9	70.5	89.2
$\sigma_c$ (MPa)			(1.40)		(1.27)
Bending strength	4	12.6	17.8	38.7	47.8
$\sigma_b$ (MPa)			(1.40)		(1.23)
Diametral compression	2	6.43	9.10	15.3	18.5
$\sigma_{nc}$ (MPa)			(1.42)		(1.21)
Electric resistance	4	2097	4241	1150	1927
$\rho$ ( $\mu\Omega\text{cm}$ )			(2.02)		(1.68)
Rockwell hardness	7	49.3	63.4	71.0	78.0
H <sub>0.15x</sub>			(1.29)		(1.10)
Impact fracture energy	2	0.12	0.09	0.41	0.42
E <sub>0</sub> (J/cm <sup>2</sup> )			(0.75)		(1.02)
Mode I fracture	4	0.82	0.90	0.78	1.01
toughness K <sub>IC</sub> (MPa <sup>1/2</sup> )			(1.45)		(1.29)
Mode II fracture	4	0.86	0.83	0.98	1.24
toughness K <sub>IIc</sub> (MPa <sup>1/2</sup> )			(1.26)		(1.29)
K <sub>IIc</sub> /K <sub>IC</sub>		1.06	0.92	1.23	1.23
Thermal diffusivity	2	34.3	21.9	48.5	26.0
$\kappa$ (mm <sup>2</sup> /s)			(0.64)		(0.54)
Thermal shock	7	9.65	4.18	31.9	21.7
resistance $\Delta$ (W/mm)			(0.43)		(0.68)
Thermal shock fracture	7	25.8	14.0	34.4	26.8
toughness $\nabla$ (W/mm <sup>1/2</sup> )			(0.54)		(0.78)
Equivalent crack size		3.47	3.36	0.13	0.14
$Ce_1 = (K_{IC}/\sigma_c)^2/\pi$ (mm)			(0.97)		(1.08)
$Ce_2 = (\nabla/\Delta)^2/\pi$ (mm)		2.28	3.57	0.37	0.49
			(1.57)		(1.32)

#### 4. Experimental Results and Discussions

Table 3 summarizes the mean values of experimental results for the specimens of fuel compact model and graphite IG-110 before and after neutron irradiations. Values inside the parentheses show the ratio of "after-irradiation" and "before-irradiation" values. Experimental results are explained in the followings mainly for the fuel compact model.

##### 4.1 Mechanical properties

Dimensional change of the fuel compact before and after neutron irradiation was about 0.58 % in shrinkage. This is larger than the value of 0.04 % for IG-110. Other data<sup>(12)</sup> for IG-110, however, are in the range of 0.2-0.5 % under similar irradiation conditions. The shrinkage of fuel compact model can, thus, be considered to be about the same order of magnitude or somewhat larger than the case of IG-110. Such shrinkage values due to neutron irradiation of fuel compact are close to those for the case of graphite matrix reported by Schulze<sup>(13)</sup>.

Young's modulus E, compressive strength  $\sigma_c$ , bending strength  $\sigma_b$  and diametral compressive strength  $\sigma_{nc}$  of the fuel compact model are smaller than those of IG-110. Among these, values of  $\sigma_c$  and  $\sigma_{nc}$  are especially small. These are the strengths related to shearing fracture in the stress field dominated by compressive stress. Therefore coated particles and the defects on their interfaces appear to be sensitive to shearing stresses.

Rockwell hardness (H<sub>0.15x</sub>) of the fuel compact was about 70-80% of IG-110. This is smaller than the difference in mechanical strengths. However, impact fracture energy E<sub>0</sub> was only about 20-30%, showing a weak tendency against dynamic stresses.

Young's modulus of the fuel compact increased 1.45 times due to neutron irradiation. Such an increase in Young's modulus due to irradiation is similar to that observed by Delle<sup>(14)</sup> for the case of graphite matrix. On the contrary, however, the impact fracture energy E<sub>0</sub> of the fuel compact decreased. The increase in mechanical properties of the fuel compact due to neutron irradiation shows similar trend to that observed for graphite IG-110<sup>(2)</sup> and other nuclear grade graphites<sup>(15)</sup>. This is in agreement with the well-known general tendency, and is believed to be due to some stiffenings brought about by the neutron irradiated interlayer atoms restraining the displacement movabilities.

Photo.2 shows the typical fracture appearances observed in the tests of (1) bending strength  $\sigma_b$  and (2) diametral compressive strength  $\sigma_{nc}$ . Crackings proceed meanderingly through the matrix parts of the spacings between coated particles. Exfoliations of coated particles from the fracture surfaces were sometimes observed. No characteristic difference of fracture surfaces was noticed compared to the cases of thermal shock fractures by SEM to be discussed later.

##### 4.2 Fracture mechanics properties

Mode I fracture toughness K<sub>IC</sub> of the fuel compact was about 80-90% of IG-110 for both before- and after- neutron irradiation. But, mode II fracture toughness K<sub>IIc</sub> was about 70% or less than that of IG-110 showing a larger

difference.  $K_{IC}$  and  $K_{IIc}$  increased by a factor of 1.45 and 1.26 respectively due to irradiations, showing a similar trend compared to the case of IG-110, for which the increase was by a factor of 1.29. Ratios of fracture toughnesses ( $K_{IIc}/K_{IC}$ ) for the fuel compact, however, were 1.06 and 0.92 respectively before and after irradiation, and are smaller than the ratio of 1.23 obtained for the case of IG-110. ( $K_{IIc}/K_{IC}$ ) represents the ratio of pure shearing strength and tensile strength of the material. It is noteworthy that shearing strength, which was slightly larger than the tensile strength before irradiation, becomes smaller after neutron irradiation. Such a reversal due to irradiation differs from the trend commonly observed for brittle materials. It is deduced that the shearing strength or fracture toughness of mode II at the interface of coated particle and matrix has a tendency to degrade significantly due to irradiation.

Photo.3 shows typical fracture appearances observed in the fracture toughness tests of (1) mode I and (2) mode II. Along the central slit, traces of exfoliation of coated particles, formed during the machining, can be seen. For (1), crackings proceed meanderingly through matrix spacing between coated particles. For (2), cracking initially proceed from the tip of slit and then gradually change the direction toward that of mode I progression.

#### 4.3 Thermal diffusivity and electric resistivity

Thermal diffusivities  $\alpha$  of the fuel compact before and after irradiations were about 70% and 84% respectively of those for graphite IG-110. The ratio of the values before and after irradiations was 0.64. It is known that, for graphite, heat is propagated by lattice vibration. For fuel compact, the SiC coated particles become a barrier for heat propagation, thus lowering the thermal conductivity compared to graphite.

Electric resistivities  $\rho$  of the fuel compact before and after irradiations were respectively about 1.8 times and 2.2 times larger than those of IG-110. The ratio of the values after and before irradiation was about 2.0, which was larger than the ratio of about 1.7 for IG-110.

Using the well-known approximate relationship between electric resistivity  $\rho$  and thermal conductivity  $k$  developed by Mason and Knibbs<sup>(10)</sup>, for graphite,  $k$  values before irradiation were calculated to be about 0.64 W/cm°C and about 1.12 W/cm°C respectively for the fuel compact and IG-110. Although the specific heat,  $C_p$ , of the fuel compact is presently unknown, assuming it to be roughly 1.00 Ws/g°C (at 125°C) after the value of graphite IG-110, the thermal conductivity is deduced from the measured value of thermal diffusivity  $\alpha$  as 0.62 W/cm°C. This thermal conductivity value of the fuel compact is close to the room temperature value of JAERI data<sup>(17)</sup>.

#### 4.4 Thermal shock resistance and fracture toughness

Fig.3 illustrates an example of recorder charts obtained in the  $\Delta$  and  $\nabla$  testings before and after irradiation, showing the electric power near the critical power at which the fracture occurs. Some fluctuations of electric power during arc discharge were noted in these charts, but the mean values were measured.

Fig.4 (a) and (b) show the ranges of thermal shock resistance  $\Delta$  and fracture toughness  $\nabla$  which were obtained from each equations<sup>(10,11)</sup>, after

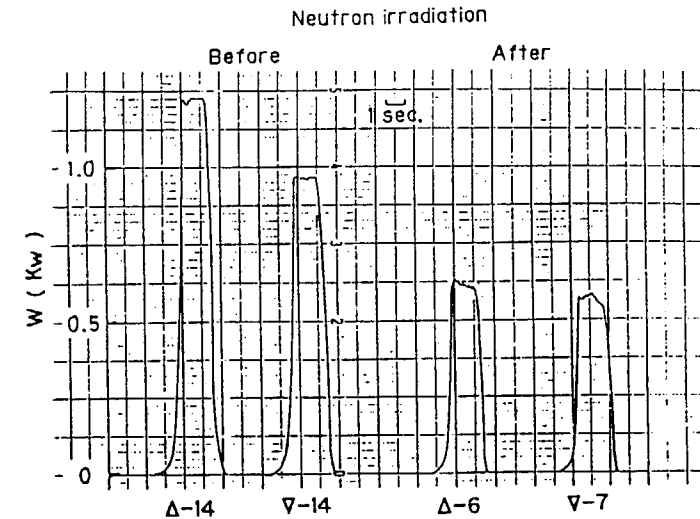


FIG. 3. Recorder charts of electric power in the thermal shock resistance ( $\Delta$ ) and the fracture toughness ( $\nabla$ ) tests for the fuel compact model.

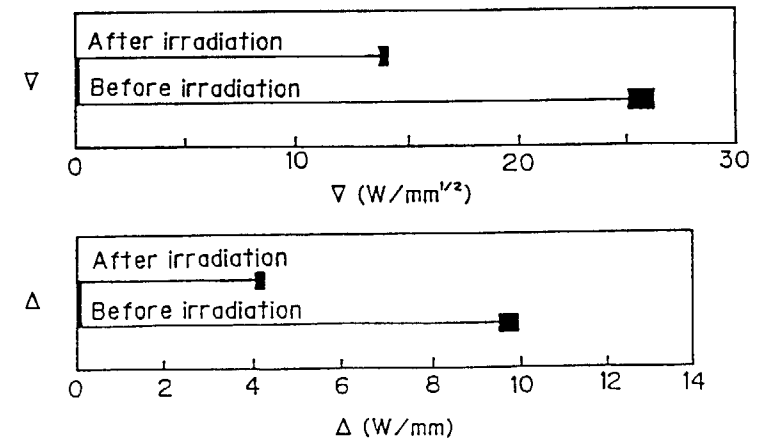


FIG. 4. Thermal shock resistance ( $\Delta$ ) and thermal shock fracture toughness ( $\nabla$ ) for fuel compact.

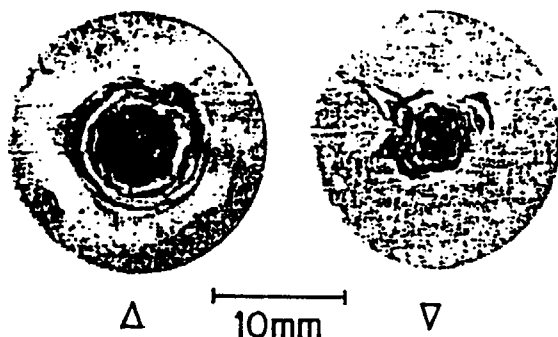


Photo 4. Typical fractures in the thermal shock resistance (left) and fracture toughness (right) tests of the fuel compact disk specimens.

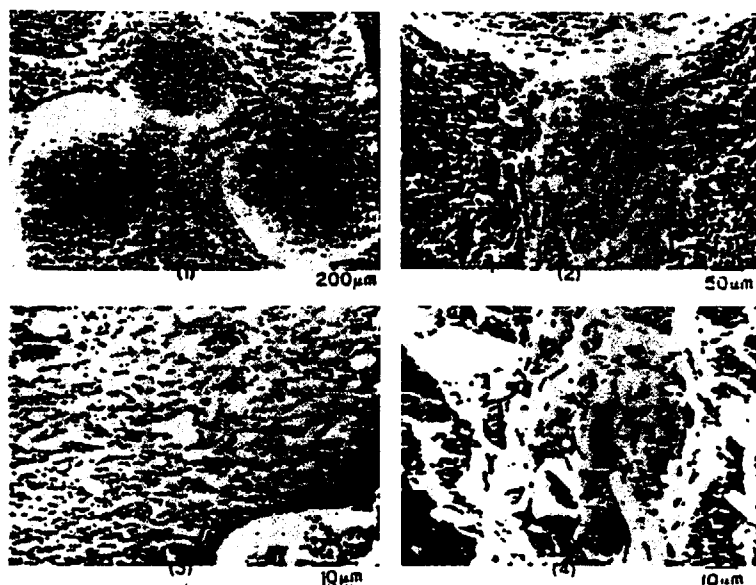


Photo 5. Typical fractographs of the fuel compact: (1) and (2) general view; (3) fuel particle; (4) matrix.

applying  $\beta$ -correction using the critical electric powers in the thermal shock testing. The mean values evaluated for these ranges were entered as the values of  $\Delta$  and  $\nabla$  in Table 3.

The thermal shock resistance  $\Delta$  and the thermal shock fracture toughness  $\nabla$  of the fuel compact are respectively about 1/3 and 1/2 of the values of graphite IG-110. After neutron irradiation, both  $\Delta$  and  $\nabla$  decrease about 50%, showing larger degradations compared to the cases of IG-110.

Photo.4 shows typical fracture appearances observed in the thermal shock resistance and fracture toughness testings of the fuel compact. For the thermal shock resistance tests, the crack proceeds from the periphery toward the center. For the thermal shock fracture toughness test, the crack propagates from the tip of the edge slit toward the center following mode I progression.

Photo.5 shows some fractographs of the thermal shock fracture surfaces of the fuel compact. Photo.(1) shows a general view of coated particles and matrixes on the fracture surface. Part of it is magnified and shown in photo.(2). From these photos, it can be seen that crackings proceed along the spacings between coated particles or along the interfaces of particles and matrixes. On the fracture surface of matrix, well developed flaky layers of apparently of natural graphite structure, can be seen. The longitudinal sizes of the flakes are seen to form a fibrous texture along spherically coated particles. Photo.(3) shows small powders of less than several  $\mu\text{m}$  and flakes of ten-odd  $\mu\text{m}$  in length adhering to the coated particles. Photo.(4) shows the well developed flaky structures on the fracture surfaces of matrixes.

#### 4.5 Equivalent crack size

According to fractographs of the fuel compact, the fracture propagates along the interfaces of the coated particles is the matrixes. The coated particles are high rigidity inclusions. Their surroundings are centers of complex stresses resulting from the interference of many defects. Matrixes are microscopically very inhomogeneous having some fibrous structures, which surround the coated particles. Hence, the microscopic distributions of stresses inside the fuel compact are presumed to be very complex.

For a fracture mechanical evaluation, the equivalent crack size  $C_{e1}$  was calculated from the fracture toughness value and tensile strength, which was deduced from the bending strength of fuel compact. The equivalent crack size  $C_{e2}$  was also estimated by the thermal shock fracture toughness and the thermal shock resistance.

Although  $C_{e1}$  and  $C_{e2}$  were calculated based on completely different experiments, they show surprisingly good agreement. The equivalent crack size represents the critical size at the final moment of fracture of a defect growing under a tensile stress. It is considerably larger than the apparent defect size. The value of  $C_{e2}$  for graphite IG-110 was 0.37-0.49mm and corresponds to several times the maximum coke grain size (about 0.10mm). In the case of fuel compact, the coated particles indwelled in the matrix act as heterogeneous inclusions, thus providing plenty of room for the defect to grow. This is thought to correspond to the fact that the critical electric power found in the thermal shock fracture toughness test of the disk (30mm in diameter) with an edge slit of 3mm depth was surprisingly closed to that found in the thermal shock resistance test of the disk without the edge slit.

#### 4.6 Thermal stresses of fuel compact under normal operating condition

According to the HTTR core engineering design of JAERI<sup>(16)</sup>, the maximum fuel temperature at the standard core (after 330 days of operation) is 1495°C and 1417°C at the outer surface of the fuel compact when the coolant temperature at the reactor outlet is 950°C. From the temperature difference  $T_d$  between the inner and outer surfaces, the maximum tensile thermal stress,  $\sigma_{\theta, \max}$ , in the circumferential direction, considering it as a cylinder of outer and inner radius  $b$  and  $a$  can be calculated as follows;

$$\sigma_{\theta, \max}/E\alpha_{(r=b)} = \frac{T_d}{2(1-\nu)} \left( \frac{\xi^2+1}{\beta^2-1} - \frac{1-\ln\xi}{\ln\beta} \right) \quad (1)$$

Substitution of  $\beta=b/a=1.3/0.5=2.6$ ,  $\xi=b/r=1$ ,  $\nu=0.2$  and  $T_d=1495^\circ\text{C}-1417^\circ\text{C}=78^\circ\text{C}$  into the equation, yields.

$$\sigma_{\theta, \max}/E\alpha_{(r=b)} = 34.2^\circ\text{C} \quad (2)$$

Now introducing the thermal conductivity  $k$  ( $0.62\text{W}/\text{cm}^\circ\text{C}$ ) of the fuel compact obtained in section 4.3 and comparing it with the thermal shock resistance  $\Delta$ , one obtains;

$$\sigma_{\theta, \max}k/E\alpha = 2.1\text{W}/\text{mm} \ll \Delta \quad (3)$$

#### 4.7 Thermal stresses of fuel compact in experiments under abnormal conditions

To evaluate the safety of real fuel compact under abnormal operating conditions, an experiment was conducted by applying high energy pulse irradiations of  $2300\text{J}/\text{gUO}_2$  maximum using the Nuclear Safety Research Reactor (NSRR) of JAERI. Based on the experimental results, it was reported that all coated particles were damaged and reticulate crackings were found on the surface of fuel compact<sup>(17)</sup>.

The real fuel compact (39mm in height and 26mm and 10mm in the outer and inner diameter) has a weight of 45gr and contains 15.3gr of  $\text{UO}_2$ . Now assuming that the aforesaid maximum energy is applied pulse-wise during a period of 15ms, the heat generation  $H$  per unit volume of the fuel compact can be calculated as follows;

$$H = 2300\text{J}/15.3\text{grUO}_2 \cdot 15\text{ms} = 2300\text{J}/1.472\text{cm}^3\text{UO}_2 \cdot 15\text{ms} = 1.042 \times 10^5\text{W}/\text{cm}^3\text{UO}_2 \quad (4)$$

No temperature data is available from this experiment under abnormal conditions. The thermal stresses in the fuel compact are regarded as that caused by the pulse-wise uniform heat generation of  $H$  in a cylindrical fuel element. The temperature at the instant the fuel compact cracking occurs is assumed to be room temperature, with equal temperature at both inner and outer surfaces. The radial and circumferential thermal stresses, in this case, are calculated by the following equations<sup>(22)</sup>;

$$\sigma_r = \frac{E\alpha}{1-\nu} \left( \frac{(r^2-a^2)\{\xi(b)-\xi(a)\}}{(b^2-a^2)r^2} - \frac{\{\xi(r)-\xi(a)\}}{r^2} \right) \quad (5)$$

$$\sigma_{\theta} = \frac{E\alpha}{1-\nu} \left( \frac{(r^2+a^2)\{\xi(b)-\xi(a)\}}{(b^2-a^2)r^2} + \frac{\{\xi(r)-\xi(a)\}}{r^2} - m \ln r + nr^2 - f \right) \quad (6)$$

where  $m = \{n(b^2-a^2) - (T_1-T_2)\} / \ln(b/a)$ ,  $n = H/4k$ ,  
 $f = \{n(a^2 \ln b - b^2 \ln a) + (T_1 \ln b - T_2 \ln a)\} / \ln(b/a)$ ,  
 $\xi(r) = r^2 \{ (2 \ln r - 1)m - nr^2 + 2f \} / 4$

Since  $\sigma_r$  is zero at the inner and outer surfaces of the fuel compact, its value at the central surface  $r=(a+b)/2$  was calculated.  $\sigma_{\theta}$ , meanwhile, was calculated based on the outer surface, as follows;

$$\begin{aligned} -\sigma_r/E\alpha_{(r=(a+b)/2)} &= 604^\circ\text{C}, \\ \sigma_{\theta}/E\alpha_{(r=b)} &= 2059^\circ\text{C} \end{aligned} \quad (8)$$

To compare with thermal shock resistance  $\Delta$ , introducing  $k$  ( $=0.62\text{W}/\text{cm}^\circ\text{C}$ ) into the above equations, one obtains

$$\begin{aligned} -\sigma_r k/E\alpha_{(r=(a+b)/2)} &= 374\text{W}/\text{cm} \gg \Delta \\ \sigma_{\theta} k/E\alpha_{(r=b)} &= 1277\text{W}/\text{cm} \gg \Delta \end{aligned} \quad (9)$$

Further, assuming that the fuel compact is free from axial restriction, the axial stress  $\sigma_z$  can be similarly calculated as follows;

$$\sigma_z k/E\alpha_{(r=b)} = 1622\text{W}/\text{cm} \gg \Delta \quad (10)$$

Based on the calculations shown in sections 4.6 and 4.7 above, it can be said that the fuel compact is sufficiently safe since the thermal stress is well below the thermal shock resistance  $\Delta$  under normal operating conditions. However, the thermal shock stresses in the experiment by NSRR for exceed  $\Delta$  in all directions, substantiating that crackings occurred on the surface of the fuel compact. Furthermore, the equivalent crack size of the fuel compact is quite large, about 3mm as deduced previously. This tends to explain well the circumstance that no final fracture ensured despite the occurrence of the crackings.

#### 4.8 Thermal shock testings of fuel compact matrix

Similar thermal shock resistance and fracture toughness testings were carried out using disk specimens of matrix containing no fuel particles. The typical fracture appearances by results of SEM observation indicated close similarity to the matrix part of Photo.5.

The mean values of the experimental results are as follows;

$$\begin{aligned} \Delta &= 18.4\text{W}/\text{mm}, \\ \nabla &= 49.8\text{W}/\text{mm}^{1/2} \end{aligned}$$

The equivalent crack size  $C_{\Delta 2}$  can, therefore, be calculated as  $C_{\Delta 2}=2.33\text{mm}$ . The fracture toughness values are

$$K_{IC} = 0.93\text{MPa}\text{m}^{1/2}, \quad K_{IC} = 1.08\text{MPa}\text{m}^{1/2}.$$

These results of  $\Delta$  and  $\nabla$  are about 2 times larger than those of the fuel compact model containing coated fuel particles. The fracture toughness values of the matrix are also larger, about 1.5 times in the model and about 1.6 times in the model.

The value of  $C_{\Delta 2}$ , meanwhile, is about the same as that of the fuel compact model, as indicated by these ratios. It can, thus, be seen that existence of coated fuel particles in the fuel compact reduces both the resistance and the fracture toughness against thermal shocks by about a half.

## 5. Conclusion

By using SiC-kernel particles instead of  $\text{UO}_2$ -kernel, HTTR fuel compact models were prepared by dispersing coated particles in a graphite matrix, and by following the same manufacturing process as that for real fuel compact.



A series of mechanical and fracture mechanics properties, as well as resistances against thermal shocks were then investigated. The results were compared with those of the core graphite IG-110 for HTTR. Effects of neutron irradiation by JMTR were also compared. Although the number of test specimens was small, especially for after-irradiation case, the obtained mean values of experimental results are tabulated in Table 3.

These results can be summarized as follows;

(1) Mechanical properties; The mechanical strengths of the fuel compact are about 1/2 - 1/3 those of graphite IG-110. Judging from the relatively small difference between Young's moduli, the enclosed coated particles appear to act as one concentrated source of structural sensitivity.

(2) Fracture toughness; Fracture toughness values of the fuel compact are about 70~80% of those of IG-110. The difference is small compared to that of mechanical strength. This implies that the enclosed coated particles become dispersed inclusions or defects, thus having a tendency to moderate the stress singularities at the crack tips.

(3) Thermal properties and electric resistivity; Thermal diffusivities of the fuel compact are about 70 % and about 84 % respectively of IG-110 for before-irradiation and after-irradiation. Assuming an identical specific heat, and judging from the difference in specific gravity, the difference in the thermal conductivities can be expected to be small. The electric resistivity is about 2 times that of IG-110.

(4) Thermal shock resistance and fracture toughness; Thermal shock resistances of the fuel compact are about 1/3 and 1/5 respectively of IG-110 for before and after-irradiations. The degradation of thermal shock resistance and thermal shock fracture toughness due to irradiation is about 43 % and about 54 %, respectively. The differences are not as significant as those of the thermal shock resistances. These circumstances resemble the characteristic differences of mechanical strengths and fracture toughnesses between the fuel compact and IG-110. This is an indication that the defects have plenty of room to grow before reaching the final fracture. The equivalent crack sizes calculated from the thermal shock tests are about 2.3 mm before irradiation and about 3.6 mm after irradiation. They are considerably larger than the value of about 0.4-0.5 mm for IG-110. Such large equivalent crack sizes of the fuel compact tend to substantiate the fact that the crackings found in the fuel safety experiment of NSSR under abnormal conditions did not lead to fuel destruction.

Thermal shock testings of matrix material containing no coated fuel particles were also carried out. Then it was revealed that both thermal shock resistance and fracture toughness deteriorate to about one-half as a result of containing coated fuel particles.

## REFERENCES

- [1] JAERI, Present Status in the Develop. of Multi - purpose High Temp. Gas Cooled Reactor (1981).
- [2] S.Sato, K.Kawamata, A.Kurumada, H.Ugachi, H.Awaji and R.Ishida, Degradations of thermal shock resistance and fracture toughness of neutron irradiated reactor graphite, J.Nucl.Sci. and Tech., 24 (1987) pp.547-556.
- [3] K.Fukuda, et al., Research and development of HTGR fuels, JAERI-M 89-007 (1989) 7.
- [4] JAERI, Present Status in the Develop. of High Temp. Engineering Test Reactor, (1987) 33.
- [5] S.Sato, A.Kurumada, et al., Influences of grain size and porosity on the thermal stress fractures of boron carbides, J. Faculty of Eng., Ibaraki University, 33 (1985) pp.31-41.
- [6] H.Awaji and S.Sato, Combined mode fracture toughness measurement by the disk test, J.Eng. Materials and Tech., ASME-H, 100 (1978) pp.175-182.
- [7] H.Awaji and S.Sato, Diametral compressive testing method, J.Eng. Materials and Tech., ASME-H, 101 (1979) pp.139-147.
- [8] S.Sato, K.Kawamata and H.Awaji, Combined mode fracture toughness of reactor-grade graphite at high temperature, High Temp. - High Press., 12 (1980) pp.23-32.
- [9] S.Sato and S.Miyazono, Studies of elastic modulus of irradiated graphite by means of an ultrasonic pulse method, Carbon, 2 (1964) pp.103-114.
- [10] S. Sato, K. Sato, Y. Imamura and J. Kon, Determination of the thermal shock resistance of graphite by arc discharge heating, Carbon, 13 (1975) pp.309-316.
- [11] S.Sato, H.Awaji and H.Akuzawa, Evaluation of the thermal shock fracture toughness of reactor graphite by arc discharge heating, Carbon, 16 (1978) pp.103-109.
- [12] JAERI, Present Status in the Develop. of High Temperature Gas Cooled Reactor (1986) 126.
- [13] R. E. Schulze, H. A. Schulze and W. W. Delle, Irradiation behaviour of graphite matrix for HTGR - Effects of irradiation parameters and influences of material variations - , 5th Inter. Conf. on Carbon and Graphite, London, (1978) pp.904-910.
- [14] W.W.Delle, H.A.Schulze and R.E.Schulze, Influences on the change in the Young's modulus of graphite materials for HTR under fast neutron exposure at irradiation temperatures between 400 and 1400°C, 12th Biennial Conf. on Carbon, Pittsburgh, (1975) pp.127-128.
- [15] S.Sato, A.Kurumada, K.Kawamata, et al., Neutron irradiation effects on thermal shock resistance and fracture toughness of graphites as plasma-facing first wall components for fusion reactor devices, Carbon, 27 (1989) pp.507-516.
- [16] B.T.Kelly, Physics of Graphite, Applied Science Publishers, London (1981) 231.
- [17] K. Fukuda, Private communication (1990).
- [18] S.Sato, Statistical analysis on the mechanical strength of graphite, Symposium on Carbon, Tokyo (1964) V-5-1~4. or NSJ Tanso, NO.38 (1964) pp.1-18.
- [19] S.Maruyama, et al., Core thermal and hydraulic design of high temperature engineering reactor (HTTR), JAERI-M 88-255 (1988).
- [20] Strength Design Databook, Revised Edition, Shokabou, Tokyo (1971) 996.
- [21] Y. Yasuno, et al., Report of the first technical meeting on high temperature gas - cooled reactor, JAERI-M 90-078 (1990) 40.
- [22] Z. Zudans, et al., Thermal Stress Techniques in the Nuclear Industry, American Elsevier Publishing Co., New York, (1965) 492.

## DISCUSSION

## Questions or Comments

Name: Chernikov

What do you think about a contribution of products interaction  $\text{UO}_2$  with pyrocarbon in stress-strain state of the compacts?

## Answer:

Thank you for your essential question.

The influence of  $\text{UO}_2$  by fission products is confined at the barrier of high density PyC and SiC, except very rare case. Therefore stress-strain state in the compact is not almost influenced. So far as our study reported today, the influences are not known quantitatively.

## Questions or Comments

Name: I.S. Mosevitskii

1. What is a volume fraction of matrix graphite in the fuel codes of HTTR?
2. What do you think about a minimal permissible volume fraction of matrix graphite for another like constructions?

## Answer:

1. It was about 70% in the fuel compact. In the fuel rod, there are ten-odd fuel compact,
2. I don't know. test results by JAERI and Nuclear Fuel Industry Ltd. on the volume ratio to obtain the optimum condition. Probably about 70% may be the best.

## Questions or Comments

Name: M. Brie

Did you measure the young's modulus before and after irradiation.

## Answer:

The measurements were carried out by ultrasonic pulse method.

## A METHOD FOR ASSESSING THE EFFECTS OF GRAPHITE PROPERTY VARIABILITY ON CORE STRUCTURAL INTEGRITY CRITERIA

R.C.B. JUDGE

Gas Cooled Reactor Assessments Department,  
AEA Reactor Services,  
Risley, Warrington, Cheshire,  
United Kingdom

## Abstract

The Reserve Strength Factor (RSF) is the factor of safety used in assessments of Advanced Gas-cooled Reactor core integrity. Values of RSF currently used are based on engineering judgement. These values should, in principle, be related to variability due to inhomogeneity of graphite, systematic error in the calculation route and uncertainties in property measurement.

A probabilistic approach, bringing the safety assessment of the graphite core into line with other reactor components, is described in this paper.

A probability distribution for the RSF may be obtained by repeatedly following the full calculation route. In each iteration, appropriate values for the key parameters will be obtained using the Latin Hypercube sampling technique. The number of key parameters will be kept to a minimum by first using the sensitivity calculations to eliminate the less important ones.

Material properties have generally been obtained from tests on small specimens. The variability in these properties would, intuitively, be expected to be greater than that found in the brick (on which the RSF calculations are based). In the case of the non-destructive properties these size effects may be treated by applying the central limit theorem. Core brick strength will be obtained from a series of on-going experiments. The statistical distribution of brick strength will be assumed to follow a Weibull function fitted to small specimen data.

Work is currently underway, applying this proposed methodology to an Advanced Gas-cooled Reactor core.

## 1. BACKGROUND

## 1.1 Introduction

The basic design of an Advanced Gas-cooled Reactor (AGR) core consists of fuel assemblies surrounded by some three thousand graphite bricks which act as moderator. The current policy is that the structural integrity of the core should be maintained and that none of the bricks should fail. This is likely to introduce excessive conservatism into safety assessments of the graphite core.

The recognition that inherent redundancies in the core structure allow a small number of cracked bricks to exist without compromising safety is preferred. An assessment of whole core performance may then be used to provide a realistic figure for an acceptable probability of brick failure.

The issues of core redundancy and the ability of the core to withstand a limited number of cracked bricks has been considered in other recent work<sup>[1]</sup>. This involved the use of advanced finite element techniques, modelling the graphite core bricks in three dimensions and taking into account the non-linearities of both graphite behaviour and contact across crack faces.

A probabilistic approach to the assessment of whole core performance is proposed in this paper. This method may be used to demonstrate the soundness of the majority of the core structure. It will also bring the techniques used in safety assessment of the graphite core into line with those used on other reactor components.

The following section gives an overview of core brick behaviour and the design criterion currently used to define brick integrity.

## 1.2 Structural integrity

Graphite bricks are stacked in columns to form an AGR core. The columns are radially keyed to allow for core movement due to temperature changes and graphite shrinkage. Keys are located in eight keyways which extend over the full height of a brick; the active keys extend over the central third of a keyway with filler keys over the remaining height.

A brick will be subject to external stress due to the weight of the column above. In addition, uneven core restraint under both normal operation and fault conditions may result in tilting of a brick column giving rise to external loads on surrounding bricks. These loads will be transmitted via the keying mechanism. Experimental work has shown that a brick will fail if sufficient load is applied via the keying mechanism with crack initiation at the corner of a keyway (the keyway root).

Fast neutron irradiation and radiolytic oxidation cause changes to the physical and mechanical properties of graphite. Structural integrity of a graphite brick is affected by:

### 1. Component failure stress ( $\sigma_f$ )

The strength of graphite is increased by fast neutron hardening but reduced by radiolytic oxidation. The net effect at the keyway root of a peak rated core brick is an initial rapid increase in strength followed by a slight fall off with time.

### 2. Irradiation shrinkage stress ( $\sigma_i$ )

Fast neutron irradiation causes graphite to change dimension with the result that shrinkage stresses develop over a graphite brick section. These stresses are considerably relieved by irradiation induced

creep. At early times in life the stress at the keyway root is compressive but towards end of life the stress distribution reverses and gives tensile stress at the keyway root. This reduces the capability of a brick to withstand applied loads.

### 3. Thermal stress at shutdown ( $\sigma_{th}$ )

Fast neutron irradiation causes changes to the coefficient of thermal expansion of graphite with the result that thermal stresses develop over a graphite brick section when the reactor is shutdown. At early times in life the thermal shutdown stress is compressive at the keyway root but at later times this stress becomes tensile. This reduces the capability of a brick to withstand applied loads.

### 4. Duty stress ( $\sigma_d$ )

External stresses arising both from the weight of the column above and from load transfer via the keying mechanism are included in the value for duty stress. In addition, brick distortion arising from graphite dimensional changes with creep strain relief can cause the tips of a keyway to close ('dovetailing'). This may result in a key becoming jammed in the keyway, which could lead to additional loads on a core brick.

These four stress terms are related by superposition to give the Reserve Strength Factor (RSF):

$$RSF = \frac{\text{Strength remaining to withstand applied load}}{\text{Stress due to applied load}} = \frac{\sigma_f - \sigma_i - \sigma_{th}}{\sigma_d}$$

The RSF is evaluated at the keyway root which is the most likely position for the brick to fail.

The structural integrity of bricks in an AGR core is embodied in the Reserve Strength Factor. Currently, values of 5, 2 and 1 are recommended for the RSF under operating, shutdown and earthquake conditions, respectively. These figures were based on engineering judgement. There has been no detailed justification for the currently used values of RSF.

As the demonstration of an adequate RSF is a major consideration in the safety case for the graphite moderator, some form of justification is clearly required for the limiting value of RSF. In principle, this should be related to scatter in the input parameters.

## 1.3 Sources of data scatter

Mean values of material properties have been used in previous studies on RSF. In any probabilistic assessment allowances must be made for uncertainties in the data.

The scatter inherent in graphite properties comes from a number of sources. These include

1. Inhomogeneity of graphite
2. Systematic error in the calculation route.  
This may be due to inadequacies in the theoretical models of graphite behaviour and dosimetry.
3. Uncertainties in measurement.  
In the controlled environment of a laboratory these uncertainties are likely to be small. The same is unlikely to hold for reactor data, which might be prone to significant errors.

## 2. METHODOLOGY

The proposed method for determining a probability distribution for the RSF involves a number of steps. These are outlined in the following sections.

### 2.1 Assessment of calculation route for RSF

The calculation route which needs to be followed to obtain the RSF is complex, with a number of interdependencies. It requires breaking down to a set of base material properties and loading conditions (base parameters).

A critical review of the calculations must also be carried out to establish where systematic errors or uncertainties may lie. These may be associated with inadequacies in theoretical models, often due to a paucity of experimental data.

### 2.2 Databasing of the material properties

The assessment of scatter requires a comprehensive data compendium which summarizes the materials data and source documents.

Quality assurance procedures during graphite manufacture required the measurement of material properties on samples taken from each furnace batch of graphite ('heats'). The mean value of the properties were recorded on 'heat certificates'. For a given station, the total number of samples tested for a single property was typically in the hundreds. The heat certificates form the largest collection of data on unirradiated graphite samples.

### 2.3 Statistical analysis of the material properties

Statistical analysis will be used to give the means and the ranges of individual material properties. In general, the data will be plotted and assessed visually. Where appropriate, formal analysis will be undertaken using recognised statistical techniques. A statistical software package linked to the database will facilitate this analysis.

It will generally be assumed that the material property data can be represented as a continuous distribution.

Initial tests will be for a normal (Gaussian) distribution. The nature of the graphite, with its inhomogeneities, would suggest that data would be normally distributed. However, the relatively small number of samples may cause skews to be apparent. Tests for the normality of a distribution include the Chi squared test and the testing of symmetry/Kurtosis. Particular features of the distribution, for instance cut-off points in the data, should be noted.

The analyses of the distributions should enable confidence limits to be established for many of the properties. An estimate of these limits is a prerequisite of any sensitivity study.

A number of correlations between graphite material properties similar to those in reference [2] have already been noted. There may also be correlations between properties and source of the graphite. It is emphasised that correlation does not imply causality.

Potential correlations will be examined using a standard method for correlation tests, the Pearson correlation coefficient. The significance of the coefficient, which is dependent on the number of samples, can be estimated using the Students *t*-distribution. The technique only identifies linear correlations.

### 2.4 Estimation of scatters

Not all the scatter in material properties will be available from the material property database. Some of the data used in the calculations, for instance temperatures, are derived using other computer codes and have a scatter associated with their own calculation route.

There may also be cases where the paucity of material property data prevents the determination of a meaningful mean and standard deviation. In these cases an estimate of the scatter will necessarily be based on engineering judgement.

### 2.5 Sensitivity studies

A great number of parameters are involved in the calculation of the RSF. In principle, it is possible to carry out a full probabilistic analysis, varying all of these parameters. However, the value of such detailed analysis, and the effort put into the calculation of the uncertainty is questionable. Source data, for instance reactor data, are themselves subject to so many uncertainties that even the final probability distribution for the RSF could be considered only as a reasonable estimate.

It is proposed to use sensitivity studies as a precursor to probabilistic assessment, as a means of minimising the number of properties which have to be considered in detail. The sensitivity studies may also highlight critical areas which require further investigation.

The sensitivity studies will involve following components of the calculation route, using upper and lower bounds for one property, whilst holding all other properties at their mean value. This differs significantly from the probabilistic analyses in which a number of parameters are varied in each iteration. The outcome of a sensitivity analysis is not a probability distribution, but an indication of the more significant parameters.

Two basic techniques are proposed studying the effect of scatter. First, an error analysis using hand calculations would be attempted. This is only possible where an exact equation is known, and where the variables behave linearly. The alternative method would involve the use of the computer codes which form part of the calculation route for the RSF.

## 2.6 Probabilistic analysis

In the probabilistic analyses the full calculation route for the RSF will be repeatedly followed. In each iteration, values for the key parameters identified in the sensitivity studies will be obtained using a statistical sampling technique. All other properties will be held at their mean value. This will enable a probability distribution to be constructed for the RSF.

It is expected that the key parameters will be single variables, rather than distributions (for instance, an annulus temperature and an arrowhead temperature rather than the actual temperature distribution through the brick). If necessary, spatial variations of properties can be accounted for by randomly choosing an entire distributions, in effect treating the distribution as a single variable.

The sampling techniques described below may be used to generate values for the key parameters in any given iteration from any continuous probability distribution; they are not limited to Gaussian distributions.

Two sampling techniques commonly used in risk analysis, Monte Carlo and Latin Hypercube sampling, techniques were considered. In both cases one sample is drawn from each material property distribution in every sampling iteration. With enough iterations the sample values will approximate the original distribution.

Monte-Carlo sampling techniques are completely random. Clearly samples are more likely to fall in the area of the distribution with higher probabilities of occurrence. This leads to the danger of clustered samples if only a small number of iterations are performed. Clustering can become particularly pronounced when the distribution includes low probability outcomes.

The problem of clustering has led to the development of stratified sampling techniques such as Latin Hypercube sampling. Stratification divides the cumulative probability distribution into a number of equal intervals. Samples, without replacement, are randomly taken from each stratification. The total number of sampling iterations is equal to the number of stratifications.

In the proposed analyses there are multiple variables (the key parameters). Independence between these variables is maintained by randomly selecting the stratification from which to draw for each variable. Linear correlations between variables may also be taken into account.

The concept of convergence is used to test the efficiency of sampling methods. This is considered in terms of the number of sampling iterations required to re-create the original distribution. Latin Hypercube sampling converges more rapidly than Monte Carlo sampling. It is proposed that this method be adopted.

Software packages for sampling of distributions exists. These codes may be used in conjunction with the software proposed for the material property database.

## 3. SPECIMEN SIZE EFFECTS

### 3.1 General

The scatter of graphite material properties can be mainly ascribed to inhomogeneities in the material.

In principle, it is possible to measure non-destructive properties of a whole core brick. In practice, the heat certificate data is obtained from smaller specimens cut from individual bricks in a heat.

If a brick was cut up into smaller specimens then, intuitively, the mean properties obtained from the smaller specimens would correspond to those of the brick. The scatter of the properties, however, would increase as the specimen size was reduced. This behaviour is clearly limited by the maximum grain size of the graphite (approximately 1 mm), which gives a lower bound to the specimen size.

The effect of the initial spatial variation of properties through a brick is not taken into account in the RSF calculations as there is no known method of treating the effects of these variations or even of choosing the scale over which they vary.

The RSF is calculated assuming initially uniform properties for the brick which are chosen from a distribution of whole brick properties. As the majority of the tests for material properties are carried out on small specimens, the relationship between whole brick and small specimen distributions is of particular significance in the analysis of the probability distribution for the RSF.

Any reduction in the scatter of small specimen data when it is used in the RSF calculations is beneficial as this would help to minimise the scatter associated with the RSF. This, in turn, should enable improved estimates to be made of the core life and also lead to substantial cost savings for the industry. There is naturally a strong desire to use a reduced scatter when dealing with bricks.

There are, however, arguments to retain the scatter of the small specimen data in RSF calculations. These arguments impinge on the validity of assumptions that have to be made to develop a technique of scatter reduction. The assumptions are discussed in the following section.

Interest centres on a mean value for non-destructive properties, whereas for destructive properties it centres on the minimum (weakest) value. For this reason, the treatment of destructive and non-destructive properties has to differ; the two are considered separately.

### 3.2 Non-destructive property variability

Technically, the only approach to derivation of a distribution of initial brick properties appears to be the following for non-destructive properties:

1. The brick property is assumed to be the mean of the same property over the  $n$  random small specimen test samples which make up a complete brick ( $n$  is the ratio of the volume of the bricks/small specimens).
2. The  $n$  samples which make up a brick are randomly selected from the number  $N$  of such samples which make up a full reactor core which have a given distribution ( $N$  is the ratio of the volume of the core production/small specimens).
3. The distribution of properties amongst the  $N$  samples is given by the heat certificate data from the manufacturers total output of AGR moderator graphite.

Intuitively these assumptions would be expected to produce a much narrower distribution of brick initial properties than the distribution of small sample properties. Clearly, all three assumptions may be incorrect.

The assumption that a brick property is the mean value of the same property measure on  $n$  samples which make up the brick is not necessarily correct since the environment of the sample within the brick may alter the response – such effects are neglected.

The random selection of samples from the entire distribution to form a single brick is an almost completely untested assumption.

It may be argued that the graphite that formed a single brick might be expected to comprise  $n$  similar rather than  $n$  random small specimens. This would be observed if the graphite properties varied spatially throughout the heat. If, as may be the case, the selection of samples from a heat was not random, then the spatial variation might not be seen in the small specimen property distribution. In this case, however, any variation in graphite properties between heats would still result in the brick comprising  $n$  similar samples. The reduction in scatter of the brick properties

based on  $n$  similar samples would be less than that predicted using random samples.

The assumption that the small specimen (heat certificate) data is representative of the core property distribution has also been carefully considered. It is believed that there is sufficient uncertainty in the validity of this assumption to warrant the use of the full range of the small specimen properties in the sensitivity analyses. Not reducing the scatter shown by the small specimen data may be considered to constitute the worst case.

Although it currently appears that reducing the small specimen scatter when applying the data to full bricks cannot be justified, the implications of this decision on the overall variability in RSF is likely to be significant. In view of this, the question of scatter reduction will need to be revisited for each of the key properties that will be varied in the probabilistic assessments. If the assumptions made above can be justified, then an appropriate technique to use for scatter reduction is that described in the following section.

### 3.3 Reduction of non-destructive property variability

The assumptions given above enable reduction of brick scatter to be carried out using the central limit theorem. This theorem states that if  $n$  random samples are repeatedly taken from a distribution with a mean  $\mu$  and standard deviation  $\sigma$  then the sample means will form a distribution that is approximately normal with mean  $\mu$  and standard deviation  $\sigma_s/\sqrt{n}$ . The proof of this theorem may be found in statistics textbooks<sup>[3]</sup>.

In this case, the heat certificate data provides the original distribution, the number of samples is the ratio of the volume of bricks/small specimens ( $R_{vol} = V_b/V_s$ ) and the brick properties are defined by the mean of the samples. Using the subscripts  $b$  and  $s$  for brick and small specimen data, respectively, this gives:

$$\mu_b = \mu_s \quad \text{and} \quad \sigma_b = \frac{\sigma_s}{\sqrt{R_{vol}}}$$

Inherent in this approach is the assumption that the mean of the brick properties is the same as the mean of the small specimens, which depends on the small specimen data being representative.

The application of this technique is limited to specimens representing bulk graphite. No allowance can be made for the presence of disparate or other manufacturing flaws.

The application of the central limit theorem to individual properties needs assessing. It is emphasised that the technique is for non-destructive properties. The treatment of strength is described in the following section.

The use of this technique could have a significant impact on the distributions assumed for key properties, and hence on the final RSF probability distribution.

### 3.4 Destructive properties

The treatment of strength must be different from that proposed for non-destructive properties since interest centres on the weakest bricks under the particular stress systems generated. Tests of AGR brick cross-sections under simulated and appropriate internal stresses and external loads have shown failures to propagate from the keyway root to the brick bore because of the local stress concentration.

It may be argued that polycrystalline graphite, because of its method of manufacture, contains two quite distinct flaw distributions which control its mechanical failure.

1. An inherent flaw distribution determined by the coke particle size distribution, number of impregnations etc. This distribution should be reproducible and should also show correlations with other properties, for instance strength and Young's Modulus.
2. Flaws produced by accidents during manufacture such as incorporation of foreign bodies and poor mixing. These flaws have been christened 'disparate' flaws by Eatherly<sup>(4,5)</sup> who first described them quantitatively in different graphites. These flaws tend not to be observed in normal laboratory test programmes because specimens containing them are rejected or cannot be prepared (flaw larger than sample dimension). These flaws do not correlate with other properties. The effect of these disparate flaws are still being considered.

The mean values of stress at failure will be obtained from a series of analyses currently underway at AEA Technology. The few bricks that are being tested are not sufficient to give a statistical variation for the properties. This information will again come from heat certificate data.

A statistical approach often used in brittle failure problems is known as a three parameter Weibull distribution. The cumulative strength distribution with strength ( $\sigma$ ) normalised to a mean strength ( $\bar{\sigma}$ ) are of the form:

$$F\left(\frac{\sigma}{\bar{\sigma}}\right) = 1 - \exp(-B)$$

where  $B$  is known as the risk of rupture and for a sample volume  $V$  was chosen by Weibull to have the form:

$$B = \int_V \left(\frac{\sigma}{\bar{\sigma}} - \frac{\sigma_u}{\bar{\sigma}}\right)^{2\alpha} dV$$

$\sigma_u$  is the threshold stress below which failure probability is zero. This parameter is often set to zero when analysing graphite data.

The parameters  $2\alpha$ ,  $\sigma_u$  and  $\bar{\sigma}$  are obtained from experimental data from best fit methods. Equal probabilities of failure apply under different situations when the risk of failure is the same. This allows comparisons between different tests to be made by equating the relevant values of  $B$ .

In this case, particularly relevant is the comparison which may be made between different volumes  $V_1$  and  $V_2$  of the same test samples:

$$\frac{\sigma_1}{\sigma_2} = \left(\frac{V_1}{V_2}\right)^{\frac{1}{2\alpha}}$$

The Weibull theory was applied to a range of tests and test volumes by Brocklehurst and Darby<sup>[6]</sup>. Consistent values for the Weibull parameters were not obtained from the various tests. Over two orders of magnitude in specimen volume there was little apparent dependence of both bend and tensile strength on volume, giving a high value of  $m$  (approximately 18). This was consistent with the value obtained for bend strengths at constant volume, but much higher than the value of  $m = 6$  required to satisfy the measured ratio between bend and tensile strengths.

Attempts to relate strengths from different laboratory tests using a statistical Weibull treatment have all concluded that the relationships predict a greater dependence on specimen volume than is experimentally observed. Nonetheless, the method is believed to offer the most reasonable means of defining the statistical variation of strength.

The approach which will be adopted in the probabilistic assessment is to analyse the heat certificate data to obtain appropriate Weibull parameters. This will define the normalised strength distribution. The mean strength of bricks will be obtained from the finite element analyses of ongoing tests of full bricks. The maximum principal stress at the keyway root will be used to define the failure stress.

## 4. DEVELOPMENTS

Work is in hand to apply this methodology to a UK AGR reactor. An assessment has been made of the calculation route and graphite material properties have been databased. In order to prove the concepts described in this paper, the methods for the treatment of both non-destructive properties and strength variability have been demonstrated. Combined experimental and analytical work to study failure criteria for core bricks is also underway.

A revised form of the RSF has recently been proposed. It is referred to as a fractional remanent strength ( $\Delta S$ ). Its format is more consistent with other engineering design criteria, in that the terms of the equation are all ratios of actual and ultimate stresses. Whilst the calculation route described in this paper is based on recommendations existing at the time of writing, the methodologies defined herein may be equally well applied to calculations of  $\Delta S$ .

## 5. CONCLUSIONS

1. The Reserve Strength Factor (RSF) is the factor of safety used in assessments of AGR core integrity. Values currently used are based on engineering judgement. These values should, in principle, be related to variability due to inhomogeneity of graphite, systematic error in the calculation route and uncertainties in property measurement.
2. A probabilistic approach to assessing variability in RSF is proposed. This will bring the safety assessment of the graphite core into line with other reactor components. The approach involves:
  - (a) A critical review of the calculation route to highlight areas in which there are uncertainties.
  - (b) A statistical analysis of the base parameters to determine distributions, means and ranges of the material properties.
  - (c) Numerous parameters are involved in the RSF calculations. The use of sensitivity studies as a precursor to probabilistic assessments is proposed as a means of minimising the number of variables that have to be considered in detail.
  - (d) A probability distribution for the RSF may be obtained by repeatedly following the full calculation route. In each iteration, appropriate values for the key parameters (identified in sensitivity studies) would be obtained using the Latin Hypercube sampling technique.
3. Material properties have generally been obtained from tests on small specimens. The variability in these properties would, intuitively, be expected to be greater than that found in the brick (on which the RSF calculations are based). In the case of the non-destructive properties these size effects may be treated by applying the central limit theorem. Core brick strength will be obtained from a series of on-going experiments. The statistical distribution of brick strength will be assumed to follow a Weibull function fitted to small specimen data.
4. Work is currently underway, applying this proposed methodology to an Advanced Gas-cooled Reactor core.

## ACKNOWLEDGEMENTS

The work described in this report was carried out by Gas Cooled Reactor Assessments Department, AEA Technology on behalf of the Health and Safety Executive.

Significant contributions to the contents of this paper have been made by the author's colleagues. Their assistance is gratefully acknowledged.

## REFERENCES

1. JUDGE RCB., To be published
2. YODA S and FUJISAKI K., Journal of Nuclear Materials, Vol. 113, p. 263, 1983
3. HOEL PG. 'Introduction to Mathematical Statistics', Wiley, 4th Ed., 1971
4. EATHERLY WP and KENNEDY CT. 'The statistical characterisation of Tensile Strengths for a Nuclear Type Graphite', IAEA Specialists' Meeting on Graphite Component Structural Design, September 1986, IWGGCR/H.
5. EATHERLY WP., George C. Skakel Award Lecture, 16th Biennial Carbon Conference, 1983.
6. BROCKLEHURST JE and DARBY MI., Materials Science and Engineering, Vol. 16, p. 91, 1974

## DISCUSSION

### Questions or Comments

Name: S. Shiozawa

How about applicability of the proposed methodology to actual reactors in their licensing processes?

### Answer:

In the United Kingdom safety cases must be written for reactor operation for the most agreed period, based on direct observations and simple predictions of behavior. Very complex cases are requested only for difficult situations - such as high power on-load refuelling, but this does not apply (yet) to the moderators which are behaving as expected.



**DESIGN CRITERIA, FRACTURE MECHANISMS  
AND COMPONENT TESTS  
Part B**

**(Session II)**

**Chairmen**

**T.D. BURCHELL**  
United States of America

**S. SHIOZAWA**  
Japan



## BENDING FATIGUE BEHAVIOR OF NUCLEAR-GRADE GRAPHITE UNDER IMPACT LOADING

M. FUTAKAWA, K. KIKUCHI, Y. MUTO  
Department of High Temperature Engineering,  
Tokai Research Establishment,  
Japan Atomic Energy Research Institute,  
Tokai-mura, Naka-gun, Ibaraki-ken

H. SHIBATA  
Institute of Industrial Science,  
University of Tokyo,  
Tokyo  
Japan

### Abstract

The graphite components in HTR ( High Temperature gas-cooled Reactor ) are subjected to impact force due to earthquake. It is important from the viewpoint of seismic safety design to investigate the difference of strength under impact loading and non-impact loading.

Both bending strength and bending fatigue strength tests, therefore, were carried out under impact and nonimpact loading on two kinds of graphite materials: isotropic and near-isotropic. The impact response analyses, which used a beam model taking account of the contact behavior between specimen and tup, were performed to evaluate the relationships between impact energy, impact force and stress.

The main conclusions obtained are summarized as follows:

- (1) A beam model taking account of the contact behavior through the Hertzian theory is applicable to describe the impact behavior.
- (2) The bending strength of graphite is independent of strain rate in the range from  $10^{-6}$  to  $5 \text{ 1/s}$ .
- (3) Despite both specimen volume and kind of graphite the strength of graphite is lower in impact fatigue than in nonimpact fatigue .

### 1. INTRODUCTION

The core of the HTR (High Temperature gas-cooled Reactor) consists of many kinds of graphite components: fuel block, reflector block, dowel, key, and so on [1]. These components are repeatedly subjected to impact forces due to collision motion among them during earthquakes. Accordingly, it is important from the viewpoint of a seismic safety design in the HTR to make clear the impact strength and the impact fatigue behavior of the graphites.

Hitherto, the impact fatigue tests for an isotropic graphite IG-11 had been carried out by using a pendulum-type impact repeatedly-bending machine, and then the relation between impact energy and the stress generated by impact was discussed through the analysis using the simple one-dimensional model taking the Hertzian contact stiffness into consideration[1]. As a result, it had been confirmed that the endurance curves evaluated using a maximum stress induced by impact are independent of the specimen size, and the fatigue strength of IG-11 is lower in impact than in nonimpact.

Additionally, the impact fatigue behavior and the impact bending strength of another kind of nuclear-grade graphite, that is, a near-isotropic graphite PGX was investigated and compared with IG-11. The impact response analyses were conducted using a finite element method in order to discuss the effect of higher vibrational modes of the beam specimen on the stress generated by impact.

### 2. EXPERIMENTAL METHOD

The impact fatigue and the impact strength tests were carried out by using the pendulum-type impact repeatedly-bending machine[1]. The maximum impact velocity, energy and cyclic frequency are  $3\text{m/s}$ ,  $1\text{J}$  and  $0.5\text{Hz}$  respectively. The impact force acting on the specimen was measured from a strain gage instrumented tup. The specimen was simply supported at each end and centrally subjected to impact as shown in Fig. 1. The size of specimen was varied to investigate the volume effect on the

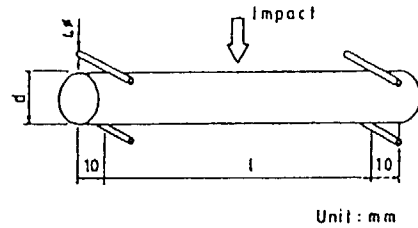


Fig.1 Specimen shape

Table 1 Mechanical properties of graphite materials

	IG-11	PGX (#)	PGX (L)
Bending strength (MPa)	40.3(2.3)	14.5(0.4)	16.5(1.4)
Young's modulus (GPa)	10.7(0.7)	6.3(0.1)	7.6(0.07)
Poisson's ratio	0.18(0.03)	0.09(0.01)	0.07(0.01)

Number of specimens; 5 (PGX), 15 (IG-11)

Standard deviation; ( )

strength, that is, S denotes that  $l=110\text{mm}$  and  $d=10\text{mm}$ ,  $M\ l=210\text{mm}$  and  $d=10\text{mm}$ , and  $L\ l=210\text{mm}$  and  $d=20\text{mm}$ . The strain at the outer fiber of the specimen was measured by using the strain gage which was fixed on its center across the impact point. The quasi-static 3-point bending fatigue tests were performed under the cyclic stress in the unidirectional bending by using an electro-hydraulic testing machine. In the quasi-static fatigue tests, the frequency of cyclic load was 1 Hz at a triangular wave.

The mechanical properties of graphite materials are shown on the table 1.

### 3. ANALYTICAL METHOD

The simple analytical model taking account of the Hertzian contact theory had been proposed to investigate the relation between the stress generated by impact, the impact force, and

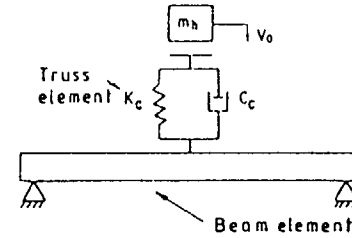


Fig.2 Analytical model

the damping effect under the impact velocity[1]. The model, however, could not represent the higher vibrational modes of the specimen which may affect the generated stress. Thereupon, the impact response analysis was performed by using the beam model, as shown in Fig.2, in which the contact stiffness used to describe the contacting behavior between the tup and the specimen was derived from the Hertzian theory[2] as in the following equation

$$F(t) = k_H X(t)^{3/2}, \quad (1)$$

where  $X(t)$  is the distance that the impactor and the target approach each other because of local compression at the point of contact. When two cylinders with radii  $r_1$  and  $r_2$  are placed in contact normally to each other, the Hertzian contact stiffness  $k_H$  of the two cylinders is given by

$$X(t) \geq 0 :$$

$$k_H = \frac{4\alpha}{3(\delta_1 + \delta_2) \sqrt{1/2r_1 + 1/2r_2}} \quad (2)$$

$$\delta_i = (1 - \nu_i^2) / E_i \pi$$

$$\text{and } X(t) < 0 :$$

$$k_H = 0, \quad (3)$$

where  $\nu$  is Poisson's ratio,  $E$  modulus of elasticity, and  $\alpha$  a constant defined by  $r_1/r_2$  [2].

It is essential for evaluating the relation between impact energy, impact force and stress to take account of the effect of the damping factor on the impact response. Unfortunately, the damping behavior results from so complicated a phenomenon that it can not be analytically represented yet. Therefore, the damping factor measured experimentally by using the FFT analyzer was adopted for the beam model.

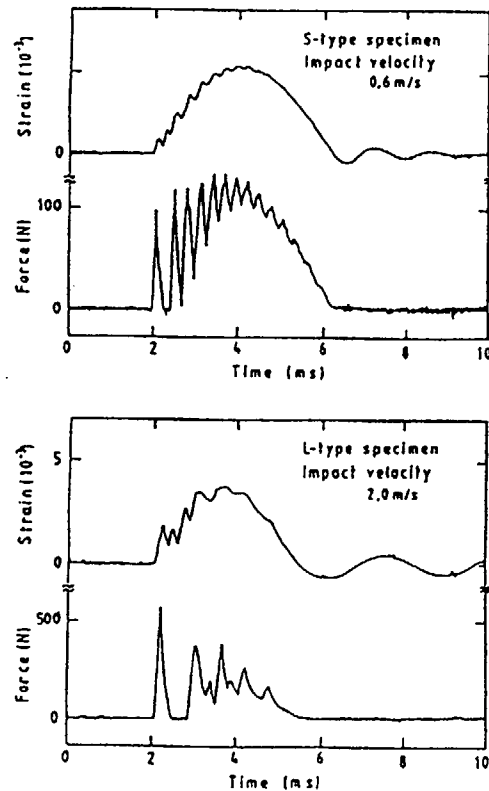


Fig.3 Impact bending-response waves

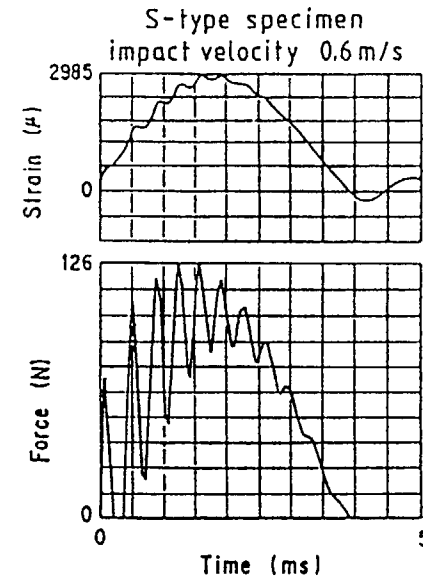


Fig.4 Analytical results of impact response waves

#### 4. RESULTS AND DISCUSSION

##### 4.1 Impact response

Figure 3 shows the impact responses of the force and the strain in the IG-11 specimens. The high-frequency components are superimposed on both the force and the strain because of the impact behavior affected by the interaction between specimen and tup. Especially in the case of the L-type specimen, the effect of the inertia of the specimen on the impact response is so conspicuous that the maximum force and the maximum strain do not occur at the same time.

Figure 4 shows the analytical results of the force and the stress in the S-type specimen of IG-11. Here, the contact stiffness  $k_c$  is a third of the Hertzian one used according to the previous paper [1]. The analytical results can represent the

experimental ones adequately where the high-frequency components are superimposed on the force and the stress. The agreement between the experimental and the analytical results can be confirmed also in the case of PGX. It can be said, therefore, that the beam model having the modified Hertzian contact stiffness between specimen and tup is useful to describe the impact bending response of the graphite beam in which the high-frequency components are developed under impact loading.

#### 4.2 Impact bending strength

In order to investigate the effect of the strain rate on the bending strength, the impact and the quasi-static bending tests were performed using the same material and size specimens as those in the fatigue test.

In the quasi-static test, the bending strain rate obtained from the gage fixed on the center of the specimen ranged from  $10^{-5}$  to  $10^{-6}$ /s. Figure 5 shows the Weibullian distributions for the bending strength obtained in the quasi-static test. Table 2 indicates the Weibull's parameters. It can be said for a Weibull plot having a straight-line portion as shown in Fig. 5 that the

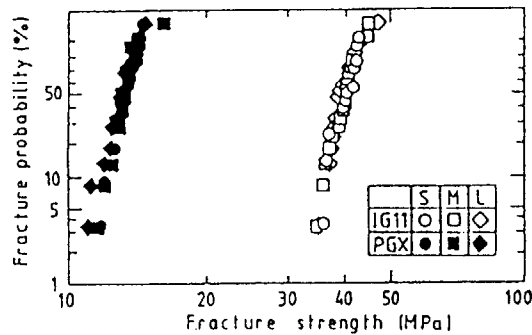


Fig.5 Weibull's distribution of bending strength

Table 2 Weibull's parameters

Weibull's parameter	IG-11			PGX		
	S	M	L	S	M	L
Number of specimens	19	20	20	20	20	20
Weibull's modulus	16.2	16.8	15.6	18.5	16.7	15.7
Mean value (MPa)	40.3	40.2	40.0	13.3	13.4	13.1

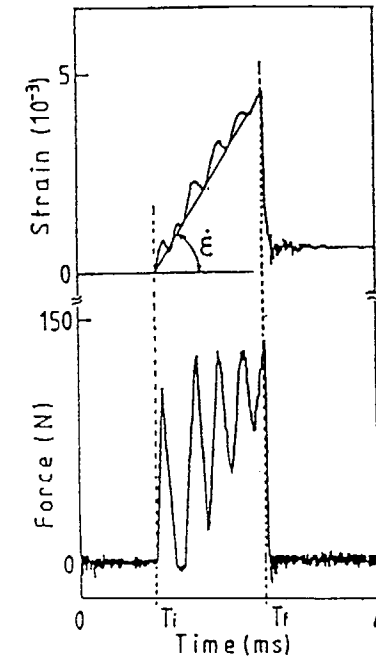


Fig.6 Impact force and strain at fracture

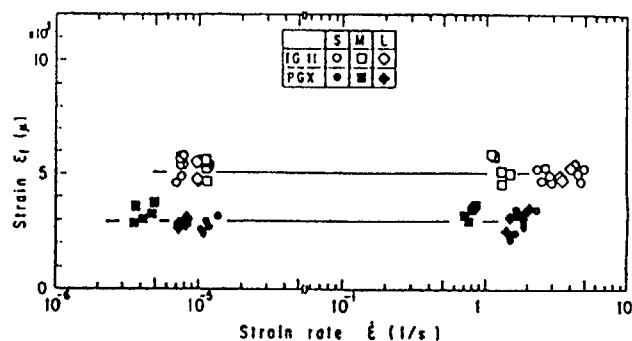


Fig. 7 Bending fracture strains of IG-11 and PGX as a function of strain rate

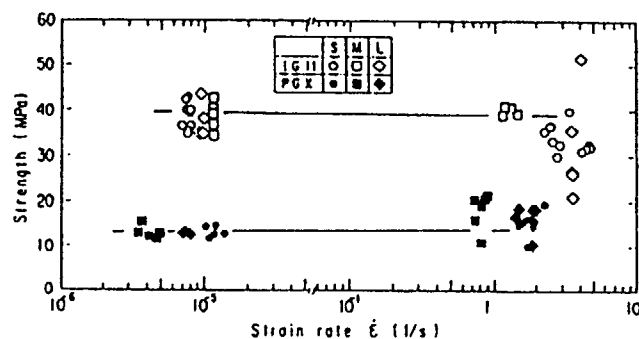


Fig. 8 Bending strength of IG-11 and PGX as function of strain rate

Weibull's function is applicable to describe not only the distribution of the strength of graphites in compression and tension[2] but also that in bending. The volume effect on the bending strength is not observed in the range of these specimen sizes.

Figure 6 illustrates the impact force and the strain at fracture. In the impact test, the strain rate  $\dot{\epsilon}$  is approximately defined to be the fracture strain  $\epsilon_f$  divided by the fracture time ( $T_f - T_i$ ). The strain rate is dependent on both the mass of impact hammer and the specimen size and ranges from 1 to 5/s.

The relation between the fracture strain  $\epsilon_f$  and the strain rate  $\dot{\epsilon}$  was shown in Fig. 7. Despite both the specimen size and the kind of graphite, it can be said that the fracture strain  $\epsilon_f$  in bending is independent of the strain rate up to 5/s.

The relation between the bending strength and the strain rate is shown in Fig. 8. The bending strength is derived from the elastic theory of a beam assuming that the impact force acts on the specimen quasi-statically. The higher the impact velocity, the larger the dispersion of the strength becomes. That is because the effect of the superimposed high-frequency components on the impact force is magnified with increasing impact velocity. The bending strength, although, seems to be independent of the strain rate up to at least 5/s regardless of both the kind of graphite and the specimen size.

#### 4.3 Behavior of impact fatigue

##### 4.3.1 Relation between impact energy and fatigue life

Figure 9 shows the relation between the impact energy  $U_i$  and the number of cycles to failure  $N_f$  (U-N diagram). The lines in

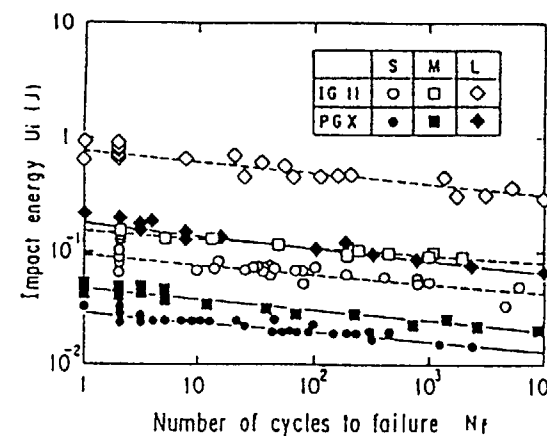


Fig. 9 U-N diagrams of IG-11 and PGX

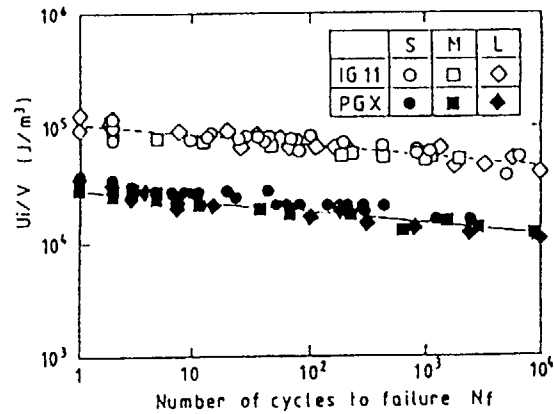


Fig.10 U/V-N diagrams of IG-11 and PGX

the figure are derived from the following equation whose constants are determined by applying the least squares method to experimental data.

$$\log U_i = A + B \log N_f \quad (4)$$

It is revealed from U-N diagrams that despite the kind of graphite the larger the specimen size the longer its fatigue life is and the impact energy at failure in PGX is a third of that in IG-11 approximately. Figure 10 shows the relation between the impact energy per unit volume  $U_i/V$  and  $N_f$ . Regardless of the specimen size the behavior of impact fatigue for IG-11 and PGX is described by each line which has almost the same inclination.

Assuming that the contact deformation under the point of impact is so small as to be ignored and the bending behavior of the specimen conforms to the elastic theory, generally, the elastic energy on bending is given by

$$U_s = \frac{\sigma_b^2 V g}{2E} \quad (5)$$

where  $V$  is the volume of specimen and  $g$  a factor to account for the stress distribution in the specimen ( $g=1/9$  for square-section bars in three point bending and  $1/12$  for round-section bars)  $\sigma_b$  a bending stress,  $E$  modulus of elasticity. Provided the impact energy is convertible into elastic energy, the stress generated by impact is proportional to the square root of  $U_i/V$ . Therefore, it is intimated through Fig. 10 that the stress generated by impact is valid to characterize the behavior of impact fatigue in the graphite materials tested here.

#### 4.3.2 Comparison between impact and nonimpact fatigue

The behavior of nonimpact fatigue in each graphite, S-N diagram, is shown in Fig.11. The ordinate in each S-N diagram denotes the normalized stress. That is, the maximum bending stress  $\sigma_{max}$  is normalized by using the static bending strength

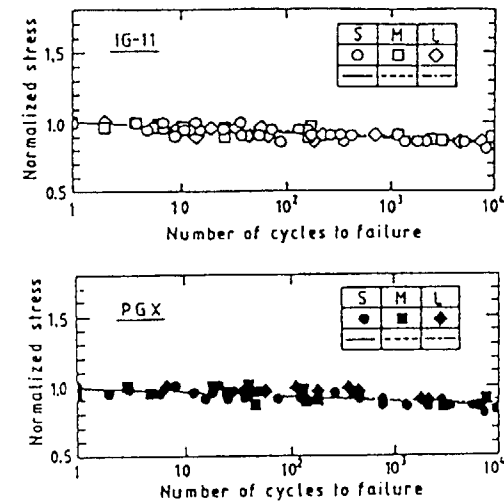


Fig.11 Nonimpact fatigue behaviors of IG-11 and PGX



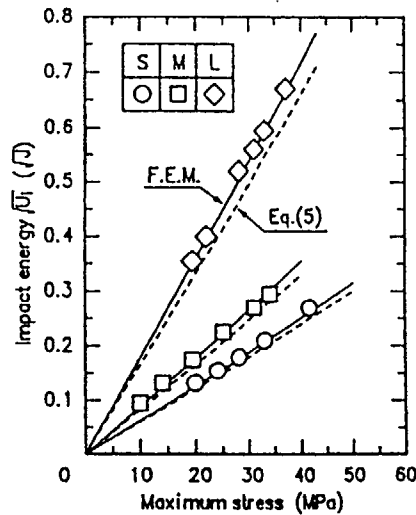


Fig.12 Relation between impact energy and maximum stress for IG-11

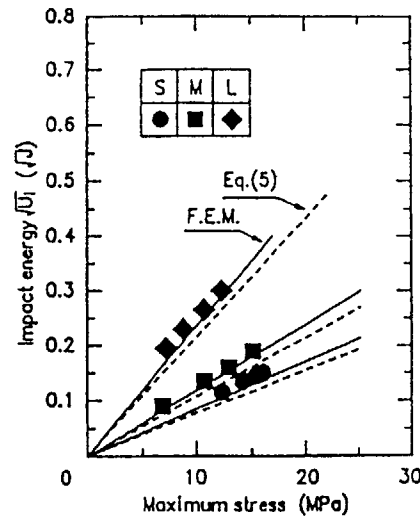


Fig.13 Relation between impact energy and maximum stress for PGX

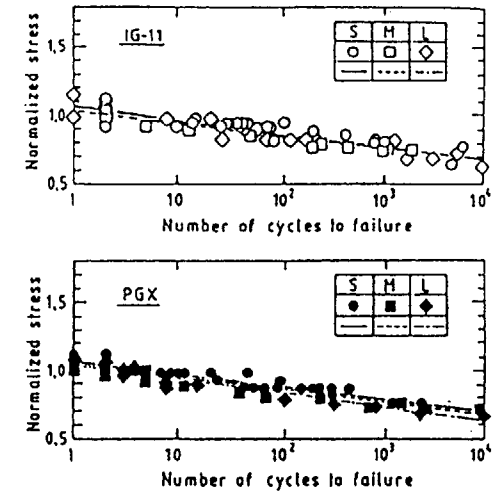


Fig.14 Impact fatigue behaviors of IG-11 and PGX

of each graphite in order to compare the behavior of fatigue between IG-11 and PGX. The regression curves in Fig.11 are given by

$$\log(\sigma_{max}/\sigma_s) = A + B \log N_f \quad (6)$$

It can be said from Fig. 11 that the normalized stress is valid to characterize the bending fatigue behavior of the graphites because the inclination of the regression curves is independent of both the kind of graphite and the specimen size.

It is necessary to transform the U-N diagram shown in Fig.9 to the S-N diagram in order to compare the impact fatigue strength with the nonimpact one. Figures 12 and 13 show the relations of each graphite between  $\sqrt{U}$  and the maximum stress  $\sigma_{max}$  generated by impact which is evaluated from the measured strain based on the elastic theory. It is clear that the stress is proportional to  $\sqrt{U}$  and the slope of line depends on the specimen size. The solid lines denoting the analytical results obtained by using the beam model are in adequate agreement with the experimental results.

The broken lines indicate the results obtained from Eq.(5). The reason why the slopes of the beam model are somewhat larger than that of Eq.(5) is attributed to that the experimental damping effect is applied to the beam model while the energy loss is excluded in Eq.(5).

Figure 14 shows the S-N diagram of impact fatigue transformed from the U-N diagram by using the relation between  $\sqrt{U}$  and  $\sigma_{max}$  shown in Figs. 12 and 13. The ordinate indicates the normalized stress and the regression curve is obtained from Eq.(6). Despite the kind of graphite, the behavior of impact fatigue in each specimen size can be almost represented by an identical curve.

The regression curves of both impact and nonimpact fatigue are put together in Fig.15. It can be said that the strength of graphite is lower in impact fatigue than in nonimpact fatigue, especially in the region of lower stress, irrespective of kind of graphite and specimen size.

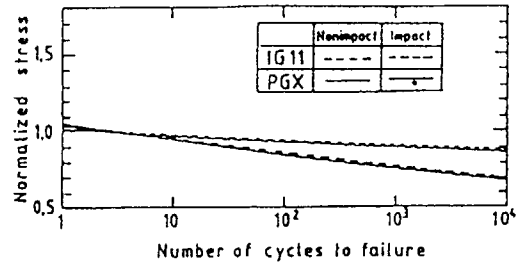


Fig.15 Comparisons of fatigue strength in impact with that in nonimpact

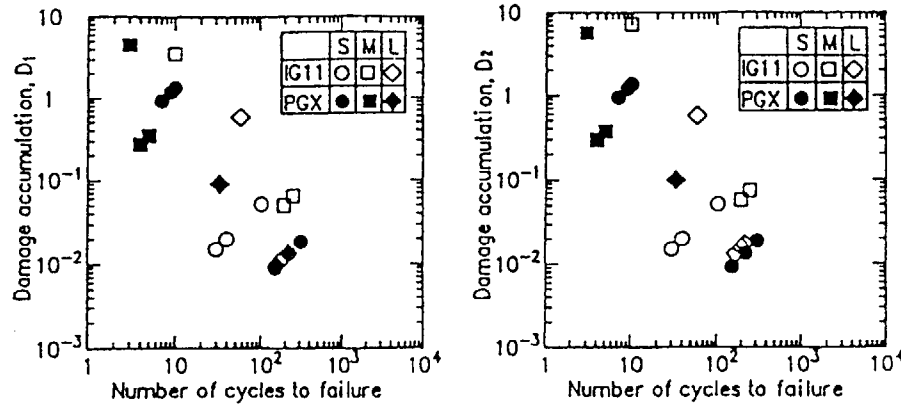


Fig.16 Linear damage accumulation based on the modified Miner's rule

The effect of the high-frequency components of the stress on the impact fatigue was evaluated assuming that fatigue damage was accumulated according to the modified Miner's rule based on the nonimpact bending fatigue. Two methods were employed to count the stress peaks on each cycle: one is to count a maximum peak and the other to count all peaks which seems to give the most conservative evaluation. Figure 16 shows the linear damage accumulation factors  $D_1, D_2$  evaluated using the maximum peak and

the all peaks count method, respectively. Because the discrepancy between  $D_1$  and  $D_2$  was hardly observed, the degradation of fatigue strength under impact loading can not be explained by considering the high-frequency components of the generated stress through the modified Miner's rule. The tendency is similar to those of many metals[4,5] and other graphites[6]. Likewise, recently observations of fatigue crack initiation and propagation under impact loading have been made by some investigators, which show that crack growth rates become higher than under nonimpact loading[7-10] as well as the crack initiation is influenced by the rising rate of load and becomes earlier than under impact loading[10]. Accordingly, in order to evaluate the impact fatigue damage rigorously, it seems to be necessary to take account of the effects of not only the high-frequency components superimposed on the stress wave but also the strain rate on the fatigue strength.

## 5. CONCLUSION

The bending strength tests were carried out under both impact and nonimpact loading on the two kinds of graphite materials by using the pendulum-type repeatedly impacting machine. The beam model with the contact stiffness taken account of the Hertzian theory was applied to evaluate the relation between the impact energy, the impact force and the generated stress.

The following conclusions were obtained.

- (1) The impact behavior of the graphite, such as the impact force, the bending stress and contacting time, can be represented using the beam model with the modified Hertzian contact stiffness.
- (2) The bending strength of the graphites is independent of the strain rate in the range from  $10^{-6}$  to 5 1/s.
- (3) The effect of specimen size on both the bending fatigue behavior and the bending strength was not observed in the experimental range.

- (4) The maximum stress generated by impact is a unique variable to describe the endurance curve of impact fatigue behavior represented on the S-N diagram irrespective of the specimen size.
- (5) It can be concluded from the S-N diagram that the fatigue strength of graphite is lower under impact loading than in nonimpact loading.

#### REFERENCES

- [1] M. Futakawa, K. Kikuchi, Y. Muto and H. Shibata, Carbon 28(1),149-154(1990).
- [2] W. Goldsmith, Impact, Edward Arnold, London (1960).
- [3] M. Eto, S.Ishiyama, T. Oku and K. Fujisaki, JAERI-M 84-148(1984).
- [4] I. Maekawa, Trans. JSME 52(473) 249-256 (1986).
- [5] T. Tanaka, H. Nakamura, J. Soc. Mater., Sci. Japan 23(252), 678-685(1974).
- [6] M. Birch and J. E. Brocklehurst, Carbon 21(5), 497-510(1983).
- [7] T. Tanaka, H. Nakamura and K. Kimura, Fatigue Fract. Engng. Mater. Struct. 8(1), 13-22(1985).
- [8] R. Murakami, K. Ito and K. Akizono, J. Soc. Mater., Sci. Japan 33(375), 1527-1532(1984)
- [9] H. Iguchi, K. Tanaka and S. Taira, Fatigue. Engng. Mater. Struct. 2, 165-176(1979).
- [10] I. Maekawa, Trans. JSME 56(525) 1051-1057 (1990).

## COMPONENT TEST OF THE CORE SUPPORT POST OF THE HTTR

M. ISHIHARA, T. IYOKU, N. TAKIKAWA, S. SHIOZAWA  
Oarai Research Establishment,  
Japan Atomic Energy Research Institute,  
Oarai-machi, Ibaraki-ken

K. JINZA, N. TSUJI, T. MIKI  
Fuji Electric Company Ltd,  
Kawasaki

Japan

#### Abstract

The component test of core support post for the High Temperature Engineering Test Reactor (HTTR) was carried out to verify its structural integrity using full-scale and 1/2-scale models of core support post and seat. The compressive fracture load (buckling load) of support post was measured under the conditions of post inclination angles to the post axis up to about 1 degree, cyclic load above maximum applied load and oxidation weight loss under about 30% at room temperature. In the cyclic load test, compressive fracture load was also measured after 200 times of cyclic load applied; the magnitude of this cyclic load was about 2.5 times of the maximum applied load in the design of HTTR. In this report the effects of compressive fracture load on post inclination angle, cyclic load and oxidation weight loss of this component were discussed and obtained fracture loads were compared with the applied load in the design of HTTR.

#### 1. INTRODUCTION

The core of the High Temperature Engineering Test Reactor (HTTR) is supported by the core support graphite structures, such as hot plenum blocks, core support posts and so on; these graphite structures are fastened by the core restraint mechanism (see Fig.1). The hexagonal hot plenum blocks are combined with each others by key elements. Three core support posts and corresponding seats made by isostatic-rubber-pressed

Keywords ; Support Post, Component Test, HTTR, Structural Integrity,  
Fracture, Buckling, Buckling Load, Graphite

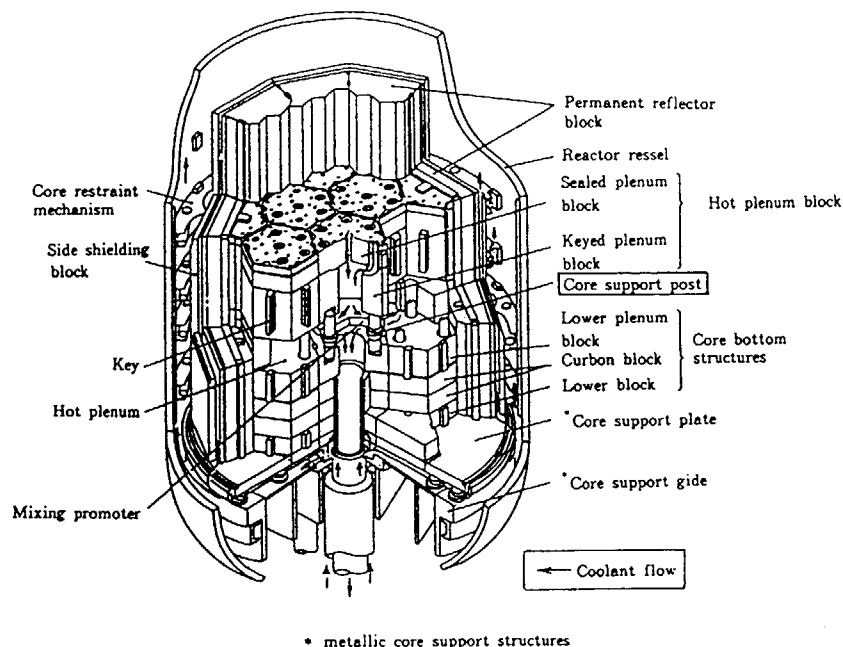


Fig.1 Core support graphite structures of HTTR.

graphite, grade IG-110, are placed below each hot plenum block. These posts can allow the relative horizontal displacement between the hot plenum and lower plenum blocks by the inclination during earthquake. The seat supports the post, 150 mm in diameter with 600 mm in length, by the spherical contact.

The main loads applying to this support post/seat component are the dead load of core components such as fuel blocks and control rod blocks etc. and the seismic load caused by the vibrations of core and core support components. At an earthquake, it is required that this component shall withstand the seismic cyclic load and eccentric load due to the inclination of the support post. At the same time the post/seat component shall withstand under the accident condition of double tube rupture at the primary coolant circuit of the HTTR; which is the most severe accident for this component from an oxidation point of view. It is also required that this component shall withstand the seismic load after this oxidation accident.

This component design had been achieved based on the buckling test results using 1/6-model<sup>(1)</sup>. However, it is well known that the strength of the graphite material shows the so-called "volume effect"<sup>(2), (3)</sup>; this volume effect of IG-110 graphite was observed on the several strengths<sup>(3), (4)</sup>.

Therefore, full-scale and 1/2-scale model tests were carried out to evaluate the fracture load of core support post/seat component on post inclination angle, cyclic load and oxidation weight loss. Then, the structural integrity of this component was estimated by the comparison between the evaluated fracture load and the applied load in the design of the HTTR.

## 2. EXPERIMENT

### 2.1 Materials and test specimen

The graphite materials employed in this component test were petroleum coke, fine-grained isostatically pressed high-purified nuclear grade graphite, grade IG-110 and its unpurified graphite, grade IG-11 manufactured by Toyo Tanso Co., Ltd.; IG-110 graphite is to be used the support post/seat component of the HTTR.

Table 1 Typical properties of core support post and seat graphite.

( IG-110 Graphite )

Density	(g/cm <sup>3</sup> )	1.78
Mean tensile strength	(MPa)	253
Mean compressive strength	(MPa)	768
Young's modulus <sup>*)</sup>	(GPa)	7.9
Mean thermal expansion (20~400°C)	(x10 <sup>-6</sup> /°C)	4.06
Thermal conductivity (400°C)	(kcal/m·s·°C)	1.9 x 10 <sup>-2</sup>
Ash content	(ppm)	< 100
Mean grain size	(μm)	20

\*)The slope of the straight line connected at the 1/3 points of the tensile and compressive specified minimum ultimate strengths.

Typical properties of IG-110 graphite are given in Table 1. The properties of IG-11 graphite are the same as those of the IG-110 graphite except for the ash content data. The test specimens of full-scale and 1/2-scale models were cut from IG-11 and IG-110 graphite blocks, respectively.

Fig.2 shows the test specimens of full-scale and 1/2-scale models. The specimen of full-scale model was mainly used for cyclic load and post inclination tests, while the 1/2-scale model specimen was used for the oxidation test.

## 2.2 Experimental method

The component test was carried out under following three types of test conditions. The test condition and the number of the test specimen are summarized in Table 2. Hydraulic testing machine with maximum loading capacity of 3000 kN was employed in this compressive loading test. Schematic of this testing apparatus with full-scale specimen is shown in Fig.3 and the photograph is shown in Fig.4.

Table 2 Test condition and the number of test specimens of component test.

(The number of test specimen)				
Oxidation test <sup>*1)</sup>	Cyclic load test <sup>*2)</sup>	Inclination test (degree)	1/2-scale model specimen	full-scale model specimen
×	×	0	2 <sup>*3)</sup>	6 <sup>*4)</sup>
		0.5	1	0
		0.62	0	2
		0.94	0	2
○	○	0	0	4
	×	0	10	0
○	—	—	8 <sup>*5)</sup>	0
	×	—	—	—

\*1) Oxidation test : ○ , un-oxidation test : ×

\*2) Cyclic load test; ○ , un-cyclic load test; ×

\*3) Seat curvature Rs=45.5 mm and 51 mm

\*4) Seat curvature Rs=88 mm and 89.5 mm, seat thickness L1=50 mm and 100 mm

\*5) For the measurement of oxidation distribution

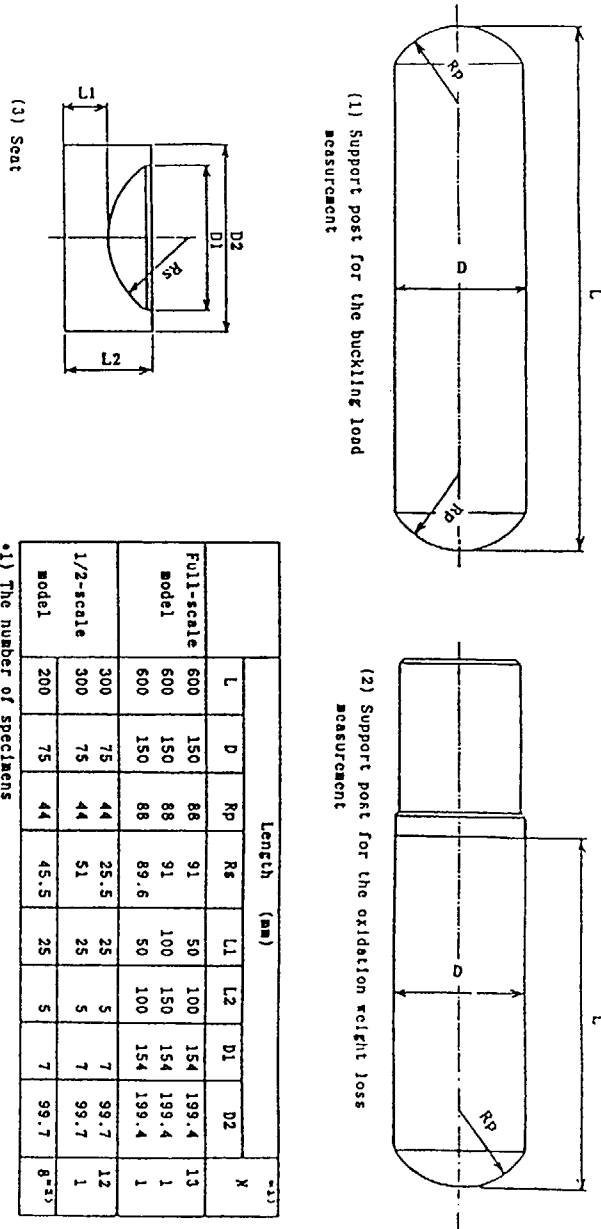


Fig.2 Geometry of test specimen.

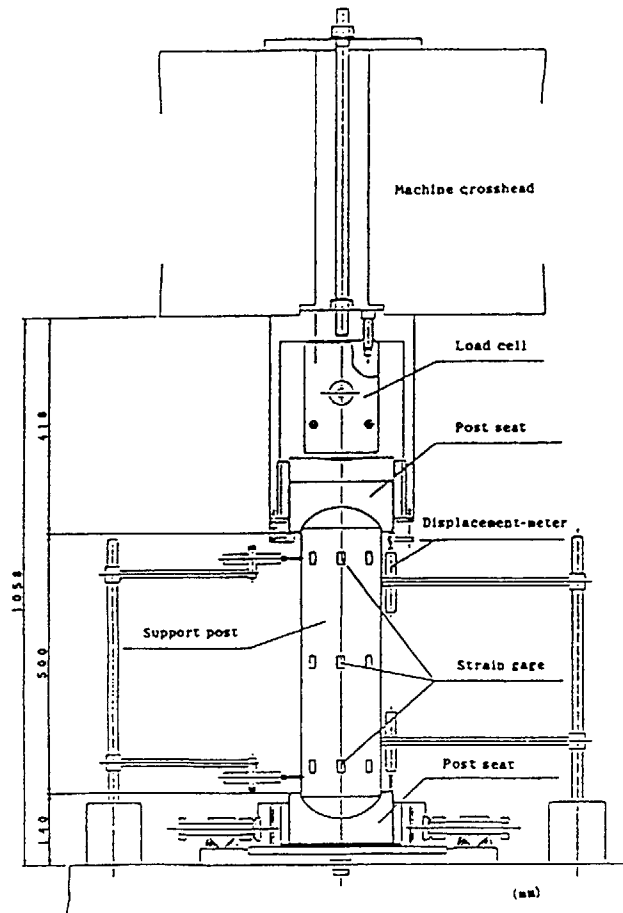


Fig.3 Schematic of the compressive load testing apparatus.

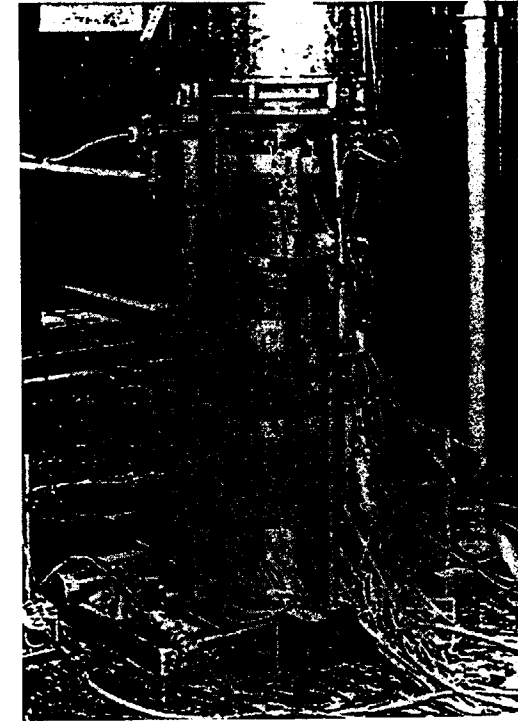


Fig.4 Photograph of compressive load testing apparatus.

#### 2.1.1 Post inclination test

In the support post design of the HTTR, the maximum inclination angle of the support post is estimated to be 0.62 degree. Then, the test was carried out at the angles of 0, 0.62 and 0.94 degree (up to the 1.5 times of maximum inclination angle). The full-scale specimen was set up at these three kinds of inclination angles by inclinometer, then compressive load was applied till the specimen was fractured. The longitudinal and circumferential deformations of specimen during the test were measured by strain gages as illustrated Fig.3.

### 2.1.2 Cyclic load test

The design maximum seismic load of support post is about 130 kN and the required load cycles for fatigue under the seismic load of the HTTR is 200 times. Therefore, the cyclic load test was performed 200 times of cyclic load between the three kinds of compressive load levels of 30 to 165 kN, 30 to 300 kN and 100 to 340 kN, then finally compressive load was applied until the specimen was fractured in order to investigate the fatigue damage of the support post/seat component. The longitudinal and circumferential deformations of this fracture test specimen were also

measured by strain gages attached at the same points as those of the post inclination test. Four test specimens of full-scale model were tested under the condition of 200 times of cyclic load.

### 2.1.3 Oxidation test

The 1/2-scale test specimen was oxidized at the temperatures of 550, 650 and 800 °C in the electric furnace under the air condition. The temperature of oxidation test specimens were measured by the three thermocouples. The magnitude of the oxidation weight loss was controlled by the oxidation time exposed in the air condition.

The oxidation weight loss,  $R$ , defined as following equation.

$$R = (\rho_0 - \rho) / \rho_0 \quad (1)$$

where  $\rho_0$  and  $\rho$  are the density of before and after oxidation treatment of specimen, respectively. The specimen for the measurement of inner oxidation distribution shown in Fig.2(2) was set up into the oxidation furnace; the oxidation furnace is shown in Fig.5. The eight specimens were oxidized in order to measure the inner oxidation distribution at the side section of the support post; this oxidation distribution was measured by the weight changes every after the surface cutting of 1 mm depth.

The ten specimens shown in Fig.2(2) were tested under the compressive load after oxidized up to about 30 % of oxidation weight loss under the different heat treatment conditions.

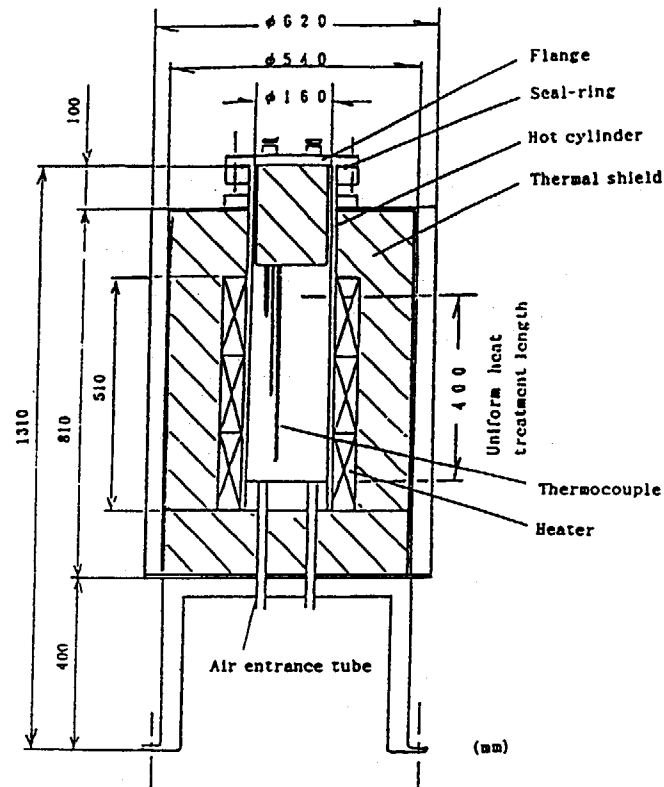


Fig.5 Oxidation furnace of 1/2-scale model specimen.

## 3. RESULT AND DISCUSSION

### 3.1 Post inclination test

The test specimen of full-scale model after the compressive load test is shown in Fig.6. The post specimen fractured at the contact spherical section. Longitudinal strains measured at the twenty points of three kinds of longitudinal positions are shown in Fig.7. Three kinds of post inclination angles showed almost the same longitudinal deformation.

Fracture loads at the different post inclination angles are shown in Fig.8. Within the 1.5 times of the maximum design inclination angle, the inclination angle has no clear effect on the fracture load (This behavior was also observed by the 1/6-scale model test<sup>(1)</sup>); moreover two types of different configuration specimens, 100 mm seat thickness and 89.5 mm seat curvature, almost show the same fracture load.

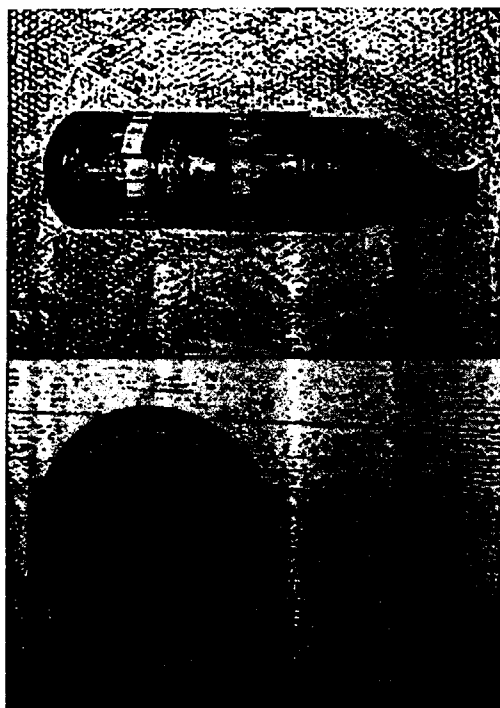


Fig.6 Fracture test specimen after compressive load test.  
(Post inclination angle is 0.62 degree)

The mean fracture load,  $P_{m}$ , and standard deviation  $s$ , containing above two types of different specimens were 904 kN and 72.6 kN, respectively. From these data specified minimum fracture load,  $P_{\min}$ , can be calculated as the 99 % survival probability with 95 % confidence level by the following equation.

$$P_{\min} = P_m - (2.326 + 1.645/\sqrt{n})s \quad (2)$$

where  $n$  is the number of test data. The specified minimum fracture load calculated by equation (2) is shown in Fig.8.

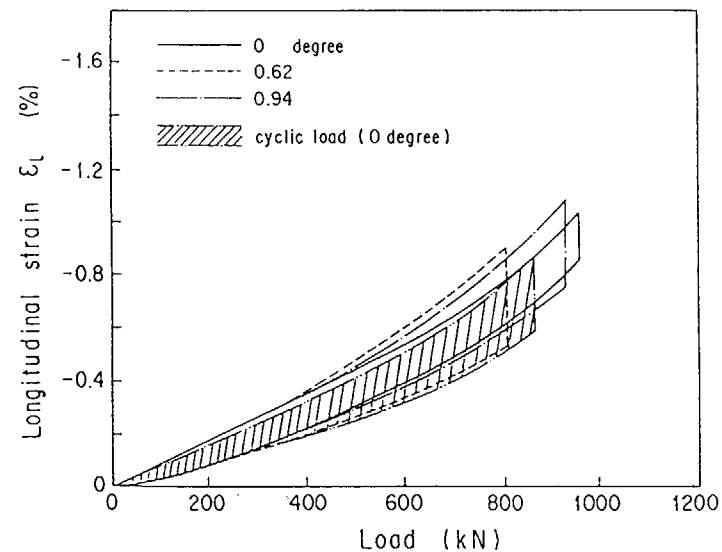


Fig.7 Relationship between longitudinal strain and applied load under the conditions of different inclination angle.

On the other hand, since the normal operation load and maximum design load applied to this component are about 35 kN and 130 kN, respectively, the safety factors (specified minimum fracture load/applied load) in the normal operation and the most severe earthquake are 20 and 5.4, respectively.

Fig.9 shows the volume effect on the buckling strength of support post of full-scale model and 1/6-scale model test. In this figure the volume effect on compressive strength of IG-11 graphite<sup>(4)</sup> is also plotted. The buckling strength exhibited slightly higher volume effect than that of observed in compressive strength on IG-11 graphite; the ratio of buckling load of the full-scale model to the 1/6-scale model was about 0.7, meanwhile in the compressive strength this ratio was about 0.8 in the same volume difference.



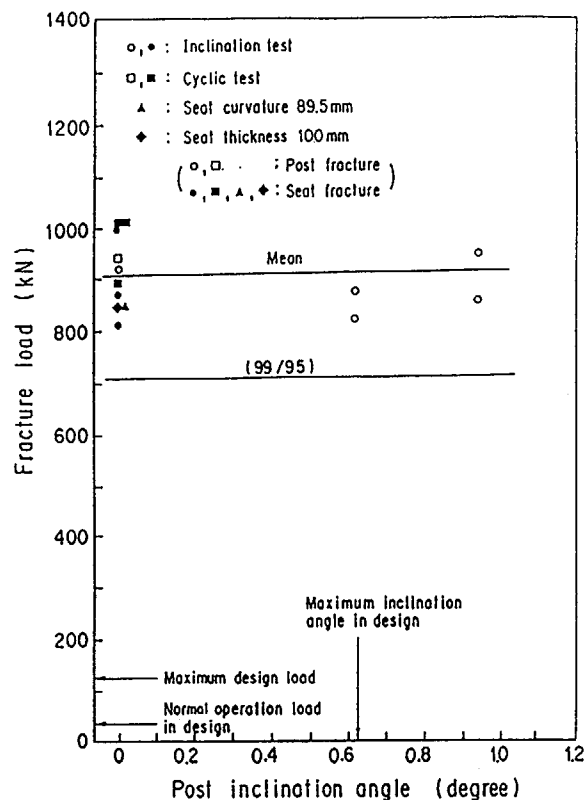


Fig.8 Fracture load dependence of support post inclination angle in a full-scale-model test.

### 3.2 Cyclic load test

The specimen after the cyclic load test is shown in Fig.10. The post specimen also fractured at the contact spherical section. Each specimen withstood three kinds of the 200 times of load cycles. Longitudinal strain in the compressive fracture test after applying cyclic load showed almost the same behavior compared with that of observed in the no-cyclic load specimen (see Fig.7). Also the fracture load after applied the cyclic load showed no decrease compared with that of observed in the no-cyclic load

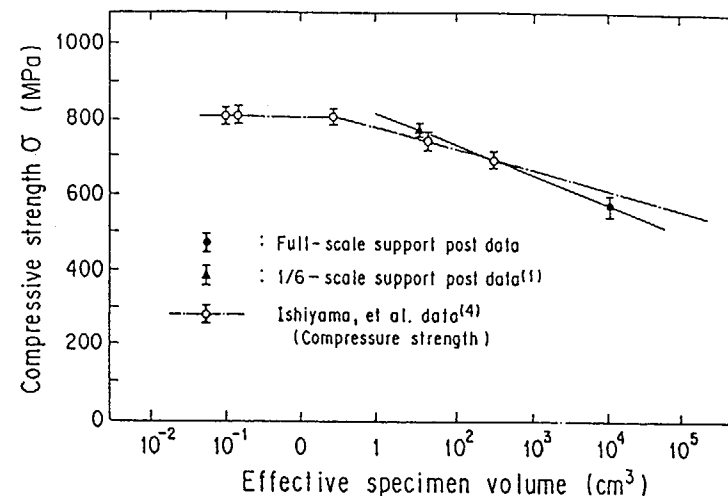


Fig.9 Volume effect on buckling strength of IG-110 graphite.

specimen. (see Fig.8) Therefore, the cyclic load below about 300 kN, which is at least two times larger than the maximum seismic load, has no damage to the support post/seat component, and then the integrity of this component was verified under the most severe cyclic seismic load.

### 3.3 Oxidation test

The test specimen about 14 % oxidation weight loss oxidized at 650 °C is shown in Fig.11. The inner distribution measurement of oxidation weight loss was done at the three kinds of oxidation temperatures, 550 °C, 650 °C and 800 °C; these results are shown in Fig.12(a) to (c).

At the 550 °C oxidation treatment in the air condition the specimen showed small dimensional change of post diameter, and measured density by every 1 mm cutting showed constant value; the oxidation must be limited at the near surface (see Fig.12(a)). On the other hand, at the 650 °C oxidation treatment specimen showed also dimensional change of post diameter, and the density diminution was observed within about 10 mm depth from the surface (see Fig.12(b)). In this figure the distribution of

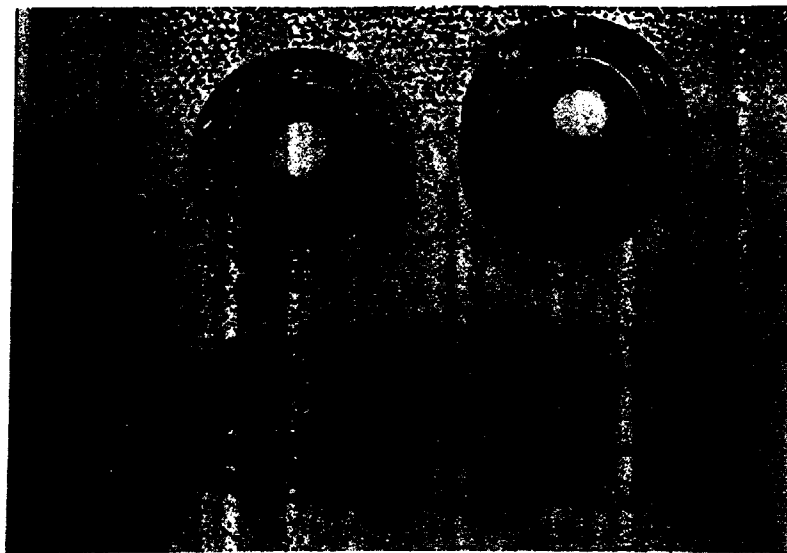


Fig.10 Fractured test specimen after the 200 times cyclic load test.

maximum oxidation weight loss in design (the mean oxidation weight loss estimated in design is about 15 %), which is occurred at the severe accident of air ingress of double tube rupture at the primary circuit, was also shown; this oxidation distribution in design is similar to that of oxidized at 650 °C heat treatment. At the 800 °C oxidation the specimen showed large dimensional change of post diameter compared with that of the 650 °C specimen (see Fig.12(c)); since the measured density from the surface showed almost the same value, it can be clear that the oxidation is limited at the near surface.

Fig.13 shows the oxidation effect on the fracture load of support post. The fracture load of oxidized post/seal component decreased with increasing oxidation weight loss. In this oxidized support post and seal specimens only the seal was fractured by the compressive load; therefore the each buckling strength of oxidized posts are higher than those obtained fracture loads.

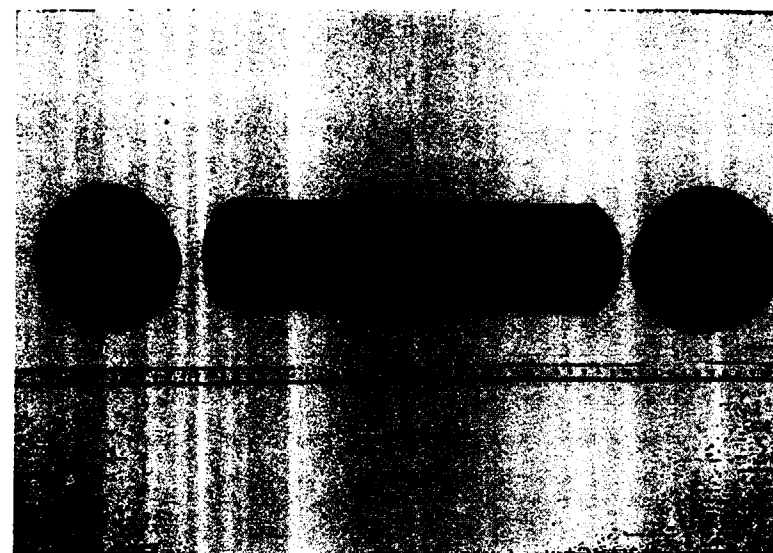


Fig.11 Test specimen of 1/2-scale model after oxidized 14% weight loss at the temperature of 650 °C

To compare with the component fracture load of full-scale model, un-oxidized 1/2-scale model specimen was tested at the inclination angles of 0 and 0.5 degree. These data are also plotted in Fig.13. Both specimens exhibit almost the same fracture load as those of the full-scale model specimens considering the scale factor of the full-scale model.

From all the 1/2-scale buckling test data the mean straight line of fracture load on oxidation weight loss is calculated by the least square method as shown in Fig.13.

Assuming that the absolute values of fracture load differences between the mean straight line in Fig.13 and each obtained data in the same oxidation weight loss conform to the normal distribution, the specified minimum fracture load on oxidation effect can be calculated by equation (2) as the 99 % survival probability with the 95 % confidence level. In the normal operation, the oxidation weight loss of support post is estimated under 1 % in design. Therefore, from the oxidation test result the normal

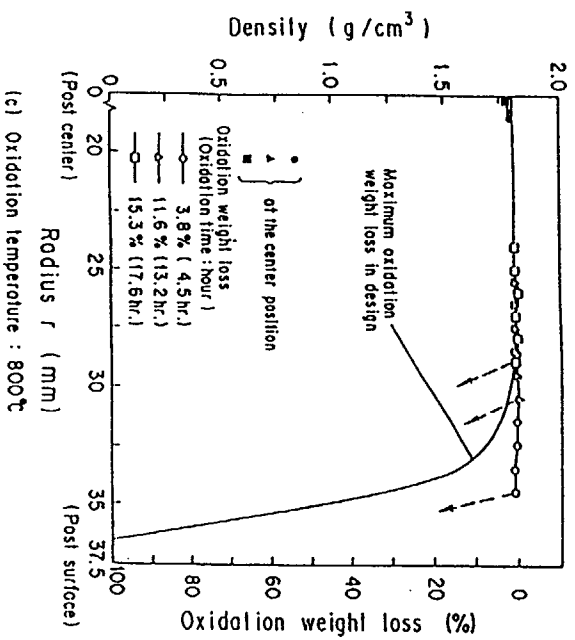
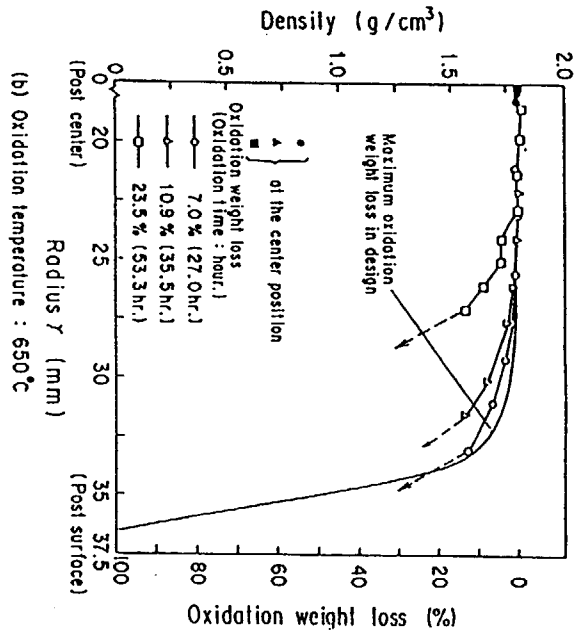
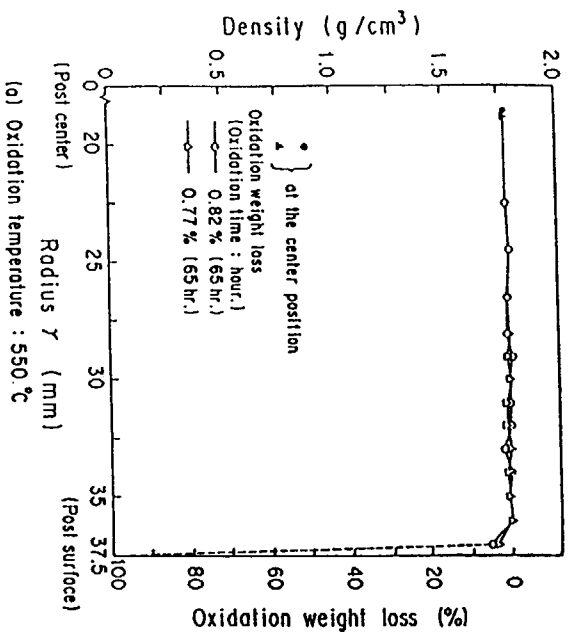


Fig.12 Oxidation weight loss distribution of 1/2-scale model specimen.

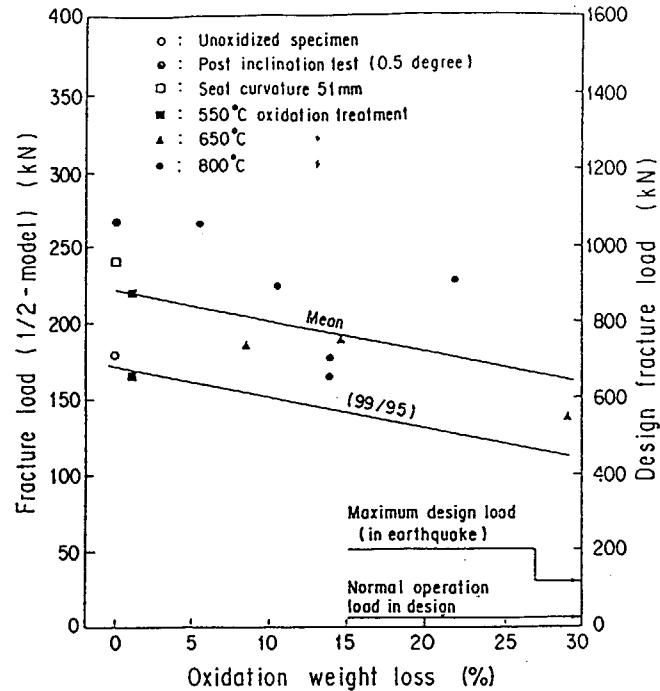


Fig.13 Fracture load vs. oxidation weight loss of support post in a 1/2-scale model test.

operation load is about 1/20 to the calculated 99%/95% value within about 1 % oxidation weight loss.

On the other hand, even if the maximum post oxidation event caused by the double tube rupture of primary coolant circuit and the severe earthquake will occur simultaneously by chance, the seismic load level is about 1/4.5 to the estimated 99%/95% value at 15 % oxidation weight loss. Therefore, the integrity of the support post/seat component was verified under the most severe oxidation accident.

#### 4. CONCLUSION

To evaluate the fracture load of core support post/seat component, full-scale and 1/2-scale model tests were carried out under the several conditions postulated in the HTTR. From the compressive strength test results, the following conclusions were obtained;

- (1) Within the maximum design inclination angle of support posts, inclination angle has no clear effect on the fracture load.
- (2) Specified minimum fracture load as 99 % survival probability with 95 % confidence level of the full-scale model was about  $7 \times 10^2$  kN. This value was about at least twenty times larger than that of the normal operation load and five times larger than that of the maximum seismic design load to the support post/seat component.
- (3) Cyclic load, which is at least two times larger than the maximum seismic load, has no clear damage to the support post/seat component.
- (4) Fracture loads of the 1/2-scale model were about a quarter of the mean full-scale ones, which indicates that the both models have almost the same fracture load of post/seat component.
- (5) Under the most severe accident of oxidation, even if the severe earthquake will occur by chance, the applied seismic load level was about 1/4.5 times of the specified minimum fracture load level (99 % survival/95 % confidence) of oxidized support post/seat component. Therefore, the structural integrity of this component was verified from these test results under the severe conditions postulated in the HTTR.

#### REFERENCES

- (1) K. Kikuchi, et al., JAERI-M 9109, 1980
- (2) Brocklehurst J.E., Chemistry and Physics of Carbon, Vol. 13, 145 (1977)
- (3) S. Sato, et al., Tanso, No. 118, 124 (1984)
- (4) S. Ishiyama, et al., J. At. Energy Soc. Japan, Vol. 30, No. 2, 181 (1988)

## DISCUSSION

Questions or Comments

Name: M. Eto

-----  
Did your experiment simulate the actual depressurization?  
-----

In what manner and how much air is supposed to be let in during accident?  
-----

Answer:  
-----

The manner in the depressurization accident was simulated actually; both  
-----  
model and actual component which were oxidized under the natural  
-----  
convection of air. The amount of the air is not used in this evaluation;  
-----  
To evaluate the fracture load of this component, we simulate  
-----  
conservatively only the magnitude of the oxidation weight loss  
-----  
(%) and the shape oxidation distribution in this oxidation test.  
-----

## ASSESSMENT OF THE LOAD CAPACITY OF THE DOWEL AND SOCKET SYSTEM IN THE HTTR HEXAGONAL BLOCK

N. TAKIKAWA, M. ISHIHARA, T. IYOKU, S. SHIOZAWA

Oarai Research Establishment,  
Japan Atomic Energy Research Institute,  
Oarai-machi, Ibaraki-ken

M. TOKUMITSU, S. KOE, M. UNO

Kawasaki Heavy Industries

Japan

### Abstract

The dowel and socket system was demonstrated of its load capacity in the seismic event using full size graphite blocks and finite element analysis.

There were good agreement between the measured fracture stress and the calculated fracture stress. That shows the propriety of 3D FEM modeling in which analytical mesh, quoted data and boundary condition were involved.

A special method was also developed for the dowel and socket system. It can estimate the stress of full 3D model from the stresses of 1/3 model.

### 1 INTRODUCTION

The reactor core of the HTTR is an array of hexagonal graphite blocks. During seismic events, the alignment of the stacked blocks in the core array must be sustained by some mechanism.

The dowel and socket system was a candidate of restraint structure of the alignment of the stacked blocks. After some researches and tests<sup>(1)</sup>, this system was selected for HTTR.

There are three dowels at the top of each block and mating three sockets at the bottom of each block in the dowel and socket system. To demonstrate the integrity of the dowel and socket system, it need to perform the full scale shear strength tests and three dimensional finite element analyses.

Especially, the socket is very important in HTTR design. The evaluation of the socket fracture strength had to be performed to assess the integrity of the dowel and socket system. However, the state of the contact between dowel-pin and socket had not been obviously, because of many difficulties in the numerical analysis of large full 3D model and in the modeling of boundary condition at the contact surface.

So, the object of this study were determined as follows.

- ① measurement of fracture load
- ② observation of the state of contact surface
- ③ development of the estimation method  
( from 1 dowel-socket to 3 dowel socket)

This paper describes the dowel and socket system's fracture test, the numerical analysis method and the stress evaluation in licensee event reports.

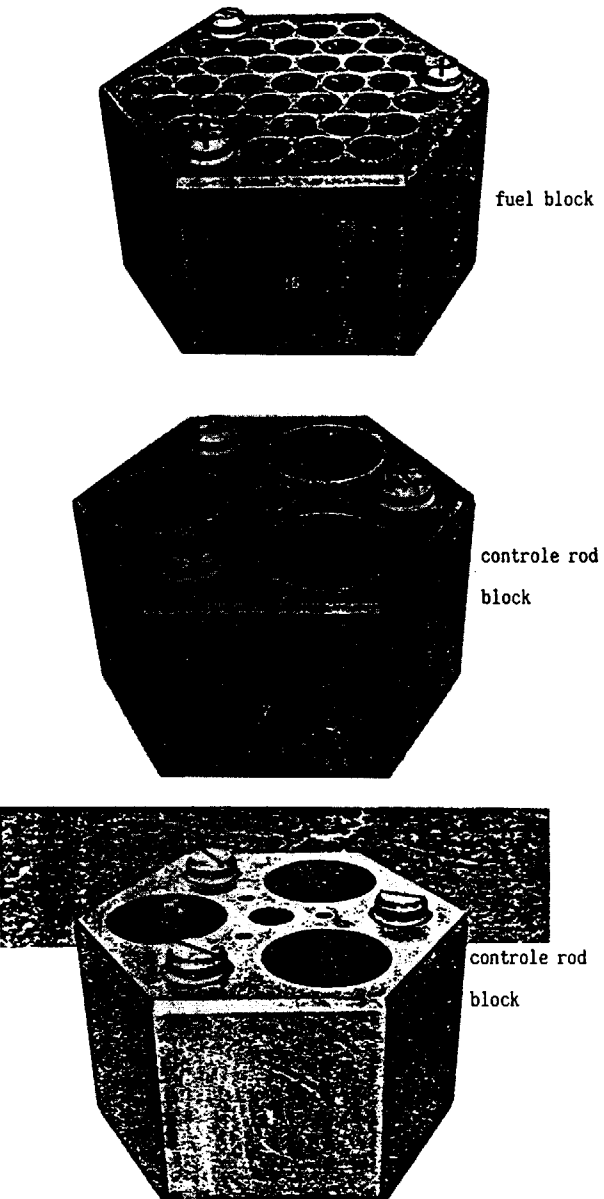


FIG. 1. Test blocks.

TABLE 1. UNIAXIAL TENSILE STRENGTH

(unit: Kg/cm<sup>2</sup>)

Lot No.	Log No.	use	blocks' number	holizon (//) axial (L)	uniaxial tensile strength				average strength	standard deviation	99/95% strength	graphite grade
					test piece's No.							
					1	2	3	4	x	$\sigma_m$	X	
7-5-58	1	fuel block	1	//	200	203	291	269	283	11.80 11.92	245	175
	2		4,5,6	//	272	268	288	266	273		235	
	3		7,8,9	//	290	279	278	270	279		241	
	4		10,11,12	//	272	243	257	283	264		226	
	5		13,14,15	//	302	288	286	300	294		256	
7-5-64	6	control rod guide block	16,K2	//	272	292	282	272	279	11.80 11.92	241	175
	7		2,3,K1	//	274	280	290	275	280		242	
	1		2,3	//	277	283	281	274	279		241	
	2		4,5,6	//	294	278	301	338	303		265	
	3		7,K1	//	302	310	304	294	302		264	
	4	dowel pin	all	//	302	302	290	319	303	11.80 11.92	265	175
	1		control rod guide block	//	306	306	293	281	295		257	
	2		7,K1	//	279	259	304	273	279		241	
	3		all	//	285	294	275	300	284		246	
	4		all	//	286	291	308	275	290		252	

// 291 Kg/cm<sup>2</sup>  $\sigma_m$  11.80  
287 Kg/cm<sup>2</sup>  $\sigma_m$  11.92

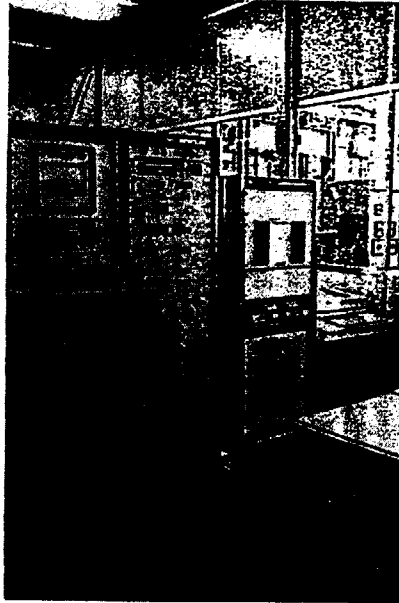


FIG. 2. Test facility.

## 2 EXPERIMENTAL

### 2.1 Graphite block and dowel

#### (1) Material

The core of HTTR consists of columns which are composed of stacked hexagonal graphite blocks. The alignment are sustained by pairs of pin and hole called dowel and socket system.

Though the material of blocks and dowels are IG-110 in HTTR, we used IG-11 in this study. Because IG-11 is same as IG-110 without purity and economy.

The kinematic and chemical test were performed with small test pieces, and the results of uniaxial tensile strength test are listed in Table 1.

#### (2) Blocks

There are two representative blocks in HTTR, one has the shape of providing coolant channels and the another one has the shape of guiding control rods.

We produced fuel blocks and control rod blocks as above two types considering which block are severe condition from the point of seismic stress. Figure 1 shows produced blocks. The size of blocks are full scale without height. The width is 360mm, the height is 250mm and the channel holes' diameter is added 1mm as a surplus.

#### (3) Dowel and socket

The shear force between two blocks is occurred from the prevention of structure's horizontal displacement at seismic event. The dowel and socket system are required

to have sufficient toughness against this shear force. On the other hand, the construction of the core array requires dimensional surplus on dowel socket system to accommodate manufacturing error and irradiational dimension change.

The consistent design of the dowel and socket system are determined with  $\pm 0.3$  mm gap between dowel and socket. Diameters of dowel are 45mm at fuel block and 55mm at control rod block, and diameters of socket are 45.6mm at fuel block and 55.6mm at control rod block.

### 2.2 Test facility

#### (1) Apparatus

We used the fatigue testing machine with electrical controlled hydraulic system. It can apply the 20ton as the maximum load.

#### (2) Configuration

Figure 2 shows the arrangement of test block, holders, testing machine and controlling panels.

The holder was designed to have a characteristic of applying shear force only. The characteristic was performed by driving force in-line from top load-cell to bottom base plate. If load-cell and the portion of test were not in-line, the additional strong moment would change the condition of the load from the accurate state, then lower strength would be measured.

In the design of holder, the force loss by friction was considered. The loss was caused from sustaining force against dead weight of block and holder. Figure 3 shows the balance of force and moment around the block. According to this figure, the friction force was calculated as follows.

$W = F$  : dead weight

$R = N$  : restraint force

a, b, c, d dimensions

The balance is

$$a \cdot R + d \cdot N = b \cdot F \dots (1)$$

Restraint force is

$$N = \frac{b}{(a+d)} \cdot W \dots (2)$$

= 88 kgf

Friction force is

$$T = \mu \cdot N \dots (3)$$

where,  $\mu$  is coefficient of friction.

$\mu$  is less than 0.3.

Then maximum friction force is

$$T = 0.3 \cdot 88 = 26 \text{ kgf.}$$

This value is 3% of fracture strength, and can be ignored.

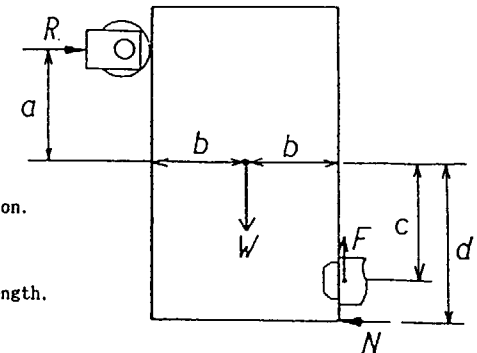


FIG. 3. Friction force.

### 2.3 Loads

#### (1) Direction

From the point of blocks' load capacity, three dowel socket systems fracture tests were performed. The number of three dowel tests were two in both fuel block and control rod block. The direction of load were determined from finite element analysis to observe the lowest load capacity. The direction is shown in Fig. 4.

To confirm the developed method, one dowel and socket tests were carried out with three load directions. The number of three is corresponding to three dowel and socket system. Therefore, directions of one dowel and socket tests are same as each direction of three dowel and socket system's test.

## (2) Loading conditions

control method : load control  
 load speed : 200 kgf/minute at one dowel socket system  
               400 kgf/minute at three dowel socket system  
 temperature : room temperature

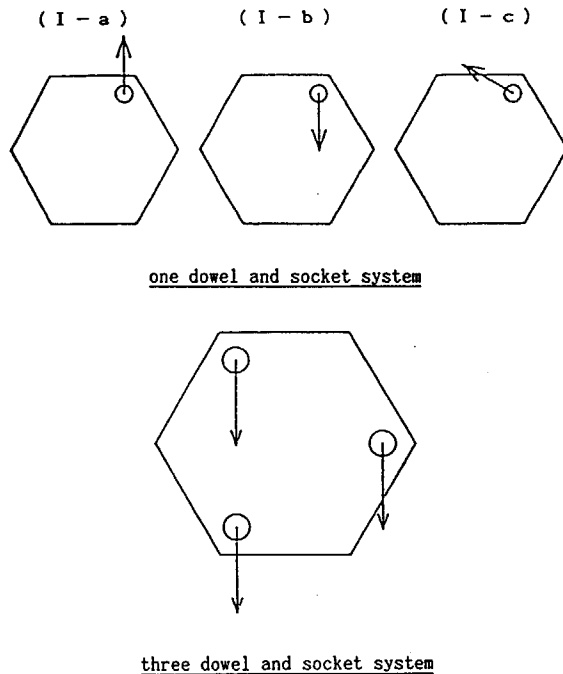


FIG. 4. Direction of load.

## 2.4 Measurement

## (1) Displacement

The displacement was measured at neighbourhood of two blocks' contact surface to get spring constant.

The detector type was strain gauge type. The X-Y recorder was used to get the relation between load value and displacement.

## (2) Strain

Positions and directions of strain gauges were determined by three-dimensional finite element analysis. That is, gauges were setted in high stress position and with directions of primary stress.

The strain gauge was electrical resistance type gauge.

The small gauge (1mm length) was selected to measure of local strain.

The accuracy of small strain gauge was certified by check test which performed comparison of 4mm and 1mm gauge length on four point bending of flat graphite.

The last consideration on selection was the error from temperature fluctuation.

The strain gauge for graphite was not obtained commercially, the steel type gauges were used. If the temperature fluctuation is 5 °C, the difference of thermal strain is

$$\Delta \varepsilon = \Delta T \cdot \Delta \alpha = 5^{\circ}\text{C} \cdot (5 \cdot 10^{-6} - 11 \cdot 10^{-6}) = -30 \times 10^{-6} \dots\dots\dots (4)$$

This strain is much less than the fracture strain.

## (3) Contact surface

The shape of the contact surface between dowel-pin and socket-hole was measured using two types of pressure detecting films. These films were used to increase accuracy of measurement by deviding the pressure range to high region and low region.

The load value is 1/3 of first test block's fracture load (about 400kgf).

After removed these films, the fracture test were carried out.

## 3. RESULT and DISCUSSION

## 3.1 Shear load capacity

The summary of fracture tests is shown in Table 2.

The shear load capacity of fuel block with three dowel socket system was 2660kgf in average.

The shear load capacity of control rod block with three dowel socket system was 3648kgf in average.

The capacity of control rod block was 37% greater than fuel block's. Therefore, the integrity of control rod block is assured from the integrity of fuel block.

The results of three dowel and socket system's test are as follows.

## (1) Three dowel socket strength of fuel block

- ① There are low scatter in strength in two blocks. The values of average strength was 2660kgf.

This value corresponds to small failure. For complete fracture in which the dowel socket system loses the performance of load sustaining, the value was 3812kgf. The functional surplus was 40% higher than strength criterion.

- ② After complete fracture, the portions of fracture were found in the ligament near socket hole, the ligament near dowel attachable hole and the dowel pin.
- ③ The average displacement were 0.259mm.
- ④ The spring ratios were 9140kgf/mm.

## (2) Three dowel socket strength of control rod block

- ① The values of average strength was 3648kgf.

This value corresponds to small failure. For complete fracture in which the dowel socket system loses the performance of load sustaining, the value was 7191kgf. The functional surplus was 95% higher than strength criterion.


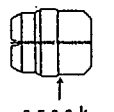


- ② After complete fracture, the portions of fracture were found in the ligament near socket hole, the ligament near dowel attachable hole and the dowel pin.
- ③ The average displacement were 0.251mm.
- ④ The spring ratios were 13280kgf/mm.



TABLE 2. SUMMARY OF TEST RESULTS

use	No pin	direction	No	first failure P <sub>r</sub> (kgf)	displace ment (mm)	spring constant (kgf/mm)	failure position	comment
fuel blk.	1	a	1	1091	0.345	2550	pin,thr.	average strength
			2	1181	0.373	2540	pin,thr.	P <sub>r.a</sub> = 1123kgf P <sub>r.b</sub> = 1140kgf P <sub>r.c</sub> = 1140kgf P <sub>r.d</sub> = 1178kgf
			3	1096	0.342	2500	pin,thr.	
			ave.	1123	0.353	2530	—	
		b	1	1093	0.360	2300	socket	(b)'s strength standard deviation $\sigma_{pb} = 53\text{kgf}$
			2	1209	0.449	2180	pin,soc.	
			3	1200	0.435	2210	socket	coeff. of variance $\sigma_{pb}/P_{r.b} = 0.047$
			4	1122	0.384	2360	pin	
			5	1179	0.403	2390	pin,soc.	99%/95% strength P <sub>u</sub> = 930kgf
			6	1188	0.414	2240	pin,soc.	
			7	1065	0.348	2360	pin	(a),(b),(c) strength by calc. P <sub>total</sub> = 3403kgf
			8	1069	0.351	2350	pin,soc.	
			1'	1137	0.379	2480	pin,soc.	average P <sub>u</sub> = P <sub>total</sub> /3 = 1134kgf
			2'	1137	0.395	2260	all	
			ave.	1140	0.392	2310	—	spring constant 1 dowel pin k <sub>a</sub> = 2530kgf/mm k <sub>b</sub> = 2310kgf/mm k <sub>c</sub> = 3370kgf/mm  3 dowel pin K <sub>s</sub> = 7898 kgf
		c	1	1278	0.297	3420	pin	
			2	1102	0.244	3460	pin,thr.	
			3	1040	0.234	3220	pin	
			ave.	1140	0.258	3370	—	
	3	a b c	1	2720	0.283	8280	pin	
			2	2599	0.235	10000	all	
			ave.	2660	0.259	9140	—	
cont rol rod blk.	3	a b c	1	3495	0.231	13560	pin	
			2	3800	0.270	12990	all	
			ave.	3648	0.251	13280	—	

TABLE 3. FRACTURE SKETCH

test No.	sketch or comment				fracture load (kgf)
	No	dowel		socket	
		hole	pin	hole	
F1-b-1	No	9	9-1	8	1093
	f				
	i	no failure	no failure		
F1-b-2	No	9	9-2	8	1209
	f				
	i	no failure			
F1-b-3	No	9	9-3	8	1200
	f				
	i	no failure	no failure		

## 3.2 Strength and spring constant of one dowel and socket

In following description, we'll mention about fuel block and its dowel and socket only. Because the assessment of the fuel blocks' strength is more critical than control rod blocks'. The example of fracture sketch is shown in Table 3.

## (1) Results of one dowel and socket

- ① There are low scatter in strength among load direction. The values of strength are in the region of 1123kgf ~ 1178kgf.
- ② The fracture occurred at socket by (b) direction load. Its crack initiation point was corresponded to high stress occurring position in finite element analysis.
- ③ The average displacements were in the range of 0.258mm~0.433mm. They were changed according to the directions of load.
- ④ The spring constants were in the range of 2180kgf/mm~ 3370kgf/mm. They were also changed according to the directions of load.

## (2) 99% survival &amp; 95% confidential strength

The load direction (b) has more accurate value because of amount of results. The single system's capacity was calculated from this direction. The result of plotting on normal probabilistic paper was shown in Fig. 5. It says that the distribution of strength may be normal probabilistic expression.

99% survival & 95% confidential strength P<sub>u</sub> is calculated as follows.

$$P_u = \bar{P} - \kappa \sqrt{\sigma} \quad \dots \dots \dots (5)$$

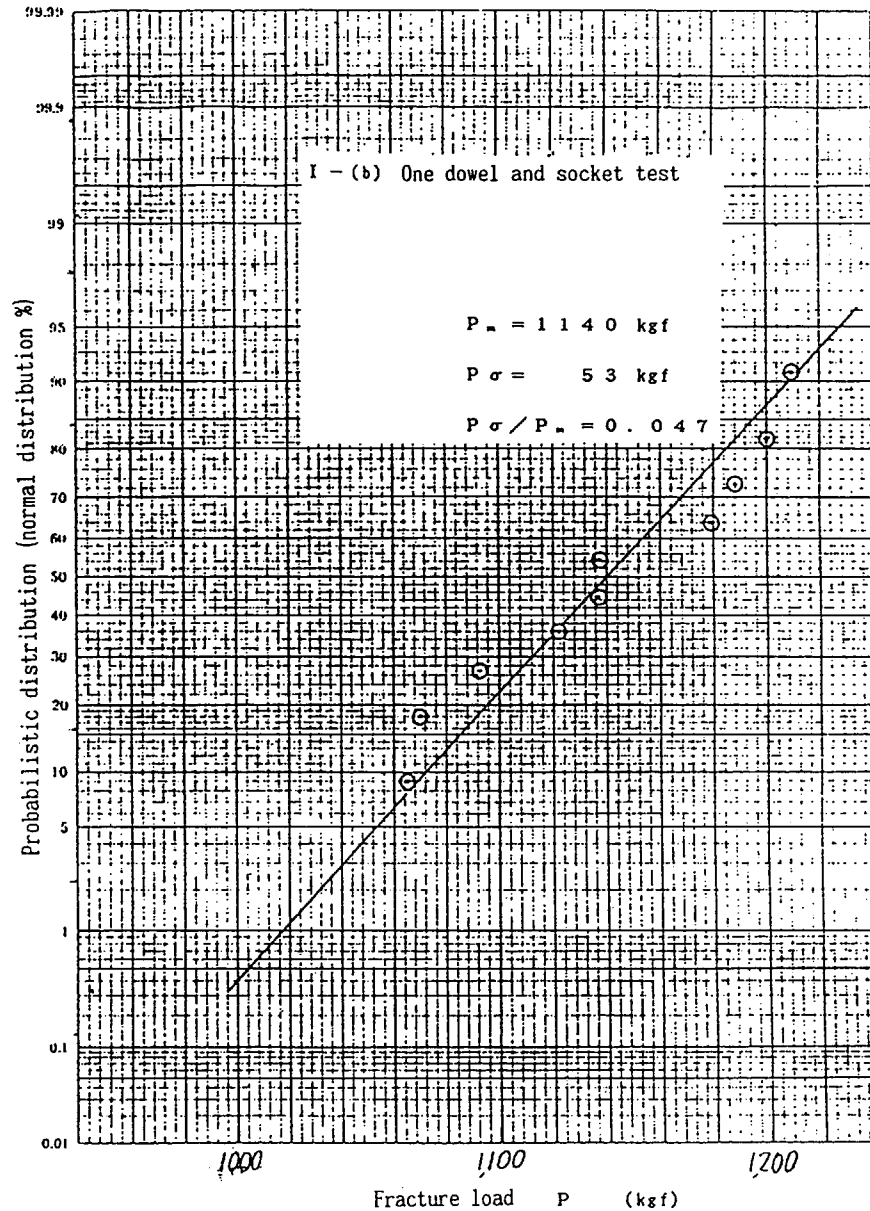


FIG. 5. Strength distribution.

Where,  $P$  is the average of results,  $\sigma$  is the variance and  $\kappa$  is the coefficient determined by limited level of 99%/95% in one side criterion.

From the test's result,  $P$  was 1140kgf and  $\sigma$  was 53kgf. Then the 99% survival and 95% confidential strength is

$$P_u = 1140 - 3.96 \sqrt{53} = 930 \text{ kgf.}$$

### 3.3 Shape of contact surface

The shape of contact surface were measured in two pressure region.

The pressure distribution was measured that its shape is the ellipse and the region of contact is 90° around socket hole. This feature agreed with Hertz's contact theory.

### 3.4 Method of estimation from 1 dowel system to 3 dowel system

#### (1) Equations of balance

3 dowel system's spring constant was certified from 1 dowel systems results which was more accurate because of amount of numbers.

The first contact occur at two dowel-socket which are (a) or (b) and (c) in Fig. 6. Because, the machining doesn't have complete accuracy.

The equations of force balance is as follows.

$$\left. \begin{aligned} P &= P_a + P_b + P_c \\ 2P_c &= P_a + P_b \\ \delta_a &= P_a / K_a \\ \delta_b &= P_b / K_b \\ \delta_c &= P_c / K_c \\ \delta_a \pm \varepsilon &= \delta_b \end{aligned} \right\} (6)$$

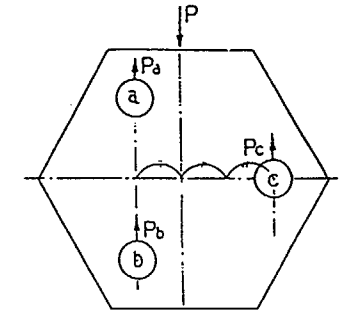


FIG. 6. Schematic balance of force.

Where,  $P_a, P_b, P_c$  are each load of dowel-socket,  $\delta_a, \delta_b, \delta_c$  are displacements,  $K_a, K_b, K_c$  are spring constants,  $\varepsilon$  is the dimensional error in production, and  $\pm$  is changed + when (a) contact first or - when (b) contact first.

The solutions are follows.

$$P_a = \frac{2}{3} \cdot \frac{K_a}{K_a + K_b} \cdot P \mp \frac{K_a \cdot K_b}{K_a + K_b} \cdot \varepsilon \quad (7)$$

$$P_b = \frac{2}{3} \cdot \frac{K_b}{K_a + K_b} \cdot P \pm \frac{K_a \cdot K_b}{K_a + K_b} \cdot \varepsilon \quad (8)$$

$$P_c = \frac{P}{3} \quad (9)$$

#### ① Fracture load estimation in 3 dowel socket system

From tests' result,  $K_a, K_b, K_c$  are 2530, 2310, 3370 kgf/mm respectively and  $\varepsilon$  is 0.1mm at (b).

The load distribution of 3 dowel system is follows.

$$P_a = 0.348 \cdot P + 121 \quad (10)$$

$$P_b = 0.318 \cdot P - 121 \quad (11)$$

$$P_c = 0.333 \cdot P \quad (12)$$

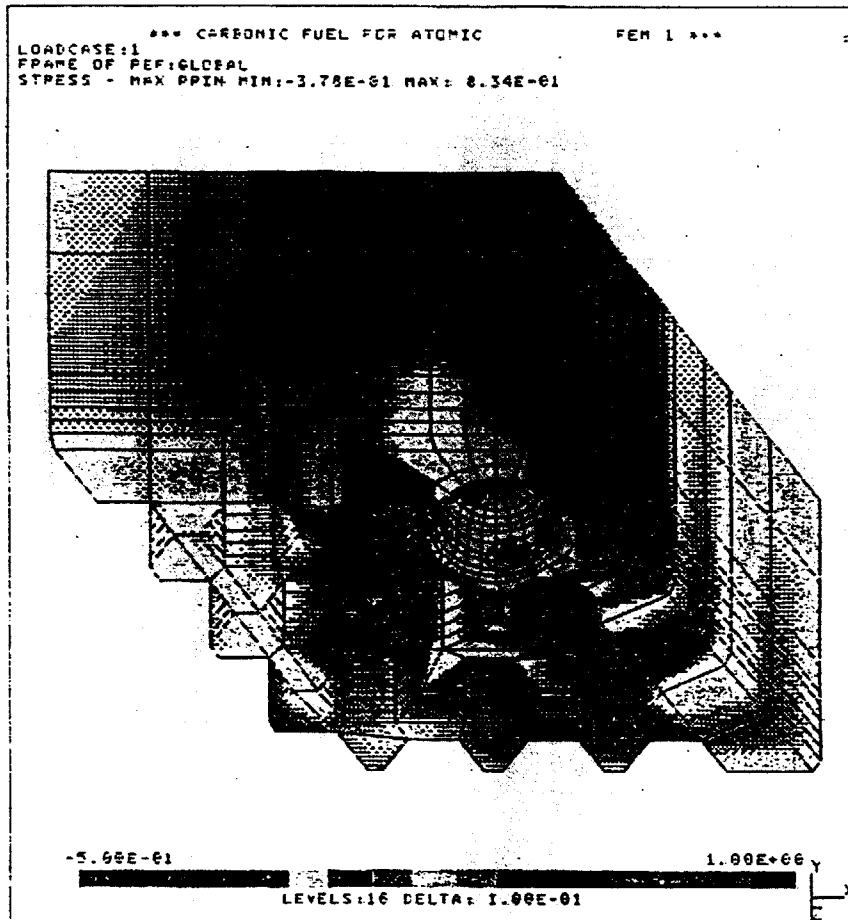


FIG. 7. Stress contour.

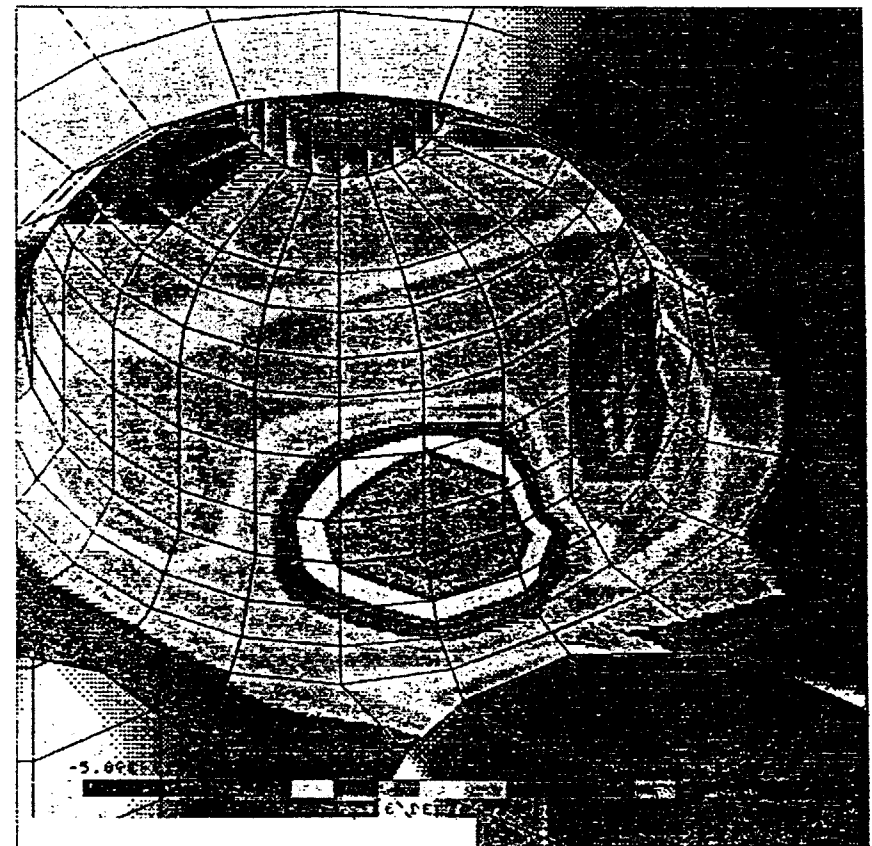


FIG. 8. Stress contour (zooming).

1 dowel systems' strength are 1123, 1140, 1140kgf in (a), (b), (c) direction respectively. Fracture of 3 dowel system is occur as soon as one of  $P_a, P_b, P_c$  exceeds above 1 dowel systems' strength. The estimated value is follows

$$P_{\text{estimated}} = 2879\text{kgf}$$

This value agrees with measured value.

$$P_{\text{measured}} = 2660\text{kgf}$$

## ② Displacement at fracture

Each displacement are calculated as follows.

$$\delta_a = P_a / K_a = 1122 / 2530 = 0.444 \quad (13)$$

$$\delta_b = P_b / K_b = 794 / 2310 = 0.344 (\therefore \delta_a - \varepsilon) \quad (14)$$

$$\delta_c = P_c / K_c = 960 / 3370 = 0.285 \quad (15)$$

## ③ Spring constant

The displacement of (b) follows (a) with distance  $\varepsilon$ . Then 3 dowel system's displacement is  $(\delta_a + \delta_b) / 2$ . The spring constant of 3 dowel system is

$$K_s = \frac{P}{(\delta_a + \delta_b) / 2} = 7898\text{kgf/mm} \quad (16)$$

This value is near the measured value of 9140kgf/mm. (The difference is 14%.)

## (2) Discussion

There are some difficulties in three dimensional finite element analysis for the graphite blocks. That are the numerical difficulty of large model for full scale of blocks and the boundary condition's difficulty simulating the turn of dowel and socket contact from manufacturing error.

The developed method provide the solution for these difficulties as follows.

The modeling is sufficient with 1/3 model and three calculations of different load directions are need.

The three dowel and socket system's stress with the manufacturing error is estimated arithmetically from the results of 1/3 model analysis for one dowel and socket system.

## 4. EXAMPLE of ANALYSIS

### (1) Method of the analysis

Three-dimensional linear elastic finite element analysis was carried out.

In the modeling, 1/3 model was adopted.

Used material data are quoted from the explication of design code<sup>[2]</sup>.

The code used for the analysis was 'NASTRAN'.

### (2) Applied load

There were three directions of load which correspond to one dowel system tests.

The distribution of contact load was determed from this test, and the magnitude of load was 1/3 average strength. (1140/3 = 380 kgf)

By the way, this load value is almost correspond to the result of core dynamic analysis code 'SONATINA-V2'. So, the blocks are expect to tolerate 3 times of seismic load.

### (3) Result

Figure 7 and 8 show the stress contour. It says the maxmum principal stress is 83.4 kgf/cm<sup>2</sup>.

If we apply 1140kgf as a load, then stress becomes 250.2kgf/cm<sup>2</sup>. This value is agree with uniaxial tensile strength (247kgf 99%/95%) of the test piece, and we could show the accuracy of modeling.

### (4) Licensee event report

Both of seismic stress and thermal-irradiation stress are to be assessed in the licensee event.

We performed two-dimensional viscoelastic stress analysis, and obtained the thermal-irradiation stress as 20 kg/cm<sup>2</sup> in thermal transient near the socket.

In the seismic event, the transient stress is added to the stress induced by S<sub>1</sub> earthquake (corresponding to Safe Shutdown Earthquake in U.S.A.).

The allowable stress in S<sub>1</sub> event is 175.09=157.8kgf/cm<sup>2</sup>. The evaluation is

$$\sigma = 20 + 83.4 \frac{190\text{kgf}}{380\text{kgf}} = 66.7\text{kgf/cm}^2 < 157.8\text{kgf/cm}^2 \quad (17)$$

In the design, we also evaluated the load capacity, that is

$$P_a = 380 \cdot (175 \cdot 0.9 - 20) / 83.4 = 620\text{kgf} \quad (18)$$

where 175 is strength of grade B graphite in HTTR design code, 0.9 is safety factor and other value are above mentioned. This value is sufficiently larger than S<sub>1</sub> load value which is 190kgf.

Even in S<sub>2</sub> event which is severer than S<sub>1</sub>, the occurred stress is less than allowable value. The evaluation is as follows.

$$\sigma = 20 + 83.4 = 103.4\text{kgf/cm}^2 < 175\text{kgf/cm}^2 \quad (19)$$

We have a plane using grade A graphite for the ligament near fuel hole in which the thermal-irradiation stress is severe. The strength of grade A is 198/cm<sup>2</sup>, and it is increased to 257kgf/cm<sup>2</sup> by irradiation.

In these case, the right side of eq. (19) changes eq. (20).

$$\sigma = 20 + 83.4 = 103.4\text{kgf/cm}^2 < 257\text{kgf/cm}^2 \quad (20)$$

## 5. CONCLUSION

The results of the strength tests have revealed the followings:

- (1) The load capacity of control rod block was 37% heigher than fuel block.
- (2) The load capacity of fuel block was 2660kgf, it has sufficient surplus.
- (3) The spring constant were 7898kgf/mm at 3 dowel-socket system.
- (4) The shape of contact surface between dowel and socket was ellipse, and range is 90° around the socket hole.

A special method was developed. That is a estimation of three dowel and socket system's stress from one dowel and socket system's stresses. Using this method, the analytical model can be reduced to 1/3, and the manufacturing error can be evaluated easily.

We could demonstrate the integrity of graphite blocks under thermal-irradiation and seismic HTTR condition using the results of this study.

## REFERENCES

- [1] N. TAKIKAWA, et al., "Structural Assessment of Prismatic Block for Pin-in-Block Fuel Element", proc. IAEA Specialist' Meeting on GRAPHITE COMPONENT STRUCTURAL DESIGN, TOKAI, JAPAN, September (1986).
- [2] T. IYOKU, et al., "An Explication of the Graphite Structural Design Code of Core Components for the High Temperature Engineering Test Reactor" JAERI-M 91-083, (1991)

# THE VIBRATIONAL CHARACTERISTICS OF THE KEYED GRAPHITE COMPONENTS IN THE HTTR

M. FUTAKAWA\*, H. SHIRAI\*\*, T. IYOKU\*,  
S. SHIOZAWA\*, S. TAKADA\*

\*Tokai Research Establishment,  
Japan Atomic Energy Research Institute,  
Tokai-mura, Naka-gun, Ibaraki-ken

\*\*CSK Company,  
Tokyo

Japan

## Abstract

The assembly system consisting of the keyed graphite components, which is employed in the core bottom structure of the HTTR (High Temperature Engineering Test Reactor), has a nonlinear vibrational characteristic. The analytical code was developed to predict the vibrational characteristic, and the validity of the code was verified through seismic model tests.

## 1 INTRODUCTION

The graphite components of the core bottom structure (CBS) in the HTTR are connected with each other through the key/keyway structure to restrict the horizontal motion during a seismic event and thus to avoid damage among the blocks, as shown in figure 1. The vibrational characteristics of the keyed graphite components indicate the complex nonlinear behavior attributed to the collision motion at key/keyway structures. Then, because of the complexity, it is necessary from the viewpoint of aseismic design for the HTTR to assess the integrity of the structure through combinations of analyses and test works.

In developing the analytical code suitable for predicting the vibrational behavior of the keyed graphite components, the basic vibrational tests were performed using a simplified model to verify the propriety of the collision model for the key/keyway

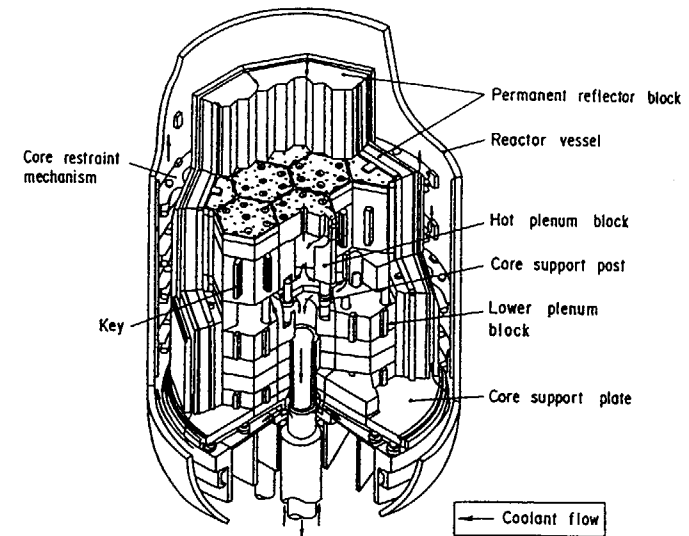


Fig. 1 Core bottom structure in HTTR

structure. In the analytical model, the dynamic response of the key/keyway structure is represented by a collision element consisting of a spring in parallel with a dashpot and the graphite block is idealized as a rigid body. The nonlinear dynamic response induced by the key/keyway structure was investigated analytically and experimentally.

The analytical code including the collision models has been used to evaluate the vibrational behavior of the CBS, especially the impact acceleration at the key/keyway structure. The analytical results were compared with the experimental ones obtained using 1/5-scale and 1/3-scale experimental models for the CBS in order to verify the propriety of the analytical code.

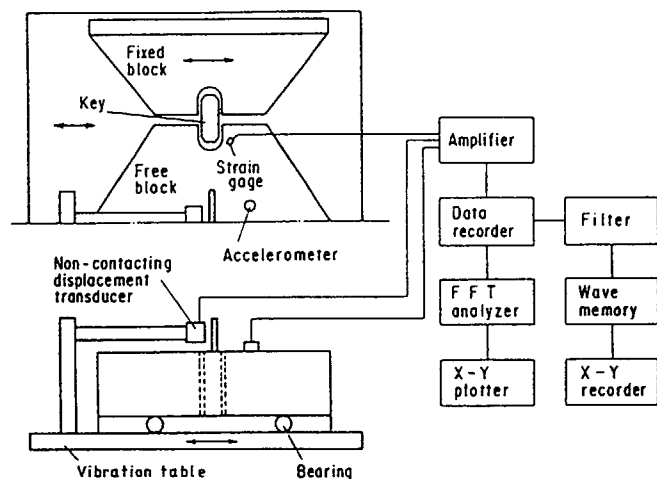


Fig. 2 Vibrational model of key/keyway structure

## 2 EXPERIMENTAL METHOD

### 2.1 Key/keyway structure

The vibrational tests were carried out using the simplified model to verify the collision model for the key/keyway structure. The vibrational model used for this study is composed of a hexagonal slice block and two fixed slice blocks, as shown in Fig. 2, and excited sinusoidally at a constant acceleration level by an electric vibrational table. The 2-type blocks are connected with each other through the key/keyway structure. The reason why the slice blocks are applied to the vibrational model of the key/keyway structure is to minimize the vertically rocking motion and therefore reduce the analytical representation to two dimensions. The material is the same as that in the HTTR, that is, the key is an isotropic graphite IG-11 and the keyway a near-isotropic graphite PGX. The size in a horizontal plane of

the model is half of the hot plenum block in the HTTR. The gap between key and keyway affecting on the collision behavior and the input acceleration level are varied in the vibrational tests.

Additionally, both the stiffness of the key/keyway structure and the stress distribution around the keyway are measured quasi-statically by using a hydraulic actuator.

### 2.2 Core bottom structure in the HTTR

The vibrational tests were performed by using the 1/5-scale and the 1/3-scale models for the CBS to confirm the validity of the vibrational analytical code, the scale effect and the structural integrity of the CBS against an earthquake<sup>2)</sup>. Both models consist of hot plenum blocks, permanent reflector blocks, key/keyway structures and so on, as shown in Fig. 3. The models

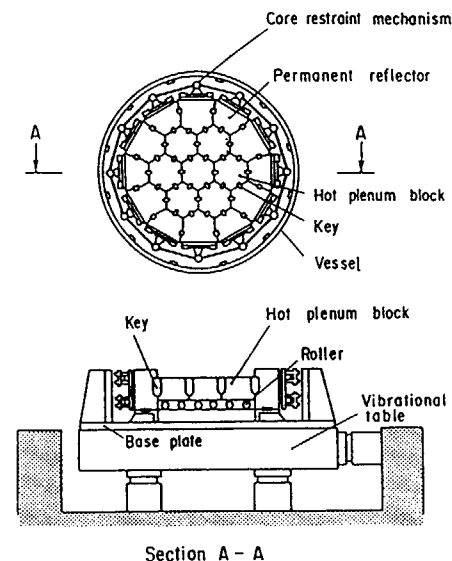


Fig. 3 Vibrational model of core bottom structure

were excited on the shaking table using sine dwell, sine sweep and equivalent ground motion induced by  $S_1$  and  $S_2$  seismic waves, where  $S_1$  means the maximum possible earthquake on a considering area and  $S_2$  the extreme design earthquake which is not supposed to occur actually. The response acceleration was measured at the center of the each block.

### 3 ANALYTICAL METHOD

#### 3.1 Equivalent stiffness of the key/keyway structure

In order to evaluate the equivalent stiffness of the key/keyway structure and the stress distribution around the keyway, the analysis of a contact problem between key and keyway was performed using a finite element code ABAQUS<sup>3)</sup>. The contact behavior was represented by using surface contact elements which take account of the relative slip and the deformation on the contacting graphite surfaces between key and keyway, as shown in Fig.4. On the other hand, the analysis in which the distributed

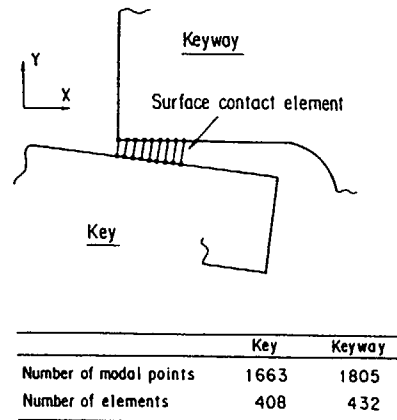


Fig. 4 Contact analysis model between key and keyway

force imposed on the contact area was carried out to investigate the effect of the contact behavior on the equivalent stiffness.

The stress-strain curves for the graphites were assumed to be bilinear relation, that is, Young's modulus  $E$ : 10GPa, work hardening coefficient  $H$ : 1.94GPa and yield stress  $\sigma_y$ : 42MPa for IG-11, while  $E$ : 6.3GPa,  $H$ : 2.22GPa and  $\sigma_y$ : 19MPa for PGX. Von Mises yield criterion was also applied to the nonlinear relation of the graphite. Additionally, the friction coefficient between graphite surfaces was assumed to be 0.25.

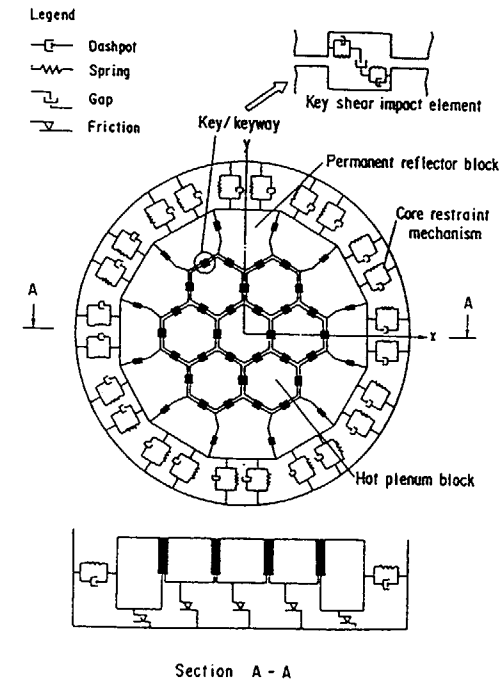


Fig. 5 Analytical model of keyed graphite components

### 3.2 Vibrational analysis for the keyed graphite components

The analytical model for the keyed graphite components shown in Fig.5 ,in the present study, is described as the following two-dimensional model:

- (1) each block is treated as a lumped mass,
- (2) each block has three degree-of-freedom, that is, two in-plane translational displacements and one rotation around the block center,
- (3) collision motion of each block is represented by a spring and dashpot model located at the corner of each block,
- (4) collision motion at the key/keyway structure is represented by a spring in parallel with a dashpot,
- (5) friction force acting between the block and the core support plate is considered as Coulomb friction.

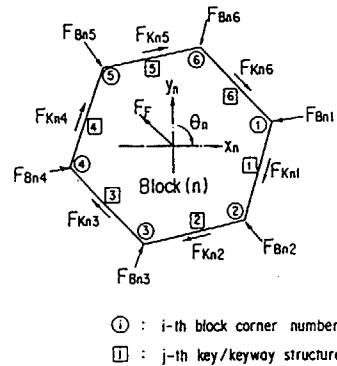


Fig. 6 Forces acting on a block

Figure 6 shows the forces acting on the block. The equations of motion for the n-th block can be written as:

$$m_n \ddot{x}_n = \sum_{i=1}^6 F_{xBni} + \sum_{j=1}^6 F_{xKnj} + F_{xFn}, \quad (1)$$

$$m_n \ddot{y}_n = \sum_{i=1}^6 F_{yBni} + \sum_{j=1}^6 F_{yKnj} + F_{yFn}, \quad (2)$$

$$I_n \ddot{\theta}_n = M(\sum_{i=1}^6 F_{xBni}) + M(\sum_{j=1}^6 F_{xKnj}) + M(\sum_{i=1}^6 F_{yBni}) + M(\sum_{j=1}^6 F_{yKnj}), \quad (3)$$

where,

$m_n$  = block mass,

$I_n$  = block mass moment of inertia,

$x_n$  = x-coordinate displacement of block,

$y_n$  = y-coordinate displacement of block,

$\theta_n$  = block rotation,

$F_{Bni}$  = impact force at the i-th block corner,

(  $F_{xBni}$  : x-component,  $F_{yBni}$  : y-component )

$F_{Knj}$  = impact force at the j-th key/keyway structure,

(  $F_{xKnj}$  : x-component,  $F_{yKnj}$  : y-component )

$F_{Fn}$  = friction force between the block and core support plate,

(  $F_{xFn}$  : x-component,  $F_{yFn}$  : y-component )

$M(F)$  = moment of force  $F$ ,

( $\ddot{\phantom{x}}$ ) = dots denote time derivatives of ( ).

The above governing equations can be solved numerically by using the fourth-order Runge-Kutta-Gill method.

## 4 RESULTS AND CONSIDERATIONS

### 4.1 Key/keyway structure

#### 4.1.1 Equivalent stiffness of the key/keyway structure

Figure 7 illustrates the relationship between the imposed force and the displacement at the center of a hexagonal block relating to the equivalent stiffness of the key/keyway structure. The relationship exhibits that the stiffness has a nonlinear characteristic. In the figure, the analytical results using the distributed force and the contact force generated through contact behavior are depicted by a dot-dash-line and a broken line.



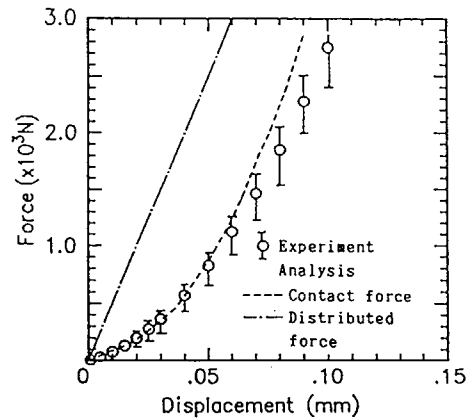


Fig. 7 Relationship between the imposed force and the displacement on the key/keyway structure

respectively. The analytical result considering the contact behavior represents the experimental one sufficiently. On the contrary, the stiffness deduced from the analytical result using the distributed force comes to be almost linear and far larger than the experimental one. It can be said from these results that the nonlinearity of the stiffness results from the contact behavior between key and keyway.

Therefore, the nonlinear spring, in the vibrational analysis, will be used to give an account of the collision motion in the key/keyway structure. In the equation (1)-(3), the impact force  $F_k$  at the key/keyway structure which is simulated by using a nonlinear spring may be represented by a polynomial function;

$$F_k = \sum_{i=0}^n K_i (|x_k| - 2d)^i \quad \text{at } |x_k| \geq 2d, \quad (4)$$

$$F_k = 0 \quad \text{at } |x_k| < 2d, \quad (5)$$

where  $K_i$  is the constant evaluated by the quasi-static test,  $x_k$  the relative displacement between the two adjacent keyways, and  $d$  the clearance between key and keyway.

Figure 8 shows the strain distributions around the keyway bottom obtained by the quasi-static and the vibrational tests and also by the contacting analysis. On the figure,  $\epsilon_0$  denotes the strain at 5mm from the bottom edge. It is clear from Fig.8 that the stress distribution is independent of whether it is induced in dynamic or in static states in the range of the tests and the contacting analysis is valid to describe the stress distribution around the keyway.

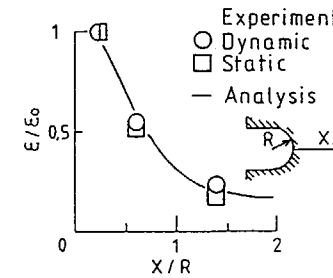


Fig. 8 Stress distribution around keyway

#### 4.1.2 Vibrational characteristics

Figure 9 shows the frequency responses of the acceleration. The key/keyway structure has the nonlinear vibrational characteristics in which the jump-down frequency shifts to the higher frequency region as an input acceleration increasing. The analytical results with the nonlinear spring considering the contact behavior can represent the experimental results sufficiently. On the contrary, the maximum acceleration in the analytical results with the linear spring becomes about 3 times as large as that in the experimental results. It is confirmed from the comparison between the experimental and analytical results that the analytical code in which the nonlinear spring was applied to express the collision motion at the key/keyway structure is useful to predict the vibrational behavior of the key/keyway structure.

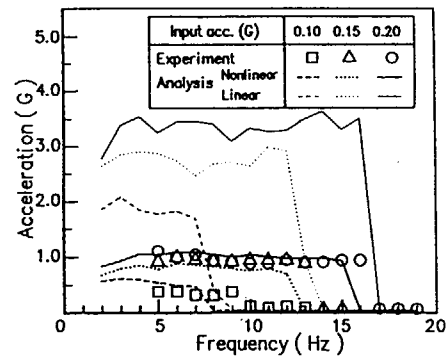


Fig. 9 Frequency response of acceleration on the key/keyway structure

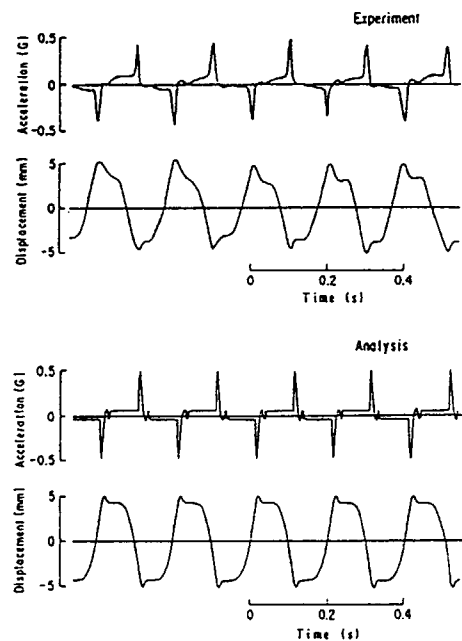


Fig.10 Vibrational wave of acceleration and displacement on the key/keyway structure

Figure 10 shows the wave shape of displacement and acceleration on the slice block when the collision motion occurred between key and keyway. The analytical results with the nonlinear spring show a favorable correlation with the experimental ones.

#### 4.2 Core bottom structure in the HTTR

Figure 11 shows the frequency responses of the acceleration in the center block of the 1/3-scale model at sine sweep of 120 and 360 Gal. The acceleration increases with increasing the input acceleration. The rapid drop in response, whose frequency increases with the input-acceleration level because of the

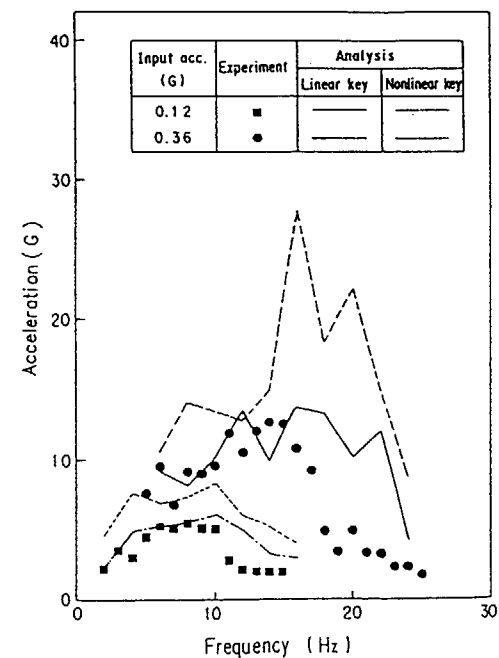


Fig.11 Frequency response of acceleration on the core bottom structure

characteristic of the nonlinear system, occurs around a resonance frequency. The analytical results using the nonlinear spring for the key/keyway structure can describe the experimental ones adequately. However, the acceleration in the results using the linear spring is larger than that in the experimental ones. It can be seen that the analytical code using the nonlinear spring for the key/keyway structure is available to represent the vibrational behavior of the CBS.

Likewise, the relations between the maximum acceleration of each block and the input acceleration under seismic motion are compared with the analytical results using the nonlinear spring, as shown in Fig.12. The maximum acceleration dose not increase proportionally with the input acceleration and the increasing rate lowers by degrees as the input acceleration increasing. This is because the unsteady collision behavior through the key/keyway structures is dependent on the relation between the input acceleration level and the clearance in the key/keyway structure. It is confirmed from the comparison that the developed analytical code can describe adequately the vibrational characteristic of the keyed graphite components such as the CBS including even the unsteady collision behavior.

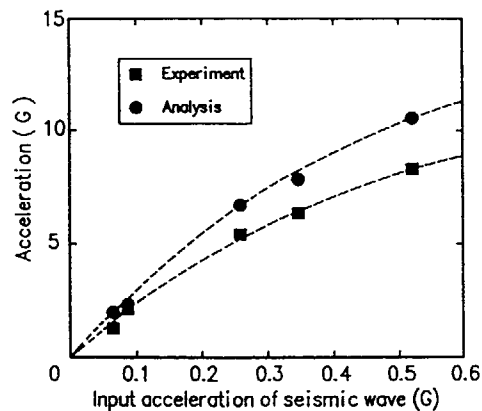


Fig.12 Relationship between maximum acceleration and input acceleration under seismic motion

## 5 CONCLUSION

The vibrational characteristics of the keyed graphite components were investigated through the vibrational tests and the analyses taking account of the collision motion in the key/keyway structure. The main conclusions are summarized as follows;

- (1) The stress distribution around the keyway is independent of whether it is induced under a dynamic or a static state.
- (2) The stiffness of key/keyway structure, which is applied to represent the vibrational behavior of the keyed graphite components, has the nonlinear characteristic due to the contact behavior.
- (3) The nonlinear stiffness of key/keyway structure can be evaluated by the contact analysis taking account of the relative slip and the deformation on the contacting graphite surfaces between key and keyway.
- (4) The analytical code employing a nonlinear spring for the key/keyway structure is available to predict the vibrational characteristic of the keyed graphite components.

## ACKNOWLEDGMENTS

The authors would like to thank Mr. Y. Muto for his helpful suggestions and comments.

## REFERENCES

- 1) IAEA Technical reports series No.312, Gas cooled reactor design and safety, Chapter 6., IAEA, Vienna, 1990.
- 2) Iyoku, T., Shiozawa, S., Futakawa, M. and Miki, T. The seismic test for HTTR core bottom structure, K15/2, 11th SMiRT, Tokyo, 1991.
- 3) ABAQUS User's Manual, Version 4.8, Hibbit, Karlsson and Sorensen, Inc., 1990.

## DISCUSSION

Questions or Comments

Name: R. Judge

Do you use ABAQUS on the model of the core bottom?  
-----Answer:  
-----

yes .-----

**MATERIALS DEVELOPMENT AND PROPERTIES**  
**Part A**

**(Session III)**

**Chairmen**

**B.T. KELLY**  
United Kingdom

**T. ARAI**  
Japan



# FABRICATION OF HTGR CORE COMPONENTS BY THE METHOD OF VOLUME GAS-PHASE IMPREGNATION OF POROUS MEDIA WITH PYROCARBON — MAIN CHARACTERISTICS OF THE MATERIALS AND PRODUCTS

V.F. ZELENSKIY, V.A. GURIN, Yu.F. KONOTOP,  
Yu.A. DERYUGA, V.V. KOLOSENKO  
Institute of Physics and Technology,  
Khar'kov, Union of Soviet Socialist Republics

## Abstract

Considered are some special features of fabricating carbon-graphite materials and products by methods of volume gas-phase impregnation of porous substances with pyrocarbon. Main characteristics of the materials of this class are given. Results from reactor tests of the materials and products with a pyrocarbon binder as well as their possible applications are discussed.

## 1. Introduction

Graphite is known to be used as a main structural material of the HTGR core for fabricating reflectors, discharge tubes, support columns, etc. It is also used as a matrix material for fuel and absorbing elements.

The classical fabrication methods for the graphite materials, which have not changed much since the second half of the past century, are founded on pressing or extrusion of coke powders with a binder, and a subsequent carbonizing and graphitizing annealing of the produced blocks [1].

The industrial technologies ensure the production of different sorts of graphite with a wide range of principal properties beneficial for solving successfully the problems of atomic power engineering, including those of HTGR. However, this may be treated as an evidence for unique properties of graphite materials rather than for the perfection of the conventional technology. Really, at high temperatures no materials can compete in strength with carbon and graphite, even though only a few percent of the theoretical strength value are realized for graphite.

In the last few decades, in the carbon technology there have appeared at least two radically new trends which make it possible to improve essentially the characteristics of carbon. Here we mean gas-phase (cvd) methods and the development of carbon fibers (CF) and carbon-carbon composites with these CF as a base. The both trends have been actively developed just for the solution of

HTGR problems [2,3]. However, they have not found wide application here, though large-scale manufactures were created for other applications, mainly, for space-rocket engineering [4].

At the Kharkov Institute of Physics & Technology (KIPT) the research work on fabricating from carbon the fuel elements (FE), absorbing elements, structural materials for HTGR by the use of the cvd methods has been started since early sixties. In our opinion, some of our developments are now ready for practical applications. Below we shall present some of our arguments.

## 2. Some special features of fabricating materials and products by the methods of volume gas-phase impregnation of powder and fibrous fillers

### 2.1. Installations for pyrolysis and process parameters

For realization of volume gas-phase impregnation of porous media, a series of pyrolysis installations have been developed at the KIPT. These installations represent hermetically sealed steel water-cooled chambers provided with vacuum pumping, gas supply, electric heating, gas flow rate and temperature control systems.

The vacuum system serves for outgassing the chambers before filling them with hydrocarbon gas to prevent the formation of an explosive mixture.

As a hydrocarbon gas, we generally use the natural gas from conventional city gas-supply lines at a pressure somewhat above the atmospheric one to exclude ingress of air into the chambers during the process.

Table 1

Installation type	Technical characteristics		
	Maximal diameter of products, mm	Maximal length of products, mm	Maximal power consumption, kw
AGAT - 1.6	160	1000	100
AGAT - 3.2	320	1200	250
AGAT - 5.0	500	2000	500
GF-2	1000	2000	1000
GF-3	2500	2600	1000



a)



b)

Fig. 1. a) General view of one of the pyrolysis sections.  
b) Pyrolysis installation GF-3.



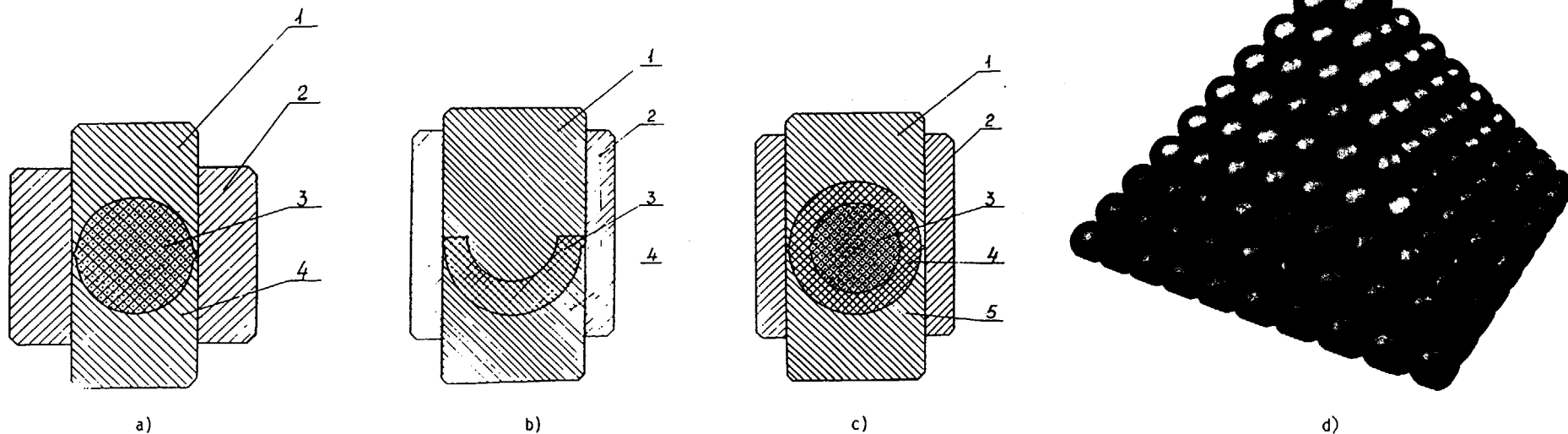


Fig. 2. Diagram of molding the billets of a core (a), shell (b) and fuel element in assembly (c); appearance of GSP fuel elements (d).

- a) 1, 4: punches, 2: casing, 3: charge material with fuel particles;  
 b) 1, 4: punches, 2: casing, 3: charge of the shell;  
 c) 1, 5: punches, 2: casing, 3: core, 4: fuel element shell.

The temperature of the process is 900 ... 1000°C, its duration depends on the size (thickness) of the fabricated products and may vary from several hours to a few thousand hours. The process is automated.

All the installations are, in principle, identical in design, differing from one another mainly by the overall dimensions (which, in turn, depend on the dimensions of the products to be fabricated) and, hence, by the power of heating sources. The main types and characteristics of the pyrolysis installations are presented in Table 1.

The general view of the pyrolysis installations is shown in fig. 1. Nearly 20 pyrolysis installations of the types listed in Table 1 are operating at the KIPT, enabling us to carry our research programs and to produce several ten tons of high-quality carbon materials per year.

## 2.2 Fabrication of fuel and absorbing elements

Fuel particles and commercial-grade graphite powder are used as basic materials for FE fabrication. An easily removable (no coke residue) plasticizer, e.g., glycerine, oil, is introduced into the graphite powder. The stock obtained is used to mold the FE shell billets.

To mold core billets, the charge material is incorporated with the necessary amount of fuel particles. The diagram of molding the FE billets is shown in fig. 2 [5,6].

On molding, we do not set as a goal to obtain a high density of billets. Generally, it is between 1.1 and 1.3 g/cm<sup>3</sup>, and this ensures sufficient strength to withstand subsequent technological procedures.

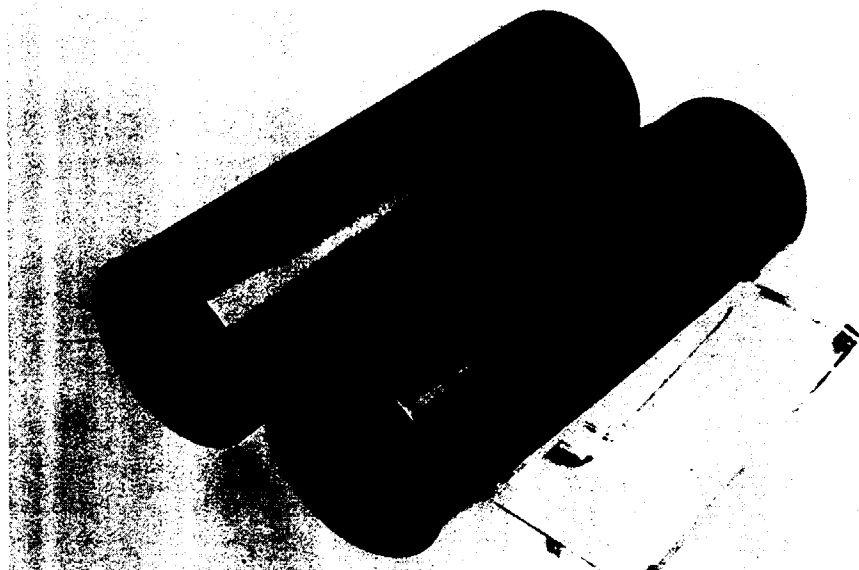


Fig. 3. Appearance of GSP fuel elements in unit form.

The billets, so molded, are placed in close rows in a porous form, then are filled with a powder of graphite, coke, quartz, etc. (to retain the shape of the products after plasticizer evaporation) and are impregnated in the pyrolysis installations to the density required (usually up to  $1.8...1.95 \text{ g/cm}^3$ ). After the impregnation procedure is completed, the FE are wheeled to get the necessary surface finish.

The fabrication process of absorbing elements is the same except that the core stock is incorporated not with fuel particles but with a  $\text{B}_4\text{C}$  powder or any other absorbing material.

Compared to the case of spherical FE, the fabrication of FE in the block form (fig. 3) or rod fuel composites, etc., by the gas-phase technology appears to be simpler. Here, a mixture of fuel particles with a graphite powder is charged into porous forms made of commercial-grade graphite or carbon cloth. The billets produced are impregnated with pyrocarbon and then their surfaces are machined.

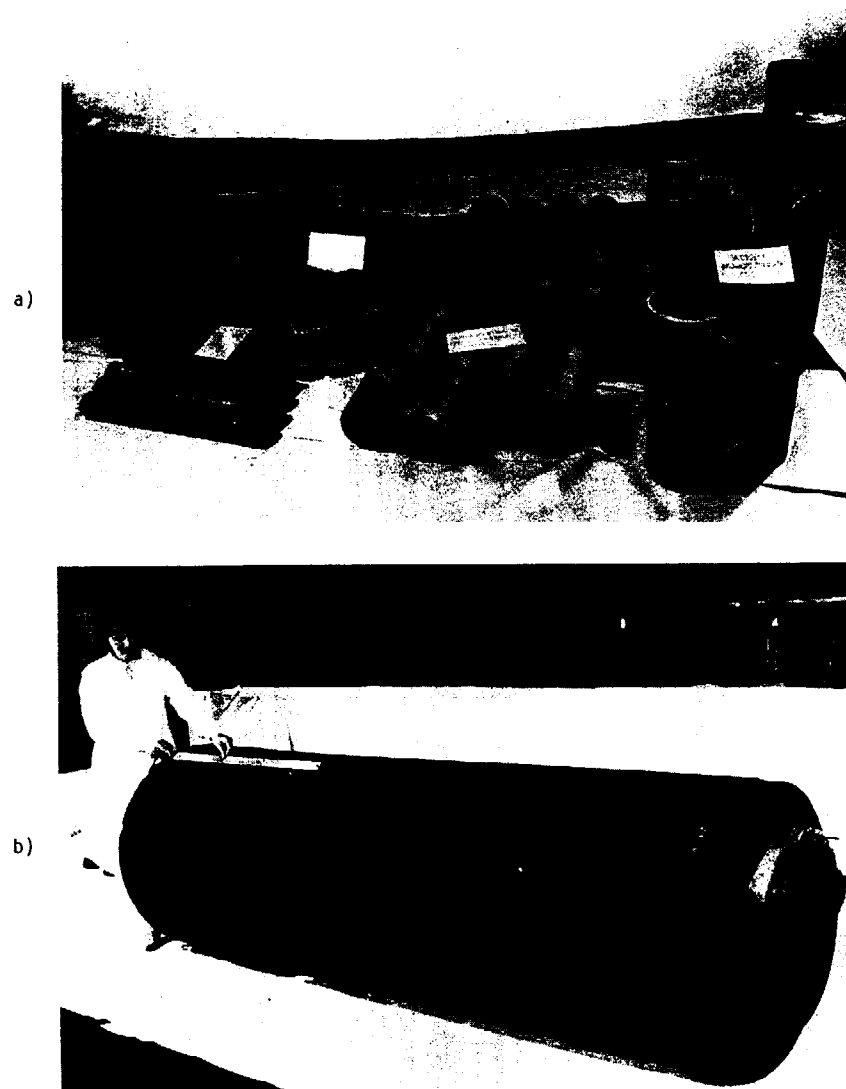
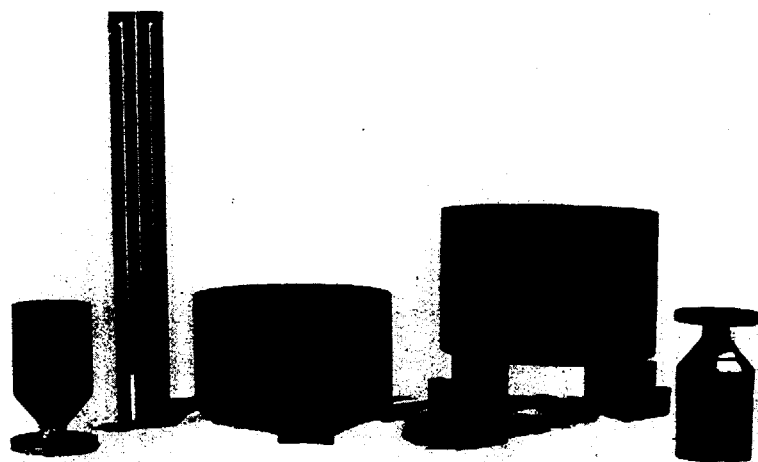


Fig. 4. GSP billets and products.

- a) Different-purpose products;
- b) GSP block,  $\sim 900 \text{ mm}$  in diameter and  $\sim 2500 \text{ mm}$  in length (without machining).



a)



b)



c)

Fig. 5. Appearance of products and structures made of carbon-carbon composites.

a): Plates and crucibles for metal melting;

b): heating elements;

c): a crucible, ~900 mm in diameter, for melting metals.

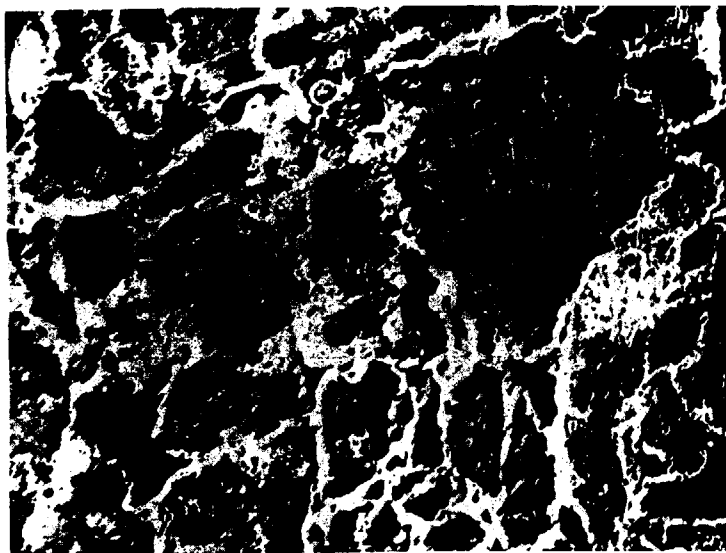


Fig. 6. GSP graphite structure, x100.

### 2.3 Manufacture of pyrocarbon-bound graphite blocks

For GSP<sup>\*)</sup> production, we also use commercial-grade graphite powders. After sieving, the required, mainly, fine-grained (the particle size being up to 630  $\mu$ m) fraction is taken. The powder is charged into porous forms and is compacted by vibration to an apparent density of 0.8 to 1.0 g/cm<sup>3</sup>, and then is impregnated in pyrolysis installations to a density of 1.7 to 1.97 g/cm<sup>3</sup> (1.97 g/cm<sup>3</sup> being the upper limit with us).

In this way we can produce GSP blocks of different sizes (fig. 4), ranging from small ones to 2500 mm in length and diameter (in GF-3).

\*) GSP is the Russian abbreviation for pyrocarbon-bound graphite.

### 2.4 Fabrication of constructions and products from carbon-carbon composites

The advantages of volume gas-phase impregnation are most successfully realized when using fillers of carbon fibers or fabrics. In this case, the moulding of required-size structures is substantially simplified. It is carried out without binders by using such known methods as winding, weaving, etc. The products obtained have a minimum of allowance for subsequent machining or even, after impregnating with pyrocarbon, can be used without any surface treatment.

By this technology we produce blocks, plates, pipes, cylinders and other structures (fig. 5), which may have extensive applications in the HTGR core.

As mentioned above, we have a possibility of fabricating carbon-carbon composite cylinders up to 2500 mm in diameter and 2600 mm in height (in GF-3). Up to now we have had no need of larger sizes, but if necessary, there are no technical or economic barriers to the construction of the installations capable of producing larger-size structures, e.g. HTGR reflectors. This offers, in our opinion, radically new possibilities of increasing the HTGR reliability.

### 3. Some properties of the materials with a pyrocarbon matrix

Fig. 6 shows the structure of the GSP-type materials. As can be seen, these materials feature a pronounced cellular structure, whose individual elements are constituted by particles of the powder-filler with pyrocarbon films settled on their surfaces. In the regions of intersection, the pyrocarbon deposits coalesce to form a continuous multidimensional framework wrapping around all particles of the powder-filler.

The characteristics of the GSP materials such as electrical resistance, thermal conductivity, thermal expansion, strength are practically isotropic.

Since the pyrocarbon, deposited from the gas phase, comprises very little of impurities (except for hydrogen), it is possible, on using high grades of graphite powder as a filler, to produce particularly pure materials which can find their application in electronic industry.

Figure 7 exemplifies the filling of pores with pyrocarbon in a carbon-carbon composite with the three-directional reinforcement.

Some characteristics of the GSP and carbon-carbon composites compared to those of industrial graphites are given in Table 2.

The limiting (minimum and maximum) values of strength characteristics for the GSP are determined by the final density of the material. In contrast, the carbon-carbon composite strength little depends on the density and is determined by the strength of carbon fibers and the reinforcement pattern.

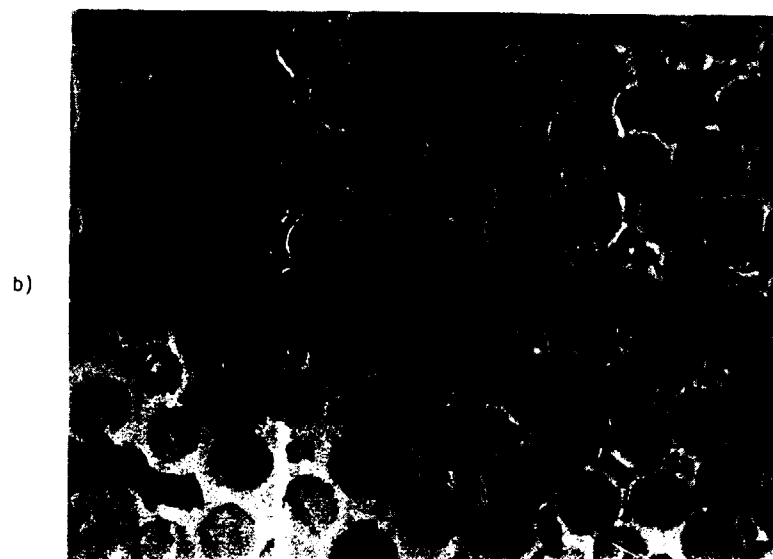
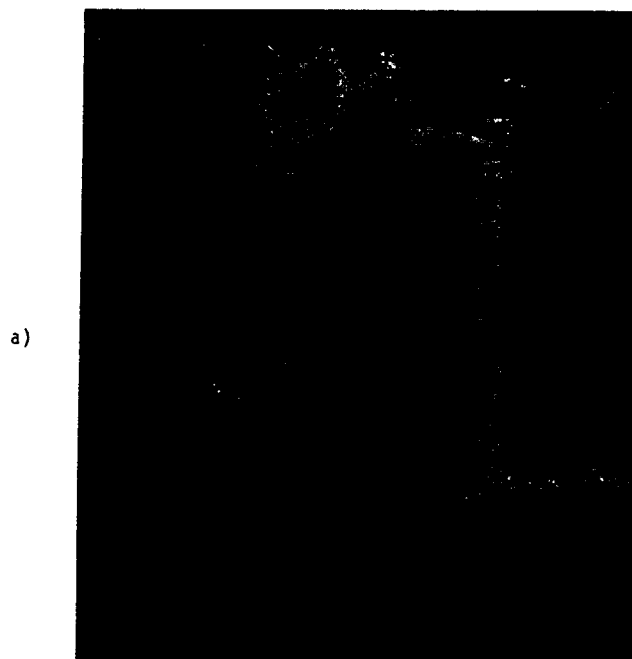


Table 2

Characteristics	Industrial graphites	GSP	Carbon-carbon composites
Density, g/cm <sup>3</sup>	1.7 - 1.88	1.7 - 1.95	1.3 - 1.9
Elasticity modulus, 10 <sup>3</sup> MPa	9 - 12	9 - 21	12 - 40
Ultimate strengths at 20°C, MPa in:			
compression	60 - 120	160 - 400	150 - 400
bending	30 - 70	30 - 70	100 - 160
tension	20 - 40	25 - 35	50 - 120
Thermal conductivity, wt(m K) at:			
20°C	90 - 130	10 - 80	5 - 7
500°C	70 - 75	100 - 60	7 - 11
1000°C	50 - 55	15 - 60	10 - 15
Thermal coefficient of linear expansion, 10 <sup>-6</sup> K <sup>-1</sup> at:			
20 to 1000°C	5 - 8	4 - 5	1 - 4
20 to 1500°C	8 - 9	4.5 - 5.5	2 - 4.5
Electrical resistivity at 20°C, Ohm mm <sup>2</sup> m <sup>-1</sup>	11 - 16	16 - 35	40 - 65
Friction coefficient (carbon-copper)	-	0.1 - 0.3	0.1 - 0.3

Fig. 7. Macro- (a) and micro-(b) structures of carbon-carbon composites with a pyrocarbon matrix. a) x50; b) x1000.

Table 3

Characteristics	$\gamma$ , g/cm <sup>3</sup>	$E_{\text{compr.}}$ , MPa	$E_{\text{bend.}}$ , MPa	$\lambda$ , wt/m K	$L$ , $10^{-6} \text{K}^{-1}$
Values	2.1 - 2.2	300 - 330	80 - 100	10 - 17	4.8 - 5.3

Table 4

Characteristics	GSP fuel elements	THTR-300 fuel elements *)
Graphite matrix density, g/cm <sup>3</sup>	1.75 - 1.95	1.72
Graphite matrix strength (MPa) in:		
compression	100	44.7 45.7
bending	45	20.4 18.6
Dynamic elasticity modulus of graphite, MPa, $10^4$	1.0	0.99 1.03
Thermal conductivity at 290 K, wt/m·K		
without additional heat treatment	40	-
with	70	67 37
Linear expansion coefficient (200 ... 1270 K) $10^{-6}$	5.0	3.59 3.92
Static strength, kN	40	17
Dynamic strength (average number of falls onto a pebble bed from a 4m height without destruction)	>3000	750
Abrasive wear, mg/cm <sup>2</sup> g	1 - 3	3
Degree of anisotropy	1.03 - 1.05	1.08 - 1.10

Note \*): numerator - parallel to the axis of pressing;  
denominator - perpendicular to this axis.

The main characteristics of the absorbing pyrocarbon-bound B<sub>4</sub>C composites are given in Table 3 (the B<sub>4</sub>C content is 1.6 g/cm<sup>3</sup>).

Table 4 gives the main characteristics of spherical GSP FE compared to THTR FE.

#### 4. Reactor test results

##### 4.1 Fuel particles

In our reactor test programs, we nearly always made tests of fuel particles in a state of free filling in parallel to tests of spherical FE, where fuel particles of a particular batch were used. In total, by the present time we have tested more than 50 batches of fuel particles of different construction.

Fuel particles differed in the material of the fuel core (UO<sub>2</sub>, UO<sub>2</sub> with additions of Al<sub>2</sub>O<sub>3</sub>-SiO<sub>2</sub>, (Th,U)O<sub>2</sub>, UCN, etc.) and in the construction (thickness, alternation and the number of pyrocarbon (PyC) or silicon-carbide (SiC) coatings). In recent years, in the fuel particle construction we have used a coating from pyrocarbon and silicon carbide (PyC+SiC) deposited simultaneously instead of dense PyC layers.

Reactor tests of fuel particles were carried out mainly at a temperature of 1250°C and burnups to 8% fima.

General regularities in the behaviour of fuel particles under reactor irradiation were observed to be the following. We observed no effect of the fuel core material on the gaseous fission product (GFP) release; the latter depends only on the fuel particle construction and the quality of protective coatings. No destruction of fuel particles was observed during irradiation, even at  $T_{\text{irr}} = 1600^\circ\text{C}$  and fuel burnups of 16% fima.

The rate of GFP release (R/B) from fuel particles ranged from  $10^{-4}$  to  $0.9 \times 10^{-6}$ ; in recent years its stable value has been at  $10^{-6}$ .

The post-reactor examinations revealed that the first layer of a low-density pyrocarbon nearly always broke down. In most cases, the denser pyrocarbon layer, following the first layer, showed serious damages.

The replacement of dense pyrocarbon coatings by combined PyC+SiC coatings has proved to be very efficient. With this replacement and with other conditions remaining the same, the GFP release rate was reduced by factors of 10 to 15. Moreover, the deposition of combined coatings is a simple and economical process as compared to the deposition of high-quality dense PyC coatings.

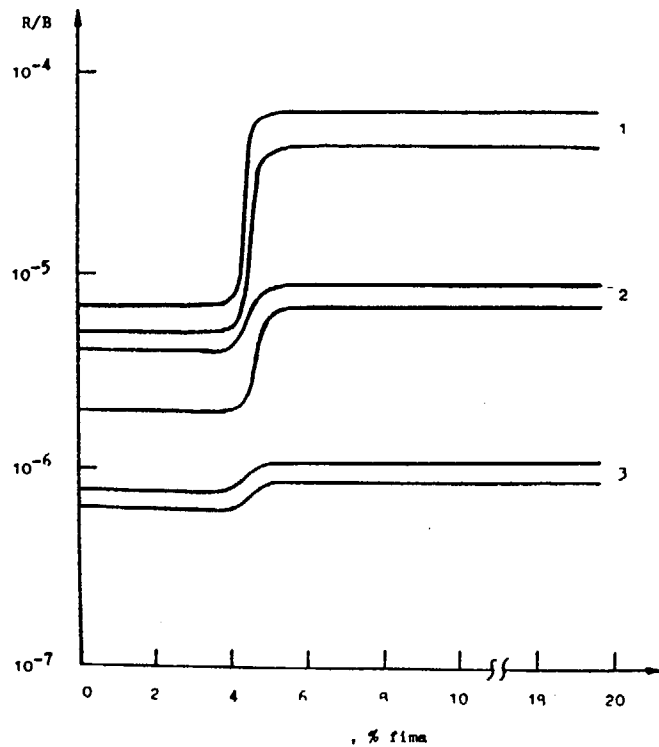
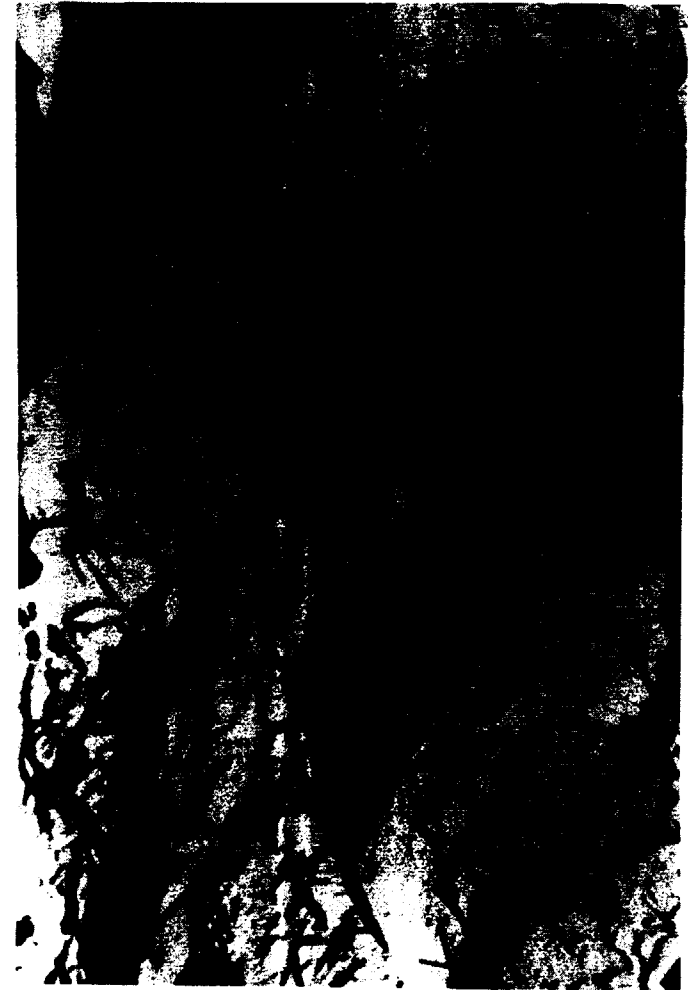


Fig. 8.  $^{85m}\text{Kr}$  release from spherical GSP fuel elements based on fuel particles with protective coatings of different types:  
 1: PyC - SiC - PyC;  
 2: (PyC + SiC) - SiC - PyC;  
 3: (PyC + SiC) - SiC - (PyC + SiC).

#### 4.2 Spherical fuel and absorbing elements, GSP and carbon-carbon composites

Spherical fuel elements (SFE) were irradiated in more than 130 experiments at temperatures between  $400^{\circ}\text{C}$  and  $1600^{\circ}\text{C}$  and fuel burnups of 8 to 16 % fima. Some experiments were performed for fuel burnups of 30 - 33% fima, this being a few times higher than the design value.

Fig. 9. Pyrocarbon sealing of a process impurity in the GSP graphite matrix, x 16000.



As could be expected, the GFP release from SFE was always lower than that from fuel particles of the same batch but in a state of free filing. In other words, the GSP matrix serves as an additional barrier, which reduces the GFP release rate; the efficiency being the greater the higher is the matrix density. Thus, the increase of the GSP density in FE from  $1.65 \text{ g/cm}^3$  up to  $1.85 \text{ g/cm}^3$  reduces the GFP release by factors of 10 to 20 [7,8]. With a further increase in the density, this effect becomes still more prominent.

The GFP release from SFE depends also on the thickness of the fuel-free GSP shell. To verify this, we have performed special experiments, namely, the  $\text{UO}_2$  pellets, 3 mm in diameter, were "packed" into GSP shells of different thicknesses and were irradiated at  $1100^\circ\text{C}$  to a fuel burnup of 8% fima. The experiments have shown that with the increase in the thickness of the fuel-free GSP shell from 3 to 7 mm the GFP release rate decreased from  $1.3 \times 10^{-3}$  down to  $5 \times 10^{-4}$ , i.e., by a factor of 2.6.

Figure 8 shows the GFP release from the GSP fuel elements under irradiation at  $1250^\circ\text{C}$ . Here we can see, first, positive effects resulting from the replacement of one or two dense pyrocarbon layers by combined layers of  $\text{PyC}+\text{SiC}$  deposited simultaneously (see above); and, secondly, jumps in the GFP release rate. These jumps are typical only of the GSP fuel elements. They are always observed after fuel burnups of 4-5 fima and are independent of  $T_{\text{irr}}$ , neutron spectrum, fuel

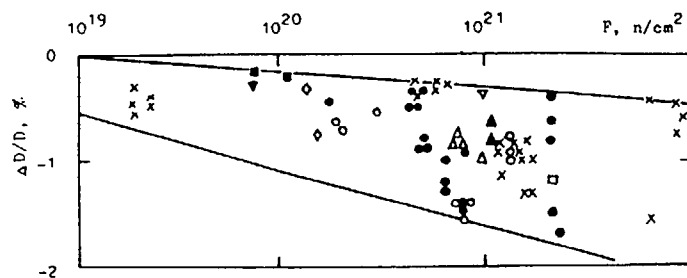


Fig. 10. Dimensional changes of absorbing (x) and fuel (the other points) elements versus the neutron fluence at irradiation temperatures of  $400 \dots 1250^\circ\text{C}$  for absorbing elements and  $500^\circ\text{C}$  ( $\nabla$ ),  $600^\circ\text{C}$  ( $\blacktriangledown$ ),  $750^\circ\text{C}$  ( $\square$ ),  $800^\circ\text{C}$  ( $\blacksquare$ ),  $1100^\circ\text{C}$  ( $\diamond$ ),  $1200^\circ\text{C}$  ( $\circ$ ),  $1250^\circ\text{C}$  ( $\bullet$ ),  $1400^\circ\text{C}$  ( $\triangle$ ),  $1500^\circ\text{C}$  ( $\blacktriangle$ ) for fuel elements.

enrichment. We attribute the jumps in the GFP release to damages caused by fission fragments and to loss of sealing by thin pyrocarbon films (fig. 9), which settled during FE impregnation with pyrocarbon, on the particles of the fissile material, impurities, which cannot be got rid of, in practice.

Fig. 10 shows the dimensional changes of spherical fuel and absorbing elements as functions of fast neutron fluence at different irradiation temperatures.

The characteristic property in the behaviour of FE, absorbing elements and GSP under irradiation is an insignificant isotropic shrinkage (not above 2%) at fluences of  $(0.5 \dots 1.5) \times 10^{21} \text{ fn/cm}^2$ . The rate of the shrinkage and its absolute values are practically independent of the irradiation temperature. The shrinkage increases with the pyrocarbon content in the material. After fluences of  $1.5 \times 10^{22} \text{ fn/cm}^2$  are attained, the shape changes are no longer observed, at least, up to fluences of  $(1 - 2) \times 10^{22} \text{ fn/cm}^2$  (the highest fluences attained in our experiments).

The strength characteristics of the materials vary little, but they do not deteriorate. On the contrary, they rather show tendency to improvement after irradiation.

The thermal conductivity of FE and GSP also slightly increases after irradiation [9].

The spherical absorbing elements, the absorbing composites based on  $\text{B}_4\text{C}$  dispersions in the GSP with a  $\text{B}_4\text{C}$  (natural) content up to  $1.6 \text{ g/cm}^3$  were also tested in wide ranges of temperatures (from  $300^\circ\text{C}$  to  $1200^\circ\text{C}$ ) and fluences.

All the materials have exhibited an extremely high radiation resistance. Even the materials containing  $1.6 \text{ g/cm}^3$  of  $\text{B}_4\text{C}$ , irradiated at  $1200 \dots 1250^\circ\text{C}$  to burnups of 90% in boron-10 showed dimensional changes by no more than 1%, while it is commonly known that the hot-pressed boron carbide exhibits swelling at a level of 10% for a  $^{10}\text{B}$  burnup of 1%.

It should be noted that during irradiation of  $\text{B}_4\text{C}$ -base dispersions in the GSP, the damages are mainly caused not by fast neutrons but rather by heavy fragments of He and Li produced on  $^{10}\text{B}$  nuclei as a result of  $(n, \alpha)$  reactions. In the number of the displacements per atom (dpa), the damage level of the matrix in the  $\text{B}_4\text{C}$  - GSP composite is much higher than one might expect in most critical HTGR units and are higher than that attained in our tests of GSP at fluences of  $(1 - 2) \times 10^{22} \text{ fn/cm}^2$ . Therefore, there will be no problem, in our opinion, of radiation resistance of the GSP, at least at temperatures of  $1200\text{--}1250^\circ\text{C}$ , when it is used in the HTGR core.

The radiation resistance of carbon-carbon composites with a pyrocarbon matrix has not been studied so extensively as in the GSP case. Tests were made



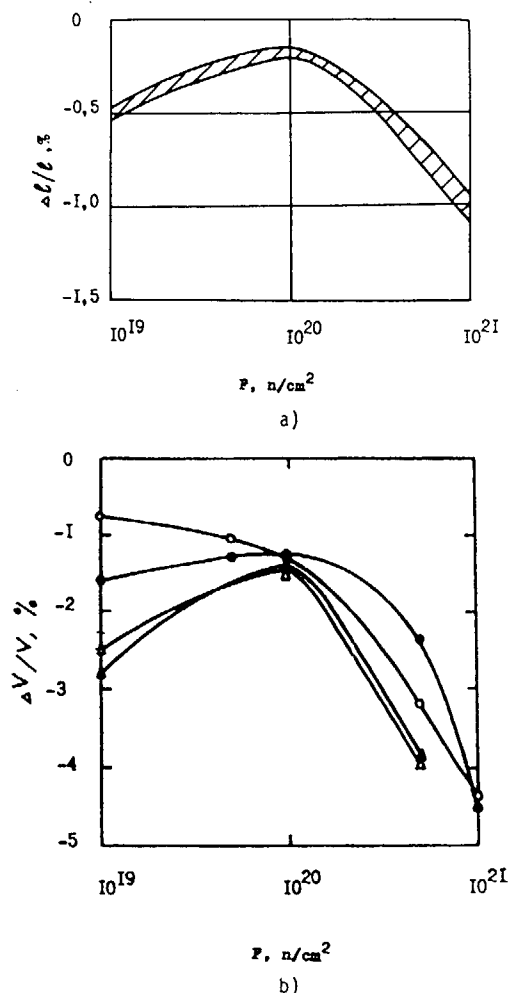


Fig. 11. Relative linear size changes in the specimens of GSP graphite (a) and carbon-carbon composites with the three-directional reinforcement (b).  
 a)  $T_{irr} = 1200^{\circ}\text{C}$ ;  
 b)  $T_{irr} = 300^{\circ}\text{C}$  (clear circles) and  $600^{\circ}\text{C}$  (full circles).  
 ○, ● : samples of x, y cut-outs;  
 △, ▲ : samples of z cut-out.

mainly with 3D-structure composites only at  $300^{\circ}\text{C}$  and  $600^{\circ}\text{C}$  to fluences of  $10^{21} \text{ fn/cm}^2$ . After irradiation, we investigated dimensional changes of the samples as well as changes in strength properties, thermal conductivity and thermal expansion.

The behaviour of carbon-carbon under reactor irradiation is in many ways similar to the behaviour of GSP (fig. 11), and the results obtained give us grounds for optimistic judgements of the prospects of these materials in HTGR applications. However, the data are still insufficient for recommending right now the employment of carbon-carbon in stressed (both in fluence and temperature) HTGR units.

#### References

1. A.S. Fialkov, Carbon-graphite materials (in Russian) Moscow, Ehnergiya publ., 1979.
2. United Kingdom, Patent N 914776, 1963.
3. Bundesrepublik Deutschland Patentschrift N 1203657, 1965.
4. F. Fitzer, The future of carbon-carbon composites, Carbon, 1987, v.25, 163-190.
5. V.E. Ivanov et al., Dispersion fuel and absorbing elements based on pyrocarbon-bound graphite for HTGR. In book: Reactor materials science (in Russ.) (Trudy konferentsii po reaktornomu materialovedeniyu, Alushta, 29 May-1 June, 1978). Moscow, TsNIIAI publ., v.6 (1978) 308-325.
6. V.A. Gurin et al., Development of fuel and absorbing pyrocarbon-bound elements of monolithic type for HTGR. In book: Atomno-vodorodnaya ehnergetika i tekhnologiya. Moscow, Ehnergoatomizdat publ., is.5 (1983) 213-225.
7. N.N. Ponomarev-Stepnoj et al., Microfuel elements and fuel element studies with the use of pre-irradiation. In: Specialists' Meeting on gas-cooled reactor fuel development and spent fuel treatment (Moscow, 18-21 October, 1983) Moscow, 1985, pp. 212-225.
8. V.A. Gurin et al., Radiation resistance of pyrocarbon-bonded fuel and absorbing elements for HTGR. In book: Gas-cooled reactor technology safety and siting (Working material). Report of a Technical Committee Meeting Organized by the International Atomic Energy Agency and Held in Dimitrovgrad, USSR, 21-23 June, 1989. Reproduced by the IAEA, Vienna, Austria, 1990, E-1.
9. V.F. Zelensky et al., The effect of neutron irradiation on carbon-graphite materials with a pyrocarbon matrix, (in Russ.). In book: Radiation materials science (Proceedings of the International Conference on Radiation Materials Science, Alushta, USSR, 23-25 May, 1990). Kharkov-1990, MAEP SSSR, v.3 (1990) pp. 160-171.

## DEVELOPMENT OF GRAPHITE FOR FUEL ELEMENT SLEEVES IN ADVANCED GAS COOLED REACTORS

D.P. BURRIDGE, J.E. NAYLOR

Fuel Engineering Department,  
British Nuclear Fuels plc,  
Springfields Works,  
Salwick, Preston, Lancashire,  
United Kingdom

### Abstract

The graphite sleeve is the prime structural member of the advanced gas cooled reactor (AGR) fuel element in that each sleeve supports the pin cluster and all of the fuel assembly above it. It must have a low oxidation rate, a low permeability to maintain coolant flow in the channel, must be dimensionally stable within certain limits and have sufficient strength at the end of life to sustain refuelling operations.

The paper describes a development programme covering design and improved graphite. Data is presented which is related to the anticipated in reactor behaviour of the material. It then proceeds to identify the quality assurance requirements of the sleeve material. Graphite sleeves produced from this programme of work are currently being irradiated as pilot loadings in UK reactors.

### 1. INTRODUCTION

The advanced gas cooled reactor (AGR) fuel element consists of 36 fuel pins of uranium dioxide clad in 20%Cr/25%Ni/Nb stainless steel. The 36 fuel pins and a central guide tube are supported by a stainless steel grid and two stainless steel braces which maintain the spatial array of the fuel pins. The prime structural component of the fuel element is a graphite sleeve which supports the pin cluster and the whole of the fuel and plug stringer above it. The fuel element sleeves, by engaging with lugs attached to the grids and braces, restrict possible axial, rotational and lateral movements of the fuel cluster.

Originally the graphite sleeve consisted of a double sleeve arrangement with a main structural outer sleeve and co-axial inner sleeves. The inner sleeves, together with a screwed retaining ring, positioned and fixed the grid and brace components and provided an insulating gas gap between the outer and inner sleeves (Figure 1). This arrangement was initially designed for irradiations of 18 GWd/tU but was extended to 21 GWd/tU and is known as Stage 1 fuel. The current design of fuel (Stage 2) consists of a single thick sleeve and is approximately 240 millimetres outside diameter, 1050 millimetres long and has a bore of 190 millimetres (Figure 2). Stage 2 fuel is designed for irradiations of 21 and 24 GWd/tU although there are proposals to extend the irradiations to 27 GWd/tU or possibly higher.

There are fourteen AGR reactors operating at seven stations in the UK. Five of the stations are operated by Nuclear Electric and two by Scottish Nuclear. All of the reactors with the exception of two are currently loading the Stage 2 fuel design.

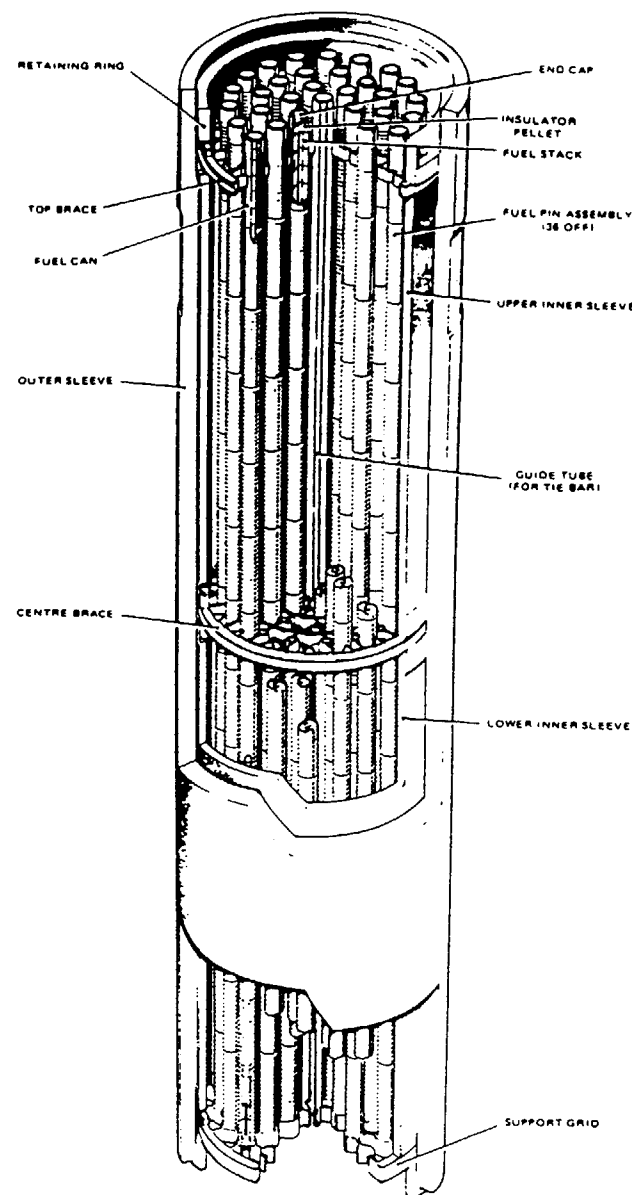
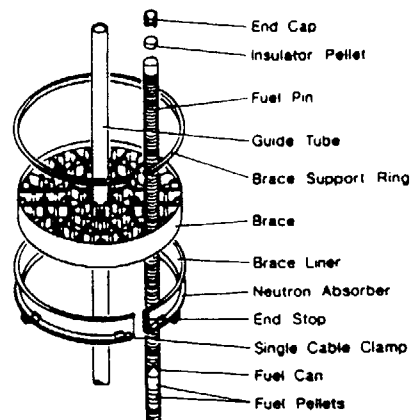
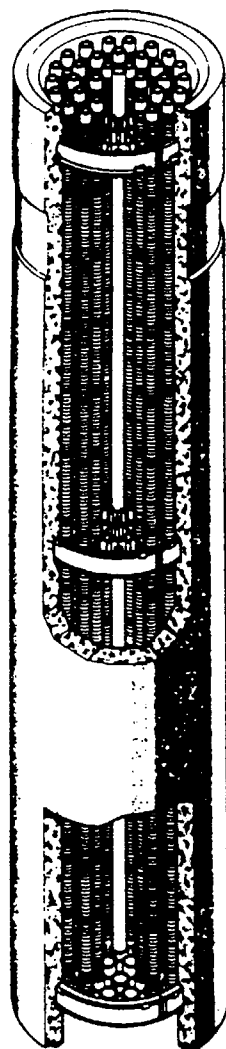
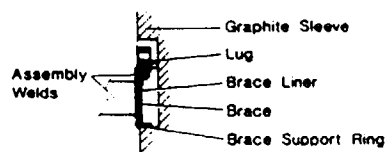


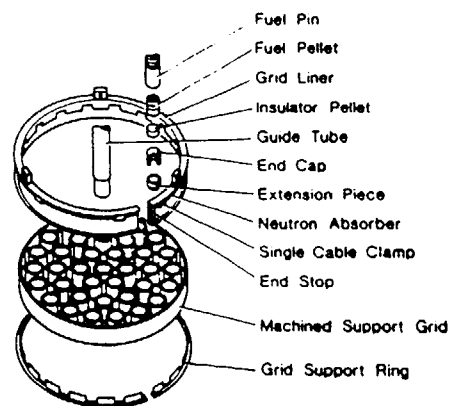
FIG. 1. Stage 1 AGR fuel element.



View at Top Brace Position



Section through Centre Brace Assembly



View at Grid Position

FIG. 2. Stage 2 AGR fuel element.

This paper summarises the operating requirements of graphite sleeves and briefly describes their manufacture. It then proceeds to illustrate how experience has been utilised to change the design and develop improved graphite sleeves. This has been achieved by assessing alternative cokes and modifying the production route to enhance both mechanical and physical properties together with improved Quality Assurance procedures.

## 2. OPERATING REQUIREMENTS

The graphite sleeves operate at temperatures of approximately 350°C on their outer surface whilst the inner surface operates at approximately 350°C at the lower (gas inlet) end increasing to 650°C at the top of the fuel assembly. The basic requirements of the sleeve are that it must have a low oxidation rate, a low permeability to maintain the coolant flow through the fuel array, exhibit reasonable dimensional stability and have sufficient strength to sustain refuelling operations at power. The properties and performance of irradiated sleeves are regularly monitored by post irradiation examination (PIE) to validate the continuing satisfactory performance.

### 2.1. Strength and Integrity

The original double sleeve design was intended for refuelling at high power but in 1978 a signal from a failed pin was detected in a Hinkley Point B reactor 4 fuel stringer which had been loaded at full flow. The stringer was discharged and examination revealed damage to a fuel element outer graphite sleeve. It was subsequently established that this damage had occurred as a result of being unable to withstand the internal pressurisation during the on-load charging operation.

During charging and discharging operations the upward flow of high velocity gas causes the fuel elements to vibrate and as a consequence there are risks of impact damage (1) which they must be able to withstand without failure. The sleeves are also subject to differential pressure during charge and discharge operations and therefore the graphite should be resistant to such a condition even in the event of impact damage. To minimise impact damage the important properties are therefore high bend strength and low modulus for high critical impact velocities, high impact strength and high fracture toughness.

### 2.2. Radiolytic Oxidation

Radiation chemically activates the carbon dioxide coolant and causes oxidation of the graphite to carbon monoxide. This reaction takes place in the porosity present in the graphite. To inhibit this reaction the coolant contains small amounts of carbon monoxide and methane (2). However, if the levels of these inhibitors are too high problems can be encountered with carbonaceous deposits on the fuel cladding which impair heat transfer. The choice of coolant is therefore a balance between these two requirements and in the event some oxidation of carbon on the surface of the graphite pores occurs due to the breakdown of carbon dioxide to form oxidising species (3). This results in some weakening of the graphite with consequential reduction in impact properties and this needs to be monitored for extended irradiation application and assessed in the development of new graphites.

### 2.3. Dimensional Change

It is necessary to demonstrate that the inevitable dimensional changes that occur as a result of fast neutron damage can be accommodated within the fuel assembly design to avoid interaction with the grids and braces as well as the fuel assembly interface with the reactor. Low shrinkage is also necessary to minimise the internal stress within the graphite. The fuel sleeves shrink in both the axial and diametral directions and it has been established that this is inversely correlated with the unirradiated coefficient of thermal expansion [cte](4). As a result of this correlation minimum values of cte are specified.

### 2.4. Permeability

Radiolytic oxidation of graphite leads to an increase in the pores available for gas transport and produces an increase in permeability. Coolant leakage through the sleeve, due to a pressure differential between the channel flow and the re-entrant flow on the outside of the sleeves, can result in increases in fuel operating temperatures that are undesirable. To prevent this, a limit is placed on the permeability level in the procurement specification and the coolant chemistry is also controlled to limit radiolytic oxidation.

## 3. MANUFACTURE

The graphite is required to be of high quality, near isotropic, with a high thermal expansion, high strength and exhibit relatively low permeability. Pitch coke has historically been used as the basic raw material primarily because of the requirement for a high coefficient of thermal expansion. The coke is milled to achieve a small particle size, and hence fine grain size, before mixing with the pitch and other additives. It is formed by extruding to tube or bar and then baked. Further pitch impregnations followed by baking are given prior to graphitisation so that the required quality is achieved.

The graphite sleeves are machined from the feedstock by BNFL in a purpose built facility that enables the graphite to be machined to tight tolerances in nuclear clean conditions. The manufacture is supported by a rigorous procurement specification which calls for a wide range of testing for important physical and mechanical properties as well as non destructive tests. The more important of these will be discussed within this paper.

## 4. DEVELOPMENT

To increase the safety margins for on load refuelling and to develop fuel for extended irradiation, BNFL embarked upon a substantial programme covering the design of the fuel element sleeve and the development of an improved graphite. The rest of this paper will briefly outline the design changes and provide an insight into the graphite development programme.

### 4.1. Design Changes

It was established that the outer graphite sleeve failure was the result of an axial crack being present in the sleeve before being subjected to the operating conditions, therefore further analysis of the charge path during on load refuelling was initiated. This led to

the conclusion that graphite fuel sleeves were subject to a level of impacting as they pass through critical points within the charge/discharge path. Bench tests established that the sleeve ends were particularly vulnerable. This work led to the development of a single thick sleeve design outlined earlier. Circumferential slots for grids and braces were moved as far away from the sleeve ends as practicable to minimise their weakening effect. A specially developed profile was added to the outer surface to suppress or significantly reduce vibration during charge/discharge operations. These changes along with other fuel element design changes which constitute the stage 2 fuel element are given in more detail elsewhere (5). Pressure burst testing of the new design revealed it to be 2.5 times stronger than the original design whilst the movement of the circumferential slots away from the sleeve ends improved impact resistance.

### 4.2. Improvements to Properties

As an interim measure improvements to the bend strength and linear coefficient of thermal expansion were made by minor changes to the additives and grist mix and baking technique. However it was recognised that to provide greater assurance there was a need to develop a new graphite.

### 4.3. New Graphites

In the search for a new graphite a number of sleeve properties were considered in need of improvement. Increases to the transverse and axial bend strength would improve resistance to pressure bursting and impact strength. Increased values of cte were sought to minimise reactor interface problems at extended irradiation. To ensure a satisfactory level of graphitisation, electrical resistivity should not be reduced. Graphite sleeves had performed satisfactorily in the reactor so it was decided that permeability should remain at the level measured in the then standard product, or be reduced if possible.

TABLE 1 PROPERTIES OBTAINED FROM LABORATORY TRIALS

PROPERTY	MATERIAL	
	STANDARD	NEW
AXIAL CTE x E-06/°C (20°C-120°C)	3.13	4.32
TRANSVERSE CTE x E-06/°C (20°C-120°C)	4.41	4.41
AXIAL BEND STRENGTH (MPa)	27.1	26
TRANSVERSE BEND STRENGTH (MPa)	29.5	36.3
ELECTRICAL RESISTIVITY (μohm.m)	9.9	8.1
COMPRESSIVE STRENGTH (MPa)	74.7	82.6
PERMEABILITY (cm/s)	6.23	5.77

Various discussions and evaluations took place prior to embarking on a full scale programme of development with over 30 different grades of graphite being considered. These were assessed using manufacturers' data and additional test data. Ultimately it was decided to develop a new graphite at existing suppliers with an alternative source of pitch coke.

#### 4.3.1. Laboratory Trials

Preliminary laboratory trials provided evidence of improvements in transverse bend strength and axial linear coefficient of thermal expansion (Table 1). It was anticipated that this would provide improved dynamic properties and reduced in-pile dimensional change. Advantages to be gained included a potentially stronger sleeve, reduced problems with in-pile length changes and increased burn-up capability. These laboratory trials provided an incentive to continue the development.

#### 4.3.2. Radiolytic Oxidation

Radiolytic oxidation tests were conducted in the DIDO materials test reactor at AERE Harwell and compared the new graphite with the standard product. The tests were conducted for 1102 hours in 1%CO/200vpm CH<sub>4</sub>/300vpmH<sub>2</sub>O in CO<sub>2</sub> at 41 bar. One of the variants tested gave an equivalent radiolytic oxidation rate to the standard product whilst a second variant exhibited a rate that was a factor of two better than the standard product.

#### 4.3.3. First Production Material

From the experience of the laboratory trials, a production route was established using a preferred pitch coke, initial grist mix, extrusion technique, baking and impregnation technique to yield a raw material on which to conduct a comprehensive programme of tests.

Some of the more important material properties of the first production material are summarised in Table 2. This provided strong support for the development with noted improvements in coefficient of thermal expansion, open pore volume and bend strength.

Special purpose full scale rigs were designed to carry out impact testing of single and multiple machined sleeve arrangements during which crack initiation was studied. Pressure burst tests were also carried out. It was found that the new product exhibited impact resistance which was some 13 to 20 % greater than the standard product and failure pressures in burst tests were higher than the standard product (Figure 3).

Small specimen tests were conducted on samples cut from sleeves and confirm the general improvement found in the mechanical and physical properties of this material (Table 3).

Bend strengths in the axial and transverse direction were higher than those in the standard product by factors of between 1.2 and 1.4. The fracture toughness was greater than that of the standard sleeve graphite by a factor of 1.3 indicating greater resistance to crack propagation.

TABLE 2 MATERIAL PROPERTIES FOR PRODUCTION MATERIAL

PROPERTY	MATERIAL	
	STANDARD	NEW
AXIAL CTE x E-06/°C (20°C-120°C)	3.06	4.38
TRANSVERSE CTE x E-06/°C (20°C-120°C)	4.30	4.53
AXIAL BEND STRENGTH (MPa)	26.60	34.75
TRANSVERSE BEND STRENGTH (MPa)	27.37	35.00
ELECTRICAL RESISTIVITY (μohm.m)	8.3	8.9
AXIAL COMPRESSIVE STRENGTH (MPa)	70.2	89.6
EFFECTIVE OPEN PORE VOLUME (cm <sup>3</sup> /100g)	6.27	5.02
AXIAL YOUNG'S MODULUS (MPa)	10776	10594
TRANSVERSE YOUNG'S MODULUS (MPa)	8809	10774

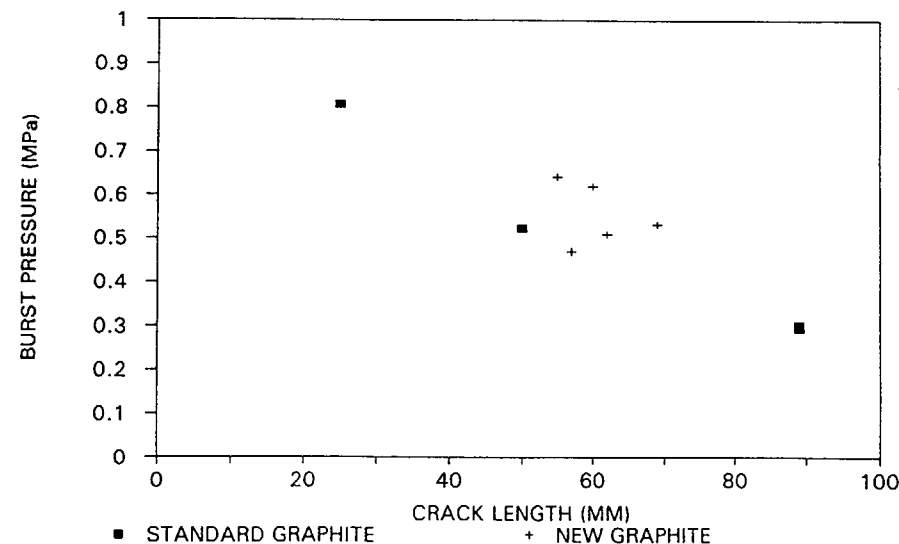


FIG. 3. Burst pressure/crack length of standard and new graphite.

TABLE 3 SUMMARY OF SMALL SPECIMEN DATA

PROPERTY	MATERIAL	
	STANDARD	NEW
AXIAL CTE x E-06/°C (20°C-120°C)	3.1	4.2
TRANSVERSE CTE x E-06/°C (20°C-120°C)	4.3	4.4
AXIAL BEND STRENGTH (MPa)	26	31
TRANSVERSE BEND STRENGTH (MPa)	28	40
ELECTRICAL RESISTIVITY ( $\mu\text{ohm.m}$ )	8.3	9.0
AXIAL COMPRESSIVE STRENGTH (MPa)		76
EFFECTIVE OPEN PORE VOLUME (vol %)	10	10.3
AXIAL YOUNG'S MODULUS (MPa)	10800	10260
TRANSVERSE YOUNG'S MODULUS (MPa)	8820	10260
AXIAL FRACTURE TOUGHNESS (MPa.m <sup>1/2</sup> )		1.50
TRANSVERSE FRACTURE TOUGHNESS (MPa.m <sup>1/2</sup> )	1.20	1.57

The increase in the axial cte values means that the predictions for dimensional change in this direction are significantly less. In the transverse direction the shrinkage is predicted to be similar to the standard material.

Porosity measurements suggested that initial radiolytic oxidation rates will be similar to the standard product whilst thermal oxidation tests indicated an insignificantly worse rate for the new material. The permeability of the new graphite was found to be superior to the standard product.

Chemical analysis to check for impurity levels found that they were comparable with the standard product. Thus there was no undue concern about additional compatibility or nuclear property issues.

Irradiation induced dimensional change has been assessed by placing samples in the PLUTO materials test reactor at AERE Harwell. These were irradiated in inert gas to fast neutron doses of up to  $43 \times 10^{20} \text{ n cm}^{-2}$  (Equivalent DIDO Nickel [EDN]) This is equivalent to a fuel element burnup of 34 Gwd/tU which is well in excess of current irradiation limits. The results which are shown in Figure 4 reveal that dimensional change in both the axial and the transverse direction was slightly better than that for the transverse direction of standard graphite. This improvement is greater than expected simply from the change in cte values. Significantly higher length change was found in the axial direction of the standard graphite which exhibited a much lower cte in this direction.

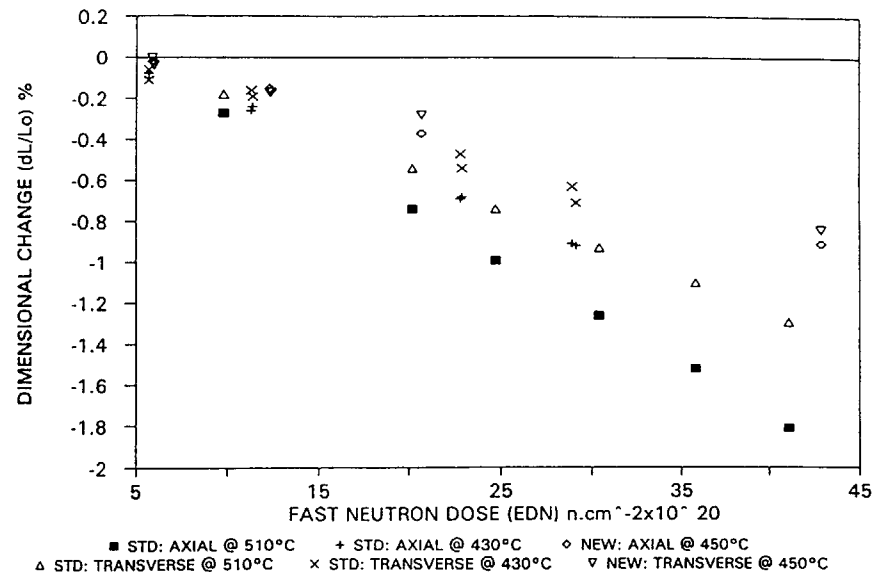


FIG. 4. Dimensional change data for new and standard sleeve graphite.

TABLE 4 SUMMARY OF IRRADIATION DATA

GRAPHITE	DIRECTION	DOSE [EDN] ( $\text{n cm}^{-2}$ )	LENGTH CHANGE (%)	RESISTIVITY INCREASE (%)	YOUNG'S MODULUS INCREASE (%)
NEW	axial	5.9	-0.02	470	65
		12.3	-0.15	650	71
	transverse	5.9	0	420	68
		12.3	-0.17	620	75
STANDARD	axial	5.9	-0.13	490	69
		12.3	-0.36	670	75
	transverse	5.9	0	480	73
		12.3	-0.16	660	79

In the same series of tests it was found that the irradiation induced changes in both Young's modulus and thermal resistivity were similar for both types of graphite. Some of the results are presented in Table 4 where all the data relates to irradiation temperatures of 510°C.

#### 4.3.4. Pilot Loadings

Detailed analysis of the data generated in the development programme was sufficient to justify a pilot loading and five stage 2 fuel stringers containing the new graphite are currently being irradiated in AGR reactors. The sleeves have been subject to comprehensive mensuration prior to loading and will be subject to detailed PIE at burnups ranging from 9 to 24 Gwd/tU. The PIE will include visual assessment, dimensional change, permeability and impact testing.

#### 5. QUALITY ASSURANCE

The importance of these sleeves is such that their manufacture is supported by a comprehensive quality assurance programme to ensure that the sleeves are acceptable for the required conditions.

It was concluded that the failed sleeve had probably contained an internal defect before being loaded into the reactor and so a comprehensive proof pressure testing strategy was developed which placed less reliance on visual evaluation. Test pressures range from 2800 kiloPascals at the graphite manufacturers to 1400 kiloPascals at the power station. Currently the sleeves are tested at 5 stages:

- (a) at the feedstock supplier
- (b) at BNFL Lillyhall before machining
- (c) at BNFL Lillyhall after machining
- (d) at BNFL Springfields following manufacture of fuel elements
- (e) at the power stations prior to stringer build

This high level of testing provides assurance that the sleeves do not contain any significant manufacturing or handling defects. As a further measure eddy current testing was developed and introduced at the station to test the critical end faces for defects.

Bend strength data in the transverse direction is used as a guide to the impact properties of the unirradiated and the irradiated material. Transverse bend strength is considered of particular importance to the ends of the sleeve where impact strength is a minimum and the risk of damage greatest. Young's modulus is also measured as this also is important for the impact properties.

All sleeves are subject to an axial proof load test to provide confidence on its load bearing capacity in reactor.

Open pore volume and chemical reactivity in air are both useful to assess the risk of oxidation attack. Open pore volume is an important parameter in determining the initial rate of radiolytic oxidation whilst the reactivity in air is of importance during air inlet shutdowns. Both these properties can ultimately affect the end of life strength of the graphite sleeve.

A minimum value for permeability is specified so that the increased permeability that develops in reactor is still acceptable. Electrical resistivity is used as a measure of graphitisation. Keeping the degree of graphitisation high ensures that the in reactor changes to properties fall within certain limits. The neutron absorption cross section of all heats is measured to ensure the graphite has no adverse effect upon the reactivity of the core.

The material test programme outlined above is included in a procurement document that deals with other Quality Assurance requirements such as precautions against contamination. This is supported by a total quality system complying with BS 5750.

#### 6. CONCLUDING REMARKS

This paper has provided a broad outline of the required properties of AGR fuel element sleeve graphite. It has shown how operational experience has been used to develop the design and improve the properties of the graphite sleeve. Comprehensive programmes of work have been conducted to demonstrate confidence that the stage 2 design in conjunction with the new graphite is suitable for the high power on load refuelling at extended irradiation.

#### REFERENCES

1. M E Ginneff, M W Parkin, K A Sansom and J G Thompson, Gas-cooled Reactors Today, BNES Conference, Bristol, September 1982, vol 2, pp 15-23.
2. B T Kelly, R L Faircloth and J V Best, Gas-cooled Reactors Today, BNES Conference, Bristol, September 1982, vol 2, pp 105-108.
3. J V Shennan, Gas chemistry in nuclear reactors and large industrial plant. Proceedings of Salford Conference, April 1980. pp98-110.
4. B T Kelly, W H Martin and P T Nettley, Phil. Trans. Roy Soc. A, vol 260, p37(1966).
5. T A Seeley, R D Stacey, J S Waddington and C E Hale, The design and development of an improved CAGR fuel element for high power refuelling and extended irradiation, Nuclear Fuel Performance, Stratford upon Avon, March 1985, BNES, pp177-184.

# MECHANICAL PROPERTIES AND THERMAL SHOCK RESISTANCES OF RECENTLY DEVELOPED HIGH PERFORMANCE GRAPHITES

S. SATO, K. KAWAMATA, A. KURUMADA, A. CHIBA

Faculty of Engineering,  
Ibaraki University,  
Hitachi-shi, Ibaraki-ken,  
Japan

## Abstract

Recently, owing to the improvement of coke properties and the advances in arrangements and molding techniques, many graphite products possessing superior mechanical and physical properties have been developed. These graphite products are being used in metallurgy and new advanced technological fields, such as semiconductor industry, aerospace rockets and first wall of plasma-facing nuclear fusion devices. At present, the candidate for use as principal core construction material in JAERI's High Temperature Engineering Testing Reactor (HTTR) is generally regarded as the isostatically molded near isotropic graphite, IG-110. For use in HTTR, it is desirable that the graphite material possesses superior mechanical and physical properties, as well as the ability to minimize neutron irradiation damage during reactor operations. This report introduces the experimental results of recent studies on the mechanical properties especially, their strength against thermal stress, fracture toughness and, for part of the graphites, the effects of neutron irradiation and thermal shock resistance of several representative graphite brands. Comparisons are made with those of IG-110. From these experimental results, these several new brands of graphites appear to have far superior properties compared to IG-110. Therefore it can be expected that, following future construction of the HTTR and during the stage of its operational tests, these high-performance graphites may have an opportunity to be utilized as the core graphite component to replace IG-110.

## 1. Introduction

Artificial Graphite is generally manufactured (ref.1) by carbonization sintering of a shaped-body of kneaded mixture, using granular cokes as filler and pitch as binder, going through pitch impregnation process if necessary, and finally applying graphitization heat treatment. Recently, owing to the improvement of coke properties and the advances in arrangements and molding techniques, many graphite products possessing superior mechanical and physical properties have been developed one after another. These graphite products are being used in metallurgy and new advanced technological fields, such as semiconductor industry (ref.2), aerospace rockets (ref.2,3) and first wall of plasma-facing nuclear fusion devices (ref.4). Progress is being made through severe competition for better product qualities.

More than twenty years have elapsed (ref.5) since JAERI contemplated the development of high temperature gas cooled reactors. During this period, many different brands of graphites have been chosen by the present authors as an object of investigation for use as reactor core construction element. At present, the most promising candidate for use as principal core construction material in JAERI's High Temperature Engineering Testing Reactor (HTTR) is generally regarded as the isostatically molded near isotropic graphite, IG-110. This graphite has been manufactured by Toyo Tanso Company and appeared on the market as the initial brand of IG-11 in 1974. For use in HTTR, it is desirable that the graphite material possesses superior mechanical and physical properties, as well as the ability to minimize neutron irradiation damage during reactor operations. The present authors have conducted studies of various brands of graphites for application in the afore-mentioned advanced technological fields, with attention mainly focused on mechanical properties, especially, their strength against thermal stress, fracture toughness and, for part of the graphites, the effects of neutron irradiation (ref.6,7). This report introduces the experimental results of our recent studies on the mechanical properties and thermal shock resistance of several representative graphite brands. Comparisons are made with those of IG-110. So far as one can observe from these experimental results, these several new brands of graphites appear to have far superior properties compared to IG-110.

## 2. Experimental Methods

### 2.1 Graphite Samples

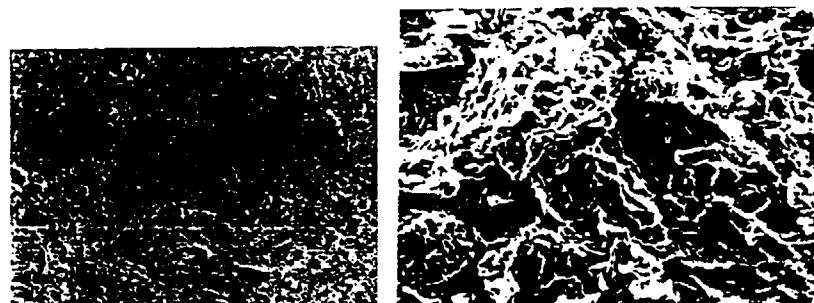
As shown in Table 1, the graphite samples discussed in this report encompass eight brands of isostatically molded isotropic graphites, including

Table 1 Main applications of compared graphites.

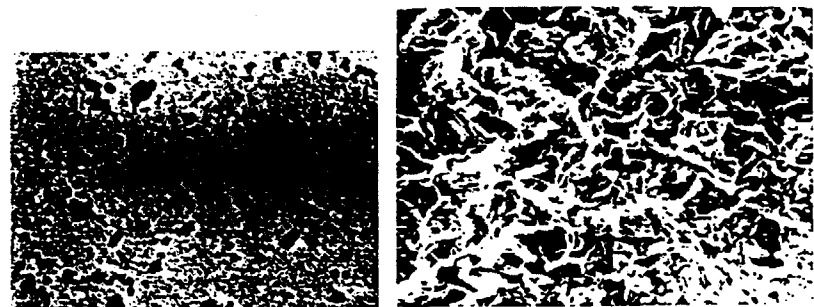
Brand	Maker	Main applications
IG-110	Toyo Tanso	Nuclear, Metallurgy
IG-430u	"	Fusion reactors
IG-720u	"	Metallurgy
IG-12	"	Metallurgy, Rocket nozzles
IG-15	"	Metallurgy, Rocket nozzles
ETP-10	Ibiden	Metallurgy, Fusion reactors
ST-60	"	Metallurgy
HCB-18	Hitachi Chemical	Machine parts
PD-330S	"	Fusion reactors
C/C-B*	Showa Denko	Fusion reactors

\* C/C-312

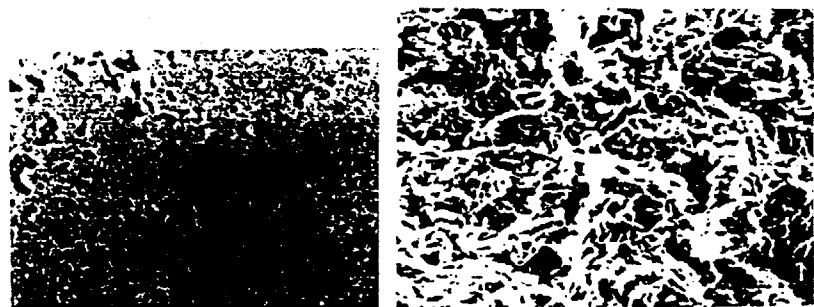




IG-110



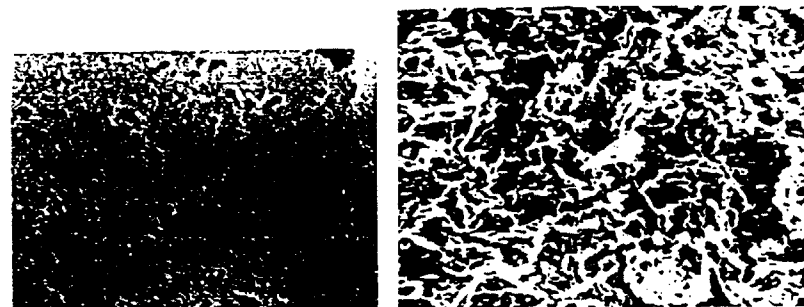
IG-430u



IG-720u

0.1mm

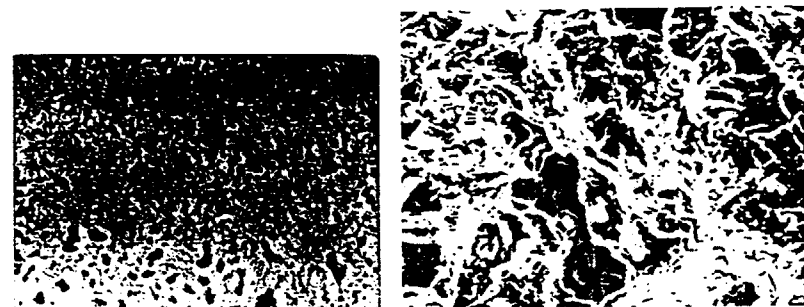
10 $\mu$ m



IG-12



IG-15



ETP-10

0.1mm

10 $\mu$ m

Photo. 1 (a) Microscopic structures and fractographs of compared graphites.

Photo. 1 (b) Microscopic structures and fractographs of compared graphites.

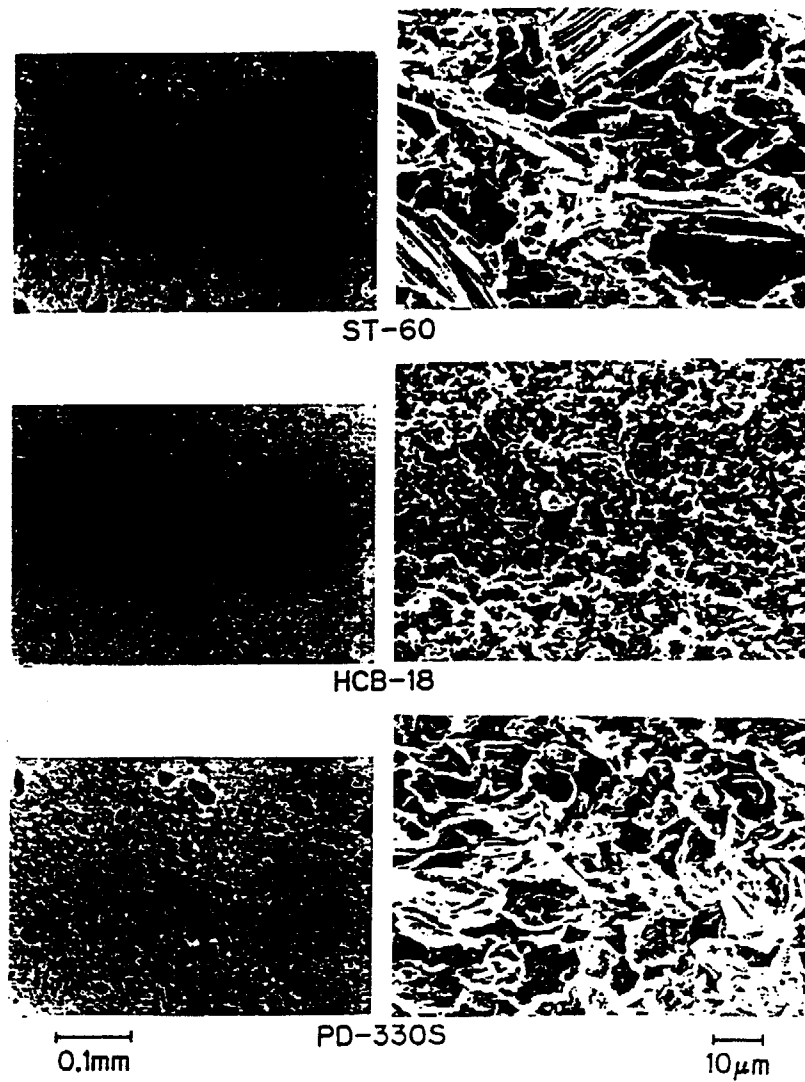


Photo. 1 (c) Microscopic structures and fractographs of compared graphites.

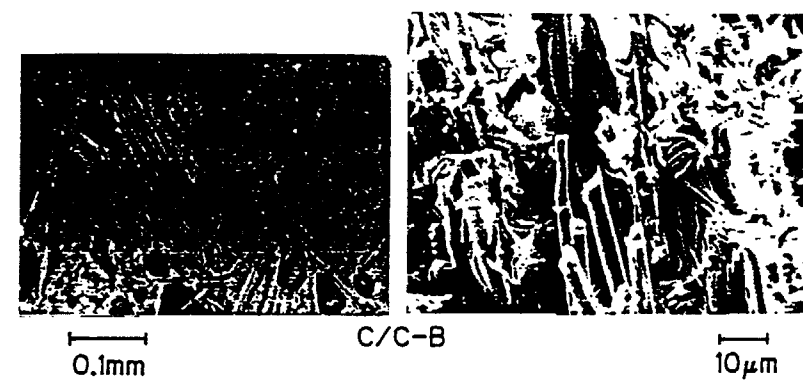


Photo. 1 (d) Microscopic structures and fractographs of compared graphites.

IG-110 and a high-strength fine-grain mesophase quasi-isotropic graphite. HCB-18. For comparison, it also includes C/C-B, a brand of felt carbon fiber reinforced C/C carbon composite. Table 1 lists the current principal use of the individual brand. Photo.1 shows comparisons of the microscopic structure of these graphite samples and their fractographs obtained after fracture toughness tests.

## 2.2 Experimental Methods

The fracture of materials containing many interior defects and cracks, such as graphites, is brought about by the propagation of the cracks that embrittle the material. For comparison of mechanical strength or fracture mechanical properties, therefore, the tests should be carried out under the conditions of fixing, as close as possible, the shape and dimension of the test specimens.

In this study, experimental results are presented for (1) bending strength,  $\sigma_b$  (ref.8), of a circular disk of 30 mm diameter and 3 mm thickness by a ball indenter; (2) Mode I and Mode II fracture toughness values,  $K_{IC}$  and  $K_{IIC}$  (ref.9), of a disk having a central slit by diametral compression; (3) thermal shock resistance  $\Delta$  ( $=\sigma_t k/E\alpha$ ,  $\sigma_t$  is tensile strength,  $k$  is thermal conductivity,  $E$  is Young's modulus and  $\alpha$  is thermal expansivity) (ref.10) and fracture toughness  $\nabla$  ( $=K_{IIC}/E\alpha$ ) (ref.11) due to arc-heating of the central part of a disk; (4) diametral compressive strength,  $\sigma_{HC}$  (ref.12), of a disk of 6 mm thickness by arc-shaped anvils and (5) compressive strength,  $\sigma_c$  (ref.13), of a circular cylinder of diameter 10 mm and length 25 mm.

These experimental methods were basically developed by the present authors, and the details are described in the relevant literature.

## 3. Comparison of Experimental Results

Table 2 shows the comparison of the mean values of the experimental results. Values shown inside parentheses represent the catalogue values provided by the individual makers.

(1) Bulk Density,  $\gamma$ ;

Bulk density,  $\gamma$ , of all the graphites was found to exceed 1.75 g/cm<sup>3</sup>, indicating high density and fineness. Especially, mesophase pitch carbon HCB-18 showed the highest density. Its very high density can be observed from the microscopic picture shown in Photo.1.

(2) Young's Modulus,  $E$ ;

Young's modulus,  $E$ , was found to be about 10 GPa for all the graphites. However, felt-like carbon fiber reinforced C/C-B showed the largest value of about 26 GPa in the direction of accumulated layer surface. This is followed by HCB-18, while has also a significantly high  $E$  value of 15.7 GPa. IG-110 has relatively low value of Young's modulus.

(3) Bending Strength,  $\sigma_b$ ;

There are considerable differences in the bending strength,  $\sigma_b$ , among the individual brands of graphites. Both C/C-B and HCB-18 have large bending strength, reflecting their high values of Young's modulus. IG-110 shows a relatively low value, which ST-60 and ETP-10 show comparatively large values of  $\sigma_b$ .

Table 2 Mean experimental results of compared graphites.  
(Values in parentheses are catalogue values by makers.)

Material	IG-110	IG-430u	IG-720u	IG-12	IG-15	ETP-10	ST-60	HCB-18	PD-310S	C/C-B
Maker			TOYO TANSO			IBIDEN		HITACHI CHEMICAL		SHOWA DENKO
Bulk density $\gamma$ (g/cm <sup>3</sup> )	1.75 (1.78)	1.85 (1.86)	1.81 (1.82)	1.75 (1.76)	1.90 (1.90)	1.72 (1.75)	1.84 (1.88)	2.00 (1.98)	—	1.77 (1.75)
Young's modulus $E$ (GPa)	9.8 (9.8)	10.8 (10.8)	10.1 (9.9)	9.9 (10.8)	10.4 (11.8)	10.4 (10.8)	10.4 (11.8)	13.7 (15.7)	—	26.3 (26.0)
Bending strength $\sigma_b$ (MPa)	48.6 (41.2)	80.8 (36.8)	1.2 (35.9)	46.3 (46.1)	11.6 (49.0)	62.3 (36.8)	70.4 (62.1)	78.4 (68.2)	56.5 (46.0)	95.9 (90.0)
Compressive strength $\sigma_c$ (MPa)	70.5 (78.4)	—	—	84.2 (88.2)	117.7 (103.0)	—	—	192.1 (176.0)	—	86.3 (88.0)
Diametral compressive strength $\sigma_{HC}$ (MPa)	14.9	19.4	23.0	16.3	21.5	18.0	—	37.1	16.6	—
Rockwell hardness	74.2	83.6	87.9	55.3	74.2	81.4	—	91.0	77.2	44.0 (4.0)
Mode I fracture toughness $K_{IC}$ (MPa $\sqrt{m}$ )	0.82	1.04	1.01	0.82	1.04	0.89	1.00	0.75	1.02	3.44 (4.0)
Mode II fracture toughness $K_{IIC}$ (MPa $\sqrt{m}$ )	0.97	1.21	1.17	1.18	1.30	1.01	1.20	0.94	1.30	4.39 (4.0)
Thermal conductivity $k$ (W/mK)	(116)	(139)	(105)	(104)	(139)	(104)	(151)	(125)	(150)	(150)
Thermal expansivity $\alpha$ ( $\times 10^{-6}/K$ )	(4.5)	(5.2)	(5.4)	(4.7)	(4.8)	(3.8)	(3.0)	(5.0)	(4.8)	(1.0)
Electric resistance $\rho$ ( $\mu\Omega cm$ )	1150 (930)	—	—	1235 (1230)	986 (950)	—	1118 (950)	—	—	400 (400)
Thermal shock resistance $\Delta$ (W/mm <sup>2</sup> /K)	29.2	90.1	37.0	38.0	61.9	85.7	100.3	27.5	50.1	>194 (194)
Thermal shock fracture toughness $\nabla$ (W/mm <sup>3/2</sup> )	30.7	48.5	35.3	36.1	43.4	39.7	63.9	20.0	50.1	196 (196)
Equivalent crack size $a_e (mm) = (\nabla/\Delta)^2/\pi$	0.352	0.092	0.290	0.287	0.156	0.068	0.129	0.168	0.318	—

(4) Compressive Strength,  $\sigma_c$  ;

The compressive strength,  $\sigma_c$ , of HCB-18 is extremely high, more than twice the value for IG-110. IG-720u, IG-15, IG-430u and ETP-10 also show relatively high strength. However, IG-110 and C/C-B have low  $\sigma_c$  values.

(5) Diametral Compressive Strength,  $\sigma_{H\Delta}$  ;

HCB-18 shows exceedingly high value of  $\sigma_{H\Delta}$ . It was not possible to measure the  $\sigma_{H\Delta}$  value for C/C-B due to fracture occurrence at the edge in contact with the anvil during diametral compressive strength tests. IG-110 was found to have the lowest value of  $\sigma_{H\Delta}$ .

(6) Rockwell Hardness,  $H_{R15X}$  ;

HCB-18 shows the highest value of hardness, followed by IG-720u. Both C/C-B and IG-12 have low values of hardness.

(7) Mode I Fracture Toughness,  $K_{IC}$  ;

C/C-B shows incomparably high value of fracture toughness value,  $K_{IC}$ . This is followed by IG-15, IG-430u, IG-720u and PD-330S in decreasing order of toughness. HCB-18 shows especially low value, indicating its sensitivity to cracking or defects. IG-110 and IG-12 show relatively low values.

(8) Mode II Fracture Toughness,  $K_{IIC}$  ;

The general trend is similar to that described above for the case of Mode I. The ratio of the Mode II and Mode I fracture toughness values can be considered to represent the ratio of pure shearing strength and simple tensile strength. With the exception of IG-12, the ratio was found to be nearly 1.23.

(9) Thermal Conductivity,  $k$  ;

ST-60 and C/C-B (in the direction parallel to accumulated layer surface) show high values of thermal conductivity. This is followed by IG-430u, IG-15, and PD-330S. ETP-10, IG-12 and IG-720u have relatively low  $k$  values.

(10) Thermal Expansivity,  $\alpha$  ;

The  $\alpha$  value for C/C-B (in the direction parallel to accumulated layer surface) is extremely low. Among the isostatically molded graphites, ST-60 has the smallest value of  $\alpha$ . This can be considered as one of the reasons for the significantly large thermal shock resistance of C/C-B and ST-60. Those which have relatively large  $\alpha$  values include IG-720u, IG-430u and HCB-18.

(11) Electrical Resistance,  $\rho$  ;

The  $\rho$  value for C/C-B in the direction of accumulated layer surface is the smallest. This is followed by IG-430u, ST-60 and IG-15. However, ETP-10 and IG-720u have relatively large  $\rho$  values.

(12) Thermal Shock Resistance,  $\Delta$  ;

The  $\Delta$  value for C/C-B is extremely large, exceeding the capacity of our thermal shock test apparatus (40 kW, 1200 A). During the test, no thermal shock fracture could be observed for this brand. Among the isostatically molded graphites, ST-60, IG-430u and ETP-10 show very large values. However, HCB-18 and IG-110 show low  $\Delta$  values, about one-third that of ST-60. Photo.2 (left side) shows the fracture appearance of some of the graphites following the thermal shock resistance tests of disk specimens. Thermal stress fractures occur along the periphery of the disk and propagate toward the central region. Within the test range, no fracture of C/C-B was found to occur.

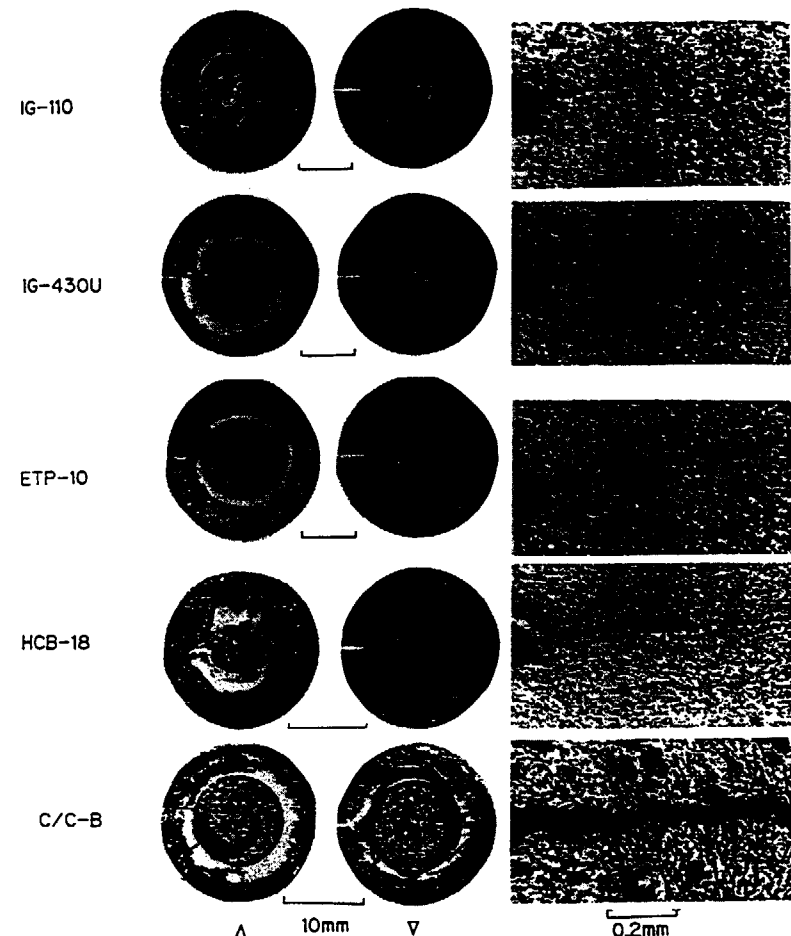
(13) Thermal Shock Fracture Toughness,  $\nabla$  ;

Photo. 2 Fracture appearances of thermal shock resistance ( $\Delta$ ) and fracture toughness ( $\nabla$ ) tests of graphites and c/c-composite.

C/C-B showed peerlessly high value of  $\nabla$ . Among the isostatically molded graphites, ST-60, IG-430u and IG-15 show high values. The  $\nabla$  value for IG-110 is relatively small, about one-half that of ST-60. HCB-18 has the smallest value of  $\nabla$ . Photo.2 (center) shows the fracture appearances of a disk having an edge-slit following the thermal shock fracture toughness test. Photo.2 (right side) is a microscopic picture showing the appearances of the occurrence and propagation of fractures from the tip of the slit. In this case, propagation of fractures from the tip of the slit was also observed for C/C-B.

(14) Equivalent Crack Size,  $C_e$ :

Among the graphite brands, IG-110 showed the largest value of  $C_e$ , followed by PD-330S. However, ETP-10 and IG-430u showed small values of  $C_e$ .  $C_e$  can be thought to correspond to allowable crack dimension or the limit to which cracks can grow. The larger the  $C_e$  value, the less sensitive the graphite is to cracks or defects. The structure of IG-110 is relatively coarse having large defects. However, HCB-18, for which  $C_e$  is relatively small, has fine structure and very small defects. It was not possible to determine the  $C_e$  value for C/C-B, but it is probably fairly large.

#### 4. Conclusions

In the foregoing sections, we have discussed the mechanical and fracture mechanical properties, as well as thermal shock resistance, of several representative graphites we have studied recently. Some of these graphites are currently in practical use as continuous casting nozzle of metals, aero-space rocket nozzles and plasma-facing wall material of nuclear fusion devices under very severe mechanical and thermal circumstances. Part of these graphite materials have been tested for neutron irradiation (ref.6,7), and many of them have been found to have far superior properties compared to IG-110. It can, thus, be expected that, following future construction of the HTTR and during the stage of its operational tests, these high-performance graphites may have an opportunity to be utilized as the core graphite component to replace IG-110.

Figure 1 shows a comparison of fracture and design criteria of IG-110 and IG-430u. This chart was prepared according to the fracture criteria established based on fracture mechanics and advocated by the present authors previously (ref.14,15). In constructing this chart, catalogue values were adopted for the tensile and compressive strengths, while pure shearing stress was estimated based on the ratio of Mode I and Mode II fracture toughness values shown in Table 2. The number of tests was chosen to be 20 and the Weibull homogeneity factor was taken to be 5 for applying probabilistic corrections. Also, following ASME Sec.III specifications (ref.16), the design standard chart was constructed for the case of 99% survival probability with 95% confidence level. According to the chart, it appears that, by using IG-430u, the design margin for mechanical strength can be significantly widened leading to improved reliability.

Besides the use of HCB-18 for the core support post is considered to increase also the safety margin in the compressive strength to almost 2 times or more of the case of IG-110.

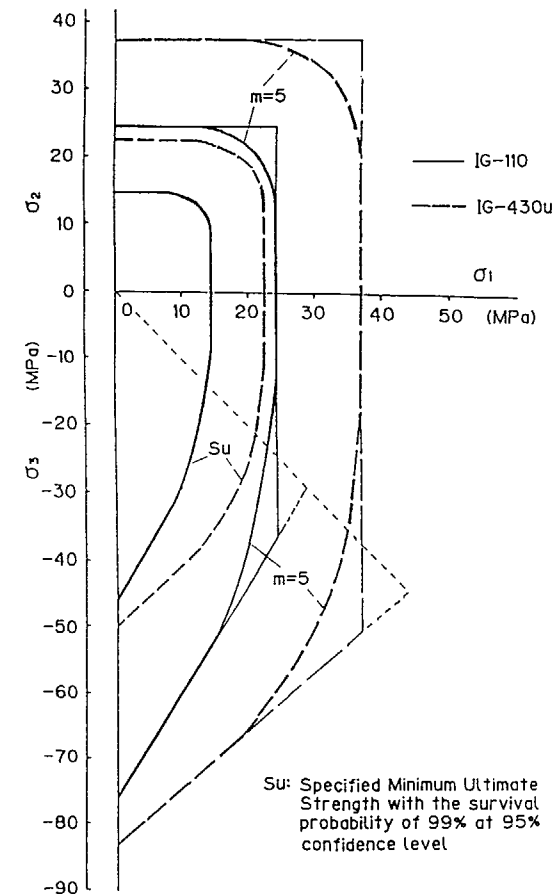


Fig.1 Fracture criteria and Design criteria of IG-110 and IG-430u graphites under multiaxial stresses.

## REFERENCES

- ( 1 ) S. Mizushima and J. Okada, Tanso-Zairyo, Kyoritsu-Shuppan, Tokyo (in Japanese), (1989) 55.
- ( 2 ) Toyo Tanso Co., Graphite Applications(catalogue),(1990).
- ( 3 ) S.Sato, et al., 20th Conference on Carbon, (1991) 610.
- ( 4 ) S.Sato, et al., Fusion Engineering and Design, 13(1990) 159.
- ( 5 ) JAERI, Present Status in Research Development of Multi-purpose High Temperature Gas Cooled Reactor (in Japanese), (1985) 2.
- ( 6 ) S.Sato, et al., J.Atomic Energy Soc., Japan, 21, (1979) 957.
- ( 7 ) S.Sato, et al., Nuclear Engineering and Design, 61 (1981) 383.
- ( 8 ) S.Sato, et al., PNC-SJ268, 84-02 (1984).
- ( 9 ) H.Awaji and S.Sato, J.Eng.Materials and Tech., ASME-II, 100 (1978) 175.
- (10) S.Sato, et al., Carbon, 13 (1975) 309.
- (11) S.Sato, et al., Carbon, 16 (1978) 103.
- (12) H.Awaji and S.Sato, J.Eng.Materials and Tech., ASME-II, 101 (1979) 139.
- (13) S.Sato, et al., Proc. Hitachi Meeting of JSME, (1991) No.103.
- (14) S.Sato, et al., J.Atomic Energy Soc., Japan, 20 (1986) 1172.
- (15) S.Sato, et al., Nucl.Eng. and Design, 103 (1987) 291.
- (16) ASME code, Section III, Division 2, Subsection CE, Design Requirements for Graphite Core Supports, (1982).

**MATERIALS DEVELOPMENT AND PROPERTIES**  
**Part B**

**(Session III)**

**Chairmen**

**O. CHUGUNOV**  
Union of Soviet Socialist Republics

**T. MARUYAMA**  
Japan





# BEHAVIOR OF GAS DESORPTION AND GAS PERMEABILITY OF CARBON MATERIALS

M. OKADA, T. SOGABE  
Toyo Tanso Company, Ltd,  
Mitoyo-gun, Kagawa-ken,  
Japan

## Abstract

Carbon materials rather easily adsorb and desorb gases such as hydrocarbons,  $H_2$ ,  $H_2O$ , CO and alcohols. It is very important to study the behaviour of gas desorption and gas permeability of carbon materials, especially when they are used in a vacuum vessel or a closed system. Gas desorption behaviour was studied by using Thermal Desorption Spectroscopy. Gas desorptions from isotropic graphites, Felt-C/C and  $B_4C$  graphite materials were measured. Thermal desorption spectra were obtained from IG-11, IG-110 and IG-110U graphites with a total ash content of 400 ppm, 10 ppm and 2 ppm, respectively.

## Introduction

Polycrystalline carbon materials are made from either a combination of coke filler and binder, or self-sintering coke. The average filler particle size ranges from  $\mu m$  to deca  $\mu m$ . While a green block is baked, volatile matters and pyrolysis gases from the carbonizing binder are released from the block and make a network of pores. The bulk density of carbon materials ranges from 1.7 to 2.0  $Mg/m^3$ , while real density of graphite is 2.2  $Mg/m^3$ . Carbon materials are porous with pore volume of about 9 to 23 %, and most of the pores are open. The surface areas of carbon materials, depending on pore size *i.e.* filler particle size, are about 1  $m^2/g$ .<sup>1)</sup> Therefore, carbon materials rather easily adsorb and desorb gases existing in the atmosphere, such as hydrocarbons,  $H_2$ ,  $H_2O$ , CO and alcohols. It is very important to study the behavior of gas desorption and, and gas permeability of carbon materials, especially when they are used in a vacuum vessel or a closed system.

Gas desorption behavior was studied by using Thermal Desorption Spectroscopy (TDS). Gas desorptions from isotropic graphites, Felt-C/C and  $B_4C$ -graphite materials were measured.  $B_4C$ -graphite materials were produced for a control rod or shielding material for HTTR. And thermal desorption spectra were obtained from IG-11, IG-110 and IG-110U with a total ash content of 400 ppm, 10 ppm and 2 ppm, respectively. Purification effects on gas desorption is also discussed.

Gas permeabilities of various carbon materials including isotropic graphites, resin or glass impregnated ones, and pyrolytic carbon (PyC) coated ones were measured. Both nitrogen and helium gases were used for the measurements.

The gas permeability of a graphite block as large as 950 mm in diameter and 800 mm in length was compared with the data obtained by small specimens such as 30 mm in diameter with 7 mm in thickness

## 1. Gas desorption

### 1.1 Experimental

#### 1.1.1 Preparation of specimens

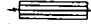

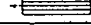
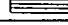
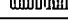
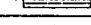
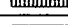
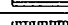
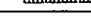
Graphites tested were IG-11, IG-110 and IG-110U with a total ash content of 400 ppm, 10 ppm and 2 ppm, respectively. IG-110 is a purified graphite of IG-11 and IG-110U is produced by purifying and outgassing IG-11.

$B_4C$ -graphite materials produced for a control rod or shielding material for HTTR were also tested. Their boron concentrations are 0, 1, 3, 10 and 30 wt%. Boron 0 % materials was prepared as a reference. Some properties of  $B_4C$ -graphites are shown in Table 1.

Table.1 Properties of  $B_4C$ -Graphites

Boron Content (wt%)	Flexural Strength (MPa)	Specific Resistance ( $\mu \Omega \cdot m$ )
0	33	20
1	33	9
3	35	10
10	55	15
30	75	25

Table.2 Thermal and Mechanical Properties of Felt-C/C Composite 2)

	Direction		remarks
Bulk Density ( $Mg/m^3$ )	—	1.5	RT
Specific Resistance ( $\mu \Omega \cdot m$ )	 (//)	4	RT
Flexural Strength (MPa)	 (//)	45	RT
Tensile strength (MPa)	 (//)	31	RT
Compressive Strength (MPa)	 (//)	44	RT
	 ( $\perp$ )	39	RT
Coefficient of Thermal Expansion ( $10^{-6}/K$ )	 (//)	2.3	RT~
	 ( $\perp$ )	7.1	1273K
Thermal Conductivity ( $W/m \cdot K$ )	 (//)	270	RT
	 ( $\perp$ )	130	
Ash Content (ppm)	—	<10	

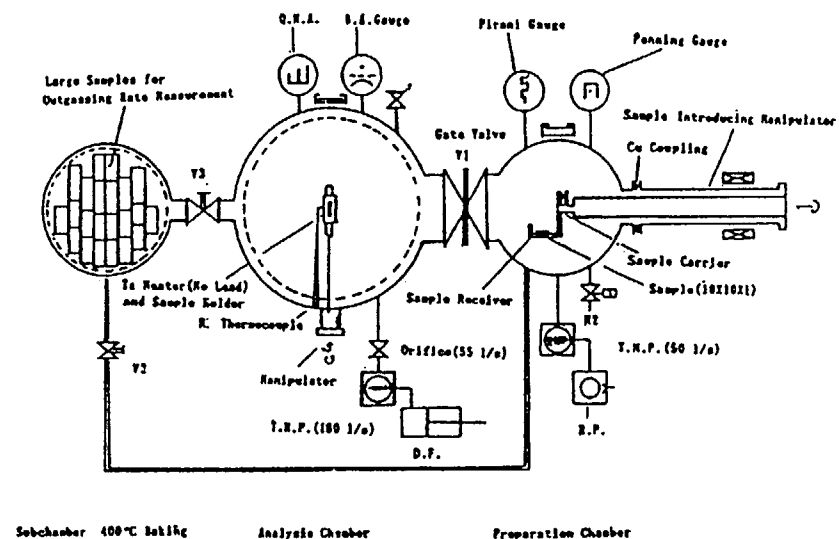


Fig.1 Thermal desorption spectroscopy device<sup>2)</sup>.

Felt-C/C material<sup>2)</sup> was prepared. This material was fabricated by infiltrating PyC into carbon felt and outgassed at 2000 °C. Some properties of Felt-C/C material are summarized in Table 2. The features of Felt-C/C material include high thermal conductivity and relatively small anisotropy.

The sample size for the gas desorption test was 10 x 10 x 1 (mm).

#### 1.1.2 Measurement of gas desorption

A schematic of the thermal desorption spectroscopy device<sup>2)</sup> is shown in Fig.1. The analysis chamber is pumped with a diaphragm pump and a turbo molecular pump. These pumps are oil free. Pumping speed is controlled to 55 l/min. by introducing an orifice between the analysis chamber and pumps. A specimen was put on a sample container made of tantalum and introduced to the analysis chamber after pre-vacuuming in the preparation chamber. The analysis chamber was vacuumed to  $10^{-7}$  Pa at room temperature.

In order to obtain thermal desorption spectra, a sample was heated up to 1500 °C at a heating rate of 1 K/s, and total pressure was measured with a B-A gauge and partial pressures were measured with QMS (Quadrupole Mass Spectroscopy:  $m/e=1$  to 60) every 15 seconds. Back ground or sample free spectrum was measured to obtain net thermal desorption spectra from the samples.

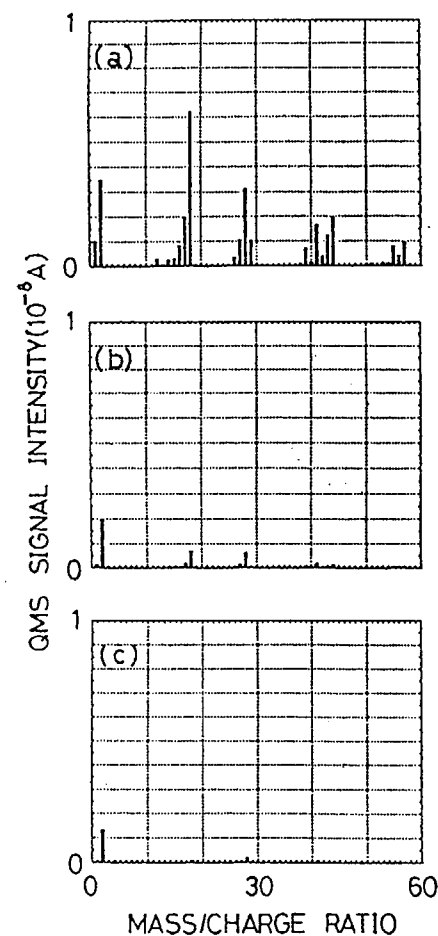


Fig.2 Mass spectra from isotropic graphites with different impurity levels at 600°C during heat-up at heating rate of 1 K/s  
(a) IG-11(400ppm);  
(b) IG-110(10ppm);  
(c) IG-110U(2ppm).

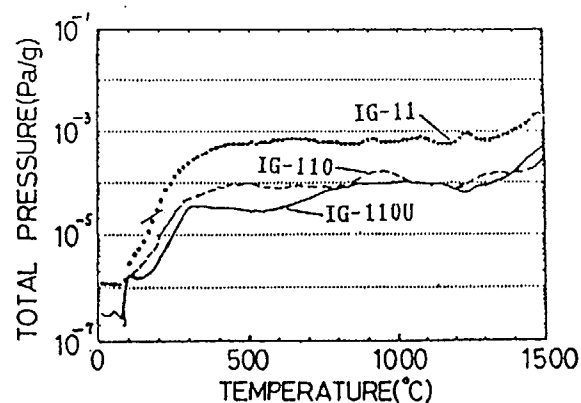


Fig.3 Thermal desorption curves  
from IG-11, IG-110 and IG-110U.

Each sample was heated up to 200, 400, 500 and 700 °C, separately at a heating rate of 1 K/s, and kept at each temperature for either 0.5 or 3 hours. Each sample was then cooled down in the chamber for one night, and it was again heated up to 1000 °C at the same heating rate. This kind of test was done in order to study pre-baking effect.

## 1.2 Results and Discussion

### Effect of purification<sup>3)</sup>

Mass spectra of the gas species detected by a QMS at 600 °C for IG-11, IG-110, and IG-110U are shown in Figs.2(a), (b) and (c), respectively. Detected gas species were  $m/e=2$ ,  $m/e=18,16,17$ ,  $m/e=28$ ,  $m/e=44$  ( $\text{CO}_2$ ),  $m/e=15$ ;  $\text{CH}_3^+$  (methane) and other  $m/e$  (hydrocarbons). It was clearly found that the amount of desorbed gases became significantly smaller after purifications. Total pressures for those graphites from room temperature to 1500 °C are shown in Fig.3. Total pressure of purified graphite IG-110 was found to be smaller than unpurified graphite IG-11, and IG-110U showed even lower pressure than IG-110. After 5 to 6 month exposure in the atmosphere, the gas desorption of these graphites were measured. No significant difference was observed in thermal desorption behavior compared with Fig.3. Hirohata et al.<sup>4)</sup> pointed out that impurities in graphite are adsorbing gases. Reduction of the amount of gas desorption after purification is mainly due to the smaller amount of impurities, a large amount of desorbed gases are degassed during the purification process, and further outgassing is applied for IG-110U. In Figs.4(a),(b) and (c), thermal desorption spectra for IG-110 are shown. Main outgases were hydrocarbons,  $\text{H}_2\text{O}$ ,  $\text{H}_2$  and  $\text{CO}$ . Peaks of total pressure correspond to peaks of above gas

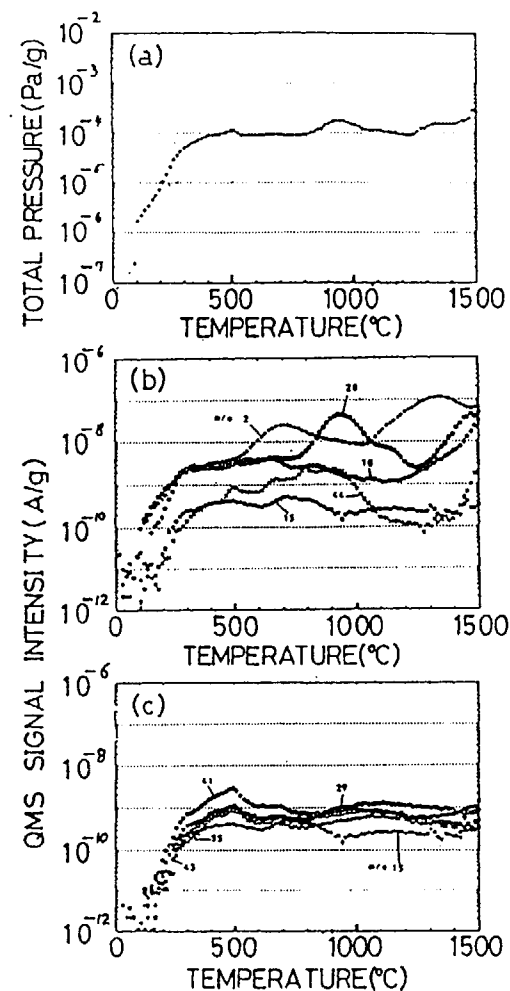


Fig.4 TDS spectra from IG-110

- (a) Total pressure
- (b)  $m/e=2(\text{H}_2)$ ,  $15(\text{CH}_3)$ ,  $18(\text{H}_2\text{O})$   
and  $44(\text{CO}_2)$
- (c)  $m/e=15, 29, 41, 43$  and  $55$  (Hydrocarbon).

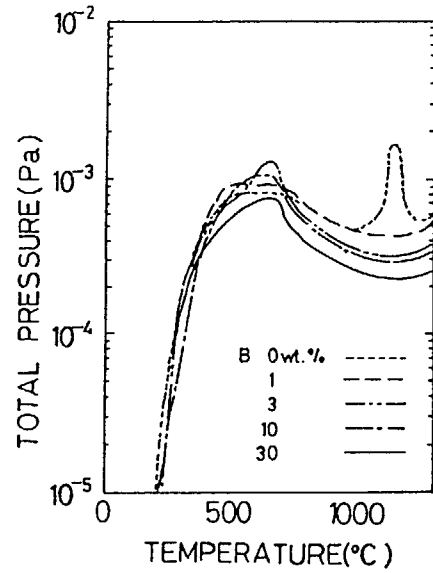


Fig. 5 Thermal desorption curves of total pressure from  $\text{B}_4\text{C}$  graphites.

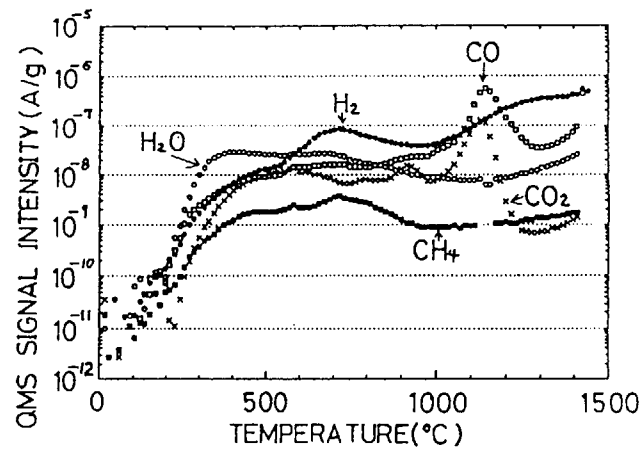


Fig. 6 TDS spectra from 0%B reference for  $\text{B}_4\text{C}$ -graphite.

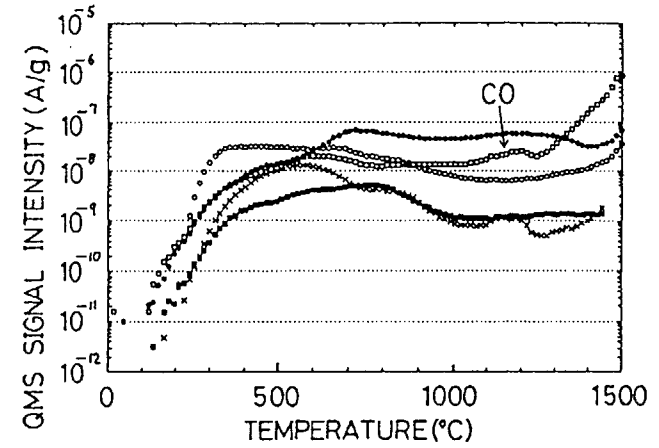


Fig. 7 TDS spectra from 1wt% B  $\text{B}_4\text{C}$   
-graphite:  $\text{H}_2$  (●),  $\text{CH}_4$  (■),  
 $\text{H}_2\text{O}$  (○),  $\text{CO}$  (□),  $\text{CO}_2$  (×).

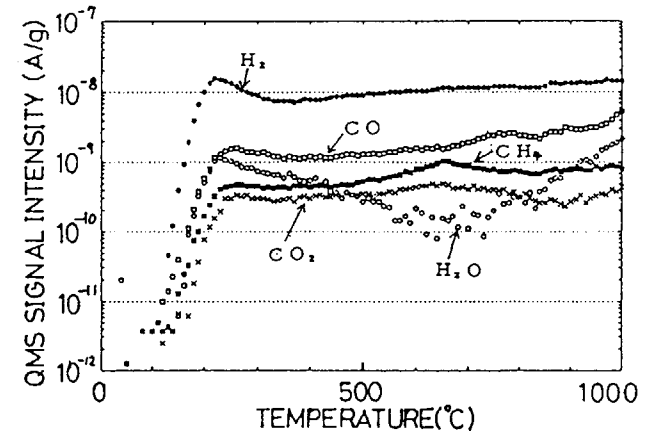


Fig. 8 TDS spectra of  $\text{H}_2$  ( $m/e=2$ ),  
 $\text{CH}_4$  (15),  $\text{H}_2\text{O}$  (18),  $\text{CO}$  (28) and  
 $\text{CO}_2$  (44) from Felt-C/C composite.

species. At high temperature region above 1300 °C, spectra are going up. This is because adsorbed gases at the chamber wall are releasing due to the radiant heat from the heating elements. At above 1000 °C, H<sub>2</sub>O and hydrocarbons are appeared in the chart, these are the delayed gases caused by a rather high heating speed of 1 K/s.

#### B<sub>4</sub>C-graphite materials

Total pressure curves for B<sub>4</sub>C-graphite materials are shown in Fig.5. A peak at around 1250 °C is not seen for B<sub>4</sub>C-graphite materials whereas there is a peak for 0 % B material. It was found that the total pressure level is smaller the more boron the material contains. Thermal desorption curves from room temperature to 1400 °C for a reference and 1 % boron contained materials are shown in Figs.6 and 7, respectively. CO and CO<sub>2</sub> desorptions appeared to be suppressed for 1 % boron sample. There were peaks of CO(m/e=28) and CO<sub>2</sub>(m/e=44) at around 1250 °C for the reference material, while no significant peaks appeared for 1 % boron contained one. These findings are probably due to the suppressed gasification of carbon by boron, and also due to enhanced graphitization by boron<sup>5)</sup>. It is also considered that oxygen from the sample is captured by boron forming boron oxide.

#### Felt-C/C

Thermal desorption curves from room temperature to 1000 °C for Felt-C/C is shown in Fig.8. The amounts of gas desorption for H<sub>2</sub>, CO and CO<sub>2</sub> can be estimated much the same as those of IG-110U. H<sub>2</sub>O gas desorption from Felt-C/C was smaller and that of Hydrocarbons were one order larger compared with IG-110U.

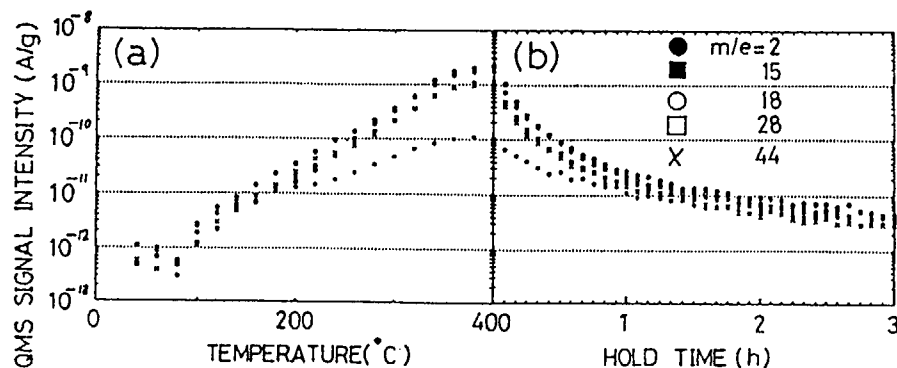


Fig.9 IDS spectra of H<sub>2</sub>(●), CH<sub>4</sub>(■), H<sub>2</sub>O(O), CO(□) and CO<sub>2</sub>(X) from felt-C/C composite during (a) heated up to 400°C and (b) held at 400°C for 3 hours.

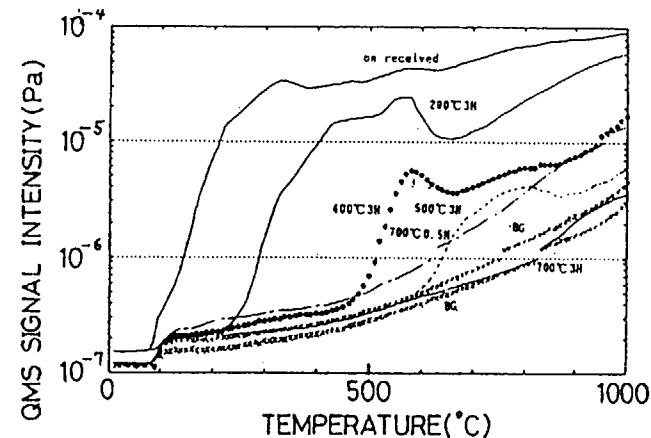


Fig.10 Thermal desorption curves of total pressure from IG-110U specimen after pre-baked under various condition.

#### Pre-baking effect

In Fig. 9 a), thermal desorption curves of m/e=2, 15, 18, and 44 for Felt-C/C from room temperature to 400 °C are shown. And after reaching 400 °C, the chamber was kept at that temperature for 3 hours. Thermal desorption curves during holding are shown in Fig.9 b). As is seen Fig.9 b), partial pressures of CO and CO<sub>2</sub> become constant in 20 min. and partial pressure of H<sub>2</sub>O become constant in 10 min. Partial pressure of CH<sub>4</sub> decreased one order after one hour hold. We can see that 3 hours is enough to attain equilibrium pressure.

Pre-baking effect for IG-110U is summarized in Fig.10. After pre-baking for 3 hours at 400 °C, the amount of gas desorption became one twentieth to that of as-received. After 3 hours at 700 °C, the total pressure curve became almost back ground level, although that of pre-baking for 0.5 hour is higher than back ground level. As indicated in Fig.10 b), about 3 hours pre-baking is required to reach back ground level.

Much the same results of pre-baking effect were obtained for Felt-C/C. Pre-baking for 3 hours at 200 °C reduced outgas amount about one tenth to as-received. The specimen pre-baked for 3 hours at 400 °C released small amount of gases above 500 °C. And gas desorption curves after pre-baked for 3 hours at 700 °C were almost back ground levels. Effectiveness of pre-baking for reducing outgas for Felt-C/C and isotropic graphites was much the same, although the structures of these materials are quite different.

Table 3 Typical Properties of Isotropic Graphites

Grade	Bulk Density ( $\text{Mg/m}^3$ )	Mean Pore Radius* ( $\mu\text{m}$ )	Remarks
IG-56	1.77	1.9	Volume effect
IG-11	1.77	1.8	Substrate for Glass Impregnation
IG-110	1.77	1.8	Substrates for PyC Coating (0-25 $\mu\text{m}$ )
IG-2520	1.37	3.8	
ISO-630	1.82	0.9	
ISO-880	1.90	0.2	

\* Hg Penetration Method

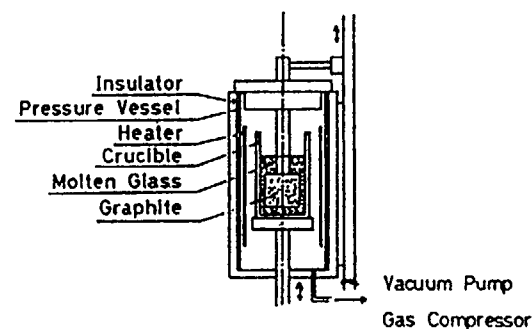


Fig.11 Autoclave for glass impregnation.

Table 4 Boro-silicate Glass 8)

Composition (wt%)	$\text{SiO}_2$	38
	$\text{B}_2\text{O}_3$	36
	$\text{Na}_2\text{O}$	21
	$\text{Al}_2\text{O}_3$	5
Glass Transition Temperature( $^{\circ}\text{C}$ )		513
Softening Temperature( $^{\circ}\text{C}$ )		620

Table 5 Properties of Graphite(IG-11)and Glass Impregnated IG-11 7)

	IG-11	Glass Impregnated (IG-11G)
Bulk Density ( $\text{Mg/m}^3$ )	1.77	2.08
Hardness (shore)	55	70
Flexural Strength (MPa)	39	59
Compressive Strength (MPa)	78	147
Modulus of Elasticity (GPa)	10	17
Coefficient of Thermal Expansion ( $10^{-6}/\text{K}$ )*	4.6	5.8

\* 350-450 $^{\circ}\text{C}$ 

## 2. Gas permeability

### 2.1 Experimental

#### 2.1.1 Preparation of specimen

A large specimen was prepared to study volume effect of gas permeability. A cylindrical specimen with dimensions of 950 mm(Outer Diameter) x 750 mm(Inner Diameter) x 800 mm(Length) was cut from a large block of IG-56 which is a fine grained isotropic graphite. Small specimens with dimensions of 30 mm(Dia.) x 7 mm(Thickness) were also cut from near both the ends of the large specimen. Bulk density and mean pore radius of IG-56 are listed in Table 3 together with other materials.

Pyrolytic carbon (PyC) coated isotropic graphites were prepared. As in Table 3, substrate graphites are IG-110, ISO-630, ISO-880 and IE-2520. Specimens were cylindrical with dimensions of 80 mm(O.D.) x 50 mm(I.D.) x 40 mm(Len.). Pyrolytic film<sup>9)</sup> was grown on those substrates by CVD.

Pyrolytic Carbon (PyC) coating was carried out for some graphites under two different conditions faster deposition rate and slower deposition rate. Glass and resin impregnated graphites were also prepared. Glass impregnation was carried out by using the autoclave<sup>7)</sup> shown in Fig.11. Impregnation was done according to vacuum and pressure method. Boro-silicate glass was impregnated into IG-11 graphite. Composition of the glass<sup>9)</sup> is shown in Table 4. Some properties<sup>7)</sup> of glass impregnated IG-11 are shown in Table 5. Phenolic resin was also impregnated into IG-11 by using another kind of autoclave. Resin impregnation was applied twice. Specimen size for impregnated IG-11 was 80 mm(O.D.) x 50 mm(I.D.) x 40 mm(Len.).

#### 2.1.2 Measurement of gas permeability

For small specimens, 30 mm(Dia.) x 7 mm(Thi.), and 80 mm(O.D.) x 50 mm(I.D.) x 40 mm(Len.), the measuring method of gas permeability<sup>9)</sup> is as follows. The

apparatus used for the test is illustrated in Fig.12.(This figure illustrates a case in which a disk like specimen is used). Only by changing specimen holding jigs, cylindrical specimens can be measured. The specimen was pressurized from the outside so that gas permeates into the space  $V_0$ (chamber B) the pressure change of the space was measured. Either nitrogen or helium gas was used for the measurement. Gas permeability  $K$  [ $\text{cm}^2/\text{s}$ ] was calculated by Eqs.(1) and (2).<sup>10)</sup>

$$K = Q L / \Delta P A \quad (1)$$

where  $Q$  is the volume of permeated gas [ $\text{cm}^3$ ],  $L$  the thickness of the specimen [ $\text{cm}$ ],  $\Delta P$  the pressure difference in two chambers separated by the specimen [ $\text{kgf}/\text{cm}^2$ ], and  $A$  the cross-sectional area for gas permeation [ $\text{cm}^2$ ].

$$Q = (p_2 - p_1) V_0 / t \quad (2)$$

where  $p_1$  is the initial pressure of chamber B [ $\text{kgf}/\text{cm}^2$ ],  $p_2$  the pressure of chamber B after  $t$  second [ $\text{kgf}/\text{cm}^2$ ],  $V_0$  the volume of chamber B [ $\text{cm}^3$ ], and  $t$  the gas permeation time [ $\text{s}$ ].

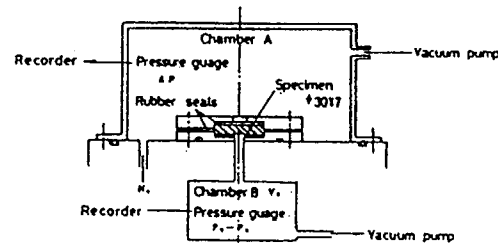


Fig.12 Apparatus for gas permeability measurement of small specimen.

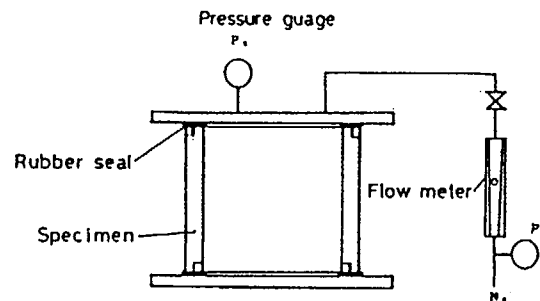


Fig.13 Apparatus for gas permeability measurement of large specimen.

For a large specimen, 950 mm(O.D.) x 750mm(I.D.) x 800 mm(Len.), another kind of apparatus was used, and its schematic is shown in Fig.13. Both ends of the specimen were supported by iron plates and were sealed by rubber. Nitrogen gas was introduced to the inside of the specimen, and nitrogen gas flow rate that makes the pressure inside the specimen maintain a given pressure was measured by a flow meter. The volume of permeated gas was calculated by Eq.(3).

$$Q = v P_0 \quad (3)$$

where  $v$  is the index of flow meter (atmospheric pressure equivalent) [ $\text{cm}^3/\text{s}$ ] and  $P_0$  the atmospheric pressure [ $\text{kgf}/\text{cm}^2$ ].

Gas permeability was also calculated by Eq.(1).

## 2.2 Results and discussion

### Gas permeability

The gas permeability  $K$  of graphite materials can be approximated by Eq.(4).<sup>11)</sup>

$$K = (B_0 / \eta) P_m + (4/3) K_0 (8RT / \pi M)^{1/2} \quad (4)$$

where  $B_0$  is the permeability constant for viscous flow [ $\text{cm}^2$ ],  $K_0$  the permeability constant for Knudsen flow or slip flow [ $\text{cm}$ ],  $\eta$  the viscosity of the gas [ $(\text{kgf}/\text{cm}^2)\text{s}$ ],  $P_m$  the average pressure between the pressure in two chambers [ $\text{kgf}/\text{cm}^2$ ],  $R$  the gas constant,  $T$  the temperature [ $\text{K}$ ] and  $M$  the molecular weight of the gas [ $\text{kg}/\text{mole}$ ].

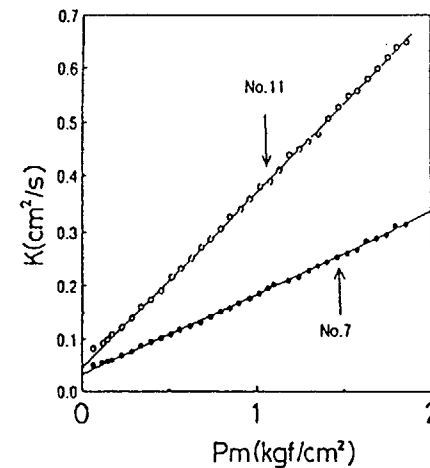


Fig.14 Mean pressure dependence of  $\text{N}_2$  gas permeability of IG-56.  
(Specimen size:  $\phi 30 \times 7t$ )

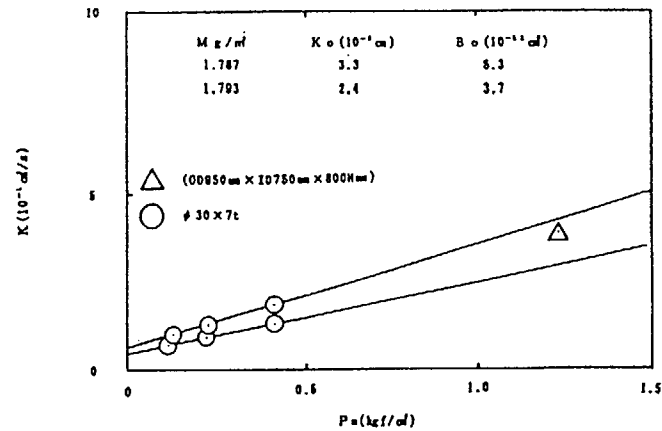


Fig.15 N<sub>2</sub> gas permeability obtained for IG-56 cutted out from a same graphite block.  
△:large specimen;  
○:small specimen

Mukaibou and Takahashi<sup>12)</sup> reported that in case  $P_m$  is less than around 150 mmHg (0.2kgf/cm<sup>2</sup>), lineality between  $K$  and  $P_m$  loses for the graphite of which  $K$  is  $5.6 \times 10^{-9}$  cm<sup>2</sup>/s at  $P_m = 1$  atm. And Hutoheon et al.<sup>13)</sup> reported that graphites with  $K$  of around  $10^{-2}$  cm<sup>2</sup>/s follows Eq.(4) in the range of 1 to 10 atm.

The plots of  $K$  against  $P_m$  for a small specimen of IG-56 is shown in Fig.14. Linearity was found in the region  $P_m$  is more than 0.2 to 3.4 kgf/cm<sup>2</sup> or 20 to 340kPa for a fine grained isotropic graphite.

#### Volume effect

Volume effect for gas permeability was also tested. In other words, we tested if the evaluation of small specimens can be used to estimate the gas permeability of large specimens. The results of gas permeability for both two small specimens and a large specimen of IG-56 are shown in Fig.15. It was found that all the data was on a single line, which can be said that the gas permeability of large blocks can be evaluated using small specimens.

#### Gas permeability of IG-11 measured by N<sub>2</sub> and He gases

Gas permeabilities of IG-11 measured by N<sub>2</sub> and He gases are shown in Fig.16a) and b), respectively.  $B_0$  values measured by N<sub>2</sub> and He gases appeared to be much the same as is indicated in Eq.(4).

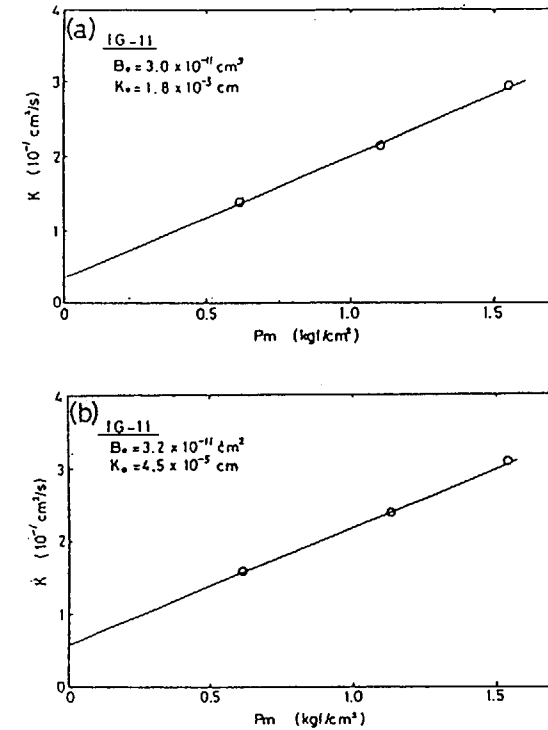


Fig.16 Mean pressure dependance of permeability of IG-11.  
(a) for N<sub>2</sub>; (b) for He

#### Impregnation of resin and glass

Phenolic resin was impregnated into IG-11 graphite. As shown in Figs.17, the specimen became impermeable after resin impregnation was applied twice. Gas permeability of resin twice impregnated graphite was found to be  $10^{-7}$  cm<sup>2</sup>/s, whereas that of IG-11 is  $10^{-1}$  cm<sup>2</sup>/s. Only slip flow was observed for the resin twice impregnated graphite. Boro-silicate glass was also impregnated into IG-11. Gas permeabilities for IG-11G, glass (shown in Table 4) impregnated IG-11, is plotted in Fig.18. It was found that gas tightness of IG-11G is slightly lower than that of the materials which are resin impregnated twice. This is due to the 10 % open pores which remained unoccupied in IG-11G. We can see that



impregnation of either resin or boro-silicate glass is very effective in reducing gas permeability. However, these impregnats cannot be effective at high temperatures since resin degrades creating pores and the softening point of the glass is only 620 °C. To overcome these problems, impregnation of high melting point substances or coating and/or infiltration of pyrolytic carbon can be done.

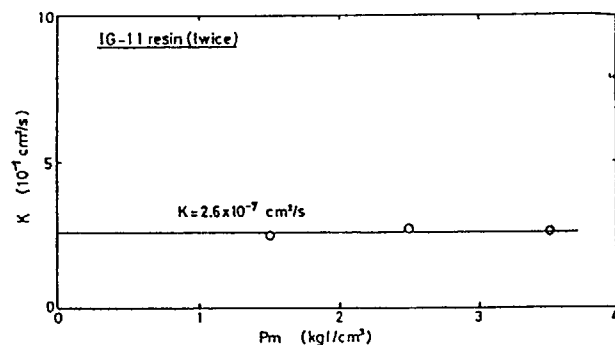


Fig.17 Pressure dependance of He permeability of phenolic resin impregnated IG-11.

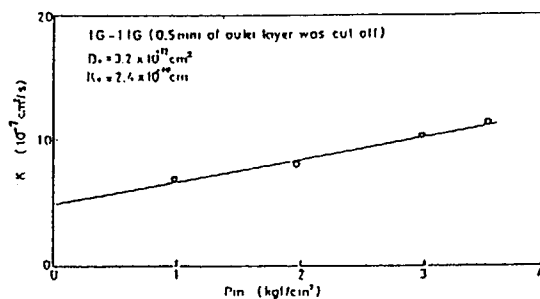


Fig.18 Pressure dependance of  $N_2$  gas permeability of glass impregnated IG-11.

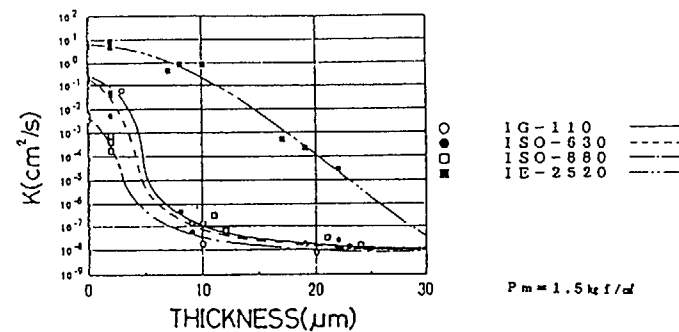


Fig.19  $N_2$  gas permeability of PyC coated isotropic graphites with various film thickness deposited under faster rate condition.

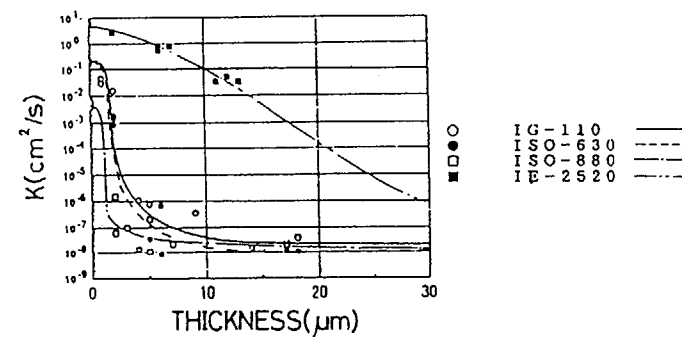


Fig.20  $N_2$  gas permeability of PyC coated isotropic graphites with various film thickness deposited under slower rate condition.

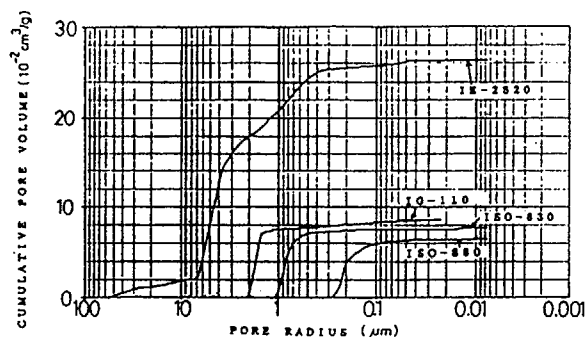


Fig.21 Pore distribution curves of isotropic graphites.

#### PyC coating

Thickness of the coating film was varied between the range of 0 to 25  $\mu\text{m}$ . Gas permeabilities of PyC coated graphites with the condition of faster deposition rate are shown in Fig.19 and those of with the slower condition are shown in Fig.20. Order of  $10^{-8} \text{ cm}^2/\text{s}$  could be achieved with the film thickness of 10 to 20  $\mu\text{m}$  for the graphites coated with faster deposition rate. Such a gas tightness was seen with the film thickness of 5 to 10  $\mu\text{m}$  for the graphites coated with slower deposition rate. The reason why the PyC film deposited with a slower rate could achieve gas tightness with a thinner film is probably because with a slower deposition rate, resource gas can get inside the specimen and form PyC film in the pores. Here, IE-2520, of which pore radius is 3.5  $\mu\text{m}$ , could not become gas tight even after 20  $\mu\text{m}$  PyC coating. As in Fig.21, IE-2520 has large pores, even larger than 20  $\mu\text{m}$ , so that it might be natural that 20  $\mu\text{m}$  of coating thickness is not enough to make gas tightness.

#### Conclusion

Behavior of gas desorption for isotropic graphites, B<sub>4</sub>C-graphite materials, and Felt-C/C were studied by using TDS.

1. Purification of graphites is very effective to reduce the amount of gas desorption, and baking pretreatment in vacuum lowers outgassing even further.
2. Adding only 1% boron suppresses CO and CO<sub>2</sub> desorption.
3. Gas desorption behavior of PyC infiltrated Felt-C/C was found to be much the same as that of isotropic graphites. Outgas amounts for H<sub>2</sub>, H<sub>2</sub>O, CO and CO<sub>2</sub> were much the same as those of IG-110U. Desorption of hydrocarbons for Felt-C/C was 10 times larger than that of IG-110U.
4. After pre-baking of isotropic graphites and Felt-C/C for 3 hours at 400 °C, the amounts of gas desorption was reduced to one twentieth to that of as-received.

5. After pre-baking of IG-110U for 3 hours at 700 °C, the thermal desorption curve of total pressure was almost back ground level ( $10^{-6} \text{ Pa} \times 55 \text{ g/s} \times (1 \times 1 \times 0.1 \text{ cm}^3)$ ).

Gas permeability was measured for isotropic graphites, resin and glass impregnated graphites and PyC coated graphites.

1. Gas permeability of large blocks such as 950 mm in diameter can be estimated using data obtained from small specimens.
2. Glass as well as resin impregnation was effective to reduce gas permeability.
3. 20  $\mu\text{m}$  PyC coating on a graphite substrate made it gas tight. However, if the pore diameter of a substrate is larger than 1.8  $\mu\text{m}$ , thicker coating is required.
4. Permeability constants for viscous flow of IG-11 measured by N<sub>2</sub> and He gas appeared to be much the same.
5. Linearity was observed between mean pressure(P<sub>m</sub>) and gas permeability(K) in the P<sub>m</sub> range 0.2 to 3.4 kgf/cm<sup>2</sup> for the isotropic graphites.

#### References

- 1) T.Yamashina and T.Hino, J.Nucl. Mater. **162-164** (1989)841
- 2) M.Okada et al. Fall Meeting of the Atomic Energy Society of Japan, Proc. p.602 Oct. 1990 Sendai
- 3) M.Okada et al. the 16th annual meeting of the Carbon Society of Japan, Proc. p.136 Dec.1989, Tokyo
- 4) Y.Hirohata et al. Shinkuu **33** (1990)293
- 5) A.Oya and S.Otani Carbon **17** (1979)131
- 6) M.Okada Youyuuen **32** (1989)121
- 7) T.Sogabe et al. FC Report of Japan Fine Ceramics Association 1989 [7]243
- 8) S.Ikeda et al. Tanso 1986 [124]2
- 9) M.Kamiyama and T.Sogabe Inter. Sympo. on Carbon Proc. p.296 Nov.4-8,1990 Tsukuba, Japan
- 10) H.P.G.Darcy "Les Fontaines publiques de la ville de Dijon" (1985)Victor Dalmont
- 11) P.C.Carman "Flow of gases through porous media" (1956) Butterworths
- 12) T.Mukaibo and Y.Takahashi Tanso 1961[28]7
- 13) J.M.Hutcheon et al. SCI Conf. on Industrial Carbon, (1957)London, UK

# RELATION BETWEEN GASIFICATION RATES AND GAS DESORPTION BEHAVIOR WITH METALLIC IMPURITIES OF CARBON AND GRAPHITE MATERIALS FOR THE HTTR

S. NOMURA\*, H. IMAI\*\*, K. FUJII\*, M. SHINDO\*

\*Department of Fuels and Materials Research,  
Japan Atomic Energy Research Institute

\*\*Research Association for Nuclear Facilities  
Decommissioning

Tokai-mura, Naka-gun, Ibaraki-ken,  
Japan

## Abstract

Gasification rates of carbonaceous materials by water vapor and carbon dioxide were strongly dependent upon both, kind of metallic impurities and their concentrations present in the materials. Similar relations were also hold for gas desorption behavior from the carbonaceous materials.

Seventeen kinds of carbons and graphite were oxidized in helium flow containing 0.65% of water vapor and carbon dioxide in the temperature range from 800 to 1000°C. The rates of reaction with carbon dioxide were relatively equal to those with water vapor.

The gasification rates increased with sum of contents of transition metal impurities Fe, Ti, V and Ni. Structural parameters of the carbonaceous materials, the degree of graphitization, the crystallite size  $a_0$  and c-axis lattice strain of the graphite crystallite hardly affected the gasification rates.

The compensation effect between the activation energies and the pre-exponential factors of the reaction was found to exist in both gasification. This means that the gasification is governed by catalytic action of the metallic impurities. Iso kinetic temperatures, at which all catalyst lose their activity, were 1230°C for the reaction with water vapor and 1120°C with carbon dioxide.

Six kinds of carbonaceous materials and some metallic impurities doped natural graphite powder compacts were used for the gas desorption experiments. Gases evolved from the materials up to 1000°C were  $\text{CO}_2$ , CO,  $\text{H}_2$ ,  $\text{CH}_4$  and physically adsorbed species,  $\text{N}_2$ ,  $\text{O}_2$  and  $\text{H}_2\text{O}$ . Total volume of the former group of gases evolved from the graphite materials was correlated to both, their ash contents and the gasification rates with water vapor at 1000°C. Effect of metallic impurities, Ca, Fe, Ni, Al and Si, on the former gas species evolution behavior were also investigated.

## 1. INTRODUCTION

The High Temperature Engineering Test Reactor (HTTR) contains large amount of carbonaceous materials for the core component and the core support component. Gasification of these materials by impurity gas is mainly water vapor and carbon dioxide in coolant helium causes degradation of their mechanical and physical integrity. It is known that carbonaceous materials evolve various kind of gases when they are heated up to 1000°C and total evolved gas volume are same order of a volume of the materials (1). Gas desorption behavior is important factor in maintenance practice of the coolant helium purity, especially in a phase of initial start up operation of the HTTR.

There are two major factors on determining the gasification behavior of the carbonaceous materials. The first is environmental factors around them, such as temperature of gasification, concentrations of impurity gases (2), ionizing radiation (3, 4), imposed stress on the materials (5), pressure of coolant helium and their flow condition in the reactor (4). The second is inherent properties of the materials, such as B. E. T. area and degree of graphitization, pore structure (6) and metallic impurities present in the materials (7).

Gasification rates of carbonaceous materials can be described by the Langmuir-Hinshelwood type rate equation (2). In this case, reacting gas species are adsorbed chemically on an active site on a solid surface and then decomposed on the site. In this connection, gas desorption processes from chemisorbed sites is one elementary process of the gasification. It is expected that some correlations are existed between the gasification rate and gas desorption behavior of the materials.

Metallic impurities, especially transition metals have catalytic activity in the gasification of carbonaceous materials (7). Therefore, existence of correlation between gasification rates and metallic impurities present in the materials was examined. Similar relation was also examined with gas desorption behavior from the materials.

Iso kinetic temperatures, at which all catalyst lose their catalytic activity, were determined for both gasification of the materials with water vapor and carbon dioxide.

## 2. EXPERIMENTAL

### 2.1 Materials

Graphite and carbon materials used in the corrosion test are listed in table 1. Test specimens for each brands were taken from single log or block with various positions, center and peripheral. The specimens were machined in the form of rod, 11 mm diameter, 50 mm long and their longitudinal direction taken with grain. The specimens were washed in a ultrasonic bath filled with reagent grade of carbon tetrachloride and dried in air at 120 °C for 48 hours.

The degree of graphitization of crystallite in the specimens was determined from 004 line (8). The height and the c-axis strain of crystallite were calculated from 002, 004, 006 lines by a method of Thrower (9).

Ash content was obtained from weight of an oxidation residue of 3 grams of powdered sample oxidized in air at 900 °C. Ash contents of the materials were ranged from 80 to 2400 ppm and distributed higher in

Table 1 Carbons and graphites used in the experiments

Brand	Coke	Compaction method	Apparent Density (g/cm <sup>3</sup> )
ATR-2E	Special Pitch coke	E**	1.81
P <sub>1</sub> JHA	Pitch coke	M***	1.73
TS-1240	—	E	1.76
H451	Petroleum coke	E	1.74
V-483T	Pitch coke	Isostatic M	1.77
ATJ	—	M	1.78
ASR-1RG	Pitch coke	Vibrational M	1.80
PGX	—	M	1.74
7477PT	Petroleum coke	M	1.74
7477	"	M	1.75
H327	"	E	1.77
IG-11(R)	"	Isostatic press	1.75
IG-11(S)	"	"	1.75
C-140A*	Pitch coke	Vibrational M	1.66
G-117	"	M	1.55
EG-38B*	Petroleum coke	M	1.57
CP101*	Pitch coke	Isostatic press	1.54

(R): Round type block, (S): Square type block

\* Carbon, \*\* Extrusion, \*\*\* Molding

Table 2 Graphite and carbon materials used in the experiment

	Density (g/cm <sup>3</sup> )	B.E.T. Area (m <sup>2</sup> /g)	Ash (ppm)	Impurity (ppm) 16)					
				Ca	Al	Fe	Ti	V	Si
IG-110	1.75	0.36	<80	2	N.D	2	0.2	N.D	<0.1
IG-11	1.75	—	1450	490	30	84	53	180	78
PGX	1.74	0.25	1000	116	25	304	38	5	58
ASR-ORB	1.69	0.55	3000	—	—	—	—	—	—
Aerolor-03	1.76	—	—	—	—	—	—	—	—
SiC (F.G.M.)	1.89	—	—	—	—	—	—	—	—

N.D.: Below Detection Limit

Table 3 Studied elements and their concentration in graphite

Element	Content	Atom %	Weight %
Ca		0.34	1.1
Al		1.34	3.0
Fe		0.84	3.9
Ni		0.10	0.5
Si		0.26	0.6

inner part than in outer especially in large logs. Eight metallic impurities (Fe, Ca, Mg, Ni, Mn, Ti, V and Al) were determined from a wet oxidation decomposition method for graphite (10). The graphite powder was decomposed with periodic acid (H<sub>5</sub>IO<sub>6</sub>) in perchloric acid at 200 °C. In purified graphite materials, major impurity element was Ti and next level contents of impurities were Fe, Ca and V. In unrefined graphite materials, contents of Fe and Ca were about 100 times higher than those of the purified graphite although Ti and V were same level in the both graphite.

Six nine grade of high purity helium was used as carrier gas. Water vapor was added to the helium by bubbling the helium through a distilled water bath held at 2 °C. JIS-K2 grade of carbon dioxide gas was further purified by passage through a column of 5A molecular sieve at room temperature. Methane and ethylene impurities contained in the carbon dioxide were removed by this procedure. Concentrations of water vapor and carbon dioxide in the helium stream were 0.65% by volume, respectively.

Carbonaceous materials used in the gas desorption experiment are listed in table 2. Brand name ASR-ORB is a carbon material, and Aerolor-03 is a carbon / carbon fiber composite. A SiC coated graphite material has functionally gradient concentration profile of SiC from specimen outer surface to inner within coating layer of thickness about 1mm. Fractional concentration of SiC at the specimen outer surface was about 99%. Specimen shape is the same as that of the corrosion test.

Specimens added metallic impurities are listed in table 3. The impurities added natural graphite pellets were prepared as follows. Natural graphite powder for spectroscopic grade containing 170 ppm ash was dipped in one normal concentration of metal chloride aqueous solution, impregnated under reduced atmosphere and then dried. After pelletizing, they are heated at 1100 °C for 3 hours under vacuum. Specimens silicon doped were prepared by mixing of the graphite powder and 1 weight percent of high purity silicon powder. After pelletizing the mixture, they are heat treated at 1800 °C for 3 hours under vacuum. The impurity content of those pellets was determined by the same method as mentioned before. Specimens the impurity added were exposed to the atmosphere during three months after preparation to attain an equilibrium of adsorption-desorption with atmospheric gases.

## 2.2 Apparatus and procedure

Apparatus used for oxidation rate and gas desorption measurement was shown schematically in Fig. 1. Gas flow rate at one atmospheric pressure was regulated at 650 ml/min for the oxidation or 60 ml/min for the gas desorption with mass flow controllers. The effluent gas, passage through the quartz reaction chamber was diverted to the gas chromatograph with helium ionization detector (H.I.D.) and flame ionization detector (F.I.D.), where the concentration of reaction products was periodically determined by comparison with standard gas mixtures. To remove the adsorbed gases, each specimen was outgassed overnight at 1000 °C under vacuum before oxidation. Oxidation rates were measured in the temperature range between 800 °C to 1000 °C. The oxidation rate was determined from both a weight change of the specimen and the concentration of the reaction product gases.

For the gas desorption experiment, the specimen was placed in the reaction chamber and then purged air with the helium stream at room

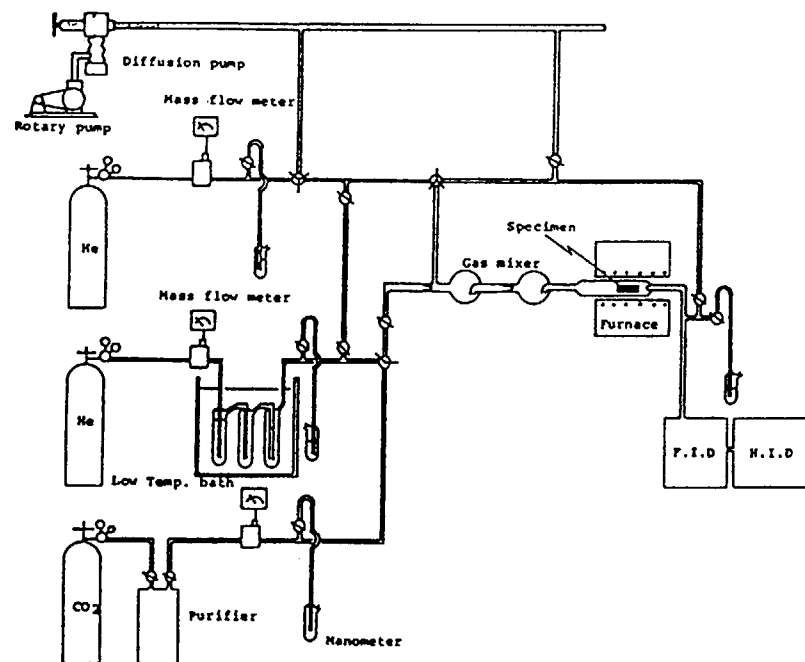


Fig. 1 Apparatus for the reaction

temperature. Specimens were heated up to 1000 °C with heating rates 2 °C/min or 3 °C/min and then held at 1000 °C for some hours. Concentration of desorbed gas in the helium was monitored periodically with time. Some specimens showed higher concentration level of desorbed gases at 1000 °C and did not fall off below quantitative analytical limits for the gases within reasonable time. In this case, the total amount of desorbed gases at 1000 °C was determined by multiplying of factor 2 an area of a concentration-time curve at which given concentration of the desorbed gas decreases to one half of its initial value. This is based on fact that the concentration of desorbed gases at constant temperature decrease exponentially with time. Amount of water adsorbed was determined from a weight loss of the specimen heated at 170 °C for 48 hours in an air oven. The weight loss was measured by a microbalance and corrected for its buoyancy using nearly same volume of an aluminum rod.

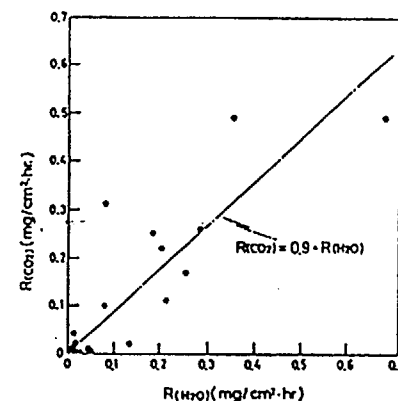


Fig. 2 Relation between the reaction rate with water vapor and that with carbon dioxide at a gas concentration of 0.65% in helium at 860°C

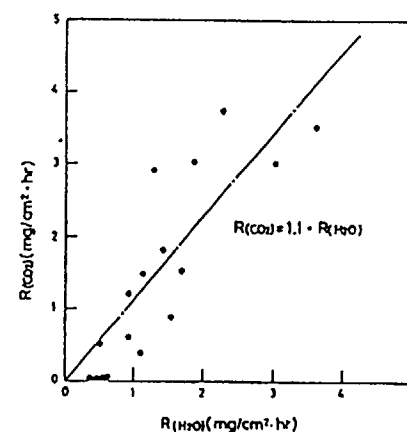


Fig. 3 Relation between the reaction rate with water vapor and that with carbon dioxide at a gas concentration of 0.65% in helium at 1000°C

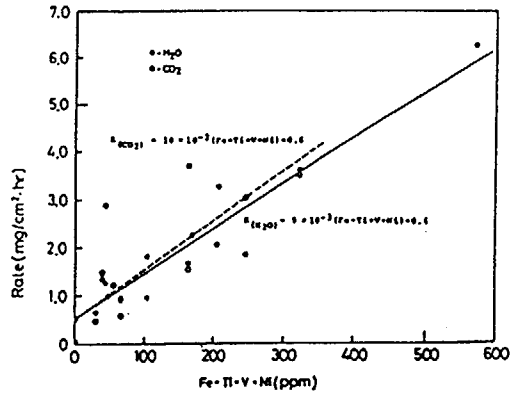


Fig. 5 Relation between the reaction rates with gases of 0.65% in helium at 1000°C and the total concentrations of (Fe+Ti+V+Ni) in the specimens

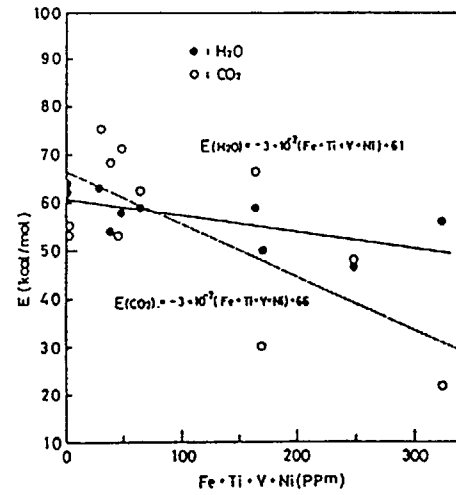


Fig. 6 Relation between the activation energies for the reactions and the total concentrations of (Fe+Ti+V+Ni) in the specimens

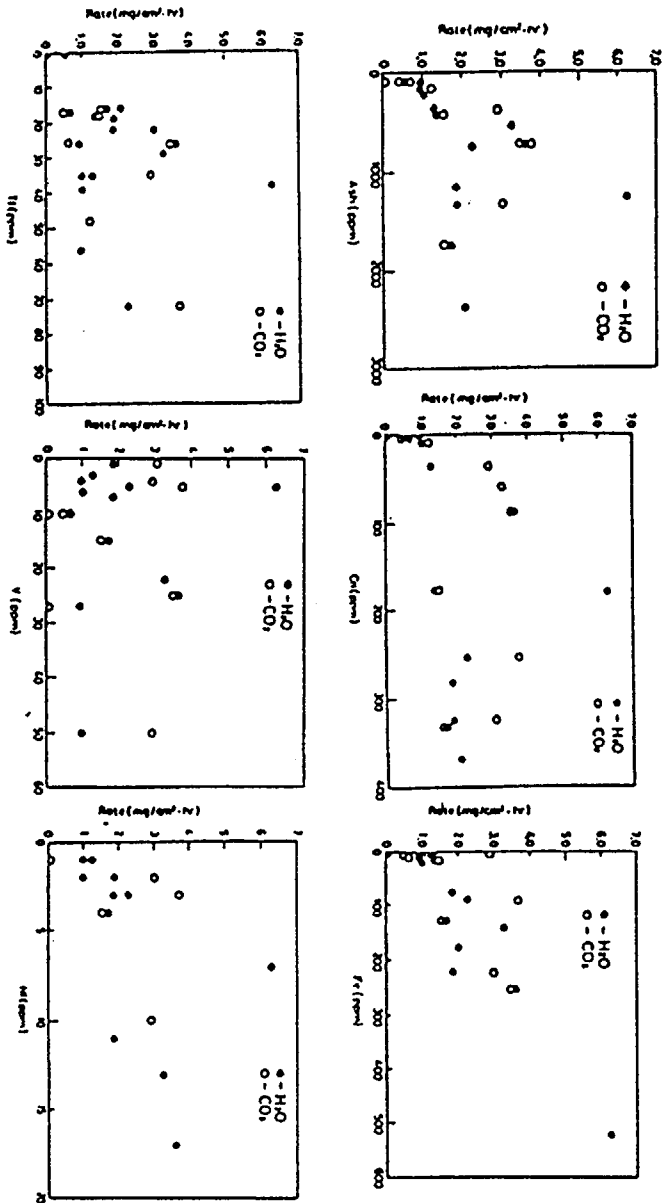


Fig. 4 Relations between the reaction rates with gases of 0.65% in helium at 1000°C and the concentrations of ash, Ca, Ti, V, Ni and Fe contained in the specimens

### 3. RESULTS

#### 3.1 Gasification rates of the materials

The oxidation rate with carbon dioxide,  $R(\text{CO}_2)$ , was compared with the rate of water vapor,  $R(\text{H}_2\text{O})$ , in two rate controlling temperature regime (2), namely chemical control regime at 860 °C and in pore diffusion regime at 1000 °C. In ordinary nuclear graphite, the oxidation rate initially increases with time as results of the increasing availability of reactive surface area and ultimately levels off. Therefore, the rates were taken a value at the reaction time 10 hours. Fig.2 and Fig.3 shows comparison between the oxidation rate  $R(\text{CO}_2)$  and  $R(\text{H}_2\text{O})$  at each temperature. Although there are considerable scatter, the least square fitting gave a linear relationship among them:

$$\begin{aligned} R(\text{CO}_2) &= 0.9 \times R(\text{H}_2\text{O}) & \text{at } 860^\circ\text{C} & \quad (1) \\ R(\text{CO}_2) &= 1.1 \times R(\text{H}_2\text{O}) & \text{at } 1000^\circ\text{C} & \quad (2) \end{aligned}$$

and correlation factor for eq. (1) and eq. (2) were 0.84 and 0.85 respectively. The oxidation rate in the in pore diffusion controlled regime influenced both intrinsic chemical reactivity and pore structure of the materials (1). Linear relationships shown by eq. (1) and eq. (2) show that inhibiting actions of the oxidation products CO and  $\text{H}_2$  are similar to each other and also the in pore diffusion rates of  $\text{CO}_2$  and  $\text{H}_2\text{O}$ .

Fig.4 shows relation between metallic impurity contents and the oxidation rates at 1000°C. Ash contents appeared to have ambiguous influence on the reaction rate, especially higher than 500 ppm. Other impurities, Ca and transition metals Ti, V, Ni, were also hardly correlate with the rates. The content of Fe could be correlated with the rates and the regression to strait line gave the correlation factor 0.85 for the water vapor and 0.65 for the carbon dioxide. The correlations were improved by taking the impurity contents as a sum of the transition metals (Fe+Ni+V+Ti). Fig.5 shows a fitting of the rates with the sum of the impurity contents. The regression analysis gave:

$$R(\text{H}_2\text{O}) = 9 \times 10^{-3} (\text{Fe} + \text{Ti} + \text{V} + \text{Ni}) + 0.6 \quad (3)$$

$$R(\text{CO}_2) = 10 \times 10^{-3} (\text{Fe} + \text{Ti} + \text{V} + \text{Ni}) + 0.6 \quad (4)$$

where unit of impurity is ppm and that of the rates is  $\text{mg}/\text{cm}^2 \cdot \text{hr}$ . Correlation factor for eq. (3) and eq. (4) were 0.92 and 0.76 respectively. The improvement in the correlations by taken the sum of the transition metals suggests that catalytic activity of these metals is nearly equal to each other. Fig.6 shows a correlation between the activation energies for the oxidation and the sum of the transition metal contents. The activation energies, which were determined in the temperature range from 800 °C to 920 °C, were decreased with increase of the sum of the impurity contents. This is similar to that of catalyzed reactions of a single materials with various concentration levels of an impurity (11).

Correlations between the x-ray parameters of the material and the oxidation rates were shown in Figs. 7 to 9. Lines connecting points represent data taken from the single log or block but different

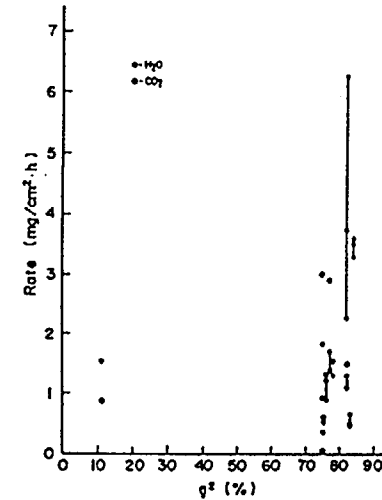


Fig. 7 Relation between the reaction rates with gases of 0.65% in helium at 1000°C and the degree of graphitization of crystallite in the specimens

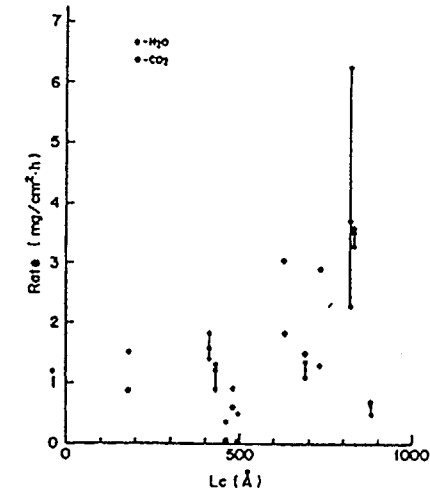


Fig. 8 Relation between the reaction rates with gases of 0.65% in helium at 1000°C and the height of crystallite in the specimens

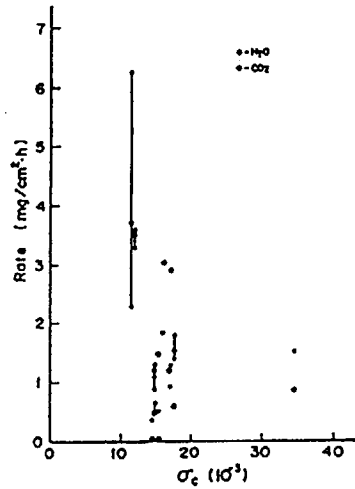


Fig. 9 Relation between the reaction rates with gases of 0.65% in helium at 1000°C and the c-axis lattice strain of crystallite in the specimens

positions. There were no clear correlations between them. An effect of the such structure parameters was masked by that of the impurities.

The oxidation rate can be written as the Arrhenius type:

$$\text{Rate} = A \exp(-E/RT) \quad (5)$$

In this case, A and E depends on impurity concentrations. Figs. 10 and 11 show a correlation between the activation energy E and the frequency factor A for the both oxidation, which indicated that an increase in the rate caused by increase of A is compensated with a decrease in the rate by an increase of E. This compensation relations observed in the present multi-couple of the impurities and the materials are similar to the compensation effect in catalytic reactions of a single materials with different concentration levels of an impurity (11, 12). The compensation relation observed in the present system indicates that 17 kinds of carbonaceous materials are oxidized as if a single carbonaceous material with the various levels of a single impurity. Least square fitting gave:

$$\ln A = 0.34xE + 3.5 \quad (6)$$

$$\ln A = 0.36xE + 2.6 \quad (7)$$

for the oxidation with water vapor and with carbon dioxide respectively. Above equations can be expressed as

$$\ln A = mxE + \ln K \quad (8)$$

where m and k is a constant. From eq. (5) and eq. (8), we get

$$\text{Rate} = kx (\exp(m-1/RT) x E) \quad (9)$$

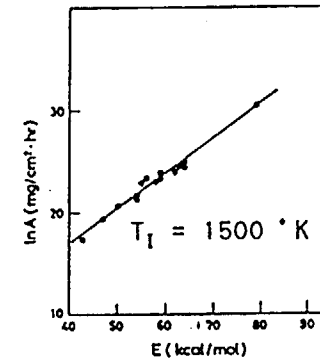


Fig. 10 Compensation effect for the reaction with water vapor

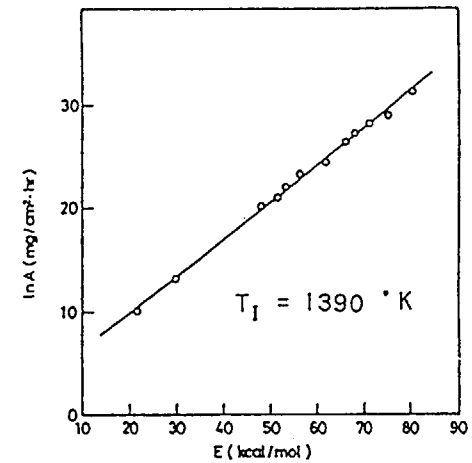


Fig. 11 Compensation effect for the reaction with carbon dioxide



A value of  $(m-1/RT)$  at lower oxidation temperature is usually negative. As the temperature increases, the sign of the value changes from negative to positive. When the temperature increased to  $T=1/RT$ , the value becomes zero. At this temperature, the catalyzed oxidation rate takes an intrinsic reactivity of the matrix. This temperature is called iso kinetic temperature(11). Iso kinetic temperatures were 1500 °K for the oxidation with water vapor and 1390 °K with carbon dioxide. The values of  $m$  obtained were within a range for semiconductor catalysis (12).

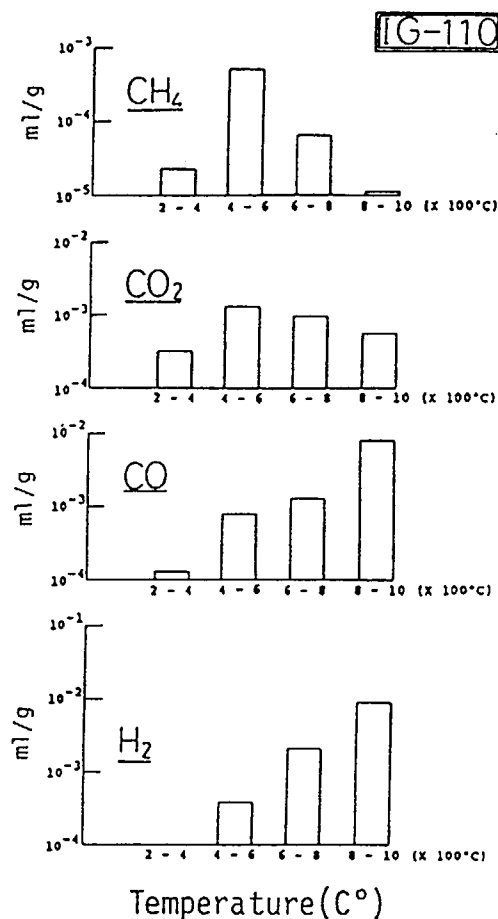


Fig. 12 Volume of gases desorbed from IG-110 graphite in interval of 200°C

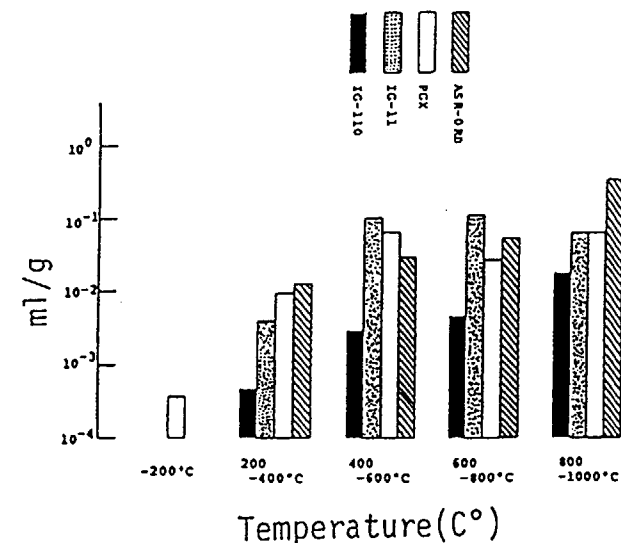


Fig. 13 Volume of gases desorbed from carbon and graphite materials in interval of 200°C

### 3.2 Gas desorption from the materials

Fig.12 shows a volume of gases evolved from IG-110 graphite at every 200 °C by heating up to 1000 °C. The desorption of CO and H<sub>2</sub> increased with the temperature, as opposed to that of CO<sub>2</sub> and CH<sub>4</sub>. A volume ratio of CO to H<sub>2</sub> which desorbed at 800 - 1000 °C was nearly unity. This shows that desorbed CO and H<sub>2</sub> in this temperature range were formed by decomposition of adsorbed H<sub>2</sub>O in the graphite matrix. The gas desorption behavior for other materials was similar to that of IG-110 graphite, with exception of H<sub>2</sub> desorption from ASR-ORB carbon material. Fig.13 shows total volume of (CO<sub>2</sub>+CO+CH<sub>4</sub>+H<sub>2</sub>) desorbed from the materials at every 200 °C. Desorbed gas volumes for purified graphite IG-110 were less than that of unrefined graphite IG-11 in every temperature range.

Fig.14 shows volume of the gases desorbed from the impurity added natural graphite pellets heated up to 1000 °C. The figure shows qualitatively an effect of impurity addition on the desorption of the gases H<sub>2</sub>, CO and CO<sub>2</sub>. Addition of Ca increased the evolution of CO<sub>2</sub>. Fe and Ni also enhanced the evolution of CO. However, Ca, Fe and Ni affected hardly on the evolution of H<sub>2</sub>. Therefore, these impurities promote the chemical adsorption by the graphite matrix of O<sub>2</sub> rather than H<sub>2</sub>O from the atmosphere. Si reduced effectively the evolution of CO, CO<sub>2</sub> and H<sub>2</sub>. Possibly this is due to blocking of active sites for adsorption by melting of the silicon during the specimen preparation at high temperature. An addition of Al, which has the maximum content of the impurities, had no effect of the gases evolution.

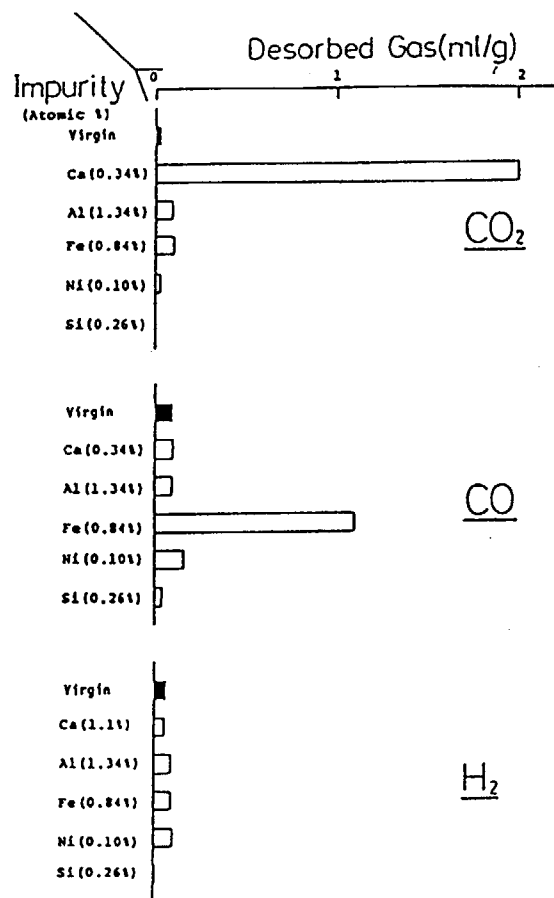


Fig. 14 Volume of gas desorbed from graphite with impurity element by heating to 1000°C

Fig. 15 shows total desorbed volumes of each gas from the carbon and graphite materials by heating up to 1000 °C. The desorbed volume of CO and CO<sub>2</sub> from the graphite could be correlated with their Ca and Fe contents. The desorbed volume of H<sub>2</sub> from ASR-ORB was larger than stoichiometry for CO as the decomposition products of H<sub>2</sub>O. ASR-ORB has other source of H<sub>2</sub> evolution. Amounts of desorbed CH<sub>4</sub> were two order of magnitude less than those of the other gases. Amounts of the desorbed gases from the SiC coated and C/C composite material were about ten times smaller than those from the other materials.

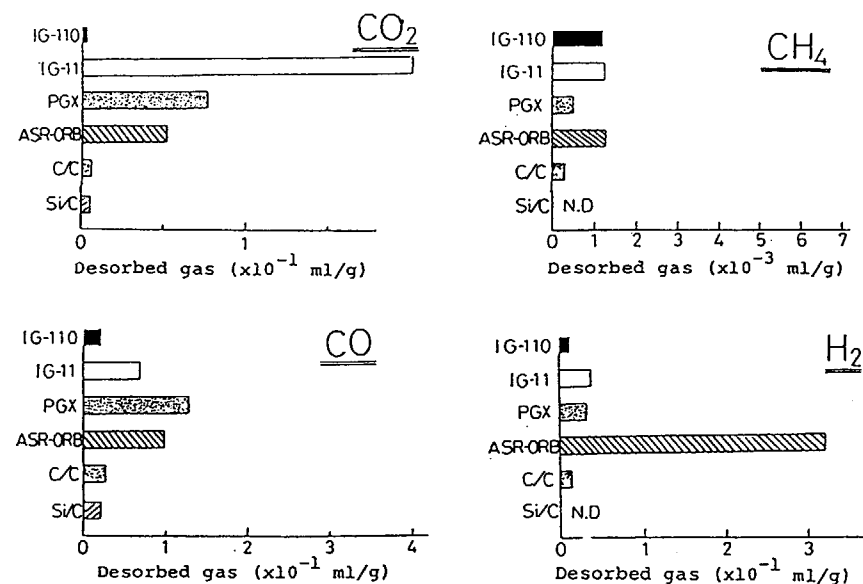


Fig. 15 Volume of gas desorbed from carbon and graphite materials by heating to 1000 °C

Fig. 16 shows relation between oxidation rates with water vapor at 1000 °C and sums of the desorbed gases volume from the materials. There were good correlations between desorbed volume (CO+CO<sub>2</sub>+CH<sub>4</sub>) or (CO+CO<sub>2</sub>+CH<sub>4</sub>+H<sub>2</sub>) and the rates, with exception of ASR-ORB which has another H<sub>2</sub> desorption site other than H<sub>2</sub>O. This good correlation shows that desorption sites for these gases are also active sites for the oxidation. Fig. 17 shows relation between the ash contents and the sums of desorbed gases from the materials. Good correlations were also observed between them. ASR-ORB was also exception in this case. The ash contains inactive metal impurities for adsorption of the gases such as Al and Si, hence the correlation between the ash content and the desorbed gas may be scatter than those of the oxidation rates.

Desorbed amounts of physically adsorbed gases N<sub>2</sub> and O<sub>2</sub> by heating up to 1000 °C for the reactor graphite were about 5x10<sup>-2</sup> ml/gr respectively. Amounts of water desorbed as water vapor were in a range from 1.5x10<sup>-2</sup> to 3.0x10<sup>-2</sup> ml/gr for the reactor graphite and 2.7x10<sup>-1</sup> ml/gr for ASR-ORB carbon materials. The desorbed amount of water vapor of the ASR-ORB was ten times larger than that of the reactor graphite.

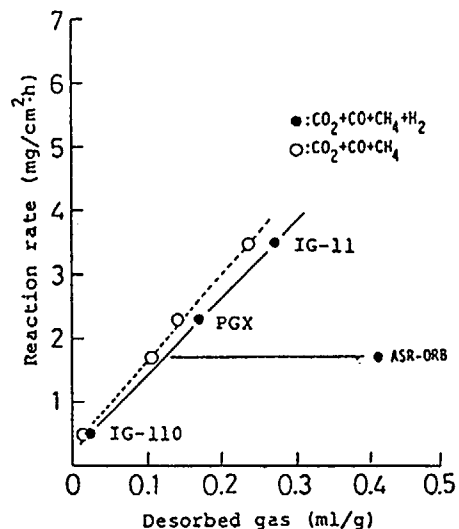


Fig. 16 Relation between volume of desorbed gas and rate of carbon gasified in reactions of carbon and graphite materials with 0.65% H<sub>2</sub>O at 1000°C

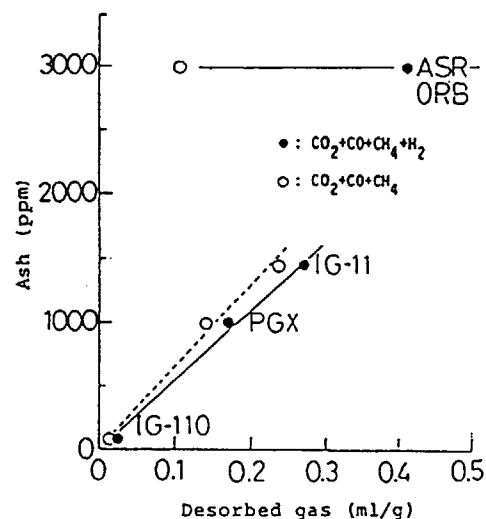


Fig. 17 Relation between volume of desorbed gas and ash contents of carbon and graphite materials

#### 4. DISCUSSION

It had been reported that oxidation rates of a carbonaceous materials by water vapor was faster than that by carbon dioxide. Walker et al. (2) reported that a ratio of  $R(H_2O)$  to  $R(CO_2)$  was 3 at 800 °C under 0.1 atmospheric pressure. Bonnetain et al. (13) also reported a value of 5 at 1000 °C under 1 atmospheric pressure. In the present study, this value averaged over 17 kinds of the materials was 1.1 at 860 °C and 0.9 at 1000 °C respectively. Some of the materials have nearly same values reported, however, the value obtained present study shows that the reactivity of water vapor toward the materials was similar to that of carbon dioxide. This result indicate that the active sites for the water vapor is common to that of the carbon dioxide.

Threuer et al. (14) reported that a catalytic activity of some metals on the oxidation of graphite is in a sequence of  $Ca > Fe > V$  for water vapor and  $V > Ca > Fe$  for carbon dioxide. In the present study, the impurity doped natural graphite pellets showed that Ca, Fe and Ni have catalytic activity, but Al and Si have not active in the oxidation with water vapor. The result obtained 17 kinds of the materials showed that Ca has no evidence of the catalytic activity in the oxidation with water vapor or carbon dioxide. There is a possibility that chemical form of Ca is different in the materials and the doped graphite caused by forming a catalytically inactive salt with other impurity elements. Correlation of the V content with the rates was observed as a sum of the transition metals (Fe+Ni+Ti+V), because the concentration level of Fe is on average one order of magnitude larger than those of the other transition metals.

Gasification of the materials takes place at solid-gas interface. If the oxidation rate is governed by the impurities at the interface, then the rate are expected to be proportional with their surface concentration. Fig. 5 shows the rate is linear with volume concentration of the impurities. This means that catalytic activity is caused by the impurities present in some layer below the interface rather than that at the interface.

Addition of only 0.26 atomic % of Si caused the decrease of the gas desorption from the natural graphite pellet. This level of Si content did not show the inhibition of the oxidation rate by water vapor. It was reported that higher content of Si increased the oxidation resistance of graphite (15). Gas desorption and oxidation behavior of Si doped graphite materials are necessary to investigate further.

The compensation effect observed between over 17 kinds of the materials shows that the oxidation rate of those materials are determined by the catalytic action of the impurities in the temperature region below the iso kinetic temperature. When the iso kinetic temperature for the water vapor is nearly equal to the maximum temperature of graphite components in HTGR, corrosion of the graphite structural components are governed by catalytic action of the metal impurities present in the graphite.

## 5. CONCLUSIONS

The results are summarized as follows:

1. The oxidation rates of the 17 kinds of carbonaceous materials with water vapor and carbon dioxide are closely related to their transition metal contents.
2. Good correlations between the desorbed gas volume up to 1000 °C and the oxidation rates of the reactor graphite are obtained.
3. The addition of Ca, Fe and Ni to the matrix enhanced the chemisorption of O<sub>2</sub> from the atmosphere. The addition of Si reduced effectively the evolution of the gases.
4. The compensation relations obtained indicate that the 17 kinds of materials are oxidized as if a single materials with the various concentration levels of a single impurity.

## ACKNOWLEDGEMENTS

Analytical Chemistry Laboratory of the JAERI performed the chemical analyses of the metallic impurities in the materials. The author would like to thank Dr. T. Saito, for the measurement of the x-ray parameters of the materials.

## REFERENCES

1. L. G. Overholser and J. P. Blakely, Proc. of 5th Conf. on Carbon, 194 (1961)
2. P. L. Walker, Jr., Frank Rusinko, Jr., and L. G. Austin, Advances in Catalysis, Academic Press, New York and London, Vol. 11 (1959) p. 133
3. H. Imai, K. Fujii, S. Nomura, and T. Kurosawa, JAERI-M 9166 (1980)
4. M. R. Everret, D. V. Kinsey, and E. Romberg, Chemistry and Physics of Carbon, Marcel Dekker, Inc., New York, Vol. 3 (1968) p. 289
5. H. Imai, K. Fujii, S. Nomura, T. Kurosawa, and Y. Sasaki, TANSO No. 105 45 (1980)
6. J. B. Lewis, Modern Aspects of Graphite Technology, Academic Press, London, (1970) p. 129
7. P. L. Walker, Jr., M. Schelf, and R. A. Anderson, Chemistry and Physics of Carbon, Marcel Dekker, Inc., New York Marsh Dekker, Inc., New York Vol. 4 (1968) p. 287
8. J. Mering and J. Maire, Les Carbons 1, 129 (1965)
9. P. A. Thrower and D. C. Nagle, Carbon 11, 663 (1973)
10. H. Hashitani, H. Yoshida, T. Adach, and K. Izawa, BUNSEKI KAGAKU 35, 911 (1968)
11. G. C. Bond, Catalysis by Metals, Academic Press, London (1962) p. 139
12. F. F. Bolikensteinn, Physics of Semiconductor and Apparatus, Moscow (1960): Japanese translation: I. Sato, Electronic Theory of Semiconductor Catalysis, Yokokawa Inc. Tokyo (1970) p. 149
13. L. Bonnetain and G. Hoynant, Les Carbons 2, 227 (1965)
14. P. A. Thrower, G. K. Mathew, and N. J. McGinnis, Carbon 20, 465 (1982)
15. R. E. Woodley, Proc. of 8th Conf. on Carbon, C117 (1967)
16. H. Kawakami, FAPIG, 105, 2 (1983)

## DISCUSSION

## Questions or Comments

Name: T. MARUYAMA

Why did the addition of Si reduce the evolution of gases? Which is more efficient between Si and B to reduce the evolution of gases?

Answer: S. Nomura

1. Reduction in the desorbed gases by Si addition is possibly due to blocking the active sites for gases adsorption by melting of Si during the specimen preparation at high temperature (1800°C for 3 hours). We think that the effect is brought from physical factor in nature, because the gasification rate with water vapor at 1000°C did not changed that of virgin graphite.
2. 2nd question is difficult to reply because we have no experience with boronated graphite gas desorption behavior. Boronated graphite show very complex behavior on the oxidation mainly by forming B<sub>2</sub>O<sub>3</sub> melt, therefore simple relation between the gasification and gas desorption was can not be drawn from the gasification data. Boronated graphites have two types, black form and grey form. In the grey form, B<sub>4</sub>C particles was partially melt and enhance the graphitization of graphite grain(1). It is known that good graphite crystals hardly adsorbed the gases from the atmosphere.

(1) R.E. Woodley., Carbon Vol.6 617/626 (1968).

# CORROSION BEHAVIOR OF SINTERED PELLET OF GRAPHITE AND BORON CARBIDE IN HELIUM CONTAINING WATER VAPOR

K. FUJII\*, S. NOMURA\*, H. IMAI\*\*, M. SHINDO\*

\*Department of Fuels and Materials Research,  
Japan Atomic Energy Research Institute

\*\*Research Association for Nuclear Facilities  
Decommissioning

Tokai-mura, Naka-gun, Ibaraki-ken,  
Japan

## Abstract

The corrosion test of the sintered pellet of graphite and boron carbide, which has been adopted as a neutron absorber material in the control rod system, the reserved shutdown system, etc. of the High Temperature Engineering Test Reactor (HTTR), was carried out in helium containing water vapor at up to 1000°C from a viewpoint of oxidation of boron carbide (B<sub>4</sub>C). Moreover, from the results obtained of corrosion test, the integrity of the reserved shutdown system was also evaluated.

It is shown that the oxidation rates of the sintered pellet do simply not increase with temperature caused by the formation of B<sub>2</sub>O<sub>3</sub>. The oxidation reaction of the sintered pellet is consisted of three competing reactions,  

$$B_4C + 6 H_2O = 2 B_2O_3 + 6 H_2 + C(F) \quad \text{first step}$$

$$C(F) + H_2O = CO + H_2 \quad \text{and} \quad C(G) + H_2O = CO + H_2 \quad \text{second step.}$$

For the integrity of the reserved shutdown system, the mutual adhesion of the sintered pellets is one of key factors because the sintered pellets mutual adhered may not be inserted into the core in an emergency. For the sintered pellet containing 30% B which is the same B concentration as the specification of the sintered pellet adopted in the reserved shutdown system, mutual adhesion yields in case of that about 2% of the contained B is oxidized and the temperature exceeds 577°C which is the melting point of B<sub>2</sub>O<sub>3</sub>. There is no possibility of both conditions yielding in the HTTR, therefore it can be concluded that the integrity of the reserved shutdown system is not damaged against the corrosion.

## 1. Introduction

The sintered pellet of graphite and boron carbide (the sintered pellet) has been adopted as a neutron absorber material in the control rod system, the reserved shutdown system, etc. of the High Temperature Engineering Test Reactor (HTTR) [1] which is under construction at the Japan Atomic Energy Research Institute (JAERI).

Table 1 Specifications of reserved shutdown system.

Moving Method	Gravitated falling of the sintered pellets
Simple Number	16 (15 in irradiation tests using center column)
Boron Carbide/Graphite Pellet	
Diameter	about 10 mm
Length	about 10 mm
Material	Sintered compact of graphite and boron carbide
Loading Mass of B-10	about 2.6 kg/ one simple

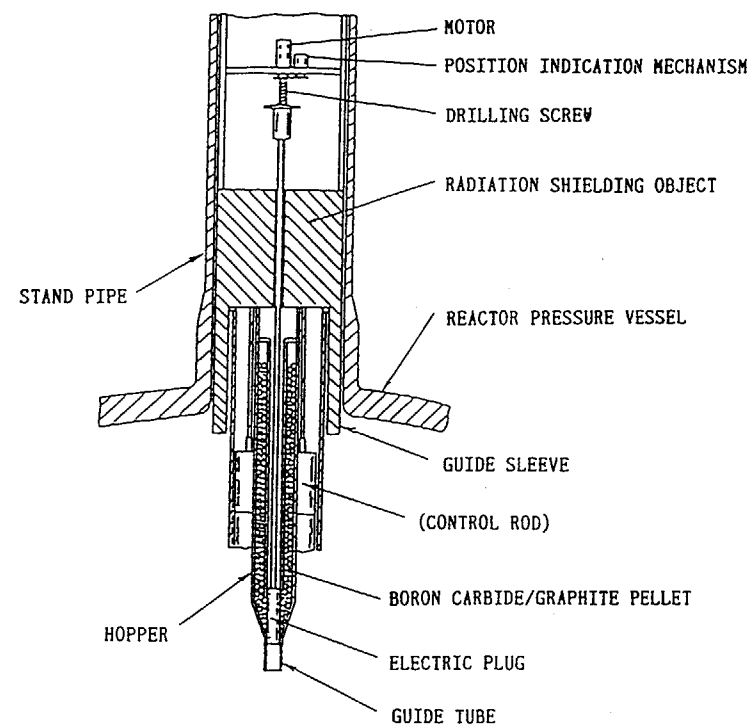


Fig. 1 Configuration of the reserved shutdown system.

Concerning boron carbide, there are various kinds of boron carbide from  $B_2C$  to  $B_{10}C$  [2], and  $B_4C$  has been used as a neutron absorber material.  $B_4C$  is thermally stable and chemically inert chemical compound, however,  $B_2O_3$  is produced by the reaction with oxidative gases at high temperature. Since the primary coolant of the HTTR contains a small amount of oxidative gaseous impurities, oxidation of the neutron absorber material is inevitable.  $B_2O_3$ , produced by the reaction has characteristics such as low melting point and relatively higher vapor pressure, therefore mass transfer phenomenon proceeds at high temperature caused by vaporization.

In the HTTR systems using the sintered pellet, the reserved shutdown system is focused. The reserved shutdown system [1] inserts the sintered pellets as neutron absorber material into the core in order to permit reactor shutdown from all operating conditions in case of failing the control rods to insert for some reasons. The specifications and the configuration of the reserved shutdown system are shown in Table 1 and Fig.1, respectively. When the reserved shutdown system is moved, the electromotive plug at the lower part of the hopper is driven by motor and the hopper is opened then the sintered pellets are inserted into the core under gravitation. The reserved shutdown system is moved by manual operation. The sintered pellets in the hopper are exposed to the stagnated primary coolant of temperature around 400°C during normal operation. For the integrity of the reserved shutdown system, specially for insertion of the sintered pellets into the core, the corrosion behavior including mutual adhesion of the sintered pellets is one of key factors.

This report describes the corrosion behavior of the sintered pellet in helium containing water vapor, mainly from a viewpoint of oxidation of  $B_4C$ . Furthermore, from the results obtained, the conditions of mutual adhesion of the sintered pellets for the reserved shutdown system are also discussed.

## 2. Experimental Procedure

### 2.1 Materials

The materials used were the porous sintered compact produced by hot-press. The density and the concentrations of boron and impurities of the sample are summarized in Table 2. The sample tested was a type of pellet of 10 diameter  $\times$  10 mm thickness. Table 3 shows the lattice parameters measured by X-ray analysis of  $B_4C$  and graphite in the sample together with comparative data for values of reference [3]. It seems that the crystal structure of  $B_4C$  is hexagonal or rhombohedral, therefore both data were shown in Table 3. Although the lattice parameters change with the ratio of boron to carbon (B/C) [4], the measured lattice parameters were slightly larger than that of  $B_4C$  in the reference. The composition of  $B_{3.7}C$  was given by the measured lattice parameters applying to the relation between B/C and lattice parameter established by Glaser[3]. Moreover, the lattice parameter  $C_0$  (002) of graphite was 6.752 Å, so that the degree of graphitization was not so high.

Table 2 Samples used in experiment.

		B <sub>4</sub> C/C (30%)	B <sub>4</sub> C/C (40%)	B <sub>4</sub> C/C (50%)	B <sub>4</sub> C
Pellet density(g/cm <sup>3</sup> )		2.04±0.03	2.06±0.03	2.25±0.03	2.31
Boron content (%)		30±3	40±3	50±3	78
Impurity(ppm)	Na	~ 100	~ 100	~ 10	~ 10
	Al	~1000	~1000	~1000	~1000
	Si	~1000	~1000	~1000	~1000
	Ca	~1000	~1000	~ 100	~ 100
	Ti	~ 100	~1000	~1000	~1000
	Mn	~ 10	~ 10	~ 10	~ 10

Table 3 Crystallite parameters of  $B_4C$  and graphite in sample together with comparative data for value of reference.

	B <sub>4</sub> C	C
Hexagonal	$a_0 = 5.612 \text{ Å} (5.61)$ $C_0 = 12.06 \text{ Å} (12.07)$	$C_0 = 6.752 \text{ Å}$
Rhombohedral	$a_0 = 5.189 \text{ Å} (5.165)$ $\alpha = 65.47^\circ (65.79)$	

( ) : data for reference [3]

### 2.2 Test condition

The experimental apparatus is shown in Fig. 2. The apparatus is consisted of helium gas supply system, water vapor injection system, reaction furnace and gas analysis system, and each systems are joined by hard glass tube. The sample set in the reaction furnace was exposed to helium containing 0.65% water vapor.

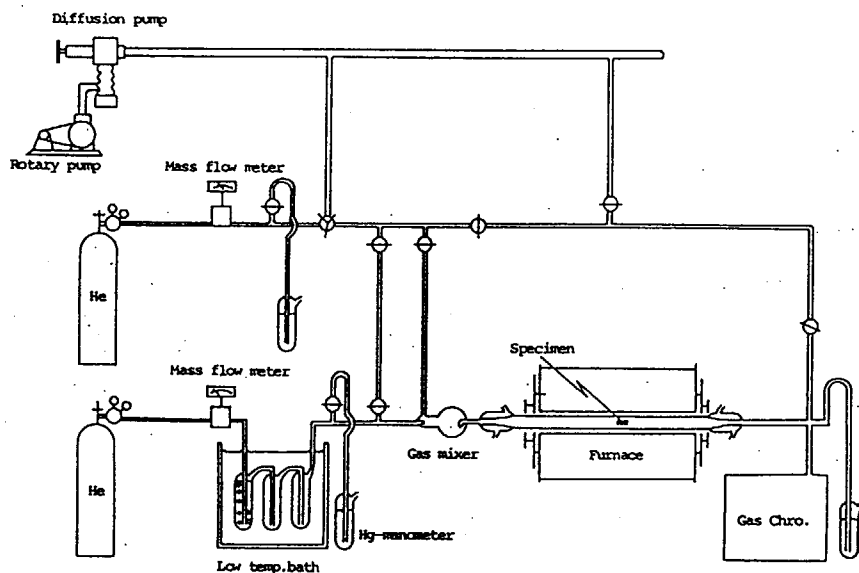


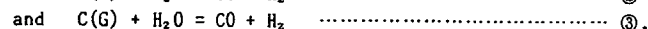
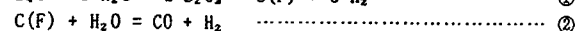
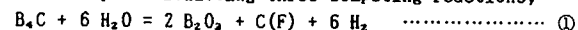
Fig. 2 Schematic diagram of experimental apparatus.

Total pressure and flow rate of helium gas were 0.1 MPa and 650 ml/min, respectively. A part of helium passing test section was led to gas chromatograph for analysis. After exposure, mass change of the sample and mass of produced  $B_2O_3$  were measured, and change in surface area caused by reaction was also examined. The measurement of mass of produced  $B_2O_3$  was possible to measure the mass of the sample after  $B_2O_3$  in the sintered pellet to be dissolved in boiling water, and the change in surface area was calculated by the mass of adsorbed Kr gas at liquid  $N_2$  temperature. The corrosion tests were carried out at constant temperature up to 1000°C and at continuous temperature changing from room temperature to 1000°C.

### 3. Experimental Results and Discussion

#### 3.1 Reaction mechanism

The oxidation reaction between the sintered pellet and water vapor in helium is proceeded by the following three competing reactions,



where C(F) is free carbon produced by the reaction ① and C(G) is graphite in the sintered pellet.  $CO_2$  and  $CH_4$  were also detected as produced gases, but the concentrations of those gases were lower compared with those of  $H_2$  and CO.

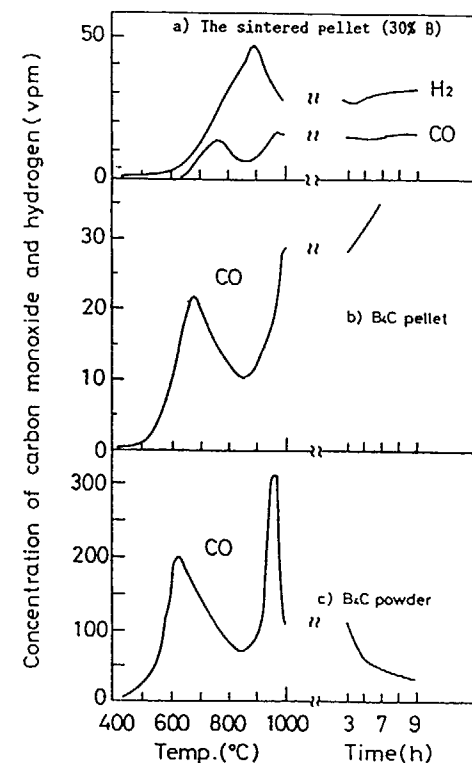


Fig. 3 Concentration change of CO and  $H_2$  with reaction temperatures and holding time at 1000°C.

Figure 3 shows the concentrations of  $H_2$  and CO which were produced by the oxidation of the sintered pellet and  $B_4C$  with water vapor under heating from room temperature to 1000°C with heating rate of 3.3°C/min. The concentrations of  $H_2$  and CO are the quantities proportioned to instantaneous reaction rates of ① and ② at each temperatures. In Fig. 3, left figures show the concentrations of produced gases at each temperatures under heating from room temperature to 1000°C and right figures show the time change in those concentrations under holding at 1000°C. The left figures indicated that the oxidation rates of free carbon produced by the reaction ① decreased from 650°C to 850°C and increased from 850°C again. It has been known [5] that the oxidation rates of carbonaceous materials with water vapor and oxygen increase with reaction temperature monotonously. Therefore, the decrease of reaction rates from 650°C to 850°C was

caused not by intrinsic character of free carbon but by molten  $B_2O_3$  produced on reaction surface which played as physical barrier against diffusion of  $H_2O$  [6,7]. From the results of surface survey for the sintered pellets reacted, it was observed that at  $550^\circ C$  the surface morphology was the same as that before reaction and at  $750$ – $850^\circ C$  the surfaces were covered by glossy glassy material. The increase of oxidation rate from  $850^\circ C$  might be due to the following two causes. The first cause is the increasing of reaction temperature. The oxidation rate of graphite materials with water vapor at  $1000^\circ C$  increased above ten times as large as that at  $850^\circ C$  [5]. In case of  $B_4C$  and the sintered pellet, the difference between at  $850^\circ C$  and at  $1000^\circ C$  was below five times, therefore, it seemed that the free carbon was oxidized under restricted condition. The second cause is the increasing of reaction surface area due to the opening of pores filled by molten  $B_2O_3$  in the sintered pellet and  $B_4C$  which was caused by the decreasing of viscosity of molten  $B_2O_3$ . The filling effect by molten  $B_2O_3$  against pores playing as diffusion paths of water vapor into matrix was explained by the time change in concentrations of CO under holding at  $1000^\circ C$ .

For  $B_4C$  pellet with large diameter of pore, the concentration of CO increased with reaction time because the filling of pores is hardly yielded, see Fig 3 (b). For the sintered pellet with small diameter of pore, the concentration of CO kept constant value because the equilibrium state between the filling and opening of pore due to the liquidity of  $B_2O_3$  is easily reached, see Fig 3 (a). On the other hand, for  $B_4C$  powder without the filling of pore, the concentration of CO decreased with the reaction time due to accumulation of molten  $B_2O_3$  and decreasing of virgin  $B_4C$ , see Fig. 3 (c). After 9 h reaction, the mass of virgin  $B_4C$  powder decreased to 50%.

In case of the oxidation rate of  $B_4C$  of the reaction ①, the peak and bottom behavior shown in the oxidation reaction for free carbon was no detected. As shown in Fig. 3 (a), the concentration of  $H_2$  increased up to  $900^\circ C$  monotonously and then decreased caused by accumulation of molten  $B_2O_3$  during heating process. The difference between the reactions of  $B_4C$  and free carbon is that the oxidation of  $B_4C$  is the reaction between virgin  $B_4C$  and  $H_2O$ , and the oxidation of free carbon is the consecutive reaction after production of  $B_2O_3$ . Fig. 4 shows the concentrations of CO and  $CO_2$  produced by oxidation of the sintered pellet in helium containing 0.65%  $O_2$  under the same thermal conditions as the reaction of water vapor, which indicated that the oxidation behavior of carbon (not limited free carbon) was about the same as that of free carbon with water vapor. Therefore, the volatile metaboric acid produced with water vapor [6–8] hardly influenced the filling of pore by molten  $B_2O_3$  and the liquidity of  $B_2O_3$ .

For the more detailed study of the oxidation behavior of free carbon, the specific surface area of the sintered pellet was measured after reaction for 1 h at each temperatures. The measured results are summarized in Table 4, which indicated that the temperature dependence of the specific surface area was similar to the results shown in Fig 3. Since the melting point of amorphous  $B_2O_3$  is  $577^\circ C$ ,  $B_2O_3$  produced at  $550^\circ C$  is a solid phase. The filling of pore at  $650^\circ C$  was hardly yielded because the specific surface area at  $650^\circ C$  was about the same as that at  $550^\circ C$ . The specific surface area at  $750^\circ C$  was 1/3 times as large as

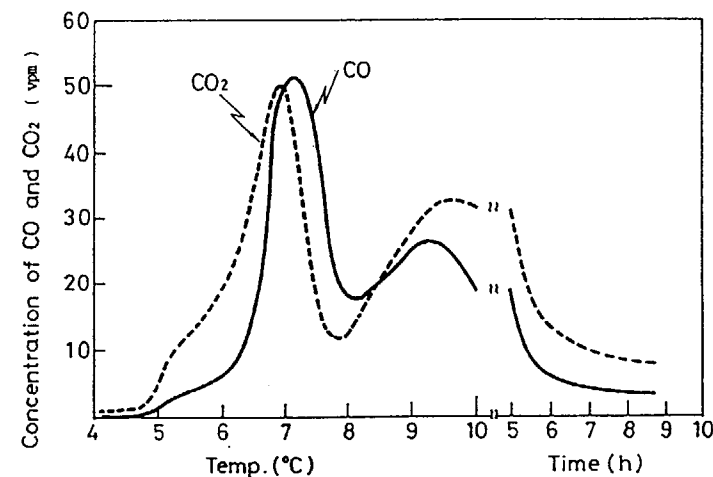


Fig. 4 Concentration change of CO and  $CO_2$  in reaction of the sintered pellet (30% B) with 0.65% oxygen in helium under heating from room temperature to  $1000^\circ C$  and then holding at  $1000^\circ C$ .

Table 4 Specific surface area of the sintered pellet (30% B) oxidized for 1 h at each temperatures.

	surface area ( $m^2/g$ )
As received	6.7
550°C	6.0
650°C	5.9
750°C	2.1
850°C	4.3
1000°C	6.6



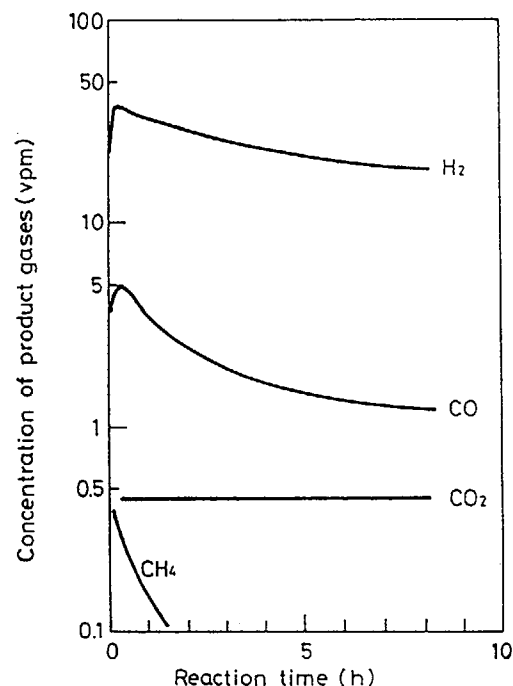


Fig. 5 Concentration change of produced gases in reaction of the sintered pellet (30% B) with water vapor in helium at 750°C.

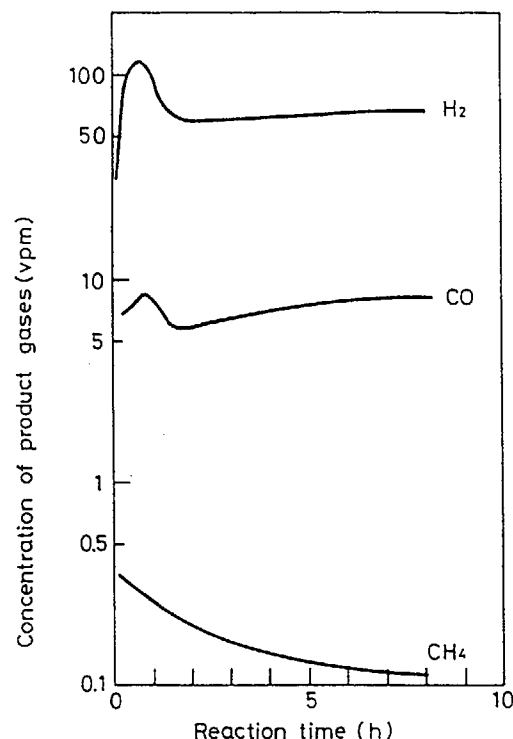


Fig. 6 Concentration change of produced gases in reaction of the sintered pellet (30% B) with water vapor in helium at 850°C.

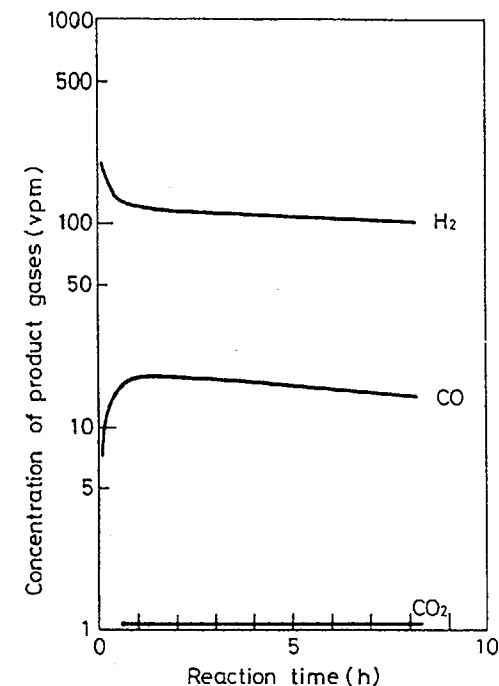


Fig. 7 Concentration change of produced gases in reaction of the sintered pellet (30% B) with water vapor in helium at 1000°C.

that at 650°C, which indicated that the filling of pore yielded briskly due to decrease of the viscosity of molten  $B_2O_3$  at 650–750°C. And with temperature the specific surface area increased resulting from opening of clogged pores due to liquidity of molten  $B_2O_3$ . For the specific surface area at 1000°C, the increase of surface area due to oxidation of graphite matrix might contribute slightly.

The change in concentrations of gases produced by reaction between the sintered pellets and water vapor at each temperatures are summarized in Figs. 5–7. The concentrations of  $H_2$  and CO gradually decreased and then kept constant values after transient state which was yielded after the beginning of the reaction. The period up to the steady state is the process for formation of physical barrier of molten  $B_2O_3$  against diffusion of  $H_2O$ . In the steady state,

the diffusion rate of  $H_2O$  reaching on the reaction surface was equal to the intrinsic reaction rates of the reactions of ①, ② and ③ on the surface.

The averaged reaction rates of the sintered pellet corresponding to the reaction ①, which were calculated by mass of residual  $B_2O_3$  in the sintered pellet after reaction for 8 h at each temperatures, is shown in Fig. 8. The temperature dependence of the averaged reaction rates exhibited the same behavior as that of the instantaneous rates for free carbon during heating process, which indicated that the effective physical barrier for  $B_4C$  and free carbon against diffusion of  $H_2O$  was homogenized by the reaction for 8 h.

The production rate of free carbon produced by the reaction ① is given from the concentration ratio of  $H_2$  to CO ( $H_2/CO$ ).  $H_2/CO$  changes from 6 to 7 corre-

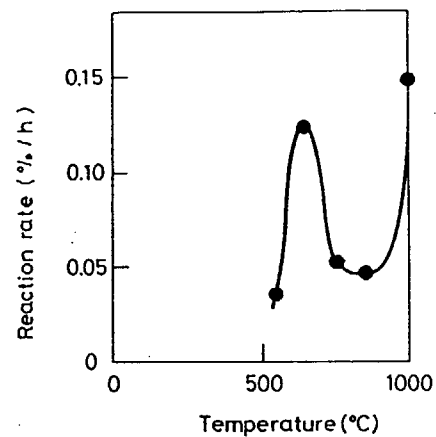


Fig. 8 Averaged reaction rate of the sintered pellet (30% B) in helium with 0.65% water vapor.

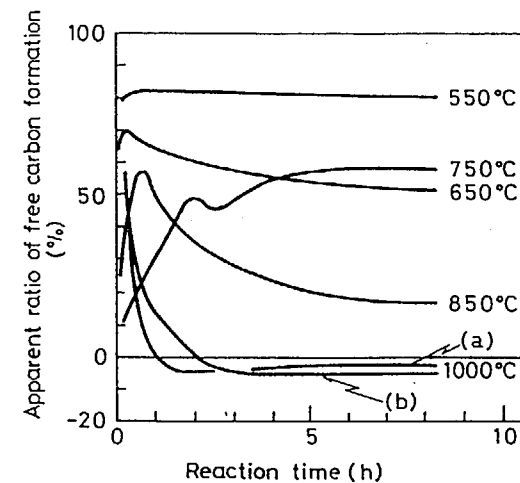


Fig. 9 Change in free carbon formation ratio in reaction between the sintered pellet (30% B) and water vapor.

Table 5 Steady state ratio of free carbon formation in reaction between the sintered pellet (30% B) and water vapor after 8 h.

Temperature (°C)	F. C. formation ratio (%)
550	8.0
650	5.2
750	5.7
850	1.7
40 wt. % B/C	-3
50 wt. % B/C	-5
1000°C	> 0

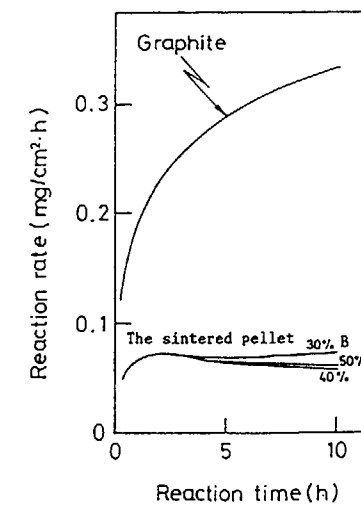


Fig. 10 Comparison of reaction rates between IG-110 graphite and the sintered pellets (30, 40 and 50% B) at 1000°C in helium with 0.65% water vapor.

sponding to the production rate of free carbon.  $H_2/CO$  is decreased by yielding of the reaction ③ and increased by production of  $CO_2$ . From the stoichiometry of reaction, the production rate of free carbon (FC) is given by the following formula ,

$$\begin{aligned} FC &= [C(F)] / \{[C(F)] + [CO]T + [CO_2]T\} \\ &= \{([H_2]T - 7[CO]T - 8[CO_2]T)/([H_2]T - [CO]T - 2[CO_2]T)\} \\ &\quad + \{6[CO]_s + 6[CO_2]_s\}/([H_2]T - [CO]T - 2[CO_2]T) \end{aligned} \quad \text{④}$$

where a note of T, [ ]T, is the concentration given by chemical analysis and a note of s, [ ]s, is the concentration of CO and  $CO_2$  produced by oxidation of graphite matrix as shown in the reaction ③. In the formula ④, the first brace is measurable quantity but the second brace is unknown quantity. Since FC is a plus quantity, the second brace is not negligible when the first brace is a minus quantity. Fig. 9 shows FC values calculated from the first brace in the formula ④, which indicated that FC values changed with reaction time corresponding to production of  $B_2O_3$  layer and then reached the constant values.

The constant values after reaction for 8 h is shown in Table 5. The values at  $1000^\circ C$ , which were the results of the sintered pellets containing 40 and 50% B (in Fig. 9, (a) and (b) are 40 and 50% B, respectively), were minus values. It has been known that the oxidation rate of graphite materials increase rapidly with burn off and then reaches the constant values. The time change in FC value at  $1000^\circ C$  shown in Fig 9 corresponded to the oxidation behavior of graphite materials mentioned above, qualitatively. The ratio of gasification rate for graphite matrix to total gasification rate, which was evaluated by supposing FC value at  $1000^\circ C$  to be zero, was about 10%.

The oxidation rates of the reactor grade graphite (brand name IG-110) and the sintered pellets with water vapor are summarized in Fig. 10. The oxidation rates of the sintered pellets at  $1000^\circ C$  were about 1/6 times as fast as that of IG-110. The oxidation rate of IG-110 increased with burn off, however that of the sintered pellets reached the constant values in an early stage of the reaction because the surface of graphite matrix was covered by molten  $B_2O_3$ . It has been well known [9-11] that the addition of B improves the oxidation resistance of graphite materials.

### 3.2 Possibility of mutual adhesion of sintered pellets

The sintered pellet adopted in the reserved shutdown system contains 30% B and is the same size as the sintered pellet tested in this report. The adhesion test of the sintered pellets was carried out for the piled up three sintered pellets under heating from room temperature to  $1000^\circ C$ . Figure 11 shows the piled up three sintered pellets after adhesion test, which exhibits that three sintered pellets were not separated due to mutual adhesion in spite of slight vibration. It can be made clear that the mutual adhesion yielded in case of oxidation of 2% of B contained in the sintered pellet, but no adhesion was observed in case of oxidation of 1.5% of B contained in the sintered pellet. The sintered pellet is porous material, so a small amount of molten  $B_2O_3$  is kept in pores and does not flow out to surface. The conditions for mutual adhesion are that the following two conditions yield simultaneously, ① temperature of the



Fig. 11 The sintered pellets (30% B) adhered mutually by reaction with water vapor.

Table 6 Estimated periods for oxidation of 2% of B contained in the sintered pellet (30% B).

Temperature ( $^\circ C$ )	Estimated period (h)
400	$1.4 \times 10^7$
550	$4.6 \times 10^4$
650	$1.3 \times 10^4$

sintered pellet exceeds the melting point of  $B_2O_3$  of 577°C even temporarily and ② above 2% of B contained in the sintered pellet is oxidized.

For the sintered pellets in the reserved shutdown system, the temperature is around 400°C during normal operation of the HTTR. Concerning oxidation rate, the periods for oxidation of 2% of B contained in the sintered pellet were estimated at 400, 550 and 650°C in helium containing 0.65% water vapor. The estimated periods are summarized in Table 6. At even 650°C, the period for oxidation of 2% of B contained in the sintered pellet was above  $10^6$  h. The maximum value of water vapor in the primary coolant of the HTTR during normal operation is 0.2 vpm, so that the water vapor concentration of 0.65% used in this experiment is a value including some margin conservatively.

From the above description, it can be concluded that the integrity of the reserved shutdown system against corrosion is maintained, i.e. the mutual adhesion of the sintered pellets in the reserved shutdown system does not yield.

#### 4. Summary and Conclusion

Corrosion tests of the sintered pellet of graphite and boron carbide, which has been adopted as a neutron absorber material in the control rod system, the reserved shutdown system, etc. of the HTTR, were carried out in helium containing 0.65% water vapor at up to 1000°C from a viewpoint of oxidation of  $B_4C$ . And from the results obtained, the conditions of mutual adhesion of the sintered pellets for the reserved shutdown system were also discussed.

The conclusions obtained showed that ;

- (1) The oxidation rates of the sintered pellet did simply not increase with temperature caused by the formation of  $B_2O_3$ .
- (2) The reaction between  $B_4C$  and  $H_2O$  was consisted of three competing reactions,  
 $B_4C + 6 H_2O = 2 B_2O_3 + 6 H_2 + C$  (F) ..... first step  
 $C$  (F) +  $H_2O = CO + 2 H_2$  and  $C$  (G) +  $H_2O = CO + H_2$  ..... second step.
- (3) The addition of B decreased the oxidation rate of graphite with  $H_2O$ .
- (4) On the sintered pellet containing 30% B which is the same specification as one in the reserved shutdown system of the HTTR, the mutual adhesion yielded when above 2% of B contained in the sintered pellet was oxidized and the temperature exceeded the melting point of the produced  $B_2O_3$  of 577°C even temporarily.
- (5) The sintered pellets for the reserved shutdown system are stored in the hopper at 400°C and the environment in the hopper is the primary coolant which is helium containing 0.2 vpm water vapor, so that the mutual adhesion does not yield.

#### Acknowledgements

The authors are indebted to Dr. T. Saito for X-ray analysis.

#### References

- [1] Department of HTTR project, JAERI-Report, to be published in 1991
- [2] Gmelin Handbook of Inorganic Chemistry B, Supplement Vol. 2, 2.1 Boron and Carbon, 117-238 (1981)

- [3] R. D. Allen, J. Am. Chem. Soc., 75 (1953) 3582
- [4] F. W. Glaser and D. Moskowitz, J. Appl. Phys., 24 (1953) 731
- [5] M. R. Everett, D. V. Kinsey and E. Roemberg, Chemistry and Physics of Carbon, 3 (1968) 289
- [6] L. M. Litz and R. A. Mercuri, J. Electrochemical Soc., 110 (1963) 921
- [7] R. E. Woodley, Carbon, 7 (1969) 609
- [8] J. T. Wenzel and D. M. Sanders, Physics and Chemistry of Glasses, 23 (1982) 47
- [9] R. E. Woodley, 8 th Conf. on Carbon, Paper C 117 Buffalo (1967)
- [10] P. L. Walker Jr., M. Shelef and R. A. Anderson, Chemistry and Physics of Carbon, 4 (1968) 287
- [11] D. J. Allardice and P. L. Walker Jr., Carbon, 8 (1970) 375

#### DISCUSSION

Questions or Comments Name: T. Sogabe

1. How did you fabricate  $B_4C/C$ ? Just sintered?
2. Have you checked  $B_2O_3$  concentration

Answer:

1. It's hot-pressed
2. Yes, (showed a example)

# EFFECT OF ATMOSPHERE ON THE BEND STRENGTH OF NUCLEAR GRAPHITE

T. MARUYAMA

Fuels and Materials Division,  
Oarai Engineering Center,  
Power Reactor and Nuclear Fuel Development Corporation,  
Oarai-machi, Ibaraki-ken,  
Japan

## Abstract

Investigations were made of effect of test environments on bend strength and fracture toughness of fine-grained isotropic graphites. Four-point bend tests were carried out in various atmospheres of air, helium and vacuum. When room temperature bend tests were carried out for specimens which had been outgassed in vacuum at high temperature, we obtained higher values than those measured in air by up to 45%. When measurements were made in helium atmosphere containing 1 to 3 ppm of water vapor, bend strength was higher by 20 to 30 % than those measured in air. When water content in helium increased to about 20 ppm, the strength became the same with that measured in air.

The high temperature bend strength of graphite specimens generally increased with increasing temperature up to 1200°C if it had not been outgassed at 1200°C. Whereas, the bend strength of specimens which had been outgassed at 1200°C showed high room temperature strength followed by negative temperature dependence up to 900°C, and then became temperature independent up to 1200°C. The fracture toughness of fully outgassed specimens measured in vacuum had higher values by about 20% than that measured in air.

## 1. Introduction

Graphite materials usually contain large amount of gases such as water, H<sub>2</sub>, CO, CO<sub>2</sub> and various kinds of hydrocarbons. The removal of these gases from graphite materials is very important for use in core structural components of HTGR. It has often been pointed out that strength of graphite is largely affected by the test environment[1-6]. The strength of graphite markedly increases when it is measured in vacuum. It also gives influence on the crack extension rates[7,8]. However, detailed study of effect of adsorbed gases on the strength has not been carried out on nuclear grade graphites.

In the present investigation, we carried out measurement of bend strength and fracture toughness of several kinds of fine grain isotropic graphites in various test atmosphere and studies were made of effect of absorbed gases on the strength of nuclear graphite.

## 2. Experiments

### 2.1 Bend tests at room temperature

Specimens used in the present investigation are fine-grain, isotropic graphite ISO-63 and ISO-630U, IG-430U (Toyo Tanso Co., Ltd) and ETP-10 (Ibiden Co., Ltd). The graphite ISO-630U is purified material of ISO-63 and the ash content is reported to be about 10 ppm, while that of ISO-63 is about 500 ppm. The graphites IG-430U and ETP-10 are also purified materials. Some physical properties of these materials are shown in Table 1.

The bend tests were carried out in accordance with the method proposed as Japan Industrial Standard Method for Bend Test of Fine Ceramics, JIS-R1601 (1981). As shown in Fig. 1, the specimen size was 3 x 4 x 40 mm<sup>3</sup>. The bend strength was obtained by the four-point bend method with the inner span 10 mm and the outer span 30 mm. The cross-head speed was 0.5 mm/min. The test jig was made of a high-density, high strength graphite with silicon carbide anvils of 4 mm in diameter.

Prior to the bend tests at room temperature, the specimens were outgassed in the temperature range from room temperature

Table 1. Physical properties of isotropic graphites.

Graphite materials	ISO-63(630U)	IG-430U	ETP-10
Density(g/cm <sup>3</sup> )	1.82	1.82	1.75
Electrical resistivity( $\mu\Omega$ )	16.5	9.0	14
Tensile strength(MPa)	53.9	37.2	35
Bending strength(MPa)	76.4	53.9	60
Modulus of elasticity(GPa)	13.7	10.8	11
Thermal conductivity (W/mK, T=20°C)	70	139	104
Thermal expansion coefficient (10 <sup>-6</sup> /K, T=350-450°C)	5.5	4.8	3.8
Average grain size( $\mu$ m)	10	10	40

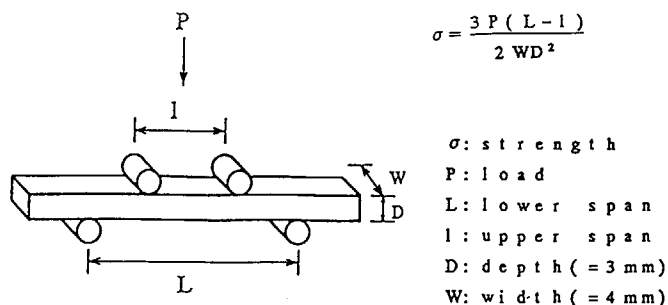


Fig.1 Schematic diagram of specimen for four-point bend tests.

to 1200°C under vacuum of  $1 \times 10^{-3}$  Pa for 15 to 30 min. After specimens were cooled down to room temperature in vacuum, the bend tests were done in vacuum of  $1 \times 10^{-3}$  Pa or in helium atmosphere containing 1 to 20 p.p.m of water vapor. The water content in helium was controlled by adjusting flow rate of dry helium to wet helium passed through a water bubbler. The water content in the helium atmosphere was measured at the outlet of the vacuum chamber with a hygrometer. A bend test in air was also conducted for the specimen which was immersed in water after outgassed at 500°C under vacuum for 30 min.

The apparatus used in this experiment was a high temperature testing machine (Instron Co. Type 8015). The testing machine provides a turning table in the vacuum chamber for automatic sample change and a bend test for twelve specimens can be carried out at one time in a high vacuum at temperatures up to 1600°C. By using this apparatus, both outgas treatments and the successive bend tests in vacuum or in helium atmosphere can be done without exposing specimens to air.

## 2.2 Bend tests at high temperature

In order to find out effect of outgas treatment on the high temperature strength, two sets of bend tests were done for IG-430U graphite from room temperature to 1200°C in steps of 300°C. In the first set of measurements, the specimens were fully outgassed and then they were subjected to the bend tests. In the second set of measurements, bend tests were made at each temperature in vacuum without outgas treatments.

## 2.3 Measurement of fracture toughness

Fracture toughness of IG-110U and IG-430U graphites were measured in air and in vacuum using SENB (Single-Edged-Notched-Beam) method as shown in Fig. 2. The specimens having

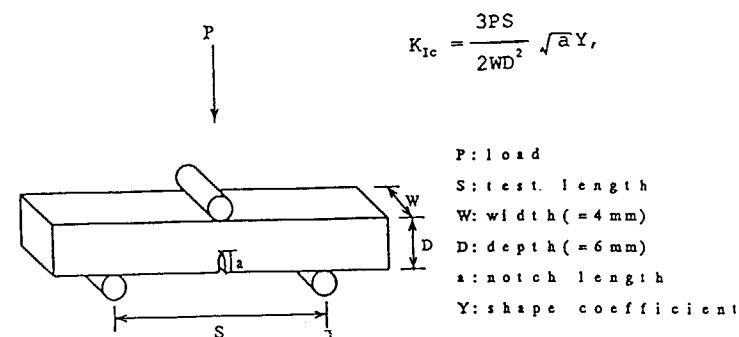


Fig.2 Schematic diagram of specimen for fracture toughness tests.

dimensions of 4 x 6 x 40 mm<sup>3</sup> provides a center notch of 2.5 mm in length. The notch radius was around 20 μm which was measured with an optical micrometer.

The fracture toughness was calculated from the following equation,

$$K_{Ic} = \frac{3PS}{2WD^2} \sqrt{aY}, \quad (1)$$

where, P is load, S the span length, W the specimen width, D the specimen height, and a the notch length. The shape factor Y is given in terms of a/D as

$$Y = A_0 + A_1(a/D) + A_2(a/D)^2 + A_3(a/D)^3 + A_4(a/D)^4. \quad (2)$$

Here, the method to obtain values of coefficients  $A_i$  ( $i = 0$  to 4) are given by Wakai et al. [9] for specimens with  $4 \leq S/D \leq 20$ . In the present investigation, since the value  $S/D = 5$ , the values  $A_i$  and the shape factor Y were calculated in accordance with the method given by Wakai et al. The notch length of each specimen was measured from the optical photomicrograph of fractured specimen.

Table 2. Effect of test atmosphere on bend strength of ISO-63 graphite at room temperature.

test condition	outgas treatment	strength $\sigma_t$ (MPa)	number of specimen	increase in strength (%)
in air	—	$80 \pm 4.3$	31	—
	dipped in water	$78 \pm 5.7$	22	-2.5
in vacuum ( $1.3 \times 10^{-4}$ Pa)	800°C, 30min	$112 \pm 16$	12	40
	500°C, 30min	$105 \pm 13$	20	30
	250°C, 30min	$99 \pm 7.2$	12	25
	20°C, 30min	$90 \pm 3.2$	12	13
	20°C, 24hr	$90 \pm 3.6$	12	13

### 3. Results and Discussion

#### 3.1 Bend tests at room temperature

Table 2 shows the bend strength of ISO-63 graphite measured at room temperature in air and in vacuum. The bend strength of as-received specimen in air was 80 MPa. When the specimen which had been outgassed at 500°C under vacuum for 30 min was immersed in water and then subjected to the bend tests, the strength was 78 MPa, which is nearly the same value with that of as-received specimen. The specimen weight increased by 6 % by the immersion in water. A large amount of water in the graphite materials gives little or no influence on the strength of the materials measured in air.

On the other hand, when materials was outgassed at 20°C for 30 min in vacuum, an increase in strength by 13% was obtained. A further outgas treatment up to 24 h at room temperature does not cause a further increase in strength.

When the materials was outgassed at 500°C in vacuum, the strength increased by 30%. The increase in bend strength has a strong dependence on the outgas temperature, as shown in Fig. 3. The bend strength increased with increasing outgas

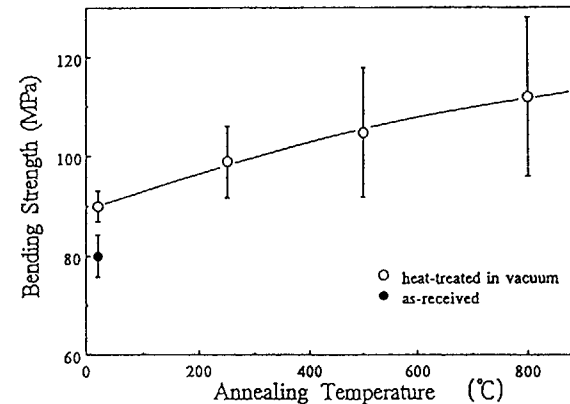


Fig.3 Bending strength vs. annealing temperature of ISO-63 graphite measured at room temperature.

Table 3. Effect of test atmosphere on bend strength of ETP-10 graphite at room temperature.

test condition	outgas treatment	strength $\sigma$ , (MPa)	number of specimens	increase in strength (%)
in air	—	$52 \pm 3.2$	12	—
	500°C, 30min	$52 \pm 1.9$	12	—
in vacuum ( $1.3 \times 10^{-4}$ Pa)	1200°C, 30min	$76 \pm 11$	12	47
	500°C, 30min	$75 \pm 10$	12	45
in He atmosphere ( $H_2O:3ppm$ )	500°C, 15min	$64 \pm 5.7$	23	23

temperature, which indicates that gases adsorbed on the surface of graphite caused a substantial degradation in strength. It is noted that scatter in strength also increased as shown in Table 2 and in Fig. 3. The cause of increase in the scatter is not clear at present.

Table 3 shows results of bend tests on graphite ETP-10. Increase in strength of 45 and 47 % were obtained after outgas treatments at 500°C and 1200°C, respectively. We note that the increase in strength of ETP-10 graphite is slightly larger than that observed in the graphite ISO-63. Since the amount of impurities contained in the graphite ETP-10 is smaller than that of the graphite ISO-63, it is inferred that gasses are more easily removed from purified graphite than that from graphites containing impurities.

When the specimen is outgassed at 500°C for 30 min and then quickly measured in air, the strength falls to the original value of as-received specimen as shown in Table 3. This result indicates that the effect of outgas treatment disappears if specimens are exposed to air.

When strength was measured in helium atmosphere containing 3 ppm of water vapor, an increase in strength by 23% was observed for the graphite ETP-10 which is outgassed at 500°C for

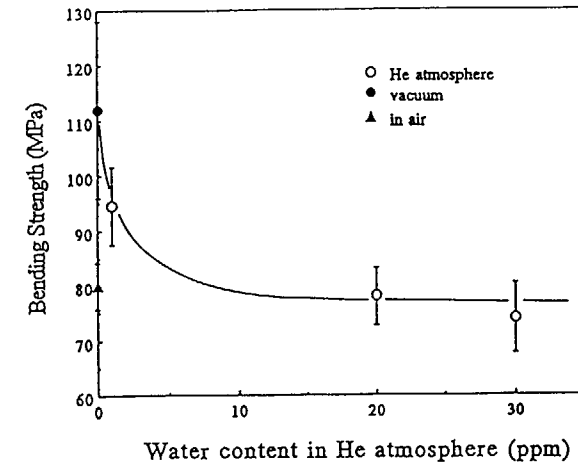


Fig.4 Effect of water content in helium on bending strength of ISO-630U graphite.

30 min in vacuum. Although the strength in helium is higher than that of as-received specimen, the value is lower than that outgassed at 500°C and measured in vacuum. It is considered that an existence of 3 ppm of water vapor in helium has caused a substantial decrease in strength of graphite. In order to find out the effect of water content in helium atmosphere, bend strength was measured in helium containing 1 to 30 ppm of water. As shown in Fig.4, a decrease in bend strength was 15% in helium containing 1 ppm. When water content in helium became 20 ppm, the bend strength is almost the same with that measured in air. These results indicate that even a small amount of water vapor in test atmosphere gives influence on the strength of graphite materials.

### 3.2 Bend test at high temperature

Figure 5 shows high temperature bend strength of graphite IG430-U. The values denoted by the symbol ○ are the strength



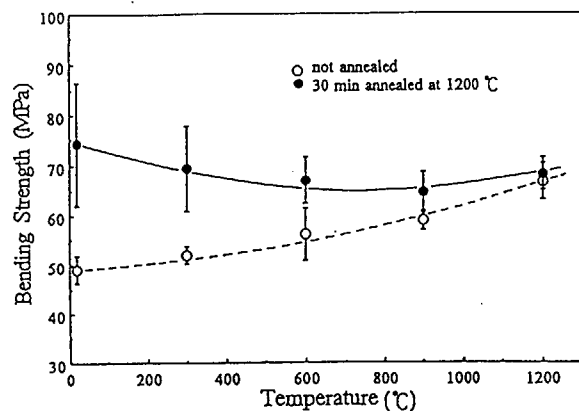


Fig.5 High temperature bending strength of IG-430U graphite.

measured without outgass treatment and the values denoted by the symbol ● are that after outgas treatment at 1200°C for 30 min. As shown in Fig. 5, there are large difference between them. The strength measured without outgas treatment (denoted by the symbol ○) increase with increasing temperature, and it showed 40% of increase at 1200°C. Whereas, the strength of graphite which had been outgassed at 1200°C (denoted by the symbol ●) showed a tendency to decrease with increasing temperature up to 900°C and then turned to increase up to 1200°C.

It has generally been accepted that strength of graphite materials increases with increasing temperature up to about 2000°C. The positive temperature dependence in strength of graphite materials is interpreted as follows[10]. Graphite crystallites exhibit large anisotropy in thermal expansion coefficient. The anisotropy in thermal expansion cause residual stress and formation of microcracks when materials are cooled down from graphitizing temperature. On heating, porosity decreases because of the closure of microcracks so that internal stress around them are relieved. The thermal

closure of these microcracks is believed to explain increase in strength as well as increase in elastic modulus with increasing temperature.

However if we treat the graphite at high temperatures to remove gases from the material, the strength of graphite shows different temperature dependences as shown in Fig. 5. We might conclude that substantial portion of increase in strength at high temperatures previously reported by many investigators may be originated from removal of gases from the graphite at high temperatures.

### 3.3 Measurement of fracture toughness

Table 4 shows results of measurement of fracture toughness of graphite IG-110U and IG-430U at room temperature. The fracture toughness  $K_{Ic}$  of graphite IG-110U measured in air was  $0.74 \text{ MPa}\sqrt{\text{m}}$ . The  $K_{Ic}$  of graphite IG-110U previously reported ranged 0.9 to  $1.0 \text{ MPa}\sqrt{\text{m}}$  which is larger than that obtained in the present investigation. The reason why present  $K_{Ic}$  exhibited a smaller value is that the specimen size is smaller than those used for the above measurements[11].

Table 4. Effect of test atmosphere on fracture toughness of IG-110U and IG-430U graphites.

graphite	test condition	outgas treatment	$K_{Ic} (\text{MPa}\sqrt{\text{m}})$	number of specimens
IG-110U	in air	—	0.74	10
	in vacuum ( $2.8 \times 10^{-3} \text{ Pa}$ )	1200°C, 30min	0.90	10
IG-430U	in air	—	0.90	11
	in vacuum ( $2.9 \times 10^{-3} \text{ Pa}$ )	1200°C, 30min	1.12	11

The fracture toughness of graphite IG-110U and IG-430U measured in vacuum after they had been outgassed at 1200°C in vacuum are shown in Table 4. They have larger values than those measured in air by 21 and 24 %, respectively. We note here that the increase in fracture toughness is a little bit smaller than those found in bend strength measurement. It may be considered that the difference is caused by the method of three-point bending and the four-point bending. However, the reason of this difference is not clear at present.

#### 4. Conclusion

The effect of test environment on bend strength and fracture toughness of fine-grained isotropic graphites was investigated. The results obtained are as follows:

- (1) If room temperature bend test is carried out in vacuum after specimen had been fully outgassed, we will obtain higher strength by about 45% than that measured in air.
- (2) If air is admitted after outgas treatments, the bend strength of graphite decrease to its original value.
- (3) If bend test is carried out in helium containing 1 to 3 ppm of water, we will obtain higher strength by about 20 to 30 % than that measured in air. It decreases to the original value if water content becomes around 20 ppm.
- (4) In regard to temperature dependence of bend strength of graphite, a substantial portion of increase in strength at high temperatures previously reported by many investigators may be originated from removal of gases from the graphite at high temperatures.
- (5) The fracture toughness measured in vacuum increased by about 20% than that measured in air.

#### ACKNOWLEDGEMENTS

This research was carried out at Research Laboratory for Nuclear Reactors, Tokyo Institute of Technology. The author

would like to thank Prof. T. Oku at Ibaraki University and Dr. T. Arai at JAERI for their encouragements and helpful discussions.

#### REFERENCES

- [1] G. W. Rowe, Nucl. Eng. (1962) 102-103.
- [2] G. W. Rowe, Wear (1960) 454-462.
- [3] R. J. Diefendorf, Proc. 4th. Carbon Conf., Buffalo, Pergamon Press, (1960) 489-496.
- [4] R. J. Diefendorf, Proc. 4th. Carbon Conf., Buffalo, Pergamon Press, (1960) 483-488.
- [5] T. Maruyama, M. Eto and T. Oku, Carbon 25 (1987) 723-726
- [6] O. H. Logsdail, AERE Report 5721 (1968)
- [7] P.H. Hodgkinson, J. S. Nadeu, J. Mater. Sci. 10 (1975) 846-856.
- [8] S. W. Freiman, J. J. Mecholsky, J. Mater. Sci. 13 (1978) 1249-1260.
- [9] F. Wakai, S. Sakaguchi, Y. Matsuno, J. Ceram. Soc. Jpn., 93 (1985) 81-82 (in Japanese).
- [10] P. L. Walker, Jr., P. A. Thrower, "Chemistry and Physics of Carbon", vol. 13 Marcel Dekker, Inc., New York and Basel pp.233-236.
- [11] T. Oku, S. Ishiyama, M. Eto et al. J. Ceram. Soc. Jpn., 96 [7] (1988) 773-777 (in Japanese).

## CORROSION TESTS OF MATRIX GRAPHITES

A.I. VAVILIN, E.T. KULIKOV,  
S.I. MOZZHERIN, A.S. CHERNIKOV  
Scientific and Industrial Association 'Lutch',  
Podol'sk, Union of Soviet Socialist Republics

### Abstract

The results of corrosion tests of matrix graphites based on calcirated (3OPG graphite) and non-calcinated (MPG graphite) petroleum cokes in the temperature range 600-1200 °C and at the water vapour concentration in helium 0.01-1 vol.% are considered. Empirical expressions of corrosion rate are obtained. Investigation results of matrix-graphite phase-components reactivity are considered. It is shown that the filler graphite 3OPG has the minimum activity towards the water vapour.

The influence of helium pressure at the constant partial pressure of water vapour, porous structure and of impurities content on the matrix graphite oxidation rate are considered.

The results of corrosion tests of irradiated specimens of 3OPG matrix graphite are given.

### I. INTRODUCTION

The presence of active impurities in helium coolant ( $H_2O$ ,  $O_2$ ,  $CO$ ,  $CO_2$ , etc.) results in graphite-matrix oxidation in HTGR core. The chemical activity of oxygen to graphite is considerably higher than that of other impurities.

However, the possibility of water ingress into the coolant through leakages in the steam generator units even under normal operating reactor conditions puts the problem of graphite corrosion by water vapour in the foreground. Under accident conditions caused by the steam generator pipes breakage water mass ingressed in the helium circuit increases considerably. That's why while HTGR fuel elements (FE) developing much attention is paid to the investigations of matrix graphite corrosion in helium containing water vapours. Some results of these investigations are considered in this paper.

### II. EXPERIMENTAL TECHNIQUE

Experiments were carried out on specimens matrix graphite based on calcinated (3OPG graphite) and non-calcinated (MPG graphite) petroleum cokes. Some characteristics of the tested specimens are given in Table 1.

Matrix graphite corrosion rate measurement was carried out by thermogravimetry method at TAG 24. Setaram. The specimen of a cylindrical form ( $\varnothing$  6 mm,  $l$  = 20 mm) cut out from the spherical FE imitator was loaded into the installation by means of the platinum suspension, after that muffles and scales volumes and gas lines were evacuated and helium washed several times. Helium was additionally purified by passing through the trap with the molecular sieve 5A placed into Dewar flask containing liquid nitrogen. This allowed to lower oxygen concentration in helium down to  $2 \cdot 10^{-4}$  vol.%.

Table 1

Characteristics of matrix graphite specimens for corrosion tests

Properties	Material	30PG-matrix graphite	MPG - matrix graphite
Filler		Calcinated petroleum coke	Non-calcinated petroleum coke
Binder		Coal-tar pitch 20%	Coal-tar pitch 20%
Manufacture method		Moulding with subsequent sintering	Moulding with subsequent sintering
Temperature of final heat treatment, °C		1800	1800
Total ash content, %		≤ 0.03	≤ 0.03
Density, g/cm <sup>3</sup>		1.9	1.9
Bending strength, MPa		24	34

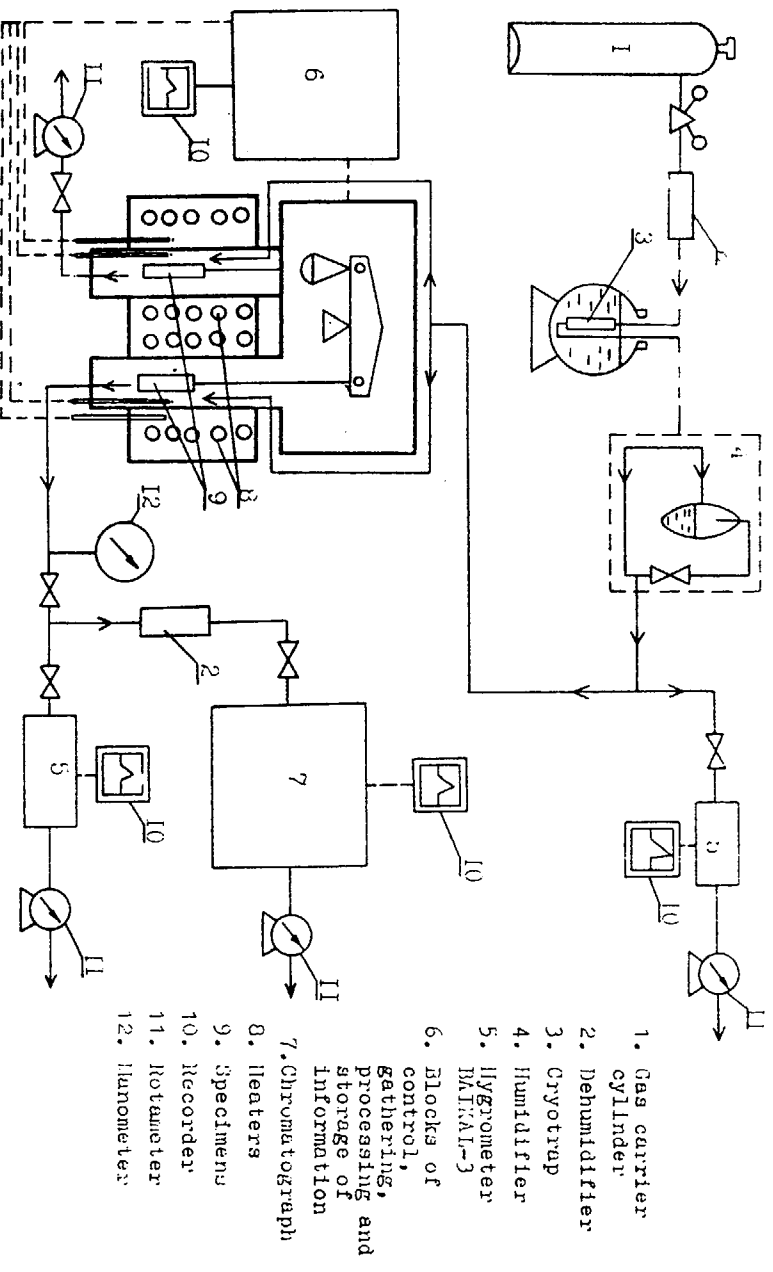


FIG. 1. Experimental rig scheme.

After washing the specimen was heated up to the required temperature in the purified helium flow, then the purified helium was replaced by the helium containing the predetermined quantity of water vapour. Helium was humidified being passed through the distilled water ampoule disposed in a thermostat. Humidity was controlled by BAIKAL-3 hygrometer and the required water vapour concentration was reached by varying the thermostat temperature.

When the degree of specimen burn-off reached the predetermined value, the humidified gas was replaced by the purified gas and the specimen was cooled. The installation schematic diagram is given in fig. 1.

Corrosion investigations were carried out at the absolute pressure 0.12 MPa in the gas mixture flow characterized by Reynolds numbers 0.1-1 (laminar regime) at the temperature range 600-1200 °C, water vapour concentration in helium ( $C_{H_2O}$ ) varying from 0.01 to 1 vol. %.

Besides the above-mentioned corrosion tests the experiments on estimation of helium pressure influence on corrosion rate were carried out. The experiments were carried out on cylindrical specimens of MPG matrix graphite ( $\varnothing$  6 mm,  $l$  = 20 mm) at the temperature 900 °C, water vapour partial pressure  $5 \cdot 10^{-3}$  MPa and helium pressure 0.5-6 MPa. The rig was an autoclave through which the humidified helium was pumped during an hour at 20 l/min flow rate. The flow rate value was chosen so that during the experiment the variation of water vapour concentration in the autoclave was less than

10%. The corrosion rate was determined from the variation of specimens mass.

Besides the above-mentioned thermogravimetry method, the standard techniques such as estimation of specific magnetic susceptibility (Faraday method), specific free surface (BET-method, low-temperature krypton adsorption), radius pore distribution (mercury porometry), specific electrical resistance (four point method), density (hydros-tatic weighing) were used to determine matrix-graphite phase - components reactivity as well as the relation of porous material structure and its corrosion rate.

### III. RESULTS AND DISCUSSION

Thermogravimetry technique with automatic scales constantly indicating specimen mass variation during the experiment allows to analyse corrosion process mechanisms. Reaction

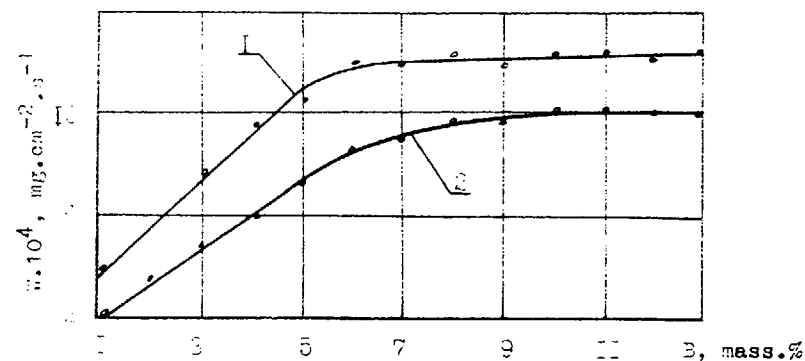


FIG. 2. Matrix graphite corrosion rate vs burn-off ( $T = 100^\circ\text{C}$ ,  $C_{H_2O} = 1$  vol.%): 1 — MPG matrix graphite; 2 — 30PG matrix graphite.

rate of water vapour matrix graphite as a function of burn-off is represented in fig. 2. The unstationary process of oxidation in a wide range of burn-off results in a significant inaccuracy of corrosion rate evaluation. Perhaps it is the maximum corrosion rate value attainable at porous reaction graphite layer stabilization which gives the full characteristic of material corrosion resistance. At the same time this value is conservative because it is obtained at high material burn-off accompanied by reaction layer crumbling. The corrosion rate conservative values are given below. Experimental dependencies of matrix graphite corrosion rate on temperature are given in fig. 3. The peculiar feature of the attained functions is their two-stage character. The experimental data were processed according to known macrokinetics equations primarily derived by Ya.B.Zeldovich /1/:

$$W = \beta(C_0 - C_s) \quad (1)$$

$$W = \sqrt{\frac{2}{n+1} \cdot D_1 \cdot K_1 C_s^{n+1}} \quad (2)$$

where  $W$  - corrosion rate,  $\text{kg/m}^2 \cdot \text{s}$ ;

$C_0$  - the oxidant concentration ( $\text{H}_2\text{O}$ ) in a volume;

$C_s$  - the oxidant concentration on the specimen surface;

$\beta$  - a mass transfer coefficient equal to  $\frac{\text{Nu}D}{d}$ ,

where  $\text{Nu}$  - the Nusselt number;  $D$  - an interdiffusion coefficient,  $d$  - a specimen typical size;

$D_1$  - an oxidant effective diffusion coefficient in a specimen volume (considered to be constant);

$K_1$  - the reaction rate constant;

$n$  - the reaction order.

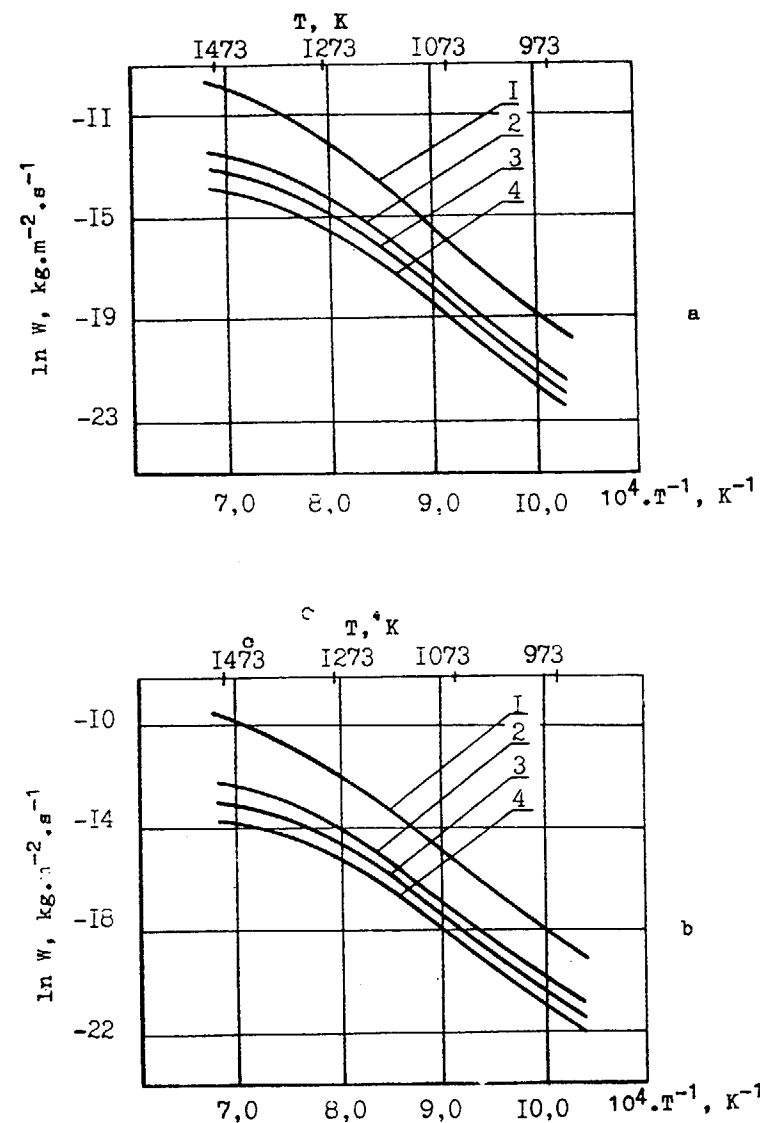


FIG. 3. Matrix graphite corrosion rate vs temperature: a - 30PG matrix graphite; b - MPG matrix graphite; 1 - 1 vol.%  $\text{H}_2\text{O}$ ; 2 - 0.08 vol.%  $\text{H}_2\text{O}$ ; 3 - 0.04 vol.%  $\text{H}_2\text{O}$ ; 4 - 0.02 vol.%  $\text{H}_2\text{O}$ .

Experimental data analysis according to equations (1) and (2) shows that the first range ( $T \leq 960^\circ\text{C}$ ) in fig.3 corresponds to kinetics determined by the chemical interaction rate. In this range the corrosion rate is satisfactorily described by the expressions:

$$\begin{aligned} W_{30PG} &= 5.5 \cdot 10^7 \cdot \exp(-33600/T) \cdot C^{0.65} \\ W_{MPG} &= 7.2 \cdot 10^6 \cdot \exp(-30800/T) \cdot C^{0.65} \end{aligned} \quad (3)$$

The second temperature range  $960^\circ < T \leq 1200^\circ\text{C}$  corresponds to kinetics determined by water vapour diffusion transfer in matrix graphite pores. In this range the corrosion rate is expressed by the equation:

$$\begin{aligned} W_{30PG} &= 123 \cdot \exp(-14344/T) C \\ W_{MPG} &= 36 \cdot \exp(-12530/T) C \end{aligned} \quad (4)$$

In the investigated temperature range ( $600-1200^\circ\text{C}$ ) the variation of apparent activation energy takes place from 267 kJ/mol. down to 115 kJ/mol. for 30PG matrix graphite and from 244 kJ/mol. down to 104 kJ/mol. for MPG matrix graphite.

The dependence of MPG matrix graphite corrosion rate on helium pressure ( $T=900^\circ\text{C}$ ,  $P_{\text{H}_2\text{O}}=5 \cdot 10^{-3}$  MPa) plotted on the base of the experimental data is given in fig. 4. As it can be seen in the range  $0.1 \leq P \leq 1.5$  MPa corrosion rate slightly depends on helium pressure containing the constant partial pressure of water vapour and in the range  $1.5 < P \leq 6.0$  MPa corrosion rate is proportional to  $1/\sqrt{P}$ .

Corrosion mechanisms realization boundaries and corrosion rate are determined not only by test conditions but

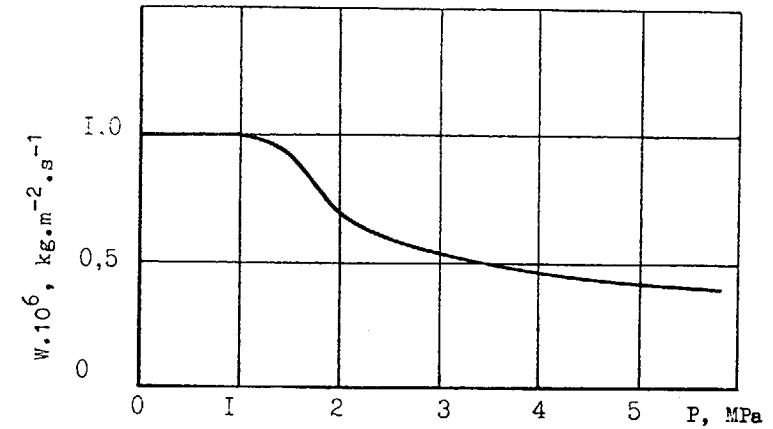


FIG. 4. MPG matrix graphite corrosion rate vs coolant pressure under constant partial pressure of water vapour ( $T = 900^\circ\text{C}$ ,  $P_{\text{H}_2\text{O}} = 5 \cdot 10^{-3}$  MPa).

also physical and chemical properties of the initial material. It is known that corrosion rate of carbon-graphite materials depends, for example, on the graphitization degree. Thus, poorly graphitized binder coke residue /2/ is subjected to corrosion in the first place. The investigations of filler and binder reactivity of 30PG and MPG matrix graphites were carried out. Magnetic susceptibility was chosen as a characteristic of matrix graphite. The magnetic susceptibility is an additive value of material phase components /3/ and submits to the equation:

$$\chi_{MG} = (1-x)\chi_f + x\chi_b \quad (5)$$

where  $\chi_{MG}$ ,  $\chi_f$ ,  $\chi_b$  is a specific magnetic susceptibility of matrix graphite, filler and binder respectively;  $x$  is the coke yield from the binder.

Table 2

Average values of specific magnetic susceptibility of matrix graphites and their phase components at the temperature 20 °C

Material	Specific magnetic susceptibility CGS/g $\times 10^6$	
	Initial	After oxidation $T=1000^\circ\text{C}$ , $C_{H_2O}=1$ vol.%
3OPG filler graphite	-6.1	-6.1
MPG filler graphite	-5.6	-5.6
Binder coke	-3.6	-3.6
3OPG matrix graphite	-5.82	-5.95
MPG matrix graphite	-5.4	-5.42

The results showed (Table 2) that 3OPG filler graphite has the minimum reactivity towards the water vapour. MPG phase components have approximately the same reactivity.

As it was shown above, matrix graphite corrosion under these conditions has the volume character. Consequently corrosion rate of matrix graphite should depend on their porous structure. Differential curves of pore radius distribution are given in fig. 5. The porous structure of these matrix graphites has bimodal pore distribution. Both materials have approximately the same pore volume of 0.065-0.066  $\text{cm}^3/\text{g}$  and specific free surface of 0.3-0.4  $\text{m}^2/\text{g}$ . Oxidation leads to

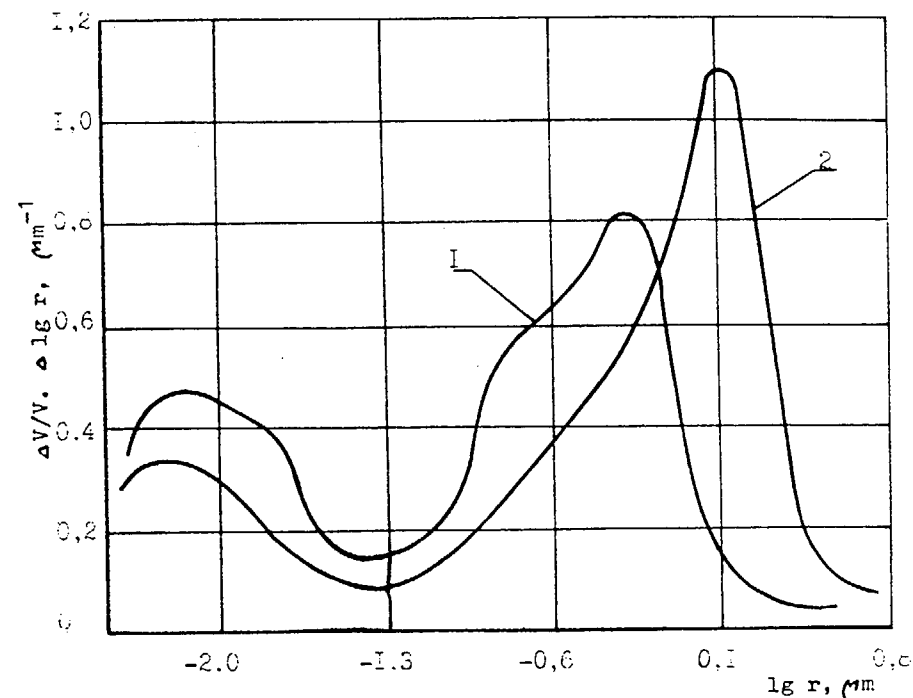


FIG. 5. Differential curves of pore distribution by sizes: 1 — MPG matrix graphite; 2 — 3OPG matrix graphite.

significant changes of the porous structure. For example, at the oxidation of 3OPG matrix graphite specimen to 3 mass % burn-off pore volume increased by 50%, and free surface increased by 1.5 order (fig. 6).

Porosity increase of matrix graphite specimens as a result of corrosion leads to their mechanical strength decrease. Thus, bending tests on MPG matrix graphite specimens after corrosion at  $T=1000^\circ\text{C}$ ,  $C_{H_2O}=1$  vol.% and burn-off of 10 mass % showed 2 time strength decrease.



Table 3

Corrosion test results of 30P3 matrix graphite specimens ( $T=1000^{\circ}\text{C}$ ,  $\text{C}_{\text{H}_2\text{O}}=1 \text{ vol.}\%$ , 10 h) in parallel and perpendicular directions to the moulding axis

Density, $\text{g/cm}^3$	Specific electrical resistance, $\text{m}\Omega \cdot \text{cm}$		Specific surface, $\text{m}^2/\text{g}$		Specific pore volume, $\text{cm}^3/\text{g}$		Cut out direction	Corro- sion rate, $\text{g/cm}^2 \cdot \text{h} \times 10^3$
	before oxidation	after oxidation	before oxidation	after oxidation	before oxidation	after oxidation		
1.80	1820	2690	0.29	3.55	0.099	0.155	"	3.76
	1480	2070	0.29	3.36	0.096	0.143	L	3.26
1.88	1500	1870	0.44	2.93	0.075	0.101	"	2.47
	1250	1470	0.32	2.28	0.068	0.097	L	2.1
1.90	1510	1920	0.4	3.15	0.066	0.096	"	2.3
	1200	1450	0.4	2.1	0.064	0.089	L	1.9

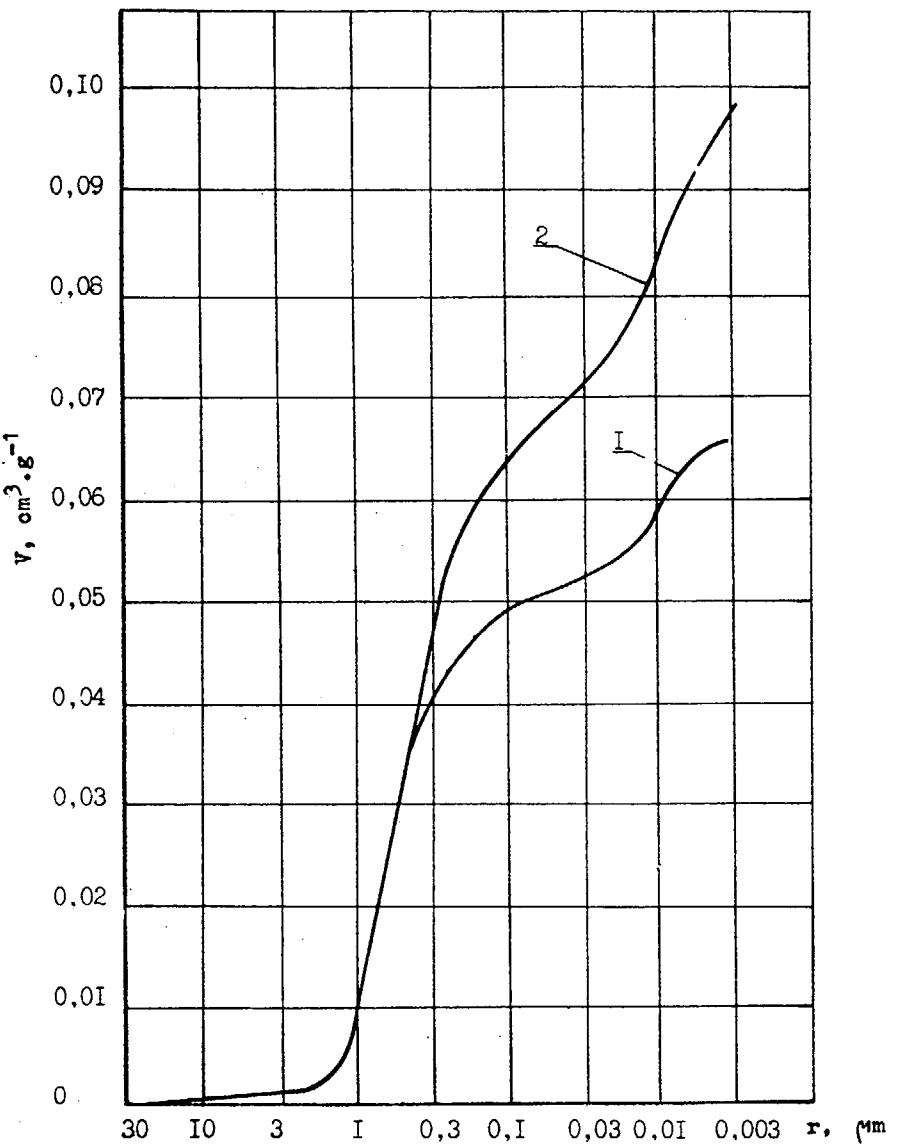


FIG. 6. Pore distribution by sizes in 30 PG matrix graphite specimen: 1 — before oxidation; 2 — after oxidation; ( $T = 1000^{\circ}\text{C}$ ,  $\text{C}_{\text{H}_2\text{O}} = 1 \text{ vol.}\%$ ).

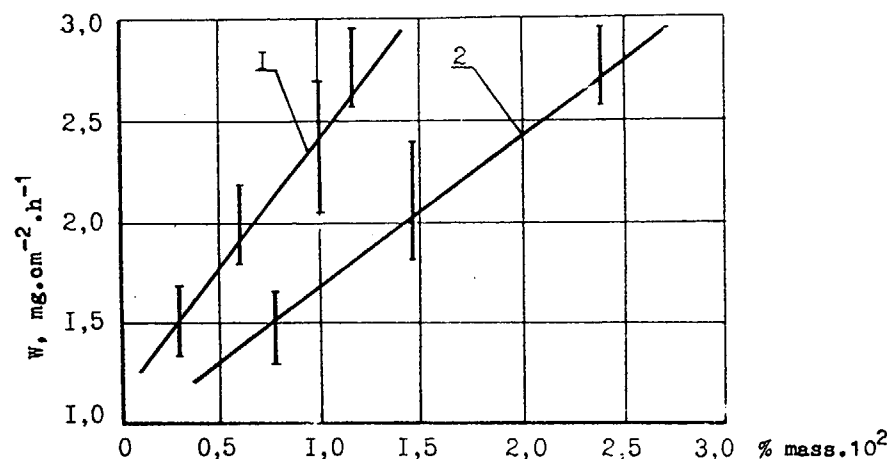


FIG. 7. Corrosion rate vs MPG matrix graphite impurities content: 1 — iron concentration (ash content is  $\sim 0.03$  mass %); 2 — ash content.

The most peculiar difference of the materials corrosion is the oxidation isotropy of MPG matrix graphite and the oxidation anisotropy of 30PG matrix graphite. 30PG matrix graphite in the initial state is an anisotropic material which can be judged by the specific electrical resistance of specimens cut out of the spherical FE imitator in parallel and perpendicular direction to the moulding axis (Table 3). Corrosion test results showed that the specimens cut out in the parallel direction to the moulding axis were oxidized more actively and the corrosion rates relationship was approximately proportional to the degree of anisotropy.

One can also observe the interconnection of corrosion rate with density and specific volume of specimen pores (Table 3). When specimen density increases from  $1.80 \text{ g/cm}^3$

up to  $1.90 \text{ g/cm}^3$  and pore volume decreases, the corrosion rate of 30PG matrix graphite decreases by a factor of 1.5.

Impurities influence much corrosion resistance of matrix graphite. Impurities quantity in graphite is characterized by such a parameter as ash residue. According to the X-ray spectrum analysis data the iron constitutes the main mass of the ash residue of MPG matrix graphite ( $1 \times 10^{-3}$ – $5 \times 10^{-3}$  mass %). The analysis of the up-to-date results permitted to determine the dependences of corrosion rate on iron and ash contents at the constant volume of the open porosity ( $\sim 0.66 \text{ cm}^3/\text{g}$ ). In fig. 7 the dependences of corrosion rate on iron content at the constant ash content (0.03 mass %) and on ash content are given. The corrosion rate increases with the increase of iron content and ash residue.

Together with unirradiated specimens of matrix graphite the specimens cut out from the shell of FE, preliminary irradiated at a temperature of  $800\text{--}1100^\circ\text{C}$  and neutron fluence  $(1.3\text{--}2) \cdot 10^{21} \text{ cm}^{-2}$ , were subjected to oxidation. The oxidation was carried out in a helium flow, containing 1 vol.% of water vapour at the temperature of  $1000^\circ\text{C}$  during 1–2 h.

In Table 4 the average results of 8 tests are given as the example of 30PG matrix graphite. The results of these tests show that under irradiation influence the specific free surface of matrix graphite increases in average by 62% and specific pores volume decreases in average by 17% and density increases. The oxidation is accompanied by the increase of the specific free surface of irradiated and unirradiated specimens by a factor of 3.1. and 4.7 for an hour and

by a factor of 4.1 and 7 for 2 hours of oxidation, respectively. Specific pores volume equally increases approximately by 20% for an hour and by 43% for 2 hours.

In this case corrosion rate of the irradiated specimens is less than the unirradiated ones by a factor of 2.

#### IV. CONCLUSION

Summerizing the results of the corrosion tests of matrix graphite on the base of 3OPG and MPG graphite fillers one can note the following:

- in the tested temperature range, water vapour concentrations in helium and pressure 0.12 MPa corrosion has a volumetric character;
- corrosion resistance of 3OPG matrix graphite is higher than that for MPG but when during the tests temperature increases this difference decreases;
- corrosion of 3OPG matrix graphite has an anisotropic character, is accompanied by a primary burn-off of the coke-liner; and higher in the direction parallel to the axis of spherical fuel element moulding;
- corrosion of MPG matrix graphite has an isotropic and arbitrary character;
- with increase of metallic impurities, in particular, iron in the graphite the corrosion rate of the material increases;
- corrosion rate of the irradiated 3OPG matrix graphite is less than the unirradiated ones by a factor of ~2;

Table 4

Average data of the porous structure and corrosion rate of the irradiated and unirradiated specimens of 3OPG matrix graphite after the tests in helium, containing 1 vol. % of water vapour, at the temperature of 1000 °C

Specimen characteristic	Specific surface, m <sup>2</sup> /g		Specific pores volume, cm <sup>3</sup> /g		Density, g/cm <sup>3</sup>	Corrosion rate g/g·h·10 <sup>2</sup>
	before oxidation	oxidation 1 h	before oxidation	oxidation 1 h		
Unirradiated	0.37	1.74	2.59	0.066	0.079	0.094
Irradiated	0.6	1.86	2.46	0.055	0.066	0.079
						1.76
						1.85
						4
						2

- corrosion rate of MPG matrix graphite poorly depends on a helium pressure (at the constant partial pressure of water vapour  $5 \cdot 10^{-3}$  MPa) in the range of  $0.1 \leq P \leq 1.5$  MPa and is proportional to  $1/\sqrt{P}$  in the range of  $1.5 < P \leq 6.0$  MPa.

#### REFERENCES

1. Zeldovich Ya. B. Journal of physical chemistry. 1939, V. 13, issue 2, pp. 163-168.
2. Virgiliev Yu. S., Cherednik F.M., Ostrovsky V.S. Chemistry of solid fuel, 1974, № 3, p. 25.
3. Fialkov A.S. Formation of the structure and properties of carbon-graphite materials, 1965, Metallurgy, pp. 58-61.

**MATERIALS DEVELOPMENT AND PROPERTIES**  
**Part C**

**(Session III)**

**Chairmen**

**B.T. KELLY**  
United Kingdom

**H. MATSUO**  
Japan



# ENGINEERING THERMOMECHANICS OF NUCLEAR GRAPHITES UNDER NEUTRON IRRADIATION, OXIDATION AND TRANSIENT HEATUP: A REVIEW

T. ARAI

Tokai Research Establishment,  
Japan Atomic Energy Research Institute,  
Tokai-mura, Naka-gun, Ibaraki-ken,  
Japan

## Abstract

Structural assessment of a GCR graphite component involves thermal and stress/strain calculations to determine local stress states. These analyses require data base and predictive models on thermomechanical behavior of graphite materials. The paper reviews state-of-the-art of graphite technology on thermomechanics with emphasis on nonisothermal irradiation, nonuniform oxidation and post-irradiation annealing. Relevant data base and predictive models are discussed. Nonisothermal irradiation behavior have now being handled partly by use of the Graphite Damage Model. Further verification of the methodology is being attempted. Some data base and analyses on deformation behavior of nonuniformly oxidized specimens are available. A few experimental evidences suggest that among various thermomechanical properties thermal conductivity should influence transient heatups after irradiations. Current knowledge and additional key data may be coordinated with a further sophistication of descriptive models for better performance and reliable operation of graphite components in actual reactors.

## 1. INTRODUCTION

Structural integrity assessment of a graphite component in gas-cooled reactors (GCRs) involves the prediction of stress states developing during lifetime on one hand, and the definition of critical stress states for specified fracture modes on the other hand. In the former part of structural designs, stress states may normally be calculated by sophisticated numerical analyses based on either a finite element method (FEM) or a finite difference method (FDM). These analyses require data base and descriptive models on thermal and mechanical behavior of graphite materials specified for individual components. Basic thermomechanical governing equations are a heat conduction equation and a linear viscoelastic constitutive law. They involve several material properties which are subject to changes due to many environmental effects in the course of reactor operations. A better predictability of local stress states and associated deviations will allow higher performance or life extension of graphite components.

The paper reviews the data base and descriptive models for thermo-mechanics of nuclear graphites which are available in the open literature. The review envisages a general operational history of a graphite component which may consists of repetitive high temperature irradiation and cool down at normal conditions, progressive oxidation at normal and/or abnormal conditions, core heatup at anticipated transients. Special relevance will be given to effects of nonisothermal irradiations, nonuniform oxidation, and high temperature annealing after irradiations.

Table 1 Design considerations on graphite structural systems in GCRs

Structural Requirements	Structural Behavior	Material Property
Mechanical Integrity (normal, accident, seismic)	Neutronic Thermohydraulic Thermomechanics (including effects of high temperature, neutron irradiation and oxidation)	Specific Heat Thermal Conductivity Thermal Expansion Dynamic Elastic Modulus Stress-Strain Relation Irradiation Creep (including effects of high temperature, neutron irradiation and oxidation)
FP Release Barrier		
Core Coolability		
Asismic Safety	Seismic excitation	

Table 2 Summary of material data base for predictive modeling

Property	Unirradiated, high temp.	Irradiated high. temp	Nonisothermal Irradiation	Uniform oxidation	Post-irrad. annealing
Specific heat	○	(○)	(○)	----	NA
Thermal conductivity	○	○	△	△	△
Elastic constants	○	○	○	○	△
Thermal expansion	○	○	○	△	△
Dimensional change	-----	○	△	△	△
Irradiation creep	-----	○	○	x	x

○sufficient, ○several, △a few, x unavailable, NA not accurate

Table 3 Computer programs for GCR graphite components

## Combined Thermal and Stress Analyses

Program	Institution	Method	Component
BARSAFE	NE(UK)	FEM	AGR moderator
TWOD	GA(USA)	FEM	MHTGR fuel element
SIGMA	HRB(FRG)	FEM	PBR reflector
ASKA	KFA(FRG)	FEM	PBR reflector
IAGUAR	IA(FRG)	FEM	PBR reflector
VIENUS	JAERI(JAPAN)	FEM	HTTR fuel element
TWOD-K	KHI(JAPAN)	FEM	HTTR fuel element
MULSHES	JAERI(JAPAN)	FDM	HTGR fuel rod

FEM:finite element method, FDM: finite difference method

## Oxidation Burnoff Analyses

Program	Institution	Method	Component
-----	NE(UK)		AGR moderator
OXIDE-3	GA(USA)	FDM	HTGR fuel element
REACT/THERMIX	KFA(FRG)	FDM	PBR core and support
GRACE	FE(JAPAN)	FDM	HTTR core and support
OXIDE-3F	FE(JAPAN)	FDM	HTTR core and support

FDM:finite difference method

## 2. GENERAL ASPECTS OF THERMOMECHANICS OF GRAPHITE COMPONENTS

Gas-cooled reactor systems are composed of graphite structures in both active core regions and core supports. Structural functions are different depending on particular reactor designs and their design philosophy. General design considerations on graphite structural systems in GCRs are listed in Table 1 with respect to structural requirements, structural behavior and material properties related to thermomechanics. Those material properties are essential to assessments of structural integrity and safety of individual graphite components under anticipated operational conditions. In general, as known well, they depend on at least current temperature, irradiation temperature, neutron fluence, oxidation burnoff, and possibly on histories of thermomechanical environments. Basic governing equations are a heat conduction equation and a linear viscoelastic constitutive equation for a specified graphite grade.

An open literature survey has led to a summary on material data base as shown in Table 2. State-of-the-art is assessed in view of availability of quantitative data base for predictive modeling. Differences and/or discrepancies between different graphite grades are disregarded for the

purpose of the present review. The material behavior at high temperatures of unirradiated and isothermally irradiated graphites seemed to be well characterized. Therefore, these aspect will be discussed to a little extent in the paper. In addition, irradiation-induced creep behavior will be spared for B. T. Kelly who will review this special topics in the Meeting. Such new aspects as thermomechanics in nonisothermal irradiations, nonuniform oxidation and post-irradiation annealing will be referred to in the following chapters.

It is of special interest for the author to identify computer programs in current use for graphite component structural designs at different institutions. Those programs for combined thermal and stress analyses (1) ~ (7) and oxidation burnoff analyses (8)(9) are listed in Table 3, although their physical models and numerical procedures are mostly proprietary.

## 3. DATA BASE AND ENGINEERING PREDICTIVE MODELS

## 3.1 Effects of Isothermal and nonisothermal Irradiations

## 3.1.1 Data Base

Thermomechanical properties of reference graphites for individual GCR systems have been measured by an uncountable number of long term irradiation tests since 1960s. Additionally they have been supported by many experiments for experimental and other grades of graphite materials in order to establish so called design curves for isothermal irradiation at different irradiation and measurement temperatures. Many grades of HTGR graphites have been irradiation tested to provide specific and general material behavior at different irradiation environments. A lot of data base on HTGR graphites have been published in 1970s by OECD Dragon Project(10). Those measurements have been bases for other near-isotropic HTGR graphites to be characterized in the wide range of irradiation temperature and neutron fluence. Recent irradiation tests on isotropic graphite IG-110 have led to more deviations of changes in thermomechanical properties due to slight irradiations at 400 ~ 1250 °C. For example, measured results on dynamic elastic modulus and tensile stress-strain relation have been reported(11) ~ (13). It should be noted that statistics of tensile deformation properties are of primary importance in assessing stress states in an actual graphite component.

Behavior under nonisothermal irradiations are, however, limited to several experimental investigations, as will be discussed later in more detail. For example, thermal conductivity of nuclear graphite has been studied intensively by British groups including effects of temperature switch during irradiations (14). Delle et al. (15) have reported dimensional changes of gilsocarbon graphite at very high and markedly changing irradiation temperatures. They have found no precise answer how to deal with measured characteristics.



### 3.1.2 Previous Engineering Predictive Models

Among several thermomechanical properties, thermal conductivity has only been studied to establish physically-based predictive models which are available for engineering design purposes. An original engineering model based on physical concepts has been developed by Taylor et al.(16). This method has been applied to American HTGR graphites by Price (17). It incorporates a numerical procedure for calculating changes in thermal conductivity at changing irradiation temperatures. For more general applications, Price and Haag (18) have discussed a practical methodology for calculating property changes at changing irradiation temperatures on the basis of several measurements on dimensional changes, elastic modulus, thermal conductivity and coefficient of thermal expansion of some nuclear graphites and fuel matrix material. They have found that a method called "Horizontal Transposition at a Scaled Fluence" provides an agreement between prediction and measurement for four properties mentioned above.

A new approach has been attempted by Aral et al. (19)(20) to formulate general numerical procedures for nonisothermal irradiation behavior. This is based on so called "Graphite Damage Model" which was originally elaborated to interpret the observed isothermal irradiation behavior by Cords and his coworkers in Research Center Juelich.

### 3.2 Graphite Damage Model

Details of physical concepts and numerical formulations of Graphite Damage Model(GDM) have been described together with comparisons with measured data on isothermal behavior in the literature(19). The GDM is capable to predict changes of dimensions, dynamic elastic modulus and thermal conductivity at ambient temperature, and mean coefficient of thermal expansion(RT-500 °C). Basic model parameters have been optimized to be common to all kinds of graphite grade, property and orientation. Those global parameters may be valid for other graphites whose data base are not included in the original data bank. A further verification of the methodology with recent irradiation data is under way at JAERI.

By means of GDM, a general recurrence formula for arbitrarily changing irradiation temperature has been proposed(20). It has been found that the predicted property changes are in fair agreement with those measured for some graphite materials(18). If the isothermal behavior could be simulated well by GDM.

### 3.3 Effects of Oxidation on Deformation Behavior

#### 3.3.1 Data Base

Effects of uniform oxidation by either O<sub>2</sub> or H<sub>2</sub>O on various properties of graphites from different manufacturing routes have been investigated by many researchers. Those data base are directly utilized for assessing deformation properties in uniformly oxidized graphite components. Most of graphite components in GCRs serve at high temperatures where oxidation processes will be controlled predominantly by in-pore diffusion or boundary layer mass

transfer of oxidizing substances. Consequently, burnoff gradient will develop in the component where thermal and mechanical loadings will induced nonuniform stress states. This requires data on oxidation-induced property changes as a function of burnoff which can be incorporated in stress-strain analyses. Quantitative relationships between elastic modulus and burnoff have been established on several HTGR graphites(21) ~ (25).

#### 3.3.2 Deformation of Nonuniformly Oxidized Graphite Specimens

A few mechanical tests have been carried out to analyze and verify deformation and fracture behavior of oxidized specimens under nonuniform stress distributions, i.e. bending loads. In the first pioneering investigation by Price and Beavan (22) nonuniformly oxidized PGX specimens have been four-point bend tested to measure deflections of the rectangular beams with different burnoffs on the surfaces where stresses are either tensile or compressive. The results have been analyzed based on a simple linear elasticity and changing Young's modulus which have been determined by tensile tests using uniformly oxidized specimens. Predicted beam deflections have been found to be in good agreement with those measured.

Another interesting work in this subject has been done by Adam and Brocklehurst (26). In the experiments radiolytic oxidation gradients in CAGR moderator graphite have been simulated by drilled holes in the specimens which are subjected to mechanical loadings to measure tensile and four-point bending deformation and fracture properties. In addition, thermal conductivities have been measured as a function of weight loss of up to 50%. These drilled specimens have been found to simulate well oxidized ones for determining oxidation-induced degradation of thermomechanical properties. Furthermore, in bending tests using the specimens with uniform and different porosity gradient, tensile stress-strain curves have been found to be unaffected by porosity gradient. As they suggest, this technique is considered to be a useful method of simulating and verifying the property changes which occur in graphite due to nonuniform oxidation in large components in reactors.

#### 3.3.3 Combined Radiation and Oxidation

Integrated effects of combined neutron irradiation and oxidation on HTGR graphites seem not to be reported in the open literature. But, results of graphite monitoring and surveillance in CO<sub>2</sub>-cooled reactors are available. They may be useful in treating with the subject in actual HTGRs although the irradiation conditions and burnoffs are different in a quantitative sense.

There have been performed a few experiments on separate effects of radiation and oxidation. Prince and Brocklehurst(27) have reported irradiation-induced dimensional changes of gilsocarbon graphite specimens unoxidized and radiolytically preoxidized. Decrease in density results in appreciably larger shrinkages in neutron fluences only above  $1 \times 10^{22}$  n/cm<sup>2</sup>(EDN) at an irradiation temperature of around 400 °C. This suggests that thermally-induced oxidation of HTGR graphite components will not pose a serious problem in normal and accidental conditions.

Delle et al.(24) have investigated the subject by measuring porosity changes due to irradiation and oxidation on different grades of graphites. Changes in coefficient of linear thermal expansion have been determined as a function of burnoff up to 3% and total porosity up to 10%. On the basis of discussions on relationships between micro- and macro-structures and some engineering properties, they have assumed qualitative property changes under simultaneous irradiation and oxidation, as shown in Fig. 1. Quantitative verification on specified graphite grades will be recommended if design data needs exist.

### 3.4 Effects of High Temperature Annealing

#### 3.4.1 Data Base

An HTGR core design may involve situations in which temperatures of graphites components may rise above normal service temperatures at anticipated transients for some ten or hundreds of hours. It is expected that thermomechanical behavior of graphite material change due to high temperature annealing. Actual necessity of design data will, of course, depends on reactor system designs.

Table 4 Data base on high temperature annealing of irradiated graphites

Researcher	Grade	Irradiation conditions	Annealing conditions	Measurements
Delle et al. (1982)	ASR-2E	425~1215°C $1.3 \sim 4.0 \times 10^{21}$ n/cm <sup>2</sup> DNE	550~2000°C 24~60 h	Dimension Young's modulus Electrical resistivity
	A3-27 matrix	425°C $1.4 \times 10^{21}$ n/cm <sup>2</sup> DNE	1455°C 0~10h	Thermal conductivity
Matsuo (1991)	IG-110	900~1250°C $0.8 \sim 2.8 \times 10^{21}$ n/cm <sup>2</sup> (E>29fJ)	900~2300°C 1h	Electrical resistivity Young's modulus Thermal expansion Dimension
	H-451	900~1250 $0.8 \sim 2.8 \times 10^{21}$ n/cm <sup>2</sup> (E>29fJ)	900~2300 1h	Electrical resistivity Young's modulus Dimension

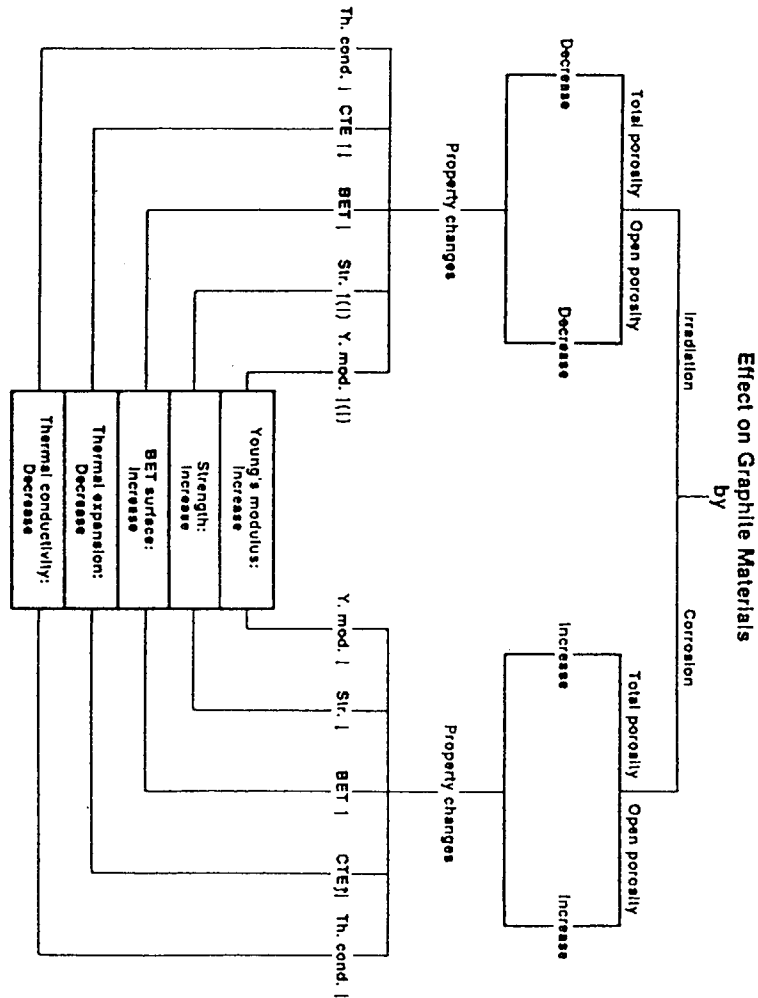


Fig. 1 Effects of fast neutron irradiation and oxidation on some properties of graphite materials(24)  
↑ = Increase, ↓ = Decrease

Here, the author refers to two experimental studies whose experimental conditions are listed in Table 4. The first data base have been reported by Delle et al.(27). It has been found that significant changes in physical properties have occurred at annealing temperatures above about 1400 °C and more pronounced at 1700 °C or above. It should be noted, however, that dimensional recovery on annealing occurs only in specimens which had been irradiated slightly.

Second experiments made by Matsuo (28) are on IG-110 and H-451 graphite specimens. Young's moduli of IG-110 graphite decrease well above 1500 °C while coefficient of thermal expansion and linear dimension exhibit no change due to annealing at temperatures up to 2000 °C for 1 hour.

Considering these experimental results and inherent scatter of thermomechanical properties of graphite materials leads to a suggestion that annealing effects may influence only thermal conductivity of graphite components subject to irradiations at lower temperatures.

#### 4. CONCLUDING REMARKS

Current graphite design technologies have been supported by long term, expensive experimental programs in individual countries. They are more or less empiricism which has been justified for respective graphite grade. It may well be understood that each graphite grade behaves differently simply because of different manufacturing processes. On the other hand, candidate nuclear graphites of current design concern possess some kinds of common characteristics, i.e. near-isotropy, nearly identical apparent density, and coke grain size, etc. Also, nuclear graphites seem not to be characterized wholly only by means of typical experiments without substantial phenomenological modelings.

This idea recalls the fact that graphite materials are inherently porous polycrystalline and pseudo-brittle whose micro- and macroscopic structures change continuously due to combined irradiation and oxidation at changing service temperatures. Material modelings may be advanced by means of further sophistication on realistic microstructural processes on deformation and fracture(29) and irradiation-induced damages(30).

#### REFERENCES

- (1) A.White, Extended Abstracts of CARBON'88 546 (1988)
- (2) R.Alloway, G.Gorholt, F.Ho, R.Vollman and H.Yu, IAEA SM Tokai, JAERI-M86-192 176 (1987)
- (3) A.Schmidt, IAEA SM Gif-sur-Yvette, Summary Report 51 (1979)
- (4) W.Theymann, W.Delle and H.Nickel, Juel-1906 (1984)
- (5) P.Rathjen, Juel-Conf-71 493 (1989)
- (6) T.Iyoku, S.Shirai, M.Ishihara, T.Arai and S.Shiozawa, Proc. of SNA'90 128 (1990)
- (7) T.Arai and S.Sato, JAERI-M5513 (1974) (in Japanese)
- (8) M.B.Peromian, et al., GA-A12493 (1975)
- (9) W.Katscher and R.Moormann, IAEA SM Tokai, JAERI-M86-192 182 (1987)
- (10) M.R.Everett, L.W.Graham and F.Ridealgh, "Graphite Structures for Nuclear Reactors" I.M.E. London, 321 (1972)
- (11) H.Ugachi, T.Arai and T.Isozaki, Extended Abstracts of Int. Symp. on Carbon Tsukuba, 538 (1990)
- (12) T.Arai, H.Schiffers, G.Haag and W.Delle, Extended Abstracts of Int. Conf. on Carbon, 268 (1990)
- (13) T.Arai, H.Ugachi, T.Oku, T.Kodaira and M.Eto, ibid (11) 162 (1990)
- (14) B.T.Kelly, private communication
- (15) W.Dell, M.R.Everett, R.Blackstone and K.Krefeld, Extended Abstracts of 13th Biennial Conf. on Carbon, 300 (1973)
- (16) R.Taylor, B.T.Kelly and K.E.Gilchrist, J. Phys. Chem. Solids 30 2251 (1969)
- (17) R.J.Price, GA-A12615 (1973)
- (18) R.J.Price and G.Haag, Juel-1575 (1979)
- (19) T.Arai, H.Cords, R.Zimmermann, W.Delle and H.Nickel, ibid (6) 122 (1990)
- (20) T.Arai, H.Cords and H.Nickel, to be published in Proc. of 1st JSME/ASME Conf. ICONE1 (1991)
- (21) G.B.Engle, GA-A14690 (1977)
- (22) R.J.Price and L.A.Beavan, GA-A16270 (1981)
- (23) S.Sato, K.Hirahara, A.Kurumada, S.Kimura and E.Yasuda, J.Nucl. Eng. Desgn. 118 227 (1990)
- (24) W.Delle, G.Haag and H.Goertz, Juel-Conf-47 18 (1982)
- (25) M.Eto, T.Oku and T.Konishi, Carbon 29 11 (1991)
- (26) R.W.Adam and J.E.Brocklehurst, Extended Abstracts of 16th Biennial Conf. on Carbon 398 (183)
- (27) N.Prince and J.E.Brocklehurst, IAEA SM Tokai, JAERI-M86-192 20 (1987)
- (28) H.Matsuo, JAERI-M91-090 (1991)
- (29) N.McNachlan, M.O.Tucker and M.J.Parry, Extended Abstracts of 19th Biennial Conf. on Carbon, 460 (1989)
- (30) R.-E.Schulze, H.A.Schulze and W.Delle, Proc. of 5th Conf. on Carbon and Graphite, Vol.II 904 (1978)

# A REVIEW OF IRRADIATION CREEP IN REACTOR GRAPHITE

B.T. KELLY

AEA Technology,  
Salwick, Preston, Lancashire,  
United Kingdom

## Abstract

The construction of graphite moderated reactors with extended lives would be virtually impossible but for the existence of irradiation creep which relaxes stresses within components due to gradients of irradiation damage which would otherwise produce failure. A very large amount of experimental data exists on many types of graphite, but there are still important differences in the constitutive equations derived by different groups and applied to calculate brick stresses. This paper summarises the results of a review of knowledge of irradiation creep recently carried out in the United Kingdom.

## 1. Introduction

The phenomenon of irradiation induced creep is essential for the construction of graphite moderated nuclear reactors because it relaxes the stresses generated by the gradients of irradiation induced dimensional changes and temperature. Many programmes have been carried out to study irradiation creep in a wide variety of graphites, but there are still considerable differences in the constitutive equations derived from these studies in different countries and used to estimate graphite brick stresses. AEA Technology<sup>(1)</sup> have recently reviewed all of the irradiation creep data available to them and carried out some new experiments on graphite containing creep strain. This review has revealed significant differences in the experimental information and generated some new theoretical considerations which are presented below.

## 2. The Constitutive Equations

The experimental studies of irradiation creep carried out in the UK may be summarised as follows<sup>(1)</sup>:

- The creep strain can be divided into primary and secondary components, both linear with stress.
- The primary creep strain is reversible with a dose constant of  $\sim 0.25 \times 10^{20} \text{ n.cm}^{-2} \text{ (EDN)}$ , and a magnitude of about one elastic strain.
- The secondary creep strain is not reversible and is inversely proportional to the elastic modulus for the same stress mode measured in the unirradiated condition.

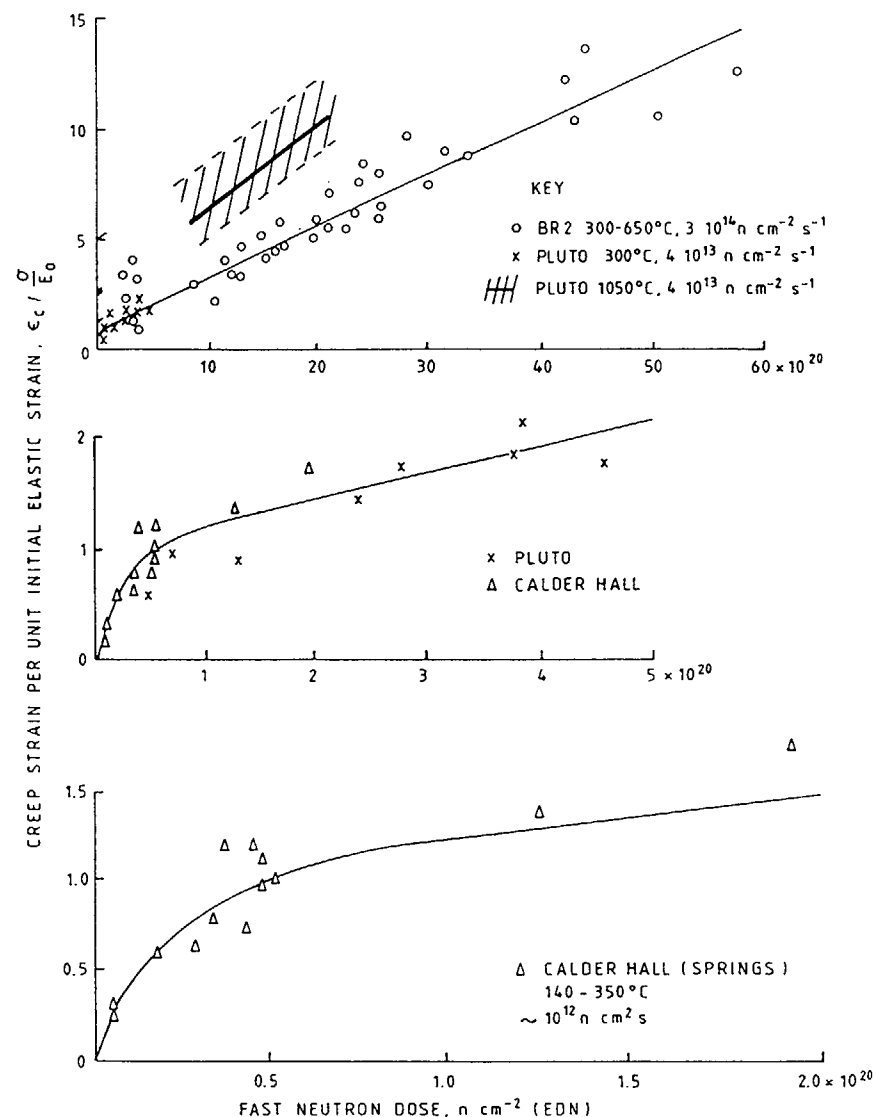


FIG.1 COMPARISON OF CONSTANT STRESS IRRADIATION  
CREEP DATA ON GRAPHITE IN DIFFERENT FACILITIES

The UK data is summarised in Fig 1 for temperatures between 140 and 650°C, it is described by

$$\text{Creep strain } \epsilon_c = a(\sigma/E_0) [1 - \exp(-b\gamma)] + c(\sigma/E_0) \gamma \quad \dots(1)$$

where  $\gamma$  is the dose in  $\text{n.cm}^{-2}$  (EDN),  $E_0$  is the unirradiated elastic modulus and  $a$ ,  $b$  and  $c$  are constants, with values

$a = 1$ ,  $b = 4$ ,  $c = 0.23$  if the dose  $\gamma$  is measured in units of  $10^{20} \text{ n.cm}^{-2}$  (EDN). Eq 1) represents data generated in shear where  $E_0 = G_0$  the shear modulus, as well as in tension and compression, and thus it was natural to suggest that  $E_0$  should be replaced by  $1/S_{ij}^0$ , the appropriate unirradiated elastic compliance. If this is the case the lateral strain ratios in uniaxial tension/compression should be the same for elastic (Poisson's ratio) and creep deformations. The lateral strain ratios obtained in tension or compression on a variety of graphites are shown in Fig 2. The results indicate a lateral strain ratio of about 0.3, compared to the initial values of Poisson's ratio 0.15-0.2. It should be noted that the elastic ratio could not be measured on these samples for practical reasons, but it is known from much earlier work that elastic ratios can be increased by irradiation damage<sup>(2)</sup> so that the two ratios, elastic and plastic may be the same.

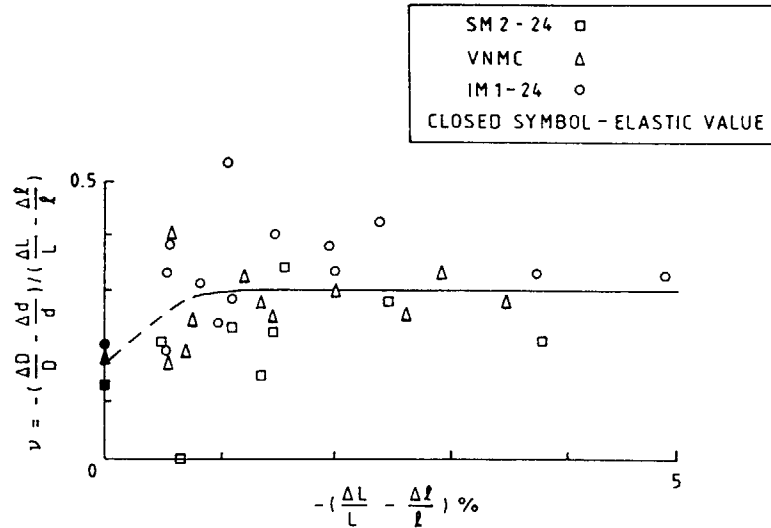


FIG. 2 CREEP POISSONS RATIO AS A FUNCTION OF LONGITUDINAL CREEP STRAIN

The changes in Young's Modulus with irradiation dose show two separate components, the first due to changes in the  $C_{44}$  elastic modulus of the component crystals and the second due to structural changes in the graphite. The first does not affect the creep rate but the second would be expected to do so and studies on samples which had been radiolytically pre-oxidised to reduce the modulus behaved as expected<sup>(3)</sup>. The normal structural changes which occur under irradiation produce an increase in Young's Modulus followed by a decrease, and thus a decrease in creep rate followed by an increase would be predicted. There is no information on changes in the shear constants or the lateral strain ratios.

Essentially the UK work resulted in the following constitutive equations<sup>(3)</sup> (neglecting primary creep).

$$\frac{de_{xx}}{d\gamma} = g_1 + S_{11} \frac{d\sigma_{xx}}{d\gamma} + S_{12} \frac{d\sigma_{yy}}{d\gamma} + S_{13} \frac{d\sigma_{zz}}{d\gamma} + K_{11}\sigma_{xx} + K_{12}\sigma_{yy} + K_{13}\sigma_{zz}$$

$$\frac{de_{yy}}{d\gamma} = g_1 + S_{12} \frac{d\sigma_{xx}}{d\gamma} + S_{11} \frac{d\sigma_{yy}}{d\gamma} + S_{13} \frac{d\sigma_{zz}}{d\gamma} + K_{12}\sigma_{xx} + K_{11}\sigma_{yy} + K_{13}\sigma_{zz}$$

$$\frac{de_{zz}}{d\gamma} = g_{11} + S_{13} \left( \frac{d\sigma_{xx}}{d\gamma} + \frac{d\sigma_{yy}}{d\gamma} \right) + S_{33} \frac{d\sigma_{zz}}{d\gamma} + K_{13}(\sigma_{xx} + \sigma_{yy}) + K_{33}\sigma_{zz}$$

$$\frac{de_{xz}}{d\gamma} = S_{44} \frac{d\sigma_{xz}}{d\gamma} + K_{44}\sigma_{xz}$$

$$\frac{de_{yz}}{d\gamma} = S_{44} \frac{d\sigma_{yz}}{d\gamma} + K_{44}\sigma_{yz}$$

$$\frac{de_{xy}}{d\gamma} = 2(S_{11} - S_{12}) \frac{d\sigma_{xy}}{d\gamma} + K_{66}\sigma_{xy}$$

for a graphite with cylindrical symmetry, where  $e_{ij}$  and  $\sigma_{ij}$  are the strains and stresses respectively in the usual notation  $S_{ij}$  are the normal elastic compliances which are dose and irradiation temperature dependent.  $K_{ij}$  are the creep constants, (initially at least proportional to  $S_{ij}^0$  the appropriate unirradiated elastic compliance).

$g_{\perp}$  and  $g_{\parallel}$  are the rates of irradiation induced dimensional changes in a free specimen perpendicular and parallel to the axis of symmetry.

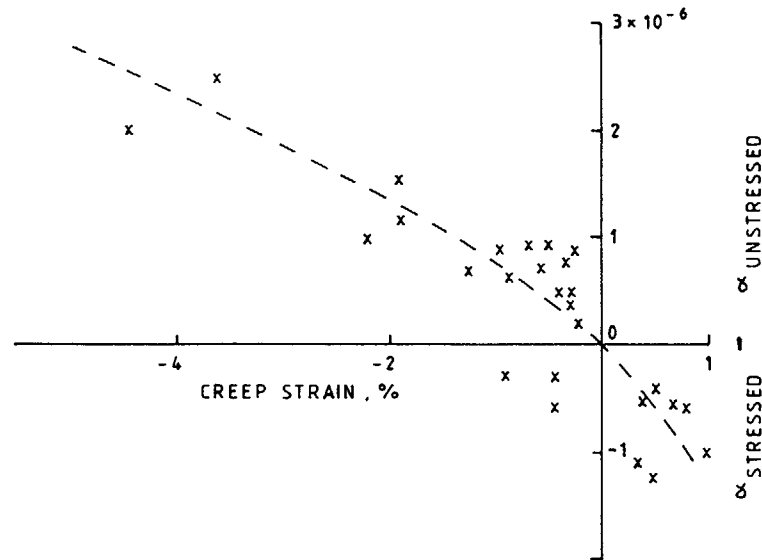


FIG. 3 EFFECT OF CREEP STRAIN ON THERMAL EXPANSION COEFFICIENT MEASURED PARALLEL TO THE STRESS AXIS (GILSO - CARBON GRAPHITE)

In practical UK calculations the creep constants are written

$$K_{1m} = \frac{K}{S(\gamma)} \beta(T_i) S^{\sigma_{1m}}$$

where  $\beta(T_i)$  allows for the temperature dependence of irradiation creep and  $S(\gamma)$  is a "structure factor" derived from Young's modulus changes and assumed the same for all  $K_{1m}$ .

The only physical property found to be significantly modified by irradiation creep is the thermal expansion coefficient. Fig 3 shows the changes in expansion coefficient measured parallel to the direction of a tensile or compressive stress as a function of creep strain<sup>(4)</sup>.

Virtually all investigators agree on the form of Eq 1, but recent work apparently shows that  $S(\gamma)$  derived from the Young's Modulus changes with dose underestimates the changes in creep rate<sup>(5,6)</sup>, both increases and decreases and proposes an alternative correlation of the form

$$K_{1m} = K S^{\sigma_{1m}} \left[ 1 - \mu \left( \frac{(\Delta V/V_o)}{(\Delta V/V_o)_m} \right) \right]$$

where  $(\Delta V/V_o)$  is the volume change of the control at the same irradiation condition.

$(\Delta V/V_o)_m$  is .. maximum volume decrease shown by the control

and  $\mu$  is a constant.

Recent measurements of the lateral creep strain ratios for creep also appear to show a value of -0.5, that is secondary creep takes place at constant volume - disagreeing with the UK work and the conclusions of an earlier review by Price<sup>(7)</sup>.

A notable feature of a number of creep studies in tension and compression have been the changes in thermal expansion coefficients produced by creep strain, an increase for compressive strain and a decrease for tensile strain in the direction of the creep strain referred to above (Fig 3). These changes are quite large and superposed upon large changes which are due to neutron induced changes in structure. These changes in expansion coefficient pose a problem for the definition of creep strain - this is normally taken to be the difference in dimensional changes between a stressed and an unstressed specimen irradiated together. It is however well established that the rate of change of dimensions of a polycrystal in direction  $x$ ,  $g_x$  is related to the thermal expansion coefficient  $\alpha_x$  measured in the same direction.

$$g_x = \left( \frac{\alpha_x - \alpha_a}{\alpha_c - \alpha_a} \right) (g_c - g_a) + g_a$$

where  $\alpha_a$  and  $\alpha_c$  are the thermal expansion coefficients of the graphite crystallites parallel and perpendicular to the basal planes and  $g_a$  and  $g_c$  are the corresponding rates of radiation induced dimensional changes. The different values of  $\alpha_x$  in the creep sample and the control sample means that the difference is not the true creep strain which is readily shown always to be greater than that due to the simple definition<sup>(4)</sup>.

The change in expansion coefficient  $\alpha_x$  due to creep strain may be due to the effects of creep on orientation or porosity or both and in both cases it would be expected that the thermal expansion coefficients perpendicular to the stress axis would also be affected and thus also the estimates of lateral strain rates. A single set of measurements of the change in thermal expansion of creep samples parallel and perpendicular have recently been published and show a significant lateral effect. This means that samples with significant creep strain may become significantly anisotropic (Table 1).

It has been remarked that these considerations do not matter since the stress to achieve a given graphite total strain is known and in-reactor calculations will give the correct result.

Table 1

Properties of BR-2 Creep samples and control

Sample	Stress/ Strain	Thermal expansion coefficient 20-120°C 1968	Current Thermal Expansion Coefficient 20-120°C	
			Parallel	Perpendicular
Irradiated	0	-	3.64 x 10 <sup>-6</sup>	-
Irradiated unstressed	0	4.1 x 10 <sup>-6</sup>	4.01 x 10 <sup>-6</sup>	4.90 x 10 <sup>-6</sup>
Irradiated stressed	-6.2 MN/n <sup>2</sup> -0.62 %	4.8 x 10 <sup>-6</sup>	4.51 x 10 <sup>-6</sup>	4.27 x 10 <sup>-6</sup>

This is only true for the uniaxial stress case. If the effects of a stress on lateral thermal expansion coefficients is significant and there are multi-axial stresses the dimensional change rates are not known. The author has suggested that creep strain effects on thermal expansion coefficient can be linearly superposed on irradiation induced changes, but there is no available evidence eg

$$\alpha_x(\gamma, \sigma_{xx}, \sigma_{yy}, \sigma_{zz}) = \alpha_x(\gamma, 0) + \left( \frac{\delta \alpha_x}{\delta e_{xx}} \right) e_{xx} + \left( \frac{\delta \alpha_x}{\delta e_{yy}} \right) e_{yy} + \left( \frac{\delta \alpha_x}{\delta e_{zz}} \right) e_{zz}$$

Table 1 suggests values  $(\delta \alpha_x / \delta e_{xx}) \sim -1.0 \times 10^{-1} \text{K}^{-1}$ ,  $(\delta \alpha_x / \delta e_{yy}) = (\delta \alpha_x / \delta e_{zz}) \sim +1 \times 10^{-6} \text{K}^{-1}$  where the  $e_i$  are the volume changing creep strains. These considerations are also important for calculating shutdown stresses.

The dose dependence of the creep constants has been directly observed<sup>(5,6)</sup>. The stiffening of the graphite structure due to volume shrinkage and the "softening" of the structure when expansion begins are reflected in decreases and increases respectively in the creep constants. The occurrence of these effects was predicted by a theoretical model<sup>(4)</sup>, but the changes are larger than predicted. It has been suggested that the changes in creep rate can be predicted by reference to the volume changes of the unstressed control<sup>(9)</sup>, but this appears to be unlikely for large creep strains because of the changes in the creep sample, compared to the control.

The  $K_{ij}$  for  $i \neq j$  determines the lateral creep strains and here there is a major experimental disagreement. The UK studies point to lateral strain ratios slightly greater than the equivalent elastic strain ratios, but US investigators in particular find secondary creep to occur at constant volume. Other investigators produce results of both types. The difference in terms of stress calculations is quite significant. In some investigations to high doses where the graphite is swelling it appears that the creep strains become negative indicating that creep strain has modified the swelling behaviour compared to the control sample.

Price<sup>(7)</sup> has examined other graphite properties for a dependence on creep strain, which must be present because of the large changes in expansion coefficient which can be produced and concluded that there is a small effect compatible with changes in thermal expansion. More recently creep at 850 - 1050°C appears to modify the change in Young's Modulus by comparison with an unstressed control, and samples failed under compressive stress of about one half of the initial compressive strength (Instability). There is some evidence that large localised creep strains can lead to crack growth and eventual specimen failure<sup>(1)</sup>.

### Discussion

The phenomenon of irradiation creep in graphite is more complex than had once been supposed. In particular more information is needed on:

- The lateral creep strain ratio due to creep.
- The dose dependencies of the creep coefficients.
- The changes in properties of the graphite due to creep strains in all three principal directions and whether they simply superpose on to change due to irradiation alone.
- The effect of creep strain on graphite strength, particularly at stress concentrations.
- The creep rate following stress reversal.

It is probable that current treatments of creep are adequate for creep strains  $\leq 1\%$  where perturbation of the graphite structure by creep strain is small. However for larger creep strains in effect the sample is now a significantly different material from the control and it may be that the effects of creep strain on properties other than thermal expansion need to be included in engineering calculations.

The moral of this tale is that engineering calculations become less accurate with increasing creep strain.

### Acknowledgement

This work was carried out under contract to the UK Health and Safety Executive.

### References

1. Brocklehurst J E and Kelly B T. "A review of irradiation creep in graphite under CAGR conditions". ND-R-1406(S) (1989).
2. Simmons, J H W. "Irradiation Damage in Graphite". Pergamon Press (1968).
3. Kelly B T and Brocklehurst J E. J. Nuclear Materials Vol 65, p 79 (1977).
4. Kelly B T. Proc 20th Biennial Carbon Conference P606, June 23-28, 1991. American Carbon Society (1991).
5. Kennedy C R, Cundy M and Kleist G. Proc Int Conference on Carbon "Carbon 88". 18-23 September 1988, p443. IOP publishing (1988).
6. Alhf J, Conrad M, Cundy M and Schurrer H J. Nuclear Materials Vol 171, p31 (1990).
7. Price R. "Irradiation induced creep in graphite - a review". GA-A16402 (1981).
8. Oku T, Fujisaki K and Eto M. J Nuclear Materials Vol 152, p225 (1988).

### DISCUSSION

#### Questions or Comments

Name: Tim Burchell

Measurements of thermal expansion coefficient have been made at ORNL on specimens subjected to compressive irradiation creep. The CTE was found to be greater for the crept specimens than for the unstressed control specimens, which is in agreement with your observation.

#### Questions or Comments

Name: A. Ide

It is recently said that not only high-energy neutron but also thermal neutron affects the neutron damage or irradiation behavior of metallic materials. Is this true with a graphite?

#### Answer:

We have carried out many experiments in different nuclear reactors, including a fast reactor and compared the observed property changes with calculations of atomic displacements - essentially due to neutrons with energies >100 keV. The agreement is very good - there is no significant effect of thermal neutrons.

#### Questions or Comments

Name: doctor Chugunov USSR

Are you discovered the third stage of coefficient of thermal expansion change under irradiation - "secondly increase stage"?

#### Answer:

We do see a third stage in which expansion increases in our Pile Grade A graphite (needle coke, anisotropic) but not in our AGR graphites (gilsonite coke, isotropic). The doses extend to about  $3 \times 10^{22}$  n.cm<sup>-2</sup> (EDN) equivalent to about  $4 \times 10^{22}$  n.cm<sup>-2</sup> in USSR units.



# SPECIFIC BEHAVIOR OF REFLECTOR AND MATRIX GRAPHITE UNDER HIGH TEMPERATURE IRRADIATION

P.A. PLATONOV, V.I. KARPUKHIN, Ya.I. SHTROMBAKH,  
V.M. ALEKSEEV, O.K. CHUGUNOV, B.A. GUROVICH,  
E.I. TROFIMCHUK  
Department of Research Reactors and Technology,  
I.V. Kurchatov Institute of Atomic Energy,  
Moscow, Union of Soviet Socialist Republics

## Abstract

Physical properties for reflector and matrix graphite for the VG-400 VGM reactors being developed in the USSR are reported. Three types of graphite have been investigated. These are: the graphite based on uncalcined coke - KPG and MPC; the graphite based on the special coke - GR1; and the graphite for spherical fuel elements - molded graphite (KPD) and graphite binded by pyrocarbon (GSP). Specimen of these graphites have been irradiated up to a neutron fluence of  $0.5$  to  $2.5 \times 10^{22}$  neutron/cm<sup>2</sup>. The dependence of the following on fluence is reported: relative volume change, Young's modulus, dimensional change, elastic modulus, electrical resistivity, thermal conductivity and the coefficient of thermal expansion.

The investigation of graphite for HTGR in the USSR are being according to materials of core of VG-400 and VGM reactors.

The specimens of three types of graphite were irradiated in reactor up to the fluence  $(0.5-2.5) \cdot 10^{22}$  neutron/cm<sup>2</sup>:

- the graphite based on uncalcined coke - KPG and MPG;
- the graphite based on the special coke - GR1;
- the graphite for spherical fuel elements - molded graphite (KPD) and graphite binded by pyrocarbon (GSP).

At the same time the radiation properties of standard reactor graphite were also investigated.

Tables 1 and 2 show the main properties of reactor block graphite [1,2].

The dependance of critical neutron fluence at different temperatures and maximum design operation conditions for the HTGR inner reflector are listed in Fig.1.

The following main properties of graphite were investigated: radiation induced dimensional change, strength (elastic module), coefficient of thermal expansion (CTE) and thermal conductivity, electrical resistivity. The main results of this investigation are listed in figures 2-10. The investigation of radiation induced dimension changes and linear thermal expansion coefficient together with the direct transmission electron-microscope examination of the graphite structure under irradiation permits us to create the model of the destruction of the graphite and using the insight thus gained a production technology for graphite with a greater radiation stability under high temperature irradiation can be developed.

Table 1. The physical properties of reflector graphites.

Graphite Characteristics	ГР-280 (GR-280)	ГРП2 (GRP2-125)	МПГ-6 (MPG-6)	ГР-1 (GR-1)
Filler	calcined coke KNPS	calcined coke KNPS	uncalcined coke	composition on the base of uncalcined coke
Formation method	extrusion	extrusion	molding	molding
Graphitization temperature, °C	2400	2800	2500	2800
Density, g/cm <sup>3</sup>	1.72	1.85	1.80	1.70
Young's modulus E <sub>d</sub> , 10 <sup>4</sup> MPa	0.65/0.50	1.2/0.85	1.05/1.06	0.75/0.77
Electrical-resistivity, 10 <sup>-6</sup> Ohm·m	10.3/14.8	8.0/10.8	11.7/10.7	15.0/14.0
Compression strength, σ <sub>с</sub> , MPa	34/24	59/59	100/100	70/84
Tensile Strength, σ <sub>ap</sub> , MPa	7.6/6.0	15.0/8.0	31.0/33.5	15/18
Coefficient of Thermal conduct. (20°C), W/m·K	103/89	160/100	138/125	86/90
C.T.E., 10 <sup>-6</sup> K <sup>-1</sup>	3.2/4.9	3.9/5.2	7.3/6.6	6.8/6.7

In the numerator - the properties of parallel orientation samples, in the denominator - of transverse one.

First of all we must note the specific feature of changing radiation induced dimension change of the domestic reactor graphite (GR-280) with the increase of irradiation temperature from 500 to 900°C, fig. 2.

This figure illustrates that even the main criterion for the selection of radiation-stable graphite (the critical neutron fluence) that permits to assess the lifetime of the graphite under irradiation must be reconsidered because the shrinkage stage may be absent completely and we should work out new approach for assessing the irradiation stability of graphite - for instance, degradation of strength of irradiated graphite (F<sub>c</sub>), when we observe irreversible destruction of the graphite structure, increased swelling, decreased thermal conductivity and so on.

Table 2. Properties of matrix graphites.

Technology	Hot pressure			Graphite binding by pyrocarbon		
	KPA	KPA-CMI-30MP	KPA-CMI-MTP	ГСМ1,85	ГСМ1,75	ГСМ1,85
Graphite						
Bulk density $d_k$ , g/cm <sup>3</sup>	1,85	1,87	1,84	1,63-1,66	1,71-1,77	1,80-1,89
Young modulus, $E$ , 10 MPa	1,0	0,95	1,05	1,3	1,5	1,6
Electrical resistivity, $\rho$ , 10 Ohm m	16,0	14,0	13,5	21,5	19,5	17,5
Thermal conductivity (at 20 °C), W/m K	85	60	80			60
C.T.E. at 400 °C, 1/K	6,0	5,4	5,7		5,5	5,4

In the numerator - the properties of parallel orientation samples, in the denominator - of transverse one.

Figures 3-6 illustrate dimensional changes, changes of elastic modulus, electrical resistivity, the coefficients of thermal conductivity and thermal expansion of graphite based on uncalcined coke (MPG and KPG) under irradiation.

Figures 7-9 illustrate the results of high temperature irradiation of the graphite GR1 and matrix graphite GSP and KPG. These figures illustrate that up to a neutron fluence of about  $2.5 \cdot 10^{22}$  1/cm<sup>2</sup> at irradiation temperature 500-600°C and  $0.5 \cdot 10^{22}$  1/cm<sup>2</sup> at irradiation temperature 900-1000°C MPG, KPG, GR1 and GSP graphites retain their radiation stability and consequently these materials quite adequate to meet VGM reactor lifetime requirement.

The nature of the structural changes in graphite under high temperature irradiation can be assessed by means of CTE changes examination. Figures 3 and 10 illustrate the relative changes of CTE (measured at 400°C) and corresponding changes of such properties as elastic modulus, dimension changes and electrical resistivity of the different graphites.

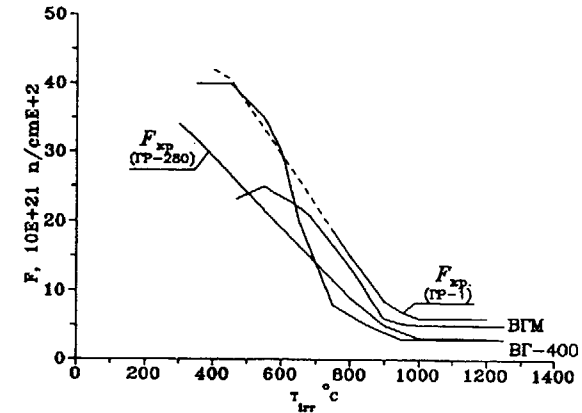


Fig. 1. The dependence of critical fluence of neutron on irradiation temperature and maximum design explore condition of graphite of HTGR inner reflector.

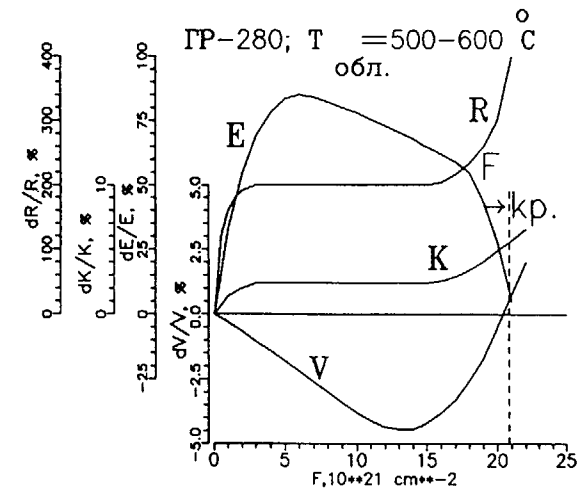


Fig. 2. The dependence of the relative volume changes and Young's module of RBMK-type reactor graphite irradiated under 500-600 and 900-1000°C, on neutron fluence.

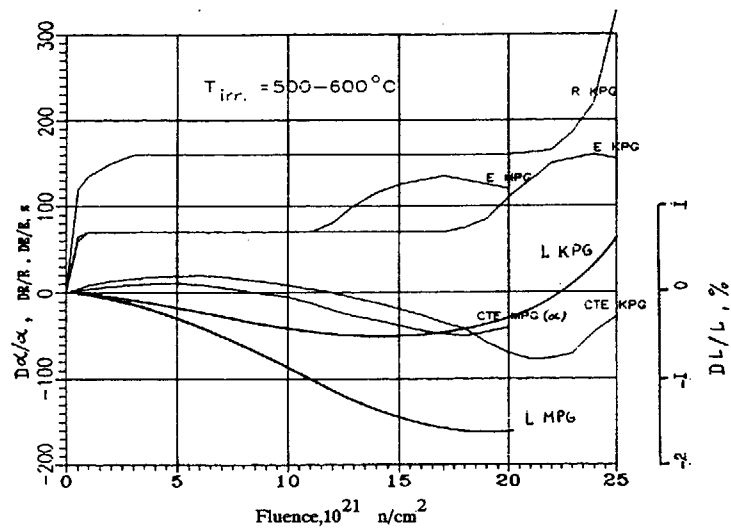


Fig. 3. The dimensional changes (L), changes of elastic modulus (E), electrical resistivity (R) and coefficient of thermal expansion (CTE) of MPG and KPG graphites transverse orientation. Irradiation temperature 500-600°C.

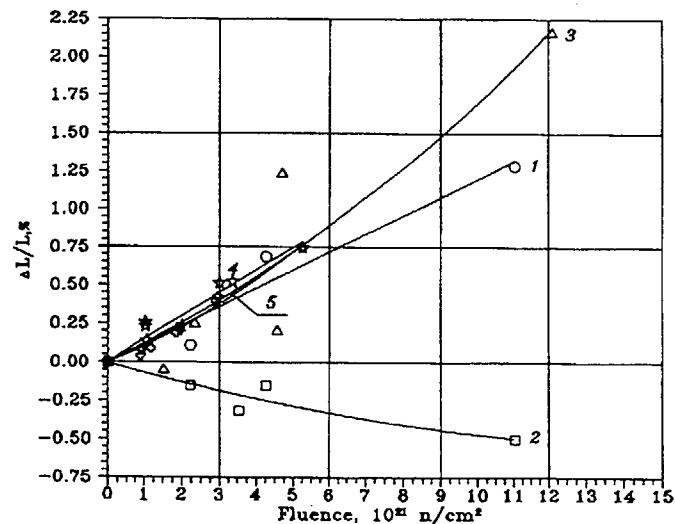


Fig. 4. The dimensional changes of MPG-6 graphite: 1 - parallel. orient.,  $T_{irr} = 600-700^\circ\text{C}$ , 2 - transv. orient.,  $T_{irr} = 600-700^\circ\text{C}$ , 3 - parallel. orient.,  $T_{irr} = 700-750^\circ\text{C}$ , 4 - transv. orient.,  $T_{irr} = 900-1000^\circ\text{C}$ , 5 - transv. orient.,  $T_{irr} = 900-1000^\circ\text{C}$ .

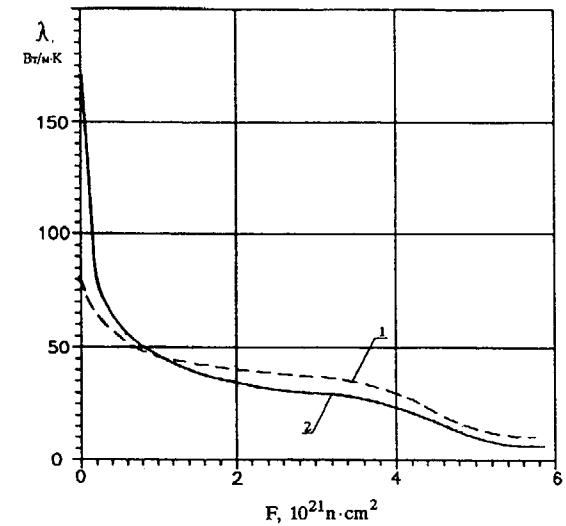


Fig. 5a. The dependence of thermal conductivity of GRP2 graphite parallel orientation samples irradiated under temperature 1150-1250°C, on neutron fluence.

- 1 -  $T_{measure} = T_{irr}$ ;  
2 -  $T_{measure} = 20^\circ\text{C}$ .

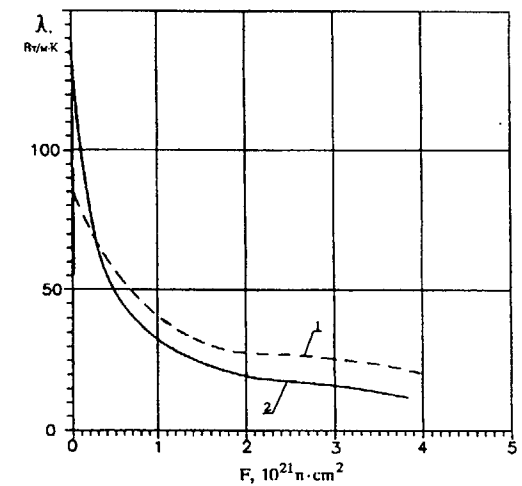


Fig. 5b. The dependence of thermal conductivity of MPG-6 graphite parallel orientation samples irradiated under temperature 950-1050°C, on neutron fluence.

- 1 -  $T_{measure} = T_{irr}$ ;  
2 -  $T_{measure} = 20^\circ\text{C}$ .

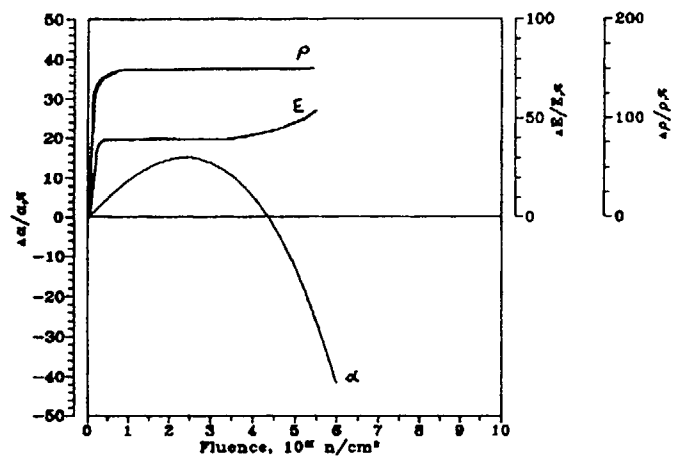


Fig. 6. Relative change of electrical resistivity (R), elastic modulus (E) and coefficient thermal expansion (CTE) MPG-6 graphite. Transverse orientation,  $T_{irr} = 900-1000^\circ\text{C}$ .

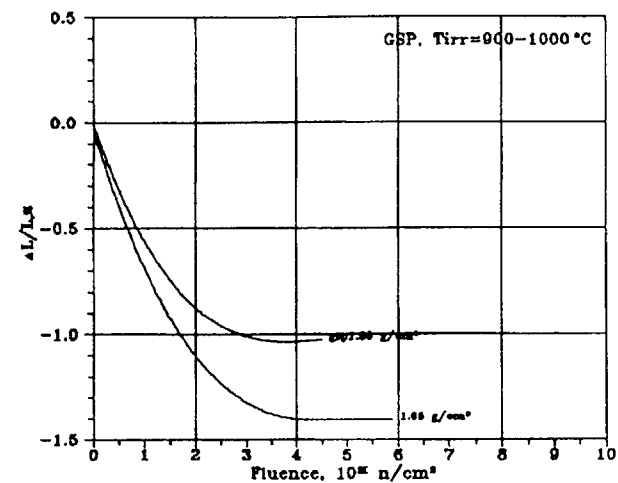


Fig. 8. Dimensional change GSP graphite with different density under irradiation temperature  $900-1000^\circ\text{C}$ .

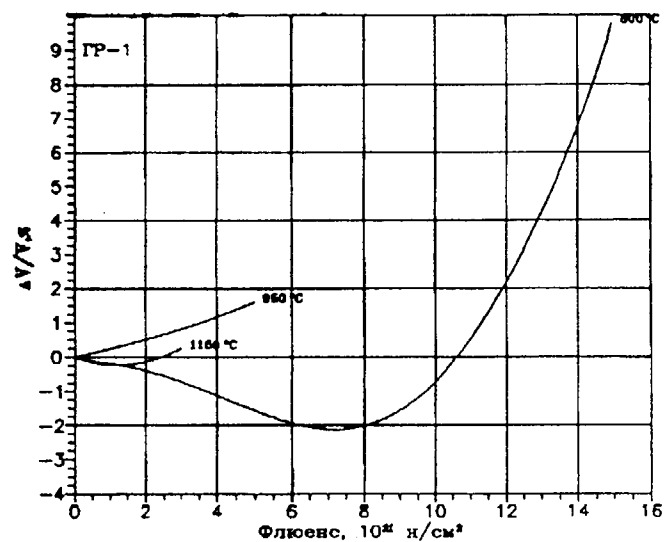


Fig. 7. Volume changes of specimens GR-1 graphite under different irradiation temperatures.

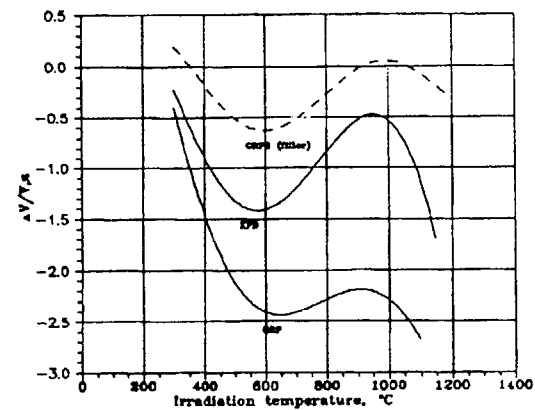


Fig. 9. Relative volume changes of GSP, KPD and GRP-2 graphites irradiated up to the neutron fluence  $0.17 \cdot 10^{22} \text{ 1/cm}^2$ , on irradiation temperature.

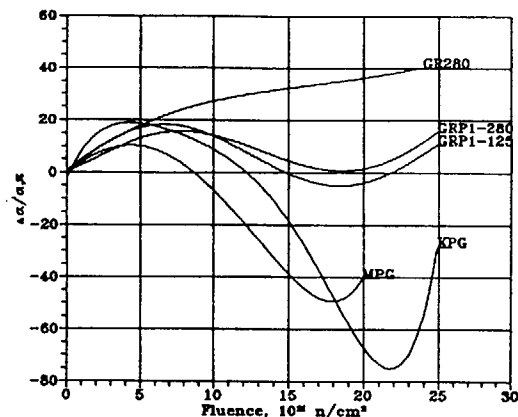


Fig. 10. Relative change of coefficient thermal expansion (CTE) of different types graphite. Transverse orientation.  $T_{irr} = 500-600^\circ\text{C}$ .

The analysis of these results shows, that the higher is the density of graphite (the worse accommodation capacity of the of the thermal expansion of single crystallites in graphite) the more is the rate of change of CTE. As for the increase of irradiation temperature the stage of "secondary increase" of CTE shifts towards smaller fluencies (following a pronounced decrease of elastic modulus) which indicates a close relation of these properties with the structural changes of irradiated graphites, manifested by the formation of inner crack in graphite.

These changes in CTE under irradiation can be described as a "three stage process":

- increase of CTE at the first stage (about 20% in the begging of irradiation),
- a rapid decrease CTE (it falls by about 80% in comparison with the initial magnitude),
- the secondary increasing stage.

Such complicated CTE behavior can be explained by existence of two competing processes: under irradiation accommodation capacity of graphite decreases (the oriented technological microporosity is reduced due to the radiation growth of single crystallites). But at the same time the accommodation capacity tends to increase due to microcracks formed inside crystallites and on their boundaries because increased stresses evolve caused by different rates of radiation growth for crystallites of different sizes, [3].

However, we can't explain the grate rate of increasing CTE at the third stage, but we should pointed out, that the increase of CTE of graphite materials correlates with "the secondary expansion stage" of dimensional change and decrease of the elastic modulus of the graphite under irradiation, fig.3.

One must also note a distinctly different behavior of CTE of the domestic reactor graphite GR-280 under these irradiation conditions. CTE of this graphite increases continuously under irradiation although the rate of increase falls with the neutron fluence, fig.12. Such behavior seems to offer only one explanation, notably that after fluencies of more than  $2 \cdot 10^{22}$  neutron/cm<sup>2</sup> the material is a conglomerate of weakly bonded single crystallites.

The transmission electron - microscope examination of the structure of these types of graphite shows that increase of irradiation temperature to over  $500^\circ\text{C}$  leads to decrease in accommodation capacity of graphite. This effect reveals itself in a decreased rate of technological cracks closure with an increase of irradiation temperature.

As the finally, the investigation of dimensional changes as well as physical properties for reflector blocs and matrix graphite for HTGR under irradiation temperatures of  $300-1200^\circ\text{C}$  gives us ground to believe that the modified critical neutron fluence criterion provides satisfactory lifetime values for the matrix and block graphite developed in USSR.

## References

1. П.А.Платонов, Я.И.Штрмбах, В.И.Карпунин, В.М.Алексеев, Б.А.Гурович, О.К.Чугунов "Действие облучения на свойства графита для ВТГР". Доклад на советско-германском семинаре "Твэлы и графит ВТГР", Москва, июль 1990 г.
2. Конструкция и основные характеристики твэлов ВТГР. "Атомно-водородная энергетика и технология", вып. 5, Энергоатомиздат, Москва, 1983, с.207-213.
3. Radiation effect on the graphite of high-temperature gas-cooled reactors. The reports of the meeting of the specialists on designing graphite moderator for HTGR, Tokyo, Japan, 8-11 September, 1986.

## DISCUSSION

### Questions or Comments

Name: Tim Burchell

Data taken at ORNL on a fine-grained graphite, Graphnol N3M, shows the material has an increasing CTE, followed by a decreasing CTE at higher irradiation fluences. The initial increase is attributed to an irradiation.

### Answer:

Induced closure of of thermal cracks. The subsequent reduction in CTE is attributed to increased accomodation with in graphite microstructure.

### Questions or Comments

Name: B.T. Kelly

We see a second increase in thermal exfasion of our Pile Grade A graphite at high doses. The first increase takes place when the MROZOWSKI cracks close, then it remmains constant until a second long increase occurs at high doses - taking the volume coefficient close to that of a crystal. However we do not see this in high thermal expansion isotropic graphite.

# IRRADIATION BEHAVIOR OF BORONATED GRAPHITE FOR THE HTTR

H. MATSUO

Tokai Research Establishment,  
Japan Atomic Energy Research Institute,  
Tokai-mura, Naka-gun, Ibaraki-ken

F. KOBAYASHI, K. SAWA

Oarai Research Establishment,  
Japan Atomic Energy Research Institute,  
Oarai-machi, Ibaraki-ken,  
Japan

## Abstract

Two kinds of hot-pressed and cold-pressed boronated graphites containing 3 wt% or 30 wt% boron for use in the HTTR were studied. Neutron irradiation was done up to a maximum fast neutron fluence  $2 \times 10^{25} \text{ n/m}^2 (E > 29 \text{ fJ})$  at 550-1070°C in the JMTR.

Irradiation-induced dimensional changes, thermal expansivity and thermal conductivity from room temperature to high temperatures were measured after the irradiation. Dimensional changes and thermal expansivity depend on the direction measured and fabrication method, and thermal conductivity decreased and its temperature dependence changed after the irradiation. Furthermore the changes depend on boron content as well.

## 1. Introduction

Boronated graphite which is a mixture of  $\text{B}_4\text{C}$  granules and graphite matrix has been used for neutron absorbing material in fission reactors, because  $^{10}\text{B}$  has large cross-section for neutron absorption, and data on the effect of irradiation on property changes have been reported<sup>1)</sup>. In the case of the HTTR (High Temperature Engineering Test Reactor), the material is the candidate to be used as neutron absorbing material such as control rod, burnable poison, reserved shutdown system and neutron shielding. Properties of the boronated graphite is considered to be dependent significantly on variation in boron concentration and fabrication technique such as kind of graphite to be used for matrix, baking temperature, forming method and so on.

Furthermore the material is degraded due to irradiation damage by helium in addition to neutron bombardment in an atmosphere of neutron environment, because absorptive isotope  $^{10}\text{B}$  is transformed to  $^7\text{Li}$  by the reaction  $^{10}\text{B}(n, \alpha)^7\text{Li}$  and helium is generated.

The present work aims at obtaining data for irradiation effect on changes in dimension, thermal expansivity and thermal conductivity of boronated graphite containing different boron concentration for use in the HTTR and the comparison of the data with those of nuclear graphite is discussed.

## 2. Experimental procedure

### 2.1 Sample

Test samples were specially prepared for use in the present experiment. Samples were baked at 2000°C for two hours in vacuum after dispersing  $\text{B}_4\text{C}$  granules in the graphite matrix and shaping by either hot-pressing or cold-pressing. Boron carbide granules were done to be homogeneously dispersed in the graphite matrix. Specimens were taken from the same block for both longitudinal (L) direction and radial (R) direction. Boron contents were either 3 wt% or 30 wt%. The samples used in the present experiment are tabulated in Table 1.

Table 1 Samples used in the present experiment

Forming method	Hot-pressing		Cold-pressing	
Boron content(wt%)	3	30	3	30
Bulk density(g/cm <sup>3</sup> )	1.79	1.93	1.78	1.90
CTE(20-400 C)				
L direction	8.22	5.07	7.01	5.53
R direction	3.03	4.00		4.32
Thermal conductivity at 20 C (W/mK)				
L direction	18	21	30	24
R direction		28		28

## 2.2 Neutron irradiation

Neutron irradiation was carried out in the JMTR (Japan Materials Testing Reactor) to a maximum fast neutron fluence of  $2 \times 10^{25} \text{ n/m}^2 (E > 29 \text{ fJ})$  at temperatures 550-1070°C by using two irradiation capsules. Fast neutron fluence was obtained from the reaction  $^{54}\text{Fe}(n,p)^{54}\text{Mn}$ , and irradiation temperatures were measured and controlled by thermocouples during irradiation.

## 2.3 Measurement method

A high accuracy comparator was used for the measurement of length changes at room temperature, where the precision of the measuring device was  $\pm 0.03\%$ , but the rough and granular nature of the surface of the specimens limited the repeatability of the measurement. Therefore, length and width of dimensions were measured at multiple locations, and the average values were taken as the measured values.

A dilatometer was used for the measurement of thermal expansivity using a quartz as a standard sample, where the samples was heated at a rate of  $5^\circ\text{C}/\text{min}$  from room temperature to high temper-

ature which is equal to irradiation temperature of each specimen. The thermal expansivity was expressed using a fourth or fifth order polynomial expression, where each coefficient was determined by least-square method.

A laser pulse technique was applied to the measurement of thermal conductivity. Specimen size was 10 mm in diameter and about 1.5 mm in thickness. A ruby laser was used and the rear face temperature rise of the specimen was measured by a remote sensor, In-Sb detector. A schematic diagram for the measurement of thermal diffusivity<sup>2)</sup> is shown in Fig.1. Thermal diffusivity was obtained from the following formula.

$$\alpha = 0.1388l/T_{1/2}$$

where  $\alpha$  is thermal diffusivity ( $\text{cm}^2/\text{s}$ ),  $l$  specimen thickness (cm),  $T_{1/2}$  half time to reach maximum temperature rise.

In order to resolve finite pulse-width effect some corrections were given using the center of gravity of laser pulse<sup>3)</sup>. Thermal conductivity was obtained from the measured thermal diffusivity, bulk density and specific heat capacity which was deduced from the literature values of specific heat capacity of  $\text{B}_4\text{C}$ <sup>4)</sup> and graphite<sup>5)</sup>, and their content ratios.

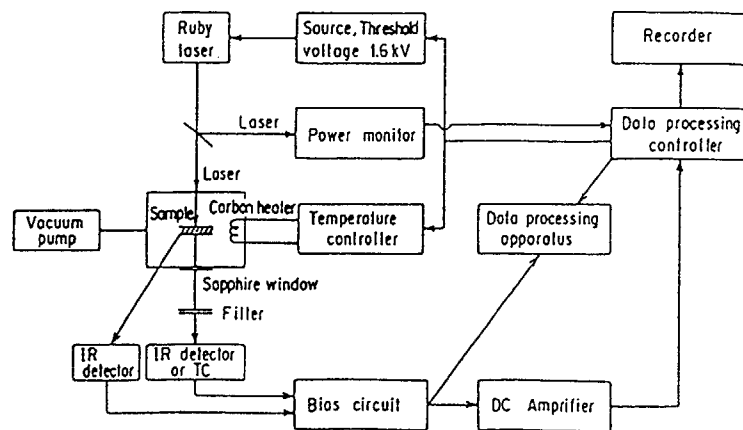


Fig.1 Schematic diagram for the measurement of thermal conductivity by laser flash method

## 3. Results and discussion

### 3.1 Thermal expansivity and thermal conductivity of unirradiated samples

Thermal expansivity and thermal conductivity parallel and perpendicular to the forming direction were measured for many specimens prior to neutron irradiation. The results on thermal expansivity and thermal conductivity are presented in Figs.2 and 4 for hot-pressed samples, and in Figs.3 and 5 for cold-pressed samples, respectively. The average values and scattering of the data arising from the measurement of different specimens are shown in Figs.2 and 3. Comparatively large scattering of the measured values was observed, even though the samples were taken from each compact made through the same fabrication technique, either hot-pressed or cold-pressed.

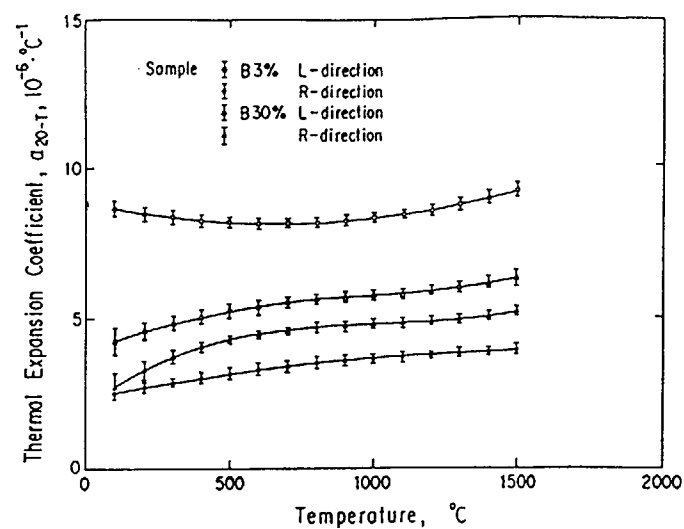


Fig. 2 Thermal expansivity of unirradiated hot-pressed boronated graphites

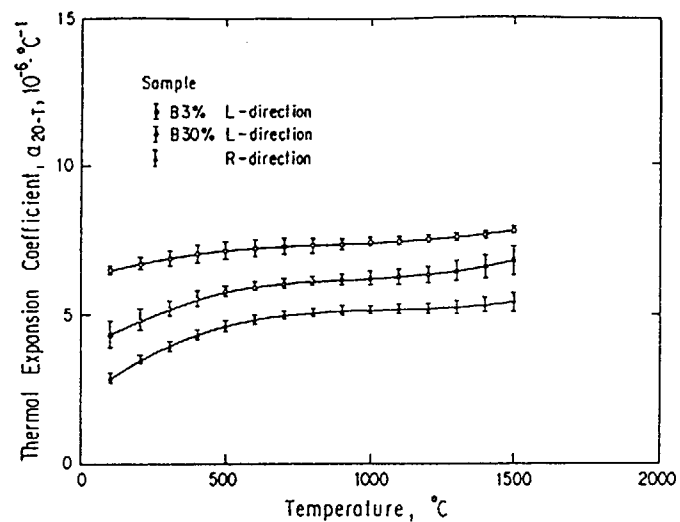


Fig. 3 Thermal expansivity of unirradiated cold-pressed boronated graphites

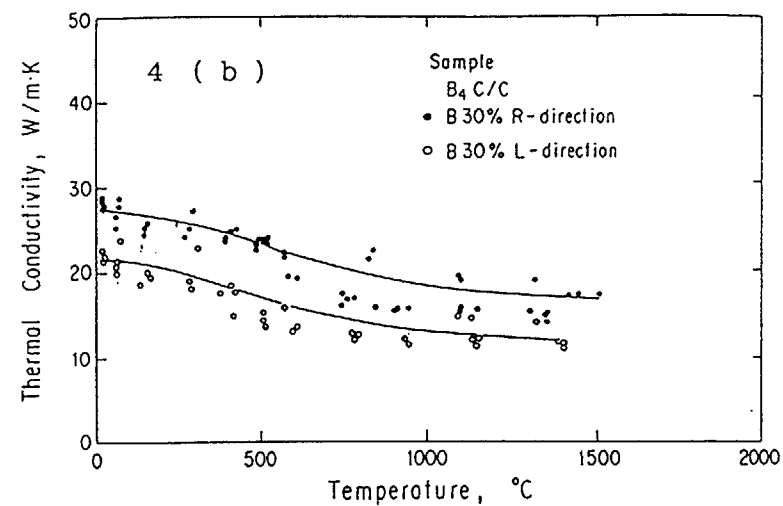
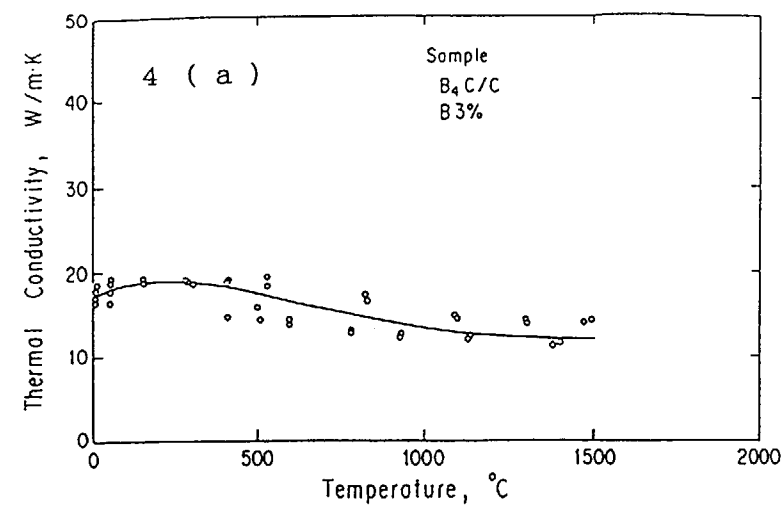


Fig. 4 Thermal conductivity of unirradiated hot-pressed boronated graphites (a) Boron content 3 wt% , (b) Boron content 30 wt%



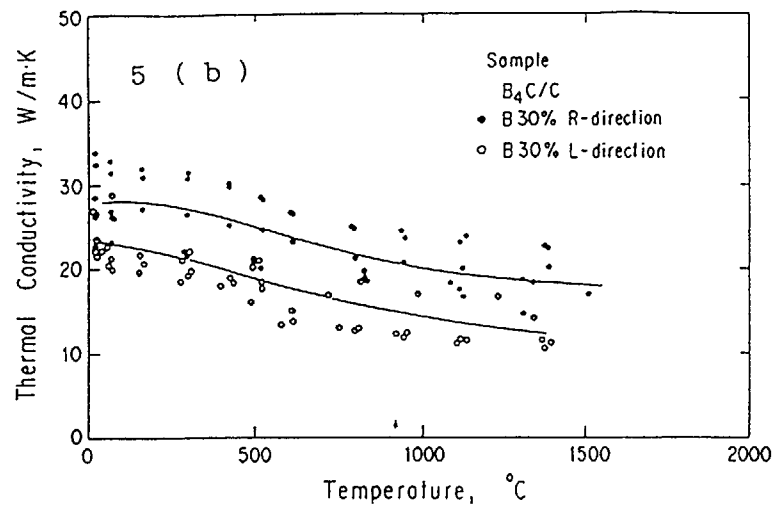
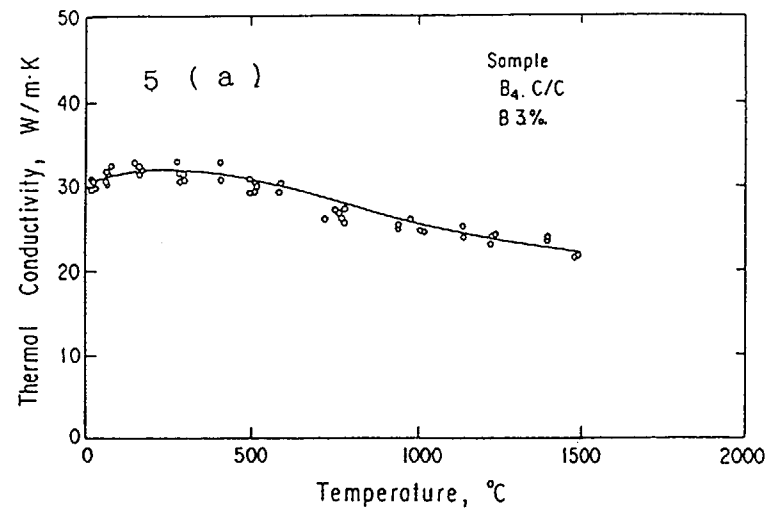


Fig.5 Thermal conductivity of unirradiated cold-pressed boronated graphites (a) Boron content 3 wt% , (b) Boron content 30 wt%

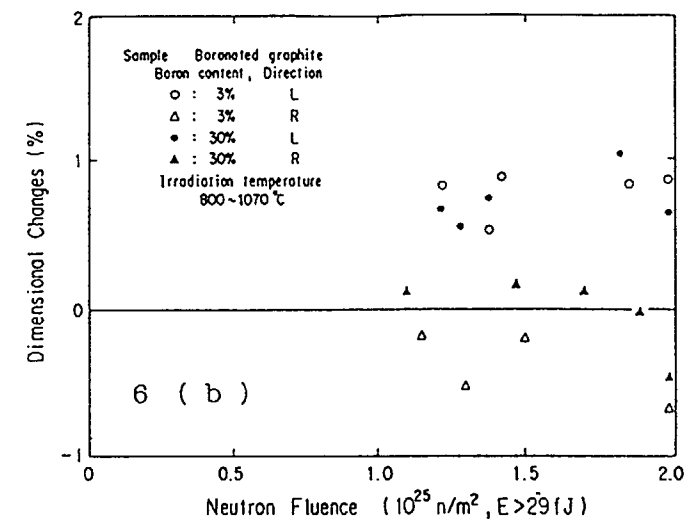
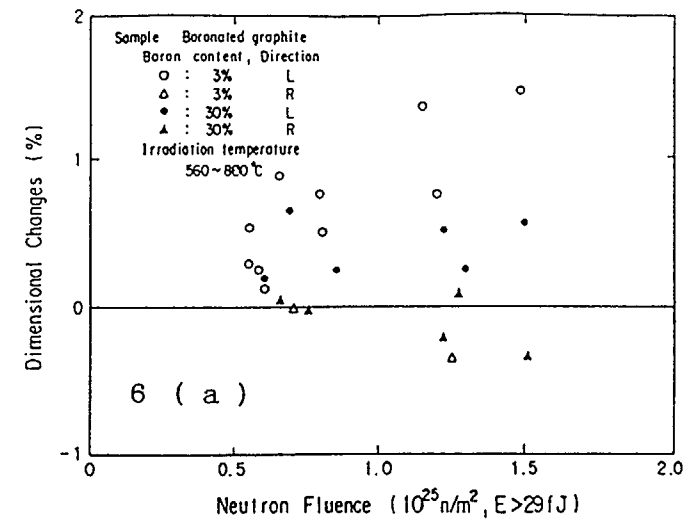


Fig.6 Dimensional changes of hot-pressed boronated graphite containing boron 3wt% or 30 wt% (a) Irradiated at 560-800 °C, (b) Irradiated at 800-1070 °C

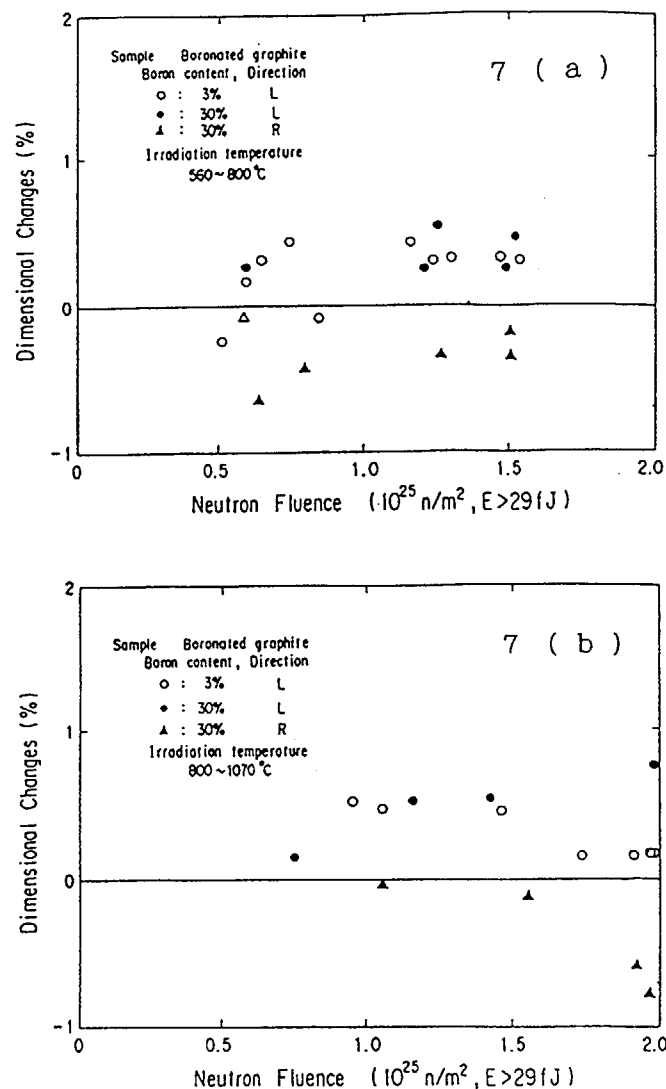


Fig.7 Dimensional changes of cold-pressed boronated graphite containing boron 3wt% or 30 wt% (a) Irradiated at 560-800°C, (b) Irradiated at 800-1070°C

### 3.2 Irradiation-induced dimensional changes

In Figs.6(a) and 6(b) irradiation-induced dimensional changes of the hot-pressed boronated graphite which boron content is either 3% or 30% are shown as a function of fast neutron fluence, where the samples were irradiated at 560-800°C and 800-1070°C, respectively. It can be seen from the figures that the dimensional changes of the samples containing 30 wt% boron are smaller than those of the samples containing 3 wt% boron. Figures 7(a) and 7(b) are the dimensional changes of the cold-pressed samples irradiated at 560-800°C and 800-1070°C, respectively. The dimensional changes seem to depend on boron content, but it is not clear because of large scattering of data. Furthermore the L direction shows the tendency of expansion compared with the R direction. These neutron fluence dependence of dimensional changes are similar to the cases of nuclear graphite. However, the most distinguished observation is that the samples containing 30 wt% boron shows smaller dimensional changes for hot-pressed samples. So, degradation of the samples containing 30 wt% boron is considered to be accelerated, because helium generated with the reaction  $^{10}\text{B}(n,\alpha)^7\text{Li}$  degrade the properties of material in addition to the effect of neutron bombardment. But the present results shows the different behavior, i.e. the sample containing 3 wt% boron shows larger dimensional changes than those of the samples containing 30 wt% boron. As pointed out by Stansfield<sup>6)</sup>, damage by fission fragment in the graphite binder matrix has important role on the changes and heavy irradiation by both fast neutron and helium has tendency to cause more contraction of dimension at the irradiation temperatures. The anisotropy of thermal expansion coefficient (CTE) is larger than that of the samples containing 30 % boron as shown in Table 1, and the irradiation-induced dimensional changes is larger for the former than the latter. This shows that anisotropy ratio of CTE is effective on dimensional changes just like the case of nuclear graphite which is more stable for isotropic graphites on irradiation-induced dimensional changes.

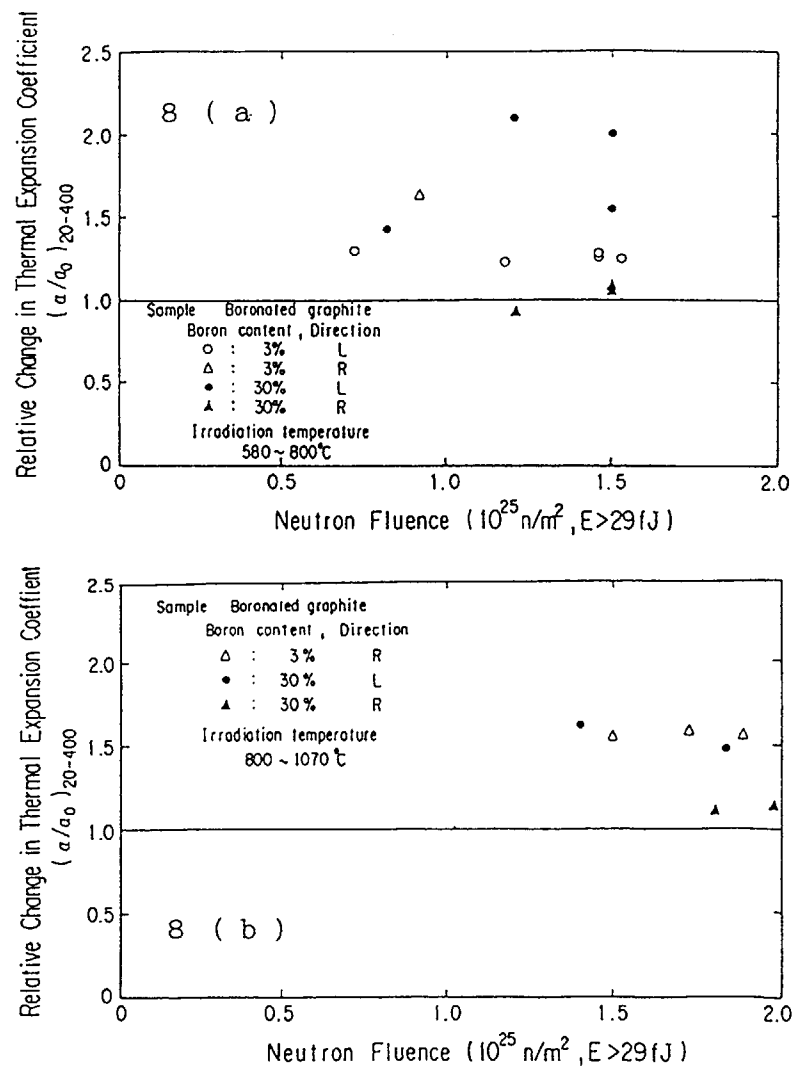


Fig. 8 Changes in thermal expansion coefficient of hot-pressed boronated graphites containing boron 3 wt% or 30 wt% (a) Irradiated at 580-800°C, (b) Irradiated at 800-1070°C

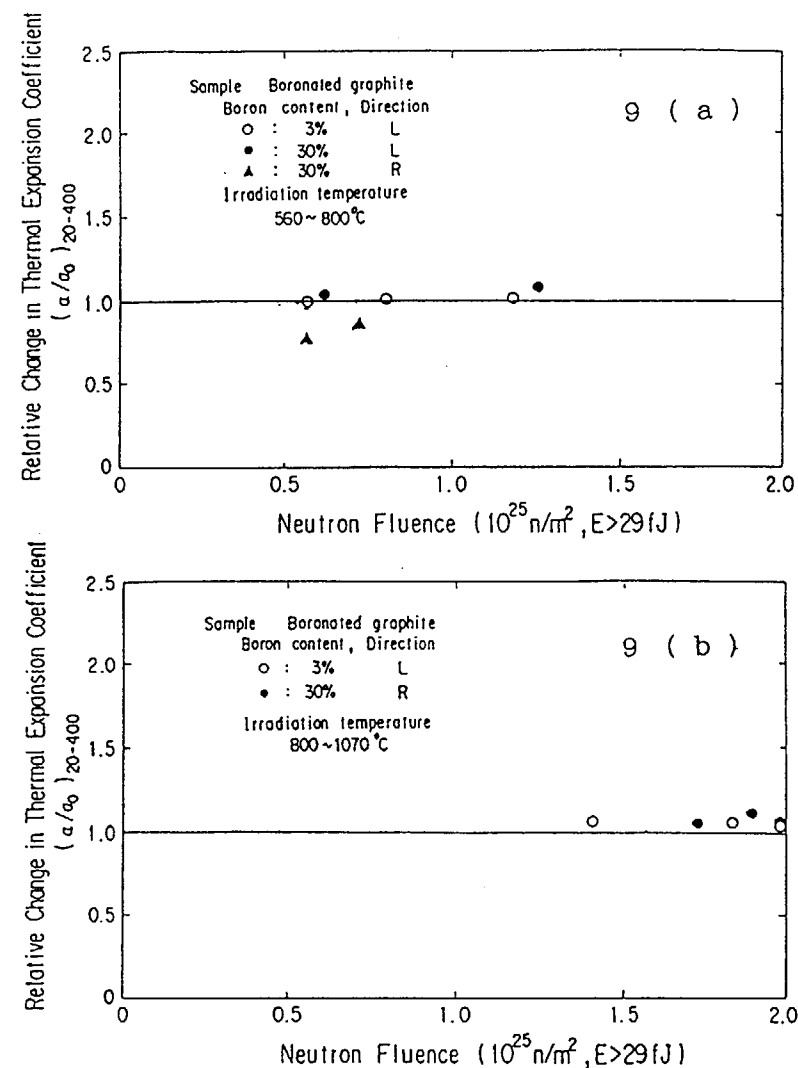


Fig. 9 Changes in thermal expansion coefficient of cold-pressed boronated graphites containing boron 3 wt% or 30 wt% (a) Irradiated at 560-800°C, (b) Irradiated at 800-1070°C

### 3.3 Thermal expansivity

In Figs.8 and 9 changes in thermal expansion coefficient (CTE) are shown as a function of fast neutron fluence, where the changes were normalized to the average measured values of unirradiated specimens. Irradiation temperatures are 560-800°C and 800-1070°C for the hot-pressed samples in Fig.8, 580-800°C and 800-1070°C for the cold-pressed samples in Fig.9, respectively. The samples containing 30 % boron has not larger changes than that of the samples containing 3 % boron for the hot-pressed samples. This leads to the suggestion that the graphite matrix degraded by helium damage is effective on the changes in CTE. But the most significant difference of the changes between the hot-pressed and cold-pressed samples is that the hot-pressed samples showed the increase after the irradiation, however the samples made through cold-pressing hardly showed the changes after the irradiation at whole irradiation temperatures in the present experiment. As described in the former section, the CTE and its anisotropic ratio of the hot-pressed samples is not so different from those of the cold-pressed samples. So, the accommodation of thermal expansivity of  $B_4C$  granules and graphite matrix of the hot-pressed sample is similar to that of the cold-pressed sample. It is therefore considered that the larger changes in CTE at lower neutron fluence for the hot-pressed samples than the case of the cold-pressed samples is due to the difference of graphite matrix and boron carbide granules, and the larger increase of CTE of the samples containing 30 % boron than that of the samples containing 3 % boron is due to helium damage.

### 3.4 Thermal conductivity

In Figs.10-12 the changes in temperature dependence of thermal conductivity are shown as a function of neutron fluence for both the hot-pressed and cold-pressed samples. Irradiation temperatures were 550-1070°C. Thermal conductivity rapidly decreased in the early stage of irradiation as shown in the figures, and its temperature dependence changed after the irradiation as well.

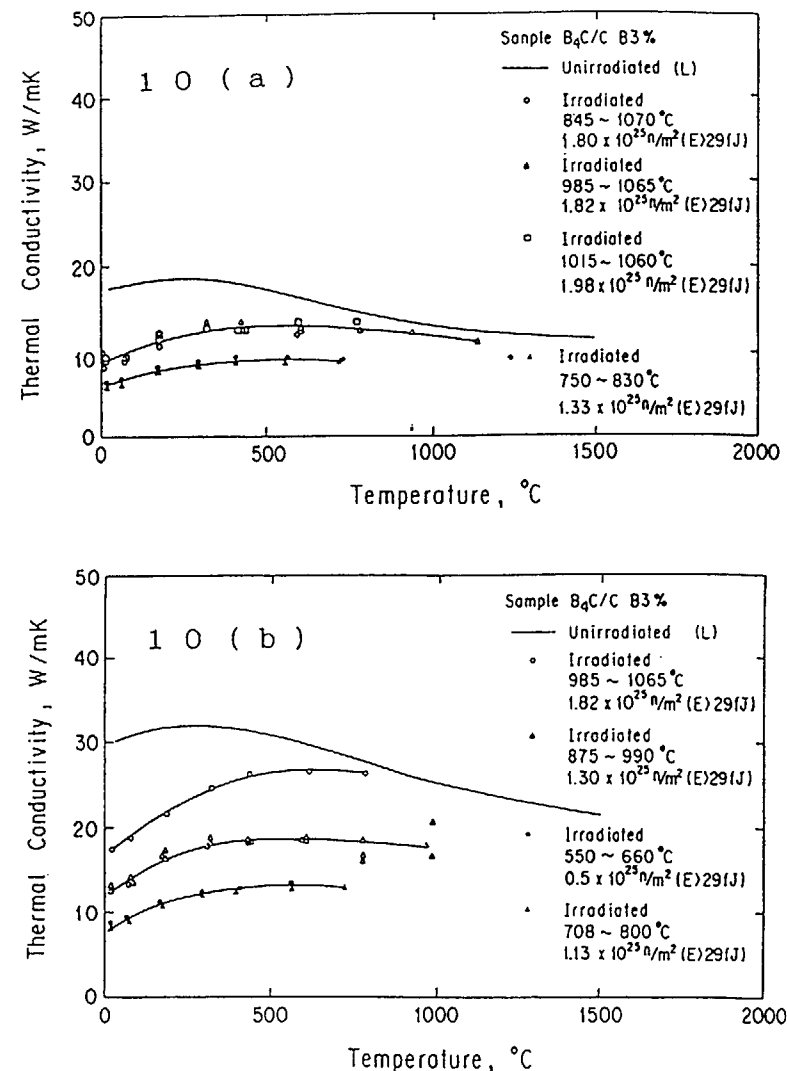


Fig.10 Temperature dependence of thermal conductivity of unirradiated and irradiated boronated graphites containing boron 3 wt%  
(a) Hot-pressed samples, (b) Cold-pressed samples

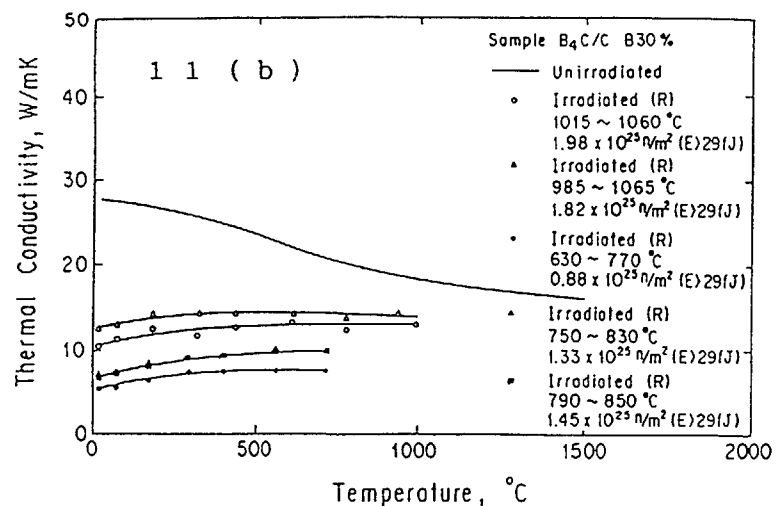
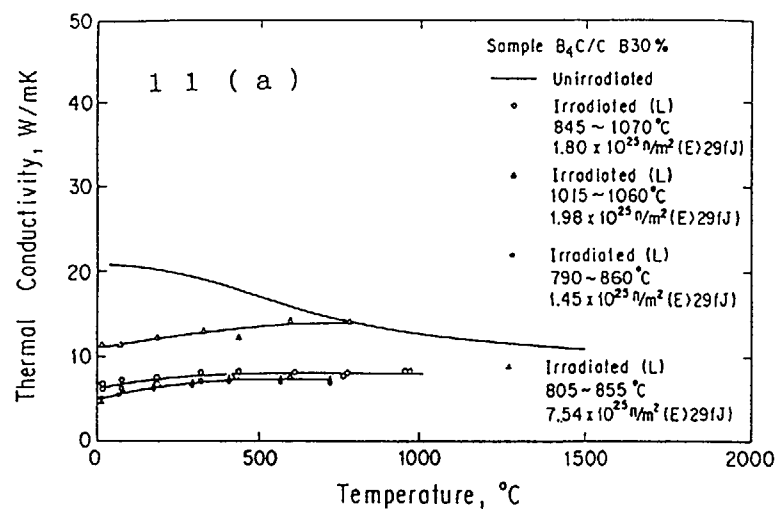


Fig.11 Temperature dependence of thermal conductivity of unirradiated and irradiated hot-pressed boronated graphites containing boron 3 wt% or 30 wt% (a) L direction, (b) R direction

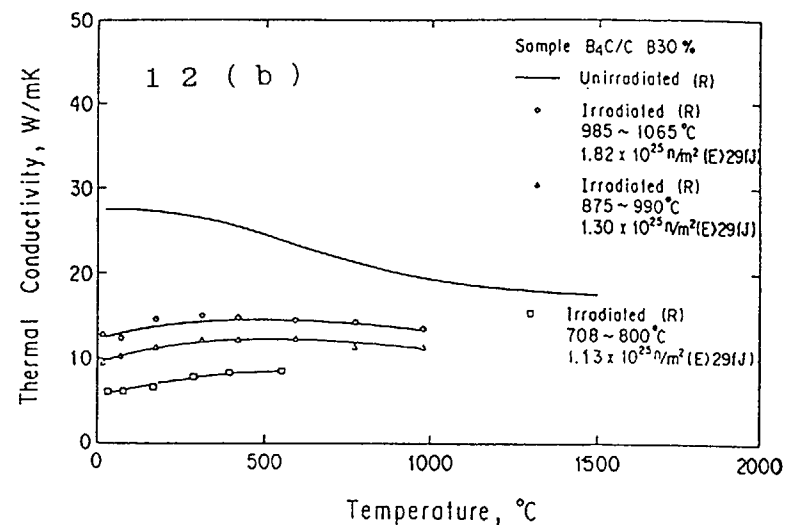
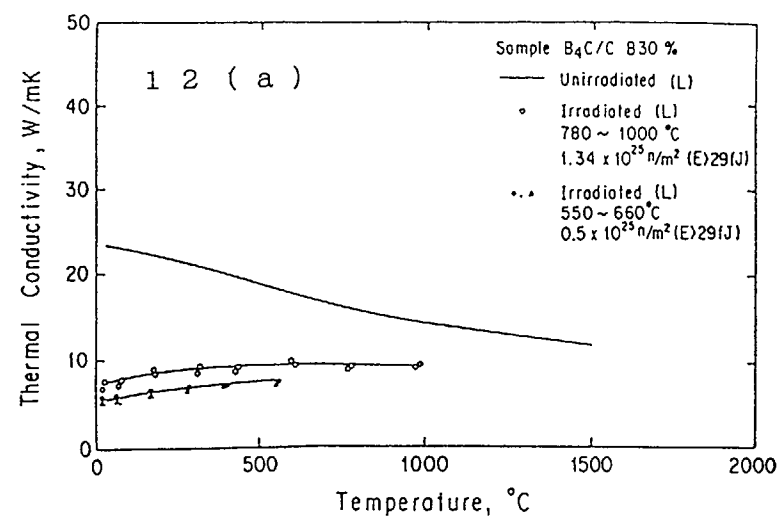


Fig.12 Temperature dependence of thermal conductivity of unirradiated and irradiated cold-pressed boronated graphites containing boron 3 wt% or 30 wt% (a) L direction, (b) R direction

The thermal conductivity of unirradiated sample shows decrease with increase measurement temperature, but the irradiated specimens show different temperature dependence. The thermal conductivity increase with temperature at low temperatures region and then decrease at higher temperatures. The peak values depend on irradiation conditions and the peak position shifts to higher temperature with increase of fast neutron fluence. This suggests that the degradation of graphite matrix occurred in addition to irradiation damage in boron carbide granules<sup>7)</sup>, and the scattering of phonon having significant role on conduction of heat above room temperature became to be effective by irradiation.

#### 4. Summary

The experimental results and discussion on the effect of neutron irradiation on the property changes of boronated graphite are summarized as follows.

- 1) Irradiation-induced dimensional changes depend on the fabrication method.
- 2) Anisotropy of CTE is effective on the irradiation-induced dimensional change.
- 3) Hot-pressed samples expand in longitudinal direction and contract in radial direction when irradiated at 560 – 800°C and 800-1070°C to fast neutron exposures up to  $2 \times 10^{25} \text{ n/m}^2 (E > 29 \text{ fJ})$ .
- 4) Cold-pressed samples expand in parallel and contract in perpendicular to the pressing direction when irradiated at 560-800°C and 800-1070 C to fast neutron exposures up to  $2 \times 10^{25} \text{ n/m}^2 (E > 29 \text{ fJ})$ .
- 5) The magnitude of expansion or contraction in either perpendicular or parallel to the forming direction for the hot-pressed samples are similar to those of the cold-pressed samples having similar anisotropy ratio of CTE.
- 6) Changes in thermal expansion coefficient depend on fabrication method. The hot-pressed sample showed increase and the cold-pressed samples hardly showed the changes by irradiation.

- 7) Neutron irradiation causes a decrease in thermal conductivity and changes in its temperature dependence. The peak of thermal conductivity shifts to higher temperatures by irradiation.

#### References

- 1) e.g. O.M.Stansfield et al. GA-A16648(1971).
- 2) H.Matsuo, Netsu Sokutei 17, 2(1990).
- 3) T.Azumi, Y.Takahashi, Rev. Sci. Instrum. 52, 1411(1981).
- 4) Y.S.Touloukin Thermophysical Properties of High Temperature Solid Materials Vol.5, New York, Macmillan (1967).
- 5) A.T.D.Butland, R.J.Maddison, AEEW-R-815(1972).
- 6) O.M.Stansfield, GA-A12035(1972).
- 7) K.E.Gilchrist, High Temp.-High Pressures 17, 671(1985).

#### DISCUSSION

##### Questions or Comments

Name: B.T. Kelly

-----  
 The boron doped samples will give different behaviors in different  
 -----  
 neutron spectra, because the boron carbide smells with burn-up of  $^{10}\text{B}$   
 -----  
 depending upon the thermal flux, while the carbon component which  
 -----  
 depends upon the fast neutron (graphite damage) flux. The behavior in  
 -----  
 an MTR will differ from that in an HTR because of the higher thermal  
 -----  
 flux.  
 -----

##### Answer:

-----  
 I quite agree with your comments. I think the irradiation behavior in  
 -----  
 the HTTR become a little different from the data presented in this  
 -----  
 meeting. We must understand irradiation behavior in the actual  
 -----  
 condition of the HTTR.  
 -----

Questions or Comments

Name: Gurin V.

Take you in account the decreasing of the neutron flux across the  
assembly because of the absorption of neutrons by B-10, and what is  
the burn out magnitude for B-10?

Answer:

In order to avoid the effect of distribution of irradiation damage  
in the samples, the samples were shaped as small as possible. Burn  
up of B-10 has not been estimated at the moment.

CAPSULE DESIGN, FABRICATION AND IRRADIATION  
FOR TENSILE CREEP TEST ON HTGR GRAPHITES  
AT 1200°C IN THE JMTR

T. SAITO

Oarai Research Establishment,  
Japan Atomic Energy Research Institute,  
Oarai-machi, Ibaraki-ken

T. KIKUCHI, T. ARAI, H. UGACHI

Tokai Research Establishment,  
Japan Atomic Energy Research Institute,  
Tokai-mura, Naka-gun, Ibaraki-ken

Japan

Abstract

An irradiation creep test under uniaxial tension in JMTR has been performed by JAERI as one of the collaborative efforts on HTGR graphite development and testing with USDOE. The purpose of the test is to determine secondary creep coefficients at 1200 °C of isotropic IG-110 graphite and near-isotropic H-451 graphite. The irradiation capsule has withstood so far c.a. 1600 EFPH irradiation in JMTR.

The paper describes outline of the design, fabrication and operational progress of the capsule designated as Capsule 89M-6A. Thermal and structural designs were devised to achieve the good thermal insulation and the mechanical integrity of key components inside the capsule. Seven dogbone type tensile specimens were encapsulated together with other unstressed control specimens. The specimen temperature control system and load control system are similar to those utilized in the previous creep tests.

In the course of three irradiation cycles in JMTR the graphite specimens have been subjected to nearly constant temperatures and the specified tensile load. The capsule will be unloaded after another irradiation cycle.

1. INTRODUCTION

An irradiation-induced secondary creep coefficient is one of the important mechanical properties which is involved in a linear viscoelastic stress analysis of an HTGR core graphite component. In-pile creep tests on graphite materials are needed to determine irradiation creep coefficient as a function of irradiation temperature. Different types of

Table 1 Summary of irradiation creep tests on IG-110 graphite in JMTR.

Experiment	Specimen temperature (°C)	Tensile stress (MPa)	Core position	Fast flux $\times 10^{14}$ n/cm <sup>2</sup> s	Fast fluence $\times 10^{25}$ n/m <sup>2</sup>	EFPH **
I (83M-2A)	756 ~ 984	9, 11, 13	G-6	1.7 ~ 3.4	0.9 ~ 1.8	1480
II (85M-5A)	~ 600	9, 11	G-6	1.8 ~ 3.7	1.0 ~ 2.1	1580
III (86M-3A)	~ 400	7, 9	I-11	0.94, 1.3	1.2 ~ 1.7	3550
IV (89M-6A) ***	(1200 $\pm$ 50)	(10)	(G-10)	(1.8 ~ 2.7)	(1.3 ~ 2.7)	(2000)

\* Neutron energy  $E > 29$  fJ

\*\* Effective operating hours of 50 MW

\*\*\* Under irradiation

experimental techniques have been adopted since 1960s. According to Price(1), they are classified into three types:

- 1) Restrained shrinkage test(2)
- 2) Fully instrumented creep test(3)(4)
- 3) Controlled load test with out-of-reactor strain measurement(5)(6)

The Japan Atomic Energy Research Institute(JAERI) has undertaken a series of controlled load tests on a fine-grained isotropic IG-110 graphite for the prismatic fuel and reflector elements of the High Temperature Engineering Test Reactor(HTTR). The creep capsules in the Japan Material Testing Reactor(JMTR) have been developed for irradiating graphite specimens under constant tensile loading at constant temperatures. Table 1 summarizes the past and present creep tests. Results of the previous three tests have been published recently(6)(7)(8).

The paper describes outline of the design, fabrication and irradiation progress of the fourth test(JMTR Capsule 89M-6A).

## 2. DESIGN AND FABRICATION OF THE CAPSULE 89M-6A

### 2.1 Design Principles

The purpose of the 89M-6A capsule is to acquire secondary irradiation creep coefficients under tension of two graphite grades at irradiation temperature of 1200 °C. The general concept of the capsule structure followed the previous one for the irradiation temperature below 1000 °C. Improvements were, however, needed to attain higher specimen temperatures by incorporating additional thermal insulation inside the outer tube having an increased outer diameter of 60mm. The radial gaps between thermal radiation reflectors and radiation shields were determined based on a 1-D radial heat transfer analysis. The arrangement

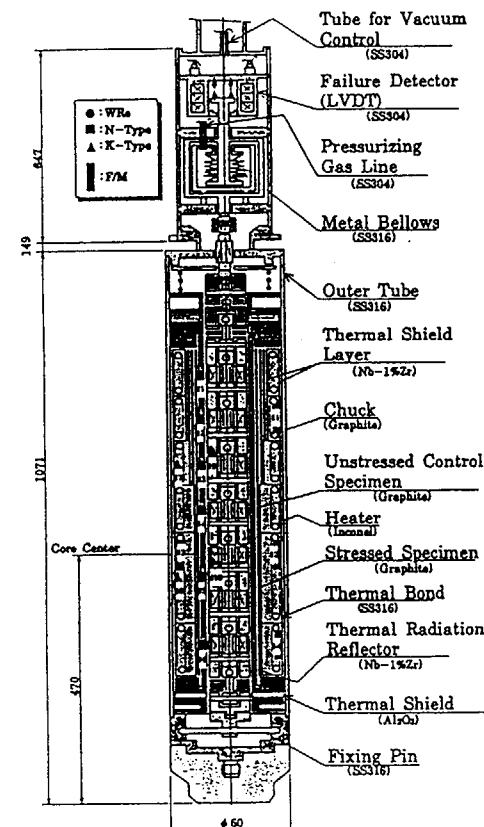


Fig. 1 Structure of JMTR graphite creep capsule(89M-6A).

of thermal and mechanical components are shown in Fig. 1. The metallic components touching the reactor coolant water are made of SS316 and SS304 while the internal metallic ones are tubes of Nb-1%Zr alloy. A tensile load generated by pressurizing a bellows is transferred to seven creep specimens connected all together by graphite chucks and pins.

Ten thermocouples are arranged in graphite specimen holders(2 W-Re type), in thermal shields(6 N type) and in thermal bonds(2 K type). Four iron fluence monitor wires are placed also in the thermal bonds. A tensile loading mechanism are similar to the previous one including the out-of-pile equipments. A temperature control system used in the previous tests are also applied in the present test.



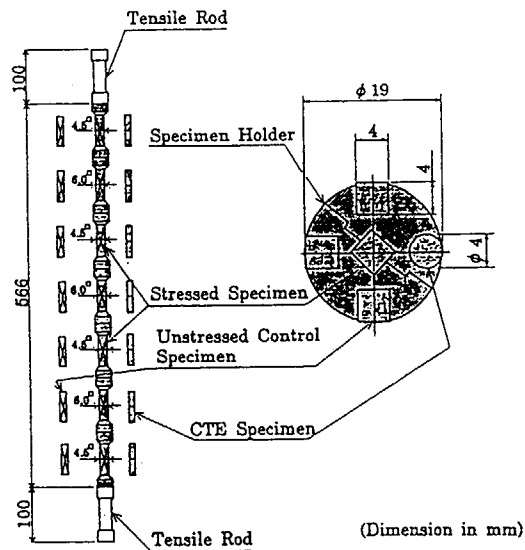


Fig. 2 Vertical and horizontal arrangement of graphite specimens.

## 2.2 Component Design and Fabrication

### Graphite specimens and their arrangement

In the graphite holders of the capsule are loaded three types of graphite specimens which compose seven sets of groups. Each group consists of one creep specimen, three unstressed control specimens and two unstressed specimens for thermal expansion measurement. The nominal dimensions and arrangement of these specimens are shown in Fig. 2. Out of seven specimen sets four sets are made of IG-110 graphite and three sets are of H-451 graphite supplied from ORNL. Considering the mean tensile strength of both graphite grades, the dimensions of the creep specimen gage section is determined to be 6x6x42mm and 4.5x4.5x42mm for IG-110 and H-451 graphite, respectively.

### Tensile loading system

A tensile loading mechanism and load controller are illustrated schematically in Fig. 3. In the present system a SS316 bellows exerts a tensile load of 20kgf(196N) to the creep specimens when pressurized to 9.9kgf/cm<sup>2</sup>(0.97MPa) by the helium gas supply line. The system was proof tested with respect to accuracy and reproducibility after the capsule assembling was completed in the machine shop and again after installed in

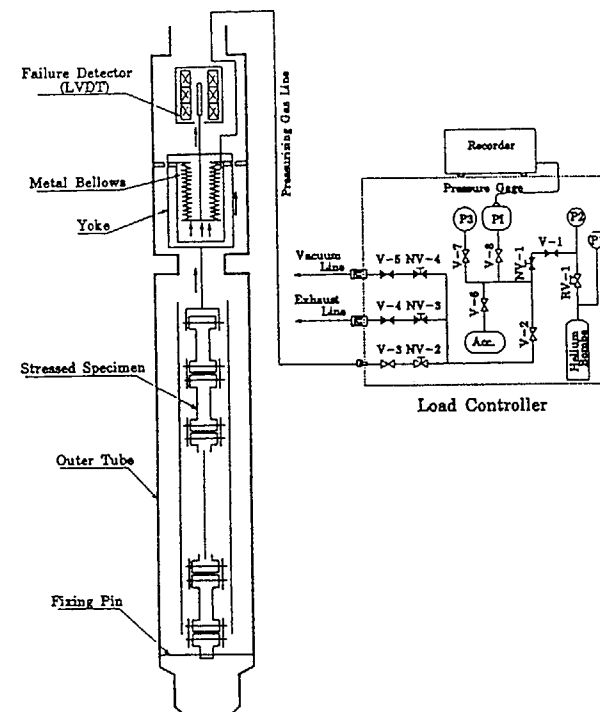


Fig. 3 Schematic loading mechanism.

the core of JMTR. The result of the proof test of the mechanism is shown in Fig. 4 which demonstrates a linear relationship between He gas pressure and applied load in the service condition. The pressure controller is actuated manually after the reactor reached the rated 50 MW power.

### Temperature control system

As mentioned earlier, two W-Re type thermocouples mounted in the specimen holders serve the indicator of the graphite specimen temperature in respective axial position. Six N type thermocouples are alternatives by taking advantage of the radial temperature distributions measured and calculated in different operating thermal conditions during the initial phase of the irradiation. A schematic representation of the temperature control system is given in Fig. 5. The temperature controller is aided by a personal computer which regulates automatically a helium gas

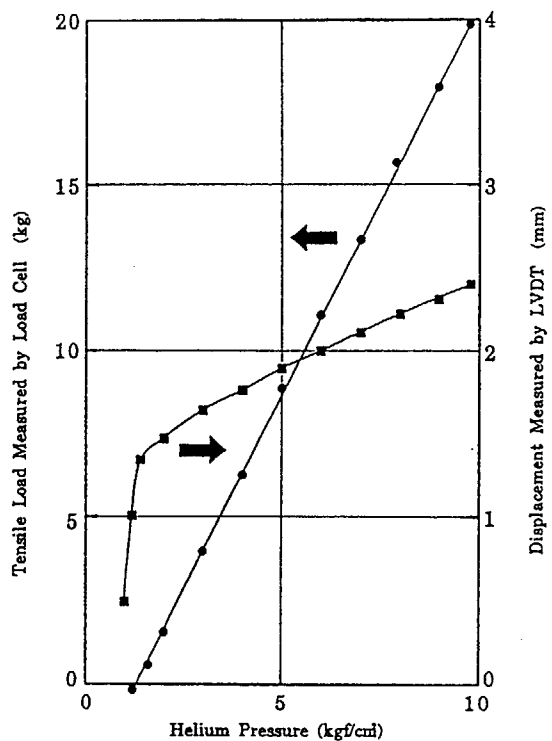


Fig. 4 Result of proof test of loading mechanism.

concentration or vacuum inside the capsule by actuating a mass flow controller, MFC. An additional manual control can be provided with six electric heaters in grooves of the thermal bonds. The temperature controller of the capsule regulates to the best of its ability in each reactor cycle. All temperature instrumentation is supported by a data acquisition/processing system, LOOCAS, which handles the load controller signals, as shown also in Fig. 5.

### 3. PROGRESS OF THE CAPSULE IRRADIATION

#### 3.1 Status of Irradiation

The capsule 89M-6A was loaded into the core position G-10 in the fuel region of the JMTR core as shown in Fig. 6. In Fig. 7 is shown the setup of the operation facility on the operating floor of the JMTR for controlling specimen temperature and tensile load.

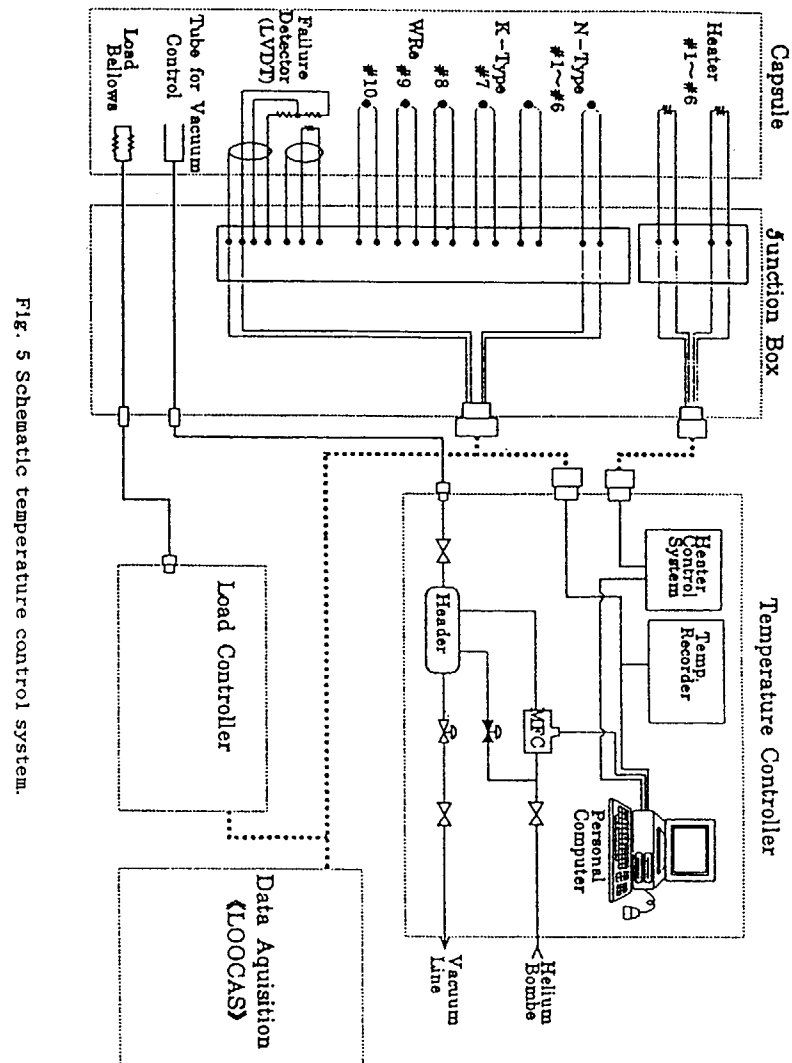


Fig. 5 Schematic temperature control system.

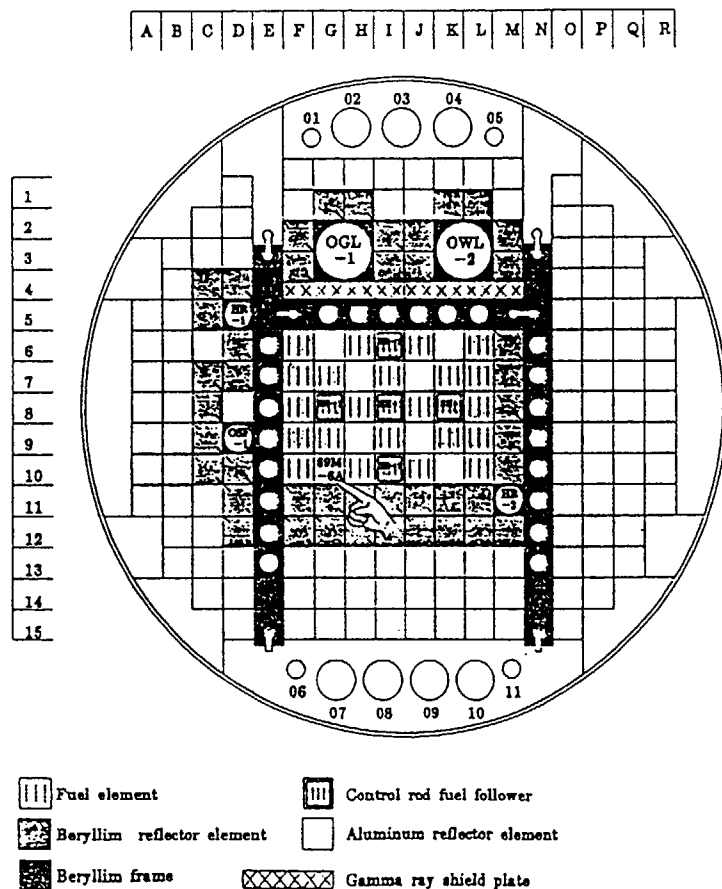
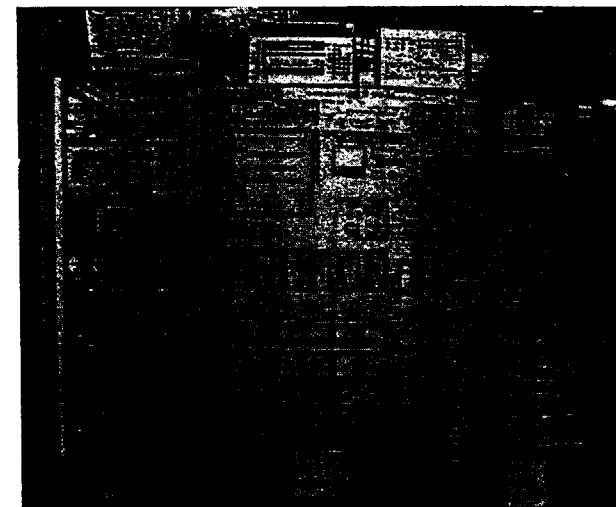


Fig. 6 Core layout of JMTR reactor.

The irradiation in the first cycle(#94 Cycle) was started on January 19, 1991. Until the beginning of last June, the capsule has been irradiated for three Cycles(1600 EFPH/effective full power hours) under controlled specimen temperature and tensile load. The next Cycle will be expected to end in the middle of the coming October which will result in a cumulative irradiation duration of c.a. 2000 EFPH and the maximum neutron fluence of  $2.7 \times 10^{25} \text{ n/m}^2 (\text{E} > 29 \text{ fJ})$ .



A: Load Control Apparatus  
B: Heater Control Apparatus  
C: Temperature Control Apparatus

Fig. 7 Photograph of capsule operating facility.

### 3.2 Specimen Temperature Distribution and History

Figure 8 shows the temperature distributions measured by the thermocouples and calculated by a thermal analysis program GENGTC for the two operating thermal conditions at the rated power: one for fully filled He gas in the internal gaps and the other for controlled vacuum/He gas. The target specimen temperature of  $1200 \pm 50^\circ \text{C}$  was maintained in five groups of specimens. The uppermost two groups were approximately at  $1100^\circ \text{C}$  and  $850^\circ \text{C}$ . These temperature decreases may be caused mainly by too low nuclear heating in the upper components and excessive upward heat conduction. In Fig. 9 is shown the measured temperature history during the Cycle #95 in which the temperature control was carried out automatically by the thermocouple #5(N type). The thermometry by other thermocouples has indicated nearly constant irradiation temperatures during three reactor cycles although there have been observed unavoidable deviations due to control rod maneuvering within respective cycle. A time-based temperature frequency of each specimen group will be analyzed after completing the planned next irradiation cycle.

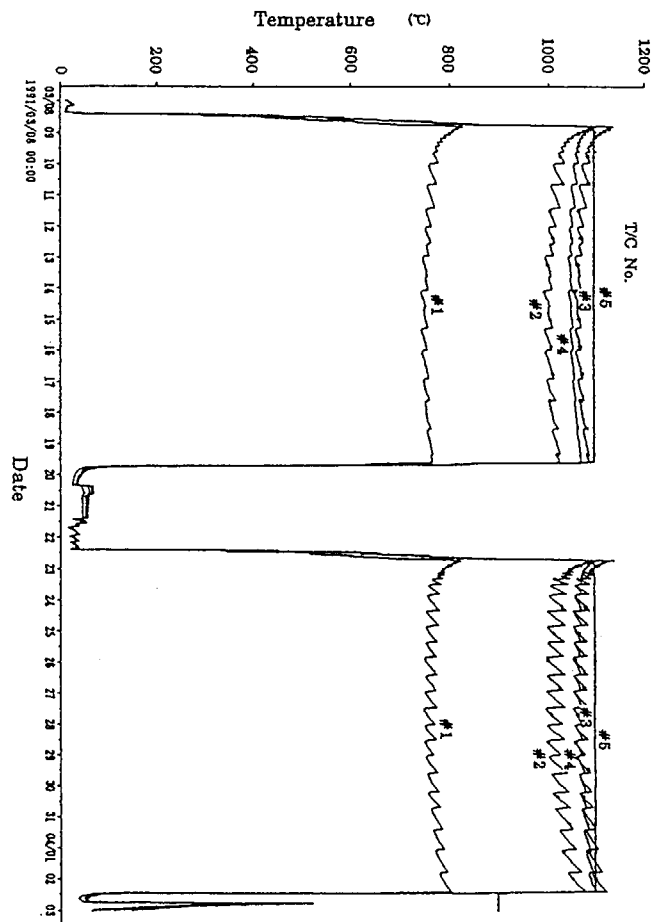


Fig. 9 Measured temperature history during #95 Cycle

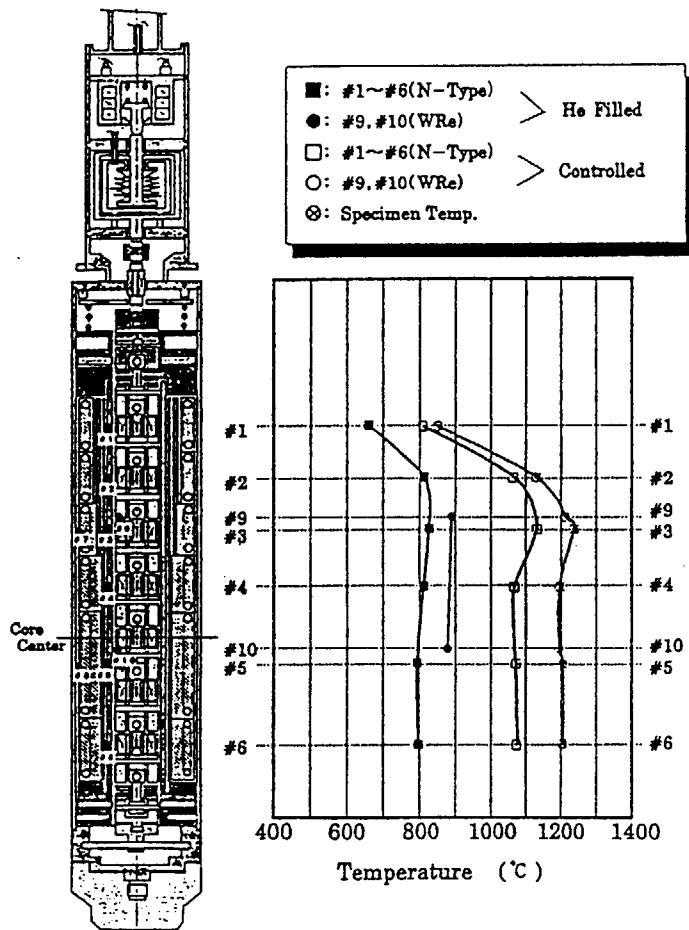


Fig. 8 Temperature distributions in the capsule.

#### ACKNOWLEDGEMENT

The authors are indebted to Messrs. Y. Ichihashi and H. Ito of Irradiation Division I of Department of JMTR Project for their support and encouragement, and to the staffs of Irradiation Division II and Reactor Division I who have operated successfully the JMTR and the test facility. Thanks are also due to the staffs of Mechanical Engineering Division of Department of Engineering Services in the Tokai Research Establishment. They are grateful to Drs. T. Oku, M. Eto and T. B. Burchell who have coordinated the test program as the collaborative work in the JAERI / USDOE Research Agreement.

#### REFERENCES

- (1) R. J. Price, GA-A16402 (1981)
- (2) H. J. Veringa and R. Blackstone, Carbon, 14, 279 (1976)
- (3) M. Masson, J. Nucl. Mater., 65, 142 (1977)
- (4) H. Hansen, R. Loelgen and M. Cundy, Ibid, 148 (1977)
- (5) R. L. Senn, W. H. Cook, J. A. Conlin and W. P. Eatherly, Ibid, 96 (1977)
- (6) R. Loelgen and F. Mason, Ibid, 131 (1977)
- (7) T. Oku, T. Arai and M. Eto, Extended Abstracts of 19th Biennial Conf. on Carbon, 486 (1989)
- (8) T. Oku, M. Eto and S. Ishiyama, J. Nucl. Mater. 172, 77 (1990)
- (9) T. Arai, H. Ugachi, T. Oku, T. Kodaira and M. Eto, Proc. Int. Symp. on Carbon vol.I, 162 (1990)

#### DISCUSSION

Questions or Comments                      Name: Tim Burchell

-----  
Is it necessary to rotate the creep capsule to even out the flux  
gradient to the specimen?  
-----

Answer:

-----  
It is actually impossible to rotate the capsule assembly in the core  
because of fixed handling and locating devices. Unavoidable flux  
gradient can be measured and estimated by flux monitors and physics  
calculations.  
-----

#### STRENGTH ANALYSIS CODE FOR GRAPHITE STRUCTURAL COMPONENTS IN URANIUM-GRAPHITE NUCLEAR REACTORS

B.S. RODCHENKOV, P.A. PLATONOV, V.N. MANEVSKIY,  
B.A. KASHIRIN, O.K. CHUGUNOV  
Research and Development Institute of  
Power Engineering,  
Union of Soviet Socialist Republics

#### Abstract

The Strength Analysis Code for Graphite Components Used in Uranium-Graphite Channel - type Reactors has been developed in the USSR on the basis of results of reactor graphite property investigations including its properties under neutron irradiation conditions as well as on the operating experience of graphite structural components in the uranium-graphite reactors. The graphite stack forms the basis for the uranium-graphite reactor design. The strength analysis of the graphite components are performed following the physics and thermal physics calculations needed to assess thermal and radiation stresses in the analyzed components as well as following the account of variations in physics and mechanical properties of graphite under neutron irradiation and temperature. Strength analysis principles in the code are based on limiting states determined for achievement of critical fluence, crack formation under static loading, accumulation of ultimate strain, and initiation of through crack under static and cyclic loading. Each of these is discussed in the paper.

#### I. Introduction

The strength analyses of structures, equipment and pipelines for uranium-graphite and other type reactors are being carried out in the USSR according to the requirements of "Strength Analysis Code for the NPP Equipment and Pipelines" /1/. The Soviet strength analyses CODE are similar to those of ASME CODE in main principles and in most part of concrete approaches. However, the Code requirements are not extended to the graphite structural components. This is due to the specific mechanical behaviour of graphite as a structural material and loading conditions of graphite structural components.

"The Strength Analysis Code for graphite components used in Uranium-Graphite Channel - type Reactors" has been developed in the USSR on the basis of results of reactor graphite property investigations including its properties under neutron irradiation conditions as well as on the operating experience of graphite structural components in the uranium-graphite reactors. The present report presents the main code statements.

## 2. Graphite Structural Components Used in Uranium-Graphite Reactors and Their Operating Conditions.

The graphite stack forms the basis for the uranium-graphite reactor design. The internal part of the graphite stack where the fuel channels are arranged, is a core (here graphite is used as a moderator) and the peripheral one using to decrease the neutron leakage, is a reflector. The graphite stack of the power reactors is a cylinder consisting of multiple vertical columns. Thermal expansion of columns takes place easily without interaction between adjacent columns. The gaps are provided between the columns to compensate thermal and radiation expansion in the transverse direction.

The columns consist of blocks being, basically, the main structural component of the graphite stack. The cross-section of the block is quadrangular or hexagonal in form. In the central part of the block there are openings for fuel channels or fuel elements to be arranged there. The sleeves or rings of various design are used to improve heat transfer from the graphite stack. For instance, there are split rings to be used in the most heat-stress part of the RBMK reactor core and sleeves - above or below this core part. The sleeves and rings can be replaced and removed from the reactor together with fuel channels. The graphite block lifetime is practically determined by the reactor lifetime as a whole.

In operation, the graphite structural components are exposed to temperature and neutron flux irradiation, the value of which is determined by the reactor neutronics. The temperature and neutron fluence gradients in the cross-section and in graphite block length give rise to initiation of thermal and radiation stresses in them. Since the physics and mechanical properties of graphite are significantly changed as a result of neutron radiation effect, the stress distribution in graphite blocks is non - uniform and can be varied during the whole reactor lifetime.

Maximum temperature of the graphite stack doesn't exceed, as a rule, 800°C, and neutron fluence during the whole lifetime is  $1-2 \times 10^{26}$  ( $E > 0.18 \text{ MeV}$ )  $\text{n/m}^2$  Helium or nitrogen or their mixture is pumped through the graphite stack to prevent graphite oxidation as well as to improve heat transfer.

Table 1 /2,3/ presents the brief characteristic of the graphite stack structures and operating conditions in nuclear power uranium-graphite reactors used in the USSR.

TABLE 1

Reactor/NPP	First in the world NPP	Beloyarsk NPP	RBMK
1	2	3	4
Reactor power, MW		(1unit)(2unit)	
electrical	5	100 200	1000
thermal		280 530	3200
Configuration of graphite stack	Cylindrical	cylindrical	cylindrical

TABLE 1 (cont.)

1	2	3	4
Arrangement of cells (channels)	vertical	vertical	vertical
Dimensions of the graphite stack, mm			
diameter	3000	9600	13800
height	4500	9000	8000
Number of cells in the graphite stack, pieces	150	1134	2488
Configuration of the graphite blocks	hexagonal	hexagonal	quadrangular
Dimensions of the graphite blocks	173x173x600	173x173x600	250x250x600- -200
Graphite temperature, Maximum, C	800	725	750

### 3. Loads and Assessment of Stress-Strain State.

Based on the operating conditions and structural features, we can conclude that the loading on the graphite structural components in uranium-graphite reactors is resulted from the effect of:

- weight,
- temperature,
- neutron irradiation,
- contact with channels (FEs) when the gaps are exhausted,
- loads during mounting or repair,
- earthquake.

The first three effects among the above ones are constant whereas the later ones are of temporary or random character.

The strength analyses of the graphite components are performed following the physics and thermal physics calculations needed to assess thermal and radiation stresses in the analyzed components as well as following the account of variations in physics and mechanical properties of graphite under neutron irradiation and temperature.

The residual stresses in the graphite components resulted from the manufacturing procedure are not accounted for.

Methods for assessment of the stress-strain state of graphite components are not specified by the strength analysis Code. In this connection, the section describing the used methods, is included in the Code as a recommendation.

The account of all the above loads as well as nonuniform distribution of temperature and neutron flux is the obligatory requirement for the methods of the graphite components stress-strain state analysis. In stress-strain analysis graphite is considered to be a viscoelastic material.

The anisotropy of physics and mechanical properties, their changes by radiation and oxidation, the irradiation induced dimensional changes and the creep are accounted for no matter whether the finite element method or the engineered calculation one is used in stress and strain assessment.

As a result of calculation, the equivalent stresses,  $\bar{\sigma}_{\text{equiv}}$ , and strain intensity,  $E_i$ , can be derived. The modified criterion of maximum elastic strain energy is used to calculate  $\bar{\sigma}_{\text{equiv}}$ .

$$\bar{\sigma}_{\text{equiv}} = \sqrt{\bar{\sigma}_I^2 + \bar{\sigma}_{II}^2 + \bar{\sigma}_{III}^2 - 2(\bar{\sigma}_I \bar{\sigma}_{II} + \bar{\sigma}_{II} \bar{\sigma}_{III} + \bar{\sigma}_I \bar{\sigma}_{III})},$$

where  $\bar{\sigma}_i = \sigma_i$  for  $\sigma_i > 0$  and  $\bar{\sigma}_i = \sigma_i (R_m^t/R_m^c)$  for  $\sigma_i < 0$

$\sigma_i$  - main stresses in the given point (i.e.  $\sigma_I, \sigma_{II}, \sigma_{III}$ )

$\nu$  - Poisson coefficient

$R_m^t$  and  $R_m^c$  - tensile and compression strengthes, respectively.

The strain intensity can be derived as a function of:

$$E_1 = \frac{\sqrt{2}}{3} \sqrt{(E_x - E_y)^2 + (E_x - E_z)^2 + (E_z - E_x)^2 + \frac{3}{2} (E_{xy})^2 + (E_{yz})^2 + (E_{zx})^2},$$

where  $E_1$  - irradiation creep strain intensity

#### 4. Strength Analysis

The following limiting states form the basis for the strength analysis principles adopted in the Code:

- achievement of critical fluence,
- crack formation under static loading,
- accumulation of ultimate strain,
- initiation of through crack under static and cyclic loading.

Let's comment upon each of them. The critical fluence is a fluence at which the volume of graphite is recovered up to the initial value with the irradiated induced dimension changes following the shrinkage stage, i.e.  $\Delta V/V=0$  (Fig.1). Under this condition graphite is in "secondary swelling" stage. Its structure is intensively degraded and the intensified cracking is mainly observed between the filler grains (coke) and the binder, which results in a drastic deterioration of all its physics and mechanical properties. The condition for conservation of graphite serviceability is the relationship of

$$F_{\text{lifetime}} < F_{\text{cr}}$$

to be satisfied for the whole volume of the component.

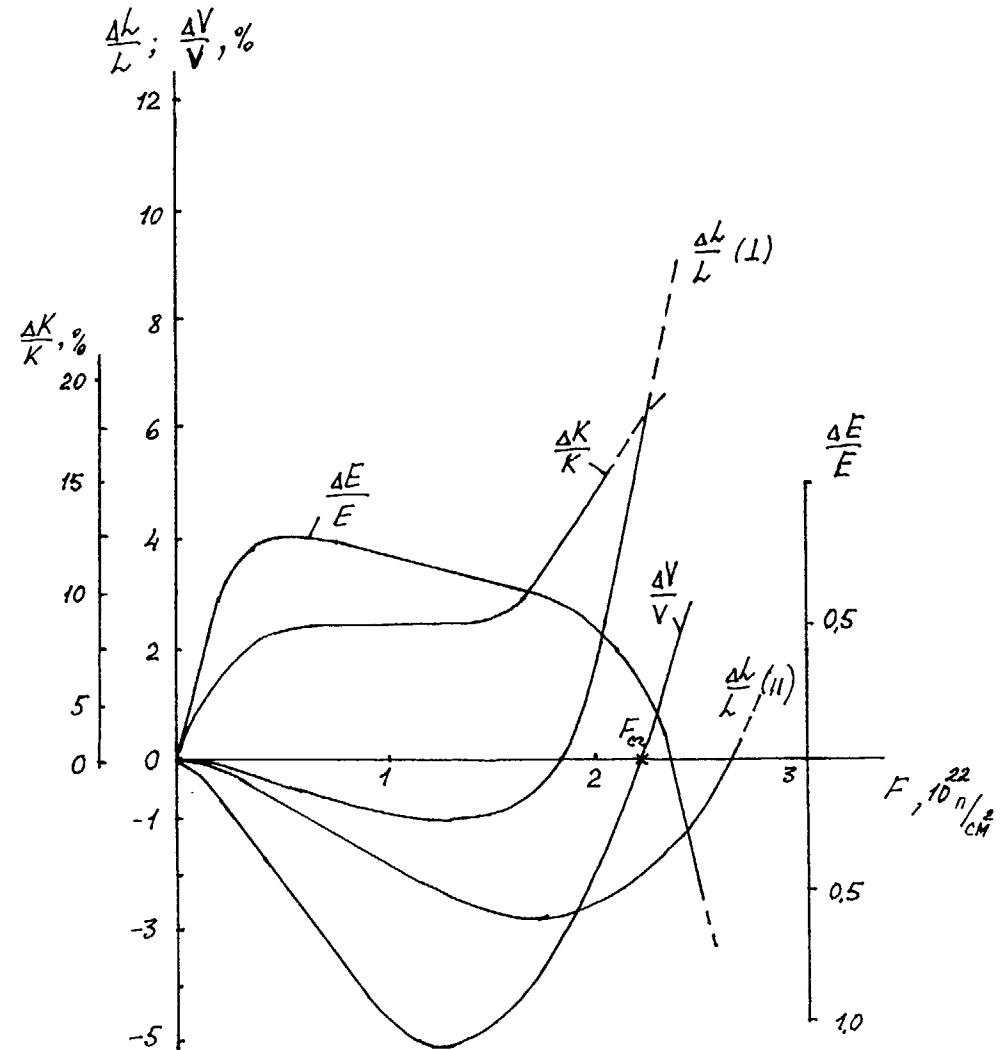


Fig.1. Relationship Between the Variation in the Standard Reactor Graphite Properties ( IP 280) and Neutron Fluence at Temperature Specific For Graphite Stack Operation in RBMK-1000 Reactor.

$$/T_{ic} = 500-600^{\circ}\text{C}/.$$



In this case, if this condition is violated for the restricted volume of the component, its integrity and serviceability are still conserved. The strength under static loading is considered to be assured, if the below condition is satisfied:

$$\sigma_{\text{equiv.}} \leq [\sigma],$$

where  $[\sigma]$  is the allowable stress, derived from the equation:

$$[\sigma] = \frac{R_m^{\dagger}}{n}$$

where  $R_m^{\dagger}$  - the average value of the tensile strength at the given fluence, and  $n$  - the margin factor for the average value of  $R_m^{\dagger}$  equal to 1.

From this it follows, that crack formation is possible if the equivalent stresses reach the values equal to tensile strength or those to be excess in the point of component analysis.

The crack can be initiated under static loading not only as a result of an excess in allowable stresses but as a result of strain accumulation by creep. The crack initiation criterion in this case is the condition of achieving the creep strain intensity of 2%, i.e.

$$E_i \leq 0,02$$

where  $E_i$  - irradiated creep strain intensity.

The initiation of surface macrocracks doesn't mean that the graphite blocks can perform their functions. In this case, the next stage of the analysis is to analyse the crack propagation which can occur by different mechanisms: either as a consequence of static loads or as a consequence of low-cycle fatigue.

The achievement of intensity factor with  $K_{IC}$  critical value is the criterion of crack propagation under static loads, i.e.

$$K_I > K_{IC}$$

To assess the crack propagation under cyclic loading, Paris relationship is used.

$$\frac{\Delta l}{\Delta N} = C \Delta K_I^m$$

where  $C$  and  $m$  - material constants,  $\Delta l$  - crack undergrowth and  $\Delta K_I$  - variation in the intensity factor per a cycle.

The condition of inadmissible through crack growth is taken to be a crack resistance criterion which guarantees the operability of graphite components. With the through crack it is required to give the additional justification of possible safe operation with regard to functional criteria of operability. Such functional criteria for the graphite stack are as follows:

- achievement of limiting gap value between the fuel channel tube and graphite blocks;
- excess of allowable operating temperature;
- excess of allowable graphite column sag;
- blocks failure.

## 5. Materials and their Physics and Mechanical Properties.

Only, the types of graphite materials specified in the Code, should be used to manufacture the structural components for uranium-graphite reactors. The semifinished items of these graphite types should be delivered according to the quality requirements specified in the standards and specifications.

The graphite characteristics listed in the delivery standards are used for strength and thermal physics analyses to be carried out. With lack of required data in the standards the Code data should be used. The following characteristics are

used as graphite material characteristics being applied for strength analyses:

- tensile, compression and bending strengthes of  $R_m^t, R_m^c, R_m^b$ ;
- elasticity modulus and Poisson coefficient, ;
- thermal expansion and heat conduction coefficient;
- characteristics of radiation changes in dimensions;
- critical coefficient of stress intensity,  $K_{IC}$ ;
- creep constants;
- crack growth constants under low-cycle fatigue.

The above characteristics are determined in parallel and perpendicular directions with respect to material ingot extrusion axis with the temperature range from 20 to 800°C at the initial state and after urradiation.

#### REFERENCES

1. Нормы расчета на прочность оборудования и трубопроводов атомных энергетических установок (ПНАЭ Г-002-86), М. Энергоатомиздат, 1989г.
2. Канальный ядерный энергетический реактор. Н.А.Доллежалъ, И.Я.Емельянов, М.,Атомиздат,1980.
3. Действие облучения на графит ядерных реакторов. М.,Атомиздат, 1978г.

**MATERIALS DEVELOPMENT AND PROPERTIES**  
**Part D**

**(Session III)**

**Chairmen**

**M. ROEDIG**  
Germany

**K. KIKUCHI**  
Japan



# THE EFFECT OF VOLUME ON THE TENSILE STRENGTH OF SEVERAL NUCLEAR-GRADE GRAPHITES\*

J.P. STRIZAK

Oak Ridge National Laboratory,  
Oak Ridge, Tennessee,  
United States of America

## Abstract

This report will present the results of a study on the effects of stress volume on the tensile strength of two nuclear-grade graphites. The materials selected were H-451, an extruded near-isotropic graphite manufactured by Great Lakes Carbon Corporation, and IG-110, a fine-grained isotropic molded graphite manufactured by Toyo Tanso Company, Ltd.

The tensile properties of H-451 were examined extensively in the past in order to characterize the variability of strength within billets, between billets, and between lots. But, the variability within a billet was, for the most part, studied only casually. The problem was the strong influence of a limited sampling plan in describing the mean strength and the variability. Therefore, an extensive, statistically sound sampling plan has been devised to fully characterize the spatial variability within a single billet. The effects of stress volume are being reexamined by comparing the strengths of four specimen sizes covering a broad range in stress volume.

Specimen configurations were machined to conform to ASTM C749-87, *Standard Test Method for Tensile Stress-Strain of Carbon and Graphite*. Test results for four specimen sizes having gage diameters of 6.35, 9.53, 15.88, and 25.40 mm will be reported for H-451 graphite. Respective gage-section volumes are 1407, 3163, 12,577, and 51,482 mm<sup>3</sup>. Likewise, tensile test results for the isotropic, high-strength IG-110 graphite will be reported. Tests will be performed on all but the largest of the four specimen sizes.

Two models will be employed for analysis of the stress volume data for the selected graphites. The popular Weibull model has previously been found to grossly overestimate the volume dependence of the strength of H-451 graphite. The model will be reevaluated using the improved statistical distribution of strength expected from the current sampling plan.

A new fracture model developed by Burchell and Tucker has potential for determining the effect of stress volume on the tensile strength of graphite. This probabilistic failure criterion combines a microstructural basis with a fracture-mechanics approach to failure. An initial evaluation of H-451 data showed that the model closely predicted the mean tensile strength for the two smaller specimen sizes.

\* Research sponsored by the Division of MHTGRs, Office of Advanced Reactor Programs, US Department of Energy, under contract DE-AC05-84OR21400 with Martin Marietta Energy Systems, Inc.

## 1. INTRODUCTION

The variability and statistical distribution of graphite strength (tensile, compressive, fatigue, flexure, and fracture toughness) must be considered in the design of critical reactor core components. A fracture model based on the governing role of flaws in the microstructure of the brittle graphite material, and relating the probability of failure to the volume of material under stress would be a useful engineering design tool. The model could be combined with finite-element stress analysis to show compliance with reliability requirements for critical structural components.

Work is currently underway to validate the existing data base on H-451 graphite, and to improve the statistical distributions used in probabilistic analysis. New data on the dependence of tensile strength on specimen size (stress volume) are reported herein. The application of several models to the data on extruded H-451 graphite as well as a high strength isotropic moulded graphite, IG-110, are reported.

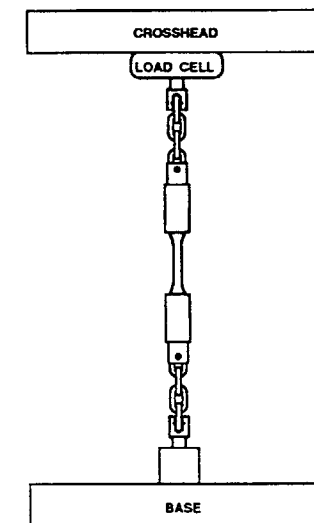


Fig. 1. Schematic diagram of tensile testing load train.

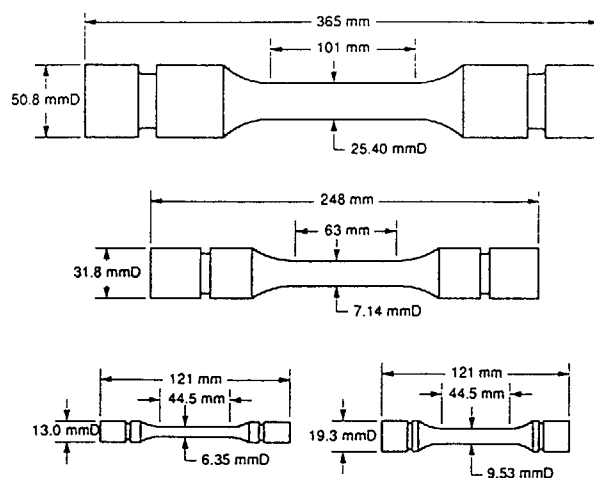


Fig. 2. Tensile specimen sizes.

## 2. EXPERIMENTAL PROCEDURE

Tensile tests at room temperature were conducted according to the ASTM C749-87 [1] method for tensile testing of graphite. Tests were performed on a microprocessor based Instron electromechanical test system equipped with specimen grips incorporating chain links which serve to minimize parasitic stresses. Figure 1 shows a schematic drawing of the test system and the specimen gripping arrangement. All tests regardless of specimen size were conducted at a constant extension rate (crosshead speed) of  $8.5 \times 10^{-3}$  mm/s. Only the fracture strength of each specimen was recorded; no strain measurements were taken in this study on the effect of stress volume (specimen size) on tensile strength.

Four specimen sizes having gage diameters of 6.35, 9.53, 15.88, and 25.40 mm were machined such that the specimens were axially aligned with the longitudinal axis of the graphite billet (log). Schematic drawings of the test specimens are shown in Figure 2, and gage section volumes are listed in Table 1.

Table 1. Tensile specimen stress volumes

Gage diameter (mm)	Gage length (mm)	Stress volume (mm <sup>3</sup> )
6.35	44.44	1,407
9.53	44.44	3,163
15.88	63.50	12,577
25.40	101.60	51,482

## 3. MATERIAL: GRADE H-451 GRAPHITE

Grade H-451, manufactured by Great Lakes Carbon Corporation, is a near-isotropic, petroleum-coke based, medium grained graphite that has been heat treated to 2,650°C and gas purified. The graphite is extruded into billets measuring 432-mm diameter by 813-mm long. An entire billet was consumed for tensile testing to determine the effects of 1) specimen size on strength, and 2) spatial variability of strength throughout the billet. The latter is the topic of another presentation by the author at this IAEA Specialist's Meeting [2].

Prior to specimen fabrication, the billet of H-451 was cut into slabs. The various specimen sizes were machined from the slabs as indicated in Figure 3. At two locations along the billet length, i.e., positions 2 and 5 in Figure 3, all four specimen sizes were available through the cross-section of

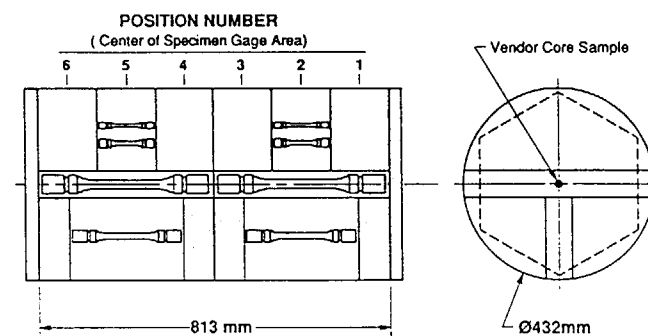


Fig. 3. H-451 Graphite billet slabbing plan.

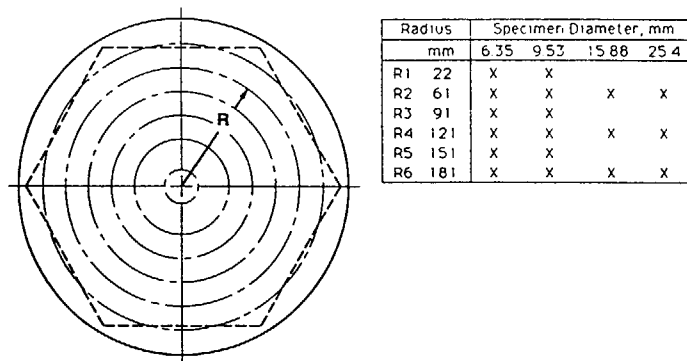


Fig. 4. Radial locations for tensile specimens in H-451 billet.

the billet. Additionally, at each position along the billet length, the specimens were located at six specific radial positions through the cross-section of the billet, as shown in Figure 4. All four specimens were obtained at the radii designated as R2, R4, and R6, while only the 6.35 and 9.53-mm gage diameter specimens were obtainable at radii R1, R3, and R6. The specimen yield from the billet included 160 of the 6.35-mm diameter specimens, 158 of the 9.53-mm diameter specimens, 20 of the 15.88-mm diameter specimens, and 18 of the 25.40-mm diameter specimens.

#### 4. MATERIAL: IG-110 GRAPHITE

IG-110 is a fine grained, isostatically moulded, high strength, isotropic graphite manufactured by the Toyo Tanso Company. Grade IG-110 is the designated graphite for the fuel element and core support structures in the Japanese High Temperature Engineering Test Reactor (HTTR). Tensile specimens were machined from a small amount of material remaining from a recent study on fracture toughness measurement techniques [3]. A limited number of three specimen sizes were machined, i.e., 23 of the 6.35-mm gage diameter specimens, 16 of the 9.53-mm diameter specimens and 8 of the 15.88-mm diameter specimens.

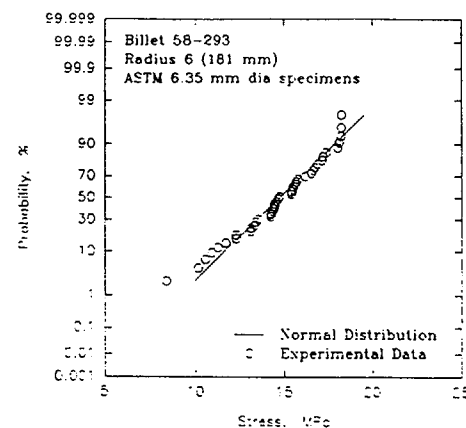


Fig. 5. Probability plot for H-451 graphite: 6.35 mm diameter specimens.

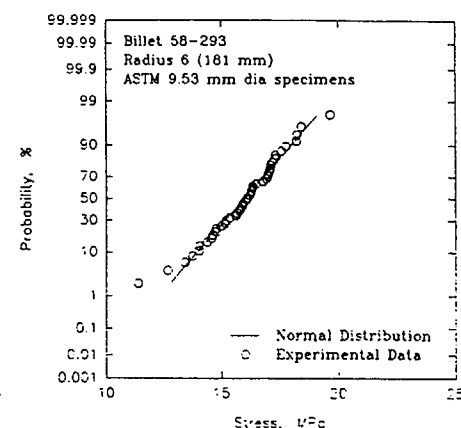


Fig. 6. Probability plot for H-451 graphite: 9.53 mm diameter specimens.

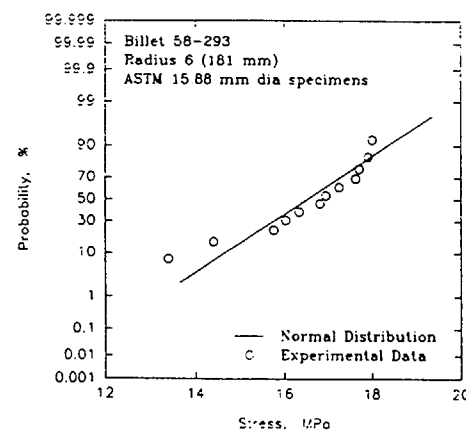


Fig. 7. Probability plot for H-451 graphite: 15.88 mm diameter specimens.

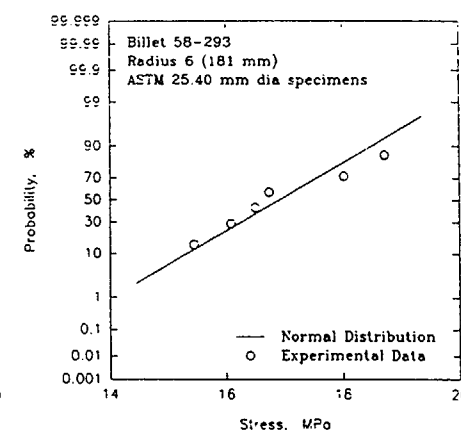


Fig. 8. Probability plot for H-451 graphite: 25.40 mm diameter specimens.

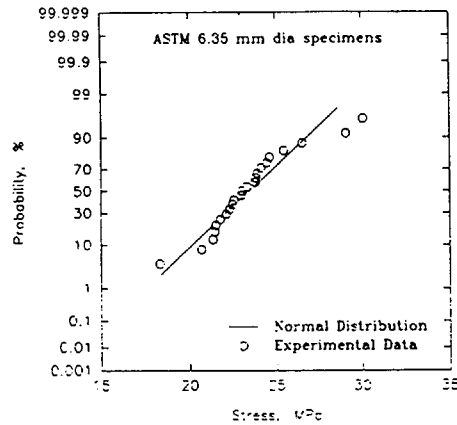


Fig. 9. Probability plot for IG-110 graphite: 6.35 mm diameter specimens.

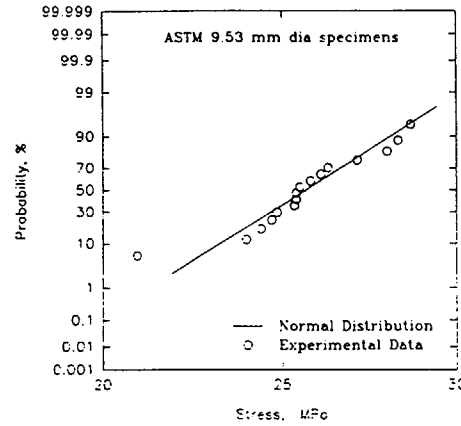


Fig. 10. Probability plot for IG-110 graphite: 9.53 mm diameter specimens.

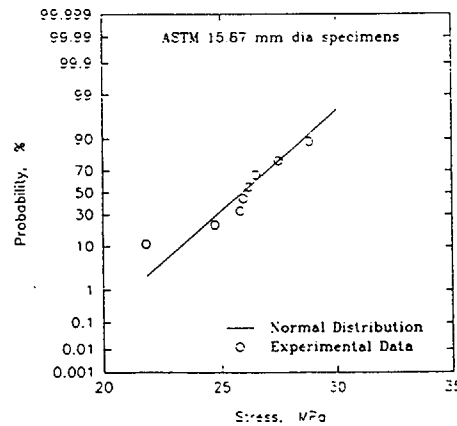


Fig. 11. Probability plot for IG-110 graphite: 15.88 mm diameter specimens.

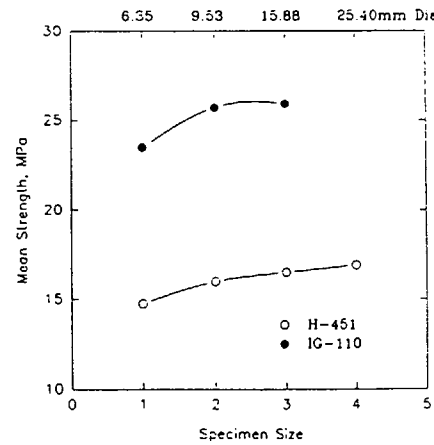


Fig. 12. Effect of specimen size on tensile strength for H-451 and IG-110 graphites.

## 5. RESULTS

Analysis of the large body of data for grade H-451 graphite obtained in this study has only just begun. Observations presented herein focus on test results for those specimens taken from the outermost radial position through the cross-section of the billet, i.e., R6. Failure probability plots for the tensile strength of H-451 at R6 for 6.35, 9.53, 15.88, and 25.40-mm diameter specimens are shown in Figures 5 through 8, respectively. The test results for the various specimen sizes appear to be reasonably well represented by a normal distribution. Price [4] had indicated in early work (1976) on H-451 that within experimental scatter normal as well as Weibull distribution functions are equally well representative of the tensile behavior of grade H-451 graphite.

Similarly, failure probability plots for the tensile strength of grade IG-110 graphite are shown in Figures 9 through 11 for 6.35, 9.53, and 15.880-mm diameter specimens, respectively. As with H-451, the tensile test results for IG-110 appear to be reasonably normally distributed.

As shown in Figure 12, both H-451 and the higher strength IG-110 graphite exhibit an effect of specimen size (stress volume) on tensile strength. The remainder of this report will 1) address the applicability of the popular Weibull Theory for describing the specimen size effects observed in H-451 and IG-110, and 2) demonstrate a new fracture model which has potential for modeling size effects on the tensile strength of graphite.

## 6. DISCUSSION

Briefly, the Weibull theory on the strength of brittle solids assumes that the material contains a distribution of flaws, either on the surface or throughout the volume; when the material is subjected to a tensile stress, the combination of the highest local stress concentration with the most severe flaw controls the strength of the bulk. This is the so-called "weakest-link hypothesis." In summary, the probability of survival,  $S$ , for a graphite tensile specimen would be written as follows:

$$S = \exp\left[-V\left(\frac{\sigma}{\sigma_0}\right)^m\right] \quad (1)$$

where

$V$  = load carrying volume of a tensile specimen

$\sigma$  = tensile stress

$\sigma_0$  = scale parameter or characteristic strength

$m$  = shape parameter or Weibull slope



For tensile specimens of volumes  $V_1$  and  $V_2$ ; with  $V_1 < V_2$  the condition for equal survival probability is:

$$V_1 \left( \frac{\sigma_1}{\sigma_0} \right)^m = V_2 \left( \frac{\sigma_2}{\sigma_0} \right)^m \quad (2)$$

and

$$\frac{\sigma_1}{\sigma_2} = \left( \frac{V_2}{V_1} \right)^{1/m} \quad (3)$$

Thus the strength of the low-volume specimen  $V_1$  is predicted to be higher than that of the high-volume specimen  $V_2$ . However, the expected dependence on volume is not generally observed for graphite. Price [4] concluded in his review that while the Weibull model appears to fit the tensile strength distribution, it greatly overestimates the volume effect.

Furthermore, Ho [5] pointed out that, in fact, the strength decreases rapidly as the least dimension (specimen diameter) approaches the grain size of the graphite. The effect of the least dimension then outweighs the volume effect. To reconcile this, Ho introduced a modified Weibull model of the form:

$$S = \exp \left[ -V \left( \frac{\sigma}{\sigma_0 f} \right)^m \right] \quad (4)$$

where  $f$  is a function of the characteristic grain size ( $h_0$ ) and the diameter ( $d$ ) of the tensile specimen. The expression for the function  $f$  chosen by Ho is as follows:

$$f(h_0, d) = \frac{2}{\pi} \cos^{-1}(h_0/d) \quad (5)$$

The ratio of tensile specimens of different volumes then becomes:

$$\frac{\sigma_1}{\sigma_2} = \left( \frac{f_1}{f_2} \right)^2 \left( \frac{V_1}{V_2} \right)^{1/m} \quad (6)$$

Ho states that the grain-size effect should be minimized when the specimen diameter is 10-15 times the maximum grain size. Thus for Grade H-451 graphite with a grain size of 1.59 mm, the specimen diameter would have to be greater than 15.9 mm. Therefore, grain-size dependence would be expected for the majority of the specimen sizes tested in this study (6.35 to 25.40-mm diameter).

Figures 13 and 14 show comparisons of the "original" and modified Weibull model predictions with the mean strengths for the various sizes of Grade H-451 graphite specimens taken at radii R6 and R4 respectively. Both figures demonstrate that the Weibull model predicts a significant increase in strength with decreasing volume. However, the strengths at R4 indicate little "real" effect of specimen size (volume), while at R6 continuing strength increase is exhibited as specimen size increases. On the other hand, the modified Weibull model appears to reasonably predict the strength at R4. However, at R6 the data still appears to exhibit a grain size effect for the 15.88 and 25.4-mm diameter specimens, though the model would predict that the grain size effect would be outweighed by the volume effect and consequently strength would decrease. It would appear then, that the expression for the  $f$  function in Equation (6) above should be refined to account for the spatial variability expected in H-451 graphite.

A new probabilistic failure model introduced by Burchell [6,7] was applied to the H-451 and IG-110 tensile data obtained in this study on volume effects. The model, developed specifically for nuclear grade graphites, combines a microstructural basis with a fracture-mechanics approach to failure. Summarily, graphite is assumed to contain inherent flaws (cracks) which under an applied stress will propagate through the material along preferred planes when the stress intensity on such a plane, in the vicinity of a crack, exceeds the critical stress intensity,  $K_{Ic}$  for a graphite particle. The material parameters used to calculate the probability of failure at a given stress include the following: filler particle size, the mean and standard deviation of the graphite pore size distribution, the number of pores, the bulk material (specimen) volume, and the particle  $K_{Ic}$ . The physical basis of the model is discussed in detail in Burchell's report [8] at this IAEA meeting.

Figures 15 and 16 compare the model predictions with the experimental data for the 9.53-mm diameter specimens of H-451 (radius R6) and IG-110 respectively. The predicted and experimental

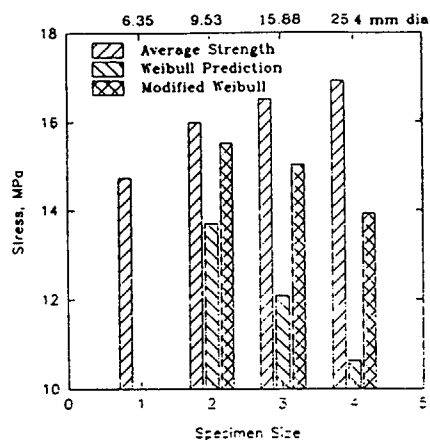


Fig. 13. H-451 data at R6 vs Weibull model predictions: 9.53 mm dia. specimens.

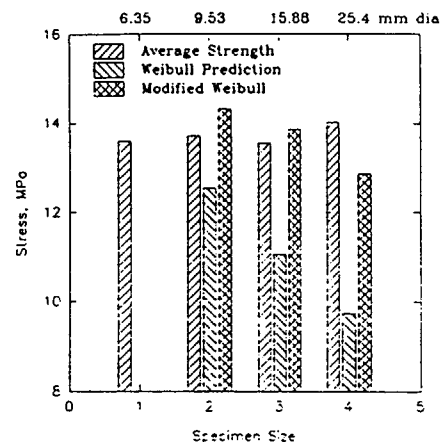


Fig. 14. H-451 data at R4 vs Weibull model predictions: 9.53 mm dia. specimens.

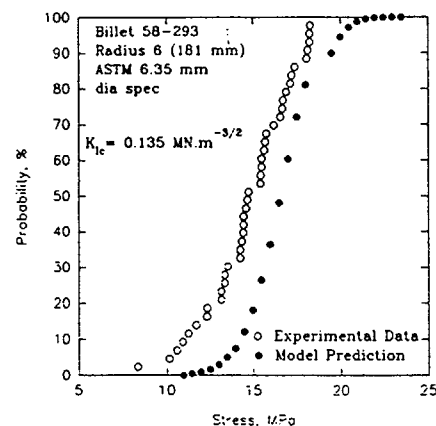


Fig. 17. Burchell model predicts higher strength for smaller H-451 specimen if toughness is not considered.

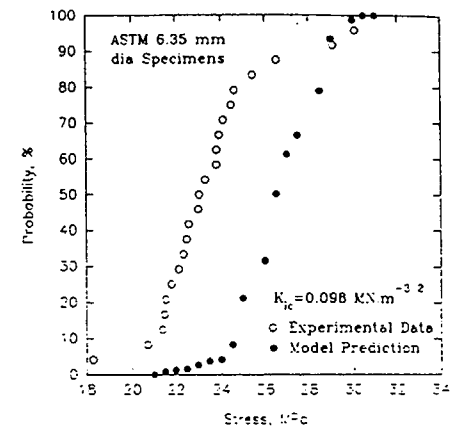


Fig. 18. Burchell model predicts higher strength for smaller IG-110 specimen if toughness is not considered.

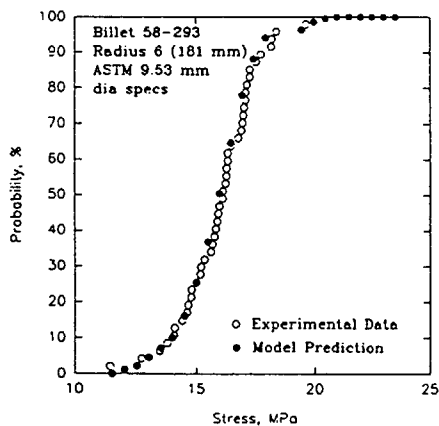


Fig. 15. H-451 graphite tensile data vs Burchell model predictions.

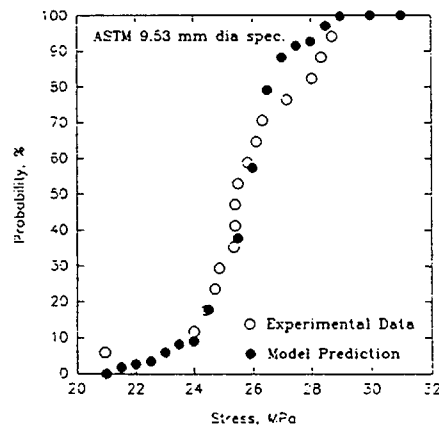


Fig. 16. IG-110 graphite tensile data vs Burchell model predictions.

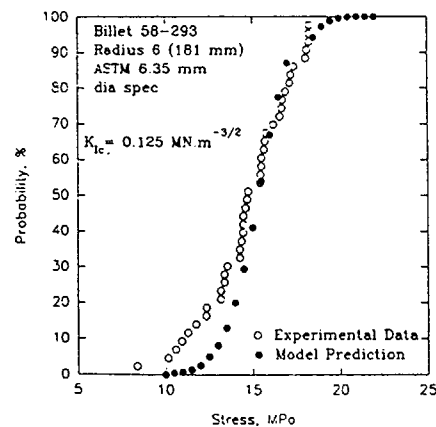


Fig. 19. Model predictions agree with H-451 data when lower toughness associated with small specimen size is recognized.

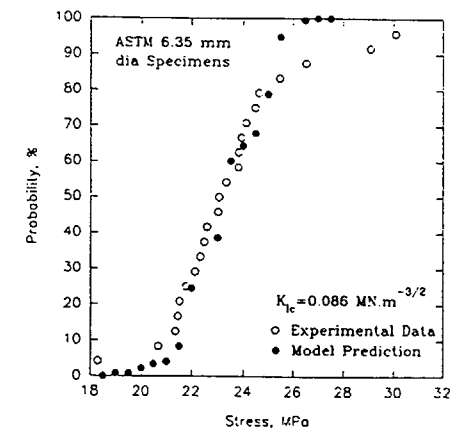


Fig. 20. Model predictions agree with IG-110 data when lower toughness associated with smaller specimen size is recognized.

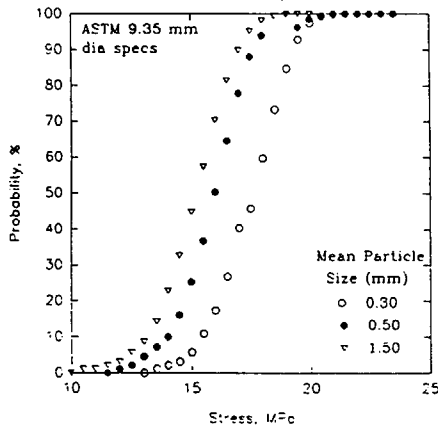


Fig. 21. Burchell model predicts decreasing strength with increasing particle size for H-451 graphite.

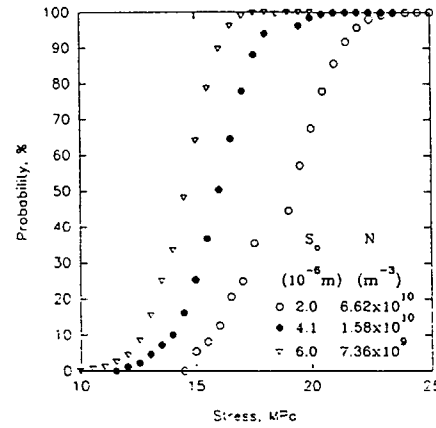


Fig. 22. Model predicts decreasing strength with increasing pore size.

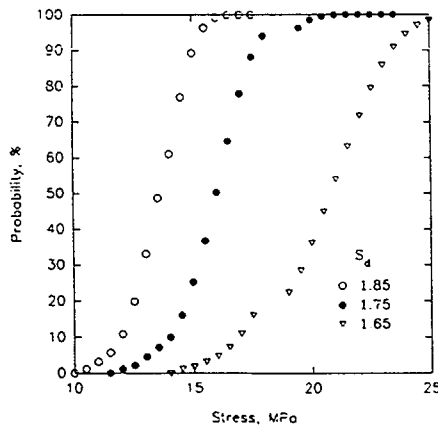


Fig. 23. Model predicts decreasing strength with increasing pore size distribution width (standard deviation).

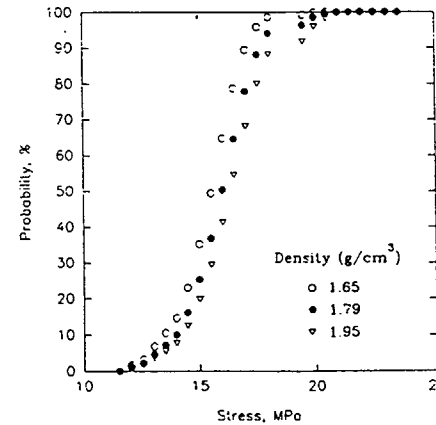


Fig. 24. Burchell model predicts decreasing strength with decreasing density.

probability failure curves are in good agreement. In particular, the model closely predicted the mean tensile failure stress, i.e., the stress at 50% failure probability.

Reducing the specimen size to 6.35-mm diameter, while keeping all the remaining model parameters unchanged, resulted in predicting increased tensile strength as was the case with the Weibull model. The predicted increased strengths were out of line with the experimental data for both H-451 and IG-110 as shown in Figures 17 and 18. Recently, Romanoski [9] reported on specimen size effects on the fracture toughness of nuclear grade graphites. Grades H-451, IG-110, as well as Stackpole 2020 were shown to exhibit decreasing fracture toughness with decreasing specimen diameter (chevron-notched short rod specimen geometry). As intuitively expected, reducing  $K_{Ic}$  in the model then shifted the predicted tensile stress failure probability down into agreement with the experimental data as shown in Figures 19 and 20.

Strength variations (edge to center, along the length and axial versus radial orientation) are common in extruded graphite billets, and result from the alignment of coke particles during extrusion and the distribution of impregnant carbon following the impregnation process. The later model discussed above appears to be particularly well suited to characterize the effects of microstructural variations on strength. Continuing analysis of the strength data on H-451 at the various radial and longitudinal locations within the billet will be proceeded by an effort to map the expected microstructural variations in the material (billet). Figures 21 through 24 illustrate the sensitivity of the model predictions of failure stress for H-451 to particle size, pore size, pore distribution and density. Note that the solid points in the figures represent the values used in the analysis above. Note too that the various parameters intuitively follow the expected effect, i.e., decreasing strength results from decreasing particle size, increasing pore size and number, and decreasing density.

## 7. CONCLUSIONS

The tensile strength of grade H-451 and IG-110 nuclear graphites exhibit dependence on specimen size (volume). Generally, the strength increased with increasing specimen size over the range of ASTM C749 specimens tested, i.e., 6.35 to 25.40-mm diameter. However, the popular Weibull model predicted behavior to the contrary. On the other hand, strength has been observed to decrease rapidly as the specimen size approaches the grain size of the graphite. A modified Weibull model introduced by Ho attempted to reconcile the grain size effect but does not currently provide for spatial variations noted particularly in H-451 graphite. A new fracture model (Burchell) incorporating microstructural elements in addition to grain size as well as the fracture toughness of

the material did show good agreement with the limited experimental data for H-451 and IG-110 analyzed to date, and shows promise for characterizing the interaction of volume effects and microstructural variations through the bulk of the material.

### REFERENCES

1. ASTM Standard C749-87, "Standard Test Method for Tensile Stress-Strain of Carbon and Graphite," Annual Book of ASTM Standards, Vol. 15.01, 1990.
2. J. P. Strizak "Spatial Variability in the Tensile Strength of an Extruded Nuclear-Grade Graphite," Proceedings IAEA Specialist's Meeting on the Present Status of Graphite Development for Gas-Cooled Reactors, September 9-12, 1991, Japan Atomic Energy Research Institute, Tokai-mura, Ibaraki-Ken, Japan.
3. T. D. Burchell, T. Oku and M. Eto, "A Comparison of Fracture Toughness Measurement Techniques as Applied to Nuclear Graphite," Proceedings, International Carbon Conference, Paris, France, July 16-20, 1990, pp. 278-279.
4. R. J. Price, "Statistical Study of the Strength of Near Isotropic Graphite," GA-A13955, General Atomic Company, San Diego, California, U.S.A., May, 1976.
5. F. Ho, "A Modified Weibull Theory for the Strength of Granular Brittle Material," GA-A15228, General Atomic Company, San Diego, California, U.S.A., May, 1979.
6. T. D. Burchell, "Studies of Fracture in Nuclear Graphite," Ph.D. Thesis. University of Bath, United Kingdom, 1986.
7. T. D. Burchell and M. D. Tucker, "A New Fracture Criterion for Graphites," Proceedings, XVII<sup>th</sup> Biennial Conference on Carbon, July 19-24, 1987, pp 486-487, Worchester Polytechnic Institute, Worchester, Massachusetts.
8. T. D. Burchell, "A Microstructurally Based Fracture Model for Nuclear Graphites," Proceedings IAEA Specialist's Meeting on the Present Status of Graphite Development for Gas-Cooled Reactors, September 9-12, 1991, Japan Atomic Energy Research Institute, Tokai-mura, Ibaraki-Ken, Japan.
9. G. R. Romanoski and T. D. Burchell, "Specimen Size Effect on Fracture Toughness of Nuclear Graphites," Proceedings Twentieth Biennial Conference on Carbon, University of California, Santa Barbara, California, U.S.A., June 23-28, 1991, pp. 584-585.

### DISCUSSION

#### Questions or Comments

Name: T. Arai

1. The increase in mean tensile strength of IG-110 graphite seems to be caused by less number of specimens.
2. In order to treat the subject both experimentally and theoretically, you need additional experiments and fits to the model for radial specimens
3. Could you compare the near tensile strength data between your recent experiments using ASTM coded specimens and the past ones using cylindrical specimens?

#### Answer:

1. Yes, I agree. The increase in strength of IG110 was not significant. The point to make (illustrate) was that IG110 did not follow Weibull theory.
2. Yes, I agree. Subsequent work will include specimens oriented axially, radially and tangentially with respect to the central axis of the billet.
3. This has not been done yet, but I intend to do it.

#### Questions or Comments

Name: B.T. Kelly

- 1) It isn't very difficult to determine Weibull parameters from this material up to need -1000 samples of homogeneous material.
- 2) I think use of models for statistics at small probabilities is to be correct for ca.50 % probabilities the Burchell model or normal distribution is satisfactory. The model is good for thinking about important parameters but cannot (unless the answer is known) the small probability.

3) H451 is inhomogeneous on a large scale-you must section many bricks to find out if all are similar so that the designer can estimate probabilities for the important regions of the bricks. This is a very large study.

4) I think given enough data (and an improvement in homogeneity ) a three parameter Weibull model be fitted to small probability - no model involved.

5) Most workers who use tensile samples on a coarse graphite(Pile Grade

A) Gilso-carbon, H451 have seen an increase in strength with volume as you do. In bend the data show a maximum then follow a Weibull behaviour with increasing volume so that it is present, but masked by sample size/grain size.

## THE EFFECTS OF SPECIMEN GEOMETRY AND SIZE ON THE FRACTURE TOUGHNESS OF NUCLEAR GRAPHITES\*

G.R. ROMANOSKI, T.D. BURCHELL  
Oak Ridge National Laboratory,  
Oak Ridge, Tennessee,  
United States of America

### Abstract

In a joint Oak Ridge National Laboratory(ORNL)/Japan Atomic Energy Research Institute (JAERI) study, various fracture toughness techniques were applied to Toyo Tanso grade IG-110 graphite to establish if specimen geometry influences on fracture toughness. The test geometries investigated were: compact tension (CT), disc compact tension (DCT), short rod (SR), chevron-notched short-rod (CNSR), cylindrical bend specimen (BS), and centrally slotted disc (CSD). Specimen geometries which allow slow crack propagation, such as the CNSR and CT, yielded higher fracture toughness values than those where fracture is very rapid, e.g., the CSD.

In a further ORNL study, the CNSR specimen geometry was selected to investigate the effect of specimen size on fracture toughness. Three specimen sizes and three grades of graphite were examined: Great Lakes Carbon grade H-451, Stackpole grade 2020, and Toyo Tanso grade IG-110. Grade H-451 was the toughest graphite, while Stackpole 2020 was the least tough. Fracture toughness increased with increasing specimen size for all graphites tested. This result was attributed to rising R-curve behavior.

### 1. INTRODUCTION

Graphite is used as a moderator and a structural material in the core of the U.S. Modular High Temperature Gas Cooled Reactor (MHTGR) and the Japanese High Temperature Test Reactor (HTTR). Core components are subject to static and dynamic loadings during assembly and operation. Although the design of core components is based on a maximum principal stress failure criterion, fracture toughness is an important consideration in material

---

\* Research sponsored by the Division of MHTGRs, Office of Advanced Reactor Programs, US Department of Energy, under contract DE-AC05-84OR21400 with Martin Marietta Energy Systems, Inc.

Figure 1. Specimen geometries used to measure the fracture toughness of graphite

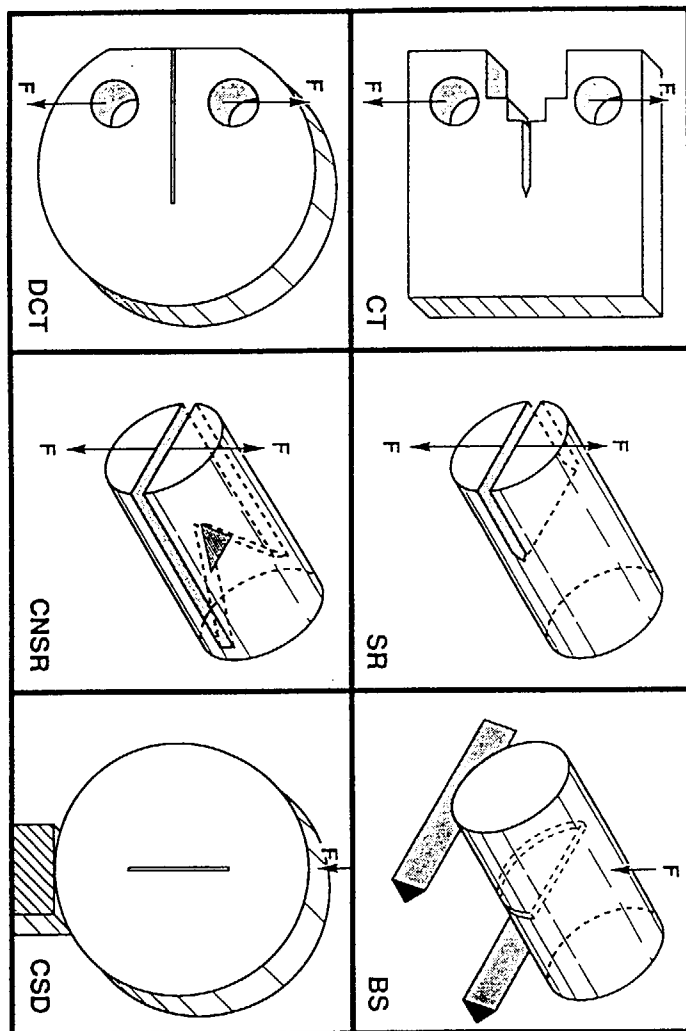


Table 1. Typical Mechanical Properties

Property	H-451	S-2020	IG-110
Density (g/cm <sup>3</sup> )	1.78	1.77	1.77
Elastic Modulus (GPa)	11.3	9.2	9.8
Poisson's ratio	0.20	--	0.14
Tensile strength (MPa)	18	27	25

selection and nondestructive evaluation. Accounting for effects of crack size and section size on fracture toughness are prerequisites to extending the fracture mechanics approach to full scale components.

## 2. EXPERIMENTAL

Specimen geometries used in this investigation are shown in Fig. 1. Typical mechanical properties are given in Table 1 for the three graphites tested. IG-110 is a fine grained isostatically molded graphite while H-451 and Stackpole 2020 are extruded graphites with somewhat larger grain size. Since no significant variation in fracture toughness was observed with position in billet<sup>1</sup>, tests on a given graphite were considered to represent specific materials. Test specimens were taken from extruded material with the crack plane perpendicular to the extrusion direction and crack propagation in the radial direction. Tests performed on IG-110 exhibited no effect of specimen orientation. The details of experimental procedure have been published elsewhere.<sup>2-5</sup>

The CNSR specimen geometry was chosen to investigate the effect of specimen size on the fracture toughness of Great Lakes Carbon grade H-451, Stackpole grade 2020, and Toyo Tanso grade IG-110. Additional details of the CNSR specimen geometry are given in Fig. 2. Specimen sizes considered included: 12.7 mm, 19 mm, and 25.4 mm. All dimensions are scaled in proportion to the specimen diameter. Fracture toughness tests were performed in displacement control using an automated Fractometer II test system manufactured by Terra Tek<sup>3</sup>. The displacement imposed on the mouth of the specimen and the resulting load was recorded

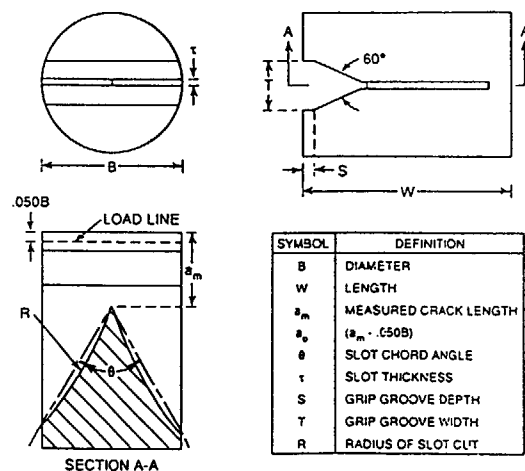


Figure 2. The chevron-notched short-rod specimen geometry

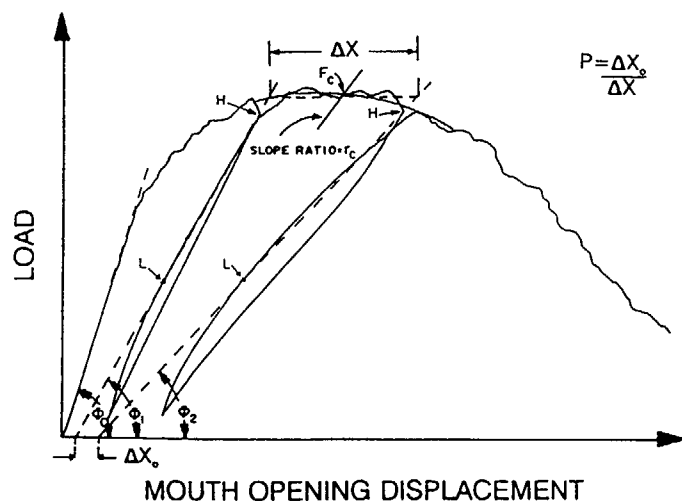


Figure 3. Typical load-displacement record for the CNSR fracture toughness test

throughout each test. Two unloading-reloading cycles were performed to determine the critical crack length, the load used to calculate fracture toughness, and to provide validity checks for the test. A typical load displacement record is shown in Fig. 3. Tests were performed in strict accordance with the procedure recommended in ASTM E 1304-89<sup>6</sup> for the determination of the plane-strain chevron-notch fracture toughness,  $K_{Ic}$ .

### 3. RESULTS AND DISCUSSION

The fracture toughness values obtained from tests on the six different specimen geometries is given in Table 2. Fracture toughness ranged from 0.83  $\text{MNm}^{-3/2}$  for the CSD specimen to 1.16  $\text{MNm}^{-3/2}$  for the CNSR specimen. The low value is in reasonable agreement with that previously obtained by Sato et al.<sup>5</sup> of 0.78  $\text{MNm}^{-3/2}$ . The CNSR and DCT are the methods preferred by ORNL and JAERI, respectively. The differences in fracture toughness determined in this study may be attributed to a true specimen size effect caused by the tendency for crack growth resistance to increase with increasing crack extension in graphites.

Table 2. Fracture Toughness of IG-110

Specimen Geometry	Fracture Toughness ( $\text{MNm}^{-3/2}$ )	Laboratory
CNSR	1.16	ORNL (1)
DCT	1.12	JAERI (2,3)
BS	1.07	JAERI (2,3)
SR	0.94	JAERI (2,3)
CT	0.92	JAERI (2,3)
CSD	0.83	ORNL (1)

At least eight CNSR fracture toughness tests were performed for each graphite and specimen size. The results are reported in Table 3 as  $K_{Qc}$ , the conditional value of the plane-strain fracture toughness. Fracture toughness versus specimen size is shown in Fig. 4. There is little scatter in the fracture toughness measurements for a given graphite and specimen size. However, the results do indicate a significant increase in fracture toughness with increasing specimen size for all three graphites. Similar results were obtained by Kennedy<sup>7</sup> using CNSR specimens.

Table 3. CNSR Fracture Toughness Test Results

Graphite	Diameter (mm)	$K_{QV}$ (MNm <sup>-3/2</sup> )	
		Mean	Std. Dev.
H-451	12.7	1.35	0.055
	19.0	1.44	0.095
	25.4	1.68	0.078
S-2020	12.7	0.91	0.058
	19.0	0.98	0.035
	25.4	1.10	0.025
IG-110	12.7	0.98	0.032
	19.0	1.07	0.036
	25.4	1.19	0.040

In a typical CNSR fracture toughness test, the load increases as a crack initiates at the chevron tip, reaches a maximum as the crack extends about halfway through the chevron ligament, and then decreases as the specimen separates. The load versus displacement test record reflects the unique design of the CNSR specimen, that is, the simultaneous requirement for the load to increase as the crack front becomes wider and to decrease as the leverage of the imposed displacement increases. The resulting mechanical driving force may be expressed in terms of the Mode I stress intensity factor. For an "ideal" brittle material which offers a constant resistance to crack extension, the minimum in stress intensity versus crack length coincides with the maximum load. The fracture toughness based on the maximum load,  $K_{IVM}$ , may be calculated using the following relation:

$$K_{IVM} = P_{max} F_{\square}^* / BW^{1/2}$$

Where B is the specimen thickness, W is the specimen width, and  $F_{\square}^*$  is the minimum normalized stress intensity factor which accounts for the CNSR specimen configuration. Rather than assuming that the peak load coincides with the minimum in the  $F_{\square}$  versus crack length curve, a determination is made of two crack lengths on the load displacement record by unloading compliance measurements made during the course of the test. Using this approach, one or more load-crack length pairs can be used to calculate toughness.

The data analysis procedure prescribed in ASTM E 1304-89 also incorporates a measure of non-elastic behavior,  $p = \Delta X_Q / \Delta X$ , which may be determined graphically from the unloading compliance measurements. For small values of p, the stress intensity factor for a CNSR fracture toughness test may be calculated using the following relation

$$K_{IV} = AP(1 + p)/B^{3/2}$$

where P is the load required to advance the crack and A is a dimensionless function of the scaled crack length.

The size effect observed for the CNSR specimen may be attributed to the possibility that one or more specimen sizes violates the requirements for a valid plane strain fracture toughness measurement according to ASTM E 1304-89.  $K_{QV} = K_{IV}$  only if all specified validity criteria are met.<sup>6</sup> Nearly all tests satisfied the validity requirements per ASTM E 1304-89 with the exception

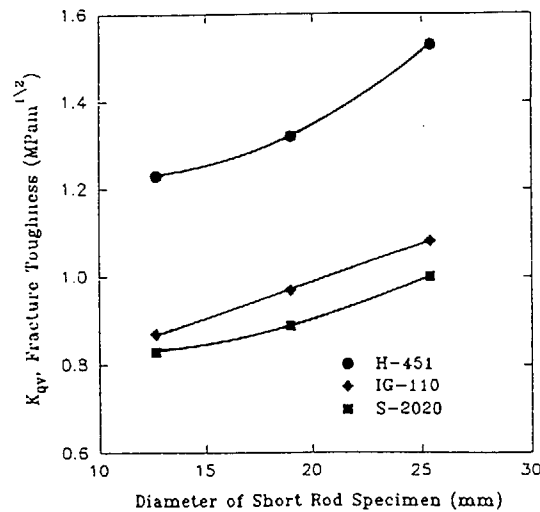


Figure 4. CNSR fracture toughness versus specimen diameter for H-451, Stackpole 2020 and IG-110 graphites



of the requirement on  $p$ , i.e.,  $-0.05 \leq p \leq 0.10$ . This requirement was violated in every test on H-451 because the unloading slopes were too high. This is likely an indication of considerable mechanical bridging along the crack wake on unloading. The higher unloading slopes observed for H-451 would result in smaller calculated crack lengths with a corresponding overestimation of  $K_{Qv}$ . At this time it is not clear how this result would cause calculated values of fracture toughness to vary with specimen size. All data were reported in Table 3 since the purpose of this investigation was to explore the suitability of the CNSR test method for determining a size independent fracture toughness.

The increase in measured fracture toughness with specimen size has been attributed to a rising R-curve. An R-curve is a plot of the stress intensity required to advance a crack,  $K_R$ , versus the distance of crack extension from a pre-test crack length. Sakai et al.<sup>8</sup> have measured the R-curve for a variant of IG-110. Their results are shown in Fig. 5. They found that the resistance to crack extension increased markedly up to a crack length of 1 to 2 mm and then increased less dramatically with further crack extension. The rising crack growth resistance may be attributed to nonlinear fracture processes including; microcracking residual strain in the crack wake region and grain bridging between crack flank surfaces.<sup>9-12</sup> The absorbed energy is not available for the creation of new crack surfaces.

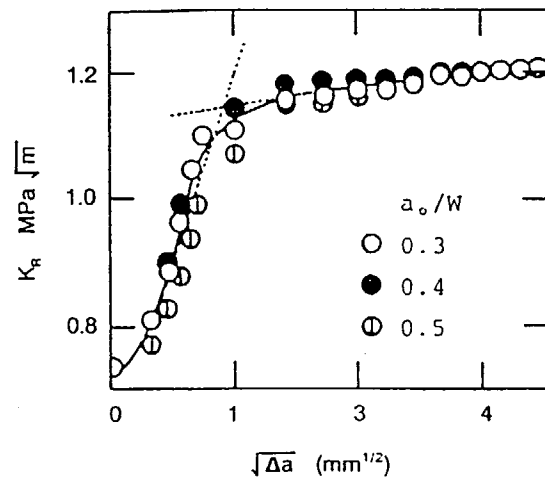


Figure 5. Crack growth resistance,  $K_R$ , versus crack extension for IG-110 graphite (Ref. 8)

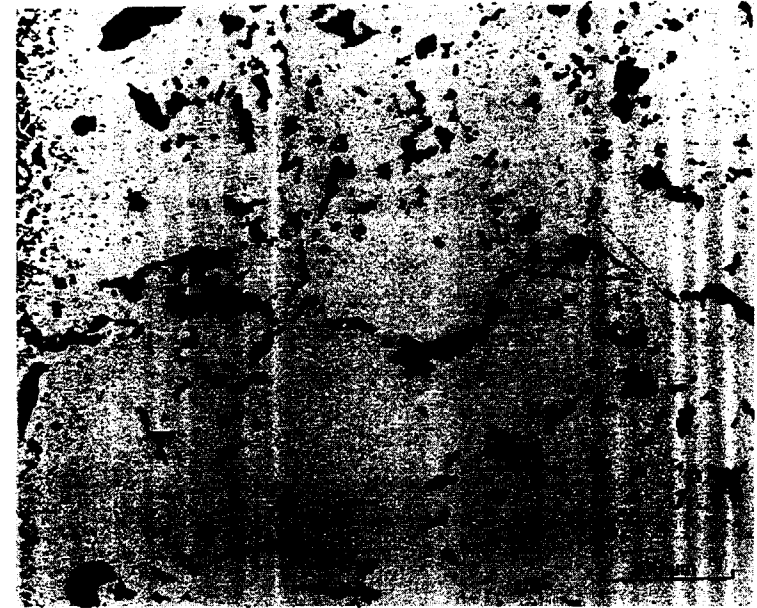


Figure 6. Fracture path trace and fracture surface for IG-110 graphite

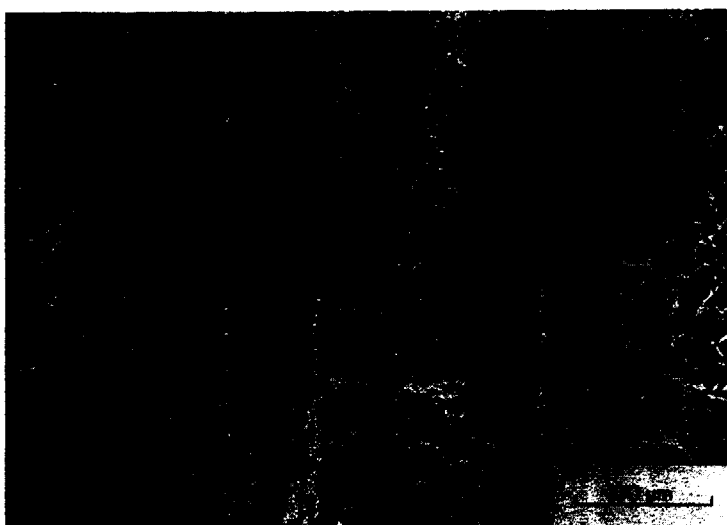


Figure 7. Fracture path trace and fracture surface for Stackpole 2020 graphite

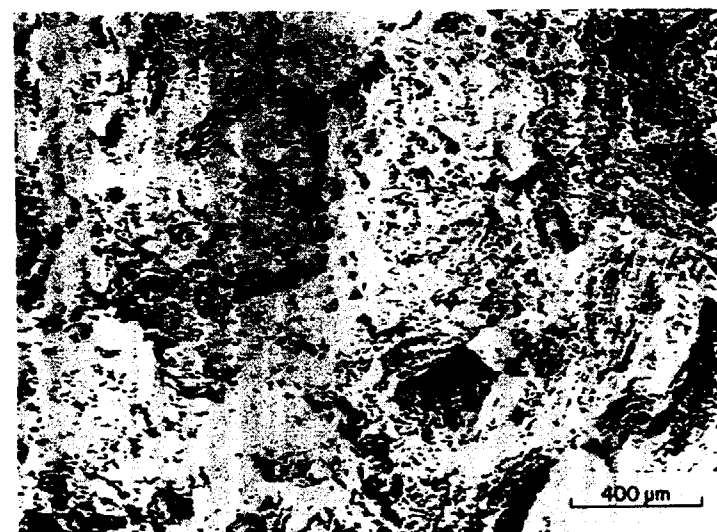
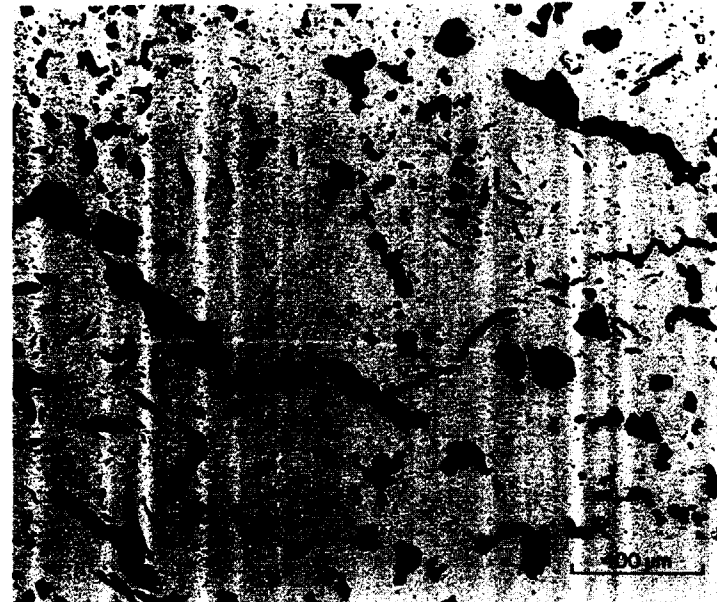


Figure 8. Fracture path trace and fracture surface for H-451 graphite

As a crack advances in polycrystalline graphite, the displacement imposed ahead of the crack tip is accommodated by irreversible slip deformation along basal planes and by extensive microcrack formation. Scanning electron microscopy studies<sup>8</sup> of stable crack growth have shown that microcracks which form in the process zone remain partially open after the applied load is removed. The absence of full closure remains when the microcrack frontal process zone becomes part of the crack wake region. The incomplete closure of microcracks leads to compressive residual strains which can impede crack extension. Following the procedures established by McMeeking and Evans,<sup>13</sup> Sakai et al. estimated the increment of enhanced toughness which could be attributed to compressive residual strains to be on the order of 20% of the total toughness increment.

A more prominent mechanism which has been identified as contributing to rising R-curve behavior is the tractions created by grain bridges between crack surfaces. The bridging tractions may take two forms: 1) intact reinforcements which require grain pull-out or fracture of individual grains, or 2) frictional interference between fracture surface asperities. The significance of grain bridging tractions was determined by crack wake removal experiments.<sup>8</sup>

Typical fracture paths and fracture surfaces are shown in Figs. 6 through 8 for IG-110, Stackpole 2020 and H-451, respectively. In every case, the fracture path follows an array of large pores generally aligned perpendicular to the applied stress. The tortuosity of the fracture path results in fracture and interlocking of microstructural constituents. Energy absorbed by frictional forces between these constituents is irrecoverable. Fracture surface asperities prop open the crack thus preventing the return to the origin on the load versus crack mouth opening curve. The presence of large fracture surface asperities for H-451 compared to Stackpole 2020 and IG-110 is evident in Figs. 6 through 8. This gives rise to high values of the inelasticity factor,  $p$ , in the CNSR fracture toughness test, particularly for H-451. More extensive inelastic fracture processes are manifest in the greater specimen size dependence on fracture toughness for H-451 as shown in Fig. 4.

#### 4. CONCLUSIONS

Due to rising crack growth resistance with crack extension, existing test methods provide a conservative measure of fracture toughness for nuclear graphites. Measured fracture toughness is higher for specimen geometries and sizes which require greater crack extension to the point

of measurement due to a rising R-curve for graphite. For the fracture toughness test specimens considered here, the CNSR specimen requires considerably more crack extension than all others and, consequently, exhibit the highest fracture toughness. Fracture toughness increased with increasing CNSR specimen size particularly when inelastic fracture processes occur.

#### REFERENCES

1. T. D. Burchell, T. Oku and M. Eto. In *Proc. Carbone 90 Conference*, Paris, France, pp. 278-279, July 1990.
2. T. Oku, S. Ishiyama, H. Takahashi, T. Fukazawa and T. Hashida. *TANSO*, No. 139, pp. 175-181, 1989.
3. T. Oku, S. Ishiyama, M. Eto, Y. Goto, K. Urashima and M. Inagaki. *J. Ceramic Soc. Japan*, No. 96, pp. 773-777, 1988.
4. Terra Tek Fractometer II Owners Manual, Terra Tek, University Research Park, Wakara Way, Salt Lake City, Utah, 1980.
5. S. Sato, K. Kawamata, H. Awaji and M. Miyauchi, *High Temperature-High Pressures*, Vol. 12, pp. 23-32, 1980.
6. Standard Test Method, ASTM E 1304-89, American Society for Testing and Materials, Philadelphia, PA 19103, USA.
7. C. R. Kennedy, High-Temperature Gas-Cooled Reactor Technology Development Program, Annual Progress Report for Period Ending December 31, 1982 ORNL #5960
8. M. Sakai, J. Yoshimura, Y. Goto, and M. Inagaki, *J. AM. Ceram. Soc.*, Vol. 71, No. 8, pp. 609-16, 1988.
9. R. W. Hertzberg, *Deformation and Fracture Mechanics of Engineering Materials*, 2<sup>nd</sup> ed., pp. 307-21. Wiley, New York, 1983.
10. H. Hubner and W. Jilek, *J. Mater. Sci.*, Vol 12, pp. 117-25, 1977.
11. R. F. Pabst, J. Steeb, and N. Claussen, pp. 821-33 in *Fracture Mechanics of Ceramics*, Vol. 4, Edited by R. C. Bradt, D. P. H. Hasselman, and F. F. Langel, Plenum, New York, 1978.
12. R. Knehans and R. Steinbrech, *J. Mater. Sci. Lett.*, Vol. 1, 327-29, 1982
13. R. M. McMeeking and A. G. Evans, *J. Am. Ceram. Soc.*, Vol. 65, No. 5, 242-46, 1982.

## DISCUSSION

-----  
**Questions or Comments**                      **Name:** Richard Judge, AEA Technology  
 -----

Particle size  $K_{IC}$  is used in the Burchell teacture model -

would this be expected to be volume dependent? It    paper III-D1.

That it is assumed to be so when particle size  $K_{IC}$  is varied to give  
 -----  
 good    between model experiment, to volume.  
 -----

**Answer:**  
 -----

Particle  $K_{IC}$  will only be constant if the particles are considered  
 -----  
 to be perfect crystals. This is not the case in reality. Therefore  
 -----  
 we can expect a distribution of particle  $K_{IC}$ 's. Such data are not  
 -----  
 available, consequently we assume particle  $K_{IC}=0.1 K_{IC}$  [Bulk].  
 -----

Since we the particle  $K_{IC}$  to the bulk  $K_{IC}$  we model reduced  
 -----  
 specimen volume with reduced particle  $K_{IC}$ , following the trend in  
 -----  
 bulk  $K_{IC}$ . Physically, the particle  $K_{IC}$  would not be expected  
 -----  
 to be change with specimen volume. H would however be expected to vary  
 -----  
 with filler particle size within the specimen. Evidently, a distribution  
 -----  
 of four particle sizes and filler particle  $K_{IC}$ 's would enhance the  
 -----  
 physical soundness of the model, but at the cost of simplicity.  
 -----

## CUMULATIVE FATIGUE DAMAGE ON HTGR GRAPHITE

S. ISHIYAMA, M. ETO

Department of High Temperature Engineering,  
 Tokai Research Establishment,  
 Japan Atomic Energy Research Institute,  
 Tokai-mura, Naka-gun, Ibaraki-ken,  
 Japan

## Abstract

To investigate the effect of cyclic ratio and stress history on cumulative fatigue damage on fine-grained isotropic nuclear graphite, two step fatigue tests were performed by the loading patterns in which peak load was changed from high level to low one( High-Low mode) and low level to high one( Low-High mode). From those results, the following conclusions were derived:  
 (1)In High-Low mode, remarkable regeneration of stress history of first step loading to fatigue damage of second step were observed at first cyclic ratio of 0.1.

(2)Cumulative fatigue damage of High-Low mode was well expressed as following equations:

$$D_1 + D_2 = 1$$

$$D_1 = n_1 / N_{f1}$$

$$D_2 = n_2 / (N_{f1} + N_{f2} (A(n_1 / N_{f1})^B))$$

where A and B are constants

(3)Cumulative fatigue damage of Low-High mode was well expressed as following equations:

$$D_1 + D_2 = 1$$

$$D_1 = n_1 / N_{f1}$$

$$D_2 = n_2 / (N_{f2} + N_{f1} (C(n_2 / N_{f2})^D))$$

where C and D are constants.

KEY WORDS: Nuclear graphite, Cumulative fatigue damage, multi-step loading, linear cumulative fatigue damage rule, HTGR

## 1. INTRODUCTION

Japan Atomic Energy Research Institute(JAERI) has been prepared for construction of High Temperature Gas-Cooled Reactor, the High Temperature Engineering Testing Reactor(HTTR) since 1990. This reactor is designed as a graphite-moderated helium gas-cooled reactor of thermal output of 30MW and maximum outlet coolant temperature of 950 °C.

Under the conditions of the reactor start-up, operation or shut-down, graphite components in HTTR are subjected to thermal stresses, the vibration caused by earthquakes and pressure fluctuations of the helium coolant. Since these stresses and vibrations may cause cumulative fatigue damages on graphite components to the graphite materials, design requires the knowledge of cumulative fatigue damage formula for graphite materials under multi-step cyclic stress.

A number of investigators have studied fatigue damage of graphites[1-4], however, studies of cumulative fatigue damage on graphites are very limited[4, 5].

This paper presents the fatigue behavior of IG-110 graphite which is nuclear-grade fine-grained isotropic graphite, examined under multi-step cyclic loading and elucidates cumulative fatigue damage in the representative High-Low and Low-High cyclic loading patterns.

## 2. EXPERIMENTAL

### 2.1 Material and specimen

IG-110 graphite is a nuclear-grade fine-grained isotropic, petroleum coke-based graphite manufactured by Toyo Tanso Co., Ltd.. Typical properties of this graphite are listed in Table 1[4,5].

Dog-bone type specimens, 10mm in diameter with 20mm gage section, were made of IG-110 graphite and used for the present tension-compression fatigue tests[4,5].

### 2.2 Apparatus and test condition

Fatigue tests were performed using a servo-hydraulic fatigue testing machine, servopulser model EHF-E01(Maximum loading capacity:  $\pm 10\text{kN}$ ) made by Shimazu Corp.

Single and two types of multi-step loading patterns were programed in programmable function generator model 4825 made by Shimazu Corp., and cyclic loading was changed automatically.

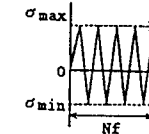
Figure 1 shows the loading patterns of single, High-Low and Low-High mode.

TABLE 1. TYPICAL MECHANICAL PROPERTIES OF IG-11 GRAPHITE

	Bulk density ( $\text{g/cm}^3$ )	Tensile strength (MPa)	Compressive strength (MPa)	Bending strength (MPa)	Young's modulus (GPa)
IG-11	1.78	25.3	76.8	37.2	10.2

### LOADING CONDITIONS

#### SINGLE STEP LOADING



#### TWO STEP MULT-LOADING

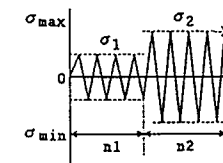
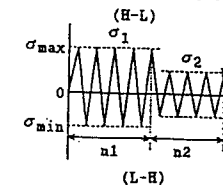


FIG. 1. Typical loading patterns of single, high-low and low-high mode multi-step loading.

Here, every terms used in this figure was defined as follows:

High-Low(H-L): Peak load was changed from high to low level during fatigue test.

Low-High(L-H): Peak load was changed from low to high level during fatigue test.

$\sigma_{max}$  : maximum applied stress

$\sigma_{min}$  : minimum applied stress

$\sigma_1$  : Applied stress at first step

$\sigma_2$  : Applied stress at second step

$\sigma_1 / \sigma_2$  : Stress history of High-low and Low-High mode

$\sigma_t$  : Mean tensile strength

$n_1$  : A number of cycle at first step

$n_2$  : Mean fatigue cycles at second step

$N_{f1}$  : Mean fatigue life obtained at single cyclic loading  $\sigma_1$ .

$N_{f2}$  : Mean fatigue life obtained at single cyclic loading  $\sigma_2$ .

$R$  : Ratio of minimum stress to maximum stress

$n_1/N_{f1}$  : First cyclic ratio

In single step cyclic loading pattern, peak load was kept constant until specimen was broken, whereas peak load were changed after the number of cycles  $n_1$  at first step in high-low and low-high two step loading tests. The number of cycle  $n_1$  at first step were determined by cyclic ratio  $n_1/N_{f1}$  and chosen as 0.1, 0.3 and 0.5 times as short as mean fatigue life  $N_{f1}$ .

During the fatigue tests, the stress ratio  $R$  was set at -1.0 and peak loading levels were chosen as from 0.9 to 0.75 times of tensile strength of IG-110 graphite. The maximum frequency of cyclic loading was 4Hz.

### 3. ANALYSIS AND DEFINITIONS

#### 3.1 Estimation of mean fatigue life

Graphite materials have wide scattering in its mechanical, physical and chemical properties and for estimation of the typical properties of those materials, statistical analysis should be applied to the data and estimate at certain estimation levels[1-5].

Statistical P-N diagram method[1] was applied to the fatigue data to estimate the mean fatigue life  $N_f$ . Fatigue data were plotted as a function of fracture probability. According to this

method, mean fatigue life  $N_f$  can be estimated as the number of cycles correspondent to 50% fracture probability in this diagram, where fracture probability  $F$  was calculated as following equation:

$$F = i / (n + 1)$$

here,  $i$  is the order of fatigue life and  $n$  is sampling number, respectively.

#### 3.2 Evaluation of cumulative fatigue damage

Cumulative fatigue damage  $D_f$  was evaluated by following definitions:

$$D_f = D_1 + D_2 \quad (1)$$

where,  $D_1$  and  $D_2$  are damage factors at first and second step, respectively and calculated by following formula[6]:

$$D_1 = n_1 / N_{f1} \quad (2)$$

$$D_2 = n_2 / N_{f2} \quad (3)$$

### 4. RESULTS

#### 4.1 Fatigue life distribution of single step loading

Fig. 2 shows the fatigue life distribution of single step loading tests as a function of fracture probability  $F(\%)$ (P-N diagram). Fatigue data were plotted on normal distribution

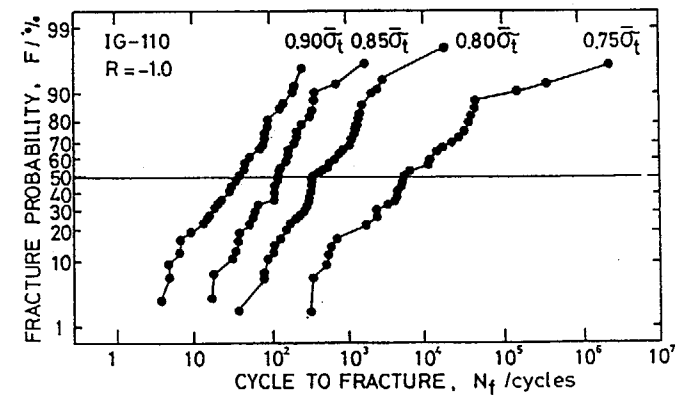


FIG. 2. P-N diagram of single mode loading patterns.

TABLE 2. TEST RESULTS OF SINGLE, HIGH-LOW  
AND LOW-HIGH MODE MULTI-STEP LOADING

High-Low									
$n_1/N_{F1}$	$\sigma_1/\sigma_s$	$n_1$	$n_2$	$N_{F1}$	$N_{F2}$	$D_1$	$D_2$	$D_1$	
0.1	0.90/0.85	4	45	42	125	0.1	0.36	0.46	
	0.85/0.80	14	130	125	404	0.1	0.32	0.42	
	0.80/0.75	40	1063	404	5266	0.1	0.20	0.30	
0.3	0.90/0.85	13	105	42	125	0.3	0.84	1.14	
	0.85/0.80	42	340	125	404	0.3	0.84	1.14	
	0.80/0.75	121	2579	404	5266	0.3	0.48	0.79	
0.5	0.90/0.85	20	70	42	125	0.5	0.56	1.06	
	0.80/0.75	202	3978	404	5266	0.5	0.76	1.28	

Low-High									
$n_1/N_{F1}$	$\sigma_1/\sigma_s$	$n_1$	$n_2$	$N_{F1}$	$N_{F2}$	$D_1$	$D_2$	$D_1$	
0.1	0.85/0.90	14	50	125	42	0.1	1.19	1.29	
	0.80/0.85	40	208	404	125	0.1	3.74	3.84	
	0.75/0.80	527	1506	5266	404	0.1	3.72	3.84	
0.3	0.75/0.80	1581	1532	5266	404	0.3	1.09	1.39	

function chart, where applied stresses were normalized by mean tensile strength  $\sigma_s$ . The experimental values of fatigue life tested at the constant stress levels are very scattered and the scatter bands became larger as the peak stress level increased. Fatigue life distribution tested at 0.9, 0.85 and 0.80  $\sigma_s$  can be stimulated by normal distribution function distribution, whereas the distribution at 0.75  $\sigma_s$  became more complex one.

Mean fatigue life  $N_F$  at every stress level were obtained by the number of cycles corresponding to fracture probability of 50% in the figure and listed Table 2.

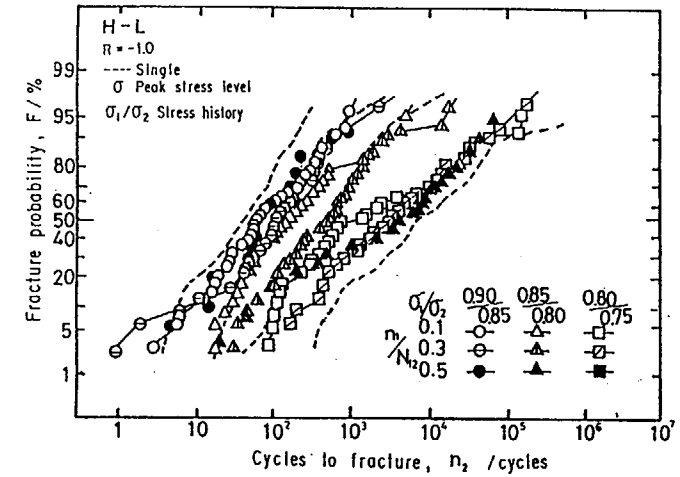


FIG. 3. P-N diagram of high-low mode loading patterns.

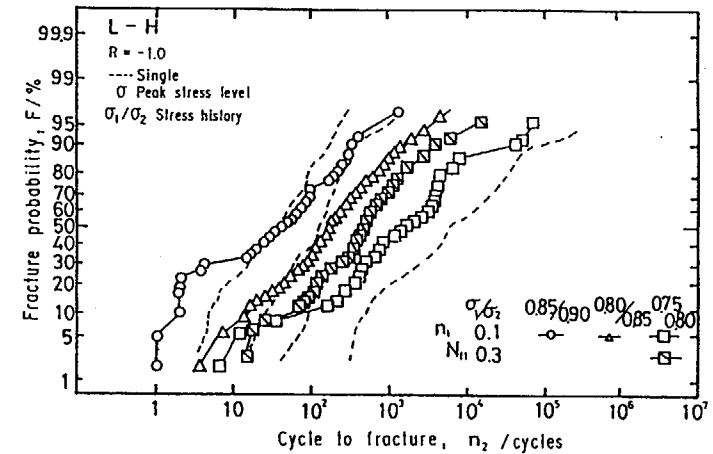


FIG. 4. P-N diagram of low-high mode loading patterns.

#### 4.2 Fatigue life distribution of H-L and L-H mode fatigue tests

Fig. 3 shows H-L mode P-N diagrams tested at first cyclic ratio  $n_1/N_{r1}$  of 0.1, 0.3 and 0.5, respectively. In this figure, cycles to fracture  $n_2$  is the number of cycles at second step and broken lines are P-N diagrams obtained by single step loading fatigue tests. Fatigue data obtained at stress history  $\sigma_1/\sigma_2$  of 0.90/0.85, 0.85/0.80 and 0.80/0.75 were distributed between P-N diagrams of single step mode tested at peak stress levels of  $\sigma_1$  and  $\sigma_2$ .

Figure 4 shows L-H mode P-N diagram tested at first cyclic ratio of 0.1 and 0.3. The results also shows that data obtained at stress history of 0.85/0.90, 0.80/0.85 and 0.75/0.80 were almost distributed between that of single step mode tested at  $\sigma_1$  and  $\sigma_2$ .

The number of cycles of first step  $n_1$ , mean fatigue life  $n_2$  and testing conditions of H-L and L-H mode were summarized in Table 2.

### 5. DISCUSSION

#### 5.1 Regeneration of fatigue history of graphite

Figure 5 shows mean fatigue life  $n_2$  of H-L and L-H mode as a function of stress history of  $\sigma_1/\sigma_2$ . In this figure, both end of divisions were mean fatigue life  $N_{r1}$  and  $N_{r2}$  obtained by single step tests at stress level of  $\sigma_1$  and  $\sigma_2$ .

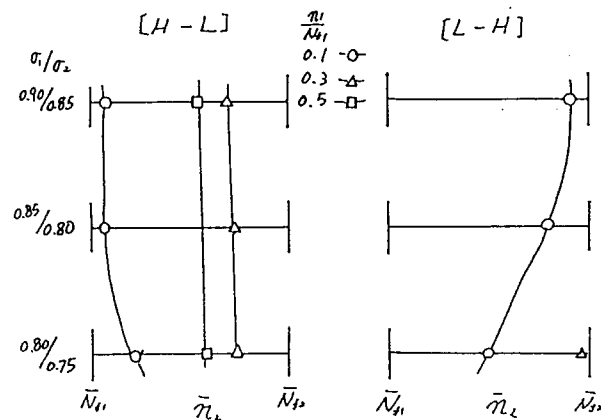


FIG. 5. Mean fatigue life of second step  $n_2$  of high-low and low-high mode.

In H-L mode, mean fatigue life  $n_2$  obtained at first cyclic ratio of 0.1 is very close to  $N_{r1}$ , whereas that of 0.3 and 0.5 were shifted to  $N_{r2}$ . Those results indicate that fatigue damage induced in graphite specimen at second step of H-L mode in which peak stress is  $\sigma_2$ , is equivalent to that induced by stress level of  $\sigma_1$  in single step mode.

Thus, it can be said that fatigue history or damage effect of first step loading still remains strongly even if  $\sigma_2$  is applied in second step of H-L mode, and stress history induced by first step loading mainly has an important role for fatigue damage process of graphite specimen.

However, those effects are remarkable only at first cyclic ratio of 0.1 and become small as cyclic ratio increases.

From the viewpoint of fracture mechanics, it is considered that the regeneration of fatigue history of first step into that of second step can be due to process zone formation at the initial stage of fatigue process.

Figure 6(a) shows the conceptual model of fatigue crack extension process in graphite in H-L mode fatigue condition. According to this model, the inherent crack extension process in graphite specimen can be explained as follows:

(1) Before crack extension, a process zone in which micro-cracking occurs, is formed in front of the crack tip. The formation of this process zone can be imagined to occur coincident with the initial stage of H-L mode fatigue process.

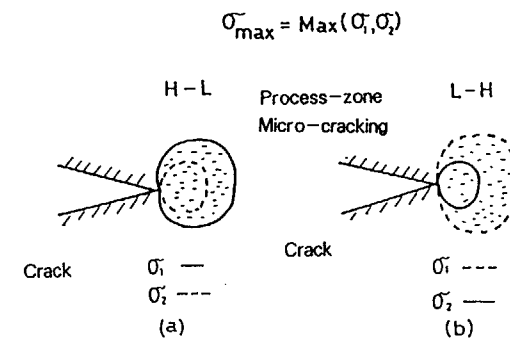


FIG. 6. Models of process zone formation and crack extension in high-low and low-high mode fatigue process.



(2) Density of micro-cracking which can be involved in those process zone reaches to a criteria after many of cyclic loading and then crack starts to extend.

Therefor process zone formed at initial stage of first step remains just as it is at second step without crack extension and works to enhance fatigue damage as if  $\sigma_1$  is applied to specimen at second step.

Figure 7 shows typical H-L mode stress-strain curves obtained at stress history  $\sigma_1/\sigma_2$  of 0.90/0.85 and first cyclic ratio of 0.3. Remarkable large deformation of graphite specimen and hysteresis loop formation was observed in initial stage of first step, and then after those initial stage those loop dose not change, but slight shift of those loop to tensile strain side also was observed. From those results, it can be considered that process zone formation and crack extension occurred correspondent to those initial deformation and loop shift, respectively

On the contrary, mean fatigue life  $n_2$  of L-H mode is close to  $N_{22}$  rather than  $N_{21}$ . It is considered from those results that process zone formed at first step is reformed as peak stress is changed at second step, and then newly reformed process zone as shown in figure 6(b) mainly controls fatigue damage process after first step cyclic loading.

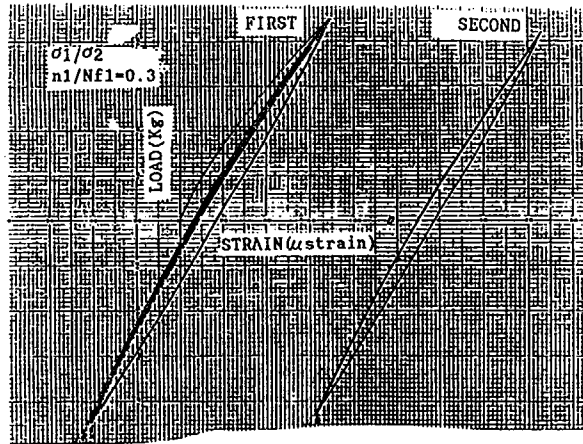


FIG. 7. Stress-strain curves obtained by high-low mode test in which stress history and first cyclic ratio is 0.90/0.85 and 0.3.

In any cases, it can be said that fatigue damage induced at second step is strongly dependent on stress history of maximum peak stress  $\sigma_{max}$  which is equal to  $\text{MAX}[\sigma_1, \sigma_2]$  in two step loading process.

The authors already reported the effect of maximum peak stress on fatigue damage and crack extension speed of lg-ll graphite[4, 7].

## 5.2 Rule of cumulative fatigue damage

Damage factors of first and second step,  $D_1, D_2$  and cumulative damage factor  $D_r$  of H-L and L-H mode fatigue tests were calculated by the eq.(1)-(3) and those results were listed in table 2.

Figure 8(a) shows cumulative fatigue damage factor of H-L mode as a function of stress history. In these figures, the solid straight line at the middle of the figure was cumulative fatigue damage derived by linear damage rule[6]. Those results shows that  $D_r$  obtained at first cycle ratio of 0.1 is very small, whereas that at 0.3 and 0.5 is close to 1, and decreased as applied peak stress decreased.

From those results, it can be considered that those dependency of  $D_r$  or  $D_2$  is due to regeneration of fatigue history above-mentioned, so that damage factor  $D_2$  should be expressed as a function of first step stress history:

$$D_2 = f(\sigma_1, N_{21}) \quad (4)$$

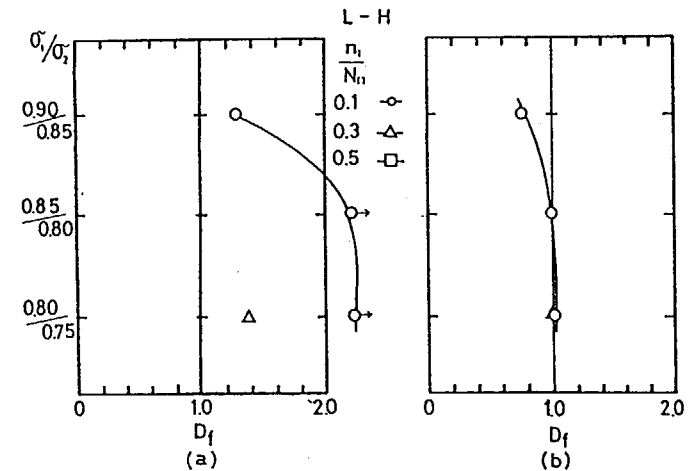


FIG. 8. Cumulative fatigue damage of high-low mode calculated by the Eqs (1)-(3) and (5)-(6).

To avoid complicating function form in eq.(4), here effect of stress level  $\sigma_1$  was ignored and the following formula of cumulative fatigue damage  $D_f$  and damage factor  $D_2$  are proposed instead:

$$D_f = D_1 (=n_1/N_{f1}) + D_2 \quad (5)$$

$$D_2 = n_2/(N_{f2} + N_{f2}(A(n_1/N_{f1})^B)) \quad (6)$$

where A and B are constants and obtained as 4.86 and 1.76 by least square method, respectively.

Figure 8(a) and (b) show the cumulative fatigue damage  $D_f$  obtained by eq.(1)–(3) and rearranged by the eq. (5) and (6), respectively. Comparing original data and rearranged data obtained by eq.(5) and (6), it is clear that rearranged  $D_f$  obtained at every first cyclic ratios is close to 1 and especially that at first cyclic ratio of 0.1 is closer to 1 than that obtained by eq.(1)–(3).

Therefore cumulative fatigue rule for H-L mode can be well expressed as following equations:

$$D_1 + D_2 = 1 \quad (7)$$

$$D_1 = n_1/N_{f1} \quad (8)$$

$$D_2 = n_2/(N_{f2} + N_{f2}(A(n_1/N_{f1})^B)) \quad (9)$$

where A and B are constants

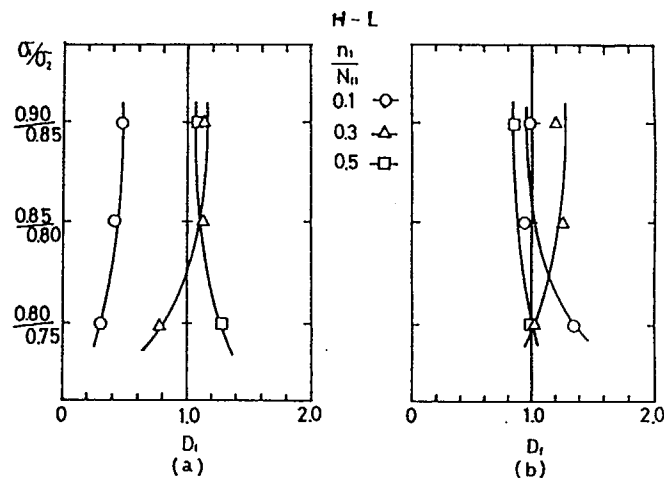


FIG. 9. Cumulative fatigue damage of low-high mode calculated by the Eqs (1)–(3) and (11)–(12).

Figure 9(a) shows  $D_f$  of L-H mode as a function of stress history.  $D_f$  of L-H mode is larger than 1 and increased as peak stress level decreased.

From those results, it is clear that in L-H mode, stress history of second step loading has rather important role to fatigue process on the contrary to the case of H-L mode, thus  $D_2$  can be expressed as a function of second step stress history:

$$D_2 = f(\sigma_2, N_{f2}) \quad (10)$$

Ignoring the effect of stress level  $\sigma_2$  to simplify above-equation forms and following equations were proposed:

$$D_f = D_1 + D_2 \quad (11)$$

$$D_2 = n_2/(N_{f2} + N_{f2}(C(n_2/N_{f2})^D)) \quad (12)$$

where C and D are constants and given as 0.01 and -1.36, respectively.

Cumulative fatigue damage  $D_f$  was calculated by eq.(11) and (12) and shown in fig. 9(b). Comparing original data and rearranged one, it is clear that rearranged data is very closer to 1 than original data, thus cumulative damage rule for L-H mode can be well expressed as following equations:

$$D_1 + D_2 = 1 \quad (13)$$

$$D_1 = n_1/N_{f1} \quad (14)$$

$$D_2 = n_2/(N_{f2} + N_{f2}(C(n_2/N_{f2})^D)) \quad (15)$$

where C and D are constants.

## 6. CONCLUSIONS

Two step multi-loading fatigue tests of High-low and Low-High mode were performed for fine-grained isotropic nuclear graphite, and effect of first cyclic ratio and stress level on cumulative fatigue damages infused in high-low and low-high mode fatigue process were discussed.

From those test results, the following conclusions were derived:

In high-low mode

- (1) Fatigue life of second step was shorter than expected results of the same loading conditions of single mode.
- (2) Cumulative fatigue damage increases as first cyclic ratio and stress level increase.
- (3) Maximum peak stress in those fatigue process has very important role in fatigue damage process of graphite and remarkable regeneration of stress history of first step loading to fatigue damage of second step were observed at first cyclic ratio of 0.1.

(4) Cumulative fatigue damage was well expressed as following equations:

$$D_1 + D_2 = 1$$

$$D_1 = n_1 / N_{f1}$$

$$D_2 = n_2 / (N_{f1} + N_{f2} (A (n_1 / N_{f1})^B))$$

where A and B are constants

In low-high mode,

(5) Fatigue life of second step was longer than expected results of the same loading conditions of single step mode.

(6) Cumulative fatigue damage decreases as first cyclic ratio and stress level increase.

(7) Maximum peak stress in test process also has important role in fatigue damage process of graphite.

(8) Cumulative fatigue damage was well expressed as following equations:

$$D_1 + D_2 = 1$$

$$D_1 = n_1 / N_{f1}$$

$$D_2 = n_2 / (N_{f2} + N_{f1} (C (n_2 / N_{f2})^D))$$

where C and D are constants.

## REFERENCES

- (1) H. Leichter and E. Robinson : UCRL REP-50337(1972).
- (2) J.B.S. Wilkins and A.R. Reich : AECL-4216(1972).
- (3) R.J. Price : Carbon, 16, 367(1978).
- (4) S. Ishiyama, T. Oku and M. Eto : J. of Nucl. Scie. and Technol., Vol.28, No.5, 472-483(1991).
- (5) S. Ishiyama and M. Eto : 20th Biennial Conf. on Carbon, 268-271(1991).
- (6) M.A. Miner : J. Appl. Mech., 12, 159(1945).
- (7) S. Ishiyama, M. Eto and T. Oku : J. of Nucl. Sci. and Technol., 24(9), 719(1987).

## DISCUSSION

Questions or Comments

Name: K. Kikuchi

What is the possible explanation to relate micromechanism of process zone to the equation proposed to evaluate combined loading?

Answer:

Our proposed formula is very simple. The most important problem is to explain the complexity of multi-loading fatigue is  $\sigma_{max}$ , namely

$$\sigma_{max} = \text{Max} [\sigma_1, \sigma_2] \text{ in multi-loading fatigue test.}$$

## FRACTURE BEHAVIOR OF NUCLEAR GRAPHITES UNDER COMPRESSIVE IMPACT LOADING

H. UGACHI, M. ISHIHARA,  
S. ISHIYAMA, M. ETO  
Department of High Temperature Engineering,  
Tokai Research Establishment,  
Japan Atomic Energy Research Institute,  
Tokai-mura, Naka-gun, Ibaraki-ken,  
Japan

### Abstract

Compressive impact fracture behavior of two kinds of nuclear grade graphites, fine-grained isotropic IG-11 graphite and coarse-grained near-isotropic PGX graphite, have been investigated as a function of various strain rates up to more than 100 (1/s) at room temperature. Two types of cylindrical specimens, 12.5 mm in diameter with 25 mm length and 25 mm in diameter with 50 mm length, were employed to investigate the volume effect on compressive impact strength. Compressive fracture load, longitudinal and circumferential strains were measured in this test. The effect of strain rate up to 100(1/s) on compressive strength and deformation behavior of these graphites are discussed and the following conclusions were derived:

(1) Compressive strength of graphites increased with increasing of strain rate up to 100(1/s) and is well expressed by the following equation:

$$\sigma_c = A \varepsilon^B$$

where  $\sigma_c$ ,  $\varepsilon$  are compressive strength and strain rate and A and B are constants respectively.

(2) Compressive strength decreased drastically with increasing of strain rate over 100(1/s).

(3) Specimen volume effect on impact compressive strength and deformation behavior was not found.

**Key Words :** Compressive Strength, Impact Strength, Impact Load, Nuclear Graphite, Brittle Material

## 1. INTRODUCTION

The Japan Atomic Energy Research Institute (JAERI) has a plan to construct an HTGR, the High Temperature Engineering Test Reactor (HTTR), which is scheduled to be critical in 1996. This reactor is designed as a graphite moderated helium gas-cooled reactor of thermal output of 30 MW and maximum outlet coolant temperature of 950 °C.

The core of HTTR consists mainly of piled up graphite components. Under the conditions of reactor operation, these components in the HTTR are subjected to impact stress due to collision with graphite component to component caused by the earthquakes.

In the graphite structural design, the data on strain rate effect of fracture strength and deformation for nuclear graphite materials are required to evaluate the integrity of the graphite components during earthquake.

Impact load tests of graphites have been carried out by several workers [1-3], however, the detailed fracture strength and deformation behavior of nuclear graphites has not been examined at high strain rates of over 100(1/s).

This paper presents the results of compressive impact load test of fine-grained isotropic nuclear graphite, IG-11 and coarse-grained near-isotropic nuclear graphite, PGX at strain rate of the order of  $10^{-3}$ (1/s) to over 100(1/s) and discussed the effect of strain rate on compressive strength and deformation behavior of graphites.

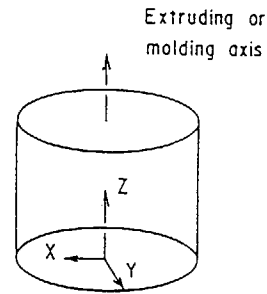
## 2. EXPERIMENTAL

### 2.1 Materials and test specimens

The graphite materials used in this experiment are petroleum coke, fine-grained isostatically pressed unpurified graphite grade IG-11 manufactured by Toyo Tanso Co., Ltd. and petroleum coke, medium-grained molded near-isotropic graphite grade PGX manufactured by UCAR. Typical properties of these materials are given in Table 1. For the near-isotropic PGX graphite, the test specimens were cut from the

Table 1 Typical properties of IG-11 and PGX graphites.

	Bulk density (g/cm <sup>3</sup> )	Tensile strength (MPa)	Compressive strength (MPa)	Bending strength (MPa)	Young's modulus (GPa)
IG-11	1.78	25.3	76.8	37.2	10.2
PGX (X) (Z)	1.73	7.8	33.6	14.9	6.6
		7.3	30.4	15.6	8.2



original block, 1140 mm in diameter with 1000 mm height, as the axial direction of the specimen corresponds to the z direction of the original graphite block. Two types of cylindrical specimens, 12.5 mm in diameter with 25 mm length and 25 mm in diameter with 50 mm length, were tested in this present compressive impact load test.

## 2.2 Experimental methods

The compressive impact load tests were carried out in low-strain rate range of the order of  $10^{-3}$ , middle-strain rate range of  $10^{-3}$  to 10 and high-strain rate range of 10 to over 100(1/s).

Three types of testing machines were employed in this impact load test. Instron-typed material testing machine(maximum loading capacity of 100kN) MODEL TOM 1000 made by Shinko company, was used for compressive strength test in low-strain rate range, servo-hydraulic fatigue machine(maximum loading capacity of 100kN) model 5041 made by MTS company, was used for the impact compressive strength test in medium-strain rate range and hydraulic impact testing machine(maximum loading capacity of 100kN and maximum accelerated speed of 15m/s) made by MTS company, was used for impact compressive strength test in high-strain rate range.

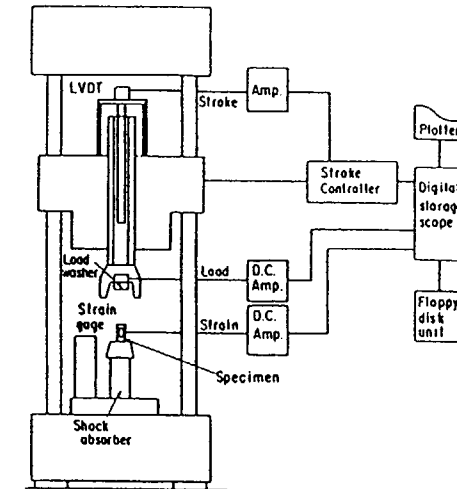


Fig.1 Hydraulic Impact testing machine and load-strain measuring systems

Figure 1 shows the hydraulic impact testing machine and the measuring systems for impact load and strain of impact compressive strength tests. The change in load in elapsed time of impact test was measured by piezo-electric load sensor(maximum loading capacity and correspond frequency of  $12.2 \times 10^6$ N and 55kHz), and dual mode amplifier, MODEL 5004 made by KISTLER company. The change of longitudinal and circumferential strain was measured by strain gages, 3mm and 5 mm in gage length, which were used for small and large size specimens respectively. Strain output was amplified by signal conditioner model CDV-230C(maximum correspondent frequency of 2kHz, 4 channel), made by Kyowa electric company.

The time histories of load and strain in elapsed time of impact test was recorded in digital oscilloscope MODEL 4094(maximum correspondent frequency of 200MHz, maximum sampling rate of  $0.5 \mu s$ , resolution of 12 bit and memory capacity of 16Words/4 channel) made by NICOLE company.

### 3. RESULTS

#### 3.1 Change in load and strain under impact loading

Figure 2 shows typical time history of compressive impact load and longitudinal strain for small size specimens of IG-11 graphite as a function of strain rates. Compressive load and longitudinal strain indicated non-linear relations to the elapsed time in low-, middle- and high-strain rate ranges. In this figure, peak point of load and strain curves correspondent to break point of specimen.

#### 3.2 Compressive stress-strain curves under impact loading

Figure 3 shows compressive stress-longitudinal strain curves of large size specimens of IG-11 and PGX graphites in various strain rate ranges. In these figures, three kinds of enveloped curves correspondent to the curves obtained in low-, medium- and high-strain rate regions. As shown these figures, compressive stress-longitudinal strain curves indicated non-linear deformation of these graphites from the beginning to the peak point of the curves and a little change of slope of those curves was observed as strain rate increased.

Figure 4(a) and (b) show compressive stress-circumferential strain curves of IG-11 and PGX graphites obtained in various strain rate ranges. Those curves of both graphites also indicated non-linearity and reduction of slope with increasing of strain rates.

#### 3.3 Change in compressive strength and fracture strain

Figure 5 shows the change of compressive strength of IG-11 and PGX graphites as a function of strain rate. Compressive strength of both graphites increased as the strain rate increased from low- to middle strain rate ranges, while compressive strength rapidly decreased as the strain rate increased in the high-strain rate range over 50(1/s) for IG-11 and 100(1/s) for PGX graphite. Compressive strength of IG-11 and PGX at strain rate of about 100(1/s) was about 10% and 8% higher than that of at the order of  $10^{-3}$ (1/s) and increase rate of compressive strength of IG-11 graphite is larger than that of PGX graphite.

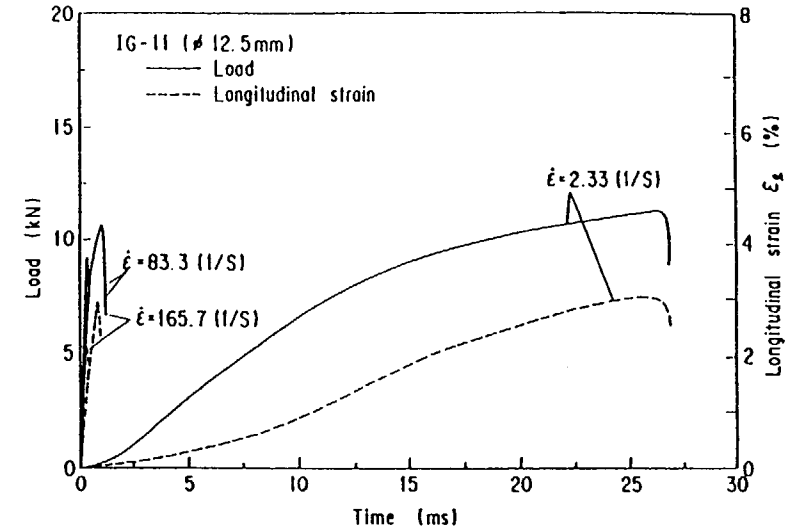


Fig.2 Typical changes of compressive impact load and longitudinal strain to the time for small size specimens ( $\phi 12.5 \times 25 \text{ mm}$ ) of IG-11 graphite.

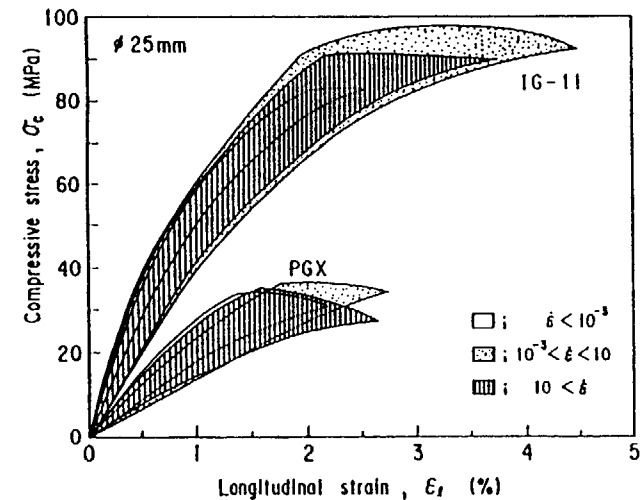


Fig.3 Compressive stress vs longitudinal strain curves of IG-11 and PGX graphites in various strain rate ranges.

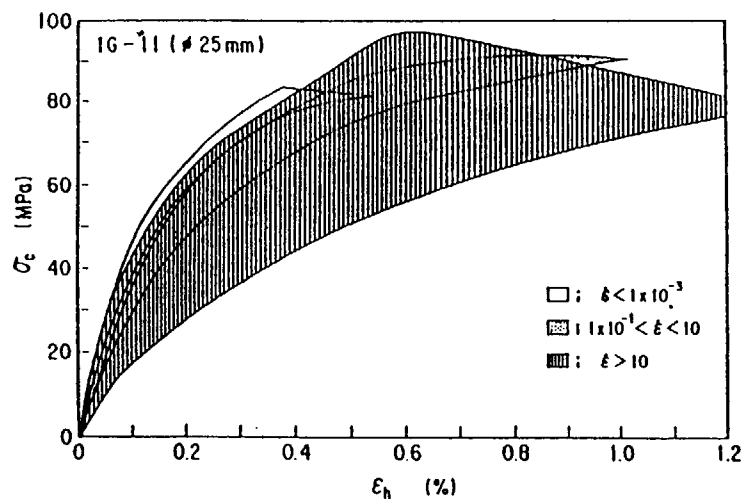


Fig. 4 Compressive stress vs circumferential strain curves of IG-11 graphite in various strain rate ranges.

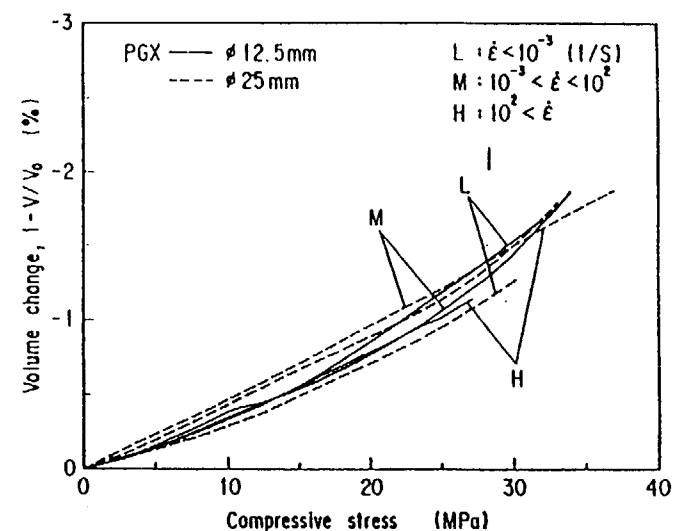


Fig. 6 The change in volume of IG-11 graphite as a function of compressive stress.

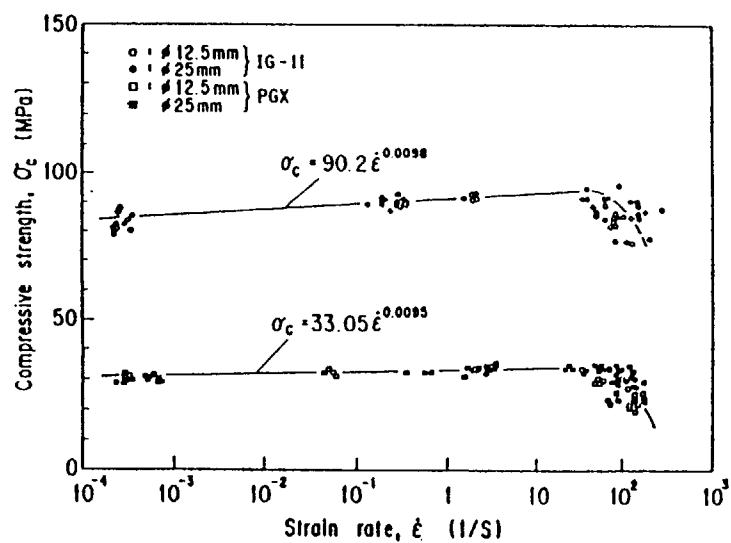


Fig. 5 The change in compressive strength of IG-11 and PGX graphites as a function of strain rate.

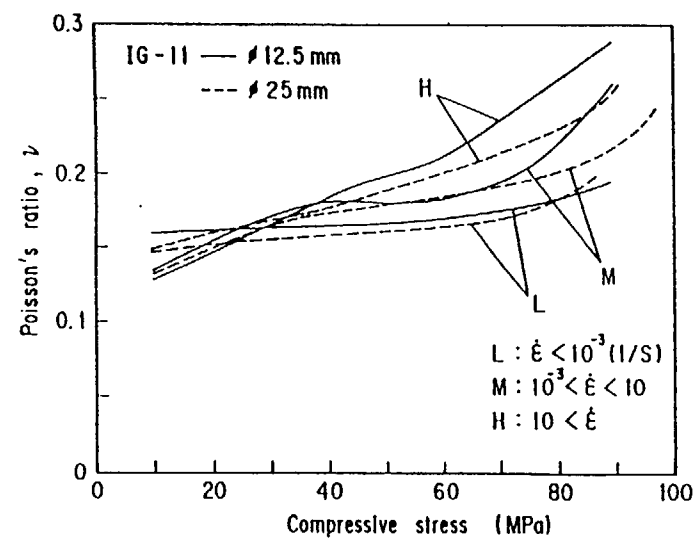


Fig. 7 The change in poisson's ratio of IG-11 graphite as a function of compressive stress.

Volume effect on of compressive strength of both graphites were not found in the low- to middle-strain rate ranges.

Compressive strength of both graphites tested at over 100(1/s) decrease as strain rate increased and that of small size specimen was smaller than that of the large one.

Figure 6 shows longitudinal and circumferential fracture strain of IG-11 and PGX graphites as a function of strain rates. Those results shows that longitudinal fracture strain dose not change in low- to high strain rate ranges, whereas circumferential fracture strain increased as strain rate increased.

Volume effect on fracture strain is not found clear in the low- to high strain rate ranges.

#### 3.4 Fracture of specimens under high strain rate

Figure 7 shows typical graphite specimens after impact load test. Fracture surface of specimen loaded in low-strain rate ranges was created on diagonal plane to the specimen axis and broken in two parts of large fragments. Test specimen loaded in middle-strain rate range also shows fracture surface on diagonal plane and was broken into many fragments, and then specimen loaded in high-strain rate range was broken to pieces.

### 4. DISCUSSION

#### 4.1 Effect of strain rate on deformation behavior of graphites

Figure 8(a) and (b) show the relationship between applied compressive stress and change in specimen volume of IG-11 and PGX graphites.

Hence volume change  $(1-V/V_0)$  is calculated by following equation.

$$(1-V/V_0) = (1+\varepsilon_h)^2(1+\varepsilon_l) \quad (1)$$

where  $\varepsilon_h$  and  $\varepsilon_l$  are circumferential and longitudinal strains. Volume of IG-11 and PGX graphite decreases with increasing of applied stress and volume reduction reaches to about -2% at peak stress. Those reduction rates does not change in low-, middle- and high strain rate ranges, however, that of PGX is about three times larger than that of IG-11.

Volume reduction caused mainly by shrinkage of graphites to the applied stress direction and cracking under volume reduction process at low strain rate of the order of  $10^{-3}$ (1/s) were already reported by Oku and Eto[4].

Solid and broken curves in the figure indicated volume reduction process of small and large specimens. Those results shows specimen volume had no effect on these reduction process

Figure 9(a) and (b) show the change in poisson's ratio of IG-11 and PGX graphites as a function of applied compressive stress, where poisson's ratio was obtained by the ratio of circumferential strain to longitudinal strain data. Poisson's ratio of IG-11 graphite changes from 0.15 to about 0.3 and that of PGX graphite also changes from 0.05 to 0.1 with increasing of strain rate.

It can be suggested from those results that graphite specimen behaves more elastically as increasing strain rate, so impact energy accumulated in the specimen as elastic deformation energy during impact loading increases as increasing of strain rate and contributes to extend micro-cracks which were created in volume reduction process above-mentioned and lead specimen to be broken to pieces.

#### 4.2 Effect of strain rate on compressive strength

The enhancement of compressive strength of graphites with strain rate is considered to be caused by dislocation pile-up at grain boundary in graphite specimen.

Here, the change in compressive strength is expressed as a function of strain rate[5]:

$$\sigma_c = A \varepsilon^B \quad (2)$$

where  $\sigma_c$  is compressive strength,  $\varepsilon$  is strain rate, and then A and B are the constant. As shown in fig. 5, solid lines were derived by the eq.(2) and the constants of A and B for IG-11 graphite were obtained 90.2 and 0.0098, for PGX graphite were 33.1 and 0.0095, respectively. This constant B obtained is very small and almost about 1/30 to the values obtained in metallic materials[5,6,7].



As shown in fig.5 and 9(a)(b) , compressive strength drastically decreased and poisson's ratio increased and reached to near elastic theoretical value 1/3 at strain rate of over 100(1/s). From these results, it can be considered that elastic deformation energy accumulated in elastic deformation process of graphite specimen can easily reach to the fracture energy criteria at strain rate over 100(1/s).

#### 4. CONCLUSIONS

To investigate the effect of high strain rates on fracture behavior for isotropic fine-grained graphite, IG-11 and near-isotropic coarse-grained graphite, PGX, a servo-hydraulic type impact testing machine has been constructed and compressive strength test were performed using this testing machine with various strain rates up to more than 100 (1/S) strain rate. From the compressive impact test results, it can be concluded:

(1)Compressive strength of both IG-11 and PGX graphites increased with increasing strain rate up to 100 (1/S), and then decreased rapidly with increasing strain rate over 100 (1/S).

(2)Increment of Compressive strength to strain rate can be well expressed as following equation:

$$\sigma_c = A \varepsilon^B$$

where  $\sigma_c$ ,  $\varepsilon$  are compressive strength and strain rate and A, B is constant and B was obtained about 0.01 for both IG-11 and PGX graphites.

(3)Fracture strain does not change at high strain rate over 100(1/s).

(4)Effect of strain rate on specimen volume change can not be found in the impact loading tests.

(5)Poisson's ratio increased with increasing of strain rate and compressive stress.

(6)Specimen volume effect on deformation behavior and compressive strength of graphites can not be found in impact loading tests.

#### REFERENCES

- (1)M.Birch, et al., Carbon 21, 479 (1983)
- (2)C.R.Smith, JAERI-M86-192, 29 (1986)
- (3)M.Futakawa, Carbon, 28, 149 (1990)
- (4)T.Oku and M.Eto, Carbon, 11, 639(1973).
- (5)M.Tokizane, et al., Proceedings of International Symposium on Intermetallic Compounds Structure and Mechanical Properties, 1015, June 17-20, Sendai, Japan (1991)
- (6)W.B.Morrison, Trans. Met. Soc. AIME, 242, 2221 (1968)
- (7)M.S.Kim, et al., Mate. Trans. JIM 30, 77 (1989)

#### DISCUSSION

Questions or Comments

Name: K. Kikuchi

Why does the compressive strength drop down drastically over than  $10^2$  of strain rate (1/s)?

Answer:

At strain rate range over 100 (1/s), elastic deformation energy accumulated in elastic deformation process reached to the fracture criteria, and this energy is used for fracture of the graphite specimen broken to small pieces which were shown in the picture.



NON-DESTRUCTIVE EXAMINATION, INSPECTIONS  
AND SURVEILLANCE

Part A

(Session IV)

**Chairmen**

**D.P. BURRIDGE**

United Kingdom

**A. IDE**

Japan



# RADIOLYTIC CORROSION OF GRAPHITE SURVEILLANCE AND LESSONS DRAWN FROM THE OPERATION OF THE BUGEY-1 REACTOR

A. PETIT

Electricité de France,  
Loyettes

C. PHALIPPOU, M. BRIÉ

Centre d'études nucléaires de Saclay,  
Commissariat à l'énergie atomique,  
Gif-sur-Yvette

France

## Abstract

This document briefly describes some of the feedback of experience from operation of the BUGEY-1 reactor (natural uranium fuelled, carbon dioxide cooled and graphite moderated).

There is a major radiolytic corrosion problem with the graphite of the stack of this reactor and small quantities of methane are added to the coolant gas to limit its effect.

Inhibition with methane has the drawback of resulting in hydrocarbon deposits forming on the fuel elements, which it is necessary to periodically eliminate by injecting oxygen.

The amount of weight loss is determined by annually taking core samples from the channel walls. At the present time, 74 of the channels of highest power (95% maximum power) have been examined (of a total of 852) and some 900 core samples have been measured (weight loss being deduced from the density as determined by measurement and weighing). Additional examinations are made, on completing each core drilling session, of the core samples with the highest corrosion factors :

- determination of the density profiles (and verification of weight loss) by gamma ray absorption,
- measurement of the compressive strength (perpendicularly to the channel wall),
- hydrogen analysis (on a few samples).

Identical examinations are made on samples taken for the purpose parallel to the channel wall.

The combined results make it possible to localize the most corroded area in the pile. The mean radial weight loss in this area (of limited height) is around 30% as compared to a maximum observed factor of 35% (mean value in one core sample). The compressive strength values ( $R_c$ ) measured in 158 samples (perpendicular direction) have made it possible to plot a curve showing the variation of  $R_c$  as a function of weight loss up to 35%. An anisotropic compression coefficient of 1.35 for a weight loss of 26% has also been established.

The mechanical behaviour of the pile is predicted using the INCA code (stress calculation) which uses the results of graphite weight loss variation determined using the USURE code. Agreement is observed between the calculated and experimental density profiles, although some parameters need to be fitted, particularly the effective diffusion coefficient for methane in the carbon dioxide determined up to 16% weight loss, as well as the parameters associated with porosity variation as a function of weight loss.

Continued operation of the BUGEY-1 reactor now depends (beyond the scope of the calculation made) on particularly careful monitoring of the variation of the physical properties of its moderator.

## I - BRIEF DESCRIPTION OF THE BUGEY-1 REACTOR

### 1.1 - Introduction

The BUGEY-1 reactor went into commercial operation in 1972 and has now reached the energetic date of 11 (fpey) full power equivalent years. This unit on the Bugey Nuclear Generating Centre belongs to the natural uranium gas cooled graphite moderated type reactor.

It has a capacity of 540 MWe and its main characteristics are the following :

- Integrated disposition : the circulation of the coolant gas, assured by 4 gas circulators, is carried out inside the prestressed concrete reactor containment and the graphite (moderator) stack on top of the main heat exchangers is also inside this building.
- The annular fuel elements, cooled both internally and externally, are held within graphite sleeves which enables them to be handled. Maximum specific power : 13 W/g.
- Each channel, containing 15 fuel elements, is directly accessible by the fuel handling machine (direct view) and refuelling is carried out during the operation of the reactor.
- The pressure of the coolant gas is 43 bar, and the average core input and output temperatures are respectively 220°C and 400°C.

Two reactors of this type are still in service in France. Their definitive shutdown dates are June 1992 for the St-LAURENT A2 unit, and April 1994 for the BUGEY-1 unit.

### 1.2 - Graphite stack constitution

The graphite stack which has a 15 m diameter is composed of 1315 columns of graphite placed side by side (height : 10.20 m). It is made up of prismatic bars with three mortice and tenon joints, the incorporated keying is a triangular link network with spaces of 370 mm.

This disposition enables the stack to have a certain suppleness or "respiration" according to the different operating regimes.

It has been constructed according to the principle of free brick deformation and lies on top of a plane steel surface, the flooring. It is encircled by a lateral structure made up of 132 steel posts which assures a corset function and supports the thermal shield hexagonal steel bricks.

The liaison between the beds is assured by the "master" columns which are placed 50 mm forward towards the bottom due to a shortening of their lower brick.

### 1.3 - Nominal channel constitution

Each nominal channel, is composed of 12 bricks ranging from 540 mm to 890 mm in height. These have an axial hole of 224 mm diameter, their thickness varying from 55 mm to 94 mm according to their azimuthal position.

The active core is composed of 852 identical columns. Operation regulation is assured by 75 control rod channel divided into 7 independant zones (1 central and 6 peripheral ones). These channels present a 88 mm bore. 9 identical columns are for the emergency control rods.

### 1.4 - Main characteristics of the active core graphite

The graphite is of P3AN quality type, made of LIMA petroleum coke, calcinated and grinded to a granulometry inferior to 1.6 mm, which has undergone a coal pitch impregnation treatment. Its main physical properties are the following :

- bulk density :	1.685 g/cm <sup>3</sup>		
- capture cross section :	3.73 mbarn		
- elasticity modulus :	in the axial direction (parallel to the extrusion axis : E// = 11 000 MPa		
- transversal direction :	E ⊥ = 7 500 MPa		
- anisotropic coefficient :	1.47		
- average mechanical resistance (in MPa) :			
	Directions	//	⊥
	Traction	14	9.2
	Compression	42	38

### 1.5 - Principal phenomena affecting the stack

#### 1.5.1 - Brick deformation due to irradiation

The graphite bricks of the active core are essentially subject to the following deformations :

- transversal contractions (perpendicular to the extrusion axis) and longitudinal ones. The latter are the source of important movements between the columns.
- differential longitudinal contractions. The fibres of the opposite faces of one graphite bar can be subject to a high flux gradient due to the cell geometry. The bricks which are the most affected by this phenomena bend slightly when this gradient is important. This effect is eventually significant compared with the passage section or with the relative vertical position of the graphite beds.
- these deformations have therefore made necessary the use of a template, on some occasions since 1989. A slight machining of the bed junctions constituting the striction areas has restored the free passage of the fuel elements.

#### 1.5.2 - Graphite radiolytic corrosion

An important radiolytic corrosion of the graphite has been encountered in some bricks, due to the high specific power attained in the most powerful core channels and to the notable coolant gas pressure.

Taken into account since reactor conception, the intensity of this phenomenon has led to adopt palliative measures to limit the evolution :

- creation of a slight flow of CO<sub>2</sub> between the external and internal faces of the bricks, by establishing a differential pressure between these faces obtained by CO<sub>2</sub> circulation in the 2 mm space between the graphite beds and the cartridge sleeves. It is a reason why the last sleeve, at the bottom of the channel, has orifices to allow the CO<sub>2</sub> passage in the internal channel made up of the train of fuel elements.

This internal "sweeping", which did not exist in 1972, was introduced in 1975 and then increased in the most sensitive zones in 1980.

- injection of small quantities of methane in the coolant gas used to limit the oxidation reaction. Weak in 1972, the methane concentration has been increased today at 420 vpm.

Although this additive allows to reduce the corrosion rate, the CO<sub>2</sub>-CH<sub>4</sub> mixture, on the contrary, induces hydrogenated-carboxy composites which form deposits on the graphite stack and fuel elements. This has led to two problems :

- \* containing about 1% of hydrogen in weight, the deposits increase the moderator capture cross section. This effect leads to a noticeable reactivity decrease, estimate at 700 pcm, now amplified by the defavorable evolution of the moderator coefficient (decrease of the moderator effect by loss of graphite). Since 1984, this persistent evolution has required the use of a slightly enriched fuel to therefore compensate this loss while reducing the fuel renewal rate, which enables a better fuel optimization. This "doping" has been fixed at 0.04% of U235.

- \* the deposits create an additional thermal screen between the CO<sub>2</sub> and the fuel element claddings degrading the exchange coefficient which could lead us, if no action is taken -and in order to respect the fuel element specifications to reduce very significantly the setpoint of the coolant gas temperature. By the way, the deposits found on the main heat exchangers have no consequence on the effective operation of the reactor.

The composition of the coolant gas is the result of a compromise between the inhibition (by CO and CH<sub>4</sub>) and the reduction of deposits on the fuel elements claddings, taking into account the limitation of the steel corrosion by steam. The joint action of the injection system and the purification circuit of the CO<sub>2</sub>, allows to maintain the concentration of impurities on the following levels :

[CO] = 1300 vpm, [CH<sub>4</sub>] = 420 vpm, [H<sub>2</sub>] = 100 vpm, [H<sub>2</sub>O] = 60 vpm.

This concentrations are controlled every day by chromatographic analysis.

## II - CLADDING DEPOSITS

The presence of deposits on the hottest claddings involves to a noticeably increase of their temperature, which could in time go over the maximum temperature authorized during normal operation (515°C).

The evolution of this phenomenon has been taken into account thanks to the temperature monitoring of the 19 instrumented channels in the reactor.

The core has an emergency protection and its role is to limit the evolution of the "temperature" and "temperature gradient" parameters of the fuel cladding. This is done by processing the results obtained by implanting 3 thermocouples on the external cladding of the hottest fuel element in each of the 2 instrumented channels found in each regulation zones. This security presents a very rapid response time during abnormal transients.

Three channels, identical to the ones described above and destined to follow the phenomenon of cladding fouling, and two other "testing" channels, equipped with thermocouples on 7 fuel elements, complete the instrumentation. It enables an accurate monitoring of the evolution of deposits through the following parameters :

- effective temperatures of the hottest fuel element claddings : the influence of the deposits is determined by comparing them with the values related to clean cladding temperatures.
- "heat transfer ratios", images of exchange coefficients. Their increase enables thermal exchange degradation to be detected.

The periodical resurgence of an abnormal evolution of these temperatures, which can reach a + 30°C increase, has led to a particular procedure designed to eliminate the deposits by oxidation. This consists of injecting about 3000 Kg of oxygen in the reactor, for a limited time (about 40 hours) to reduce the operating time without methane.

This process is regularly used (the last time was in April 1991). These injections usually give positive results, restoring the reactor to a "clean" situation [2]. Their influence on graphite corrosion remains quite weak compared with the high weight losses now reached.

## III - MONITORING THE EVOLUTION OF THE STACK CORROSION

A periodical monitoring has been set up in 1981 because of the important radiolytic corrosion of the graphite stack which could in time seriously change the mechanical properties of some bricks. This is done through :

- a set of corrosion monitors loaded in the sleeves of some fuel elements. They have been abandoned because their geographical position and the methane sweeping did not enable the recorded results to be easily extrapolated.

- samples taken directly from bricks belonging to different beds. The determination of the bulk density of these samples gives us the weight loss of these blocks.

They are taken by milling according to the perpendicular direction to the brick's axis. These core drillings - 20 mm to 30 mm long, with a 17 mm diameter, are then analysed by the C.E.A. (Commissariat à l'Energie Atomique).

The measurement of a weight loss that reached 22% in 1985 on one of the samples and the evolution prospects of the phenomena until definite reactor shutdown (the date had not then been fixed) has led to a detailed analysis carried out by the C.E.A. and BUGEY 1 and meeting the D.S.I.N. (Safety Authorities) requirements to define the evolution of the mechanical behaviour of the most affected bricks.

This study lays on the follow up of the evolution of the physical characteristics of the graphite in the most sensitive areas and also on the determination of the behaviour of these areas using "USURE" (determination of the increase of the corrosion rate in time) and "INCA" (thermomechanical calculation of the mechanical behaviour of one brick in time) calculation codes [3].

### 3.1 - Monitoring the effective evolution of graphite properties

A test programme has been established based on the samples taken in the 3 most exposed beds in the most powerful core channels (3 core drillings per level) and on video recordings of the sight of these channels. This allows to determine the effective state of these blocks.

Carried out on about 15 channels per outage (135 samples), the test programme has been finished in August 1991.

The maximum weight loss, revealed on one core drilling reaches 35% (average value on 22 mm, for a maximum point value of 38.3%). This was found in 1990 at the energetic date of 10.79 f.p.e.y. The average rate defined on the 94 mm brick thickness for this azimuthal position is about 27%.

About 25 columns have been found today with a weight loss going over 30% on at least one sample.

### 3.2 - Evolution of compression resistance as a function of the weight loss

The 20 core drillings which have the most important weight loss (U) after each campaign have their compression resistance measures taken.

The numerous values which are now available have enabled an experimental graph to be established showing the evolution of the compression resistance (perpendicular direction to the extrusion axis) as a function of the weight loss.

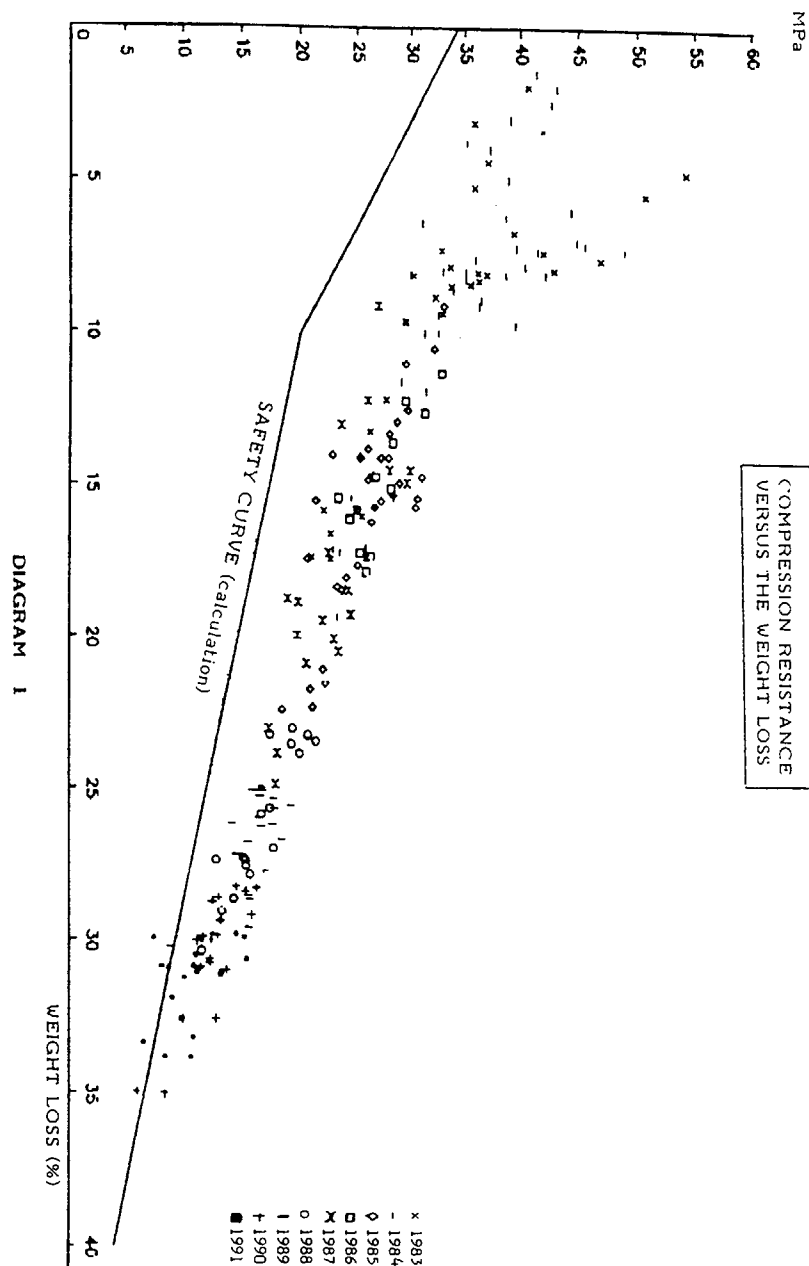
It is very important, looking at the rates which have been obtained, to detect an eventual increase of the negative gradient of the evolution of the compression resistance. This would be significant of a very noticeable, and non linear degradation, of the mechanical qualities of the graphite.

The cloud of points available on the 25% - 35% weight loss range has enabled 2 average evolution statistic laws to be validated on the 25% - 30% and 30% - 35% intervals. These equations have been established using 43 and 25 experimental points (Diagram 1).

The right segments traced on the previously designed intervals show a perfect continuity for the whole range which has been studied and are also quite close of the average law established for the weight loss held between 10% and 35%. No inflection has been noted.

The lowest resistance noted : 6.2 MPa (U = 34.9%)

Average value, U = 35% (statistical law) : 8 MPa (initial graphite : 38 MPa).



It is important and necessary for us to try to establish an identical graph for the samples which have been machined parallel to the extrusion axis. The theoretical evolution law was defined until now by extension to the parallel direction of the law formulated for the perpendicular direction, that is :

$$R (// \text{ or } \perp) = R_0 (// \text{ or } \perp) \cdot f(U)$$

Since the 1990 outage, core drillings of a diameter and length of about 30 mm have been taken out. From each of them, and perpendicular to their axis, 2 cylindrical samples of a 13 mm diameter and 26 mm length have been machined and then had their compression resistance measured.

The first results show an experimental anisotropy coefficient ( $K(\text{an, exp}) = 1.325$ ,  $U = 26\%$ ) higher than the theoretical value retained up to now. ( $K(\text{an, th}) = 1.105$ ).

### 3.3 - Determination of density

After machining and examination the surface in order to estimate the volume correction due to eventual splinters or cracks, each sample is weighted with a precision of  $4 \cdot 10^{-3}$  g. The diameter is measured by means of a laser micrometer with 15 to 20 measures on two perpendicular directions (precision  $\leq 1 \mu\text{m}$ ). The value of the length measured with a micrometer represents the average of 5 measures (precision  $\leq 2 \mu\text{m}$ ).

The weight loss is obtained through  $U (\%) = 100 (1 - \frac{\rho}{\rho_0})$

The initial bulk density of the BUGEY-1 graphite on average is  $1.685 \pm 0.02 \text{ g.cm}^{-3}$ . To calculate the weight loss the maximum value is taken in a conservative manner  $\rho_0 = 1.70 \text{ g.cm}^{-3}$ .

### 3.4 - Determination of density profiles

The bulk density, locally measured by gamma absorption every 2 mm along a sample, gives the density profiles from the distance of the channel-wall. The principle of this method consists in measuring the attenuation of a collimated beam of gamma photons emitted by a source of  $^{152}\text{Eu}$  and  $^{154}\text{Eu}$  passing through the diameter ( $\phi$ ) of the sample

$$\frac{I}{I_0} = \exp(-\mu(E) \times \rho \times \phi)$$

with  $\mu(E)$  = mass absorption coefficient of the graphite determined by graphite samples of known density.

$$\mu(344 \text{ KeV}) = 0.0984 \text{ cm}^2 \text{ g}^{-1}, \quad \sigma = 5 \cdot 10^{-4}$$

With a probability of 95%, the local bulk density ( $\rho_m$ ) is in this field defined by :

$$\rho_m - 0.6\% < \rho < \rho_m + 0.6\%$$

This method has been qualified by comparison with the method giving bulk density by measurement and weighing.

### 3.5 - Results

Presently 74 of the channels of highest power ( $P > 95\% P_{\text{max}}$ ) have been examined of a total of 852. Since 1983, some 900 samples have been measured (weight loss being deduced from the density as determined by measurement and weighing). The whole results obtained made possible to localize the most corroded area of the stack which is situated between 16.2 and 18.0 m from the upper surface of the moderator. Diagram 2 represents the evolution of weight loss as a function of time expressed in full power equivalent year. On this graph, showing a total of 256 measures carried out on samples taken at

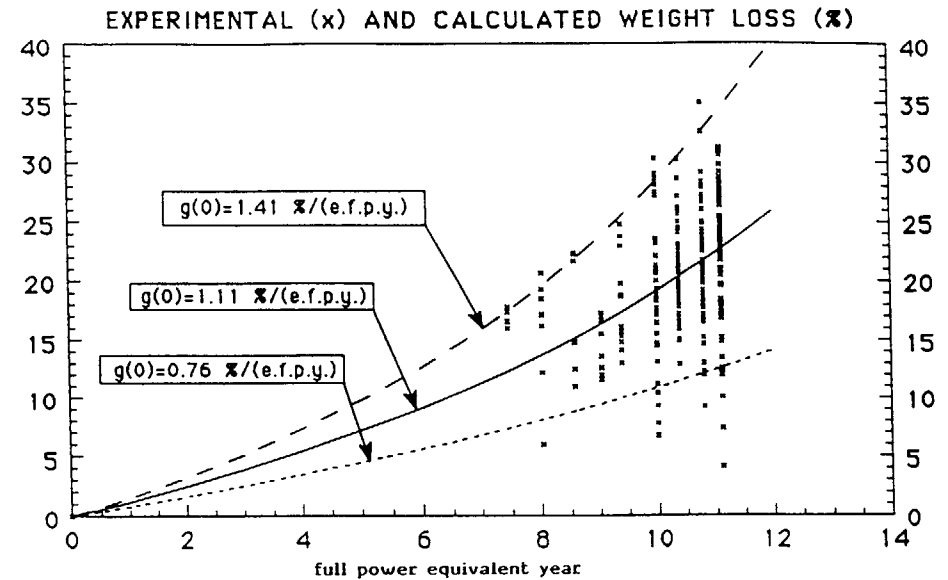


DIAGRAM 2

17.20 m, we can observe a relatively large scattering which essentially results from the heterogeneous distribution of  $\text{CH}_4$  in moderator and temperature and power variations in time. The heterogeneity of the initial bulk density of graphite contributes little to the scattering observed.

A great number of experiments carried out in the BFB loop in the SILOE reactor [4], show that the STANDRING relation [5] underestimates the accumulated weight loss of the moderator versus the lifetime of the reactor.

$$C_r (\%) = \frac{100 \pi e}{1 - \pi e} \left[ \exp\left(\frac{1 - \pi e}{100 \pi e}\right) \cdot g_0 \cdot t - 1 \right] \quad \dots\dots\dots (8)$$

$\pi_e$  = open porosity of graphite

$g_0$  = initial oxidation rate

$t$  = time expressed in full power equivalent year.

Samples from various channels have been taken successively at virtually the same levels (17.20 and 17.30 m from the upper part of the stack), at different time. From the different weight loss observed, we obtain the initial oxidation rate

$$g_0 = 1.11 \pm 0.30 \text{ \% (f.p.e.y.)}^{-1}$$



AXIAL CURVE OF DENSITY

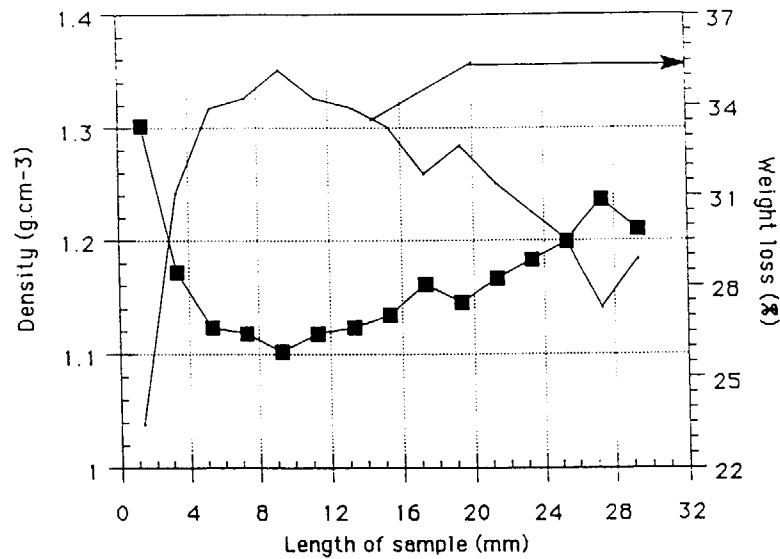


DIAGRAM 3

On the other hand, when replacing  $\pi_e$  in the relation (8) by  $\pi_R$  (reactive pore volume) with  $\pi_R = 0.10 \text{ cm}^3/\text{cm}^3 [6]$ , we get an average curve and the maximum and minimum curves of diagram (2) which include most of the points.

RPV represents the porosity of pore diameters from 0,05 to  $2 \mu\text{m}$  where most of the radiolytic oxidation takes place [7].

Diagram (3) represents the density profile determined by gamma absorption, and from which the weight loss profile is deduced. All samples show a maximum weight loss at approximately 10 mm of the channel wall. This sample presents an average weight loss of 31.4%, the maximum being 35.2%.

#### IV - ESTIMATED RADIOLYTIC REACTION OF GRAPHITE - "USURE" CODE

A code to calculate the radiolytic corrosion of graphite has been elaborated to forecast the development of weight loss of the most corroded part of the moderator.

This "USURE" code is based on the following formalism :

The number of  $\text{CH}_4$  molecules consumed per second and per gram of  $\text{CO}_2$  is given by :

$$\frac{dN}{dt} \text{ moles} = - \frac{\gamma \cdot G(-\text{CH}_4)}{100 \times 1.602 \cdot 10^{-19}} \quad (9)$$

$G(-\text{CH}_4)$  represents the radiochemical yield expressed in numbers of vpm of  $\text{CH}_4$  reacting for 100 eV absorbed by the  $\text{CO}_2$ . In the case of BUGEY-1, the dose rate  $\gamma$  is related to the linear power rate ( $\phi$ ) in uranium ( $\text{w}/\text{cm}^2$ ) by the relation  $\gamma = K \cdot \phi/r$ , being the distance of the fuel axis and  $K = 3.24 \cdot 10^{-4} \text{ cm}^2/\text{g} [8]$ .

Finally the relation (9) becomes :

$$\frac{dN}{dt} \text{ mole} = - K_{AB} \cdot \frac{\text{CH}_4}{r}$$

On the other hand, if  $J_{\text{CH}_4}$  represents the total flow of  $\text{CH}_4$  penetrating the graphite porosity through diffusion and by leakage of  $\text{CO}_2$  ( $Q_{\text{CO}_2}$ ) induced by a drop in pressure on both sides of the block, we obtain :

$$J_{\text{CH}_4} = -D_{\text{eff}} \cdot \frac{d\text{CH}_4}{dr} + K_{BA} \cdot \frac{\text{CH}_4}{r}$$

$K_{BA}$  is related to the flow of  $\text{CO}_2$  leakage by  $K_{BA} = Q_{\text{CO}_2} / 2\pi h \varepsilon \cdot \rho_{\text{CO}_2}$  with ( $\varepsilon$ ) open porosity of graphite and  $h$  unit of graphite height = 1 cm.

CALCULATED (T) AND EXPERIMENTAL (M) WEIGHT LOSS PROFILES

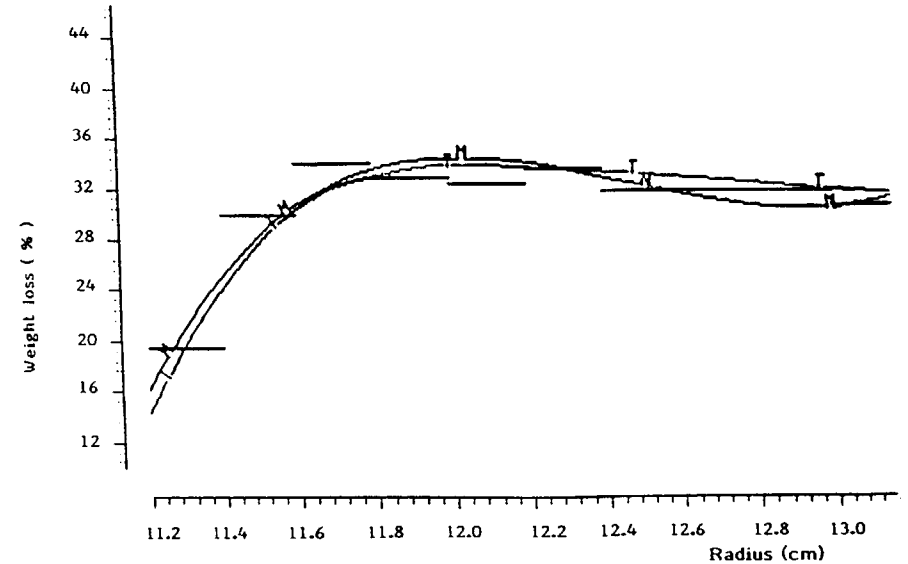


DIAGRAM 4

The conservation of the  $\text{CH}_4$  mass is expressed by :

$$\text{div}(J_{\text{CH}_4}) = -K_{\text{AB}} \frac{\text{CH}_4}{r}$$

When assimilating the graphite block of prismatic shape with a cylinder of equivalent section, we get in cylindrical coordinates

$$\frac{1}{r} \frac{d}{dr} (r \cdot J_{\text{CH}_4}) = -K_{\text{AB}} \frac{\text{CH}_4}{r}$$

The calculation consists in the numerical solution of the differential system :

$$\frac{d}{dr} \begin{bmatrix} C_{\text{CH}_4} \\ r J_{\text{CH}_4} \end{bmatrix} = \begin{bmatrix} \frac{K_{\text{BA}}}{r \cdot D_{\text{eff}}} & -\frac{1}{D_{\text{eff}}} \\ -K_{\text{AB}} & 0 \end{bmatrix} \begin{bmatrix} C_{\text{CH}_4} \\ J_{\text{CH}_4} \end{bmatrix} \quad \dots\dots\dots (10)$$

with the boundary condition :

$$C_{\text{CH}_4}(r = R_{\text{in}}) = C_{\text{CH}_4}(r = R_{\text{out}}) = \text{known value}$$

At each time, the effective diffusion coefficient ( $D_{\text{eff}}$ ) and the porosity ( $\epsilon$ ) are calculated to take into account their evolution as a function of the weight loss.  $C_{\text{CH}_4}(r)$ , solution of (10), allows to determine  $G(-C)$  from the variations of  $G(-C)$  according to the  $\text{CH}_4$  concentration and  $G(-C) = f(T)$ . The local bulk density  $\rho(r, t)$  is deduced from  $G(-C)$  locally calculated.

Diagram (4) shows a good agreement between the calculated weight loss profile and the weight loss profile determined experimentally after 10 (f.p.e.y).

## V - MECHANICAL BEHAVIOUR : "INCA" CODE

### 5.1 - Calculation hypothesis

In order to define the evolution in time of the mechanical behaviour of the most corroded block of the core, the C.E.A. developed the thermomechanical code "INCA" and defined a criteria of local rupture.

The following hypothesis have been retained :

- assignment to the brick concerned of the experimental defined maximum weight loss according to the identical profile of the one revealed on the first 22 mm of the thickness, and flat after that,
- assignment to this brick of the maximal integrated damage dose after setting up an historical account which shows the evolution of the power rate and flux graph deformations since 1972.

The criteria retained for local rupture for the graphite is the criteria of maximum stress, or Rankine criteria, which, in our case is translated by the following inequalities :

$$\begin{aligned} \sigma_c \perp &< \text{principal stress in the plan} < \sigma_t \perp \\ \sigma_c // &< \text{principal stress in the // direction} < \sigma_t // \end{aligned}$$

Rupture happens when one of these two inequalities are no longer respected.

### 5.2 - Principal factors which must be integrated

The behaviour of a graphite brick is complex and depends notably on the following factors :

- \* orthotropy : graphite properties are different according to the parallel or perpendicular directions to the extrusion axis. This is particularly true when determining Young's modulus. Poisson's coefficient,

thermal expansion coefficient, dimensional changes under irradiation, creep under irradiation and compression and traction rupture stress.

- \* irradiation : the principal consequences of integrated damage dose are the Wigner contractions and the creep. However many of the graphite properties depend also on the dose.
- \* Radiolytic corrosion : this leads to degradation of the texture of the graphite in time, altering its mechanical properties.
- \* Temperature : although it has little influence on the graphite properties inside the range which interests us (400° C - 500° C), it does intervene on the Wigner deformations and must be taken into account during important reactor operation transients.

Two opposing factors mainly takes place : the Wigner deformations (only contractions in our case) which generate stress similar to those due to a thermal gradient in the brick thickness, and which increase with dose damage, and the creep which brings about a relaxation of this stress with time. Therefore the entire state of the stress in the brick thickness must be calculated taking into account time in order to detect an eventual lack of respect of the local rupture criteria.

### 5.3 - Geometry and modelisation

The first thermomechanical calculation was made without taking into account the variation of mechanical properties according to bidimensional model of a block section. For symmetry reasons, only 1/6 of the section was modelised. The grid was composed of 252 triangular elements with 563 knots. A logarithmic cut, in 10 layers of concentric elements was established to display local stress and to take into consideration the evolution of the different physical parameters according to the radius of the block (weight loss, dose).

The following studies were then conducted on the basis of a cylindrical model. Validated according to the initial model it allows to provide correctly the mechanical properties variations versus the dose and the weight loss.

This axisymmetrical model of an infinite cylinder is made up of 138 elements in the brick thickness, 88 on the first 22 mm, precision made necessary due to the existence of very important weight loss and dose gradients in this area, generating parasite oscillations when calculating on the less precise mesh which leaves a doubt.

### 5.4 - General characteristics of the material [9]

- weight loss : the corrosion rates come directly from the "USURE" code with, from the 22 mm position, a constant weight loss imposed up to the exterior radius. These values have been reset according to the most penalizing experimental result ( $U = 35\%$ , average value on the first 22 mm, energetic date 10.79 f.p.e.y).
- Wigner deformations : as the Wigner contraction graphs relative to the graphite of our stack were only defined for weak values of integrated dose, new graphs have been established based on the dimensional evolution of series of monitors carried out on the axial and radial directions and initially destined to follow the corrosion evolution.

These samples are placed inside the sleeves of the fuel elements of powerful channels since 1972. Having integrated an important damage dose, they are used subjected to diverse dimensional measures according to fuel renewal rhythm. Only the length measures are used.

In order to define the evolution of the integrated damage dose for each analysis, an historical account has been realised to retrace the power of the fuel elements which contained the samples. The calculations of rapid flux has been made by the Nuclear Calculating Division using the "APOLLO" code.

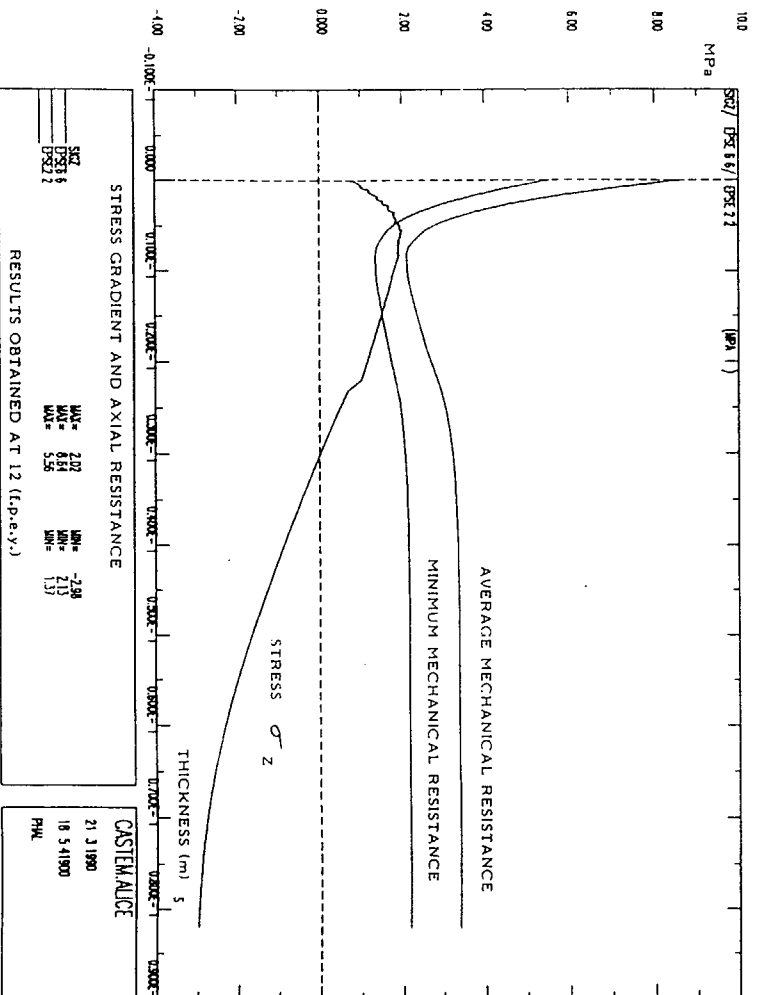


DIAGRAM 5

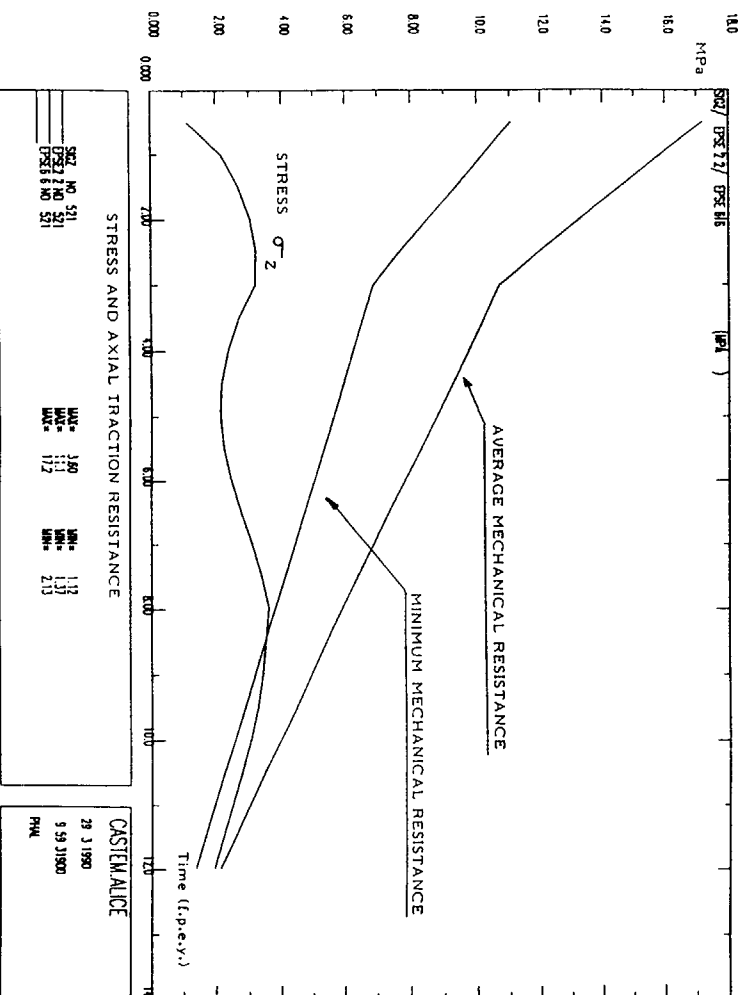


DIAGRAM 6

Using the measured contractions and corresponding dose values which go beyond  $10^{22} \text{ n/cm}^2 \phi \text{ FG}$ , 2 Wigner deformation curves have been established according to the parallel and perpendicular directions to extrusion axis ( $T = 350^\circ \text{ C}$ ).

- Creep : secondary creep coefficient  $K_{//} = 1.6 \cdot 10^* (-25)(\text{MPa n/cm}^2 \cdot \phi \text{ FG})^{-1}$

$$\text{and} \quad \frac{K_{\perp}}{K_{//}} = \frac{E_{//}}{E_{\perp}} = 1.47$$

- Young's modulus : presenting few variation in the temperature interval  $20^\circ \text{ C} - 600^\circ \text{ C}$ , the evolution law as a function of the dose D and weight loss U is therefore the following :

$$\frac{E_{//}}{E_{0//}} = \frac{E_{\perp}}{E_{0\perp}} = (2 + 1.6 \cdot 10^* (-23) D) (1 - 1.95 U) \text{ for } D > 10^* (21) \text{ n cm}^2 \phi \text{ FG}$$

- Permanent stress : the axial stress applied to the reference brick situated in the middle of the column remains weak (less than 0.3 MPa) and is practically negligible with regard to total stress level.

- Mechanical resistance : variations due to irradiation and oxidation

$$\frac{R_{\text{irr, ox}}}{R_0} = \frac{R_{\text{irr}}}{R_0} \times \frac{R_{\text{ox}}}{R_0} \quad \text{and } R_{\text{irr, ox}} = 1.3225 R_0 (0.7345 - 1.535 U), \text{ for } U > 10\%$$

### 5.5 - Results

Two calculations have been done, integrating the initial values of respectively average and penalizing (average values less than 3 standard deviations) mechanical resistance so as to know the effective behaviour of the most affected brick. The collected results of the "enveloppe" or safety study shows the existence of stress levels going beyond traction resistance (parallel and perpendicular directions) on a 10 mm thickness at the energetic date of 12 f.p.e.y. The very localized aspect of this phenomenon (radially and azimuthally) do not question the global behaviour of the brick. This overstepping happened at 8 f.p.e.y for the most used knot (diagram 5 and 6). Large margins exist for compression.

Notable margins are conserved when taking into account the average resistance values [10].

### VI - CONCLUSION

The intensity of the graphite radiolytic corrosion phenomenon of some moderator bricks of the BUGEY-1 reactor has led the power station, in collaboration with the C.E.A., to undertake a very important monitoring programme based on the surveillance of the evolution of the graphite mechanical properties of the most sensitive beds, and on a theoretical approach destined to apprehend the mechanical behaviour of these bricks until the definitive reactor shutdown date.

The calculations, carried out using the "USURE" and "INCA" codes allow to define eventual available margins with regard to the non-exceeding of the considered mechanical resistances and to establish the most affected localised zone.

The numerous analysis made on the samples carried out in the actual sensitive regions have allowed to define the maximum weight loss effectively reached, to establish the real value of oxidation rate, to validate the density profile determined by calculation, and to define the evolution laws of compression resistance (parallel and perpendicular directions to the extrusion axis) as a function of the weight loss on the 10% - 35% range.

These analysis have therefore allowed to verify that no brutal degradation of the mechanical properties of graphite happens for the high rates reached.

This element, ensuring the global positive behaviour of the bricks, will be regularly verified thanks to further samplings carried out in target areas.

### ACKNOWLEDGEMENTS

The authors wish to thank Mr. M. BRUET\*, Mr. C. BAUDUSSEAU\*, Mr. C. ROYON\* for assistance with the experimental work. Thanks are also due to Mr. Y. KAUFFMANN\* for the determination of density profile by gamma absorption.

(\* C.E.A. - CEN/GRENOBLE - France).

### REFERENCES

- [1] G. JOUQUET  
Note technique STA/STMA/83-NT-443 d'octobre 1983
- [2] M. VIEILLE BLANCHARD, A. PETIT  
Note technique D 5111/NT/9110 du 17.5.1991
- [3] Note technique D 5111/NT 126 du 1.6.1988
- [4] P. CAMPION  
Ph.D. Thesis University of Salford - 1977
- [5] J. STRANDRING  
J. of Nucl. Energy. 20-101.1966
- [6] R.J. BLANCHARD, M. MONTAGNE  
Gas cooled reactors today - Brit. Nucl.Ener.Soc. LONDON 1982
- [7] P. CAMPION, R.LIND, R.J.BLANCHARD, C.KOCH  
A th.Inter. Carbon and Graphite conf. - LONDRES. 1974
- [8] C. FICHE  
CEA-N 1280. April 1970
- [9] C. PHALIPPOU  
Rapport DMT 88/240 (SYST/EFF/88/42) du 13.7.1988
- [10] C. PHALIPPOU  
Rapport DMT 90/192 (SYST/LEFF/90/26) du 12.6.1990

# GRAPHITE SURVEILLANCE IN N REACTOR

E. M. WOODRUFF

N Reactor Facility and Operation Assurance,  
Westinghouse Hanford Company\*,  
Richland, Washington,  
United States of America

## Abstract

Graphite dimensional changes in N Reactor during its 24 yr operating history are reviewed. Test irradiation results, block measurements, stack profiles, top of reflector motion monitors, and visual observations of distortion are described.

## 1.0 INTRODUCTION

When N Reactor was last shut down on January 7, 1987, all the original load-bearing blocks were still in service and capable of continuing should a status change occur. Thus, N Reactor's 24-yr life represents an opportunity to examine behavior of a core in which most of the graphite in the fueled region has experienced the full cycle of transverse contraction, turnaround, and following growth. A recent U.S. Department of Energy (DOE) directive initiated transition activities that will ultimately lead to the decontamination and decommissioning of N Reactor.

Although N Reactor was light-water cooled and used a highly anisotropic graphite in the core and reflector regions, these departures from contemporary gas-cooled-reactor (GCR) design provide a study in contrasts. In effect, the core experienced exaggerated radiation-induced changes compared to modern GCRs constructed from more isotropic graphites.

## 1.1 GENERAL DESCRIPTION OF N REACTOR

N Reactor shares many similarities with the eight special-materials production reactors that were constructed earlier at the then-Atomic-Energy-Commission, now DOE, Hanford Site. Among the similarities are the basic core design, which has always been based on horizontal fuel tubes for front-to-rear charge/discharge operations, and the associated horizontal crisscross layering of graphite moderator and reflector blocks used to construct an unrestrained graphite stack. Light-water cooling and a low-flow, low-pressure, inert-gas blanket are also common to all Hanford Site reactors.

N Reactor (or N Production Reactor [NPR] in early references<sup>1</sup>) was the first to adopt a recirculating pressurized water cooling system designed for power recovery. Larger graphite blocks (6 in. x 6 in. in cross section) were used to accommodate both the larger tubes and an interlocking key structure that provides steam-venting passages between blocks to dissipate steam that would be ejected if a pressure tube burst. The arrangement of core components illustrated in Figure 1 also shows the side-to-side core cooling tubes that were introduced in the N Reactor design to limit filler block temperatures. Table 1 summarizes design and operating parameters of interest. Note that the core dimensions given in the text are for the graphite stack, while those shown in Figure 1 are at the outside of the biological shield.

## 1.2 CORE GRAPHITE

The choice of using an anisotropic type of graphite for N Reactor construction was influenced by several compelling factors that created the decision environment in 1958. The then newest Hanford reactors (KE and KW) were beginning to contract vertically at rates high enough to create concerns about impairment of control rod function. Then available irradiation test results indicated that a needle coke graphite with high-temperature processing and a fine particle mix would, by enhancing anisotropy, reduce the transverse contraction. The nuclear-grade TSX graphite eventually used in the core was manufactured by the National Carbon Division of Union Carbide using an extruded fine-grained needle coke and graphitization at 3000 °C.

Reflector graphite blocks were made of Speer Carbon Company Nuclear Grade 2 and Great Lakes Carbon Company Nuclear Grade R-1. These grades are almost identical to the TSX in the core, except for slightly higher impurity levels.

\* Hanford Operations and Engineering Contractor for the US Department of Energy under contract DE-ACU6-87RL10930.

Table 1. DESIGN AND OPERATING PARAMETERS

GRAPHITE	
Overall Core Dimensions . . . . .	39' 5" Long, 33' Wide, 33' 4" High
Weight Graphite . . . . .	2800 Tons Raw, 1800 Tons Finished
Number of Pieces . . . . .	78,000 Blocks, 17,000 Sleeves
Density . . . . .	1.7 g/cc Material, 1.29 g/cc As Stacked
PRESSURE TUBES, ZR-2	1003 Installed, 53' Long, 2.7" ID, 3.25" OD
COOLING TUBES, ZR-2	640 Installed Side to Side 42' Long, 3/4" OD
SAFETY SYSTEMS	
Control . . . . .	87 Horizontal water cooled, B <sub>4</sub> C Absorber Hydraulically Driven, Screen Speed 76 FPS
Safety . . . . .	108 Vertical Safety Channels, 3" ID Graphite Liners 3/8" Dia. Balls, Samarium Oxide Absorber Now Replaced by B <sub>4</sub> C
OPERATING PARAMETERS	
Power Level . . . . .	3800 Megawatts Thermal (MWT), 860 Megawatts Electrical (MWE)
Graphite Temperatures . . . . .	550 to 1050° F
Average Cumulative Fluence in 1987 . . .	Tube Block - 20.1 x 10 <sup>21</sup> , Filler Block - 17.7 x 10 <sup>21</sup> , (E>50 keV) (ref. 2)

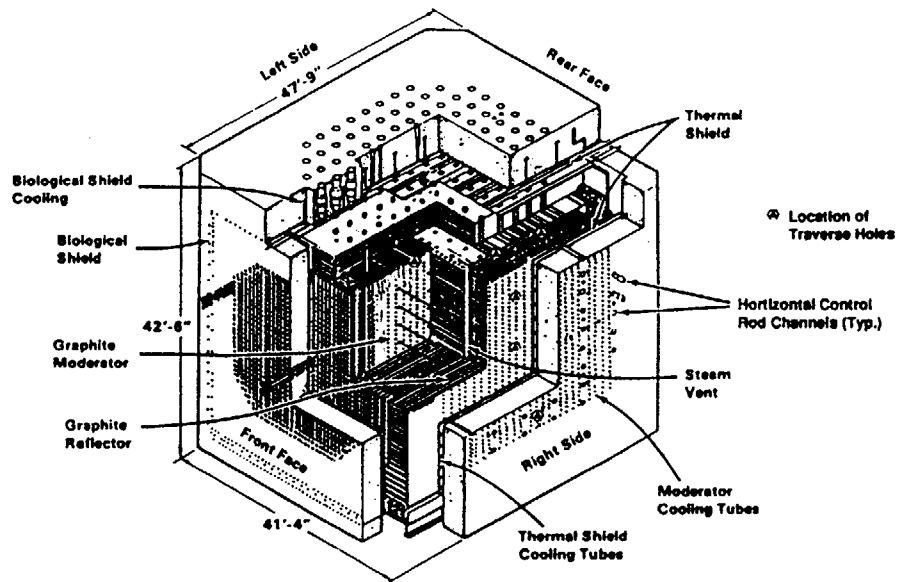


Figure 1. N Reactor Cutaway.

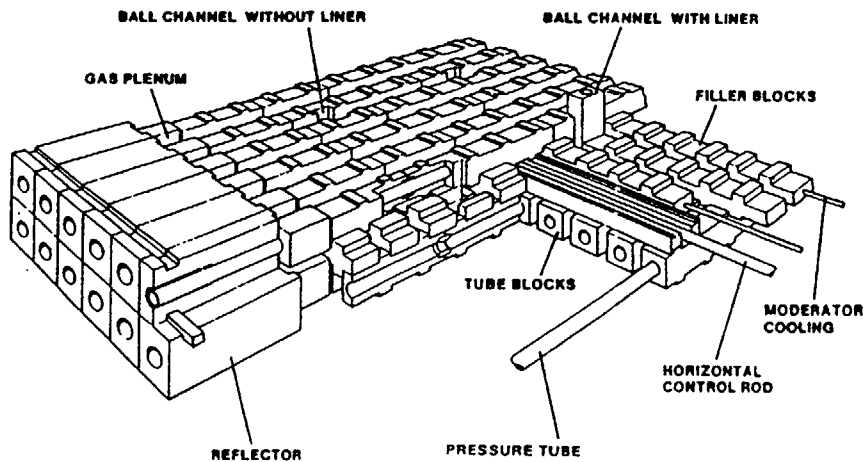


Figure 2. Graphite Layer Arrangement.

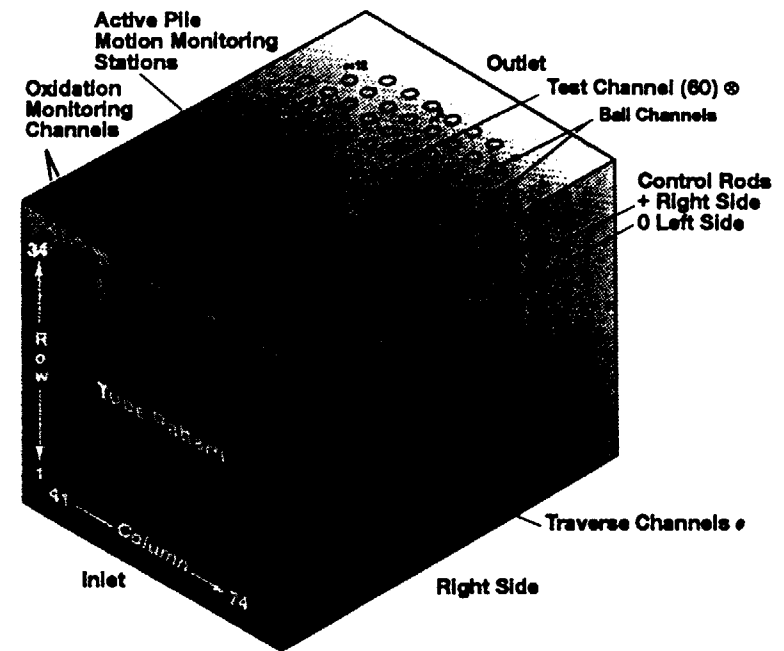


Figure 3. Surveillance Access Locations.

### 1.3 CORE CONFIGURATION

The interlocking-block design used in N Reactor is shown in Figure 2. The key recesses in the blocks (0.25 in. on tube blocks and 1.25 in. on filler blocks) establish block separations forming 2-in.-wide by 3-in.-high interconnected steam vent passages from front to rear and side to side and 2-in. x 2-in. vertical openings that intercept the horizontal channels. These passages give sufficient cross-sectional area for steam and water dissipation to limit potential damage to a particular graphite bar in which a tube might break.

Access locations for surveillance activities to be discussed are shown on the simplified core diagram in Figure 3. The side-to-side traverse channels are accessible from both the right- and left-side inner rod rooms. Horizontal control rod channels are accessed only from the rod-entry side and ball channels only through the top shield.

### 2.0 DIMENSIONAL CHANGE

When production blocks of TSX graphite arrived at the Hanford Site samples were taken for accelerated irradiation tests of dimensional behavior<sup>4,5</sup> in the Engineering Test Reactor, National Reactor Testing Station, Arco, Idaho (ETR); General Electric Test Reactor, Vallecitos, California (GETR); and later in High Flux Isotope Reactor, Oak Ridge, Tennessee (HFIR)<sup>6,7</sup>. In preparation for N Reactor start-up a set of test blocks was premeasured for insertion directly into a vertical ball safety channel (BC60) set aside as a test channel. Some of these test blocks were bored with axial holes to contain smaller samples.

Direct, in-place measurements of structural blocks in the core were made periodically throughout the reactor's life<sup>8,9</sup>, most commonly by access to tube blocks (transverse width measurements) through side-to-side traverse channels and horizontal control rod (HCR) channels. The translation of block changes

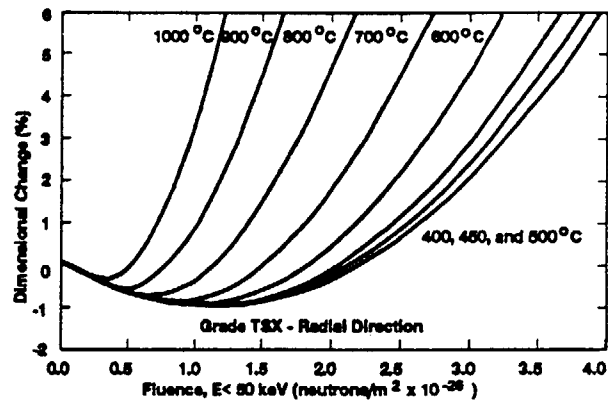


Figure 4. Calculated Against-Grain Irradiation Growth of Grade TSX Graphite.

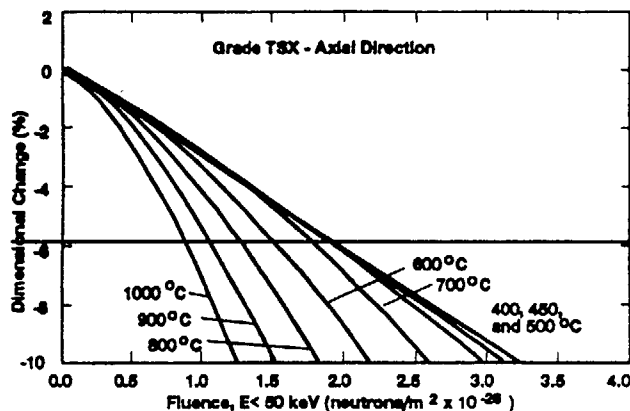


Figure 5. Calculated With-Grain Irradiation Growth of Grade TSX Graphite.

to cumulative core distortion effects was determined by a variety of surveillance techniques. This comprised the largest portion of the dimensional surveillance activities. These included profiling traverses, measuring layer heights, and monitoring pile motion.

Directional core responses to block contraction and growth are governed by block orientations and their interrelations from block to block. The vertical direction responded to cumulative transverse behavior contributed by the across-bar direction in both tube and filler layers, while horizontal front-to-rear or side-to-side responses were combined effects of both parallel and transverse behavior. However, in the vertical stack direction the transitional turnaround from transverse contraction followed by growth was protracted in time by flux and temperature gradients that introduced different timing for the turnaround phenomenon at different radial distances from the fuel. This range of timing for maximum contraction also reduced the magnitude of cumulative stack contraction compared with an individual block or a sample cut from a block and included in test irradiations because at no time did all components of the cumulative stack reach maximum contraction together.

The results of dimensional studies and their relative significance are briefly described in the following sections.

## 2.1 TEST IRRADIATIONS

Test blocks charged into BC60 at start-up were plagued from the onset with the inevitable lag in fluence accumulation because after the first sample discharge the reactor was always one or more operating periods ahead of the samples. Other problems included: difficulty in removing samples when the reactor and the test channel became distorted, a sample retrieval-tool-grip failure that resulted in sample drops and breakage, loss of effective dosimetry control after long in-reactor residence times, and the complexities of a changing flux distribution over the column of sample blocks as they subsided vertically while the adjacent tube blocks and alternate filler blocks were in the opposite transverse vertical growth mode.

On the positive side, one block retrieved in September 1984 was sectioned to provide samples for physical property determinations.

In 1981, test irradiations were conducted in HFIR at 575 °C and 620 °C to fluences up to  $2.3 \times 10^{26} \text{ n/m}^2$  ( $E > 50 \text{ keV}$ ). Analysis of the test results concluded that operating W Reactor to approximately twice its exposure level at that time would result in no "surprises" from the graphite. Additional refinements in high-exposure data were obtained from HFIR irradiations in 1986 that extended data up to an exposure of  $3.0 \times 10^{26} \text{ n/m}^2$  ( $E > 50 \text{ keV}$ ) at 450 °C. An analysis of TSX dimensional behavior using the HFIR and earlier irradiations of TSX and similar graphites combined with a modification of dimensional change theory<sup>11</sup> developed the families of length change curves shown in Figures 4 and 5 for radial (transverse) and axial (parallel) orientations respectively and irradiation temperatures between 400 and 1100 °C.

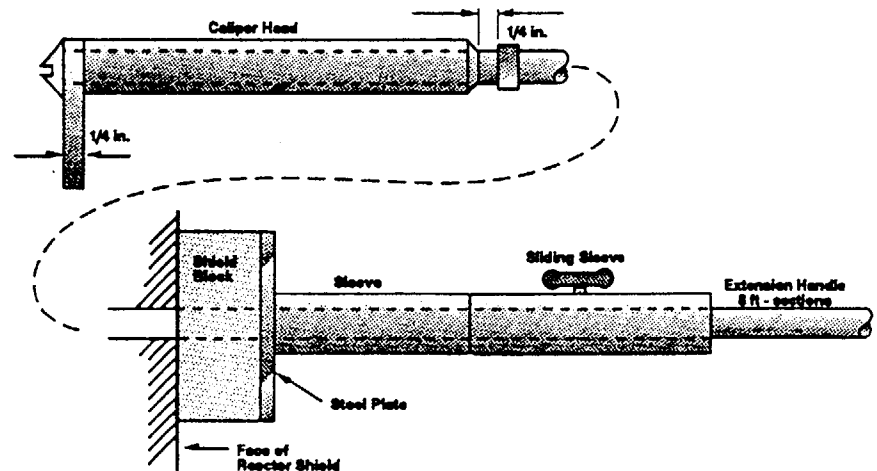


Figure 6. Calibrated Rod for Determining Tube Block Width and Position.

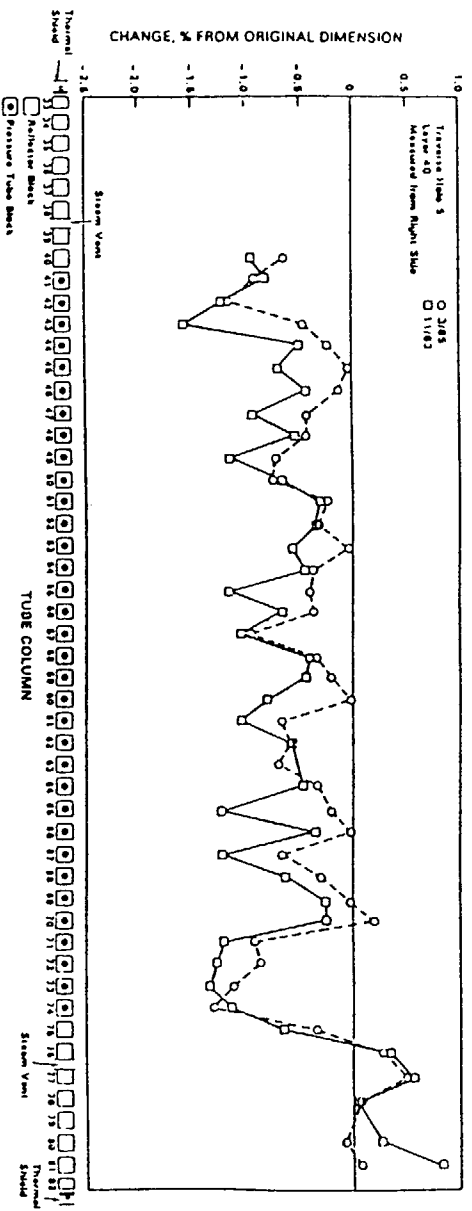


Figure 7. Block-width Change - Traverse Hole No. 5

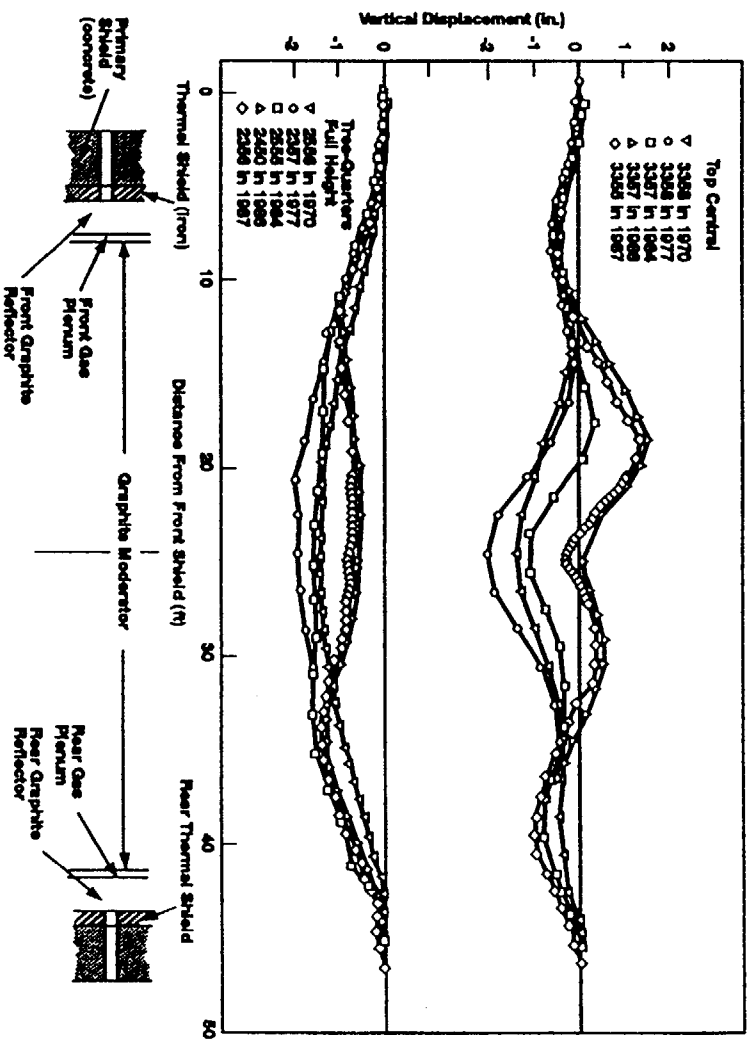


Figure 8. Pressure Tube Profiles as a Function of Time.



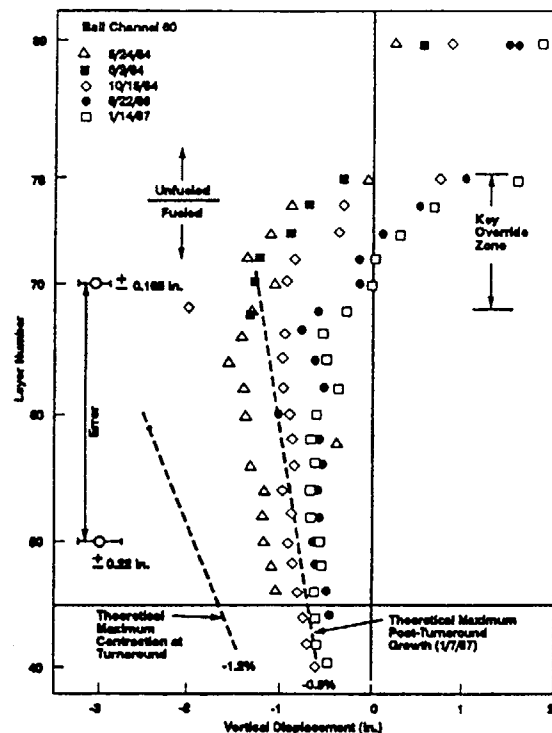


Figure 9. Layer Displacement History in Ball Channel 60.

## 2.2 REACTOR BLOCK MEASUREMENTS

Direct measurements of tube block widths were obtained in traverse holes and HCR channels with a modified caliper device illustrated in Figure 6<sup>12</sup>. In practice the technique is to remotely position the caliper head on the far side of the block to be measured, lock the sliding sleeve on the extension handle pole, and then reposition the caliper head on the near side of the block. The distance between sleeves is then measured with a dial caliper to give the block width. Tool precision is estimated to be approximately 0.004 in. for out-of-reactor measurements, and 0.012 in. for in-reactor measurements. The width of gaps between blocks and block positions with respect to as-built positions scribed on push poles are also recorded using this tool.

Block data for 1983 to 1985<sup>10</sup> provides examples of measured block-by-block changes. Data from the centrally located Traverse Hole No. 5 are given in Figure 7. The layer shown (40) is the third row of pressure tube blocks below the side-to-side core centerline. Block-to-block data scatter is typical for this surveillance, however the general trend of growth approaching the original block dimensions is clearly evident.

No comparable measurements of changes in block lengths that would represent behavior in the axial or parallel orientation were included in surveillance procedures in recent years.

## 2.3 LAYER DISTORTION

The transfer of changes in block dimensions to the core structure were detected directly by profiles in the front-to-rear direction obtained from traverses through pressure tubes or empty tube channels.

Side-to-Side measurements were made in traverse holes or HCR channels. Measurements were made using manometer equipment for vertical-only profiles or optically with a theodolite (light transit) technique that measured both vertical and horizontal displacements. Displacements were determined with respect to fixed reference points on the biological shield. Probable error for the manometer method was estimated to be less than 0.10 in.

Probable error for theodolite measurements was  $\pm 0.001$ -in. deflection from the zero reference line.

Historic changes in stack height are shown by repeat profiles in tubes at top center and at three quarters of full height in Figure 8. At the lower level in the stack, curves for tubes 2357 (tube row 23, column 57), 2958, 2555, and 2556 show that contraction had reached -1.3 in. at the center in 1970, continued subsidence to -1.7 in. in 1977 and then returned to -1.3 in. in 1984 as turnaround and growth became the predominant (transverse (vertical) behavior in the bars.

Near the top, in tubes 3357 and 3358, the same sequence occurred, but profile shapes and height are modified by key overriding that occurred early and created the shoulders of low subsidence toward the front and rear. As the core began to contract, the rigid response of the top reflector assembly prevented conformity with subsidence occurring below. This relieved vertical loads on the upper fueled region allowing horizontal displacements between layers where filler bars overrode the 0.25 in. high keys on tube blocks. The result compensated for contraction where the front and rear profile shoulders now appear, but not in the central region where key omissions in the design had intentionally created slip zones (front to rear and side to side). These zones were designed to prevent translation of the high parallel contraction across the entire width and length of the core. The combined absence of keys and decoupling of horizontal forces at the center eliminated key overriding effects near the center. During recent operating years, growth in lower regions of the core was approaching lay-up levels from below and in upper regions movement was above and away from original lay-up heights.

Another view of layer distortion was obtained from stack height measurements, which used the ball channels for vertical access into the core. Distances from the top shield (reference point) to successive graphite layers below were determined using a calibrated pole with an angled foot at the lower tip that could be positioned on successive tube blocks with the aid of a closed-circuit television (CCTV) camera. Tests of the stack-height tool determined that measurement error increased as the depth to the measurement point increased. The largest error, when six rod sections were used (to reach the bottom of the stack), was  $\pm 0.34$  in., and the error was  $\pm 0.165$  in. when two rod sections were used near the top of the core.

Repeat measurements were possible in the test channel, BC60, which was unlined exposing tube blocks down to the level of remaining test block samples near layer 40. The BC60 stack height measurements from 1984 to 1987<sup>14</sup> are plotted in Figure 9. The graphic format follows a well log approach using the abscissa to depict contraction to the left of a vertical zero or lay-up elevation line and growth to the right.

Key override effects causing the net cumulative stack height shifts back toward zero above layer 64 are typical in ball channels in the central core region. In these upper layers, many of the layer-to-layer height displacements are on the order of 0.25 in. (equivalent to one overridden tube block key). This override pattern continues to the top of tube layer 78; little change occurs within the top reflector layers. From May 1984 to January 1987 height of the top of the reflector increased from +0.2 in. to +1.9 in., which yields 1.7 in. in 2.6 yr or a growth rate (cold) of 0.66 in./yr normalized for an average production of 650 KMMO/yr.

The dashed lines in Figure 9 represent theoretical cumulative contractions of 1.2 percent and 0.5 percent, the maximum contraction at turnaround and the maximum growth at shutdown in 1987, respectively.

## 2.4 TOP-OF-STACK SURVEILLANCE

The major surveillance techniques used to monitor distortion at the top of the reactor stack included top-layer heights obtained during Ball Channel surveillance described Section 2.3, similar depth measurements obtained during calibration of the pile motion monitoring system, and the continuous readouts from the pile motion system sensors.

The depth measurements converted to heights above layup are summarized graphically in Figure 10. Numbers beside the symbols represent Ball Channel numbers and pile motion positions with the measured heights relative to the lay-up level entered below the position numbers. Note that maximum growth is indicated at left front of center. This agrees with upper-layer tube channel profiles. Negative elevations still occur in the right front perimeter region.

The pile motion system installed during reactor construction was upgraded in 1985 to replace the old manually activated data acquisition system with an automatic system for recording pile motion data at 6-hr intervals. Motion responses are detected by Linear Variable Differential Transformers (LVDT). During renovation, error analysis showed that although the system response may contain some error caused by component thermal expansion, the database is still a valid source to generate accurate growth-rate and gap-closure data. The thermal error could produce a height error bias of 0.199 in., which would be a constant bias on the dimensional readout and, therefore, would not affect growth-rate parameters or gap-closure derivatives.

The pile motion database for calendar year 1986<sup>14</sup> is shown in Figure 11. The outputs for each sensor position are adjusted to show change relevant to zero on the date the system was reactivated in October 1985. The position locations are near front-to-rear and side-to-side centerlines, as shown in Figures 3 and 10. Six of the 12 positions were included in the first phase of the renovation program before

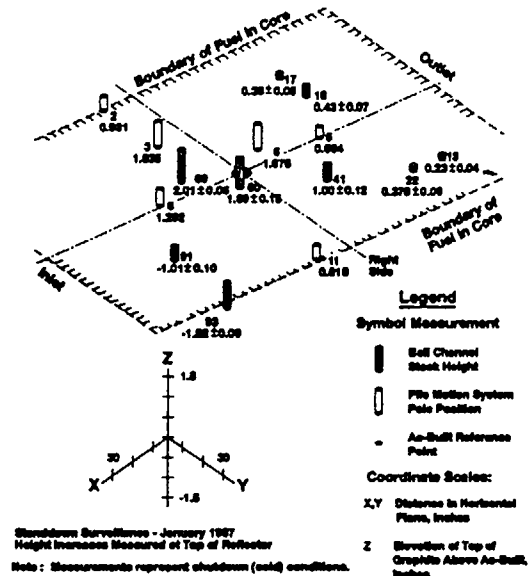


Figure 10. Changes in Height of Top of Reflector Since Initial Construction (measurements represent shutdown (cold) conditions).

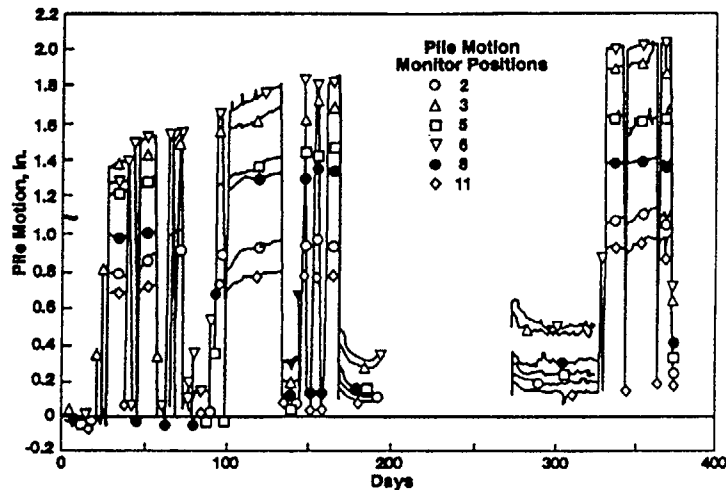


Figure 11. N Reactor Graphite Stack Motion Indicated by the Pile-Motion Monitor System for CY 1986.

final shutdown. Other positions were reactivated in 1987, in anticipation of resumption of operation. Position 8 was found after April-May 1986 to be range limited when the reactor was fully thermally expanded and is correctable by mechanical adjustment of compression springs that maintain positive pressure forcing the pushrod against the graphite stack.

The lower plateaus in the traces in Figure 11 show the reactor stack in a shutdown or thermally contracted condition. When the reactor is operating, the stack thermally expands producing the upper plateau traces.

Each monitor location shows a different rate of upward motion with those near the center (positions 3, 5, 6, and 8) showing a much greater rate of expansion than the perimeter locations: 2 and 11. Fewer fuel tubes are under positions 2 and 11, which would account for some of the differential growth. Lower graphite temperatures would account for some more of the differential growth.

During analysis of growth rates, an unanticipated difference between growth rates during operation and shutdown appeared. During operation the upward expansion in the central core area is 0.59 in./yr (650 K/MMD yr) with a growth rate envelope for this area of 0.48 to 0.70 in./yr. Growth rates derived from shutdown measurements show a smaller growth factor of 0.47 in./yr with a 0.31-in. to 0.63-in. envelope. These rate differences remain unexplained; however, thermally activated graphite bar or tube bowing may contribute to stack height at operating temperature, but relax and are masked at shutdown temperatures.

### 3.0 VISUAL OBSERVATIONS

Visual examinations of conditions in the core have played a vital role in the interpretation of distortion-related phenomena and an equal role in devising corrective maintenance procedures when needed.

Events associated with early subsidence when upper layers became unkeyed and horizontal shifting was prevalent were followed with both borescopes and CCTV cameras. The illustration of an incident involving partial obstruction of a control rod (HCR 59, upper row center on right side) shown in Figure 12 resulted from information obtained from borescope surveys<sup>16</sup>. The corrective measure that has successfully eliminated the problem was to overbore the top row HCR channels, remove the T-bars, and insert liners to prevent further intrusion by surrounding blocks or fragments. These liners were not keyed into the core and recent CCTV surveillance<sup>17</sup> indicates they are still in good condition, remaining unbroken with separations 0.5 in. wide between liner ends.

After the value of visual inspections was established in HCR channel renovation work and similar activities involving the liners in the vertical Ball Safety Channels, CCTV traverses became an integral part of annually scheduled surveillance. The frequency of Ball Safety Channels inspections was about once every 2 yr. In 1987, 43 of the 108 channels were inspected including BC60, the test channel. Fringe channels are on a somewhat longer cycle.

Six of the 87 HCR channels were scheduled annually for routine inspection; however, should manual rod motion tests conducted during every startup procedure indicate resistance to rod motion, these channels were added to the inspection schedule.

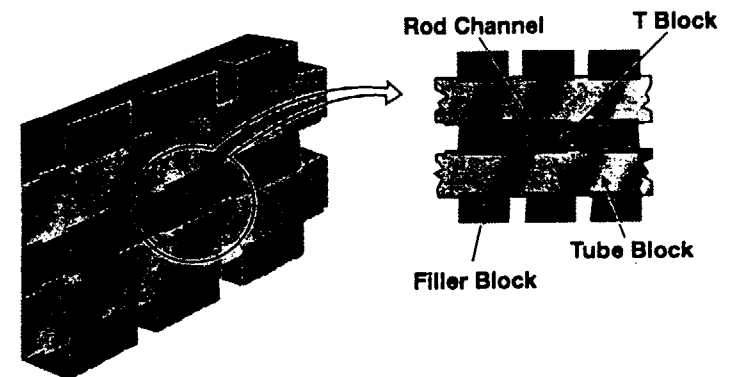


Figure 12. Rod Channel Partial Obstruction, December 1972.

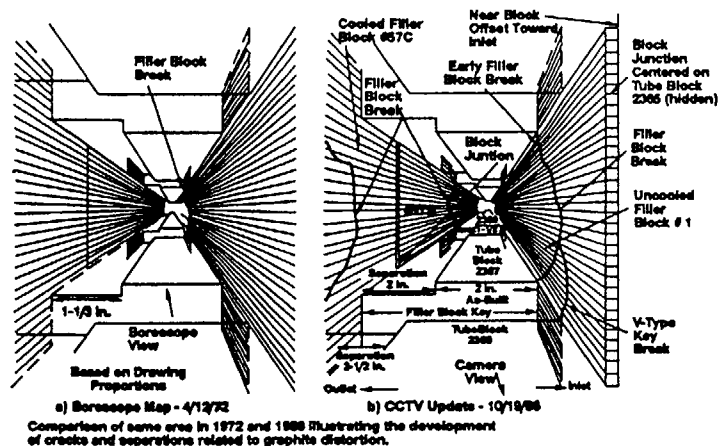


Figure 13. Comparison of Areas in Traverse Hole No. 4 Viewed in 1972 and 1986.

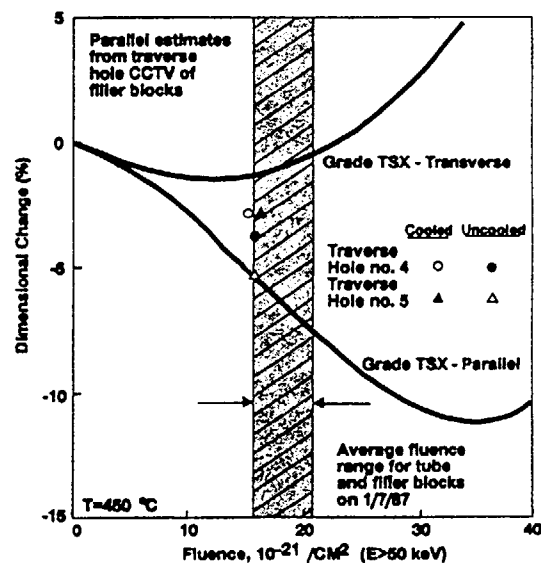


Figure 14. Comparison of Filler Block Contraction with Irradiation Tests and Visual Observations.

Inspections in the side-to-side Traverse Holes enabled the documentation of a history of distortion-related phenomena appearing in the filler blocks that parallel these channels and the tube blocks above and below. A view obtained with a boreoscope in Traverse Hole No. 4 in 1972 is compared with a CCTV view of the same area in 1986 in Figure 13. The filler blocks on the sides of these channels were both originally layed up immediately adjacent to the 1/4 in. keys on the tube blocks above and below. The left filler blocks were displaced on the order of 1.33 in. toward the reactor outlet side in 1972 and up to 2 in. in 1986, indicating much of the horizontal displacement occurred early. Traverse holes are in the central slip zone and displacements of the magnitude indicated here are not common away from the slip zone. Filler block breakage was beginning in 1972 and ultimately involved both cooled and uncooled filler blocks in 1986. Gaps between the ends of filler blocks developed and were used to estimate the filler-bar contraction across the fueled region, as shown on Figure 14.

#### 4.0 SUMMARY AND CONCLUSIONS

Observation of graphite distortion effects described in the paper illustrate how large and often unexpected consequences can be managed when sufficient information is available from surveillance. Some of the changes that have occurred within the stack suggest that a self-correcting redesign process has been operative and that this process arrested some distortion impacts. For example, the cross-bar breakage prevalent in filler blocks reduced the effective block lengths in the central core from the original 48 in. to an average between 8 and 9 in. or near the 8 in. horizontal lattice pitch. The breaks effectively interrupt the transmittal of the large parallel contraction isolating it into smaller units that can no longer generate the key overriding and shearing actions so common in the early operating years.

Another factor that has contributed to M Reactor's long life was the presence of high quality pressure tubes (no tube ruptures experienced) and cooling tubes. These not only sustained long-term functionality but provided a reinforcement structure not unlike rebar in concrete.

Recommendations based on M Reactor surveillance experience would include the following:

- Easily accessible flux dosimeters tailored to the energy spectra causing radiation effects in graphite. Access for measuring dimensions of in-reactor components should take precedence over removable dimension samples that will begin to lag behind total core fluences.
- Irradiation testing to full reactor life exposure preferably before design completion. Modern test reactors like the Hanford Site's Fast Flux Test Facility or the NFIR now make these studies feasible.

With modern dimensionally stable graphites and deference to the smaller block sizes that evolved in M Reactor's core over its 24-yr operating history, the M Reactor core design concept could have an even longer life expectancy today.

#### REFERENCES

1. R. E. Nightingale, ed., *Nuclear Graphite*, Academic Press, New York, 1962.
2. Staff, *Defense Reactor Operations Assessments and Engineering Analysis, M Reactor Core Component Surveillance Report for 1988*, UHC-SP-0229A, Westinghouse Hanford Company, Richland, Washington, February 1989.
3. P. A. Carlson, *M Plant Life Factors*, UNI-391, United Nuclear Industries, Inc., Richland, Washington, June 1975.
4. J. W. Helm, *The M-4, M-5 and M-6 Irradiation Experiments: Irradiation of M Reactor Graphite -- Interim Report No. 1*, HW-81250A, General Electric Company, Richland, Washington, October 1964.
5. J. W. Helm, *Irradiation of Graphite at Temperatures of 300 to 1200 °C*, BNWL1056 A & B, Battelle Northwest, Richland, Washington, June (1056A) and August (1056B), 1969.
6. W. K. Alexander, *Accelerated Irradiation Testing of M Reactor TSX Graphite*, UNI-1821, UNC Nuclear Industries, Richland, Washington, July 1, 1981.
7. C. R. Kennedy and E. M. Woodruff, *Irradiation Effects on the Physical Properties of Grade TSX Graphite*, UHC-EP-0211, Westinghouse Hanford Company, Richland, Washington, September 1989.
8. B. A. Ryan, *Monitoring Dimensional Changes of Graphite in Ball Channel 60 at M Reactor*, HW-84503, General Electric Company, Richland, Washington, December 1964.
9. W. K. Alexander, *M Reactor Graphite Distortion Measurements - Summer 1979*, UNI-1365, UNC Nuclear Industries, Richland, Washington, July 1979.
10. R. W. Carpenter, et al, *M Reactor Graphite Stack Surveillance Profile and Block Data Review through 1985*, UNI-3681, UNC Nuclear Industries, Richland, Washington, October 1986.

11. Bokros, J. C. and R. J. Price, 1967, "Dimensional Changes Induced in Pyrolytic Carbon by High-Temperature Fast Neutron Irradiation," Carbon, An International Journal, No. 5, p.301.
12. Technology Staff, N Plant Systems Surveillance Report for 1984, UNI-391-I, UMC Nuclear Industries, Richland, Washington, March 1985.
13. P. J. Lee, Test Report for Stack/Height Measurement Tools, UNI-4023, UMC Nuclear Industries, Richland, Washington, July 1986.
14. Defense Reactor Programs and Pressure Tube Analysis Staffs, N Reactor Core Component Surveillance Report for 1987, UMC-SP-0229, Westinghouse Hanford Company, Richland, Washington, March 1988.
15. F. R. Reich, N Reactor Growth as Indicated by the Pile Motion Monitor System, UNI-4351, UMC Nuclear Industries, Richland, Washington, May 1987.
16. J. P. Schmidt, Summary of Graphite Related Rod Insertion Incidents, UNI-600, United Nuclear Industries, Richland, Washington, June 1976.
17. E. M. Woodruff, Visual Inspection of N Reactor Horizontal Control Rod Channels, UMC-SP-0600, Rev. 1, Westinghouse Hanford Company, Richland, Washington, September 1990.
18. E. M. Woodruff, N Reactor Graphite Block Inspections, Television Camera Surveillance in Traverse Noles, UMC-SP-0450, Westinghouse Hanford Company, Richland, Washington, January 1989.

## DISCUSSION

### Questions or Comments

Name: B.T. Kelly

Did you make calculations of stresses in the bricks to compare with the Time at which brick failures occur.

### Answer:

My original response was no but on second thought I should think there is a possibility that a study by W.C. Margan done before or at the time of start-up (early '60s) probably includes the calculation. I will search for it and if I can locate it, have it changed for release, and send it to you.

### Questions or Comments

Name: Tim Burchell

Will the N reactor graphite core be dismantled during decommissioning?

### Answer:

No, stabilization in place is the proposed disposition.

### Questions or Comments

Name: M. Eto

Would you give us information on the procedure for descontamination and decommissioning? How will it be organized and who will take charge of it?

### Answer:

Decontamination will be concerned with ex-reactor systems,--sumps, pits, fuel basin and tanks that need to be stabilized for the long term.

Removal of deposits and transfer to on-site burial grounds will be the method. These activities will be performed by the operating personnel still assigned to N Reactor. No core internals will be removed since the shield and building will become the containment in the decommission date. There is an existing decommissioning organization who will inherit responsibility for the area along with the older reactors after external stabilization is complete. Spent fuel is now in storage at the KE+KW fuel basins where provisions for up to 20 storage are in progress. Final disposition by processing or burial has not been selected since fuel processing capabilities on-site are uncertain at this time. Both federal and state regulatory guidelines are being followed to achieve the condition acceptable the decommissioned unit.

# NON-DESTRUCTIVE TESTING AND ACCEPTANCE TEST FOR HTTR GRAPHITE COMPONENTS

N. TAKIKAWA, T. IYOKU,  
S. SHIOZAWA, N. OOKA  
Oarai Research Establishment,  
Japan Atomic Energy Research Institute,  
Oarai-machi, Ibaraki-ken

M. KAMBE, A. IDE  
Fuji Electric Company Ltd,  
Kawasaki

Japan

## Abstract

The HTTR core is an array of hexagonal graphite blocks. It is supported by graphite core support structures and permanent side reflector blocks. The structural integrity of these graphite components is assured by the detail mechanical design and the acceptance test to guarantee the design.

The acceptance test is planned for the graphite components as follows.

### 1) Material identification tests

To identify the graphite grade of received materials.

### 2) Impurity tests

To limit impurities to the level specified by the nuclear and shielding designs.

### 3) Strength tests.

To guarantee the strength of received materials.

### 4) Non-destructive tests

To eliminate components with harmful flaws in them.

Achieving the 4th objectives, ultrasonic and eddy current tests were selected for internal and surface flaw detection, respectively. Preliminary tests were carried out to obtain flaw detectability for the graphite grade used as a material of the HTTR components.

## 1. INTRODUCTION

The HTTR core is an array of hexagonal graphite blocks which provides the physical structure for arrangement and confinement of the fissile fuel materials, neutron moderation, heat transfer, and the positioning of control/shielding absorber materials. It is supported by the graphite core support structures and permanent side reflector blocks, and confined by the lateral restraint structure. The view of the HTTR core arrangement is shown in Fig.1.

The present study concerns only the graphite components given below:

### 1) Replaceable hexagonal graphite block

Fuel blocks, Control rod blocks, Top and bottom reflector blocks, hexagonal side reflector blocks

### 2) Permanent side reflector block

### 3) Core support structure

Hot plenum blocks, Core support posts, Core bottom structures.

The structural integrity of the graphite components installed within the reactor vessel are assured by the mechanical design. The nuclear, thermal-hydraulics and shielding performances are confirmed by their designs, respectively. The actual core characteristics and structural integrity are realized by the acceptance test to guarantee the designs.

The present study summarizes the acceptance test plan including non-destructive testing for the graphite components in the HTTR reactor vessel.

## 2. ACCEPTANCE TEST

The mechanical, nuclear, thermal-hydraulics and shielding designs are conducted by using the graphite design property data specified for the graphite grade. To guarantee these designs for an actual core, it is necessary to be confirmed by the acceptance test that the characteristics of a received material are the same as those specified in the designs.

The acceptance test is categorized by objectives into the following four items;

### 1) Material identification test to identify the graphite grade of a received material.

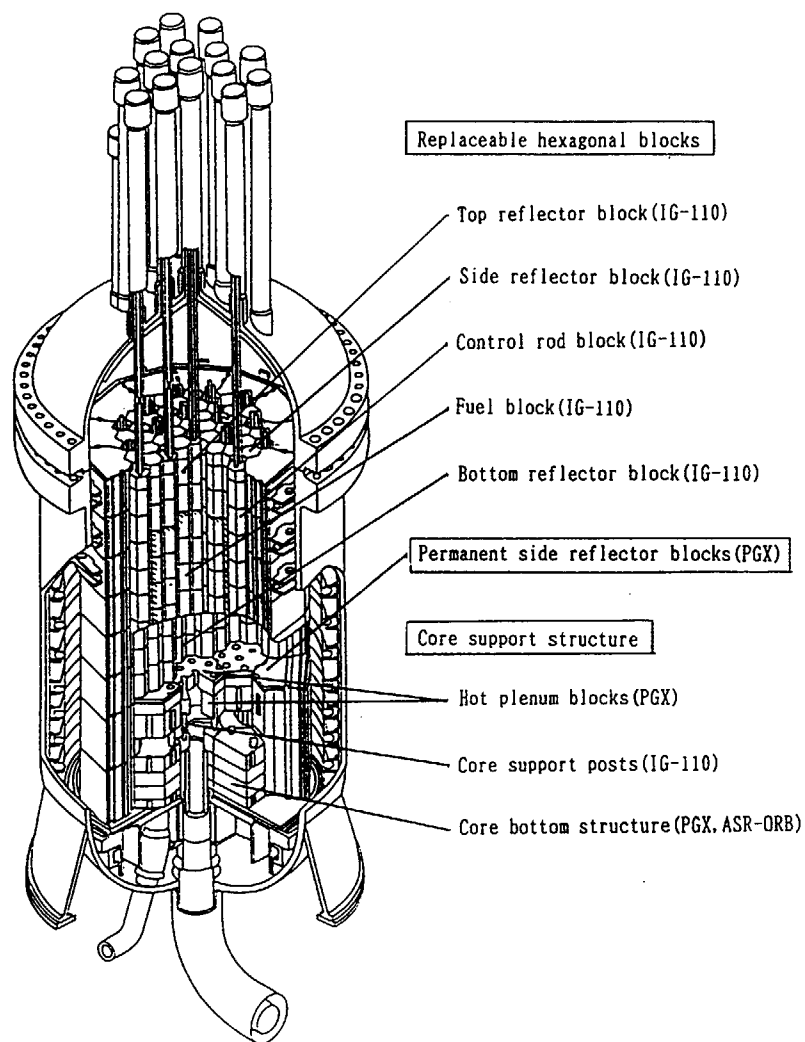


Fig.1 Arrangement of graphite and carbon components

- 2) Impurity test to limit received material impurities to the levels specified by the nuclear and shielding designs.
- 3) Strength test to guarantee the strength of a received material.
- 4) Non-destructive testing to eliminate components with harmful flaws in them.

The test items and details for the above-mentioned tests are shown in Table 1. Test plans for each manufacturing process are proposed as shown in Fig.2.

## 2.1 Material identification test

As for a graphite, material characteristics are depending on the type of raw materials and manufacturing process. The material identification test is conducted to confirm that fabrication and processing conditions of a received material shall be the same and in the same sequence as those used to manufacture production logs of the graphite grade that have been qualified by characterization and irradiation tests and found to have satisfactory properties and irradiation behavior.

The error or difference in manufacturing processes is thought to lead directly to the variation of bulk density, resistivity, coefficient of thermal expansion and anisotropy. Therefore, measurements of these properties are involved in the material identification test.

In the HTTR acceptance test, ash, bending strength and microphotograph are added to the test items because they are commonly measured in graphite manufacturers. The whole test items are listed in Table 1 and are conducted in accordance with the directions in the table. For raw materials, it is confirmed that the filler particles consist of the same generic type of a calcined coke and are the same size as production logs in the past.

Raw materials are inspected before kneading process and the other test items are measured for a graphite log as shown in Fig.2.

## 2.2 Impurity test

### (1) Boron equivalent

The nuclear characteristics of the reactor are affected by impurities with a large neutron absorption cross section in the core graphite blocks.

Table 1 Acceptance testing for graphite components

Item	Inspection plan	Sampling frequency	Rejection criteria proposed	
			IG-110	PGX
1. Material identification test (1) Row material	Inspection of a kind of coke and grain size by mill-sheet	One specimen for each graphitizing lot	as in the past	as in the past
(2) Bulk density	Determination from measurements of weight and dimensions at room temperature	One specimen for each graphitizing lot	a minimum of 1.74g/cm <sup>3</sup>	a minimum of 1.68g/cm <sup>3</sup>
(3) Specific electrical resistivity (SEI)	Measurement with voltage drop method at room temperature	One specimen for each graphitizing lot	a maximum of 1300 $\mu\Omega$ cm	a maximum of 1550 $\mu\Omega$ cm
(4) Coefficient of thermal expansion (CTE)	Measurement with vitreous silica dilatometer up to 400°C	One specimen for each graphitizing lot	within a range of 3.4~4.6 $\times 10^{-6}/^{\circ}\text{C}$	within a range of 1.8~3.4 $\times 10^{-6}/^{\circ}\text{C}$
(5) Ash	To determine by weighing the residue remaining after burning	two specimens for each graphitizing lot	a maximum of 100ppm (lot average)	a maximum of 7000ppm (lot average)
(6) Bending strength	Determination from three points bending test	one specimen for each graphite lot	a minimum of 320kg/cm <sup>2</sup>	a minimum of 70kg/cm <sup>2</sup>
(7) Microstructure	Observation of microphotograph	one specimen for each graphite lot	No significant difference comparing with standard specimen	No significant difference comparing with standard specimen
(8) Anisotropy	Ratio of $\alpha/L/\alpha_T$ $\alpha$ : CTE from room temp to 400°C SER L: Axial direction in blocks T: Radial direction in blocks	one specimen for each graphite lot	a maximum of 1.15	a maximum of 1.40
2. Impurity test (1) Boron equivalent	See Table 2.	One specimen for each lot	a maximum of 1 ppm of boron equivalent (lot average)	
(2) Radioactive impurity	See Table 3.	One specimen for each lot	a maximum of 45ppm for Si 20ppm for Fe 10ppm for Al 2ppm for N 8ppm for V 0.01ppm for Ca 0.01ppm for Li	a maximum of 380ppm for Si 370ppm for Fe 35ppm for Al 80ppm for N 130ppm for V 160ppm for Ca 0.05ppm for Li
3. Strength test (1) Tensile strength	Strength with 99%/95% is determined by uniaxial tensile tests and statistical procedure	four specimens for each lot	a minimum of S <sub>ut</sub> specified for each class in Table 4	Same as the left
(2) Compressive strength	Strength with 99%/95% is determined by uniaxial compressive tests and statistical procedure	four specimens for each lot	a minimum of S <sub>ut</sub> specified for each class in Table 4	Same as the left
4. Non-destructive testing	Ultrasonic test for detecting internal flaws in a as-graphitized lot Eddy current test for detecting surface flaws on a as-machined component	Whole number of the components possessing important safety function	a minimum S/N of 4 for UT 3 for ECT	a minimum S/N of 3 for ECT

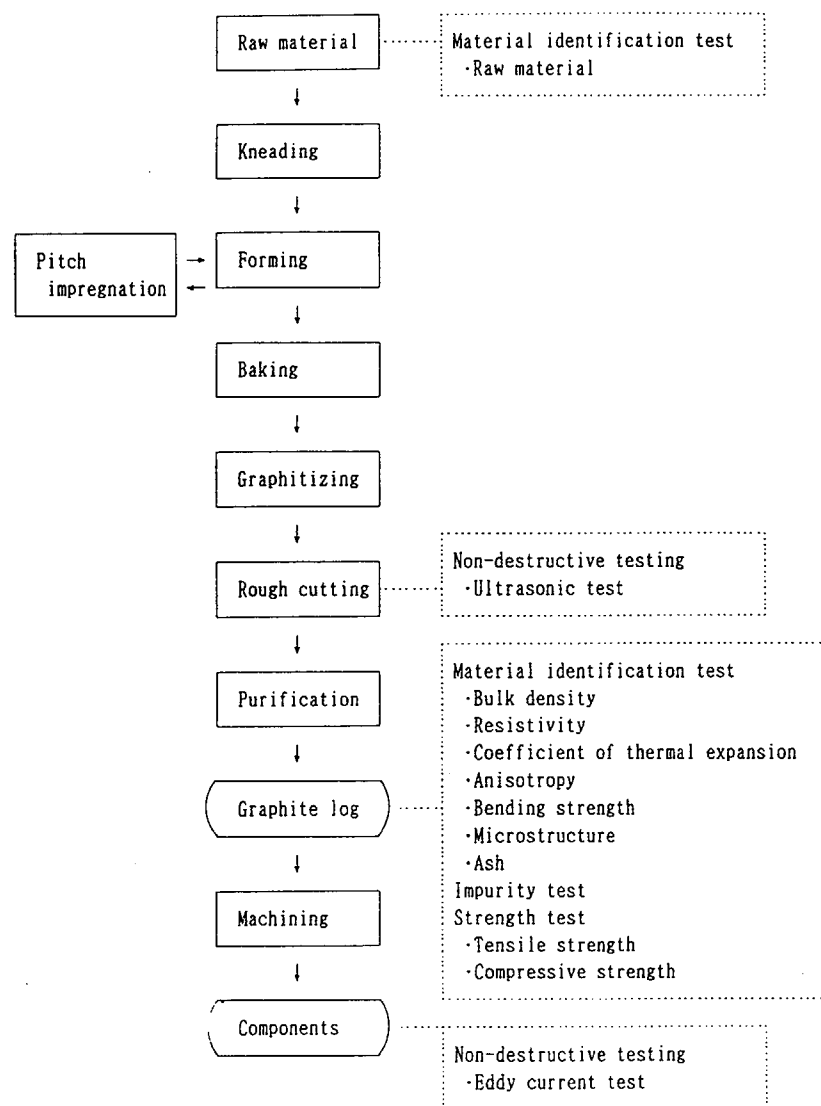


Fig.2 Manufacturing process and acceptance test

Table 2 Borron equivalent inspection

Element	Method	Conversion Ratio(a)	Rejection criteria
B	Absorption spectrophotometry	1.00	Summation of $a \times c \leq 1\text{ppm}$
Gd	ICP-AES*	1.57	
Sm	ICP-AES*	0.941	
Cd	ICP-AES*	0.855	

C = Concentration of each element

\* Inductively coupled plasma - atomic emission spectrometry

The concentrations of the impurities existing in the core blocks should be limited to the levels specified by the nuclear design. Therefore, the graphite grade IG-110 is purified for use as the core blocks.

The four elements listed in Table 2 shall be selected for the impurity test, because they have large cross sections and the large concentration records actually measured for each grade so far. The concentrations of these elements are measured for an as-graphitized log machined into the hexagonal blocks as shown in Fig. 2. The limit required by the HTTR nuclear design is 1 ppm of boron equivalent. Boron equivalent is calculated by the summation of concentration times conversion factor of each element, where conversion factors are defined below;

$$\text{Conversion factor} = \frac{\text{Neutron absorption cross section of an element}}{\text{Neutron absorption cross section of boron}}$$

## (2) Radioactive impurities

In the shielding design, the radioactivation of the impurities existing in the hexagonal graphite blocks and permanent side reflector blocks is taken into consideration. The radioactivation in the core support structures can be neglected, because it is located far from the fuel region.



Table 3 Radioactive impurity inspection

( ppm )

Element	Method	Rejection criteria	
		IG-110	PGX
Si	Absorption spectrophotometry	45	380
Fe	ICP-AES	20	370
Al	ICP-AES	10	35
Ni	ICP-AES	2	80
V	ICP-AES	2	130
Ca	ICP-AES	8	160
Li	ICP-AES	0.01	0.05

The seven elements listed in Table 3 are selected because they have large neutron absorptions, long half times of radioactive productions and also large actual concentrations. The concentrations of these elements shall be determined for an as-graphitized logs machined into the hexagonal blocks and permanent side reflector blocks. The summary of this test is described in Tables 1 and 2.

Boron equivalent and radioactive impurity concentrations are measured for an as-graphitized log. The sampling frequency of specimen is one per a log, but the measurements can be done for each graphitizing lot to obtain the average concentration of the lot. It has been confirmed by tests that there was no increase of the pollution during machining process following after measurements.

### 2.3 Strength test

The strength of a material is the most important property to guarantee the mechanical design. The reliability of the components depends directly on the strength. The most likely actual strength of a graphite component can not

be obtained without the following acceptance test including rejection, because the brittle nature provides the wide scattering of strength data. It leads to decrease of the component reliability.

The use of graphite as a structural material requires that the uncertainty in the strength should be minimized by ensuring that the actual material fabricated into the nuclear components has larger strength than the minimum ultimate strength  $S_u$  specified by the mechanical design.

The HTR graphite structural design criteria requires that the minimum ultimate strength  $S_u$  shall be specified such that there is a 99% probability with 95% confidence that the actual strength of the material is at, or above,  $S_u$ .

In order to ensure compliance with the 99/95 requirement, the statistical procedure is proposed, that is, only logs which satisfy the following criterion will be accepted:

$$\bar{X} \geq S_u + a \cdot \sigma_{WL} + \frac{b}{\sqrt{N}} \cdot \sigma_{WL}$$

where,

$\bar{X}$  = average strength of N replicate specimens from the weakest location in the log. The weakest location is determined by mapping of production logs. If it is not possible to take specimens from the weakest location, it will be permissible to take them elsewhere in the log and adjust their average strength on the basis of the mapping to represent the weakest location. For the grade IG-110, there is no significant distribution in the strength. So, it will be permissible to take specimens elsewhere without adjustment.

$S_u$  = specified minimum ultimate strength. This value is used in the mechanical design to satisfy the stress limits in the design criteria.

N = Number of replicate specimens, at least 4.

$\sigma_{WL}$  = Standard deviation of the within log strength at a given location, as determined by the production mapping.

a and b = Statistical coefficients corresponding to 99% probability and 95% confidence respectively. In the grade IG-110 and PGX graphites, a Gaussian distribution of the strength is a close approximation, in which the coefficients a and b are 2.236 and 1.645, respectively.

Table 4 Minimum ultimate strength

Strength class	IG-110		PGX	
	Sut	Suc	Sut	Suc
A	1 9 8	6 2 6	4 5	1 8 0
B	1 7 5	5 5 0	4 0	1 8 0
C	1 6 0	5 0 0	3 5	1 8 0

(kg/cm<sup>2</sup>)

Table 5 Non-destructive test plan

Component	UT	ECT	Portions to be inspected
Control rod block	○	○	Surface near to dowel system (Fig.3 (a) )
Hot plenum block	—	○	Surface near to key way (Fig.3 (b) )
Support post and post seat	○	○	Contact area between post and seat (Fig.3 (b) )

UT : Ultrasonic test

ECT : Eddy current test

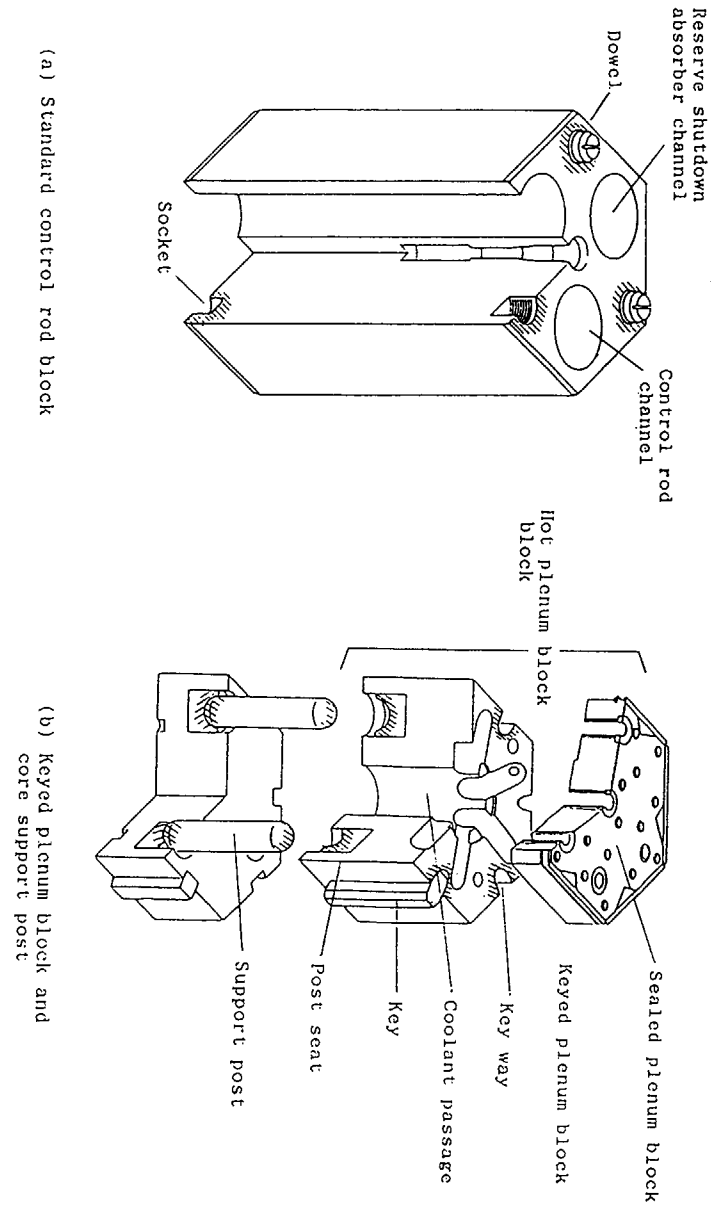


FIG. 3 Tested portions in eddy current test

Graphite logs which fail to satisfy the above criterion shall be rejected. In order to reduce the rejection rate, it is allowed to use the lower strength logs for the components where only low stresses are induced. In the HTTR, the multi-strength requirements are identified as classes A, B and C as shown in Table 4. The received logs are grouped into the each strength class. For each graphite log, the mean strength shall satisfy the above equation by substituting  $S_u$  described in the table.

#### 2.4 Non-destructive testing

To actually maintain the strength estimated by the mechanical design, a graphite block with harmful flaws in it shall be rejected by non-destructive testing.

Screening tests were conducted to select the non-destructive testing methods available for detecting internal flaws of a graphite body and surface flaws. In the tests, Ultrasonic test ( UT ), eddy current test ( ECT ), radiographic testing, X-ray computed radiography and acoustic impact technique were included. The test results showed that UT and ECT are the most available and practical for internal flaws and surface flaws, respectively, because of operationability and flaw detectability.

The non-destructive testing plan is summarized in Table 1. The tested components are selected by the reason that their failures may lead to the serious damage of safety and are listed in Table 5. ECT shall be inspected only for the portion of the components where high stresses are introduced, as shown in Fig. 3. UT is performed for an as-graphitized log, and ECT is done for an as-machined block.

#### 3. PRELIMINARY NON-DESTRUCTIVE TESTING

The preliminary non-destructive tests are conducted for the grade PGX used as the material of core support structures and permanent side reflector blocks and the grade IG-11. Here, IG-11 is substituted by IG-110 used as the material of hexagonal blocks, because it has the same characteristics as IG-110, except purity of it.

Table 6 Minimum detectable flaw size in ultrasonic test

( mm )

Grade	Method	Probe frequency	Inspected direction	Depth of*		
				200	400	600
IG-11	Single probe	0.5MHz	Axial Radial	2 - 4 2 - 4	2 - 5 2 - 5	2 - 5 -
				12 - 13 20 - 36	17 - 44 23 - 45	20 - 57 25 - 55
PGX	Single probe	0.2MHz	Axial Radial	12 - 13 20 - 36	17 - 44 23 - 45	20 - 57 25 - 55
	Double probe	0.2MHz	Axial Radial	12 - 24 12 - 27	18 - 41 18 - 38	23 - 55 20 - 43

\* Position of artificial flaw

Table 7 Minimum detectable flaw size in eddy current test

( mm )

Grade	Location of flaw	Flaw direction	Scanning angle*	Flaw depth	
				0.5	1.0
IG-11	Coolant channel	Axial	0°	2	2
			45°	-	2
		Tangential	0°	2	2
			45°	2	2
	Dowel socket	Axial	0°	x	1
		Tangential	0°	x	1
PGX	Support post end	Tangential	0°	1	1
			45°	2	1
	Key way	Tangential	0°	-	5
	Key way end	Axial Radial	0°	x	5
			45°	x	3

- Not detected

x Not prepared

\* Angle between slit flaw and scanning directions

### 3.1 Ultrasonic test

The testing conditions which was found to be suitable for IG-11 and PGX in the past tests are selected. Single probe reflection method with the probe of 0.5MHz and 34mm diameter is applied for IG-11. For PGX, both single probe reflection method and double probe reflection method with the probe of 0.2MHz and 28mm diameter are applied. Couplant is water. Both axial and radial testing for test blocks are conducted. Test blocks with artificial flaws are prepared, which are drilled such that the holes have flat bottoms and the effective distance of the sound axis are from 150mm to 550mm for IG-110 and from 130mm to 950mm for PGX.

The test results show that the minimum size of detectable circular flaw size is 2 to 5mm within 600mm depth for IG-110 and there is no difference between axial and radial directions. For PGX, the minimum detectable flaw size presents the wide scattering of 12 to 57mm for the depth. But, there is no difference of detectable flaw sizes between single and double probe reflection methods. The test results are shown in Table 6.

### 3.2 Eddy current testing

The self-induction type coil arrangement with 2 X 1mm ferite is used in this test. This is a differential type. Test frequency and lift-off are 1MHz and approximately 0.1mm, respectively. The probe is scanned at the speed of 100mm/s.

The tests are performed by using blocks which simulate the portion of the actual components and possess the artificial slit flaws on the surface of it.

Table 7 shows the test results. The detectable flaw size is 1 to 2mm for the grade IG-110, irrespective of the flaw direction, probe scanning angle and flaw depth. For the grade PGX, it is 3 to 5mm.

## 4. CONCLUSION

The above-mentioned acceptance test will be applied to the manufacturing processes of the HTTR graphite components. The reactor characteristics and structural integrity are actually ensured by the acceptance test as well as the nuclear, thermal-hydraulics and mechanical designs.

## DISCUSSION

### Questions or Comments

Name: T. Oku

What is the minimum size which should be detected for each component?

### Answer:

We don't have strict limitation for the maximum allowable flaw size. However, it is calculated to be the order of several millimeters and several tens millimeters for the components made of IG-110 and the components made of PGX, respectively, according to fracture mechanics approach. These values seem to be almost same or larger than the expected detectable flaw size.

### Questions or Comments

Name: David Burridge

Why do you not include cobalt in your radioactivity impurity inspection?

What are the typical levels of cobalt in the graphite?

### Answer:

Only minimal compulsory inspection items necessary for the governmental acceptance test are selected in our inspection criteria. Cobalt impurity in IG-110 graphite is generally hard to be measured due to its low concentration of the order of 0.01 ppm or less.

Cobalt concentration can be presumable from the iron concentration which is included in our inspection criteria. We think that the measurement of cobalt concentration shall be done, when we observe abnormally high concentration of iron in the acceptance test.

**NON-DESTRUCTIVE EXAMINATION, INSPECTIONS  
AND SURVEILLANCE**  
**Part B**

**(Session IV)**

**Chairmen**

**E.M. WOODRUFF**  
United States of America

**S. ISHIYAMA**  
Japan



# NON-DESTRUCTIVE TEST OF HTGR GRAPHITE COMPONENTS

M. ISHIHARA, T. ISHII, S. ISHIYAMA, M. ETO  
Department of High Temperature Engineering,  
Tokai Research Establishment,  
Japan Atomic Energy Research Institute,  
Tokai-mura, Naka-gun, Ibaraki-ken,  
Japan

## Abstract

Prototype NDT model units for HTTR graphite components was constructed and optimizing regulation tests of eddy-current Nondestructive Test(NDT) units and NDT for drill hole on the surface of plates made of IG-110 and PGX graphites were carried out. From those test results, the following conclusions were derived:

- (1)Recommendable probe-testing material distance(lift-off) and scanning speed for the evaluation of diameter of drill hole on the surface of graphite plates are within 0.1mm to 0.3mm and 25mm/s to 30mm/s, respectively, however, for the evaluation of depth of drill hole, more than 30mm/s scanning speed should be chosen.
- (2)Measurable minimum diameter and maximum depth of drill hole measured by C-scan technique were 2mm and 3mm on the surface of IG-110 and PGX graphite plates.

KEY WORDS HTGR, Graphite, NDT, Eddy current, C-scan, Lift off, Scanning speed.

## 1. INTRODUCTION

Japan Atomic Energy Research Institute(JAERI) has a plan of construction of a High Temperature Gas Cooled Reactor, The High Temperature Engineering Test Reactor(HTTR), which will be critical in 1996. The core of the HTTR is mainly consisted of graphite components and those components will be loaded by thermal stress, irradiation induced stress and cyclic stress due to irradiation and earthquakes during reactor operations.

Graphite is very brittle material and very sensitive to defects, so that requirements for the high quality of industrial graphite productions are more and more demanded recently, and especially for the use of nuclear grade graphite those requirement is very severe(1)(see Fig.1).

Thanks to the introduction of modern digital signal processing methods, the quality of detection of events in the NDT signal may be appreciably improved and for many years the reliability of defects detection of NDT has been increased and allows consideration of automatic

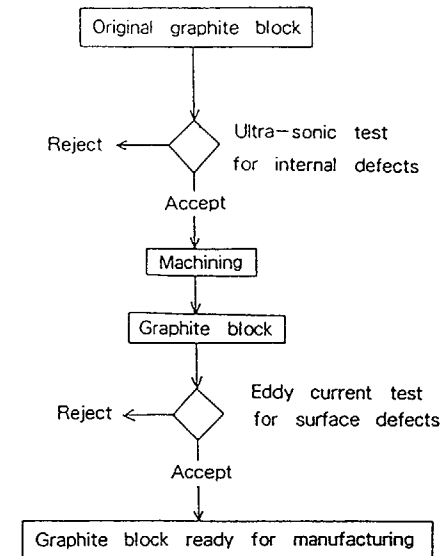


Figure 1 The concept of acceptance test for HTTR graphite.

testing in recent industrial use. With help of recent modification of NDT methods and machines, the role of non-destructive testing of graphite components for HTTR has become more significant and improvement of testing method and fundamental acknowledgement including theory, instrumentation, data analysis and applications has been required.

However, reports of non-destructive tests of graphite materials is very limited and optimization of testing method and conditions has not been discussed in detail.

This paper mainly presents fundamental test results of eddy-current NDT applied for evaluation of drill hole on nuclear graphite plates and discussed its applicability and optimization regulations of those technique for HTTR graphite components.

## 2. EXPERIMENTAL

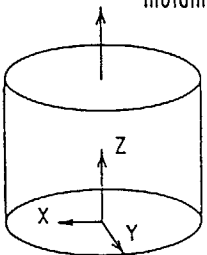
### 2.1 Materials and specimen

Two brands of graphites, fine-grained isotropic graphite, IG-110 manufactured by Toyo Tanso company and coarse-grained near isotropic graphite, PGX manufactured by UCAR were used in the present tests. Typical mechanical properties of both graphites were listed in table 1.

Table 1 Typical properties of IG-110 and PGX graphites.

	Bulk density (g/cm <sup>3</sup> )	Tensile strength (MPa)	Compressive strength (MPa)	Bending strength (MPa)	Young's modulus (GPa)
IG-11	1.78	25.3	76.8	37.2	10.2
PGX (X)	1.73	7.3	33.6	14.9	6.6
(Z)		7.3	30.4	15.6	8.2

Extruding or  
molding axis

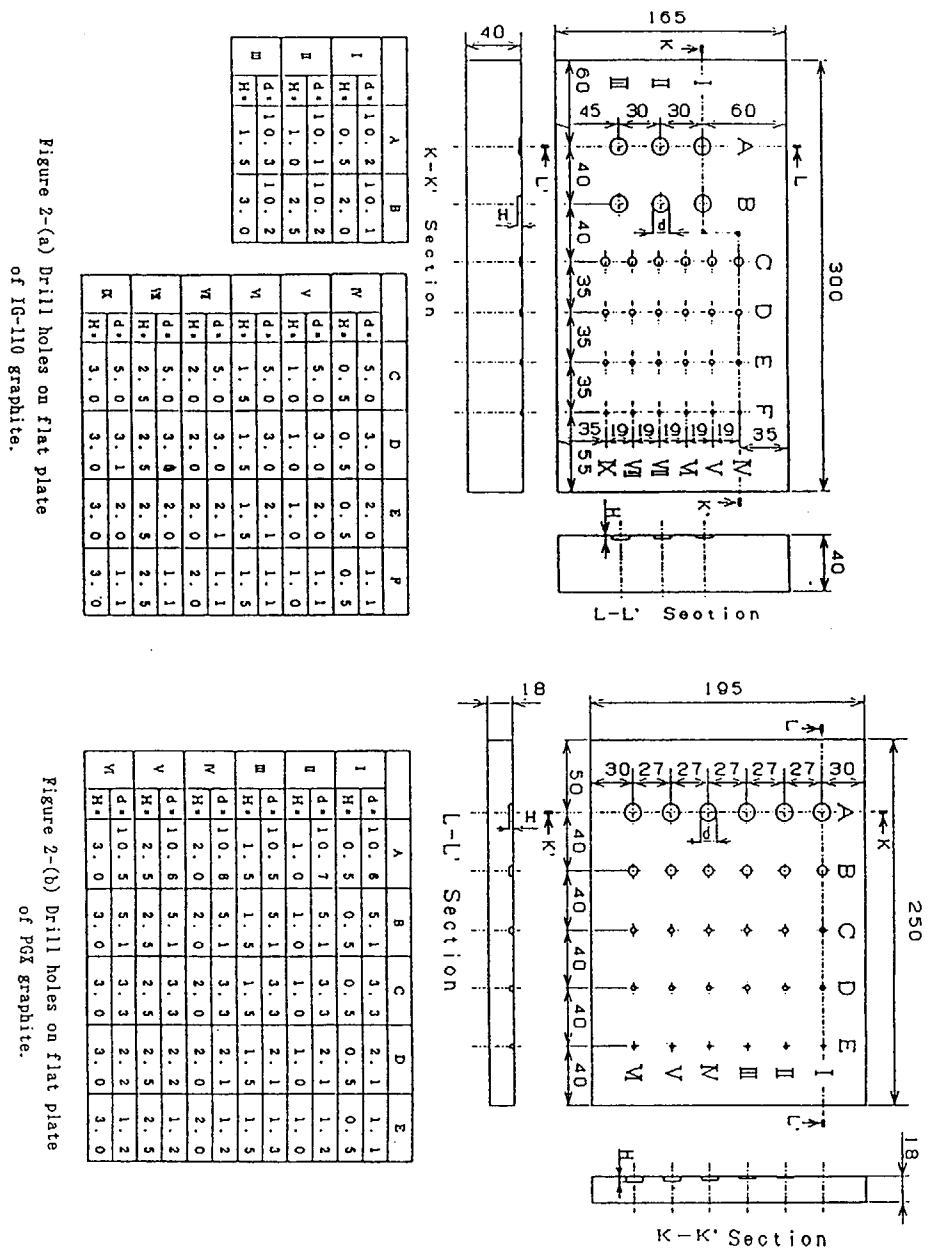


Flat plates made of IG-110 graphite, 165mm x 300mm in width and length and 40mm in thickness and of PGX graphite, 195mm x 250mm in width and length and 18mm in thickness were prepared for eddy-current test. Surface of those plates were polished by sand paper of #1000 and machined to make drill hole of 1mm to 10mm in diameter and 0.5mm to 3mm in depth. Figure 2(a) and (b) show drill holes machined on the surface of flat plates.

## 2.2 Apparatus and test conditions

A complete diagram of the eddy-current test installation and measurement systems of prototype NDT model are shown in Fig. 3 and 4.

The eddy-current probe is mutual induction type differential pencil probe model 12.832.01-2500(10g in weight, 5mm in diameter of active surface, 125mm in length) made by Krautkramer Branson company. Two micro-coils are mounted in the probe and primary current and frequency range of those coils are max.80mA and 0.1 to 10MHz, respectively. The defect-response signal including information of defect-response angle, magnitude and depth was detected by defectscope AF2.833.01(maximum gain: 100dB, frequency range: 100Hz to 10MHz),





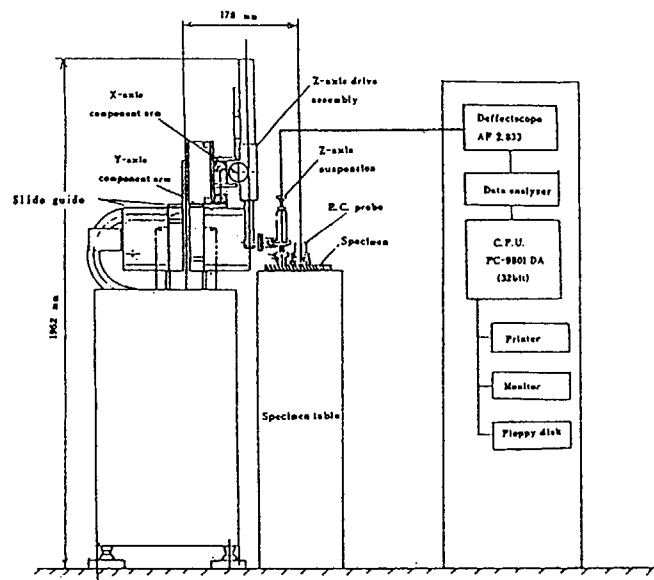


Figure 3 Prototype eddy-current measuring system for HTTR graphite components.

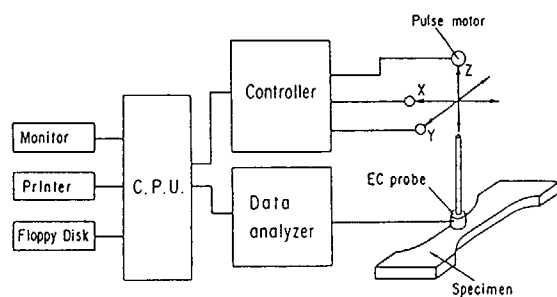


Figure 4 A conceptual diagram of prototype eddy-current test installation.

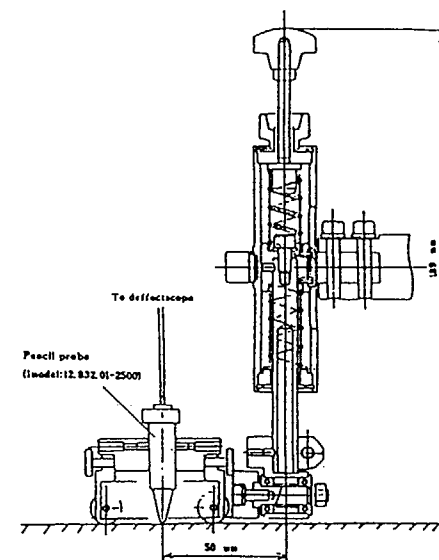


Figure 5 Mechanism of second device for eddy-current probe.

IG-110 10.2mm in diameter 2mm in depth

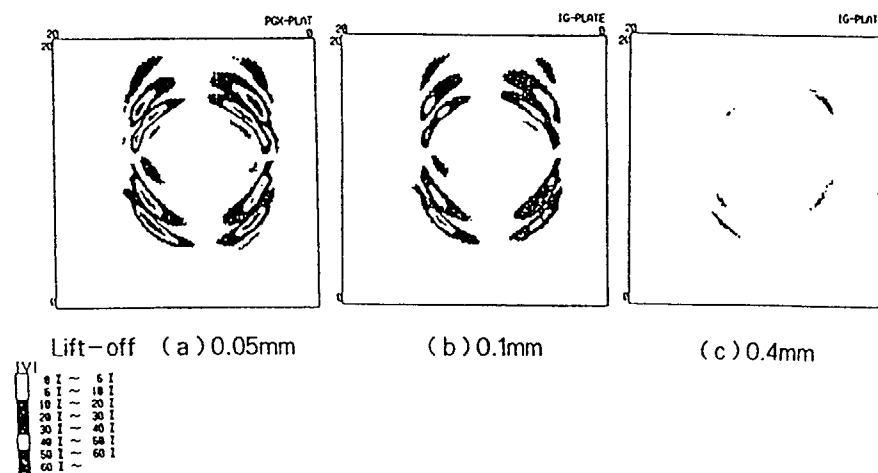


Figure 6-(a),(b),(c) C-scan defect images of a drill hole which was measured with lift-off distances of 0.05mm, 0.1mm, 0.4mm.

made by Krautkramer Branson company and probe-impedance data were gathered to the computer and calculated the type and depth of the defect. Finally, defects are describes by their magnitude and calculated depth and displayed graphically by colors(red, green, blue and et.) used to display the calculated depth of the defect, and shading used to show relative magnitude of the defect response within each color. In the present test, gain level, phase of defectscope were chosen as 71.5dB and 90 ° and high pass and low pass filter were set at 10Hz and 100Hz, respectively.

A sensor carriage pulled by a step motor and guided by three rails has a travel of 300mm x 300mm x 250mm in X, Y and Z directions along sample plate and drives at maximum speed of 100mm/s. Moreover, the probe carriage has two devices allowing precise regulation of the position of the probe with respect to graphite plates. The first device shown in Fig. 3 is slide gauge which allows the drive to X, Y and Z directions and the second device is a screw-bolt system ensuring adjustment of the vertical probe-graphite plate distance(lift-off). The mechanism of the second device is shown in Fig. 5.

Information on the intermediate positions of the carriage is given by a pulse generator. This is mounted on the transmission system of the probe carriage and delivers pulses about every tenth of a millimeter during longitudinal movement of the probe. The data acquisition system links the signals of the installation and those of the computer and to this effect includes analogue and digital input-output modules. Acquisition of the (X,Y,Z) signals coming from the electronics unit is done in an asynchronous manner using a 32 bit analogue-digital converter with multiplexed inputs and with sampling command by pulse generator pulses. The output data from the analogue-digital converter are bussed to the memory of the personal computer. The allows storing, processing and visualization of the data either on its own screen or on a high resolution color graphics printer.

### 2.3 Data analysis

In the present experiments, C-scan data display is available to identify detect size on the surface of graphite plates. This image is generated by painting each point of searching plane using the color(res, green, blue and et.) depending on response signal magnitude for the defect depth.

Real-time C-scan presentation is also available to finding defects in present experiment. The real-time display shows defect-response vectors on the normalized impedance plane, optionally displays the numerical defect-response magnitudes and angles, and will interpret the data for the operator to differentiate between defects and other material characteristics.

## 3. RESULTS AND DISCUSSION

### 3.1 Optimizing regulation of probe lift-off for detection of defects on graphite plates

To optimize probe lift-off in the present experiments, drill holes, 10mm in diameter and 2mm in depth were made on the surface of IG-110 and PGX graphite plates and scanned with changing lift-off from 0.05mm to 0.5mm.

Figure 6(a), (b) and (c) show C-scan defect images of drill hole, 10mm in diameter and 2mm in depth on the surface of plate of IG-110 graphite, where C-scan test were performed at lift-off of

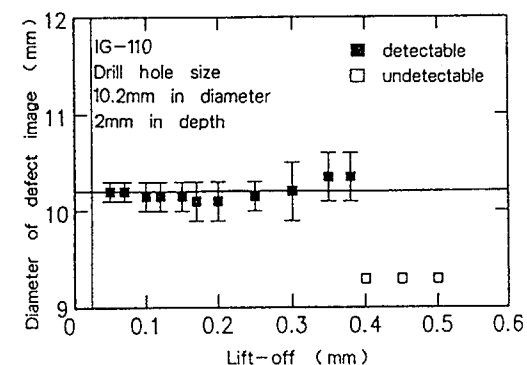


Figure 7 The relationship between diameter of defect image and drill hole made on IG-110 graphite plate as a function of lift-off distance.

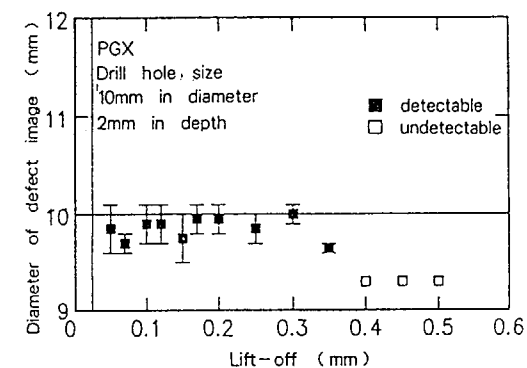
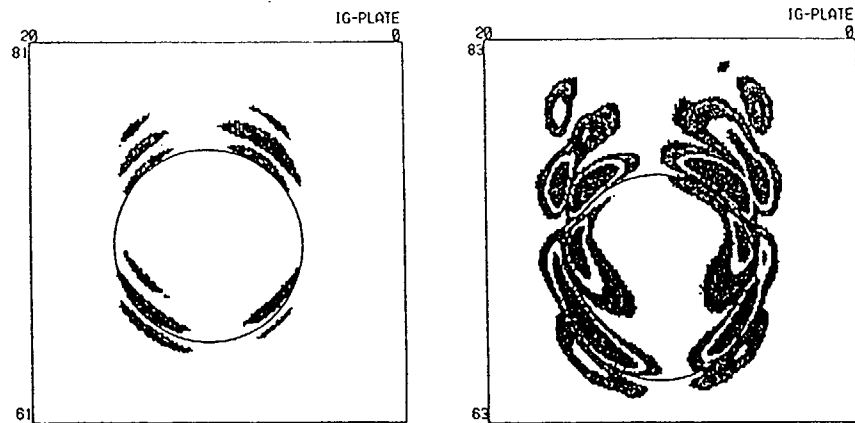


Figure 8 The relationship between diameter of defect image and drill hole made on PGX graphite plate as a function of lift-off distance.



(a) 30 mm/s

(b) 100 mm/s

Figure 9-(a),(b) C-scan defect images of a drill hole measured at scanning speeds of 30mm/s and 100mm/s.

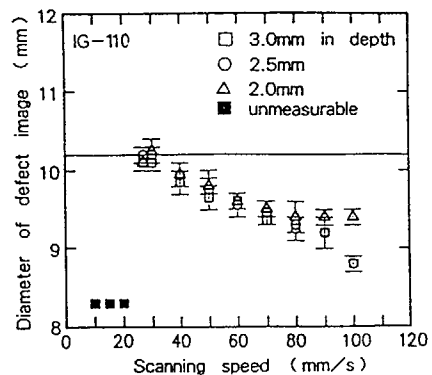


Figure 10 Diameter of defect images of drill holes made on IG-110 graphite plate as a function of scanning speed.

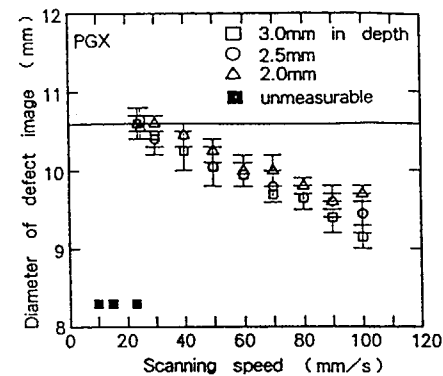
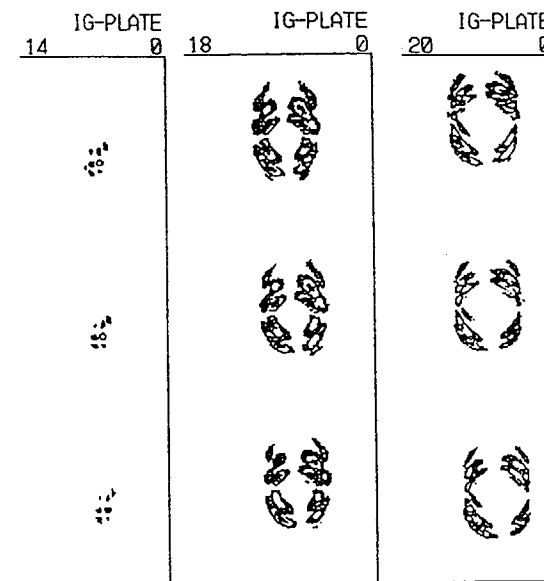


Figure 11 Diameter of defect images of drill holes made on PGX graphite plate as a function of scanning speed.



Drill hole diameter

(a) 1mm

(b) 5mm

(c) 10mm

Figure 12-(a),(b),(c) Typical C-scan images of drill holes with diameters of 1mm, 5mm and 10mm.

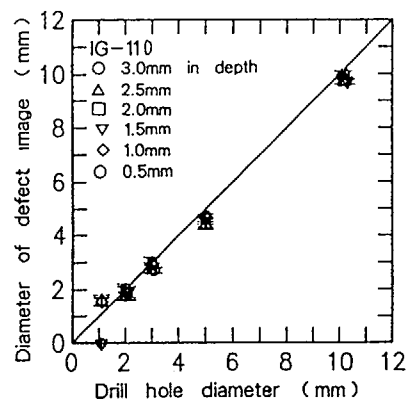


Figure 13 The relationship between diameter of defect image and that of drill holes where the depths varied from 0.5mm to 3.0mm.

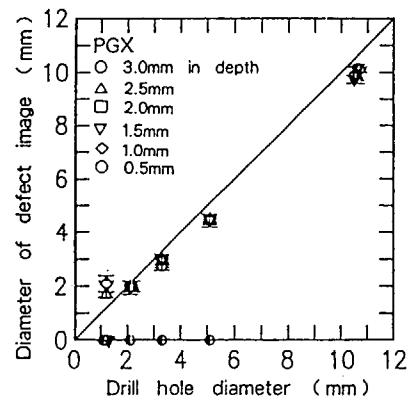


Figure 14 The relationship between diameter of defect image and that of drill holes where the depths varied from 0.5mm to 3.0mm.

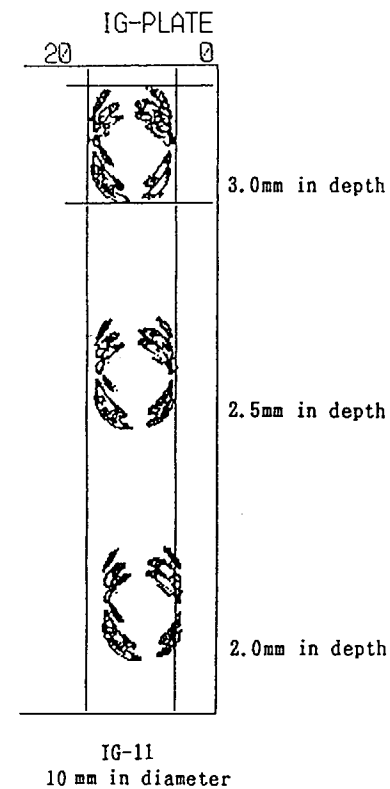


Figure 15 Typical C-scan defect image and the area surrounded by cursors, in which the occupation of colored areas are calculated.

0.05mm, 0.1 and 0.4mm. Imaging shades No. 1 and No.2 in this figure correspond to the change of impedance detected by di-pole coils No.1 and No.2 mounted in the probe, so that diameter of the imaging defect were determined by measuring inscribed circles diameter of the edges distance from the beginning to the end of shade No.2.

Figure 7 and 8 show the diameter of C-scan defect image of drill holes made on the surface of IG-110 and PGX graphites as a function of lift-off. Those results shows that the diameters of defect images on IG-110 and PGX plates measured at lift-off of 0.05mm to 0.4mm and 0.05 to 0.3mm

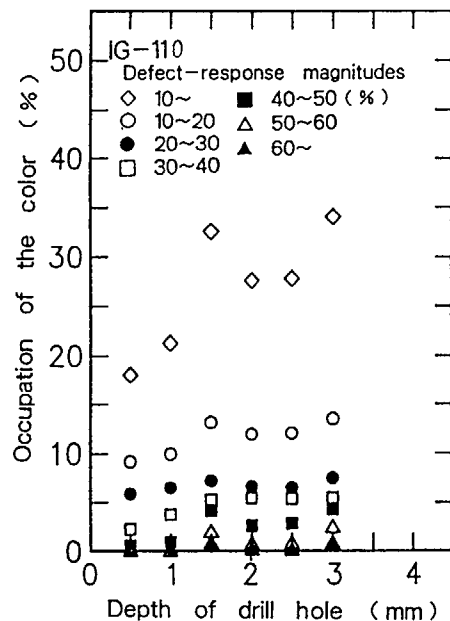


Figure 16 The occupation of colored area in C-scan defect image as a function of depth of drill holes

were well correspondent to that of drill hole, however the diameter can not be measured at lift-off over 0.4 for IG-110 and 0.3mm for PGX graphite, respectively.

Since standard roughness of surface of HTTR graphite components shown as solid line in the figure is about 0.025mm, available distance between the probe to the surface of graphite component should be required to avoid collision of the probe with the surface during NDT test. From the point of practical use, desirable regulation of lift-off should be between 0.1 to 0.3mm.

### 3.2 Optimizing regulation of scanning speed for eddy-current test

Reduction of operation time for NDT is very important problem for practical use, so that optimizing regulation of maximum scanning speed for eddy-current test was discussed here.

Figure 9(a) and (b) show typical C-scan defect image tested at scanning speed of 30mm/s and 100mm/s, where inscribed circle using for measurement of diameter of defect images is written as solid circles.

Figure 10 and 11 show the diameters of C-scan defect image of drill holes, 10.0mm in diameter and 2mm to 3mm in depth, made on the surface of IG-110 and PGX graphite plates as a function of scanning speed. Those results show that measurement of the diameter of defect image is impossible at the scanning speed less than 30mm/s, whereas the diameters measured at scanning speed over 30mm/s decreased with increasing of drill hole diameters. From those results, it can be recommended that optimizing regulation of scanning speed for measurement of diameter of drill holes should be chosen within the range from 25mm/s to 30mm/s for both graphite plates.

### 3.3 Inspection of defect size on the surface of graphite plates

Considering the above-mentioned test results, subsequent eddy-current tests to inspect defect size on the surface of graphite plates were carried out in the conditions in which lift-off and scanning speed were 0.1mm and 50mm/s, respectively.

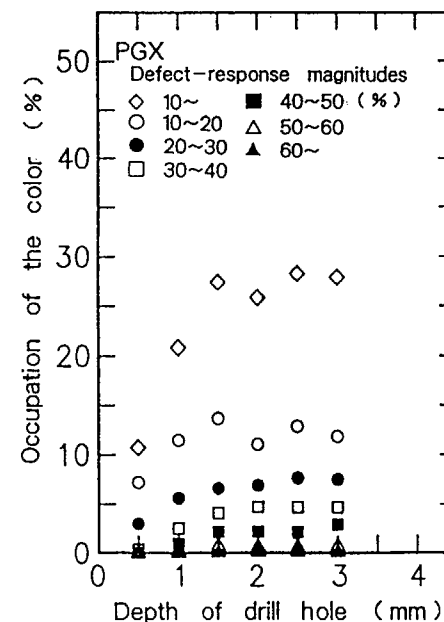


Figure 17 The occupation of colored area in C-scan defect image as a function of depth of drill holes

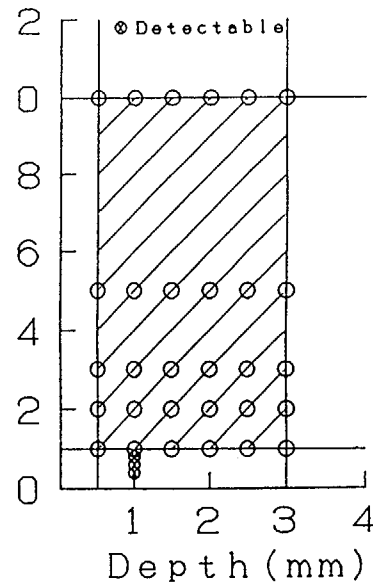


Figure 18 Detectable limitations of eddy-current NDT tests performed in the present test conditions.

Figure 12(a), (b) and (c) show typical C-scan image of drill hole, 1mm, 5mm and 10mm in diameter and those diameter of defect images on IG-110 and PGX plates were measured and shown in Fig. 13 and 14 as a function of drill hole diameter, where the depth of drill hole were changed from 0.5mm to 3mm. Those results show that good correlations between image diameter from 10mm to 2mm and that of drill holes on the surface of both graphite plate were given even if the depth of hole was changed, whereas the diameter of drill holes, 1mm in diameter and less than 1.5mm in depth on the surface of IG-110 plate and 3.0mm, 2.0mm, 1.5mm and 0.5mm in depth on the surface PGX plate can not be measurable in the present test conditions.

Figure 15 shows typical C-scan image of drill hole, 10mm in diameter and 3mm in depth and occupation rate of colored image shades (red, yellow, pink, blue and et.) in the area surrounded by 4 cursors were calculated, where NDT was carried out at scanning speed of 50mm/s for lack of colored image shades (see Fig. 9(a) and (b)). Figures 16 and 17 show the occupation rate of colored image shades as a function of depth of drill hole. Those results show that the

occupation of colored area increases as depth of hole become deep, and drill hole in depth of 0.5mm to 3.0mm can be detectable by this experimental test conditions.

Figure 18 shows the test results and detectable limitation of defect in the present test conditions. It is clear from those results that minimum diameter of 2.0mm and maximum depth of 3.0mm of drill hole can be detectable in the present test conditions.

#### 4. CONCLUSION

To inspect the availability of eddy-current NDT technique for HTTR graphite components, eddy-current test units were constructed and optimizing regulation tests of those units and C-scan imaging test for the drill hole on the surface of IG-110 and PGX graphite plates were carried out and the following conclusions were derived:

- (1) Optimizing regulation of probe lift-off is recommended within 0.1mm to 0.3mm for the evaluation of the diameter of drill holes on the surface of graphite plates.
- (2) Recommendable scanning speed for the evaluation of diameter of drill hole on graphite plates was within 25mm/s and 30mm/s, however, more than 30mm/s scanning speed should be chosen for the evaluation of depth of drill hole.
- (3) Measurable minimum diameter and maximum depth of drill hole in this experimental test conditions were 2.0mm and 3mm, respectively.

#### REFERENCE

- (1) J. Toyota, T. Ikoku, M. Ishihara and et. al. : JAERI-M91-1024(1991).

# THE CORRELATION OF HARDNESS WITH YOUNG'S MODULUS AND STRENGTHS OF NUCLEAR CARBON MATERIALS

T. OKU, S. OHTA

Department of Mechanical Engineering,  
Ibaraki University,  
Hitachi-shi, Ibaraki-ken

M. ETO

Tokai Research Establishment,  
Japan Atomic Energy Research Institute,  
Tokai-mura, Naka-gun, Ibaraki-ken,  
Japan

## Abstract

Since mechanical properties of carbon materials are, in general, necessary and important for the structural design of the components of HTGRs, lots of data on each candidate material have been obtained so far. A correlation between the Vickers hardness and strengths of different grades of graphite has been examined and as a result a good correlation with compressive strength was found. According to recent results of the instrumented hardness test that enables to measure the load and the depth continuously, some parameters obtained from the load versus depth relation had good correlations with the Young's modulus and strengths. Also, correlations of the hardness value with Young's modulus, bending strength and compressive strength were examined on the different kinds of carbon materials including the nuclear grades of graphite. As a result, the hardness values defined in the instrumented microhardness test, as well as the normal Vickers hardness value, had comparatively good correlations with Young's modulus, bending strength and compressive strength.

## 1. INTRODUCTION

The mechanical properties of nuclear carbon and graphites are important for the core structural design and safety evaluation of nuclear reactors. Different kinds of attempt for evaluating mechanical properties of carbon materials by means of nondestructive approaches have been done so far. One of the typical approach will be one by using an ultrasonic wave detector which makes possible the prediction of Young's modulus and strengths of nuclear graphite. The hardness

test is a kind of nondestructive one and it is well known that there is a good correlation between the Vickers hardness and the strengths for metallic materials<sup>1)</sup> and nuclear graphites<sup>2)</sup>. Recently an ultra-microhardness tester that enables to measure the load and the indented depth continuously, in the case of the load around 1 gf, has been fabricated and applied to the metallic and carbon materials.

It is considered that for the carbon materials the ultra-microhardness test will not be influenced by the microstructure of pores, as compared to the normal Vickers hardness test using over 1 kgf considering the size of indentation. In the case of carbon materials, it is usually difficult to define the Vickers hardness value that is based on the indentation. Therefore, in the case of the ultra-microhardness test, it is probable that correlations between mechanical property parameters or hardness values defined by using the load versus depth curve are not always the same as ones obtained by normal hardness tester.

The purpose of this study is to examine correlations between macrohardness values by the normal hardness tester and modulus/strengths and between mechanical property parameters or hardness values defined by the load-depth curve by the ultra-microhardness tester and modulus/strengths.

## 2. EXPERIMENTAL

Tested materials were fifteen grades of nuclear graphite, a carbon/carbon composite and a pyrolytic graphite. Table 1 shows the typical properties of the tested materials. In the macrohardness tests(>1 kgf) specimen size were 15x10x5mm. As to the ultra-microhardness test(<30 gf) 10x10x5mm specimens were used. The size of the specimen for Young's modulus and bending tests were 5mm dia.x50mm long or 5x5x50 mm. The compressive specimen measured 6mm dia.x12mm.

The macrohardness test(>1 kgf) was conducted using the Vickers hardness tester by Akashi Co. The hardness value for the indentation size  $d$  and load  $L$  was defined by the equation,

$$H_v = 1.854L/d^2 \quad (1)$$

,with the diamond pyramid indenter of an angle of 136 degrees between opposite faces. On the other hand, the ultra-microhardness test was done using DUH-50 by Shimadzu Co. with the trigonal pyramid indenter whose angle between edges was 115 degrees, at a loading speed of  $2.6 \times 10^{-3}$  gf/s and with the holding time of one second. The hardness value for the depth  $h$  was defined by the equation,

$$H = 37.838L/h^2. \quad (2)$$

TABLE 1. TYPICAL PROPERTIES OF TESTED CARBON MATERIALS

No.	Material	Apparent Density kg/m <sup>3</sup>	Youngs Modulus GPa	Bending Strength MPa
1	IG-11	1760	9.8	34.7
2	EPT-10	1750	10.8	58.8
3	HCB-18S	1980	15.4	88.2
4	ISO-88	1900	12.7	93.1
5	ISEM-3	1850	11.8	49.0
6	IG-56	1770	10.3	43.1
7	IG-43	1820	10.8	53.9
8	SIC-6	1850	11.8	49.0
9	CC-312(A) (C)	1770 ~1810	40.3 5.1	78.0 19.0
10	PyG (A) (C)	2229	59.3 28.3	112.0 4.4
11	IM-2 (A) (R)	1780	12.0 11.9	33.6 34.4
12	H-327 (A) (R)	1780	14.8 7.0	25.5 14.6
13	IE1-24(A) (R)	1800	13.9 11.6	34.3 -
14	SE2-24(A) (R)	1720	11.4 8.8	30.3 18.7
15	G163AS(A) (R)	1770	12.9 11.7	22.0 23.3
16	7477 (A) (R)	1760	11.4 11.4	32.7 33.9
17	SMG (A) (R)	1760	10.6 8.3	21.4 20.7

\*:Catalogue data., No.1,4,5,6,7,8:Toyo Tanso Co.  
 No.2:ibiden Co., No.3:Hitachi Chemical Co.  
 No.9,17:Showa Denko Co., No.12:Great Lakes Carbon Corp.  
 No.11,13,14:Anglo Great Lakes Corp.  
 No.15:Tokai Carbon Co., No16:Le Carbone Lorraine Co.

## 3. RESULTS AND DISCUSSION

## 3.1 LOAD DEPENDENCE OF HARDNESS VALUE

It is generally known that hardness values of carbon materials depend on the load level as well as metallic materials. Fig.1 shows the load dependence of the Vickers hardness values for seven grades of nuclear graphite in the range from 1 kgf to 10 kgf. The load dependence for four grades of graphite was not seen except for IM-2, IM2-24 and IE1-24 graphites which are the gilsonite coke ones containing larger pores(10 ~ 100  $\mu$ m). The pore size for these graphites is larger as compared with the indentation size. Other graphites, however, have relatively

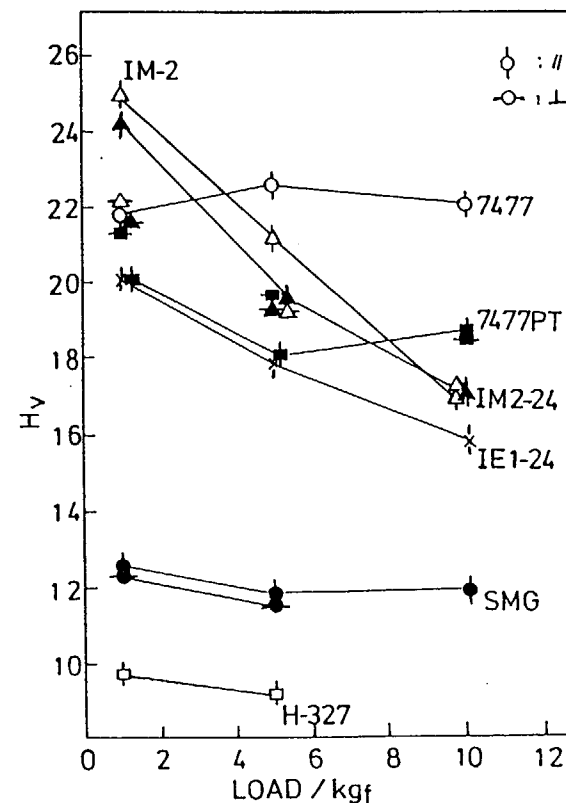


Fig.1 Vickers hardness values of seven grades of nuclear graphite as a function of the maximum load (1 kgf - 10 kgf).



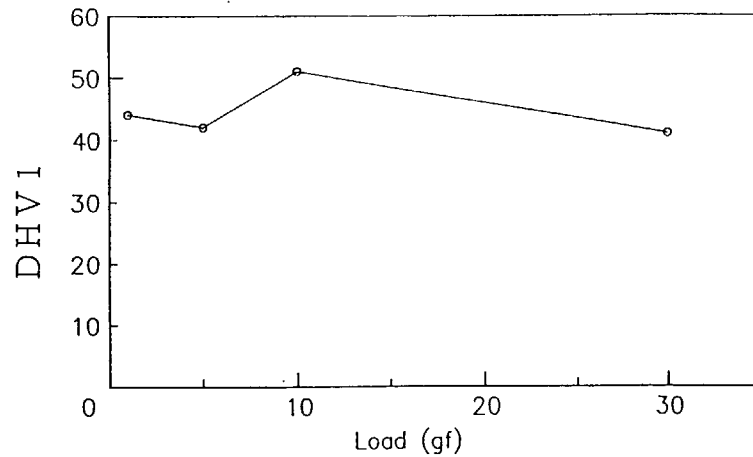


Fig.2 The DHV1 hardness values of ISO-88 graphite as a function of the maximum load (1 gf - 30gf).

fine grains and many pores less than  $10 \mu\text{m}$ . It is considered that the fine structure of the graphites may contribute to the load dependence of hardness.

In the case of the ultra-microhardness test (1 gf ~ 30 gf), a hardness value for the maximum depth  $h_m$  was calculated by the eq. (2), designated as DHV1. The hardness values defined as the above are shown to be almost constant in Fig.2 between 1 gf and 30 gf for ISO-88 graphite. DHV1 and other mechanical property parameters were defined and used during loading and unloading processes by using the load versus depth indented curve for 10 gf and 30 gf tests.

### 3.2 MECHANICAL PROPERTY PARAMETERS

The measurements of load-depth curves for No.1 to No.12 and No.16 carbons were performed during loading and unloading processes. Fig.3 gives an example of the load-indent depth curve as to ISO-88 graphite. Fig.3(a) indicates the load (L) versus indented depth (h) curves during loading and unloading processes. The hardness value for the residual depth (about  $2 \mu\text{m}$  in Fig.3(a)) was defined as DHV2. The  $L/h$  versus h relations are shown in Fig.3(b) where the slopes of tangent for the loading and unloading curves were B and D, respectively. That is, the loading curve can be expressed by

$$L/h = A + Bh, \quad (3)$$

and the unloading curve near the maximum load was approximated by

$$L/h = D(h - h_m) + L_m/h_m. \quad (4)$$

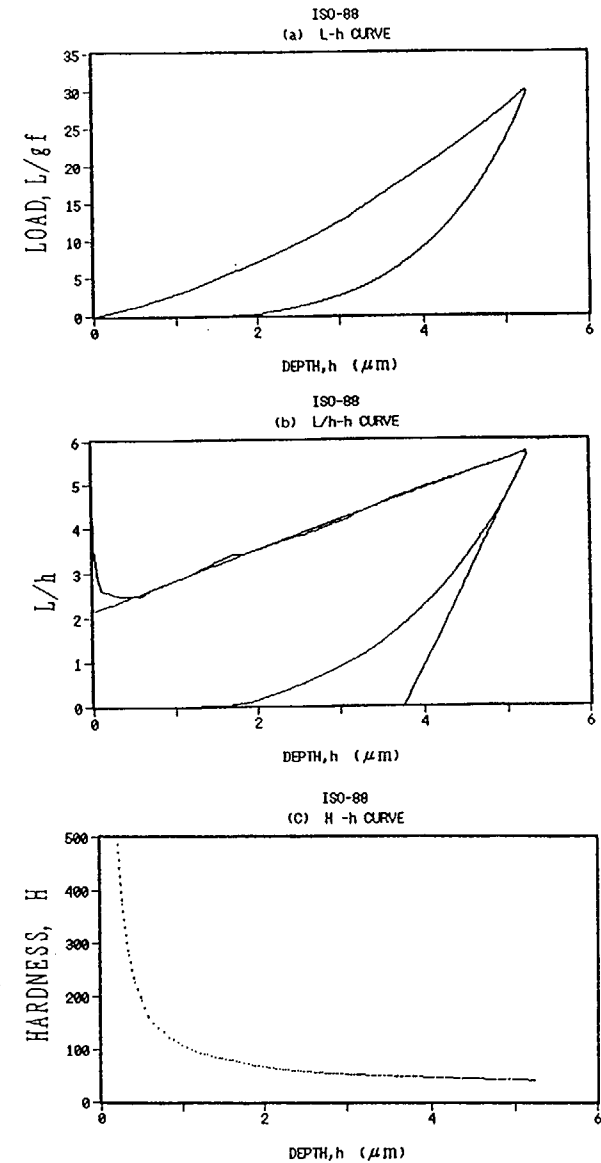


Fig.3 The load (L),  $L/h$  and hardness values as a function of indented depth. (a) L-h curve, (b)  $L/h$ -h curve, (c) DHV-h curve.

As easily seen from Fig.3(b), it turned out that the loading curve,  $L/h-h$  relation, is practically linear, otherwise it can be approximated by a line in a wide range containing the maximum loading point. In the case of the unloading curve, however, there were two cases, the one was that the eq.(4) is a good expression for the curve in a wide range of  $h$  values and the other was that the slope of a tangent of the curve at the maximum loading point  $h_m$  could be done no other than taken. Fig.3(b) corresponds to the latter case.

Fig.3(c) gives the hardness value calculated by eq.(2) to  $h=h_m$ . Since the curve tends to approach an asymptotic value as  $h$  increases, the asymptotic value was defined as Hv2 which is virtually proportional to the value  $B$  of eq.(3). The values  $B$  and  $D$  for metallic and graphite materials are known<sup>3),4)</sup> to be in proportion to strengths and Young's modulus, respectively. In this study the correlations between the Vickers hardness(Hv), DHV1 or Hv2 and Young's modulus/strengths have been examined and it will be described in the later sections.

### 3.3 CORRELATION OF HARDNESS WITH YOUNG'S MODULUS

Fig.4 shows the correlation between Hv or Hv2 and Young's modulus. Clearly from this figure, there is no consistent and definite correlations for all of the carbon materials. It turned out, however, that there exists a relatively good correlation between Hv or Hv2 and Young's modulus for the parallel direction to the layer plane of anisotropic graphite or pyrolytic graphite and the axial direction of fiber of C/C composite materials. In particular, Young's modulus values of fine grained isotropic graphites were in the range of 10 GPa to 15 GPa, although the hardness values were largely different from each other. It seems that the reason why the Young's modulus is relatively small compared to the hardness value is that many fine pores may contribute to it. The correlation between DHV1 and Young's modulus indicated the same tendency the above one also.

### 3.4 CORRELATION OF HARDNESS WITH STRENGTHS

Fig.5 shows the correlation between the DHV1 hardness value and the four point bending strength  $\sigma_b$ . Although it could not be regarded that there is a definite correlation between them on the whole, the DHV1 for some carbon materials can be deemed to be proportional to  $\sigma_b$ .

The correlation between the Hv2 value and  $\sigma_b$  is given in Fig.6. A linear correlation between them may be seen for some grades of graphite material from the figure. The relationship is described by

$$\sigma_b = 2.4 \text{ Hv.} \quad (5)$$

As easily seen from Figs.5 and 6, the Hv2 value has the relatively good correlation with the bending strength than the DHV1.

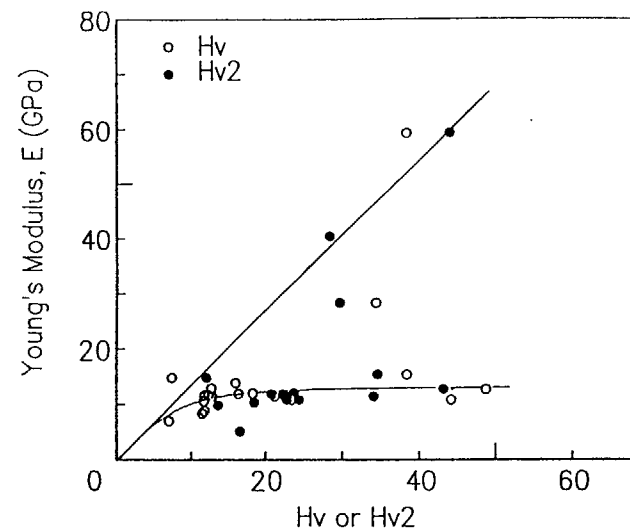


Fig.4 The correlation between Young's modulus and Hv or Hv2 for different grades of graphite.

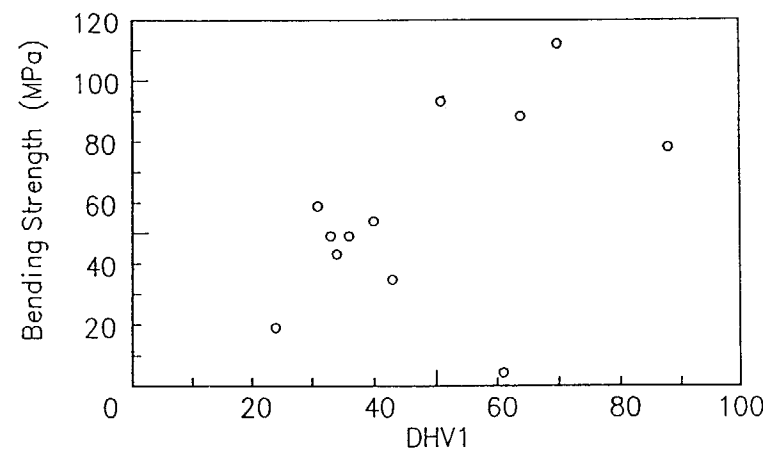


Fig.5 The correlation between bending strength and DHV1 hardness.

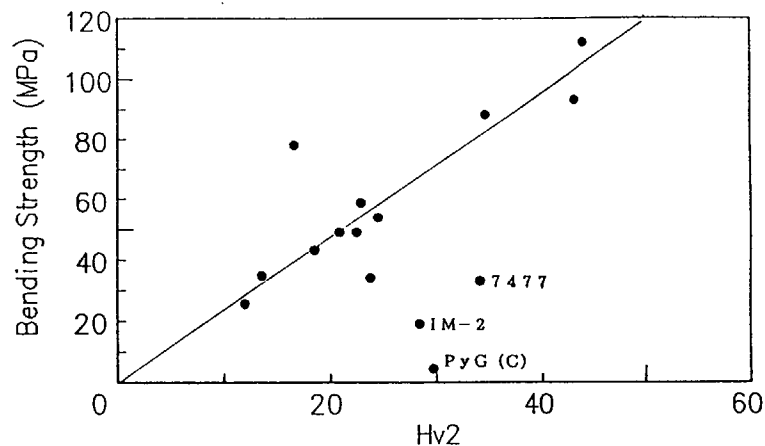


Fig.6 The relationship between bending strength and Hv2 hardness.

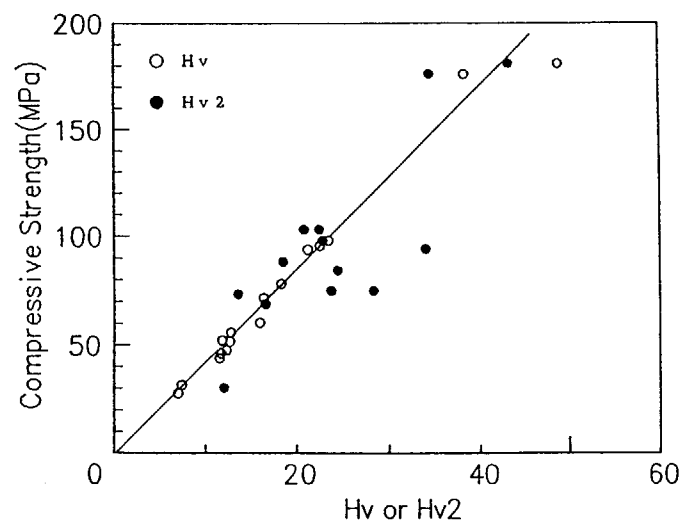


Fig.7 The relation between compressive strength and Hv or Hv2 hardness values.

Fig.7 indicates the relationship between the Hv or Hv2 value and the compressive strength. This figure shows that the correlation is expressed by  $\sigma_c = 4.3 \text{ Hv} = 4.3 \text{ Hv2}$ , (6) which has been obtained<sup>2)</sup> before.

#### 4. CONCLUSIONS

The Vickers hardness tests (1 kgf to 10 kgf) and the ultra-microhardness tests (1 gf to 30 gf) have been performed for nuclear carbon materials. The correlations of hardness values with Young's modulus and strengths have been examined and the following conclusions have been drawn:

- (1) The hardness values hardly depend on the load level applied to the material between 1 gf and 10 kgf except for the graphite materials that contain larger pore diameters
- (2) The Young's modulus of parallel direction to the layer plane of anisotropic and pyrolytic graphites and that of axial direction of C/C composite have the good correlation with the hardness values. The Young's modulus of the fine grained isotropic graphite has the good correlation with the hardness value. The Young's modulus of fine grained isotropic graphites took the values of 10 GPa to 15 GPa though the hardness value changed largely.
- (3) It was the Hv2 hardness defined from the Hv-h relation that gave a relatively good correlation with the bending strength. The correlation was expressed by the equation,  $\sigma_b = 2.4 \text{ Hv2}$ . On the other hand, the DHV1 hardness did not indicate a good correlation with the bending strength.
- (4) The compressive strength showed a good correlation with the Hv2 hardness also. The relationship can be expressed by  $\sigma_c = 4.3 \text{ Hv2}$ .

#### References

- 1) J.H. Westbrook and H. Conrad, "The Science of Hardness Testing and Its Research Applications", ASM(1973).
- 2) T. Oku, M. Eto, Carbon, 12, 477(1974).
- 3) T. Suzuki, M. Inamura, Seisan Kenkyu, 42(1990)257.
- 4) T. Oku, S. Ohta, M. Eto, Extended Abstracts, 20th Biennial Conf. on Carbon, 1990, p.608.

# QUANTITATIVE ANALYSIS OF TRACE AMOUNTS OF IMPURITIES CONTAMINATING PURE GRAPHITE WITH ICP-MS AND METAL ATOMIZER FLAAS

T. MIYATANI, H. SUZUKI, O. YOSHIMOTO

Toyo Tanso Company Ltd,  
Mitoyo-gun, Kagawa-ken,  
Japan

## Abstract

Graphite has excellent properties for the moderator or reflector of the high temperature gas-cooled reactor. In semi-conductor engineering, graphite is also available widely. For these applications the determination of the extremely low impurity level for graphite is one of the most important problems. Using an inductive coupled plasma mass spectrometer, the impurity level of elements Li, B, Na, Mg, Al, Ti, V, Cr, Fe, Mn, Ni, Co, and Zn were analyzed. Using a metal atomizer-flameless atomic absorption spectrophotometer the impurity level of K, Ca and Cu were analyzed. The highly purified graphite (IG-110) manufactured by TOYO TANSO was used for the sample. It was found that the quantitative analysis of a trace amount of impurities in graphite with high sensitivity is possible with these analyzing methods.

## 1. Introduction

Graphite has excellent properties for the moderator or reflector of the high temperature gas-cooled reactor. In semi-conductor engineering, graphite is also available widely. From these points of view, the determination of the extremely low impurity level for graphite is one of the most important problems. The determination of these impurities with high sensitivity was investigated by using both ICP-MS (Inductive Coupled Plasma-Mass Spectrometer) and MA-FLAAS (Metal Atomizer-Flameless Atomic Absorption Spectrophotometer).

The 13 elements such as Li, B, Na, Mg, Al, Ti, V, Cr, Fe, Mn, Ni, Co, and Zn were analyzed with ICP-MS, and the 3 elements such as K, Ca, and Cu with MA-FLAAS. Furthermore, a qualitative analysis for the rare earth were also tested.

## 2. Experimental

### 2.1 Equipments and reagents

The analytical instruments of an ICP-MS/SPQ-6500 and a MA-FLAAS/SAS 760+715 are both manufactured by SEIKO Instruments Inc.. The equipments made by polytetrafluoroethylene was used to avoid the contamination during

the preparation of the test sample. Ultra high pure hydrochloric or nitric acids were diluted to the proper concentration with the ultra pure water which specific resistance is 17 MΩ-cm. Calcium carbonate with its purity 99.9% was also used as a boron capture. The highly purified graphite (IG-110) manufactured by TOYO TANSO was used for the sample.

### 2.1.1 ICP-MS

As an inductively coupled plasma has a high temperature for ionization of the elements, the efficiency for ionization is more than 90%.

The characteristic points are summarized here.

- (1) The 70 elements can be determined with high sensitivity. The detection limits for a test solution is as low as ppt in average. (shown in Fig.1)
- (2) The time required for an analysis is very short. Many elements can be analyzed by this method at a time.
- (3) As the spectrum is very simple and has wide dynamic range, ICP-MS can be conveniently available for a qualitative analysis.

The restrictions are as follows.

- (1) Quantitative analysis becomes harder for some elements whose mass number is below 80.
- (2) Test solution should be diluted to as low as 500 ppm to avoid a matrix and memory effects of the equipments.

( p p b )

H	
0.027 Li	0.05 Be
0.03 Na	0.018 Mg
0.5 K	0.015 Ca
0.005 Rb	0.004 Sr
0.002 Cs	0.006 Ba
Fr	Ra

$$DL = \frac{3 \times \sqrt{10 \times BG}}{I \times 10} \times C$$

C : concentration of reference solution (ppb)  
BG : background (cps)  
I : ion count (cps)

0.1 B	0.1 C	0.1 N	0.1 O	0.1 F	0.1 Ne
0.015 Al	5 Si	5 P	10 S	0.37 Cl	0.3 Ar
0.004 Ga	0.013 Ge	0.031 As	0.27 Se	0.3 Br	0.02 Kr
0.002 In	0.010 Sn	0.012 Sb	0.032 Te	0.02 I	0.02 Xe
0.003 Tl	0.010 Pb	0.004 Bi	0.004 Po	0.02 At	0.02 Rn
0.004 Ce	0.003 Pr	0.007 Nd	0.013 Pm	0.007 Sm	0.009 Eu
0.0003 Th	0.0003 Pa	0.0003 U	0.0003 Np	0.0003 Pu	0.0003 Am

FIG. 1. Detection limits (ICP-MS).

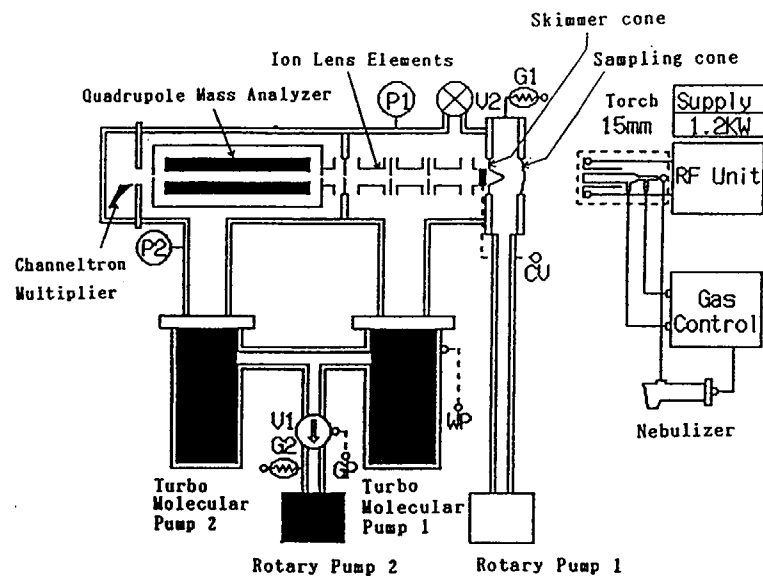


FIG. 2. Schematic diagram of ICP-MS.

Fig.2 is a schematic diagram of the ICP-MS equipment. The nebulizing test solution was ionized in the inductively coupled plasma. The ionized elements are led to the quadrupole mass analyzer through the cones and lens system. The ionized elements are separated into the groups of each mass number with quadrupole mass analyzer, and they are counted with channeltron multiplier.

#### 2.1.2 MA-FLAAS

A sample is placed in a metal head made of tungsten with high purity. And then a metal head is heated by the electrical furnace to get the atomized sample. The advantages of MA- FLAAS compared with a conventional one include:

- 1)High sensitivity (ppt to ppb level)
- 2)Less memory
- 3)Less contamination
- 4)Excellent repeatability

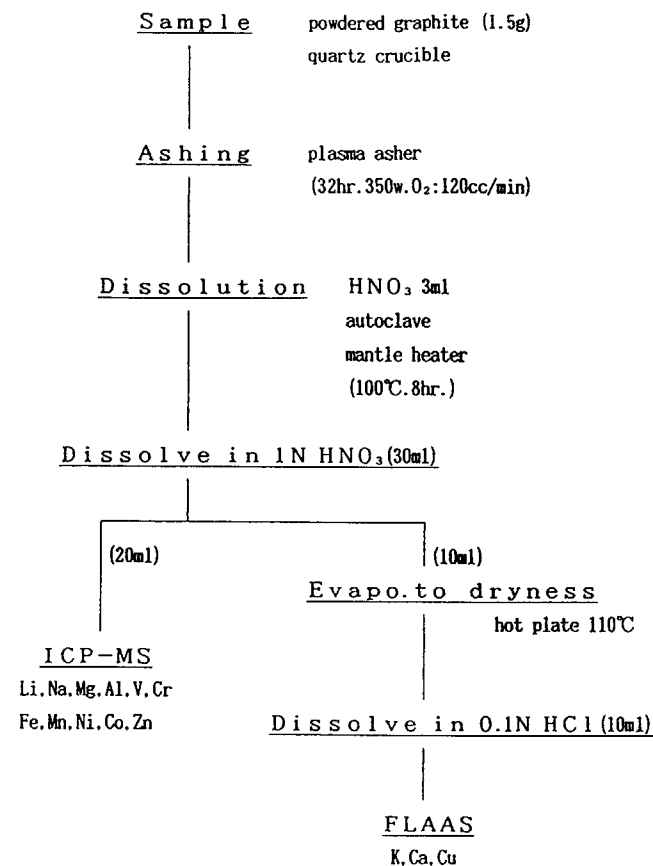


FIG. 3. Pretreatment method for 14 elements other than Ti and B.

#### 2. 2 Experimental method

The trace amount of impurities in the carbon was dissolved in the test solution according to the following three methods.

- 1) Pretreatment method for 14 elements other than Ti and B.

After the carbon was eliminated with a plasma asher, the sample was dissolved in the pressurized solution of nitric acid at 100°C for 8 hours.

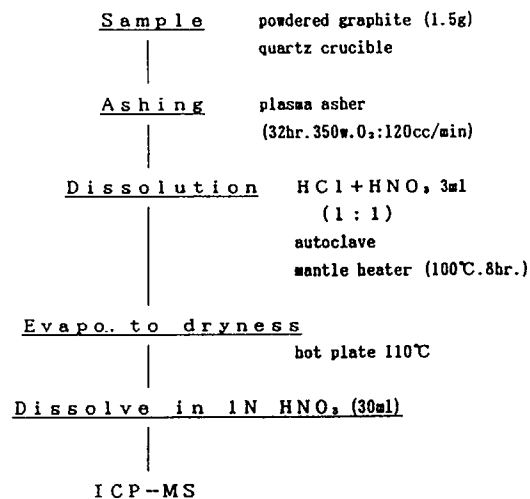


FIG. 4. Pretreatment method for Ti.

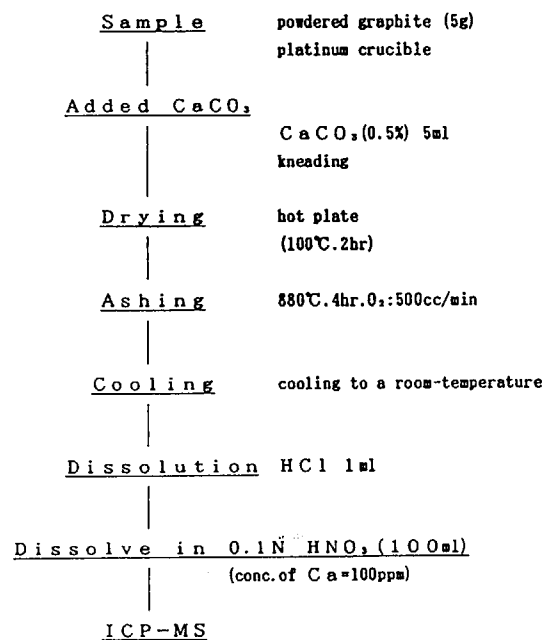


FIG. 5. Pretreatment method for B.

Table 1 Determined value of the impurities  
in the highly purified graphite (IG-110)

Element	Determined value	Lower limit of determination
	ppm	ppm
Li	0.002	0.0004
B	<0.02	0.02
Na	0.05	0.02
Mg	<0.006	0.006
Al	0.06	0.02
Ca	0.08	0.07
K	0.03	0.03
Ti	<0.006	0.006
V	0.018	0.002
Cr	0.006	0.006
Fe	0.06	0.01
Mn	<0.004	0.004
Co	0.014	0.003
Ni	0.006	0.006
Cu	<0.05	0.05
Zn	0.06	0.02

## 2) Pretreatment method for Ti.

After the carbon was eliminated with the same method as (1), the sample was dissolved in the pressurized solutions of nitric and hydrochloric acids at 100°C for 8 hours.

## 3) Pretreatment method for B.

Proper amount of CaCO<sub>3</sub> (conc. of Ca ≤ 100ppm) and carbon was burnt to ashes under the oxygen stream at 880°C for 4 hours. After the ash was cooled to a room temperature, it was dissolved in the solution of hydrochloric acid.

Those pretreatment methods are illustrated in Figs. 3, 4 and 5.

## 3. Results and Discussion

The determined value of the impurities in the highly purified graphite (IG-110) was listed in Table 1. From these results, it was found that the quantitative analysis of a trace amount of impurities in graphite with high sensitivity is possible with these analyzing methods.

A qualitative analysis for the rare earth were also carried out. This kind of analysis can be possible due to the small noise level of ICP-MS for the elements whose mass number is larger than 81. The obtained spectra were

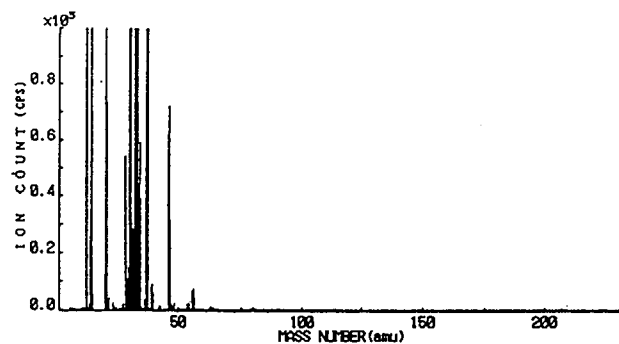


FIG. 6. Mass spectrum (1-230).

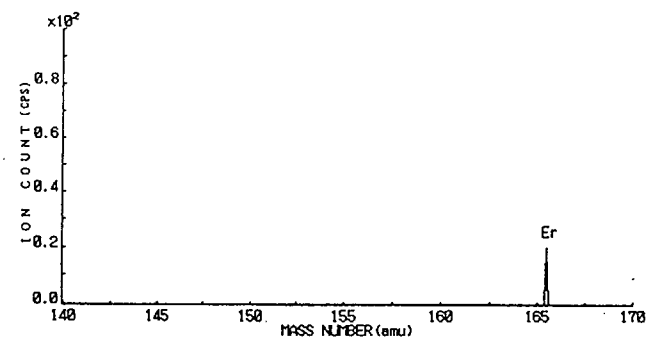


FIG. 9. Mass spectrum (140-170).

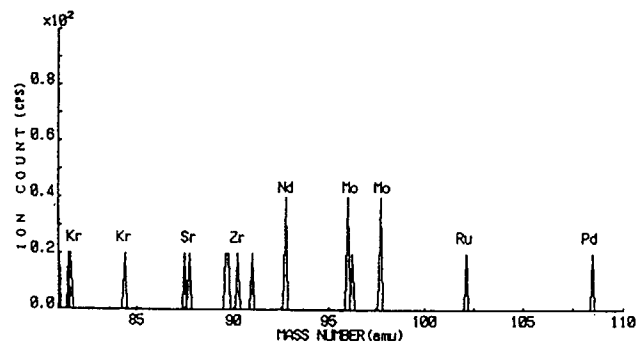


FIG. 7. Mass spectrum (81-110).

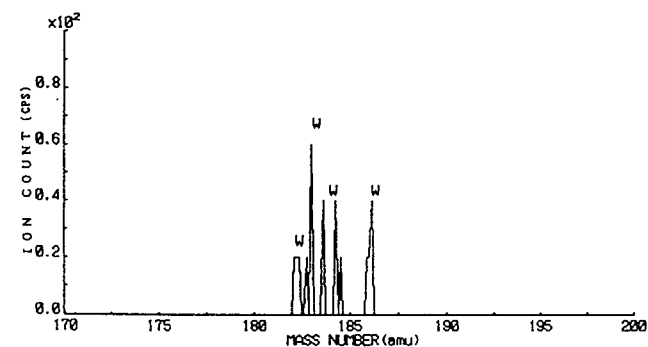


FIG. 10. Mass spectrum (170-200).

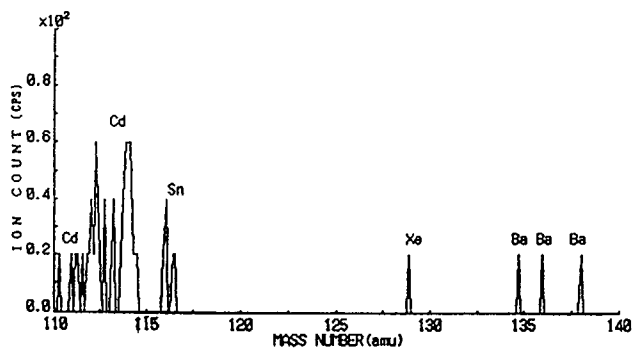


FIG. 8. Mass spectrum (110-140).

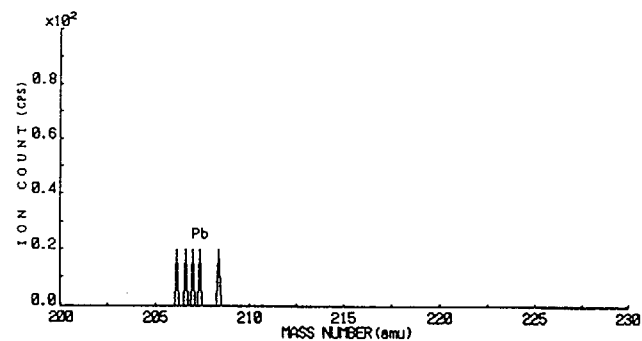


FIG. 11. Mass spectrum (200-230).

shown in from Figs.6 to 11. Fig.6 is the scanning spectrum from mass number 1 to 230, and fairly large background peaks due to the influence of Ar gas or solvent could be observed for the elements whose mass number below 80. From Figs.7 to 11 are the enlarged spectra of Fig.6 which are enlarged both ion count and mass number scale axis. It was found that the existence of the rare earth was trace from those figures.

#### Acknowledgment

The Authors would like to express cordial thanks to Mr. T.Sogabe, and Mr. K.Ohashi for their fruitful discussions.

## Appendix. 1

Lower limit of determination		
Element	ICP-MS, MA-FLAAS	ICP-AES, FAAS, etc.
	ppm	ppm
Li	0.0004	0.01
B	0.02	0.1
Na	0.02	0.05
Mg	0.006	0.02
Al	0.02	0.08
Ca	0.07	0.07
K	0.03	0.1
Ti	0.006	0.09
V	0.002	0.07
Cr	0.006	0.07
Fe	0.01	0.04
Mn	0.004	0.03
Co	0.003	0.06
Ni	0.006	0.1
Cu	0.05	0.08
Zn	0.02	0.1

## DISCUSSION

### Questions or Comments

Name: S. Nomura

Do you try to detect a presence of uranium impurity in your graphite?

### Answer:

U and Th are possible to analyze by ICP-MS

We are trying now

### Questions or Comments

Name: Tim Burchell

Is grade 1a-110 graphite thermally purified or halogen-gas purified?

If the latter, do you detect any residual halides?

### Answer:

Yes, halogen-gas is used for purification.

No, detected holides, cause it's difficult be detect them by ICP-MS on FLAAS.



## LIST OF PARTICIPANTS

Akimoto, S. Babcock Hitachi K.K Kure Works  
6-9, Takara-mach, Kure-City  
Hiroshima-ken 737, Japan

Arai, T. Japan Atomic Energy Research Institute  
Tokai-mura, Naka-gun,  
Ibaraki-ken 319-11, Japan

Araki, T. Toshiba Corporation  
Isogo Nuclear Engineering Center  
8, Shinsugita-cho, Isogo-ku  
Yokohama 235, Japan

Brié, M. Commissariat à l'Energie Atomique  
DTA/DIR/CEN de Saclay  
F-91191 Gif-sur-Yvette Cedex  
France

Burchell, T.D. Oak Ridge National Laboratory  
Building 4508, MS 6088  
P.O. Box 2008  
Oak Ridge, Tennessee 37831-6088  
USA

Burridge, D.P. British Nuclear Fuels plc  
Springfields Works  
Salwick, Preston  
Lancashire, PR4 0XJ  
United Kingdom

Bystrov, I.P. Ministry of Nuclear Power and Industry  
Staromonetny Pereulok, 26  
109180 Moscow  
Russia

Chernikov, A.S. Scientific & Industrial Association "Lutch"  
142100 Podol'sk, Moscow Region  
Zheleznodorozhnaya, 24  
Russia

Chugunov, O.K. I.V. Kurchatov Institute of Atomic Energy  
Ulitsa Kurchatova  
P.O. Box 3402  
123182 Moscow  
Russia

Cleveland, J.C. International Atomic Energy Agency  
Division of Nuclear Power  
Wagramerstrasse 5  
P.O. Box 100  
A-1400 Vienna  
Austria

Eto, M. Japan Atomic Energy Research Institute  
Tokai-mura, Naka-gun  
Ibaraki-ken 319-11, Japan

Fujii, K. Japan Atomic Energy Research Institute  
Tokai-mura, Naka-gun  
Ibaraki-ken 319-11, Japan

Futakawa, M. Japan Atomic Energy Research Institute  
Tokai-mura, Naka-gun  
Ibaraki-ken 319-11, Japan

Gurin, V.A. Kharkov Institute of Physics & Technology  
310108 Khar'kov, Ukraine

Hayano, M. Mitsubishi Heavy Industries, Ltd.  
Showa Shiba Park Building  
4-1, Shbakoen 2-Chome, Minato-ku  
Tokyo 105, Japan

Hishida, M. Japan Atomic Energy Research Institute  
Tokai-mura, Naka-gun  
Ibaraki-ken 319-11, Japan

Ide, A. Fuji Electric Co., Ltd  
Nuclear Power Promotion Department  
New Yurakucho Building,  
12-1 Urakucho  
1-chome, Chiyoda-ku, Tokyo 100, Japan

Ishihara, M. Japan Atomic Energy Research Institute  
Oarai-machi, Higashi-Ibaraki-gun  
Ibaraki-ken 311-13, Japan

Ishii, T. Japan Atomic Energy Research Institute  
Tokai-mura, Naka-gun  
Ibaraki-ken 319-11, Japan

Ishiyama, S. Japan Atomic Energy Research Institute  
Tokai-mura, Naka-gun  
Ibaraki-ken 319-11, Japan

Judge, R. AEA Technology  
Chadwick House, Risley  
Warrington, Cheshire WA3 6HY  
United Kingdom

Kambe, M. Fuji Electric Co., Ltd.  
Production Technology Laboratory  
1-1, Tanabesinden, Kawasaki-Ku  
Kawasaki-City 210, Japan

Kelly, B.T.	AEA Technology Thermal Reactor Services NRL-S, Springfield Salwick, Nr. Preston PR4 ORR United Kingdom	Muto, Y.	Japan Atomic Energy Research Institute Tokai-mura, Naka-gun Ibaraki-ken 319-11, Japan
Kikuchi, K.	Japan Atomic Energy Research Institute Tokai-mura, Naka-gun Ibaraki-ken 319-11, Japan	Nishiyama, Y.	Japan Atomic Energy Research Institute Tokai-mura, Naka-gun Ibaraki-ken 319-11, Japan
Kobayashi, H.	Tokyo Institute of Technology Ohokayama 2-12-1, Meguro-ku, Tokyo Japan	Nomura, S.	Japan Atomic Energy Research Institute Tokai-mura, Naka-gun Ibaraki-ken 319-11, Japan
Kurumada, A.	Ibaraki University 4-12-1, Nakanarusawa-cho, Hitachi-shi Ibaraki-ken 316, Japan	Notake, T.	Nihon Cabon Co., Ltd 2-6-1 Hachiyobori Chiyoda-ku Tokyo, Japan
Maruyama, T.	Power Reactor and Nuclear Fuel Development Corporation Narita-cho, Oarai-machi, Higashi Ibaraki-gun Ibaraki-ken 311-13, Japan	Okada, M.	Toyo Tanso Co., Ltd 2181-2, Ohnohara-cho, Mitoyo-gun Kagawa-ken 769-16, Japan
Matsuo, M.	Japan Atomic Energy Research Institute Tokai-mura, Naka-gun, Ibaraki-ken 319-11, Japan	Oku, T.	Ibaraki University 4-12-1, Nakanarusawa-cho, Hitachi-shi Ibaraki-ken 316, Japan
Matsuzaki, S.	Japan Atomic Energy Research Institute Narita-cho, Oarai-machi, Higashi Ibaraki-gun Ibaraki-ken 311-13, Japan	Petit, A.	Electricité de France Centre de Production Nucléaire du Bugey Centrale 1 - B.P. 14 F-01980 Loyettes, France
Miki, T.	Fuji Electric Co., Ltd Design Department Nuclear Power Division 1-1, Tanabesinden, Kawasaki-ku Kawasaki-City 210, Japan	Rodchenkov, B.S.	Research and Design Institute for Power Technology (NIKIET) 107113, Moscow Malaya Krasnosel'skaja street, 14/8 Russia
Minatsuki, I.	Mitsubishi Heavy Industries, Ltd. Showa Shiba Park Building 4-1, Shbakoan 2-chome, Minato-ku Tokyo 105, Japan	Roedig, M.	Forschungszentrum Jülich Werkstoffe (IRW) Postfach 1913 D-5170 Jülich Germany
Miyamoto, Y.	Japan Atomic Energy Research Institute Tokai-mura, Naka-gun Ibaraki-ken 319-11, Japan	Saito, S.	Japan Atomic Energy Research Institute Oarai-machi, Higashi Ibaraki-gun Ibaraki-ken 311-13, Japan
Miyatani, T.	Toyo Tanso Co, Ltd 2181-2, Ohnohara-cho, Mitoyo-gun Kagawa-ken 769-16, Japan	Sato, S.	Ibaraki University 4-12-1, Nakanarusawa-cho, Hitachi-shi Ibaraki-ken 316, Japan
Mosevitskij, I.S.	I.V. Kurchatov Institute of Atomic Energy Ulitzs Kurchatova P.O. Box 3402 123182 Moscow, Russia	Sawa, K.	Japan Atomic Energy Research Institute Oarai-machi, Higashi Ibaraki-gun Ibaraki-ken 311-13, Japan

Shimomura, K. Japan Atomic Energy research Institute  
Tokai-mura, Naka-gun  
Ibaraki-ken 319-11, Japan

Shindo, M. Japan Atomic Energy Research Institute  
Tokai-mura, Naka-gun  
Ibaraki-ken 319-11, Japan

Shiozawa, S. Japan Atomic Energy Research Institute  
Oarai-machi, Higashi Ibaraki-gun  
Ibaraki-ken 311-13, Japan

Shirai, H. CSK Company  
4-2-3, Taga-machi, Hitachi-shi  
Ibaraki-ken 316, Japan

Sogabe, T. Toyo Tanso Co., Ltd  
2181-2, Ohnohara-cho, Mitoyo-gun  
Kagawa-ken 769-16, Japan

Strizak, J.P. Oak Ridge National Laboratory  
Building 4508, MS 6087  
P.O. Box 2008  
Oak Ridge, Tennessee 37831-6087  
USA

Sudo, Y. Japan Atomic Energy Research Institute  
Oarai-machi, Higashi Ibaraki-gun  
Ibaraki-ken 311-13, Japan

Takada, S. Japan Atomic Energy Research Institute  
Tokai-mura, Naka-gun  
Ibaraki-ken 319-11, Japan

Takikawa, N. Japan Atomic Energy Research Institute  
Oarai-machi, Higashi Ibaraki-gun  
Ibaraki-ken 311-13, Japan

Tsuji, N. Fuji Electric Co., Ltd  
Design Department Nuclear Power Division  
1-1, Tanabesinden, Kawasaki-Ku  
Kawasaki-City 210, Japan

Ugachi, H. Japan Atomic Energy Research Institute  
Tokai-mura, Naka-gun  
Ibaraki-ken 319-11, Japan

Wakayama, N. Japan Atomic Energy Research Institute  
Tokai-mura, Naka-gun  
Ibaraki-ken 319-11, Japan

Wilson, J. AEA Technology  
Building 329, Thermal Reactor Services  
Harwell Laboratory  
Oxfordshire OX11 0RA  
United Kingdom

Woodruff, E.M. Westinghouse Hanford Company  
N Reactor Plant  
Facility and Operations Assurance  
P.O. Box 1970, MS X1-72  
Richland, Washington 99352  
USA

Yamawaki, M. University of Tokyo  
7-3-1 Hongo, Bunkyo-ku, Tokyo  
Japan

